Geotechnical Hazard Mitigations

Experiment, Theory and Practice

Proceedings of the 5th International Conference on Geotechnical Engineering for Disaster Mitigation and Rehabilitation

Year: 2017

Editor: Professor Meei-Ling Lin

5th International Conference on Geotechnical Engineering for Disaster Mitigation and Rehabilitation

CONTENTS

Paths Forward to Evaluating Seismic Performance of Geotechnical Structures

S. Iai[a]

[a]President, FLIP Consortium; Professor Emeritus, Kyoto University, Japan
E-mail: iai.susumu@flip.or.jp

Abstract

This paper presents an overview of the developments of seismic performance evaluation of geotechnical structures, from the simplified limit equilibrium approach to the detailed approach based on the deeper understanding of the soil behavior during earthquakes. The overview covers the period spanning from 1923 Great Kanto earthquake, Japan, to 2011 Tohoku Off Pacific Ocean earthquake, and thereby offers a journey from the early developments in the discipline of geotechnical earthquake engineering to the present and paths forward for future developments.

Keywords –
Earthquakes; Liquefaction; Seismic Performance

1 Introduction

The history of seismic design and seismic performance evaluation in Japan is overwrapped with the history of occurrence of major destructive earthquakes (Figure 1) and the history of the developments in modern urban areas and associated facilities in the form of buildings and civil engineering structures. The history includes many cycles of new construction followed by destruction with a period of five years each somewhere in Japan. In each cycle, engineering is gradually advanced with incremental improvement.

In what follows, an overview of these developments of seismic performance evaluation of geotechnical structures are presented. Some of the important issues that seem less known or recognized among the practicing geotechnical engineers are also pointed out in this overview.

2 Journey from Simplified Limit Equilibrium Analysis to Detailed Evaluation of Seismic Performance

In the history of seismic evaluation of geotechnical structures, Mononobe-Okabe equation of seismic earth pressure published in the next year of 1923 Great Kanto earthquake may be the first example which forms the basis for evaluating seismic stability of geotechnical structures through limit equilibrium analysis (Mononobe 1924, Okabe 1924). This equation is derived by modifying Coulomb's classical earth pressure theory to account for inertia forces (Figure 2). The equation has still been widely used in practice in simplified seismic design for weak to moderate earthquake motions up to a peak ground acceleration (PGA).

Less known about this widely used equation is in the fact that the paper by Mononobe was published one month earlier than that of Okabe. The paper by Mononobe was written in Japanese whereas that by Okabe was written in English. These facts lead to a certain confusion in the manner these two papers are referred to outside Japan; the Mononobe's paper is often sited with the one published in English several years after).

Apart from the limit equilibrium analysis of geotechnical structures, the 1964 Niigata and Alaska earthquakes triggered the studies on liquefaction of sandy ground (Figure 3). These studies lead to a simplified liquefaction potential assessment procedure such as shown in Figure 4 (Tsuchida, 1970). The procedure is based on grain-size distribution curve of soil and a critical SPT N-value of soil deposit for triggering liquefaction in accordance with PGA. The simplified procedure was incorporated into a technical standard for designing port structures in Japan in 1970s and formed the basis for early development of geotechnical earthquake engineering based on the framework of simplified limit equilibrium analysis.

1964 was the year when the recording of strong earthquake motions was initiated in Japan and the recorded PGA at Niigata site was 0.18g. Since then, the network of the strong motion recording systems has been deployed throughout Japan and recording of the earthquake motions during the major destructive earthquakes has been accumulated to form a solid data base of strong earthquake motions. The major

destructive earthquakes in Japan since 1964 include 1968 off Tokachi, 1973 off Nemuro peninsula, 1978 off Miyagi, 1983 Nihonkai-chubu, 1993 off Kushiro, 1993 off Hokkaido South-West, 1994 off Hokkaido East, 1994 off Sanriku with Japan Meteorological Agency (JMA)-Richter magnitude ranging from 7.4 to 8.1 (Figure 1). PGA recorded during these destructive earthquakes ranges from 0.2 to 0.5g.

Application of the simplified limit equilibrium analysis combined with appropriate mitigation measures against liquefaction, if applicable, had provided a reasonable enhancement in seismic resistance of geotechnical structures against earthquakes. Obviously, with each earthquake event, damage to geotechnical

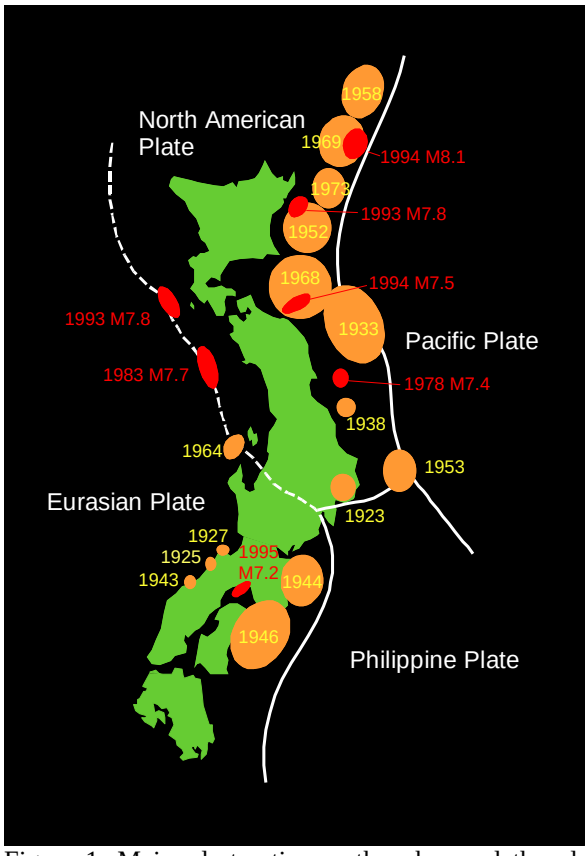

Figure 1. Major destructive earthquakes and the plate tectonic boundaries, Japan (1923-1999)

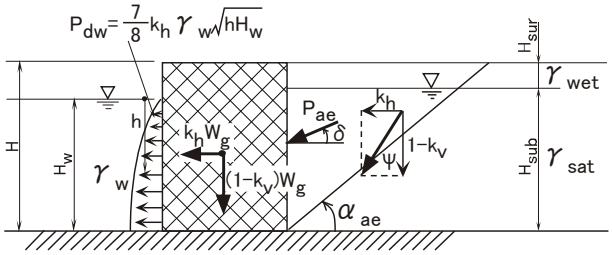

Figure 2. Active seismic earth pressures P_{ae} induced by a peak horizontal and vertical accelerations $k_h g$ and $k_v g$.

Figure 3. Damage to a RC four story building due to liquefaction (1964 Niigata earthquake, Japan)

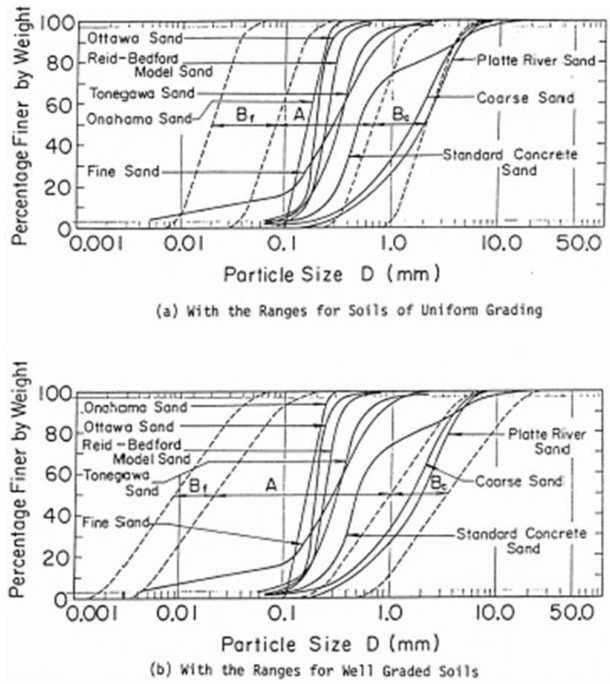

(a) Grain-size distribution of liquefiable soil

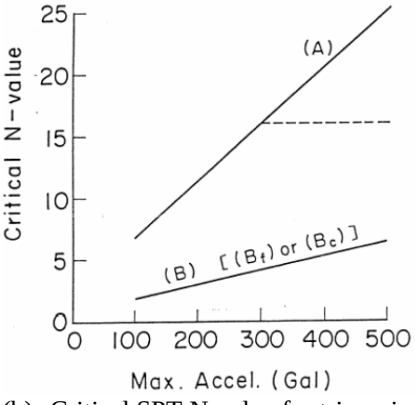

(b) Critical SPT N-value for triggering liquefaction

Figure 4 Simplified liquefaction potential assessment procedure (Tsuchida, 1970)

structures continued to occur. Most of the damage to geotechnical structures was because of the lack of implementation of mitigation measures against liquefaction (Figure 5). It was often the case that the standard liquefaction measures, such as by compaction of ground, was difficult to implement for the existing geotechnical structures. Consequently, up to 1994, engineering focus was more or less directed toward developing appropriate and practical implementation techniques of the mitigation measures against liquefaction.

Figure 5 Damage to a sheet pile quay wall due to liquefaction of backfill soil at Akita Port during 1983 Nihonkai-chubu earthquake (after Akita Prefecture)

Despite the continuous success in the early stage of development of earthquake geotechnical engineering within the framework of the simplified limit equilibrium analysis procedure coupled with the simplified procedure for liquefaction potential, 1995 Hyogoken Nambu earthquake (JMA magnitude 7.2) changed the whole picture of the engineering confidence in earthquake engineering, both for structural and geotechnical aspects. Damage to the buildings and other urban structures induced by the earthquake was extensive. This earthquake occurred just below the urban area of Kobe city and the PGA recorded by this earthquake ranged from 0.5 to 0.8g, exceeding the level of PGA recorded during the preceding earthquakes since 1964 up to 1994.

During the 1995 Hyogoken Nambu earthquake in Kobe, Japan, many of the caisson quay walls suffered damage as shown in Figures 6 and 7. These caisson quay walls were constructed on a loose saturated backfill foundation of decomposed granite, which was used for replacing the soft clayey deposit in Kobe Port to attain the required foundation bearing capacity. Subjected to a strong earthquake motion having peak accelerations of 0.54g and 0.45g in the horizontal and vertical directions, these caisson quay walls were displaced an average of 3m (maximum 5m) toward the sea, settled 1 to 2m and tilted about 4 degrees. Although a sliding mechanism could explain the large horizontal displacement of the caisson quay walls, this mechanism did not explain the large settlement and tilt of the caissons. Reduction in the stiffness of foundation soils due to development of excess pore water pressure was speculated as a main cause of the observed caisson damage at Kobe Port.

This speculation was confirmed by a series of effective stress analyses based on the strain space multiple mechanism model (Iai et al. 1992). The model parameters were evaluated based on in-situ velocity logging, the blow count of Standard Penetration Tests (SPT N-values) and the results of cyclic triaxial tests. The specimens used for cyclic triaxial tests were undisturbed samples obtained by an in-situ freezing technique. Input earthquake motions were those recorded at the Port island site about 2km from the quay wall. The spatial domain used for the finite element analysis covered a cross sectional area of about 220m by 40m in the horizontal and vertical directions.

The effective stress analysis resulted in the residual deformation shown in Figure 8. As shown in this figure, the mode of deformation of the caisson wall was to tilt into and push out the foundation soil beneath the caisson. This was consistent with the observed deformation mode of the rubble foundation shown in Figure 9, which was investigated by divers. The order of wall displacements was also comparable to that observed and shown in Figure 7.

The extensive seismic damage during the 1995 Hyogoken Nambu earthquake and the successful effective stress analysis of those damage, both in terms of deformation/failure mode and degree of damage, led to the turning point of seismic performance evaluation from the simplified limit equilibrium analysis to detailed evaluation through the effective stress analysis. Nowadays the detailed evaluation of seismic performance forms the basis for adopting performance-based design of geotechnical structures in Japan.

Figure 6 Damage to a caisson quay wall at Kobe Port, Japan, during the 1995 Hyogoken Nambu earthquake

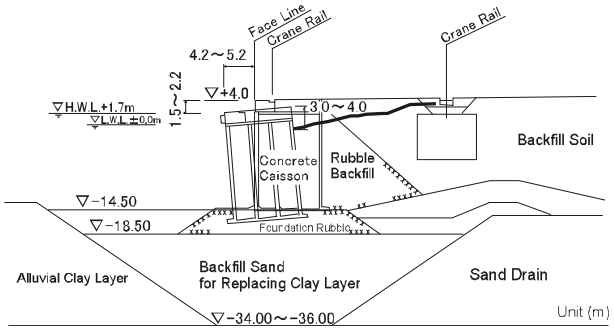

Figure 7 Cross section of gravity quay wall at Kobe Port and deformation/failure during 1995 Hyogoken Nambu earthquake, Japan

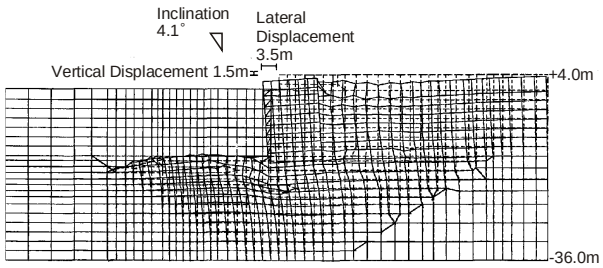

Figure 8 Computed deformation of a gravity quay wall

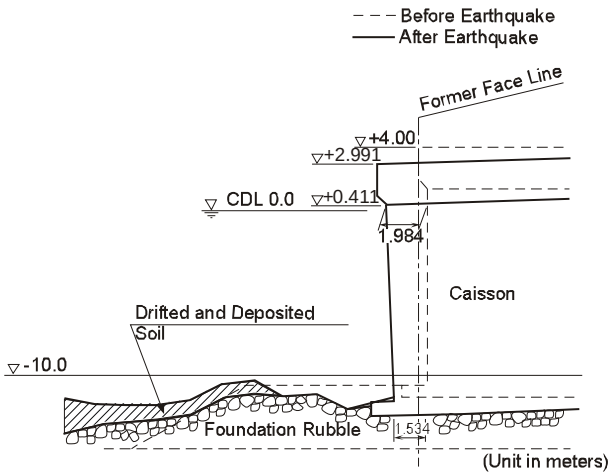

Figure 9 Deformation of rubble foundation of a quay wall investigated by divers

3 Assumption on Mechanics of Saturated Soil in Simplified Limit Equilibrium Analysis

Shear strength of cohesionless soil is defined by Mohr-Coulomb failure criterion and specified by

$$\tau_f = \sigma_m' \sin\phi_f \qquad (1)$$

where τ_f , σ_m' , and ϕ_f denote shear strength, effective confining pressure defined as an average of major and minor principal stresses, and internal friction angle, respectively. Equation (1) is fundamental and applicable to both the simplified limit equilibrium analysis and the detailed analysis based on effective stress analysis.

The assumption specifically made for the simplified limit equilibrium analysis is in the fact that the effective confining pressure remains unchanged during the earthquake. In reality, the effective confining pressure drastically changes during the earthquake due to dilatancy induced by shear deformation of soil. Although this reality is fully reflected in the detailed analysis, this reality is completely ignored in the simplified limit equilibrium analysis for simplicity. The effect of this departure from the reality, i.e. ignoring the mobilization of dilatancy, in the simplified limit equilibrium analysis may be not significant when the earthquake shaking is small or moderate. Obviously when the earthquake response of the geotechnical structures becomes highly non-linear and involves the mobilization of dilatancy, applicability of the simplified limit equilibrium analysis may become limited.

The simplified limit equilibrium analysis is further extended to the simplified dynamic analysis in order to evaluate induced deformation of geotechnical structures during earthquake. In the case of gravity retaining wall, the method is based on the sliding block model. First, the stability of the wall and the backfill are evaluated using the lateral earth pressure theory based on Monobe-Okabe's equation. The threshold acceleration is determined by the value resulting in a factor of safety of unity for sliding of the wall-backfill system. Then, a set of acceleration time histories are selected for sliding block analysis. When the ground motion acceleration exceeds the threshold acc3eleration, a_t, the wall-backfill system begins to move by translational along the based on the wall and the failure plane through the backfill. By double integrating the area of the acceleration time history that exceeds a_t, and continuing the time integration until the sliding stops, the displacement of the wall relative to the firm based below the failure plane can be determined as shown in Figure 10. This computation ca be easily performed using common spreadsheet routines or a simple computer code.

The serious limitation in this simplified dynamic analysis based on the sliding block analysis is in the fact that the effect of dilatancy is completely ignored when the threshold acceleration is evaluated. Mononobe-Okabe's equation, when applied to submerged soil structure profile, does not include the effect of dilatancy. The only effect of the submergence in the water is the buoyancy and corresponding reduction in the effective confining pressure. Back to Equation (1), the simplified dynamic analysis reflects the effect of reduction in shear strength of soil due to the buoyancy but does not reflect

the effect of dilatancy induced in reality during sliding along the sliding plane going through the saturated backfill soil. The departure from the reality in the simplified dynamic analysis can result in either conservative or unconservative evaluation of the seismic performance of geotechnical structures. The evaluation is conservative if soil is highly compacted and dilative behavior of soil is involved during sliding. The evaluation is unconservative if soil is loosely deposited and contractive behavior of soil is involved during sliding.

How the effect of dilatancy of soil affect the shear resistance of soil will be discussed in more details in the next chapter.

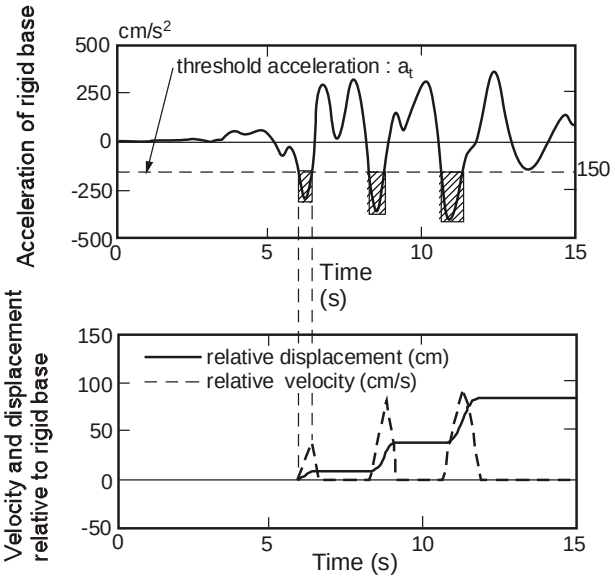

Figure 10 Example of sliding block analysis

4 Behavior of Saturated Soil under Undrained Shear

When Toyoura sand is sheared monotonically under undrained conditions to large shear strains (≧ 10%), the stress-strain relationship and associated effective stress path demonstrate dilative, strain-hardening behavior as shown in Figure 11 (Yoshimine and Ishihara 1998). When the shear strain increases in the range beyond those shown in this figure, the steady state will eventually be reached in an asymptote manner.

If the effect of dilatancy is ignored, then the effective stress path shown in Figure 11(b) becomes a vertical line, originating from the same p=100kPa point where all the stress paths originated from, reaching up to the shear failure line at about τ_{xy}=60kPa, which

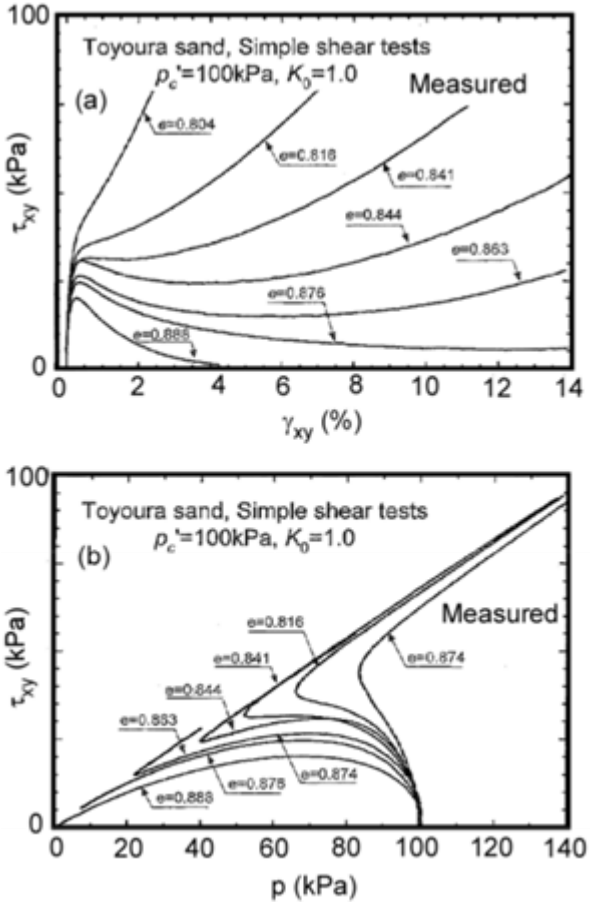

Figure 11 Measured undrained monotonic shear behavior (Yoshimine and Ishihara 1998)

corresponds to the shear strength to be adopted for the simplified limit equilibrium analysis and simplified dynamic analysis discussed earlier. The measured behavior of saturated soil under undrained monotonic shear is extensively affected by the mobilization of dilatancy and becomes very different from those assumed for the simplified analyses.

The undrained monotonic shear behavior of sand is idealized in the strain space multiple mechanism model by specifying the dilatancy at the steady state as shown in Figure 12 (Iai et al. 2011). This model is typically used for detailed analysis through effective stress analysis. Comparison of measured and computed results shown in Figures 11 and 12 indicates that the strain space multiple mechanism model has reasonable capability to capture the essential features of undrained monotonic shear behavior of sand including the steady state as asymptote. The detailed analysis through the effective stress analyses reflect the stress-strain behavior of soil under undrained monotonic shear such as shown in Figures 11 and 12.

When the steady state strength is less than the initial

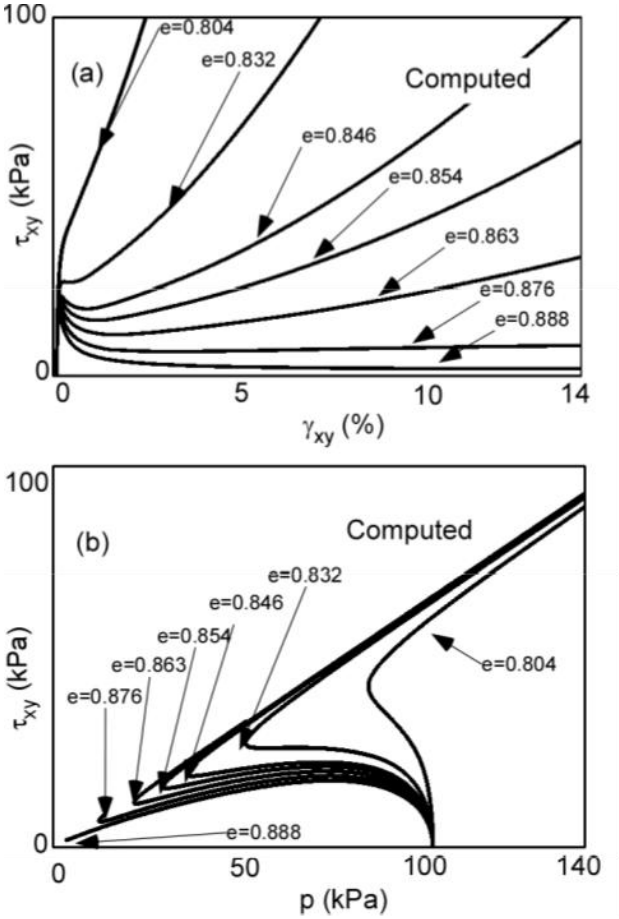

Figure 12 Computed undrained monotonic shear behavior (Iai et al. 2011)

shear induced in the slope, earthquakes may trigger liquefaction-induced flow failure (Ishihara et al. 1990). The steady state strength of engineering interest to evaluate the liquefaction-induced flow failure is typically on the order of 10 kPa. Although the steady state of sand is unaffected by the initial confining stress provided that the initial void ratio after consolidation is kept the same, it is very sensitive to the fines content and void ratio (Papadopoulou and Tika 2008).

Figure 13 shows the relationship between the void ratio and the effective confining pressure at steady state P_{us} based on triaxial tests of Toyoura sand with DL clay mixture performed by the author and his colleagues at the FLIP consortium. The residual shear strength, S_{us}, is obtained as P_{us} multiplied by $\sin\phi_f$ in the case of plane strain shear. The steady state is indeed sensitive to the fines content. In the case of Masado, a decomposed granite used for reclamation in the Kobe port, the steady state strength can be about 10 kPa at a void ratio as low as 0.4 (Ishihara et al. 1998, Tsukamoto et al. 1998).

The shear resistance at the quasi-steady state, which corresponds to the transition over the phase transformation line that can induce a large shear strain in engineering sense, is highly dependent and almost proportional to the initial confining stress (Yoshimine and Ishihara 1998). There remains a question of how cyclic loading during an earthquake affects the stress strain behavior of soil on its way to a steady state.

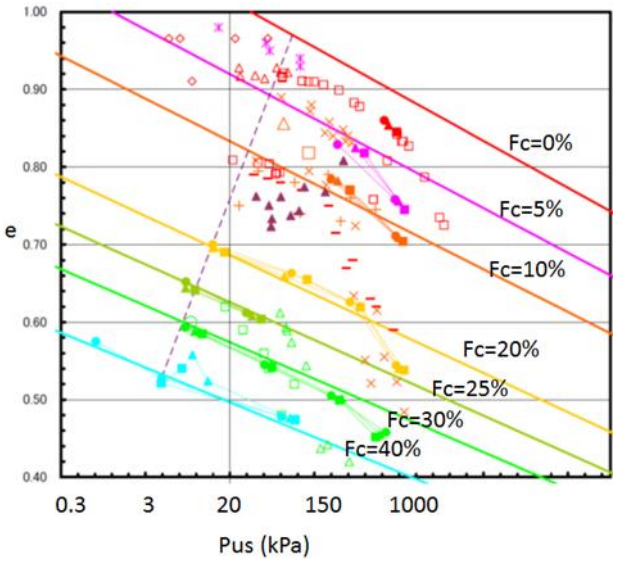

Figure 13 Effective confining pressure at steady state Pus and void ratio relationship

A series of laboratory tests, performed by the author and his colleagues, using Toyoura sand with DL clay mixture (Figure 14) indicates that the peak shear resistance is significantly affected by the cyclic loading, and a large shear strain can be induced due to cyclic loading before reaching the steady state.

Most of the damage to river dikes and embankments in port and coastal areas can be analyzed based on the undrained cyclic deformation of soil without considering the effect of the steady state. However, recent experience in the analysis of one case study, river dike No. 1 of the Shiribeshi-Toshibeshi river, Hokkaido, Japan, during the 1993 Hokkaido-Nanseioki earthquake, poses a new challenge (Matsuo et al., 2000). This river dike, which was constructed on loosely-deposited sand with a thickness of about 5 m (Figure 15), was heavily damaged during the earthquake (Figure 16).

The results of the analysis performed assuming undrained conditions, performed by the author and his colleagues (Ozutsumi et al. 2002), show a typical pattern of deformation (Figure 17). However, the degree of deformation is excessively sensitive to the type of stress-strain algorithm and the details in the constitutive modeling in the vicinity of the failure line. Without considering the steady state, the result suggests very small settlements as shown in Case A in Figure 18.

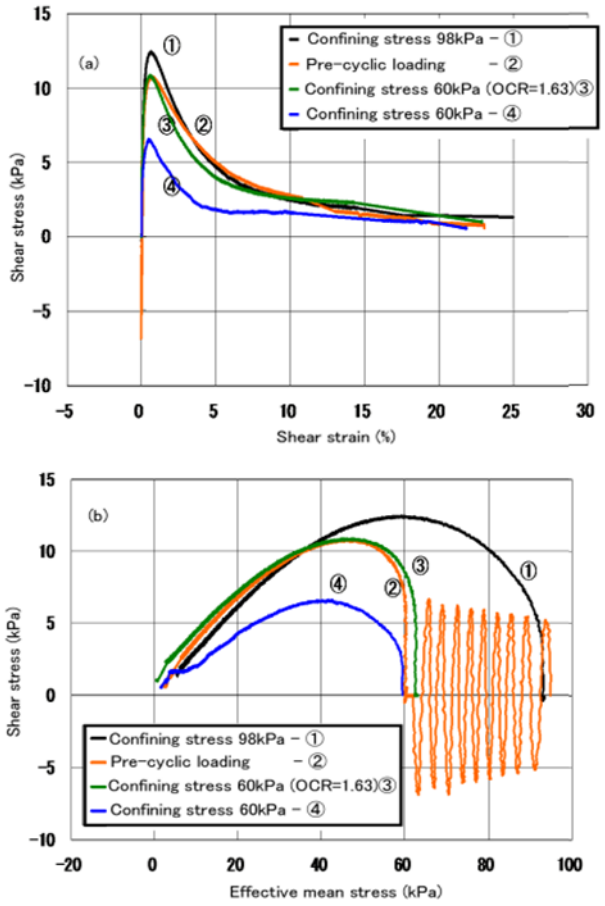

Figure 14 Hollow cylinder test results on the effects of cyclic loading before reaching the steady state (Toyoura sand with DL clay mixture)

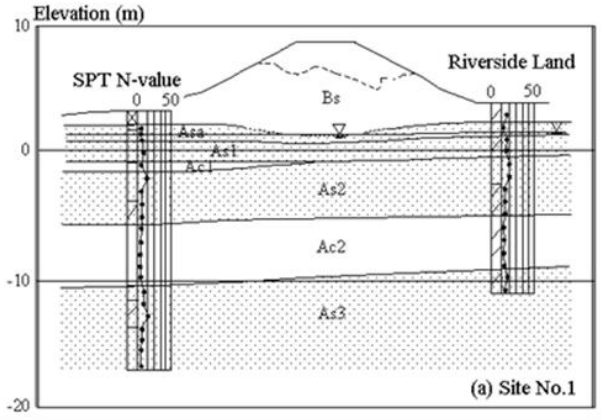

Figure 15 Cross section of dike

Figure 16 Damage to a dike at the Shiribeshi-toshibetsu river, Hokkaido, Japan, during 1993 Hokkaido-Nansei-oki earthquake

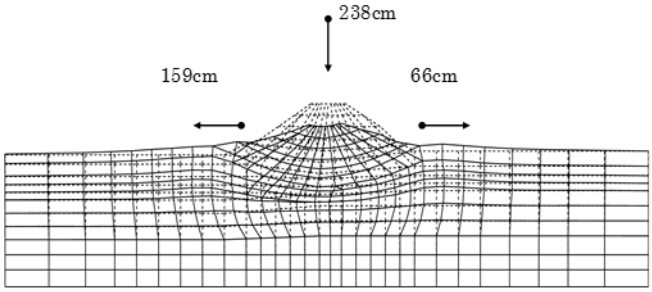

Figure 17 Computed deformation of dike

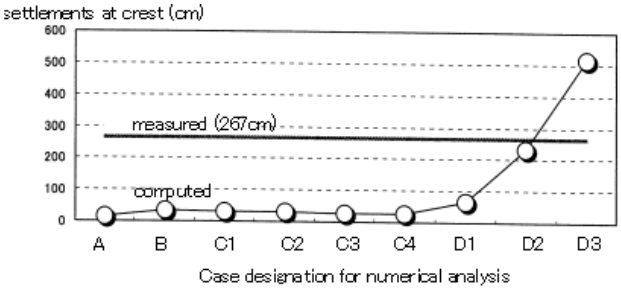

Figure 18 Computed settlements at crest

Table 1 Case designation for numerical analysis

Case No.	S_{us} (kPa) for A_{sa}	S_{us} (kPa) for A_{s1}	S_{us} (kPa) for A_{s2}
A	∞	∞	∞
B	0.1	180	50
C1	25	180	50
C2	50	180	50
C3	75	180	50
C4	100	180	50
D1	0.1	100	25
D2	0.1	25	7
D3	0.1	15	5

5 Effects of Pore Water Flow and Void Redistribution during and after Earthquakes

The duration of the earthquake motions in the case studies that have been discussed in the preceding sections is about 30 seconds or less, therefore the undrained behavior of sand provides a reasonable representation of the seismic performance of geotechnical structures. For a longer duration of earthquake motions such as those recorded during 2011 N 9.0 East Japan earthquake that were on the order of 200 seconds, the effect of partial drainage during this duration can be significant. Thus, the effective stress analysis allowing dissipation and redistribution of excess pore water pressures during and after earthquake should become the primary analysis procedure to appropriately evaluate the seismic performance of geotechnical structures.

When the ground consists of inter-layered stratigraphy of permeable and impermeable layers, the effects of void redistribution due to pore water flow within the inter-layered deposits become more complicated than in the uniform sandy deposit discussed in the previous section. The simplest most representative example is the two-layer level ground consisting of liquefiable sand deposit overlain by a non-liquefiable capping crust layer typically above the ground water table. The crust often consists of clay or silt materials, which are less permeable than the sand below the crust.

Field evidence indicates that the capping crust layer tends to prevent the direct manifestation of the effects of liquefaction at the surface (Figure 19). Depending on the conditions such as the ground shaking intensity and thickness and overall strength of the capping crust layer, there might not be serious consequences of liquefaction for geotechnical structures above the capping crust layer (Ishihara et al. 1993, Acacio et al. 2001). Evidence from the 1999 Chi-chi earthquake seems to support this notion (Juang et al. 2005).

Despite the apparent simplicity in the proposed relationship shown in Figure 19, the phenomenon involved behind this empirical approximation is complex, including potential redistribution of excess pore water pressures towards the ground surface and, in the extreme case, formation of water film below the capping layer during or after shaking for a certain period of time.

A case study analysis is performed to evaluate the redistribution of excess pore water pressures in the level ground with the capping crust layer. In this case study, the soil deposit within reclaimed land in Urayasu-city along the margins of Tokyo Bay is idealized in Figure 20: soil profile consists of a 2m thick surface crust layer (B,F), underlain by a 10m thick sandy layer (As), with 15m thick underlying clayey layers (Ac1, Ac2, and Ac3). In particular, the surface crust layer (B, F) is assumed to have the same properties as those of the clayey layers. The effective stress analysis allowing partial drainage is performed for a one-dimensional soil column, with the coefficient of permeability in the sandy layer $k=10^{-6}$ m/s and in the clayey layer $k=10^{-9}$ m/s. The ground water table is assumed to be at the ground surface level.

The downhole earthquake motion recorded at the Shinagawa site along the margins of Tokyo Bay, about 10 km west of Urayasu city, during 2011 East Japan earthquake was input at the bedrock for the effective stress analysis. In particular, the recorded earthquake motion with PGA=0.06g was scaled to a value of 0.30g for the effective stress analysis in order to clearly demonstrate the effects of void redistribution during and after earthquakes. In this case study analysis, no comparison is intended with the measured field performance; the intention of the analysis is to study the potential effects of the redistribution of excess pore water pressures and void ratios in the idealized inter-layered stratigraphy using the idealized earthquake motions.

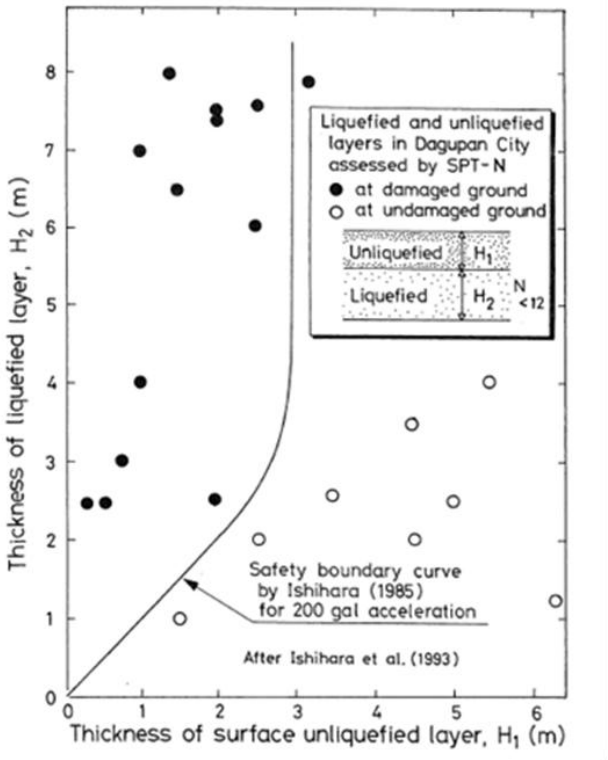

Figure 19 Effect of capping crust layer without evidence of subsoil liquefaction (Ishihara et al. 1993)

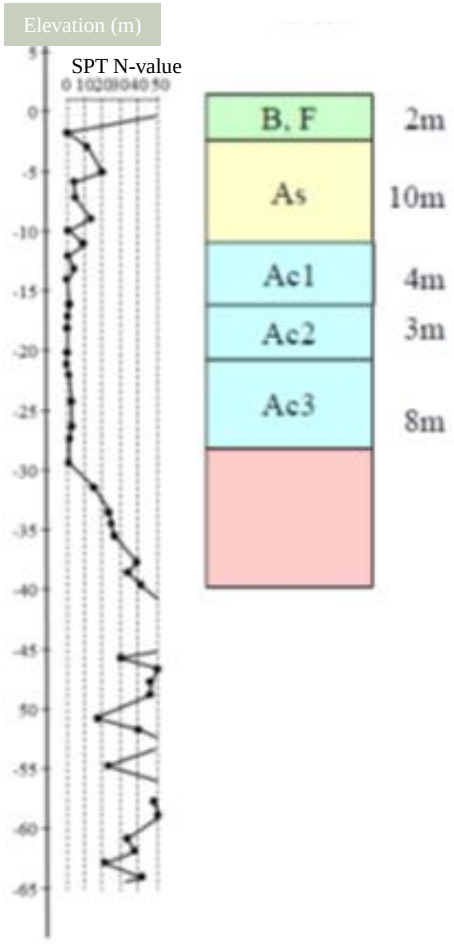

Figure 20 Idealized soil profile for a case study of redistribution of excess pore water pressures for level ground with a capping surface crust layer

Computed earthquake response of the idealized soil profile in terms of acceleration and displacement is shown in Figure 21, and computed excess pore water pressures and the ratios in the middle of each layer are shown in Figure 22. As shown in these figures, the PGA at the ground surface reaches 0.1g with a maximum horizontal displacement of 4m in a long period motion of 20s at the time from 100 to 200s, which corresponds with the initiation of liquefaction of the sandy layer (As). This large displacement is presumably due to the combined effects of the scaled earthquake motions (five times larger than those recorded), effect of liquefaction of 10m thick sandy layer combined with the long period (about 20s) components of the input earthquake motions associated with the magnitude 9.0 event. Excess pore water pressure ratios in the clayey layers, including the surface crust, reach 0.5 to 0.8 but do not yet reach the state of 1.0.

The variation of computed vertical displacements and excess pore water pressures over 60 years ($2.0x10^9$s) are shown in Figure 23. As shown by the red curve in Figure 23, the top of sandy layer (as) below the surface crust settled rapidly during shaking for the duration of 450s as indicated by almost vertical line at the left side of the figure and then settled more slowly after the shaking. As shown by the green, purple, and sky blue curves in Figure 23, the clay layers Ac1, Ac2, and A-3 settled more slowly during shaking and then follows the trend of settlement similar to that of the sandy layer As after shaking. These trends of settlements are more or less consistent with the understanding of the settlement of uniform ground. However, a different settlement behavior is depicted by the blue curve in Figure 23 at the top of the crust layer (i.e. the ground surface). In comparison to the rapid settlement of As1 layer during shaking, the settlement of the top of the crust layer (the ground surface) is negligibly small. The ground surface continues to settle linearly with time over 30 years, eventually reaching 0.45m. The logical interpretation of this behavior of ground settlement is that difference in the settlements between the ground surface and the top of the sandy layer during and after shaking should be consistent with the volume of pore water flow provided from the liquefied sandy layer. These complex phenomena are presumed due to the effect of void redistribution underneath the surface crust layer.

Figure 24 depicts the computed volumetric change of soil layers associated with void redistribution during and after the earthquake. In this figure, the color contour indicates the excess pore water pressure ratio as shown in the index on the left side. The deformation in this figure is magnified by 20 times relative to the original scale of soil profile to clearly depict the deformation associated with the void redistribution. During the shaking, the sand layer (As) is completely liquefied as indicated by red color contour in Figure 24(a). The surface crust layer above the sand layer also shows certain increase in excess pore water pressure as indicated by the yellow color contour, but does not fully reach 1.0 state as indicated by yellow color contour in the same figure.

After the earthquake (t = ten days), pore water pressures in the lower part of the sand layer begin to dissipate and pore water is flowing into the area just below the surface crust layer as shown in Figure 24(b). It is possible to interpret the volumetric expansion in the soil element (indicated by the white arrow) below the surface crust layer as formation of water film. Pore water continues to flow into the sand layer beneath the surface crust layer for over 15 years, as shown in Figure 24(c). The volumetric expansion in the soil element below the surface crust layer depicted in this figure corresponds to the volume of pore water flow into this region, and accounts for the difference in settlement

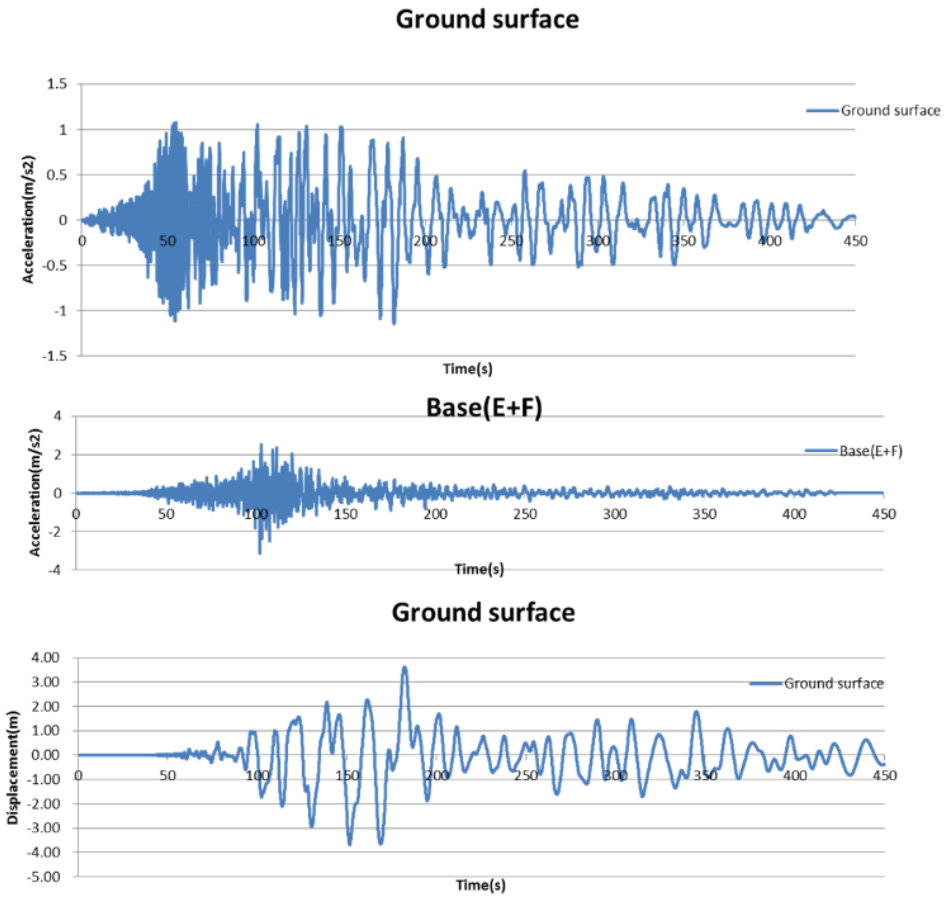

Figure 21 Computed acceleration at the ground surface (top), input bedrock acceleration (middle), and computed relative horizontal displacement at the ground surface (bottom)

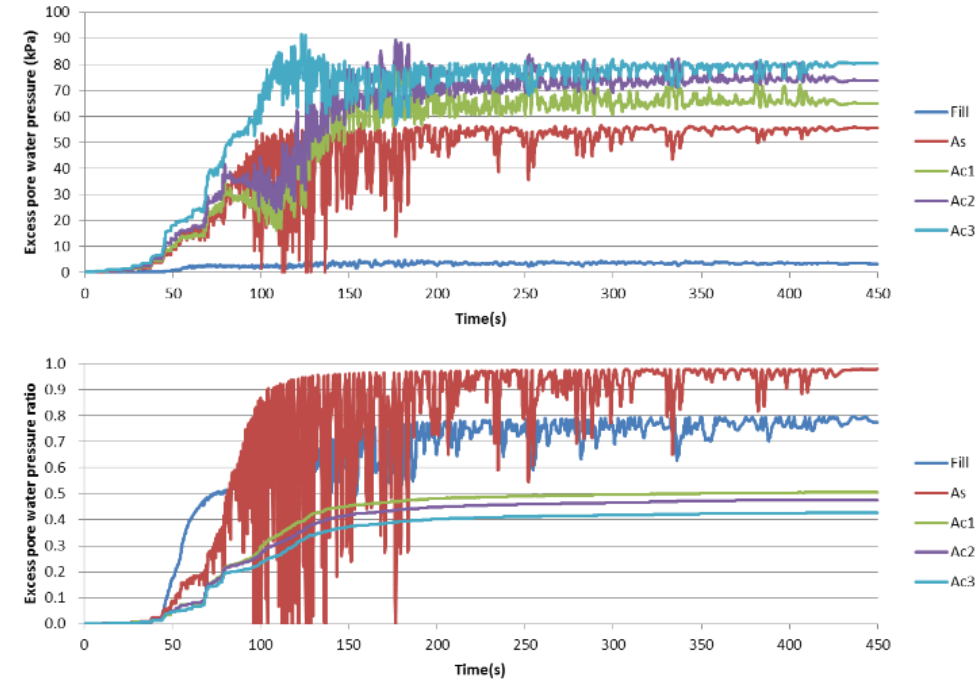

Figure 22 Computed excess pore water pressure (top) and excess pore water pressure ratios (bottom)

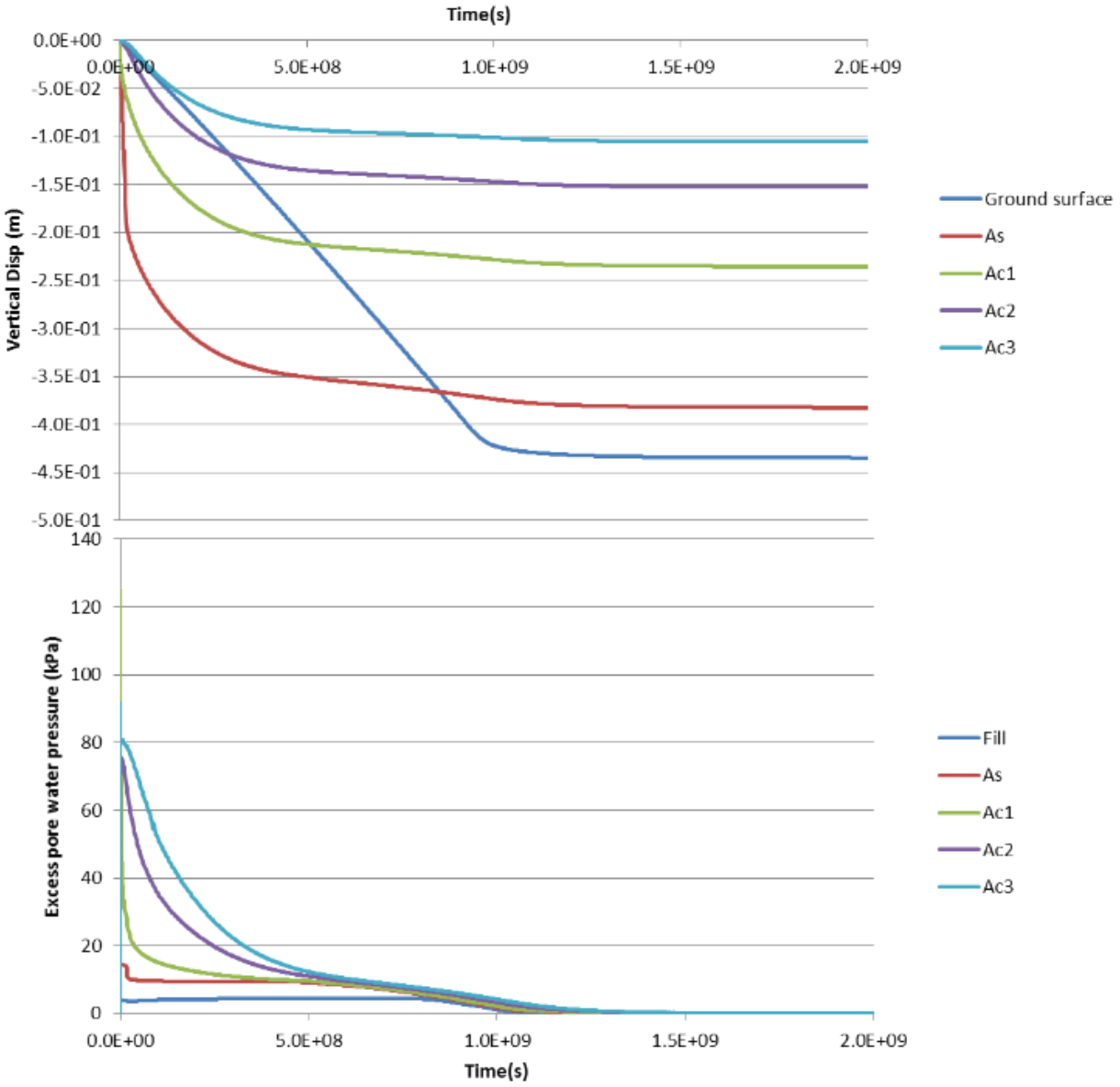

Figure 23 Vertical displacements (top) and excess pore water pressures (bottom) in long term over 60 years ($2.0x10^9$s) after the earthquake

behavior at the ground surface and at the top of the sandy layer as described earlier (Figure 23).

The high excess pore water pressure remaining under the surface crust layer eventually dissipates through the surface crust layer and results in the ground surface settlements as shown in Figure 24(d). In this simulation, a one dimensional profile of the ground is imposed throughout the analysis and 30 years is required to complete the dissipation pf excess pore water pressure and settlement after the earthquake. If other elements of soil property change over 30 years is taken, such as formation of cracks at the surface crust layer or two or three dimensional pore water flow is allowed at the lateral boundaries, the results of the simulation can be different in terms of time scale and other details.

Consequently, the effects of capping crust layer of clayey material can result in the more complex void redistribution than that in the case of uniform ground. A closer look into this aspect of the behavior of soil is needed for improving the practice in evaluating the seismic performance of geotechnical structures.

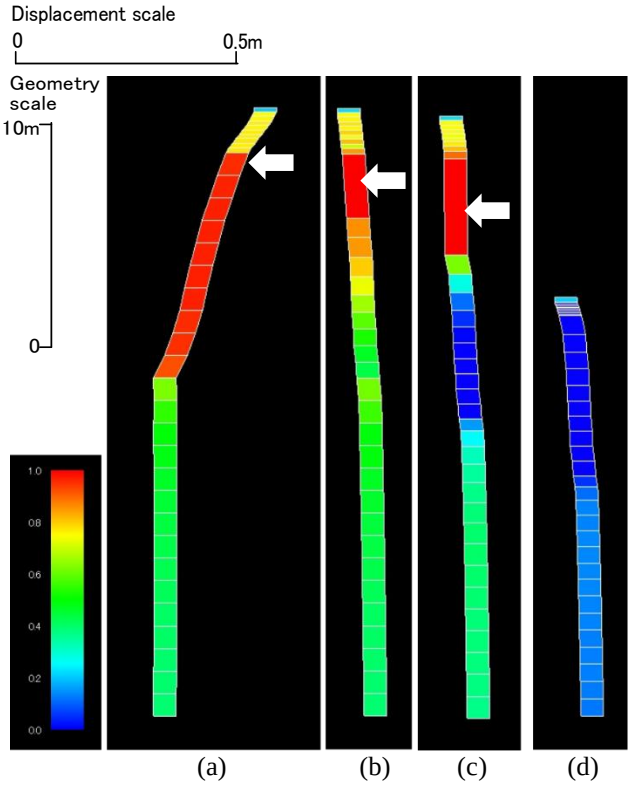

Figure 24 Computed deformation of soil column at (a) t=3.6x10^{2}s (during shaking), (b) t=8.8x10^{5}s (ten days), (c) t=4.9x10^{8}s (15 years), and (d) t=1.05x10^{9}s (30 years)

6 Delayed Flow Failure of Mild Slope

The foregoing discussions on the effects of a capping crust layer on the level ground leads our attention to the effects of a capping crust layer in a more generalized case involving a capping crust layer on the seismic performance of a mildly sloping ground. An analysis is performed by inclining the same ground profile shown in Figure 20 by two degrees. The upper 12m of this mild slope consisting of the 2m surface crust clay layer underlain by the 10m sand deposit analysis as shown in Figure 25. The section for the one-dimensional analysis of an inclined soil column is indicated by the green rectangle area. In this analysis, the steady state shear resistance of sand deposit before the earthquake response analysis is specified as *q*us=50kPa with the internal friction angle of ϕ_f=36.5degree. This steady state shear resistance is approximately two orders of magnitude higher than the induced static shear stress of τ = 0.3kPa at the interface of the sand and surface clay layer. The ground water table is assumed to be at the sloping ground surface.

Figure 26 depicts the computed deformation of the one-dimensional cross section cut out of the sloping ground subject to the same earthquake motion used for the level ground analysis described earlier.

The deformation of the soil column in this figure is depicted in the original scale of the soil profile. As shown in this figure, the sand layer is brought up to the state of liquefaction during shaking but the deformation toward to downstream of the slope is not visible except for the surface crust clay layer. However, at 7 hours after shaking, the surface crust clay layer begins to flow due to the localized shear deformation of the sand deposit just beneath the surface crust layer. The flow does not stop, resulting in the unlimited deformation of the mild slope.

The mechanism of this delayed flow failure can be explained as follows (Figure 27). During the shaking, the sand deposit liquefies. However, the void ratio of the sand layer basically remains the same as that at the initial state. Thus, the liquefied sand deposit keeps sufficiently high steady state shear resistance and does not exhibit visible deformation toward downstream side.

As time goes on, pore water from the lower portion of the sand deposit flows toward the sand just below the capping clay layer. However, the capping clay layer tends to prevent flow further up toward the ground surface. This situation induces volume expansion of the sand just below the capping clay layer. The volume expansion of this portion of the sand results in reduction in the steady state shear resistance. This situation can be interpreted in the void ratio – steady state strength diagram shown in Figure 13 as a path parallel to the straight lines with a constant fines content. When the steady state shear resistance qus becomes less than the induced static shear stress below the surface capping clay layer, delayed flow failure is triggered.

The pore water migration can result in the formation of water film in the extreme case (Kokusho 2000). However, the analysis performed above suggests that the void redistribution in the mildly sloping ground can be sufficient to trigger the delayed failure, provided that the steady state shear resistance of the soil underneath the capping crust layer is reduced less than the induced static shear stress due to the surface crust layer of mild slope.

The analysis described above is intended to study the behavior of mildly sloping ground affected by the pore water migration and associated void redistribution in the ground. Computed results such as the delay of 7 hours before the initiation of flow failure depends on the parameters used for the analysis, such as coefficient of permeability of the sand and crust clay layers and the shear strength at the steady state qus. Further study is required to verify the analysis by performing a study using case histories of delayed failure.

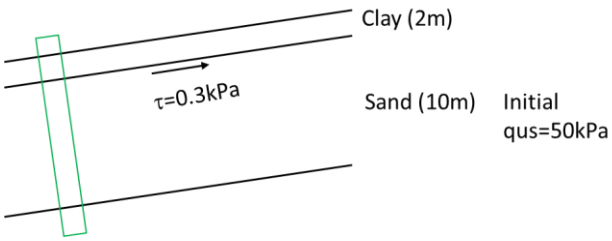

Figure 25 Schematic figure of the upper 12m profile of mild slope subject for case study

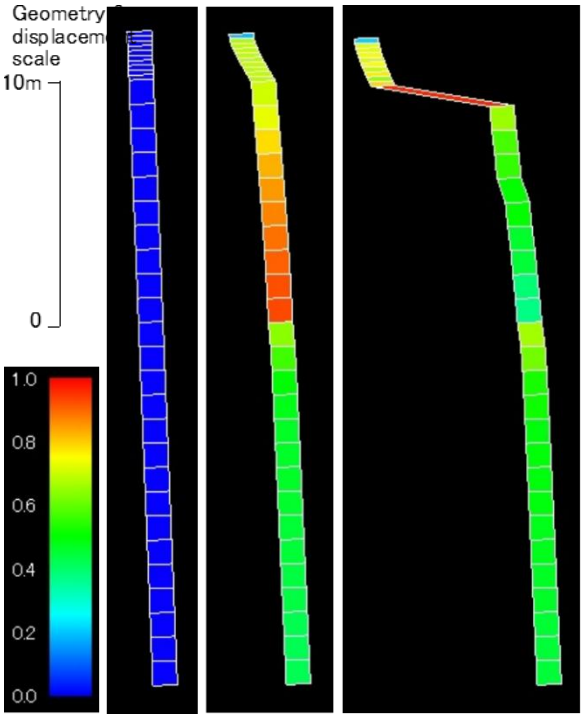

(a) (b) (c)

Figure 26 Computed deformation of soil column out of the mildly sloping ground at (a) t=1s, (b) t=229s, and (c) t=27350s (7 hours)

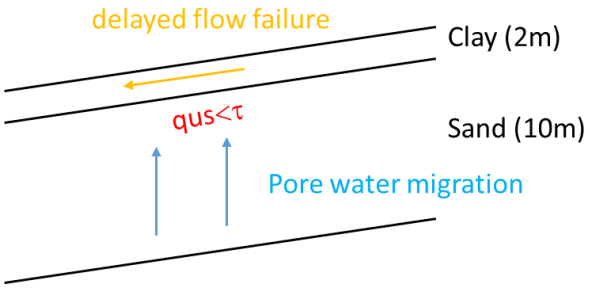

Figure 27 Schematic figure of the mechanism of delayed flow failure

7 Conclusions

This paper presents an overview of the developments of seismic performance evaluation of geotechnical structures, from the simplified limit equilibrium approach to the detailed approach based on the deeper understanding of the soil behavior during earthquakes. The overview covers the period spanning from 1923 Great Kanto earthquake, Japan, to 2011 Tohoku Off Pacific Ocean earthquake, and thereby offers a journey from the early developments in the discipline of geotechnical earthquake engineering to the present and paths forward for future developments.

Conventional simplified limit equilibrium analysis has been widely used for evaluating seismic performance of geotechnical structures during weak or moderate earthquake motions. In this approach, an assumption of no dilatancy is made on the behavior of soil and this assumption limit the applicability of this classic approach for saturated soil.

Detailed analysis for evaluating seismic performance of geotechnical structures affected by soil liquefaction have been conventionally based on undrained cyclic behavior of sandy soil. Recent developments and paths forward in evaluating seismic performance of geotechnical structures include additional mechanisms of soil behavior, such as the effects of steady state (residual strength) and combination of cyclic and steady state effects.

For longer duration earthquake motions such as those recorded during the 2011 M 9.0 East Japan earthquake with duration on the order of 200 seconds, the effect of partial drainage during shaking will likely to be significant. Thus, effective stress analysis allowing dissipation and redistribution of excess pore water pressures during and after earthquake should become the primary analysis procedure to appropriately evaluate the seismic performance of geotechnical structures. The effect of void redistribution in the interlayered ground with a surface crust layer can cause delayed settlements in level ground and delayed flow failure in mildly inclined ground.

In comparison to studies on fully drained or fully saturated sands, studies on the mechanical properties of partially saturated sand are relatively new and can be considered as a generalization in understanding the behavior of sand under cyclic loading. The effects of increasing average volume compressibility in a mixture of air and water and the effect of suction together with degree of saturation should be appropriately evaluated.

References

[1] Acacio, A. A., Y. Kobayashi, I. Towhata, R. T. Bautista and K. Ishihara. Subsidence of building foundation resting upon liquefied subsoil: case

studies and assessment. *Soils and Foundations* **41**(6): 111-128, 2001.
[2] Iai, S., Y. Matsunaga and T. Kameoka. Strain space plasticity model for cyclic mobility. *Soils and Foundations* **32**(2): 1-15, 1992.
[3] Iai, S., T. Tobita, O. Ozutsumi and K. Ueda. Dilatancy of granular materials in a strain space multiple mechanism model. *International Journal for Numerical and Analytical Methods in Geomechanics* **35**(3): 360-392, 2011.
[4] Ishihara, K., A. A. Acacio and I. Towhata. Liquefaction-induced ground damage in Dagupan in the July 16, 1990 Luzon earthquake. *Soils and Foundations* **33**(1): 133-154, 1993.
[5] Ishihara, K., M. Cubrinovski and T. Nonaka. Characterization of undrained behaviour of soils in the reclaimed area of Kobe. *Soils and Foundations, Special Issue on Geotechnical Aspects of the January 17 1995 Hyogoken-Nambu Earthquake No.2*: 33-46, 1998.
[6] Ishihara, K., S. Yasuda and Y. Yoshida. Liquefaction-induced flow failure of embankments and residual strength of silty sands. *Soils and Foundations* **30**(3): 69-80, 1990.
[7] Juang, C. H., S. H. Yang, H. Yuan and S. Y. Fang. Liquefaction in the Chi-Chi earthquake - effect of fines and capping non-liquefiable layers. *Soils and Foundations* **45**(6): 89-101, 2005.
[8] Kokusho, T. Mechanism for water film generation and lateral flow in liquefied sand layer. *Soils and Foundations* **40**(5): 99-111, 2000.
[9] Mononobe, N. Considerations on vertical earthquake motion and relevant vibration problems. *Journal of JSCE* **10**(5): 1063-1094 (in Japanese), 1924.
[10] Okabe, N. General theory on earth pressure and seismic stability of retaining wall and dam. *Journal of JSCE* **10**(6): 1277-1323, 1924.
[11] Ozutsumi, O., S. Sawada, S. Iai, Y. Takeshima, W. Sugiyama and T. Shimazu. Effective stress analyses of liquefaction-induced deformation in river dikes. *Soil Dynamics and Earthquake Engineering* **22**: 1075-1082, 2002.
[12] Papadopoulou, A. and T. Tika. The effect of fines on critical state and liquefaction resistance characteristics of non-plastic silty sands. *Soils and Foundations* **48**(5): 713-725, 2008.
[13] Tsukamoto, Y., K. Ishihara and T. Nonaka. Undrained deformation and strength characteristics of soils from reclaimed deposits in Kobe. *Soils and Foundations, Special Issue on Geotechnical Aspects of the January 17 1995 Hyogoken-Nambu Earthquake No.2*: 47-55, 1998.
[14] Yoshimine, M. and K. Ishihara. Flow potential of sand during liquefaction. *Soils and Foundations* **38**(3): 189-198, 1998.
[15] Tsuchida, H. Prediction of and mitigation measures again liquefaction of sandy ground, 1970 Annual Seminar of Port and Harbor Research Institute, (3)-1-33, 1970 (in Japanese)

Failure Investigation of A Multi-tier Geosynthietc-Reinforced Soil Slope with Marginal Backfill Subject to Heavy Rainfall

K.-H. Yang[a], J. N. Thuo[b], J.-W. Chen[b] and C.-N. Liu[c]

[a]Department of Civil Engineering, National Taiwan University
[b]Department of Civil and Construction Engineering, National Taiwan University of Science and Technology
[c]Department of Civil Engineering, National Chi-Nan University
E-mail: khyang@ntu.edu.tw, josnet2@yahoo.com , wiwi820217@gmail.com , cnliu2009@gmail.com

Abstract –

This paper presents a failure case study on a geosynthetic-reinforced soil slope with marginal backfill subject to rainfall infiltration. The considered slope is a 26 m high, 4 tier geogrid-reinforced structures constructed for traffic demands in mountain area in Taichung, Taiwan. Contrary to the backfill recommendations in design guidelines, low plasticity silty clay (CL) with over 60% of fines was used as backfill in the reinforced zone. This could have been as a result of attempting to reduce cost and environmental impact associated with transportation of recommended backfills to construction site and disposal of excavated in-situ soils. The backfill material is a locally available residual soil from weathered mudstone and shale whose soil shear strength can be significantly reduced when soil become wet. The GRS slope first experienced excessive deformation after seasons of typhoon and heavy rainfall from 2010-2012. The measured settlement and horizontal deflection at slope crest were 140 and 80 cm from June to December 2012. Although an immediate remediation had been conducted for the slope excessive deformation, the slope final collapse was caused by two sequential typhoon events with total accumulated rainfall over 600 mm in August 2013. A series of physical and numerical investigation were performed to examine the failure mechanism and causes contributing to the failure. Using recorded rainfall, measured shear strength parameters and site geology, a series of coupled hydro-mechanical finite element analyses were performed based on the framework of unsaturated soil mechanics. Lessons learned from this case history are discussed.

Keywords –

Geosynthetic-reinforced soil; Marginal backfill; Rainfall infiltration; Failure

1 Introduction

Geosynthetic reinforced soil (GRS) walls and slopes have been preferred due to increased economic advantages and reported successful performances. To minimize transportation cost and environmental impact associated with the disposal of the excavated soil, locally available soils with relatively low hydraulic conductivity (usually referred to as marginal fills) have been used as alternative backfills where granular backfill is not readily available [1] contrary to design guideline recommendations (Fig. 1).

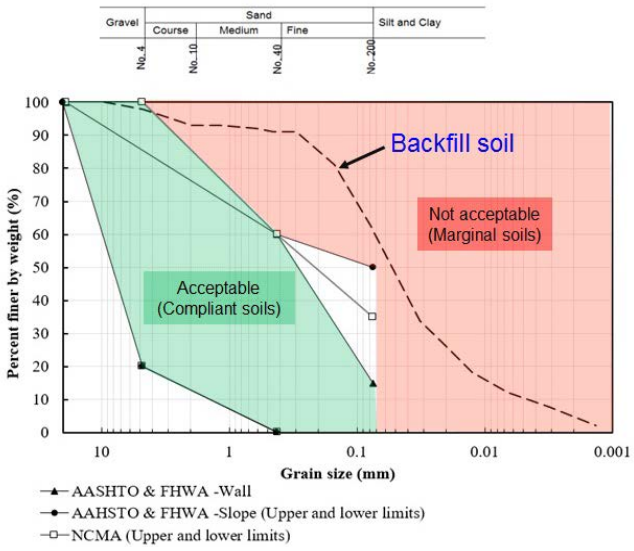

Figure 1. Backfill soil grain size distribution

Under unsaturated soil conditions, marginal backfills have been reported to perform satisfactorily due to presence of matric suction [2]. Matric suction plays a crucial role in the inter-particle or effective stress state of unsaturated soils [2]. The presence of suction can

increase soil effective stress, and thus enhance performance and stability of reinforced soil structures through increasing soil stiffness and shear strength [3], increasing soil-reinforcement interface strength [1, 2] and reducing mobilized reinforcement load..

However, upon wetting by infiltrating ground water or rainfall, low draining capacity of fine soils has also been reported to compromise performance (excessive deformation) and even cause failure of reinforced soil structures owing to the development of positive porewater pressure [1, 4]. Studies have demonstrated that the concern of porewater pressure accumulation within marginal backfills can be appropriately alleviated by adopting suitable design, construction techniques and drainage systems. It has been suggested that marginal backfill can be used as alternative backfill provided adequate drainage is provided[1] .

Conventionally, reinforced soil walls are designed using earth pressure theory while slopes are designed using limit equilibrium methods [5-7]. Among other limitations, earth pressure theory do not consider the effect of seepage forces to wall stability given that sufficient and adequate drainage is assumed[8]. On the other hand, although the effect of pore water pressure to the stability of the reinforced slope (in limit equilibrium analysis) can be factored during design, the location of the phreatic surface within to be constructed slope is usually not known and is usually assumed without clear guideline in most cases. Furthermore, both methods do not evaluate the effect of pore water pressure to the mechanical behavior (deformation) of the wall structure or backfill soil [8].

Assessing the hydrological response of unsaturated slopes subject to rainfall infiltration is critical and challenging, especially when determining the variation of pore water pressure (PWP) within slopes. To more accurately describe the physical responses (i.e., variation of soil moisture, matric suction, effective stress, soil shear strength, and slope stability) of unsaturated soil under infiltration conditions, coupled and uncoupled hydro-mechanical analyses based on the framework of unsaturated soil mechanics have recently been performed [9-11]. Coupled analysis has been found to produce a reasonably well defined wetting front [9, 11] and hence leads to a more accurate assessment of slope stability under infiltration conditions and demonstrates a better physical representation of water flow and stress variation within unsaturated soils [10]. Numerous studies have been conducted on the performance of reinforced soil walls and slopes subject to rainfal infiltration. However, there is limited studies on the effect pore water variation caused by rainfall infitration to mechanical performance of the wall and evaluation of potential remedial measures.

This paper presents a case study of a 26 m high, 4 tier geogrid-reinforced soil slope constructed for traffic demands in mountainous area of Taichung, Taiwan. Contrary to the backfill recommendations in design guidelines, low plasticity silty clay (CL) with over 60% of fines was used as backfill in the reinforced zone (Fig.1). The GRS slope first experienced excessive deformation after seasons of typhoon and heavy rainfall from 2010-2012. The measured settlement and horizontal deflection at slope crest were 140 and 80 cm from June to December 2012. Although an immediate remediation had been conducted for the slope excessive deformation, finally this slope collapsed after two sequential typhoon events with total accumulated rainfall over 600 mm in August 2013. A series of coupled hydro-mechanical finite element analyses were performed based on the framework of unsaturated soil mechanics. Field and laboratory test data obtained from site investigations were applied as input material properties and initial conditions in the numerical model. The objectives of this paper are as follows: (1) to investigate the failure and deformation mechanisms of this slope; (2) to suggest potential remedial measures to mitigate the catastrophic damage and failure caused by heavy rainfall; (3) to propose design approach and construction implication for GRS structures with marginal backfill. This study demonstrated the suitability and applicability of hydro-mechanical analysis to predict the failure and deformation of unsaturated reinforced structures by using the selected case study. The causes of slope deformation and failure are discussed, remediation measures based on the revealed failure and deformation mechanism are suggested, and lessons learned are discussed. The significance of this study is to mitigate the catastrophic damage and failure caused by failure of GRS structures with marginal backfill during rainfall

2 Case history

The slope discussed in this study was constructed in 2010 to provide traffic access to a landfill in mountainous area in Dali District, Taichung County, Taiwan. The slope height was 26m consisting of 4 tiers. An access road to nearby landfill passed just beside the toe of the reinforced slope and at the crest of the topmost tier. A few meters below the slope toe there was a creek. Presence of the creek is an indicator of a possible high ground water table in the area. Fig. 2 is a summary of the slope history. A tension crack first developed at the slope crest, followed by excessive deformation, the slope was repaired but finally failed on September 2013.

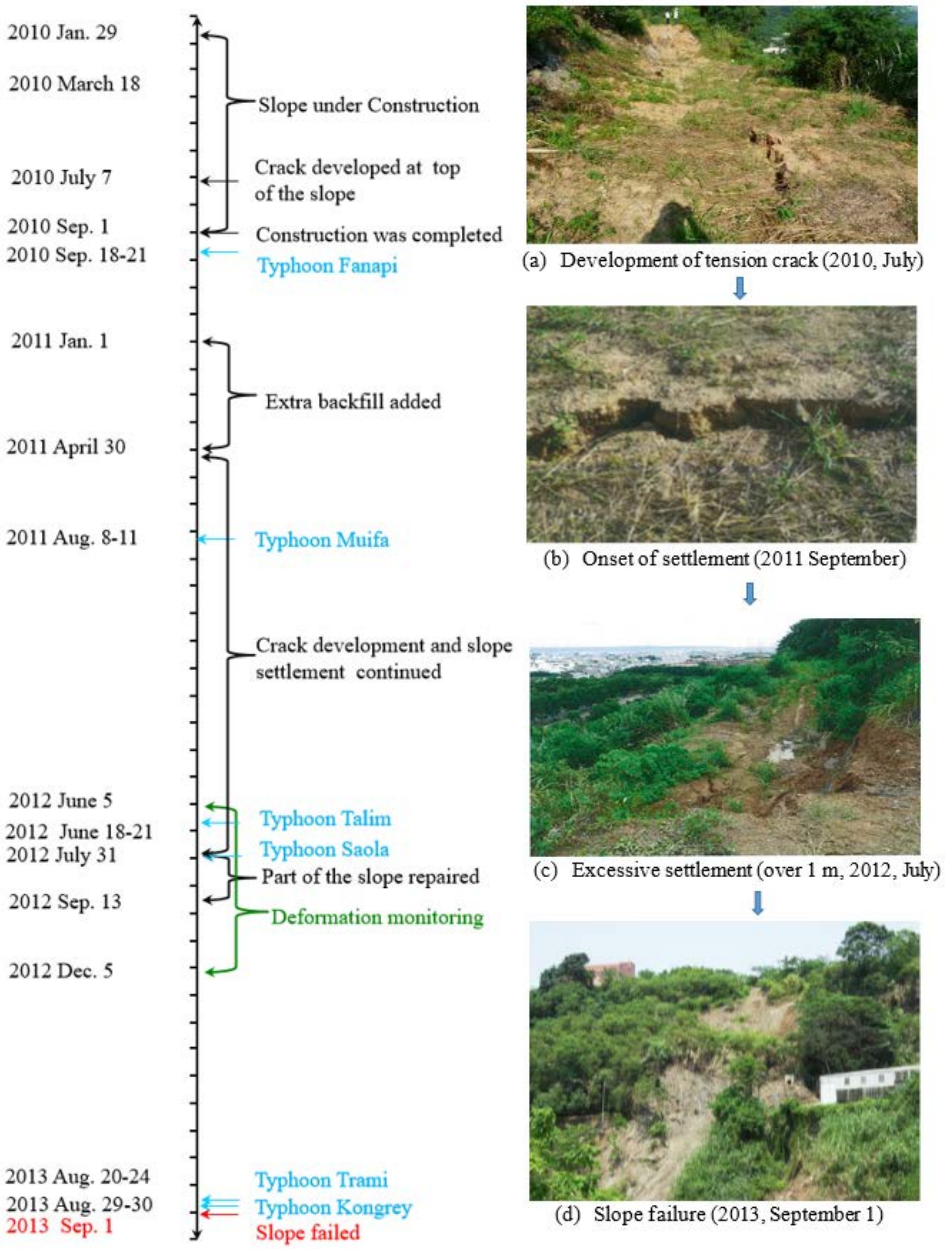

Figure 2. Summary of slope history

2.1 Slope design and construction

Fig.3 shows a typical cross section of the GRS slope discussed in this study. Wrap-around geogrid reinforcements with sandbag at front and rear side were used. Locally available, low draining soil from weathered mudstone and shale was used as backfill material. Contrary to the design guideline [5-7] recommendations, the backfill soil contained 60% of fines (Fig. 1). This could have been as a result of attempting to reduce cost and environmental impact associated with transportation of recommended backfills to construction site and disposal of excavated in-situ soils. A review of the original design revealed that as proposed by design guidelines limit equilibrium analysis was carried to check both the internal and external stability of the GRS slope. During the design, phreatic surface was assumed to be at the middle of the slope backfill (between retained weathered layer and the slope surface). No attention was paid to soil hydraulic conductivity during design.

Geocomposite back drains were place at back slope and connected to 150 mm transverse drain pipes which were laid at a spacing of 2 m at the bottom of each tier (Fig. 4a).

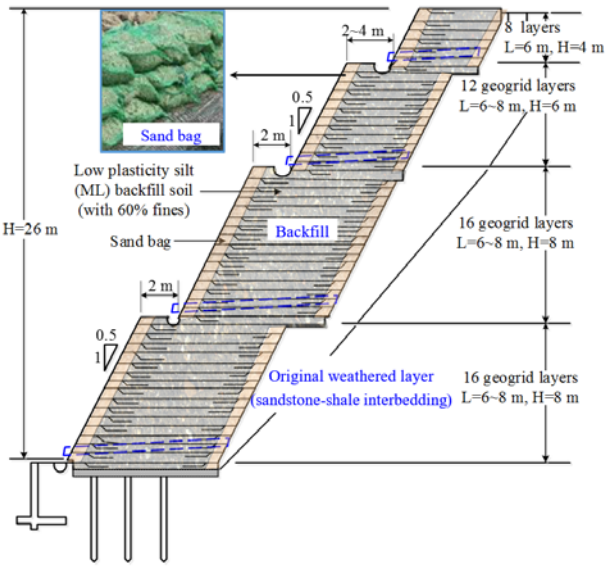

Figure 3. Multi-tier GRS slope

The 150 mm transverse drainage pipes were perforated on the upper surface to allow seeping out of accumulated water from the backfill soil. To prevent soil particles from getting into the pipe, nonwoven geotextile was used to wrap the transverse drains. However, no filtration check to prevent clogging of nonwoven geotextile was reported. Back drain and transverse drain connection joint is shown in Fig. 4b. As shown in Fig.4b, the connection joint details were poorly done and attention was not paid to easy getting disconnected during settlement.

2.2 Monitoring

Two months prior to completion of the construction process, a tension crack was formed at the crest of the slope and thereafter there was noticeable settlement (Fig. 2). The slope was repaired by placing additional 1 m high of extra backfill material on the top of the 3rd and 4th tier. After typhoon Muifa on August 2011, crack development and excessive settlement was sustained (over 1 m). In order to establish the cause of settlement and design for the remedial measures, slope deformation was monitored for a period of 7 months between June and December 2012. Deformation monitoring was done by means of recurrently recording relative heights of three established points on the top of each tier using a dumpy level machine. Fig. 5 shows recorded settlement of the top tier during this period. It was observed that after seasons of heavy rainfall (typhoon), considerably settlement was observed at the top of the top tier (Fig. 5). Therefore, it was concluded that heavy rainfall brought by typhoon induced large slope settlement.

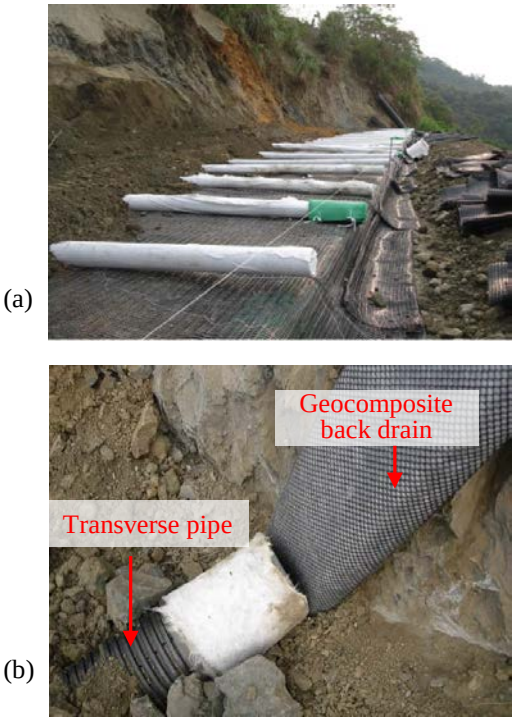

Figure 4. Drainage installations: (a) transverse drains; (b) back drain and transverse drain connection joint

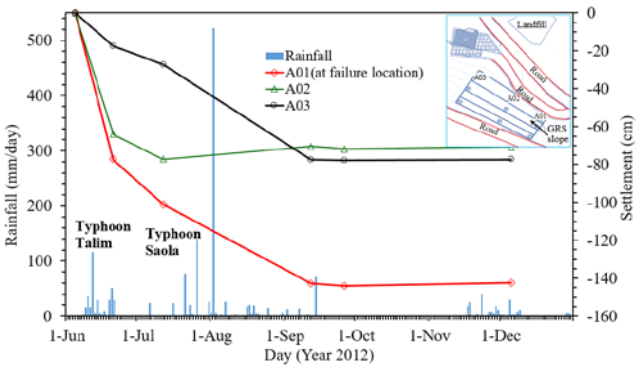

Figure 5. Slope settlement history

2.3 Slope failure

The slope final collapse happened on September 1, 2013, (Fig 2) exactly three years after completion. The collapse was preceded by two consecutive typhoon events, typhoon Tranmi (cumulative precipitation, R = 338 mm) and typhoon Kong-rey (cumulative precipitation, R = 310 mm) bringing a total precipitation of 647 mm. Immediately after the slope failure ground water seeped out of the backfill soil (Fig. 6). This suggested that pore water brought about by typhoon may have accumulated within the backfill soil. Fig. 7 shows a typical cross section of the failed slope showing the original GRS slope profile and the observed failure surface. It is observed that the failure surface cuts partially through the retained weathered layer and

partially through the retained soil thus compound failure mode occurred. From the preliminary investigations, causes of wall failure are:

i. The use of marginal soil (over 60% of fines) as backfill contrary to the backfill recommendations in design guidelines. Porewater pressure developed within the poorly draining backfill soils
ii. The original design and site investigation overlooked the existence of retained weathered rock layer, which has shear strength properties less than that of intact rock.
iii. Settlement and tension crack at the slope top surface allows rain water ponding at the slope top surface and consequently infiltrating into reinforced zone.
iv. Drainage system malfunctioned because drainage joints were poorly connected during construction and likely dislocated due to excessive slope deformation.
v. The soil fine particles may have clogged the nonwoven geotextile filter and hence retarded the drainage capacity

In order to evaluate the effect of poor backfill hydraulic conductivity to slope settlement and eventual failure, coupled hydro-mechanical analysis was performed.

Figure 6. Close view of failed slope at the toe

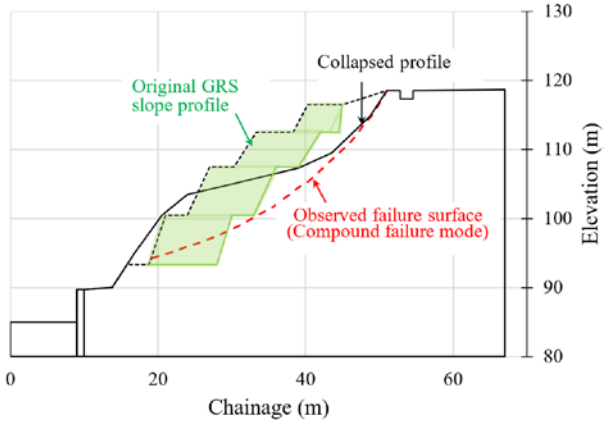

Figure 7. Failed GRS slope cross-section profile

3 Numerical simulation

3.1 Numerical model and boundary conditions

GRS slope two-dimensional FE model is displayed in Fig. 8. The slope geometry was constructed according to topographic maps and the subsurface soil profiles were interpolated from the borehole logging readings.

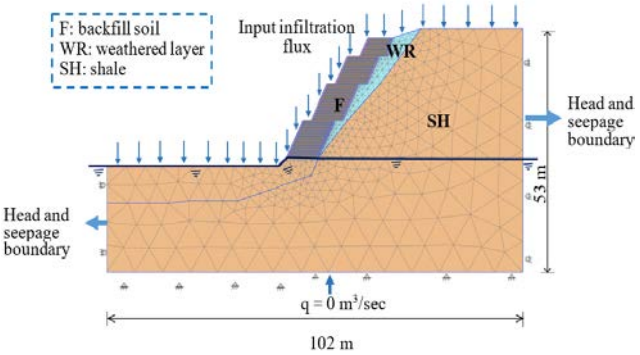

Figure 8. Geologic profiles and numerical models

The numerical model consists of a total of 3195 fifteen-node triangular elements. Fine-element meshes were specified for the backfill and weathered soil layers whereas medium-element meshes were applied to rock layers (Fig. 8). Standard fixity was applied as the mechanical boundary; the two lateral boundaries were allowed to move only in the vertical directions whereas the bottom boundary was restrained from movement.

Hydraulic boundaries at two lateral ends were initially set to be constant head boundary conditions on the basis of the assumed ground water table (GWT) levels. During the analysis, the hydraulic boundaries were switched to seepage boundary conditions to enable variations in GWT levels because of wetting and drying cycles. Downward vertical influx was prescribed on the slope surface to model rainfall, whereas upward influx was imposed on the surface boundary to simulate evapotranspiration. The input values of downward flux during rainfall were obtained from the actual rainfall records from the nearest precipitation measuring station. The value of upward flux on dry days was estimated to be 10 mm/day based on studies on the average evapotranspiration rate of mountain areas in Taiwan.

3.2 Initial conditions

Upon simulating the wall construction, the initial PWP was generated by prescribing a specified flux at the top of the slope model for a considerable time until steady state conditions were reached. The quantities of the prescribed flux were first adjusted until the calculated initial matric suction value fell within the range of expected field suctions. Considering that

during the construction of earth-retaining structures in the field, backfill soils are compacted at ±2% of the optimum moisture content [4], target suction of 40 kPa was obtained from SWCC (Fig. 9) corresponding to optimum moisture content of 11.8 % obtained during standard proctor test. In addition, a pre-rainfall period of 20 days was simulated using the actual rainfall data from July 1 up to July 20, 2013 in order to establish initial hydrology conditions.

3.3 Material properties

Backfill soil was modelled as a stress-dependent, hyperbolic, elastoplastic material by using the Hardening Soil model and was analyzed using effective stress parameters under drained conditions. Table 1 lists the input soil parameters of the Hardening Soil model.

Table 1. Input parameters for hardening soil model

Property	Values
	Backfill soil (F)
Stiffness properties	
E_{50}^{ref}, secant modulus (kPa)	29500
E_{oed}^{ref}, tangent oedometer modulus (kPa)	20650[1]
E_{ur}^{ref}, unloading-reloading modulus (kPa)	88500[2]
ν_{ur}, unloading-reloading Poisson's ratio	0.3
m, modulus exponent	0.5
R_f, failure ratio	0.9
Strength properties	
ϕ', friction angle (degree)	37
c', cohesion (kPa)	6
ψ, dilation angle (degree)	7[3]
Bulk unit weight	
γ_{unsat}, unsaturated unit weight (kN/m^3)	20.1
γ_{sat}, saturated unit weight (kN/m^3)	21.1

[1] assumed to be $0.7\,E_{50}^{ref}$ as the default value in PLAXIS

[2] assumed to be $3\,E_{50}^{ref}$ as the default value in PLAXIS

[3] estimated by $\psi = \phi - 30^o$ (Bolton 1986)

Soil residual shear strength properties were determined from isotropically consolidated undrained (CU) triaxial compression tests [12] with pore pressure measurements. Backfill soil saturated hydraulic conductivity test was determined through conducting a series of constant volume – constant head hydraulic tests using a flexible wall permeameter [13] while the water characteristic curve (SWCC) of the backfill soil was determined through applying various suctions to soil specimens in a pressure plate extractor (pressure plate test), [14]. Fig. 9 shows backfill soil unsaturated hydraulic properties. Retained soil consisted of sandstone interbedded with shale (SS/sh). Retained soil residual shear strength properties were determined using standard test method for direct shear test under consolidated drained conditions (ϕ'=31°, c'= 1.4 kPa) Retained weathered soil layer SWCC was assumed to be similar to that of similar soils (weathered sandstone) reported in literature [15]. Retained weathered sandstone and rock layers were modeled as linear, elastic-perfectly plastic materials by using the Mohr–Coulomb model and were analyzed using saturated, total stress properties under undrained conditions. The shear strengths (i.e., cohesions) of rock layers were calculated from the measured uniaxial compression strength (*qu*/2=98 kPa). The rock moduli and saturated hydraulic conductivities were estimated according to the properties of similar rock types suggested by [16]. Sand bags were also modeled as linear, elastic-perfectly plastic materials using the Mohr–Coulomb model and were analyzed using unsaturated, effective stress properties under drained conditions. Sand shear strength (ϕ'=40°, c'= 0 kPa) and saturated hydraulic conductivities were tested and reported by [17]. Additional cohesion value of 5 kPa to simulate confinement was used in sandbags. Table 2 is a summary of materials van Genuchten-Mualem model [18] curve fitting hydraulic parameters.

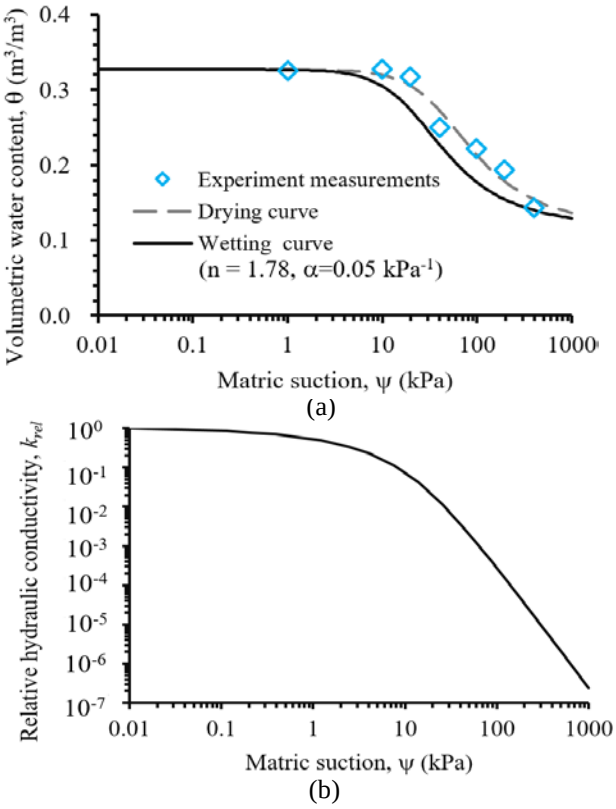

Figure 9. Backfill soil hydraulic properties: (a) SWCC; (b) *k*-function.

Table 2. Material hydraulic properties

Parameter	Backfill soil	Weathered layer	Bedrock shale	Sand
k_{sat} (m/s)	1×10^{-8}	1×10^{-6}	1×10^{-13}	1.35×10^{-4}
θ_s (%)	32.7	32.4		38
θ_r (%)	10	0.02		1
n	1.78	2.8	–	2.3
α (kPa^{-1})	0.106	0.1	–	16.667

Geogrid specimen was retrieved from failed slope in the field and tested by Single Rib Tensile Method to determine it long-term tensile strength. Test results indicate the long-term tensile strength of the retrieved geogrid $T_{ult\ (retrieved)}$ =113 kN/m.

4 Results and discussion

Fully coupled flow deformation module was implemented into the PLAXIS (version 2D 2015) finite element (FE) program [19]. Fig. 10 shows model validation for the failure of GRS slope in 2013 by comparing the predicted and observed failure timing. Fig. 10 shows the variation of the FS for period between July 20 to the day the slope collapsed (September 1). The FS of the slope dropped at each rainfall event and recovered during dry days because of the effect of modelling evapotranspiration. Predicted failure timing for FS =1 corresponds with the observed failure timing. Therefore, the developed hydro-mechanical model is capable of accurately predicting the timing of rainfall-induced slope failure.

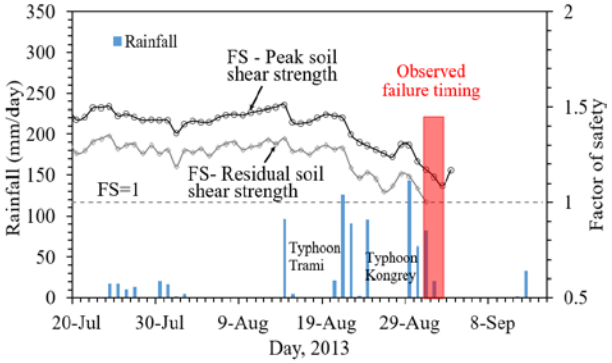

Figure 10. Predicted factor of safety variation

Predicted deformed mesh at failure is shown in Fig. 11. The deformed mesh shows that large deformations occurred in both the backfill soil and the retained weathered layer. The failure surface partially cuts through the bottom tier of the GRS slope and partially passes through the weathered rock (Fig. 12). This suggests compound failure mode occurred within the slope. Weathered layer, though overlooked in the initial reinforced slope design may have been unstable. The predicted deformed shape imitates the shape of the failure mass observed after slope failure (Fig. 6).

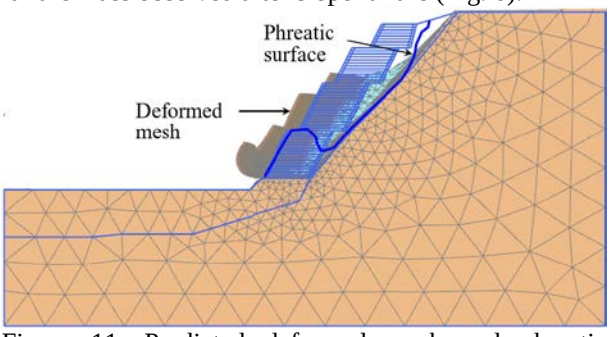

Figure 11. Predicted deformed mesh and phreatic surface at failure

From Fig. 11, it is also observed that the GWL had risen to the top of the bottom tier. The bottom tier is fully submerged. This is contrary to the initial design assumption where GWL was assumed to be at the middle of the backfill soil (between retained fill and ground surface). Therefore, slope failure was attributed to the increase of PWP (loss of soil matric suction) due to the rise of phreatic surface level.

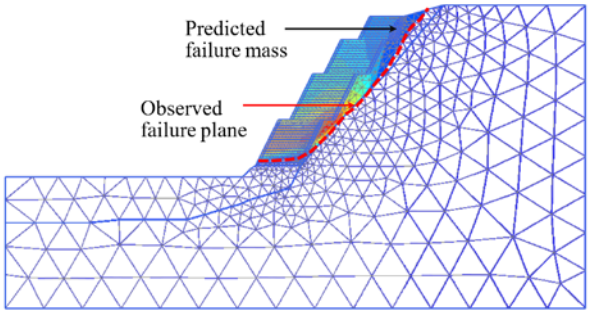

Figure 12. Predicted failure surface

5 Lessons learned and suggested remedial measures

From the discussed failure investigation and couple hydromechanical analysis, the following lessons were learned and remedial measures were suggested:

i. The use of marginal soil as backfill compromised the performance of the GRS slopes upon rainfall infiltration because its low draining capacity could cause the build-up of PWP, and finally lead to the slope failure.
ii. The original site investigation failed to identify the existence of the weak soil layer (weathered rock layer). More detailed site investigation is required during design of GRS structures
iii. Because of the compound failure mode, it is crucial to stabilize unstable weathered rock prior to the construction of the GRS slope in front of it.
iv. Because high positive pore water pressures

accumulated at the slope toe, sufficient drainage should be provided, especially at the bottom tier of the GRS slope.

v. The rear sand bags which show daylight at the top of the slope could provide a flow channel to facilitate rainfall infiltration. It is suggested that rear sand bags should not show daylight.

vi. Filter criteria should be checked for nonwoven geotextile used to wrap drainage pipes or in geocomposite to avoid clogging of geotextile by fine soil particles.

vii. Excessive deformation of marginal soil could occur upon rainfall infiltration. Hence flexible drainage joints should be used to avoid drainage joints disconnection caused by slope deformation.

6 Conclusions

From the findings of this study, the following conclusions were made:

1. This study demonstrated that using recorded rainfall, measured soil parameters, site geology and slope geometry, the hydro-mechanical model based on the framework of unsaturated soil mechanics is capable of accurately predicting the failure timing of a GRS slope.
2. The slope failure was attributed to increase of pore water pressure (loss of matric suction). The phreatic surface level advanced to the weathered rock and increase to the top of the bottom tier of the GRS slope.
3. Efficient and sufficient drainage systems are required to improve system drainage capacity and hence enhance the system stability during rainfall.

Acknowledgement

The data of site investigation and soil tests provided by Taiwan Geotechnical Professional Engineers Association are sincerely appreciated.

References

[1] Zornberg J. G. and Mitchell J. K., Reinforced Soil Structures with Poorly Draining Backfills. Part I:Reinforcement Interactions and Functions, *Geosynthetics International*, 1(2):103-148, 1994.

[2] Vahedifard F., Mortezaei K., Leshchinsky B. A., Leshchinsky D., and Lu N., Role of suction stress on service state behavior of geosynthetic-reinforced soil structures, *Transportation Geotechnics*, 8:45-56,2016.

[3] Khalili N., Geiser F., and Blight G., Effective Stress in Unsaturated Soils: Review with New Evidence, *International Journal of Geomechanics*, 4:115-126, 2004.

[4] Yoo C. and Jung H.-Y., Case History of Geosynthetic Reinforced Segmental Retaining Wall Failure, *Journal of Geotechnical and Geoenvironmental Engineering*, 132:1538–1548, 2006.

[5] Elias V., Christopher, B.R., and Berg. R., *Mechanically stabilized earth walls and reinforced soil slopes design and construction guidelines.* Report No. FHWA-NHI-00-043, National Highway Institute, Federal Highway Administration, Washington, D.C. March, 2001.

[6] AASHTO, *Standard Specifications for Highway Bridges.* , Seventeeth ed. Washington, D.C., with interims.: American Association of State Highway and Transportation Officials, 2002.

[7] NCMA, *Design manual for segmental retaining walls,* . Virginia, USA: Herndon, 2010.

[8] Christopher B. R., Leshchinsky D., and Stulgis R. P., Geosynthetic-Reinforced Soil Walls and Slopes: US Perspective, *proceedings of International Perspectives on Soil Reinforcement Applications. ASCE* Geotechnical Special Publication No. 141, Reston, Virginia, 2005.

[9] Qi S. and Vanapalli S. K., Hydro-mechanical coupling effect on surficial layer stability of unsaturated expansive soil slopes, *Computers and Geotechnics*,70:68–82, 2015.

[10] Oh S. and Lu N., Slope stability analysis under unsaturated conditions: Case studies of rainfall-induced failure of cut slopes, *Engineering Geology*, 184:6–103, 2015.

[11] Yang K.-H., Uzuoka R., Thuo J. N., Lin G.-L., and Nakai Y., Coupled hydro-mechanical analysis of two unstable unsaturated slopes subject to rainfall infiltration, *Engineering Geology*, 216:13-30, 2017.

[12] ASTM D4767, Standard Test Method for Consolidated Undrained Triaxial Compression Test for Cohesive Soils1, *ASTM International*, West Conshohocken, PA,USA.

[13] ASTM D5084, Standard Test Methods for Measurement of Hydraulic Conductivity of Saturated Porous Materials Using a Flexible Wall Permeameter, *ASTM International*, West Conshohocken, PA,USA.

[14] ASTM D6836-16, Standard Test Methods for Determination of the Soil Water Characteristic Curve for Desorption Using Hanging Column, Pressure Extractor, Chilled Mirror Hygrometer, or Centrifuge, *ASTM International*, West Conshohocken, PA,USA.

[15] Azam, S., Ito, M., and Khan, F. (2013). "Influence of cracks on soil water characteristic curve." *Advances in Unsaturated Soils* C. e. a. (eds), ed., Taylor & Francis Group, London.

[16] Goodman R. E., *Introduction to Rock Mechanics. Second ed.* : Wiley, 1989.

[17] Yang K.-H., Yalew W. M., and Nguyen M. D., Behavior of Geotextile-Reinforced Clay with a Coarse Material Sandwich Technique under Unconsolidated-Undrained Triaxial Compression, *International Journal of Geomechanics and Engineering*,16(3)DOI:10.1061/(ASCE)GM.1943-5622.0000611, 2015.

[18] van Genuchten M. T., A closed form equation for predicting the hydraulic conductivity of unsaturated soils, *Soil Science Society of America Journal*, 44:892-898, 1980.

[19] Brinkgreve R. B. J., Kumarswamy S., and Swolfs W. M., *PLAXIS 2016 Manual*. Balkema, Rotterdam, The Netherlands, 2016.

Preliminary Evaluation of Liquefaction Potential in Ilan Area

S.J. Chao[a], A. Cheng[a], H.L. Lee[b], S.M. Lu[bc], C.H. Chen[d], W.C. Chiao[d], and Z.Y. Hsiao[a]

[a]Department of Civil Engineering, National Ilan University, Taiwan
[b]Economic Affairs Department, Yilan County Government, Taiwan
[c]Graduate Institute of Architecture and Sustainable Planning, National Ilan University, Taiwan
[d]Department of Geotechnical Engineering, CECI Engineering Consultants, Inc., Taiwan
E-mail: chao@niu.edu.tw, man0403power@gmail.com

Abstract –

Ilan County is located between the east and the northeastern earthquake regions of Taiwan. Lanyang Plain is a sedimentary deposit from several rivers. As a result, the subsurface conditions of the Lanyang Plain generally contain several layers of loose uniform grained soils. Furthermore, groundwater table of the entire Lanyang Plain is fairly close to the ground surface. Together with the high probability of earthquake occurrences in this area, the soil liquefaction phenomenon needs to be considered with high attention. Tainan earthquake occurred on February 6, 2016 with the magnitude of 6.6 caused many severe disaster and makes the soil liquefaction issue being the government concern. In view of this, the primary soil liquefaction potential map was distributed within a limit time and needs to be refined for the purpose of accuracy.

Langyang Plain is located in the liquefaction-sensitive area and the liquefaction potential map is desired to be upgraded with more precision. This paper can be divided into two parts for Ilan soil liquefaction issue. The first part is to do a short introduction for the Ilan area liquefaction condition. The second part is to improve the accuracy of liquefaction potential map by planning a supplementary drilling holes distribution, which increases the accuracy of the liquefaction potential map. The purpose of liquefaction potential map is to provide information for formulating disaster reduction strategy. It can also reduce the property loss from earthquake damage. The most important thing is to let people stay away from the dangers of liquefaction and live comfortably in Ilan area.

Keywords –

Soil liquefaction; Liquefaction map; Ilan

1 Introduction

On 6 February 2016, a strong earthquake of magnitude 6.6 occurred in the Tainan area and resulted in many serious disasters. Soil liquefaction is then becomes one of the government's focus. As a matter of fact, soil liquefaction potential issue was studied by some researchers in Taiwan about 20 years ago without formal achievement. At this moment, the important issue of soil liquefaction once again is taken seriously in order to achieve safety, prevention, early warning, response and other purposes. The original soil liquefaction potential map as well as the primary one must be improved for the accuracy purpose. Especially in densely populated cities and areas that are susceptible to liquefaction, including Ilan County. The living population is concentrated in several important cities located in the Langyang Plain in Ilan County. However, Langyang Plain not only has a poor geological condition near the Pacific Ocean, but also is located in the seismic belt. Above mentioned factors make the Ilan area mush more sensitive to soil liquefaction. Therefore, Ilan area liquefaction potential map needs to be more representative. By doing so, the Ilan County Government can be more ready to prepare for disaster prevention and early warning operations. As a result, people can get a safe and comfortable living condition.

2 Story of Soil Liquefaction

The study of liquefaction of granular soils using the concept of critical void ratio was first introduced by Casagrande. Mogami and Kubo (1953) suggested that the soil will be deformed as “liquefied” when cohesionless soil is disturbed. Seed (1979) mentioned that high pore water pressure would reduce the effective confining pressure of soil. At this condition the soil residual shear strength becomes lower, thus the soil is likely to produce deformation. Overall, static load and cyclic loading are both likely to cause this phenomenon. The particles in the original soil are separated due to disturbance when the earthquakes occur. At this moment the soil cannot afford the original stress suddenly. As a result, the soil pore water pressure increases and shear stress intensity becomes smaller. This condition provides the opportunity to produce soil

liquefaction, when the excess pore water pressure continues to rise up to the original effective stress (i.e., $\sigma=\mu$). From another point of view, when the earthquake causes the local average shear stress being greater than the local soil can provide resistance to liquefaction of the shear strength, soil liquefaction happens.

3 Extra Geological Drilling Plan

The subground investigation report of geological drilling can be used to estimate the soil liquefaction status. It can also use to produce the soil liquefaction potential map directly. If the precision and accuracy of the drilling hole layout is for sure, the precision of the liquefied potential map is better. To this point, the ability to reflect the actual soil liquefaction in the Ilan region is more reliable and stronger.

On February 6, 2016, the shocking earthquake caused serious disaster in Tainan region, including the soil liquefaction phenomenon. In view of this, the original soil liquefaction potential of the primary map will be refined for more accuracy request. Especially in the Ilan area, with weak geological conditions as well as close to the seismic zones, which makes the region more sensitive to soil liquefaction. Therefore, there is a strong need to increase drilling holes to provide intermediate soil liquefaction potentials. An accurate soil liquefaction potential map can not only provide disaster prevention and control related operations, but also to bring people to a safe and comfortable living environment.

3.1 Existing Borehole Situation

In this study, the three townships (Ilan, Luodong, and Wujie) in Ilan area are located on alluvial plain. This study has collected about 350 borehole data as shown in Figure 1 for their distribution. It can be clearly found that in the central parts of Ilan City and Luodong Town demonstrate more dense distribution of boreholes. The reason for these two places showing higher degree density is the regional center of educational district for Ilan City and business district for Luodong Town.

In addition, some other boreholes are located along the National Highway No. 5. As the standards for highway construction are higher than the general public road, geological conditions of the highway must be considered more seriously. As a general rule, boreholes are mainly selected on the Lanyang Plain while more infrequent in the remote mountain area. Nevertheless, the borehole distribution is quite uneven for the whole Ilan area. As a result, the existing collected borehole data cannot accurately accomplish the needs to establish a higher level soil liquefaction potential map. Thus, it is necessary to obtain more accurate information by means of supplementary drilling operation in the study area.

Figure 1. Existing collected borehole distribution map

3.2 Supplementary Drilling Program

The existing collected boreholes are mainly concentrated among the urban areas and along important roads. Although for the densely populated areas, the primary liquefaction potential map announced by the government seems to have sufficient representative borehole data, the other areas still need more borehole data to enhance the reliability of the liquefaction potential map. Therefore, we must conduct supplementary drilling operation to improve the accuracy of liquefaction potential map. Therefore, it is required to arrange a supplementary drilling program to improve the accuracy of liquefaction potential, which is in line with the boreholes density of 4 per square kilometer (so called the intermediate level).

As the main factors affecting soil liquefaction are weak soil, high groundwater, seismic energy, etc. The drilling program of borehole distribution can be accomplish by considering following aspects: (a). The existing boreholes distribution map can not only be analyzed at the current drilling layout of the precision and accuracy, but also mainly consider for determining the decision to add the drilling point; (b). The terrain and water data over the years in this area can determine the distribution of weak soil layer and find out the regions where liquefaction is prone; (c). The data related to geology can be used to comprehend the geological distribution, to determine the correction of the drilling report and to adjust the placement of the drilling holes position. Through the screening and adjustment supplementary boreholes location and other essential pre-operation can also help to improve the accuracy of soil potential map.

4 Liquefaction Influence Factors

The terrain of Langyang Plain is mainly deposited by the soil particles carried down from Lanyang river. The composition of soil layer is commonly as uniform and loose sand. Coupling with the high groundwater level condition and with the adjacent convergent plate boundary, where earthquakes occur frequently, the seismic disaster caused by earthquake should not be ignored of any kind. These conditions make the soil liquefaction problem need to be assessment objectively and carefully in Ilan area.

This paper simply describes the key points of soil liquefaction assessment and roughly divides the occurrence of soil liquefaction into three influence parts as soil factors, seismic factors, and environmental factors.

4.1 Soil Factors

Soil factors are the ability of soil itself to resist liquefaction. Once the soil resistance to liquefaction capacity is poor, a middle size earthquake may lead to soil liquefaction. Conversely, if the soil has sufficient resistance to liquefaction, it has considerable ability to resistance a larger earthquake. In this condition, only strong earthquake with higher energy can terminate the soil bearing capacity, which leads liquefaction to occur.

The soil factors, in other words, are the features of the nature of the soil. The soil factors are based on four soil properties. The four soil properties influencing on liquefaction degree are composition of the soil, tightness of the soil, groundwater level, and overburden stress.

4.1.1 Composition of the Soil

If the in-situ soil is composed by gravel, the large void between the gravel particles make pressurized groundwater can be discharged easily. If the soil is composed by clay, the pore water pressure due to poor permeability and thus is not susceptible to disturbance. That is to say, the clayey soil has a certain degree of cohesion, which makes liquefaction hard to take place. Seed (1971) pointed out that the composition by sand and silty sand is the most prone to be liquefied. Because the sand and silty sand, during the seismic force generated, are in the undrained condition, relatively. The continuous increase of pore water pressure and the decrease of effective stress cause the soil structure to be in an unstable condition as a final point. At this point, it is likely to lead the soil liquefaction occurrence.

4.1.2 Tightness of the Soil

Granular soils can usually be judged by their relative density or by standard penetration test. The soil particles of relatively tight are less prone to relative displacement, and their resistance to liquefaction is better. The process of soil liquefaction is that the soil particles change the arrangement between the particles by repeated earthquake movements. Of course, after the moment, it will produce a more state soil structure than the initial soil particle state. Similarly, when the soil particles are stacked more closely with each other, the chance of liquefaction and the resulting damage will be reduced greatly. Consequently, due to the getting closer relationship between the particles, liquefied soil particles can also have a good liquefaction resistance.

4.1.3 Groundwater Level

The effect of water in the soil has always been a matter of concern to civil engineers. Whether it is slope stability, excavation construction, and soil liquefaction, once the soil pores filled with water would make the soil in a relatively unstable state. In the case of soil liquefaction, the soil below the groundwater level is saturated and is increasing pore water pressure under repeated earthquakes. With the condition that the total stress is constant, the effective stress must decrease. Therefore, raising groundwater table would directly raise the security concerns.

On the other idea, the weak soil more close to the surface, the impact to the liquefaction potential becomes more serious. When the soil elevation deep enough it can be sure that the soil has good liquefaction resistance, of which the impact of liquefaction potential is smaller. When the high groundwater level condition occurs, the more soil is soaked in water and is saturated. At this moment, the security to the soil liquefaction will become lower for sure.

4.1.4 Overburden Stress

In general, the soil weight itself can provide a downward pressure to the lower soil, which also called overburden stress. As this stress increases with the depth, the subsurface soil gradually thickens and provides the lower soil greater overburden stress. It can make the lower soil become more closely. Because the deep soil overburden stress is bigger than shallow soil, shallow soil layer is more prone to liquefaction than the deep soil layer. The more excess pore water pressure required for liquefaction when the effective overburden soil stress is greater At the same time, liquefaction potential is also lower. In other words, once the soil reaches a certain depth, the chance of liquefaction will be reduced. According to Iwasaki (1982), who proposed the liquefaction method with depth, we accept that the depth comes to 20m or more, the soil liquefaction situation will not happen anymore. By the way, fill deposits are most susceptible to liquefaction with thick accumulations of clean, cohesionless sand that are saturated and do not strengthen substantially with depth.

4.2 Seismic Factors

When the earthquake occurs, it will release a lot of energy from the epicenter to the periphery. The energy will transmit to the surrounding rock or soil through the form of seismic waves. In the process of energy passing through the soil mass, the shear stress inside the underground soil is produced. If the site of the soil liquefaction resistance is poor, it may present soil liquefaction phenomenon.

As a general rule, the influence factors of earthquake action on soil liquefaction include earthquake scale, cycle shear stress, duration of earthquake, frequency of earthquake, vibration waveform, and so on. The following sections simply describe the earthquake scale and cycle shear stress.

4.2.1 Magnitude

Because of Chi-Chi Earthquake and Tainan Earthquake caused serious disaster, is the reason to make the important issue of soil liquefaction be noticed by government for the safety of people and property again. The magnitude is based on the energy released by the earthquake to describe the scale of this earthquake. Usually it is expressed as a real number without a unit. Taiwan uses to adopt the Richter magnitude to describe the scale of the earthquake.

When the problem of liquefaction is discussed, the earthquake magnitude can be considered as the energy obtained for the soil. At the same place, the magnitude of the earthquake comes greater, the shaking on the surface becomes more intense and the duration last longer. It may lead to continuously increase in pore water pressure, which increases the chance of liquefaction.

4.2.2 Cycle Shear Stress

When the earthquake occurs, the center of the earthquake propagates energy through the soil or rock formation in the form of seismic waves. In the process of transmission of energy, soil bears the repeated deformation from the shear stress. Once the soil strength is not enough to resist the shear stress, the impact of seismic shear stress is bound to make happen the soil liquefaction phenomenon.

The repeated shear stress is usually considered in the form of seismic acceleration, Chao and Hsu (1997) pointed out that the max. acceleration of the ground surface transmitted by the seismic wave in the Ilan area during the 475-year period was 0.29g. In recent times, referring to the Seismic Design Specifications and Commentary of Buildings modified by Ministry of Interior, the max. earthquake surface level acceleration is recommended to be 0.4SDSg to assess the probability of occurrence of liquefaction.

4.3 Environmental Factors

In addition to soil factors and seismic factors, the impact of the environment factors on the site is also an important consideration. However, the effects of environmental characteristics are likely to be overlooked during the discussion of soil liquefaction. Here we explore the geological and time conditions of environmental factors for soil liquefaction.

4.3.1 Geological Conditions

As the geological conditions of the various regions are different, one can refer to the geological impact of liquefaction, which has been included in the relevant assessment. Within a better geological area, soil has a better resistance to liquefaction; Within a poor geological area, it is easy to have soil liquefaction.

In terms of geological formation, the formation of the surface crust can be divided into two kinds of effects, the endogenetic force (Plate tectonics) and the exogenic force (Sedimentation). The former formed by the rock, arranged closely and bind with each other. The stability of the foundation provides structural support, due to poor water permeability and strong carrying capacity. The latter mainly from the soil layer follow the procedure of the original rock erosion and deposition. The arrangement of soil particles and bearing performance is not as good as rock. Moreover, the thickness of the deposited soil layer to a certain extents, may have a serious effect of the site amplification. Under the action of seismic force, the acceleration and duration will both increase. It can be seen that the resistance to liquefaction on the former is significantly better than the latter.

Considering the site geological composition of hard rock or broken gravel, it has a better bearing capacity. Impermeable or good drainage can make the anti-liquefaction capacity improved. As the geological composition of the site for the smaller soil particles, such as sand and silty sand, the opportunity to liquefaction will greatly increase, especially the weak soil and high groundwater level together. In addition, due to the depth influence, the more close to ground surface of the soil is composed by hard rock or gravel, site anti-liquefaction capacity can be improved. On the contrary, when near ground surface of the soil composed by small soil particles, the site anti-liquefaction capacity may be reduced.

4.3.2 Geological Time

In assessing soil liquefaction potential, time factor can also be one of the important considerations. For conservatism, simplification or other reasons, time factor is often not included in the assessment, though. In general, soil layers are stacked upwards. The soil age of

upper layer is younger, on the contrary is older. In addition, as the soil deposited time getting longer, the upper soil will increase in thickness. The role of overburden stress or inter-particle forces, will lead to more tightly arranged between the soil particles. This phenomenon is like the soil is compaction. Youd and Perkins (1978) mentioned that the longer the soil deposition, the longer the binding time. At this moment the soil density increases, the arrangement of soil particles also be more closely. It can be seen that the site of the soil can improve the liquefaction resistance after a sufficient time to compaction.

5 Up-to-date Liquefaction Study in Langyang Plain

Due to the activity of erosion by Lanyang river between Central Mountain Range and Snowy Mountain Range, the mainstream and tributaries of the Lanyang river are sedimentary in the midstream and downstream area. After a long period of development, a Lanyang alluvial plain is formed. Lanyang plain has several layers of weak and loose soil. Furthermore, Langyang Plain is not only rich in groundwater, but also endangered by frequent earthquakes. Above mentioned characteristics make Lanyang plain to become the area that pretty sensitive to soil liquefaction.

5.1 Evaluation Method Description

When assessing soil liquefaction, soil strength and earthquakes are considered simultaneously. The evaluation items can be divided into Cyclic Resistance Ratio (CRR) and Cyclic Stress Ratio (CSR). It is done by taking its ratio to represent its safety factor for a design earthquake. This safety factor can be used to assess the soil liquefaction potential. If the nature of soil materials cannot resist the disturbance of seismic force, the soil is easy to have the liquefaction failure. At this condition the safety factor is less than 1. If the resistance capacity of soil materials is greater than seismic force, the soil is less prone to liquefaction. At this point the safety factor greater than 1. Additionally the liquefaction potential of the site can be further evaluated, the safety factor of each layer of soil assessment is multiplied by the respective depth weighting functions to get liquefaction potential index (PL). Through the help of liquefaction potential index, the liquefaction situation of the site can be understood comprehensively.

Lanyang plain is liquefied sensitive area. For liquefaction issues, both in government and related institutions have done research so far. As we can see in Figure 2, Ilan area is prone to liquefaction, especially in Ilan City, Luodong Town, Juanwei County, and Wujie County. Highly liquefied potential occupies a considerable proportion all over the Langyang Plain. The primary results of this assessment can be found to have a greater relevance between liquefaction and geological conditions. Normally, alluvial plain area and the mountain area have different liquefaction potential situation. Liquefaction may occur in the deposition of soil along the rivers. Meanwhile the direction of the coastal of the Pacific ocean is likely to have a tendency to high liquefaction development trend.

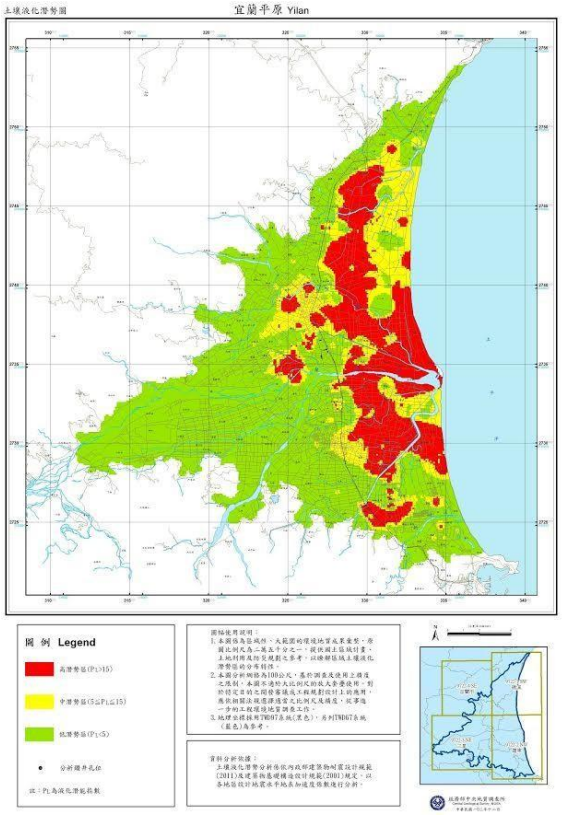

Figure 2. Ilan area primary liquefaction potential map (courtesy of the Central Geological Survey)

On the other hand, the faculty of National Ilan University adopted the use of liquefaction potential indicators to determine soil liquefaction, but also has a lot of research on the regional soil liquefaction primary assessment. The geological conditions of each subdivision were analyzed by geotechnical engineering zoning map of Ilan county to make initial primary evaluation. Soil liquefaction is also divided into three liquefaction levels by those researchers, no liquefaction, moderate liquefaction, and highly liquefied. This liquefaction identification method is followed USGS approach by assessing the Ilan region for the village

level units with the soil data and geotechnical engineering zoning map. Assessment for the situation of Ilan area liquefaction is shown in Figure 3. It can be seen that the results are quite similar to Figure 2. Both figures illustrate the high degree of soil liquefaction warning in the Lanyang alluvial area. Medium and high soil liquefaction significantly increased along the Langyang river. It is noteworthy that the predicted soil liquefaction situation by Ilan University is more conservative than the one provided by government.

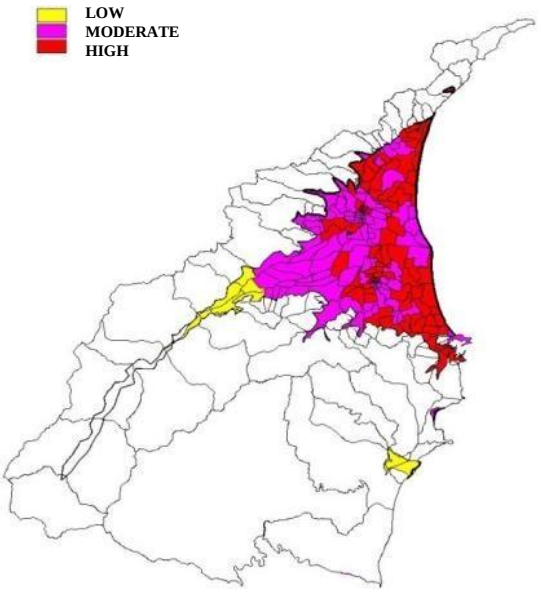

Figure 3. Ilan area preliminary liquefaction potential map (in village level units)

5.2 Upgrade Ilan Area Liquefaction Potential

Although the earthquakes happened in recent years do not produce any serious liquefaction disaster in Ilan area. However, one cannot ignore the facts that Ilan area (especially in Langyang Plain) is no doubt highly liquefied sensitive. Furthermore, there are many seismic belts near Ilan area. The issue of life and property safety of inhabitants is surely a big matter of concern when a more violent or adjacent earthquake happen around Ilan area. The improvement of liquefaction potential accuracy is helpful for the assessment as well as the prevention of soil liquefaction disaster.

In the future study, the proposed supplementary drilling holes plan, which will be distributed of the three townships in Lanyang Plain, is shown in Figure 4. The gray point in the figure is the existing collected drilling holes in the townships. The red point in the figure is the drilling point will be added. Supplementary drilling holes are evenly distributed within the three townships.

Moreover, the boreholes density in the figure can be used to view the supplementary drilling plan. The low density of drilling holes will result in the interpolation less ideal and can lead the predicted result inadequate to reflect the liquefaction situation. Therefore, there is desirable density when drawing liquefaction potential maps. The drilling density in the figure is illustrated with three colors to distinguish them: represents the boreholes density of 4 holes/km^2 or more; represents the boreholes density is above 2 holes/km^2 but less than 4 holes/km^2; represents the boreholes density is less than 2 holes/km^2. According to the figure, the three townships (Ilan City, Luodong Town, and Wujie County) within the drilling density of 4 holes/km^2 above the total area of about 95%, which can be expected to improve the accuracy of liquefaction potential map.

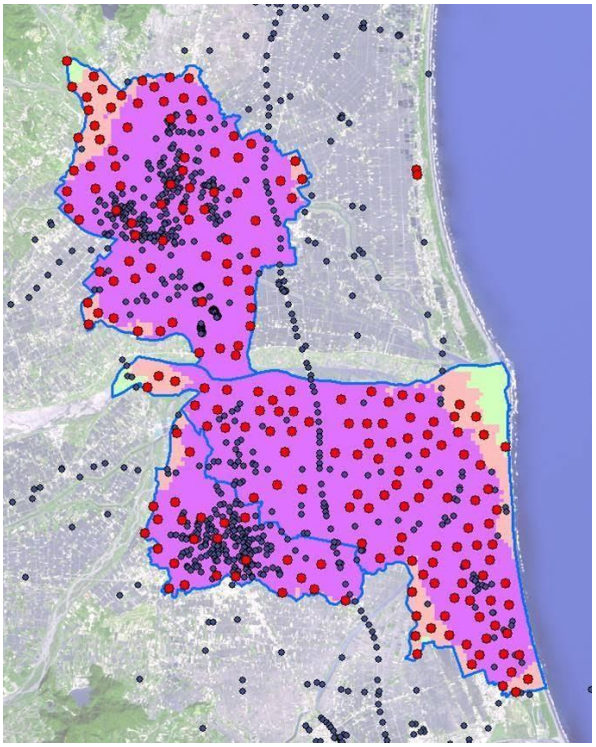

Figure 4. Supplementary drilling holes distribution map

6 Conclusion

There is considerable literature discussion about soil liquefaction potential related issues for Ilan area. Whether it is geotechnical engineering zoning map, characteristics value acceleration, soil liquefaction primary evaluation method, liquefaction initial assessment method, and others, the study for its liquefaction problem has been quite a few in Ilan area. However, Ilan area in the liquefaction assessment has

been classified as liquefaction potential highly sensitive area. With the experience of several major earthquakes, there is no significant liquefaction damage in Ilan area. Therefore, the evaluation of the liquefaction formula and other conditions related to soil liquefaction can be recommended as a future research direction.

The supplementary distribution plan of the boreholes in the three townships of the Ilan area (Ilan City, Luodong Town, and Wujie County) has been proposed as shown in Figure 4. The area of the boreholes with a density of 4 holes/km^2 is about 95% of the total area. The lack portions of density requirement are located on the township borders and the coastline. As a whole, the proposed supplementary drilling holes distribution has reached the project requirements. Follow-up progresses need to wait for the drilling operations to be completed by the end of year 2017.

References

[1] Chao S.J., Hsu H.M., and Hwang H. Soil Liquefaction Potential in Ilan City and Lotung Town, *Taiwan, Journal of GeoEngineering*, 5(1):21-27, 2010.

[2] Chao S.J. and Hwang H. Engineering Properties of Soft Ground Condition of Yilan Area, *Sino-Geotechnics*, 133:19-30, 2012.

[3] Hsu Y.C. *Evaluation of Liquefaction Potential in ILan Area*, Master Thesis, Department of Civil Engineering, National Ilan University, 2007.

[4] Iwasaki T., Arakawa T., and Tokida, K. Simplified Procedures for Assessing Soil Liquefaction During Earthquakes, *Soil Dynamics and Earthquake Engineering Conference*, Southampton, pages 925-939, 1982.

[5] Mogami T. and Kubo K. *The behaviour of sand during vibration*, Proc. 3rd Int. Conf. Soil Mech. and Foundation, 1953.

[6] Seed H.B. and Idriss I.M. Simplified Procedure for Evaluating Soil Liquefaction Potential, *Journal of the Soil Mechanics and Foundations Division*, ASCE, SM9(97):1249-1273, 1971.

[7] Seed H.B. Soil Liquefaction and Cyclic Mobility Evaluation for Level Ground During Earthquake, *Journal of the Geotech Engng Division*, ASCE, GT2(105):201-255, 1979.

[8] Seed H.B., Tokimatsu K., Harder L.F., and Chung R.M. Influence of SPT Procedures in Soil Liquefaction Resistance Evaluation, *Journal of Geotechnical Engineering*, ASCE, 111(12):1425-1445, 1985.

[9] Youd T.L. and Perkins D.M. Mapping Liquefaction Induced Ground Failure Potential, *Journal of the Geotechnical Engineering division*, ASCE, 104(4):433-446, 1978.

Development of the PDC equipped with the blow energy measurement and its application

Kazuaki UEMURA[a] and Shun-ichi SAWADA[b]

[a] Core Laboratory, OYO Corporation, Saitama pref., Japan
[b] Engineering Headquarter, OYO Corporation, Saitama pref., Japan
E-mail: uemura-kazuaki@oyonet.oyo.co.jp, sawada-shun@oyonet.oyo.co.jp

Abstract –

Conventional sounding overestimates the penetration resistance (N_d-value) compared with the SPT-*N* value due to the influence of the friction between the rod and the ground etc.. This overestimation becomes larger when the measurement depth becomes deeper. iPDC, PDC equipped with the blow energy measurement, is a newly developed in-situ sounding device equipped with the pore water pressure and the load measurement at the cone tip. The fines content of the tested soil can be estimated based on the residual value of the excess pore water pressure u_R, and the blow efficiency can be obtained from the load response at the blow. Furthermore, the penetration resistance can be corrected using the blow efficiency. Then, iPDC can evaluate soil liquefaction accurately and fast because it can evaluate the penetration resistance considering the blow efficiency and the fines content at the same time from the in-situ measurement. In this paper, iPDC device is introduced. In addition, the liquefaction analysis based on the Japanese standard (JRA method and T-Y method) and the Taiwanese standard (HBF method) using iPDC result is introduced as an application example.

Keywords –

Liquefaction; Sounding; Blow efficiency

1 Introduction

Piezo Drive Cone (PDC) can evaluate the penetration resistance indicated by a N_d-value for 200mm penetration, and fines content estimated from the pore water pressure at the cone tip (Sawada, 2012).

The penetration device installed to PDC is Swedish ram sounding or Mini ram sounding. These sounding devices usually overestimate the penetration resistance compared with the SPT-*N* value (i.e. N_d-value> SPT-*N* value) due to the influences of friction between the rod and the ground etc.. This overestimation may become larger in deeper ground.

Inteligent Piezo Drive Cone (iPDC), introduced herein, improves N_d-value evaluation by considering the blow energy measured by a load cell at the cone tip.

2 Outview of iPDC

2.1 Test equipment

Figure 1 shows the outview of iPDC equipment, which includes the following main elements.

1. Cone: The penetration cone with a built-in pore water pressure gauge and a load cell.
2. Penetration device: The penetration device by hammer free-fall method (Mini ram sounding, MRS, with 30kg hammer or Swedish ram sounding, SRS, with 63.5kg hammer).
3. Displacement sensor: A displacement sensor to measure penetration displacement.
4. Trigger: A sensor detecting start of penetration.
5. Data logger: An apparatus to record time history data of pore water pressure, load and penetration displacement.

2.2 Energy correction of N_d value

2.2.1 Mesurement example

Figure 2 shows a measurement example. It seems that the peak amplitude of the load in sandy soil is bigger than that in clayey soil. On the other hand, penetration velocity amplitude of the sandy soil is similar to that of the clayey soil.

2.2.2 Blow energy at the cone tip

The blow energy at the cone tip is calculated from Equations (1) and (2) using the load and penetration velocity.

$$E_3 = \int_0^t F(t) \cdot v(t) dt \quad (1)$$

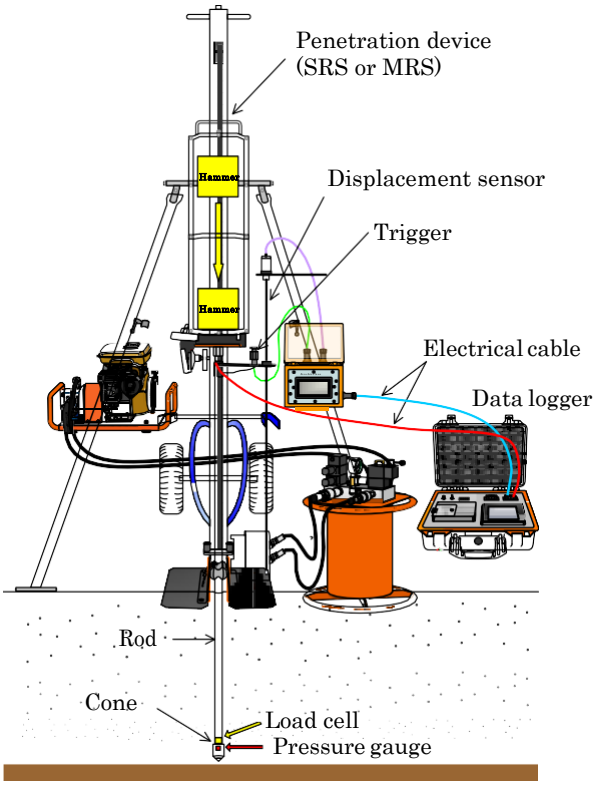

Figure 1. The outview of iPDC equipment

$$v(t) = \frac{dP(t)}{dt} \tag{2}$$

Here, E_3: Blow energy (J)
$F(t)$: Penetration load (N)
$v(t)$: Penetration velocity (m/s)
$P(t)$: Penetration displacement (m)

Since the initial motion of the load at the cone tip is delayed from the displacement measured on the ground, the delay of the initial movement is corrected from the Equations (3) and (4) for the load at the cone tip.

$$F(t) = F(t+\Delta t) \tag{3}$$
$$\Delta t = L_r / V_p \tag{4}$$

Here, Δt: Delay of the initial movement of the load at the cone tip
V_p: P wave velocity of the rod (= 5120m/s)
L_r: Rod length (m)

2.2.3 Energy efficiency at the blow

In the dynamic penetration test by the method of free fall of the hammer, it has been clarified in the past research (Japanese geotechnical society, 2013) that the potential energy of the hammer is partially consumed in the transferred process from the rod head to the rod tip. Figure 3 shows the components of energy consumption in terms of energy efficiency in dynamic penetration test.

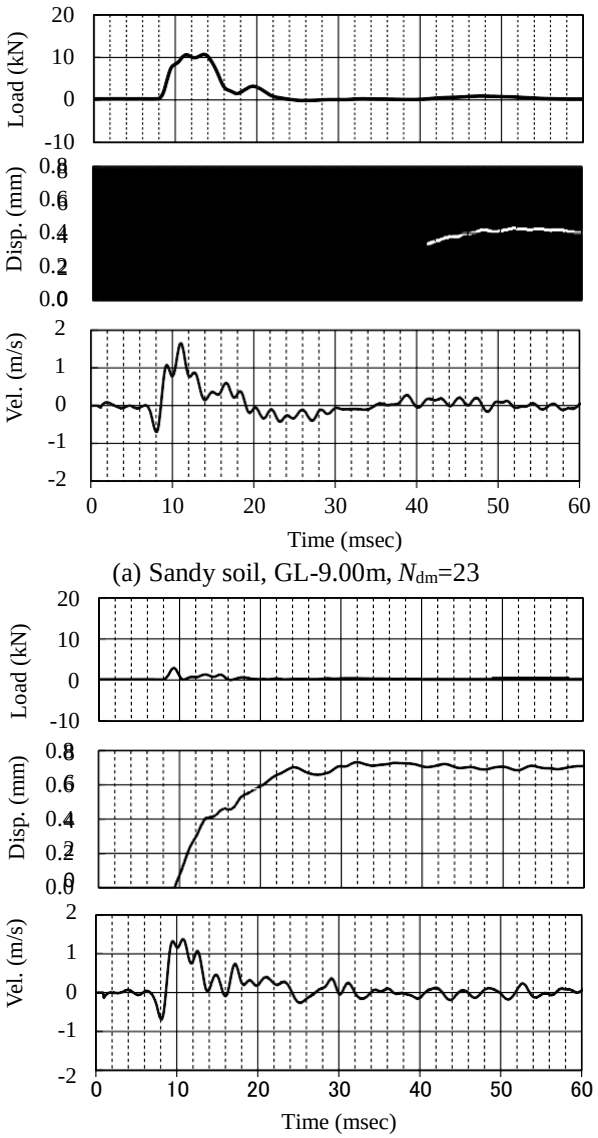

Figure 2. Measurement example

The position energy E^* of the hammer is consumed by friction occurring with the guide rod, lateral vibration of the hammer at the time of blow with the anvil, deflection of the rod and circumferential friction.

The energy efficiency of each components is defined as follow:

Friction efficiency: $e_1 = E_1/E^*$ (5)
Collision efficiency: $e_2 = E_2/E_1$ (6)
Transfer efficiency: $e_3 = E_3/E_2$ (7)
Blow efficiency: $e_1 e_2 = E_2/E^*$ (8)
Total efficiency: $e = e_1 e_2 e_3 = E_3/E^*$ (9)

Here, E^*: Position energy of the hammer (= Mgh)

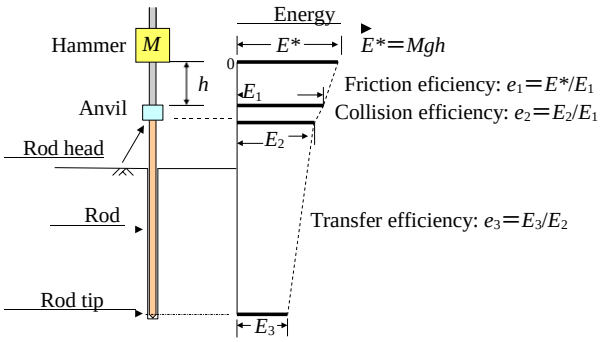

Figure 3. The components of energy consumption in terms of energy in dynamic penetration test

2.2.4 Energy correction of N_d value

The penetration resistance, N_d, was corrected using the total efficiency e obtained from Equation (9).

Equation (10) was used for calibration by penetration resistance energy efficiency (ISSMFE, 1988).

$$N_d = \frac{e_{1iPDC} \cdot e_{2iPDC} \cdot e_{2iPDC}}{e_{1SPT} \cdot e_{2SPT} \cdot e_{3SPT}} (\alpha \cdot N_{dm}) \quad (10)$$

Here, $e_{1iPDC} - e_{3iPDC}$: Energy efficiency of iPDC
$e_{1SPT} - e_{3SPT}$: Energy efficiency of Standard penetration test
α: Energy correcting factor (SRS:1.0, MRS:0.5)
N_{dm}: Number of blow required for 200mm penetration

For estimating the N_d value, energy efficiency of SPT is required. The blow efficient of SPT $e_{1SPT} \cdot e_{2SPT}$ was reported that the average value was 0.59 (Matsumoto et al., 2013).

About the transfer efficiency of SPT e_{3SPT}, it was reported that the blow stress of SPT is hardly attenuated up to the rod length of 25m (Makihara et al., 1996).

Therefore, it is assumed that blow efficiency $e_{1SPT} \cdot e_{2SPT}$ is 0.59 and transfer efficiency e_{3SPT} is 1.0 in this study.

Figure 4 shows the comparison between conventional N_d-value and energy corrected N_d-value. It can be seen that conventional N_d-value apparently overestimated SPT-N from GL-10m. However, energy corrected N_d-value is agree with SPT-N well.

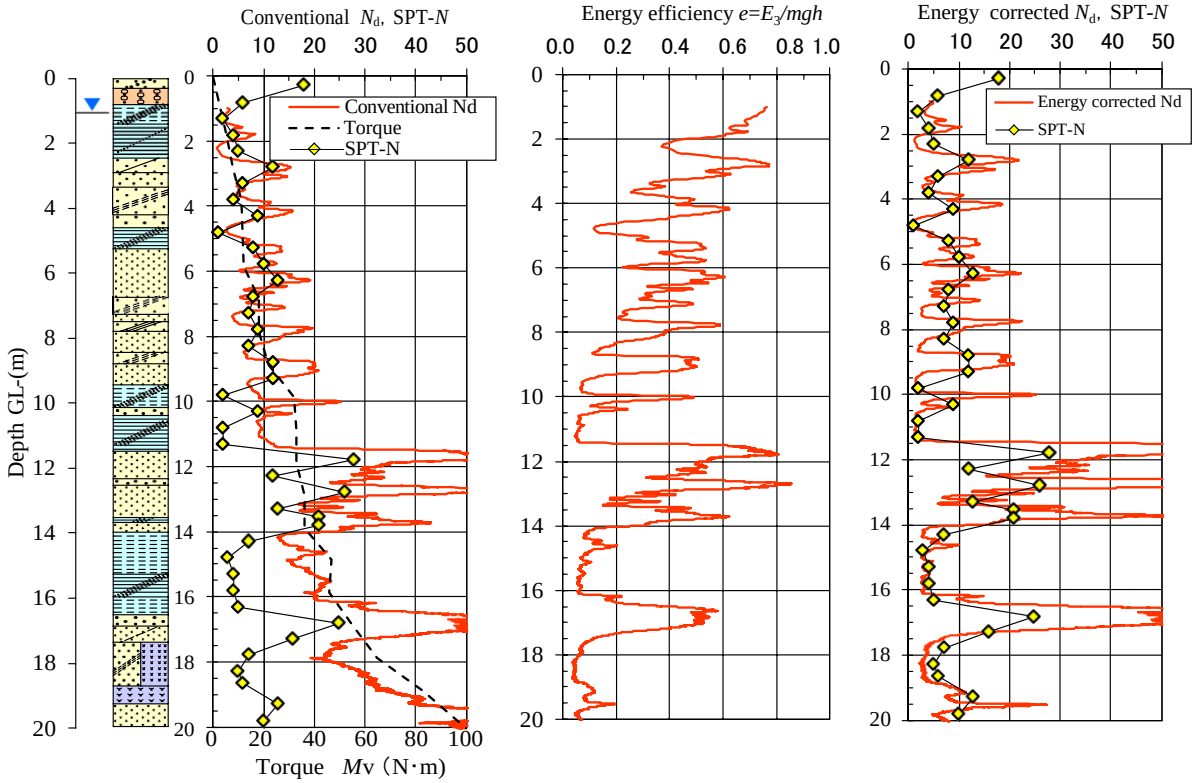

Figure 4.Comparison between conventional N_d-value and energy corrected N_d-value

2.3 Evaluation of fines content

The fines content, F_c, can be estimated as a function of the excess pore water pressure ratio Δu / σ_v' measured by the PDC as shown by the equation (11), which was established based on data of field surveies using PDC and boring as well as the laboratory tests as shown in Figure 5 (Fujii et al., 2013).

$$F_c=20(\Delta u/\sigma_v')+15 \quad (11)$$

Here, F_c: Fines content (%)

Δu: Excess pore water pressure at the blow (kPa)

σ_v': Effective overburden pressure (kPa)

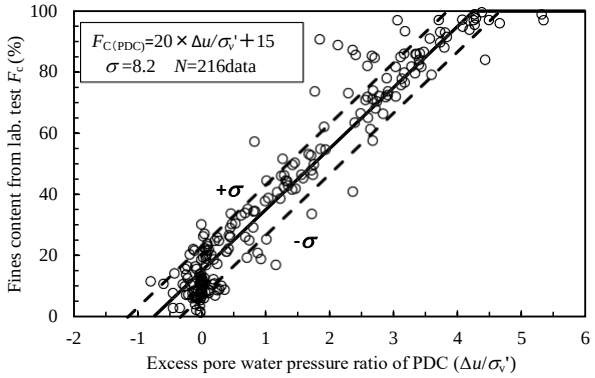

Figure 5. Relationship between excess pore water pressure ratio of PDC and fines content

3 Application example of iPDC for liquefaction analysis

3.1 Evaluation flow of liquefaction analysis using iPDC

Figure 6 shows the evaluation flow of the liquefaction analysis using iPDC. The groundwater level and unit volume weight, γ_t, are required in addition to N_d-value and F_c. The ground water level can be measured after iPDC test. On the other hand, the unit volume weight, γ_t, is assumed tentatively at the beginning. Then, data analysis is executed, and the validity of first assumed γ_t is confirmed by comparison with general value of γ_t corresponding to F_c obtained by analysis.

Then, liquefaction resistance ratio R_L and shear stress ratio L are calculated based on design guidelines of various structures. And the safety factor against liquefaction F_L is obtained.

3.2 Application example(JRA method, T-Y method, HBF method)

Figure 7 – 9 shows application example for liquefaction analysis (Japan Road association method, 2012, T-Y method, 2001, HBF method, 2012). Energy corrected N_d-value is well agree with SPT-N. Also, fines content from iPDC is well agree with laboratory test result.

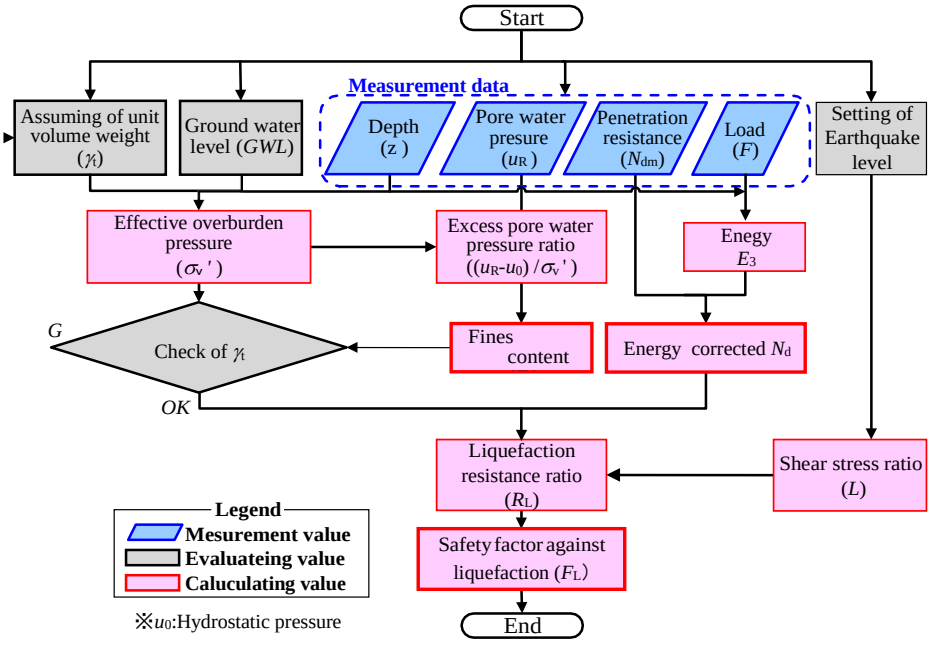

Figure 6. Evaluation flow of liquefaction analysis using iPDC

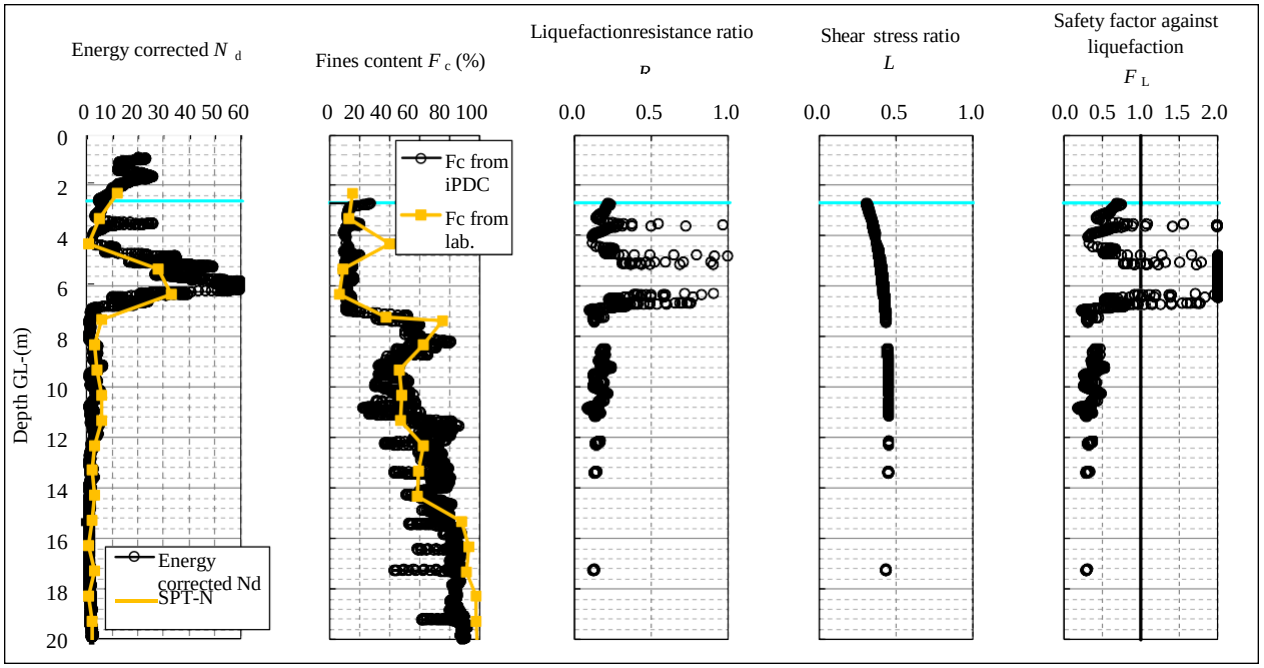

Figure 7. Example of liquefaction analysis (JRA method, k_h=0.35)

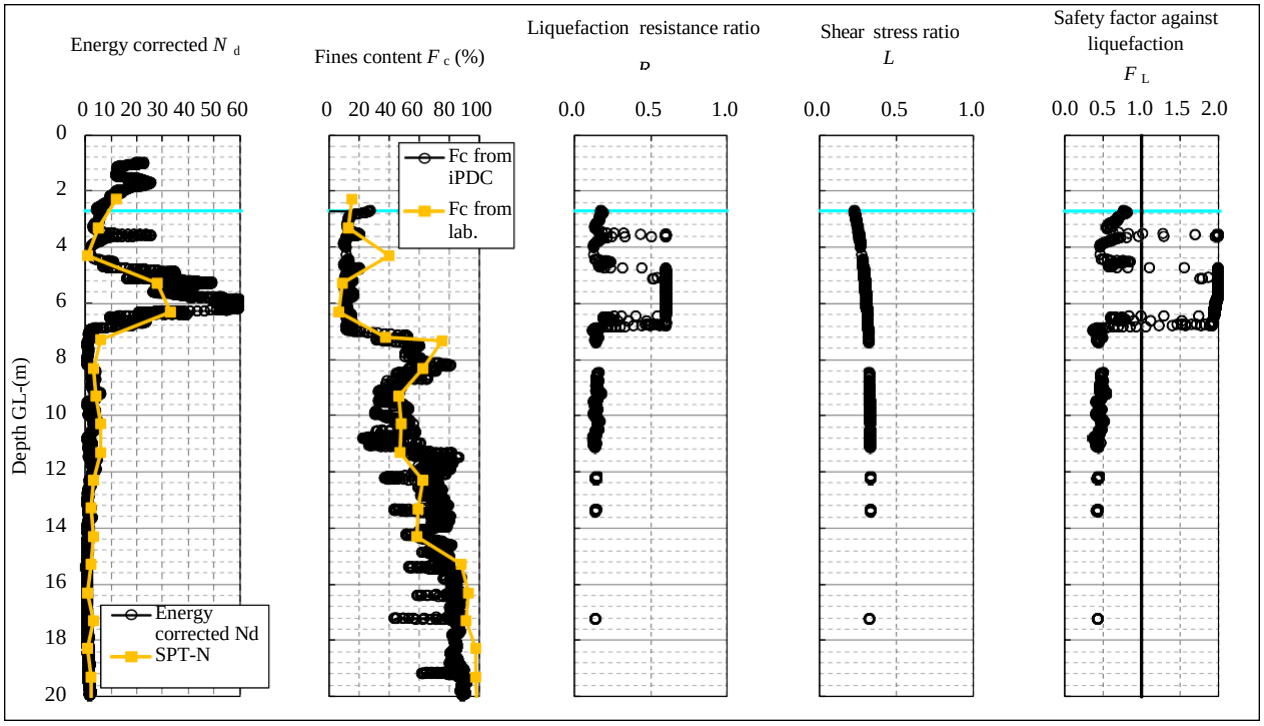

Figure 8. Example of liquefaction analysis (T-Y method, max. acceleration =350gal, M=7.5)

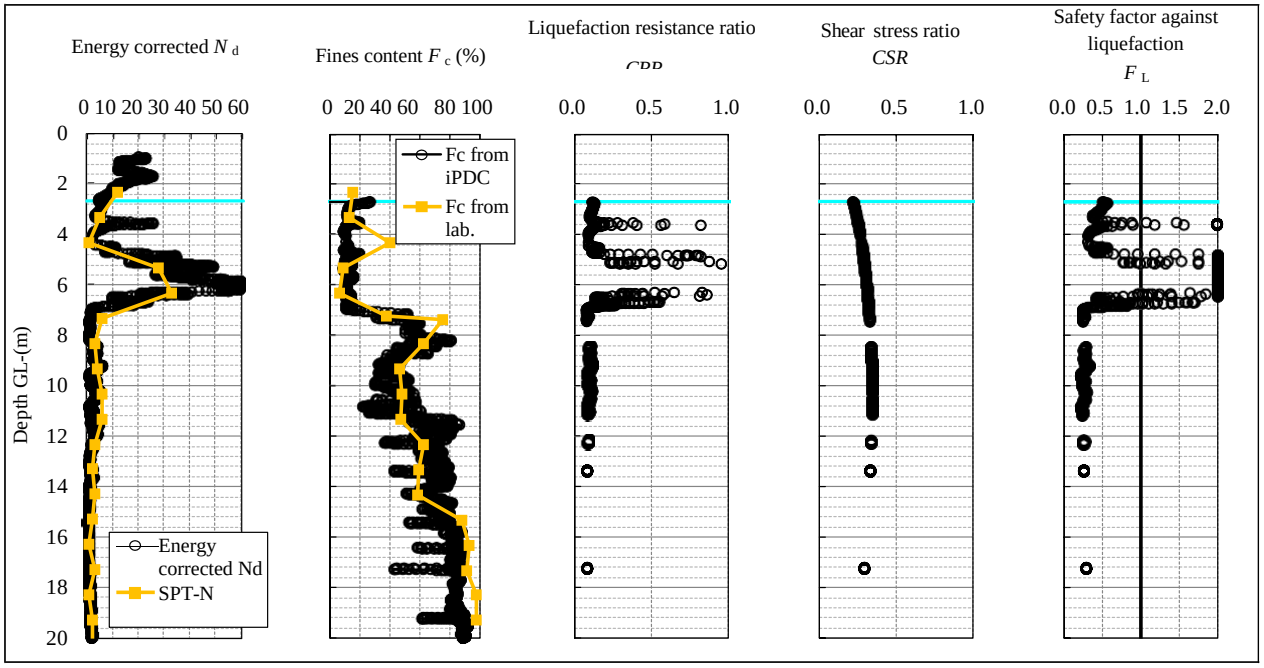

Figure 9. Example of liquefaction analysis (HBF method, max. acceleration=350gal, *M*=7.5)

4 Conclusion

In this study, the newly developed in-situ sounding equipment named intelligent Piezo Drive Cone (iPDC) is introduced. Conclusions are following:

1. iPDC can evaluate N_d-value more accurately by considering energy efficiency. Together with the fines content estimation iPDC can evaluate risk of ground liquefaction accurately, economically and quickly without laboratory test.
2. iPDC result was applicated to several standards for liquefaction analysis.

References

[1] Sawada,S. Use of Piezo Drive Cone for evaluation of subsoil settlement induced by seismic liquefaction, Second International Conference on Performance-based Design Earthquake Geotechnical Engineering, Taormina, Italy, 2012.

[2] ISSMFE Technical Committee on Penetration Testing, SPT Working. International Reference Test Procedure, ISOPT, Balkema, Rotterdam, 1988.

[3] Japanese geotechnical society JAPANESE GEOTECHNICAL SOCIETY STANDARDS Geotechnical and Geoenvironmental Investigation Methods, p.299, 2013. (in Japanese)

[4] Matsumoto,T., Shimono,S., Le Ta PHAN, Ohshima,A., and Nishimura,S. Concurrent ground survey in Moriyama city, Shiga prefecture ,48th Japan National Conference on Geotechnical Engineering ,pp.185-186,2013. (in Japanese)

[5] Makihara,Y. and Kubota,Y. Measurement of impact stress in standard penetration test, 31st Japan National Conference on Geotechnical Engineering, pp.413-414, 1996. (in Japanese)

[6] Fujii,N., Sawada,S., Yoshizawa,D., Nobumoto,M., Uemura,K.,Towhata,I. and Kiku,H. Dynamic Penetration Test with measuring pore water pressure - Part 16 Estimation of Fc value making use of pore water pressure-, 48th Japan National Conference on Geotechnical Engineering ,pp.355-356,2013. (in Japanese)

[7] Japan road association Specifications for highway Bridges Part V: Seismic Design, 2012. (in Japanese)

[8] Architectural institute of Japan Recommendations for Design of Building Foundations, 2001. (in Japanese)

Cavity survey in ground using Piezo Drive Cone

S. Sawada[a], Y. Kakihara[b], K. Uemura[b], M. Hayashi[c], T. Ono[c], Y. Uto[d] and Y. Inoue[d]

[a]Engineering Headquaters, OYO corporation, Japan
[b]Core laboratory, OYO corporation, Japan
[c]Shikoku Branch, OYO corporation, Japan
[d]Kyushu Branch, OYO corporation, Japan

E-mail: sawada-shun@oyonet.oyo.co.jp, kakihara-yoshihi@oyonet.oyo.co.jp, uemura-kazuaki@oyonet.oyo.co.jp, hayashi-mannen@oyonet.oyo.co.jp, ono-tetuji@oyonet.oyo.co.jp, uto-youichi@oyonet.oyo.co.jp, inoue-yumi@oyonet.oyo.co.jp

Abstract -

Piezo Drive Cone (PDC) penetrometer is a newly in-situ sounding equipment which economically evaluates the soil liquefaction of the ground. PDC penetrometer combines dynamic sounding and measurement of excess pore pressure at the cone tip that is generated by the dynamic sounding. Though no sample is retrieved with this penetrometer, fines content F_C of the soil is evaluated based on the residual excess pore water pressure u_R. PDC can not only estimate the soil compaction of the ground with the N_d value but also can evaluate the soil classification using fines content F_C with the residual pore water pressure response.

On the other hand, the peak pore pressure response immediately after the blow is also obtained the compressional wave velocity. It was found that it can be evaluated whether the cavity consist of foreign matter such as air or water. The system of cavity survey was using three kinds of data, for instance, N_d value, peak value immediately after blow and integral value of tremble motion of pore pressure response.

In this report, evaluation results are reported on the ground where the cavities, submerged cavities, soft clayey soil and foamed polystyrene are buried as test specimens.

Keywords -

Cavity, Cone penetration, Pore water pressure, Dynamic penetration

1 Introduction

In the river levee, there is concern that leakage will occur due to the cavitation phenomenon around the river facilities such as sluiceway and conduit pipe caused by long term ground deformation and the function of river levee will deteriorate. Figure 1 shows a schematic diagram of a cavity observed around a typical river facility. The number of river facilities to be constructed in a river levee with long extension is large. Therefore, there is a need for a economical technique to efficiently survey whether or not it exists of cavities around the facilities.

This paper is reported the results of verification experiments of surveying cavities using Piezo Drive Cone [1) ~ 3)] which developed for soil liquefaction assessment.

2 Piezo Drive Cone

Piezo Drive Cone (hereinafter referred to as “PDC”) is the geothchnical investigation equipments for measuring excess pore water pressure generated in the ground at the tip of cone during dynamic penetration, and it has been used to evaluate the liquefaction susceptibility of soils. PDC is a one of the Sounding tool that enables investigation economically and easily in a short time.

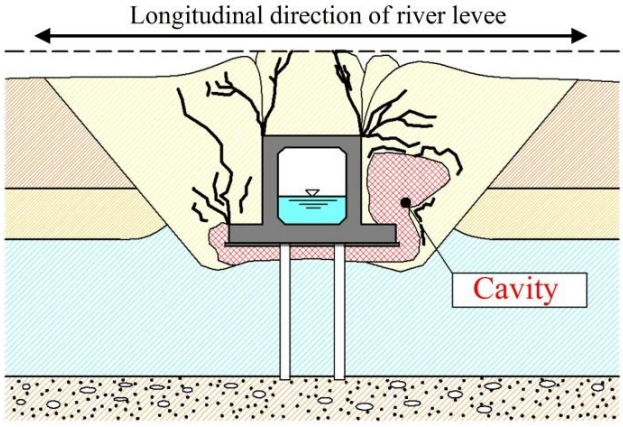

Figure 1. Schematic diagram of cavity in a river levee.

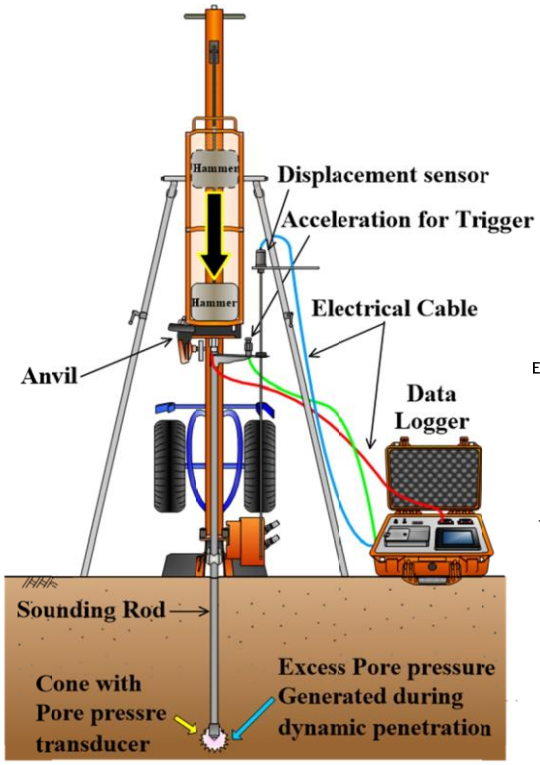

Figure 2. Schematic illustration of Piezo Drive Cone

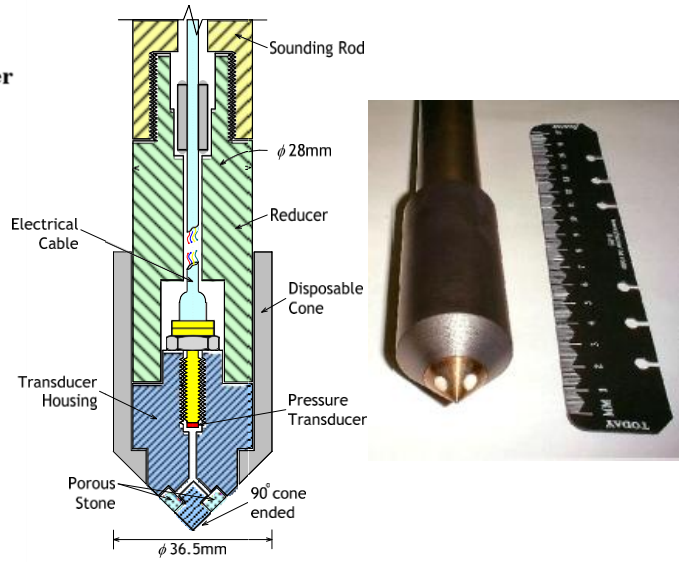

Figure 3. Detailed structure of cone apex with pore pressure transducer.

Figure 2 shows the schematic illustration of the PDC, and Figure 3 shows the detailed structure of the cone apex with pore pressure transducer. Figure 4 shows typical measurement results of the excess pore pressure response during dynamic penetration. In the measurement, the trigger is applied at the timing when the hammer weight hit the anvil for the pre-trigger, and the response value is recorded for each blow. The measuring values are the penetration resistance N_d value that is almost equivalent to the N value of SPT and an excess pore pressure response.

As shown in figure 4, the excess pore pressure responses are used for the cavity survey. The peak value of pore pressure response u_{max} during dynamic penetration indicates whether there is cavity or not existed. And the integral value of the tremble motions of excess pore pressure response ratio $D_{t=15\text{-}25ms}/u_{max}$ immediately after peak response indicates the kind of filling material of cavity.

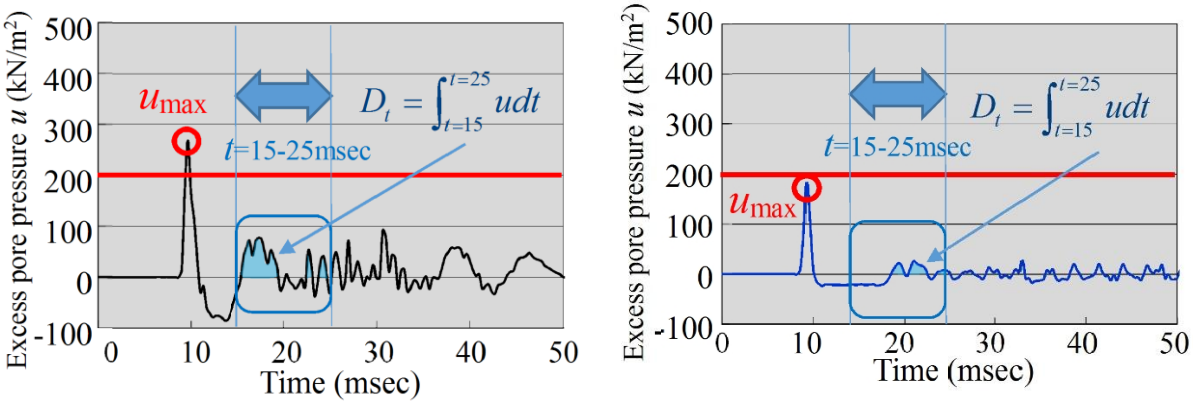

Figure 4. Typical pore pressure responses during dynamic cone penetration.

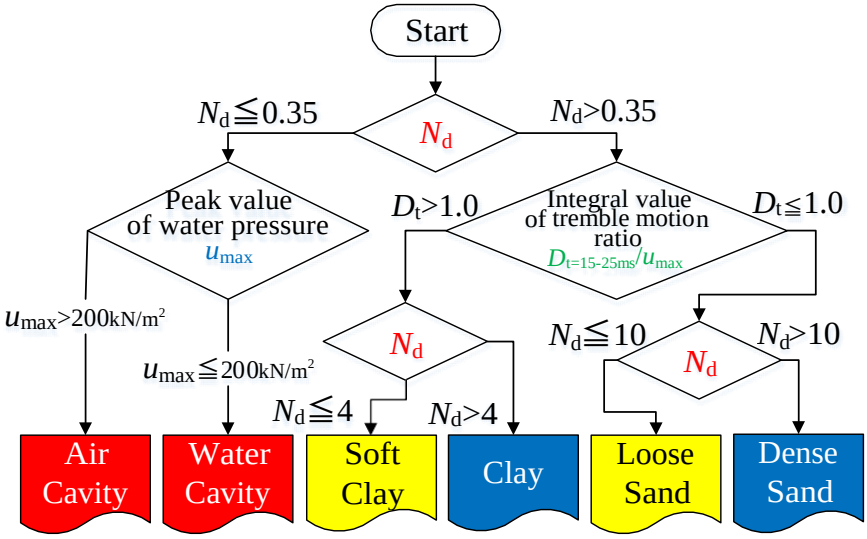

Figure 5. Flow chart to classification of cavity (foreign matter).

The integral value of the tremble motion $D_{t=15-25ms}$ was set to be a positive value of the excess pore pressure response during the 10 milliseconds from 15 to 25 after the pre-trigger at 10 milliseconds.

3 Various types of foreign maters

Cavities formed around the river facilities such as sluiceway and conduit pipe buried in the river levee are caused by water flow in the ground flowing parallel to the facilities. It is presumed that the cavity is formed by suction erosion of fine grains of soil in the levee. Cavities are filled with foreign matters such as cavity, submerged cavity, or filling the soft clay.

4 Principle of cavity survey

As measured by PDC, there is N_d value that indicates the degree of soil compaction of the ground, and as a survey method on the ground around the river facility, it is basically based on this N_d value whether there is cavity or not exsisted. If the existance of cavities can be detected by the N_d value, excess pore pressure response during dynamic penetration will be able to evaluate the kind of foreign matter fill in the cavity. This proposed method is shown in the flowchart of Figure 5.

The evaluation uses the N_d value and the integral value of the tremble motion ratio of the excess pore pressure

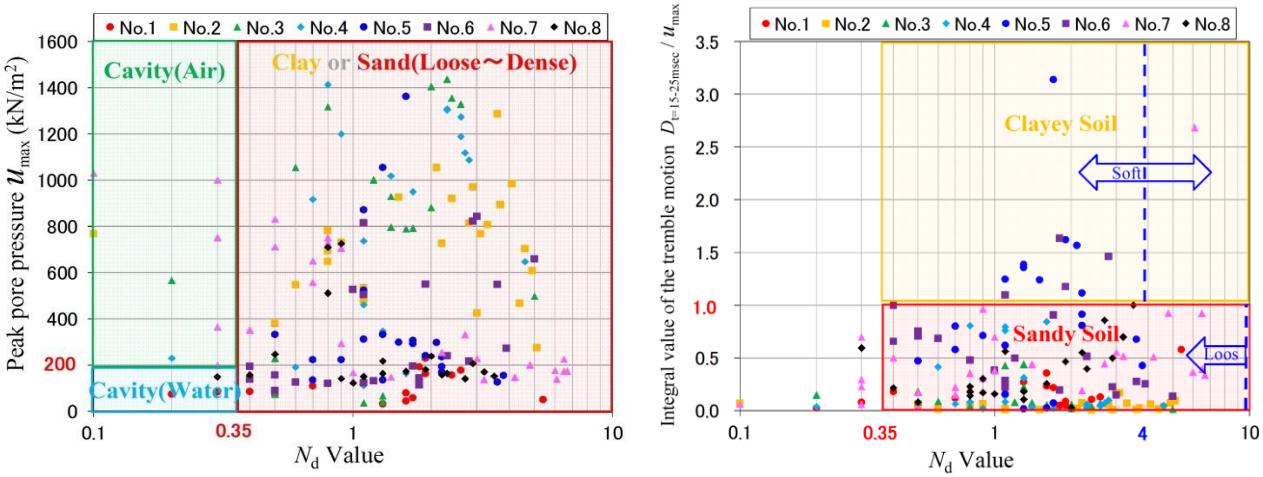

(a) N_d Value and Peak pore pressure (b) N_d Value and Integral value of the tremble motion ratio

Figure 6. Classification charts of the kind of cavity (foreign matter).

response during dynamic penetration normalizing the excess peak pore pressure shown in Figure 6.

5 Outline of verification experiment

The verification experiment was carried out by a blind experiment of class “A”. The class “A” blind test means the test to examine the survey by making an evaluating without disclosing the results. On the other hand, the blind test of the class "C" means a method of evaluating the survey after knowing the result. Initially, only the planar position of artificially embedded foreign matter (for example, air or water cavity) was disclosed, and the verification survey was conducted under conditions that the kind of matter and embedded depth of verification foreign matter were not notified. We reported the results of the blind tests in class "A". However, we could not get a reasonable survey results because the backfilling soil was not successfully well compacted. Therefore, the results of re-evaluated are shown in Figure 7. Therefore, the result shown in Figure 7 is the verification result of the class "C". The number of verification sites were eight. Eight surveys were conducted in only a day.

6 Results evaluated by verification survey

Figure 7 shows the evaluation showing the results of measurement based on the classification flowchart shown in Figure 5 for each point by verification experiment using PDC.

Based on the classification chart, the estimated depth and the estimated layer thickness are indicated together with the type of foreign matter artificially buried, and the correct result known after the measurement is superimposed on the figure.

As a result, it was possible to estimate the types of air, water, clay, etc. including foamed polystyrene buried as artificial foreign matter. In addition, although the depth of the lower end can be roughly estimated with regard to the depth of the foreign matter, the upper end depth was estimated to be shallow in many cases. The reason why the embedding of foreign matter is the work on the previous day, upper part of the extraneous matter is not sufficiently compaction, and it became loose embedding ground.

7 Discussion

Photo 1 shows the situation picture of the ground surface at the time of survey. In addition, the burying situation and depth of specimens (foreign matter) are shown in Figure 8 and Table 1. The excavated condition after the experiment is shown in Photo 2.

Based on the new index called the peak value and integral value of the tremble motion ratio in the excess pore pressure response using PDC, it was possible to identify the foreign matter in the ground by the blind test on Class “C”. Although the accuracy of the depth distribution etc. is still insufficient yet, it was confirmed that there is a possibility of increasing the accuracy by accumulating future data. It is necessary to decide to accumulate data as the threshold adopted as the boundary value this time..

8 Conclusion

By using the simple and economical geothecnical sounding tool called PDC, it was found that existanse or not the foreign matter which is cavity around the facility in the levee can be confirmed.The PDC equipment was originally a geothecnical survey instrument developed for evaluating the liquefaction assessments of soils. The test principle of PDC is to determine the degree of soil compaction of the ground and the classification soil materials. The determination of the soil compaction degree and the identification of soil material are applied to the cavity exploration. For this report, the peak value of pore pressure response and the integral value of the tremble motion of the pore pressure ratio immediately after hitting were used. This is the use of a response value different from the residual pressure response which is used for liquefaction evaluation so far. There is still unknown utility value in pore pressure response. In the future we plan to increase accumulated data further and increase accuracy.

References

[1] Sawada S. Estimation of liquefaction potential using dynamic penetration with pore pressure transducer. In *proceedings of the International Conference on Cyclic Behavior of Soils and Liquefaction Phenomena*, pages 305-312, Bochum, Germany, 2004.

[2] Sawada S. Valuation of strength of soils against liquefaction using Piezo Drive Cone, In *proceedings of the 4th International Conference on Earthquake Geotechnical Engineering*, Paper ID:1146, Thessaloniki, Greece, 2007.

[3] Sawada S. Evaluation of differential settlement following liquefaction using Piezo Drive Cone. In *proceedings of the 17th Inter-national Conference on Geotechnical Engineering*, pages 1064-1067, Al-exandria, Egypt, 2009.

Photo 1. Surface condition of the survey site.

Photo 2. Situation of foreign matters.

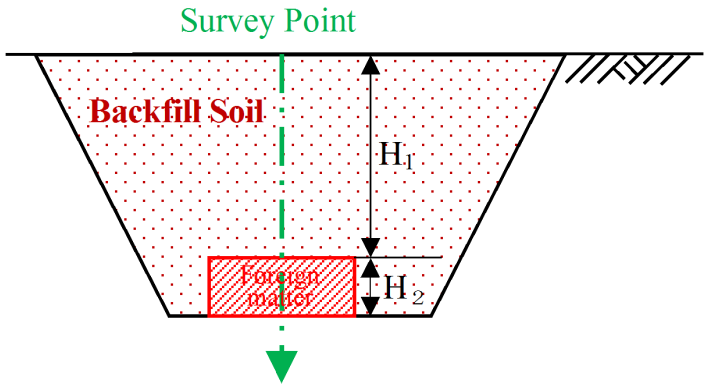

Figure 8. Sectional view of buried foreign matter.

Table 1. Covering and thickness of buried foreign matters.

No.	Covering H_1 (mm)	Thickness H_2 (mm)	Foreign matter
1	1,200	300	Cavity(water)
2	1,200	100	Foam polystyrene
3	1,050	300	Clay
4	1,150	300	Cavity(Air)
5	950	100	Clay
6	1,200	100	Cavity(water)
7	1,200	300	Foam polystyrene
8	1,450	100	Cavity(Air)

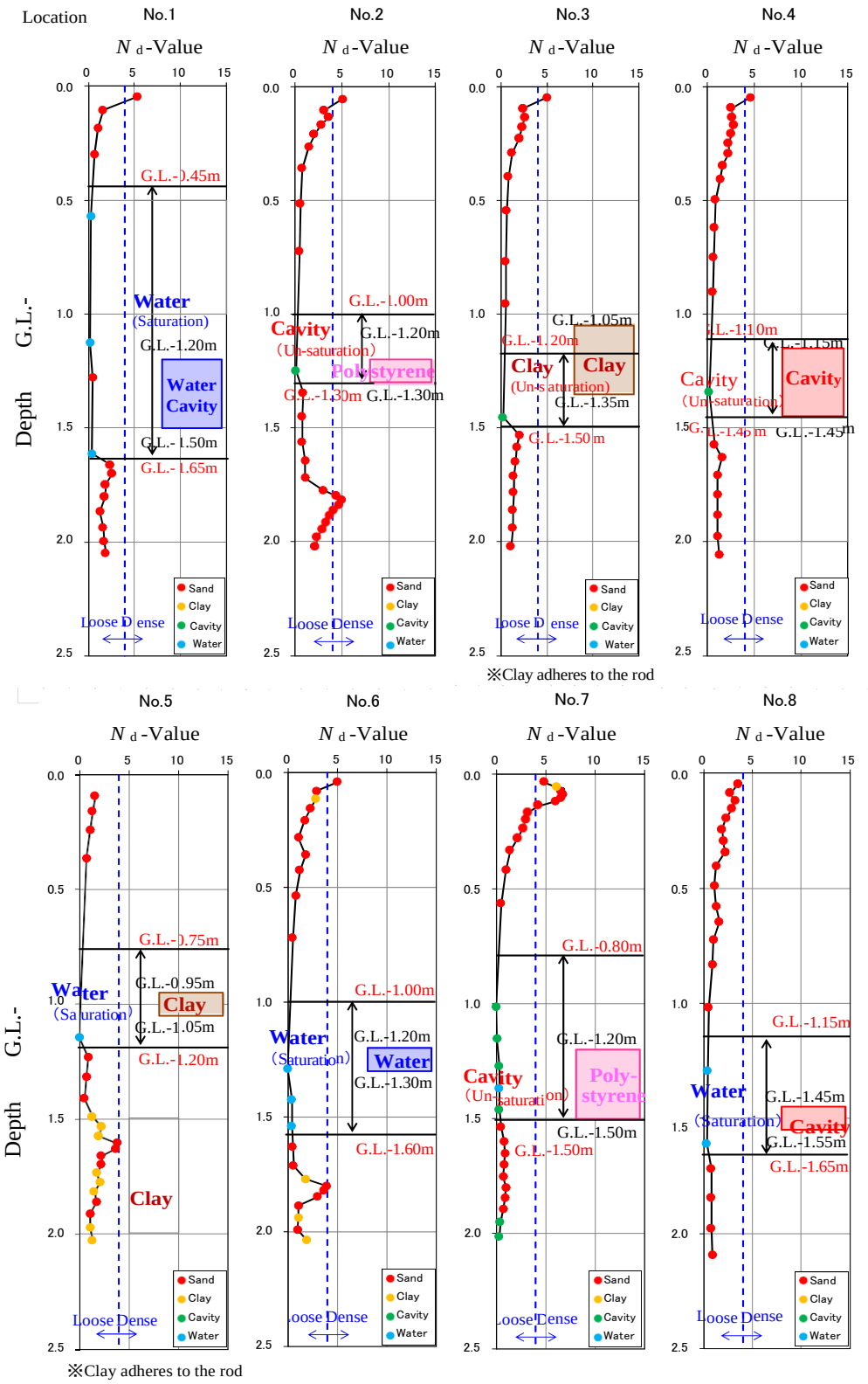

Figure 7. Depth of foreign matters and survey results using PDC.

Planning of Emergency Rescue Routes after Strong Earthquake in Myanmar, A case study of Mandalay

Yu Nandar Hlaing[a] , Koji Ichii[b] and Kyaw Zaya Htun[c]

[a]Graduate school of Engineering, Hiroshima University, Japan
[b]Faculty of Societal Safety Science, Kansai University, Japan
[c]Remote Sensing Department, Mandalay Technological University, Myanmar
E-mail: yunandar.tgyi@gmail.com, ichiik@kansai-u.ac.jp, kyawzaya.htun@gmail.com

Abstract –

Mandalay is the second largest and urbanized city in Myanmar. However, Mandalay is 8km from the east of Sagaing fault, the most active fault in Myanmar. Although many researchers have been developing on the Hazard Map of Mandalay City, this study approaches the emergency evacuation for strong earthquake by adopting a simple model of Sagaing fault considering three scenarios locations with different magnitudes, we estimated the road interval damage based on the exit road network. The estimated damage of road network in different scenarios can be used for the fundamental information for the following rescue routes planning process in Mandalay.

Keywords –

Emergency rescue route; Earthquake ; Hospital; Mandalay; Myammar

1 Introduction

Mandalay is the second largest city of Myanmar and it has more than 1.2 million populations according to 2012 census. It is located quite closed to the active fault, Sagaing fault as shown in Figure 1. It is located nearly 8 km from Mandalay. Mandalay has been historically being suffered many shocks from the Sagaing fault. Moreover, since the level of urban development is relatively proportional to increasing population, severe problems might be encountered when the urbanized regions meet the strong natural disaster like Earthquake. It is a must for a human to have way of escaping and higher level of living chances so that planning and practicing what to do shall be critical considerations.

In this study, we focused on 5 townships of Mandalay and we proposed a framework for an appropriate planning of emergency rescue routes in Mandalay.

There are similar studies on emergency route such as Stepanov and Smith[1], Sakuraba et al.[2], and Ohgai and yamamoto[3]. For example, Stepanov and Smith simulated multi-objective evacuation routing. Sakuraba discussed the road network accessibility problem and work-troops scheduling problem in rehabilitation. Ohgai estimated the non-arrival probability and arrival distance for each building. Although these studies show good challenges on the issue of the emergency route, the complexity of the problem suggests the necessity to propose something simple framework to discuss the goal setting in emergency route planning.

Unlike previous study, authors will only focus on the emergency routes from residents to hospitals without considering material supply from other area. This is due to the emergency routes planning that is the most important and easiest understanding issue to save resident lives. Therefore, we focused on the travel time of all residents in the township to hospitals and propose some index to discuss the performance of emergency routes within townships.

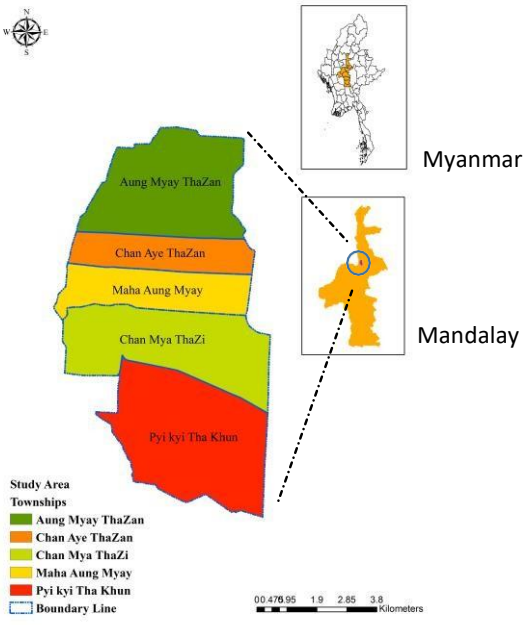

Figure 1. Target-area in Mandalay, Myanmar

2 Emergency Road Networks

2.1 Importance of Emergency Road

Golden hour principal in medicine shows that death rate of injured person increases with time as shown in Fig. 1. For example, in the case of massive bleedings, some people will die after 10 minutes and half of the people will die after 30 minutes. Although the real value of death rate depends on the extent of the injury, the concept of Golden hour principle indicates the importance of emergency route for both the transporting injured person to hospitals and the rescue teams to damaged site. Therefore, planning of emergency route from residents to hospitals could directly decrease the loss of life.

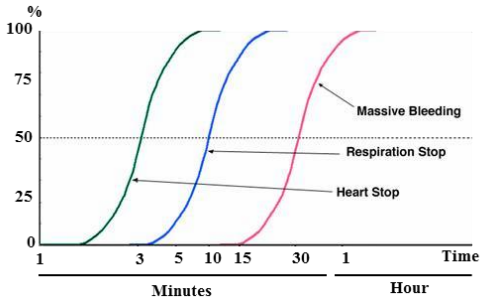

Figure 2. Golden hour principal in medecine[4]

2.2 Performance Index of Rescue Routes

In this study, we focused on the transporting of injured people to hospitals. Although the real transportation ability depends on various factors such as the number of available ambulances and speed limitation of vehicles on the damage road, we assume the injured person will be carried to the rescue route by walking speed (4 km/hour) and injured person will be carried to hospital by vehicle speed (60 km/hour) as shown in Figure 3.

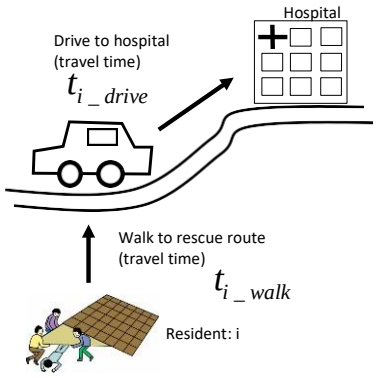

Figure 3. Travel time from a residence to a hospital

Then, as a simple performance index of emergency route, the authors propose average time of transport as follows.

$$T = \sum_i \left(t_{i\_walk} + t_{i\_drive}\right) / N \quad (1)$$

Where, T:average time, i:origin of transport (residential house), t_{i_walk}: travel time from i to rescue route, t_{i_drive}: travel time on rescue routes to hospital, N:total number of origin of transport.

Or, if we define the allowable travel time such as 15 minutes (some people will die in case of massive bleeding) or 30 minutes (50 % of the people will die in case of massive bleeding), we can define the coverage ratio as follows.

$$R = N_a / N_T \quad (2)$$

Where, N_a: Number of residents which can be reached within the allowable travel time, N_t: Number of total residents.With these indexes (total time:T or coverage ratio:R), we can discuss many issues such as the appropriate location of emergency route, priority of road improvement, etc.

In this paper, the authors demonstrate a simple case study on road networks in Mandalay, Myanmar. The research is still in the initial phase and the purpose of the paper is just demonstrate the proposal of the framework on the discussion of the appropriate emergency rescue route.

3 Estimation of Road Network Damage

3.1 Scenario Cases

It is impossible to predict the future earthquake. However, it is a good approach to assume some possible sceneario of future earthquakes. Therefore, the authors assume 3 possible scenarios as the first step of this study to demonstrate the framework. The scenario cases are summarized in Table 1. Case A is the previous earthquake occurred at Sagaing Fault in 2012. At that time, we did not have significant damage in Mandalay. Therefore, the results of Case A is the demonstration for the case without any damage (or the situation before earthquake). Case B is the case with the same magnitude of earthquake occurring at the closest location of Sagaing fault. Although most of time, the fault rupture occurs along the fault in reality, a simple point-source model is considered. Case C is one of the worst case with large magnitude occurring at the same closest point to Mandalay. The locations of the sources in these scenario cases are shown in Figure 4.

Table 1. Scenario cases in this study

Case	Location (Epicenter)	Magnitude
Case A	Same with Shwe bo earthquake (120 km North of Mandalay, depth 14 km)	Same with Shwe bo earthquake (M = 6.8)
Case B	Severe one (Closest point to Mandalay, depth 14 km)	Same with Shwe bo earthquake (M = 6.8)
Case C	Severe one (Closest point to Mandalay, depth 14 km)	Severe one (M = 7.9)

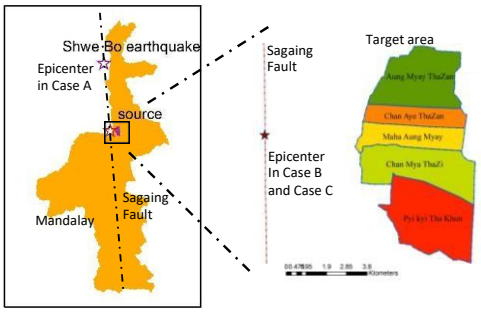

Figure 4. Location of sources in scenario cases

3.2 Major Road Network in Mandalay

In the five targeted townships in Mandalay, there are hundreds of roads with various width. However, in case of earthquake, we can easily imagine that most of the narrow roads cannot be used due to the debris of broken buildings, parked vehicles, etc. Therefore, as the first step of the study, we just focused on the major roads: roads width of 4 m or more. The number of selected roads are 384, as shown in Figure 5.

In Figure 5, present hospitals to be expected to work in case of ocuuring earthquake are also plotted. As shown in Figure 4, major roads connect to these major hospitals. But the problems are, for example, some area in these townships are far from major roads and may have difficulties to keep access to hospitals, and some of these major roads cannot be used in case of earthquake due to the earthquake induced damage.

3.3 Shaking Intensity

We used attenuation relationship[5] to estimate the seismic shakings at all the major roads within the townships. The attenuation relationship is as follows.

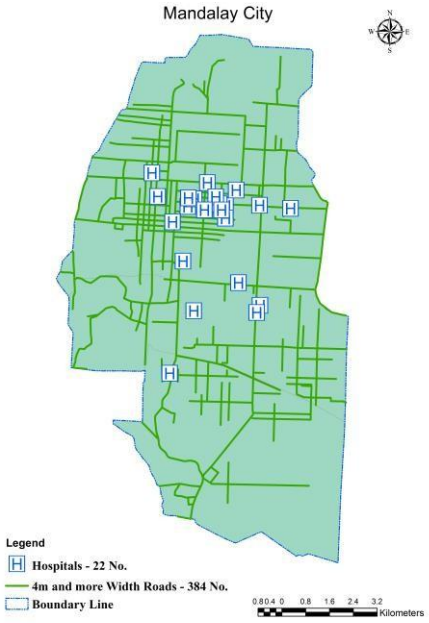

Figure 5. Major road networks in Mandalay and hospitals in the targeted townships

For D ≤ 30km,

$$\text{Log PGV } 600 = 0.65Mw + 0.0024D + d - \log (X+0.0028x\ 10\ 0.5M)-0.002X-1.77 \quad (3)$$

For D > 30 km,

$$\text{Log PGV600} = 0.65Mw + 0.0024D + d + 0.61 \log (1.7D+0.0028 \times 10\ 0.5M) - 1.6 \log (X+0.0028x\ 10\ 0.5M)-0.002X-1.77 \quad (4)$$

Where,

PGV600= peak ground velocity at engineering firm ground(cm/s)

M_w = earthquake moment magnitude

D = fault depth (km)

X = minimum distance (km)

d = constant values (0.05 for intra-plate EQ, 0.00 for crustal EQ, 0.15 for intra-plate EQ)

For simplicity, we neglect the site amplification at the first step and PGV600 is considered as the PGV at the ground surface. At the following step of the study, the authors will classify the soil class and more realistic ground shakings.

The estimated shaking intensity is summarized in Figure 6. Since the distances to the major roads to epicenter are almost uniform, there is no big difference in estimating the shaking intensities in each cases.

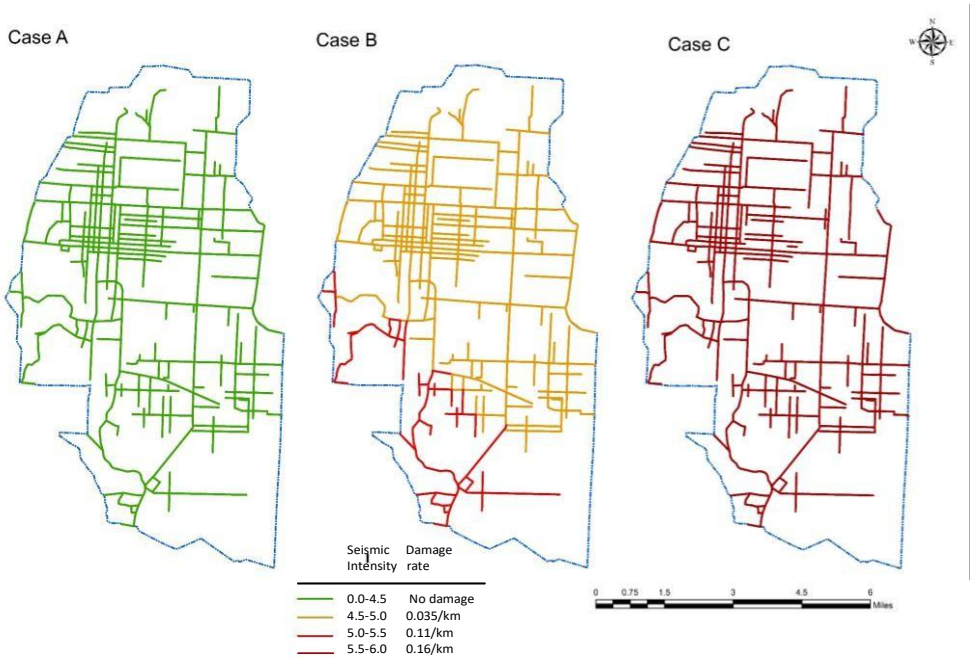

Figure 6. Shaking intensity at road network and estimated damage rate

3.4 Damage to Road

There are several former studies on the road damage caused by seismic shakings. In this study, the authors applied the damage rate evaluation from JMA seismic intensity[6], which is shown in Table 2. This table is often used in seismic damage evaluation by prefectural government in Japan. Calculated PGV is converted to JMA seismic intensity with the following formula[7].

$$I = 2.68 + 1.72 \log PGV \quad (5)$$

Where,
I = JMA earthquake intensity
PGV = peak ground velocity (cm/s)

Table 2. Damage rate estimate of road [6]

Seismic intensity	Damage rate (no./km)	
	National highway controlled by country	Prefecture roads, city roads
I < 4.5	-	-
4.5 ≤ I < 5.0	0.035	0.016
5.0 ≤ I < 5.5	0.11	0.049
5.5 ≤ I < 6.0	0.16	0.071
6.0 ≤ I < 6.5	0.17	0.076
I > 6.5	0.48	0.21

The evaluated damage rate for the target roads in 3 scenarios is also shown in Figure 6. We assume the major roads are same as national highway class so far.

4 Planning of Emergency Routes

4.1 Connectivity to Hospitals

We need to consider the difficulty of usage in damaged roads. Therefore, the authors check the conectivity or roads to hospitals. Since the damage rate in Tabel 2 is the expected number of damages per km, expected damage to all major roads were calculated by the damage rate and length of the roads. Then, the authors assume that there is no connectivity to hospitals if there are 0.5 or more damage on the way to hospitals. It agrees with the 50 % chance of disconnectivity. Figure 8 shows the summary of the major roads connected to hospitals. Since there are no damage in Case A, Case A is classified as the situation before earthquake damage. In Case C, due to the most severe condition of road damage rate, the connectivity is less than Case B and Case A.

4.2 Travel Time Evaluation

We assume the resident habitat uniformly in the targeted townships. Then, we can calculate the total time of transport, considering the origin as residential house and destination as the closest hospitals. However, since the driving time is smaller than walking time, only the walking time to the emergency route is computed at the first step of the study.The calculated walking travel time from residents to major road is in Figure 8. Due to the loss of connectivity in Case C, the walking travel time is larger than that in Case B and Case A.

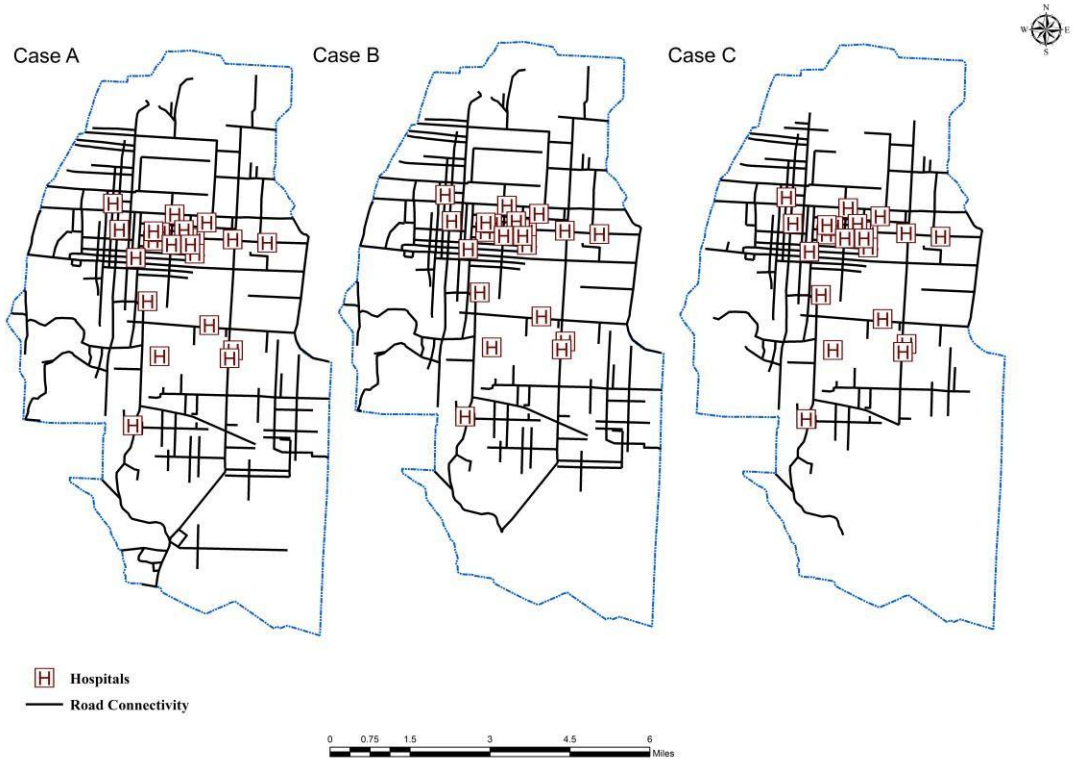

Figure 7. Estimated connectivity of road network in Mandalay

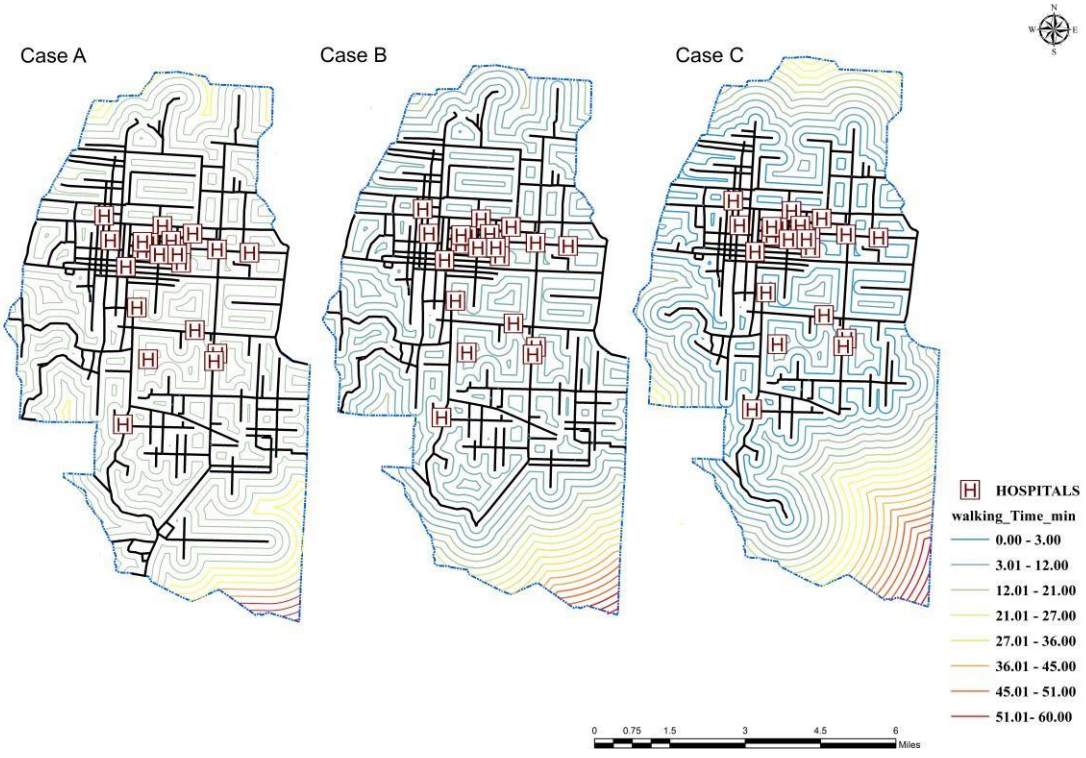

Figure 8. Estimated walking travle time to major road network in Mandalay after earthquake

4.3 Performance Indexes

From the results shown in Figure 8, the authors calculate the performance indexes. Here, not only the total time of transport, average time of transport is also calculated as shown in Table 3. Although, many issues such as shaking amplification, population distribution, driving time to hospitals are remained for future improvement, the quantitative indexes shown in Table 3 can be a good index for the discussion on the planning of emergency rescue route.

Table 3. Performance index

Case	Max time (min)	Average time (min)	Coverage ratio for 10 min.	Coverage ratio for 30 min.
A	36	5.3356	0.8792	0.9866
B	60	7.808	0.8219	0.9315
C	69	7.808	0.8219	0.9315

4.4 Estimation of critical area to be improved

The contour map shown in Figure 8 indicates the critical area. For example, residents in East Chan Aye Thar Zan and Myothit which are shown in Figure 9 need longer time to access the emergency route in case of earthquake. Thus, we can pick up the area to be improved, and set a quantitative target to be improved in urban planning process.

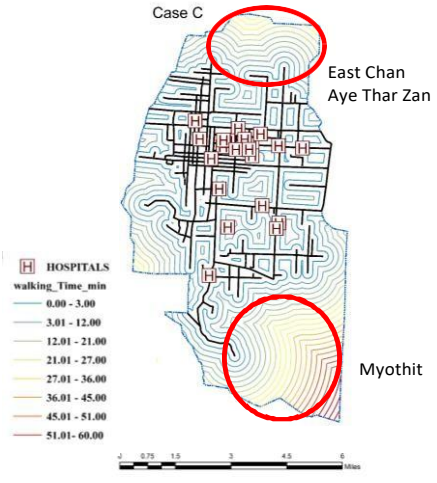

Figure 9. Critical area in Mandalay in terms of access to emergency rescue routes

5 Conclusions

The authors focused on 5 townships of Mandalay and proposed a framework for appropriate planning of emergency rescue routes. Followings are conclusions obtained in this study.

1. As simple quantitative indexes of the performance of emergency rescue route,the average time to reach hospital and coverage ratio with allowable travel time to the hospital are proposed.
2. Major roads with the width of 4 m or more are selected, and the damage rate to these roads in 3 scenario earthquake cases are evaluated.
3. Based on the damage rate of the road network, the connectivity of road to hospitals is evaluated.
4. Assuming the residents distribute uniformly in the targeted area, the walking distance and walking travel time to major road connected to hospitals are evaluated for 3 scenarios.
5. From the walking travel time to major road, it is possible to obtain performance index of road network, and the critical area to be improved can be indicated.

As the future study, the authors will consider the site amplification of ground shaking, population distributions, and the driving travel time on rescue route.

References

[1] Stepanov and Smith. Multi-objective evacuation routing in transportation networks. *European Journal of Operation Research*, 198:435–446, 2009.

[2] Sakuraba et al. Road network emergency accessibility planning after a major earthquake. *EURO Journal on Computational Optimization*, 4:381-402, 2016.

[3] Ohgai and Yamamoto. Evaluating Emergency Response Activities during Earthquakes in Local Cities of Japan. *International review for spatial planning and sustainable development*, Vol.2 No.1:4-22, 2014.

[4] Wikipedia. Golden Hour (medincine). Online : https://en.wikipedia.org/wiki/Golden_hour.

[5] Midorikawa, S., and Y. Ohtake (2002). Attenuation relationships of peak ground acceleration and velocity considering attenuation characteristics for shallow and deep earthquakes, in *Proc. 11th Japan Earthquake Eng. Symposium*, 609–614 (in Japanese with English abstract).

[6] Hiroshima Prefecture. *Earthquake Damage Prediction Survey Report*, 2013. (in Japanese)

[7] Midorikawa et al. Correlation of New J.M.A Instrumental Seismic Intensity with Former J.M.A Seismic Intensity and Ground Motion parameters , *Journal of Regional Safety*,Vol 1:51-56, 1999.

Effects of Spatial Variability of Soil Properties on Liquefaction Behavior of Horizontally Layered Ground

Kyohei Ueda[a], Vargas Tapia Ruben Rodrigo[a] and Susumu Iai[b]

[a]Disaster Prevention Research Institute, Kyoto University, Japan
[b]FLIP Consortium, Japan
E-mail: ueda.kyohei.2v@kyoto-u.ac.jp, vargas.rodrigo.35m@st.kyoto-u.ac.jp, iai.susumu@flip.or.jp

Abstract –

Effective stress analyses based on the finite element method are often used to predict liquefaction occurrence in soil-structure systems during earthquakes. In the analyses, the soil properties are typically specified by using a deterministic model although they intrinsically have spatial variability. In this study, nonlinear finite element analyses are performed to investigate the effects of soil heterogeneity on the liquefaction behavior of stochastically heterogeneous soil deposits through a Monte Carlo simulation approach. The material nonlinearity of soils is expressed by using a strain space multiple mechanism model. In the simulation, the spatial distribution of the SPT N value, shear wave velocity, and internal friction angle is independently taken into account by using sample functions of discretized Gaussian, triangular, and exponential stochastic fields. A series of analyses has revealed that the heterogeneity of the shear wave velocity has no significant effect on the distribution of the computed excess pore water pressure (EPWP), while the maximum value of EPWP ratio is partially influenced and becomes less by considering the spatial variability in the internal friction angle and the N value. In particular, the heterogeneity of the internal friction angle has a possibility to reduce the mean value (i.e. averaging over all the finite elements) of the computed EPWP ratio to about 80% of that in the case of homogeneity.

Keywords –

Liquefaction; Spatial variability; Numerical analysis

1 Introduction

In order to predict liquefaction-induced damage to soil-structure systems during earthquakes, effective stress analyses based on the finite element method are often used as a reliable tool in seismic design. The analyses require accurate modeling of liquefiable ground properties, which greatly affect the numerical results. Although the soil properties are typically specified by using deterministic models in the standard design, they intrinsically have spatial variability even in the case of horizontally layered ground. In addition, the heterogeneity of soil properties has been proven to affect the dynamic behavior of ground and to induce significant variability in the predicted response for some cases [1-3]. However, the effect has not yet been fully studied in a quantitative way.

In this study, two-dimensional nonlinear finite element analyses are carried out to investigate the effects of soil heterogeneity on the liquefaction behavior of stochastically heterogeneous soil deposits subjected to seismic loading. The analyses build on a Monte Carlo simulation approach [1]. The material nonlinearity of soils is expressed by using a strain space multiple mechanism model [4]. Numerical simulation procedures using the model in the finite element program FLIP are described. In the simulation, the spatial distribution of the SPT N_1 value, the shear wave velocity and the internal friction angles in liquefiable deposits are separately taken into account by using sample functions of discretized triangular and exponential stochastic fields [5] in addition to Gaussian one. Simulation results for stochastic models are compared to those for deterministic models by focusing on ground lateral displacement and excess pore water pressure (EPWP) build-up.

2 Modeling of Spatial Variability

The SPT N_1 value, shear wave velocity (V_s), and internal friction angle (ϕ_f) are separately considered as probabilistic variables in this study. That is to say, only one property among them expresses the variability with the other two properties kept constant for simplicity, although correlation between shear wave velocity and friction angle has been pointed out [6]. However, when the SPT N_1 value is considered to be a stochastic field, the other two properties automatically vary following a simplified method for parameter identification of FLIP

program [7] as described later.

For the each soil property, a one-variate, two-dimensional (1V-2D) stochastic field [8], which produces the probability and cumulative distribution functions (PDF, CDF), is required in order to perform stochastic analyses. In this study, nine sample functions of the 1V-2D field are generated for the Monte Carlo simulation by using sample functions of discretized Gaussian, triangular, and exponential stochastic fields. In other words, each type of stochastic fields creates three possible realizations for the each soil property over the analysis domain.

Spectral density functions of the two-dimensional stochastic fields are given as shown in Table 1 by applying the following Wiener-Khinchin theorem [5]

$$S = \frac{1}{(2\pi)^2} \int_{-\infty}^{\infty}\int_{-\infty}^{\infty} R \exp\left\{-i\left(\kappa_x \xi_x + \kappa_y \xi_y\right)\right\} d\xi_x d\xi_y \quad (1)$$

where $R(\xi_x, \xi_y)$ is the correlation function (CF) of the stochastic fields, ξ_x (=x_1-x_2) and ξ_y (=y_1-y_2) is the distance between two points in x and y direction, respectively, and $\boldsymbol{\kappa}=(\kappa_x, \kappa_y)^T$ is a wave number vector.

In Table 1, σ denotes the standard deviation of variational parameters, and d_x, d_y is the correlation distance in x and y direction, respectively. By following Nadim et al. [9], d_x=10.0 m and d_y=1.0 m were used.

A random process following the spectral density functions are derived, by assuming the mean value is zero, as follows [10]:

$$f(x,y) = \sqrt{2}\sum_{k=1}^{K_x}\sum_{l=1}^{K_y} A_{kl} \times\left[\cos\left(\kappa_{xk}x + \kappa_{yl}y + \Phi_{kl}^{(1)}\right) + \cos\left(\kappa_{xk}x - \kappa_{yl}y + \Phi_{kl}^{(2)}\right)\right] \quad (2)$$

$$A_{kl} = \sqrt{2S\left(\kappa_{xk}, \kappa_{yl}\right)\Delta\kappa_x\Delta\kappa_y} \quad (3)$$

where Φ_{kl} is an independent random phase angle distributed with uniformity between 0 and 2π. K_x and K_y is the division number for calculating wave number in x and y direction, respectively, and may be different from the division number of finite element mesh, and $\Delta\boldsymbol{\kappa}=(\Delta\kappa_x, \Delta\kappa_y)^T$ is an incremental vector of wave number. In this study, K_x=K_y=1000 and $\Delta\kappa_x$=$\Delta\kappa_y$=0.01 were used. Finally, the spatial distribution F of stochastic variables representing the heterogeneity of soil properties is given as follows:

$$F(x,y) = f_m + f(x,y) \quad (4)$$

where f_m denotes the trend component and corresponds to the mean value μ. In this study, V_s=128 m/s and ϕ_f=34.1 degree were used as the mean value assuming a loose sandy ground, whose mean value of SPT N_1 value was 5, prone to liquefaction. The coefficient of variation was set to 0.1 for all of the stochastic variables by referring to past studies [9, 11].

As an example of generated stochastic variability of soil properties, a spatial distribution of N_1 value is depicted in Figure 1 for the three types of stochastic fields. The thickness and width of soil stratum is 16 and 32 m, respectively. Figures 2 and 3 show the comparison between targets and realizations with respect to CDFs and CFs, respectively.

Table 1 Spectral density functions of two-dimensional stochastic fields.

Type	Spectral density function $S(\kappa_x, \kappa_y)$
Gaussian	$\frac{\sigma^2 \cdot d_x d_y}{4\pi} \exp\left\{-\left(\frac{d_x^2}{4}\kappa_x^2 + \frac{d_y^2}{4}\kappa_y^2\right)\right\}$
Triangular	$\frac{\sigma^2 \cdot 4\sin^2\left(d_x\kappa_x/2\right)\sin^2\left(d_y\kappa_y/2\right)}{\pi^2 d_x d_y \kappa_x^2 \kappa_y^2}$
Exponential	$\frac{\sigma^2}{(2\pi)^2} \cdot \frac{1}{\left(d_x\kappa_x\right)^2+1} \cdot \frac{2d_x}{\left(d_y\kappa_y\right)^2+1}$

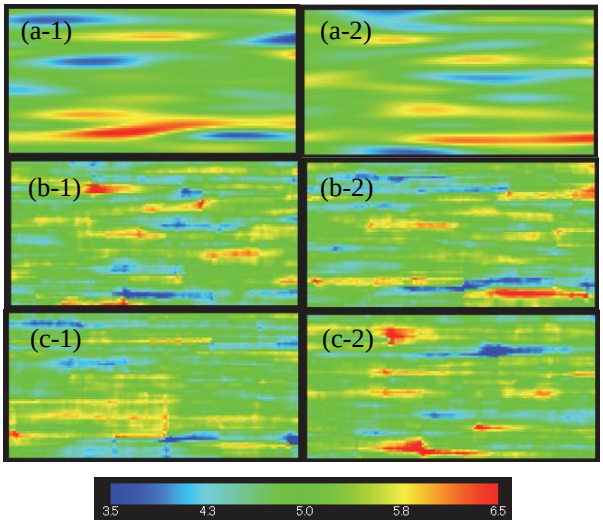

Figure 1. Spatial distribution of SPT N_1 value: (a) Gaussian, (b) Triangular, (c) Exponential

3 Numerical Simulation Procedure

Two dimensional nonlinear seismic response analyses were performed on a liquefiable sand deposit shown in Figure 4 using a finite element program for soil-structure systems (FLIP) [4]. The finite element mesh has 64 rows with 128 columns, for a total of 16,384 elements (including 8,192 pore water elements). The liquefiable deposit, consisting of clean sand, was

modeled using a strain space multiple mechanism model, called multi-spring model [4]. Model parameters (e.g. initial shear modulus, internal friction angle), including dilatancy parameters, were determined by a simplified method for parameter identification of FLIP program [7] based on the SPT N value (=5 in this study) with effective overburden pressure (=98 kPa) and fines content (=0%). Simulated liquefaction resistance curve is shown in Figure 5 with the cases of N=10 and 15.

The boundary conditions were selected to replicate horizontally layered ground. The displacement degrees of freedom on the left side boundary were slaved to move together with their counterparts on the right boundary. Rigid base boundaries were used at the bottom of the model, with the input motion shown in Figure 6. The ground water table was set at the ground surface. In the simulation, stochastic variability for the SPT N_1 value, the shear wave velocity (V_s), and the internal friction angle (ϕ_f) described in the previous section was separately taken into account to investigate the effects of soil heterogeneity on the dynamic response of stochastically heterogeneous liquefiable deposits subjected to seismic loading. The simulation was carried out under undrained condition, and thus the ground settlement after shaking is out of scope.

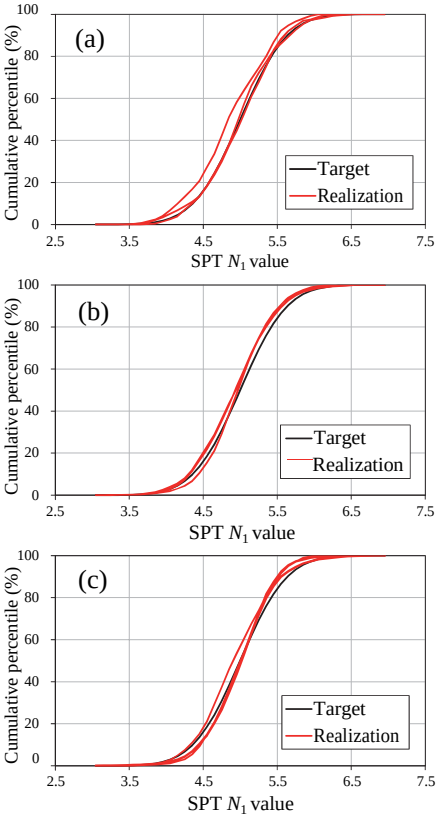

Figure 2. Cumulative distribution function for N_1 value: (a) Gaussian, (b) Triangular, (c) Exponential

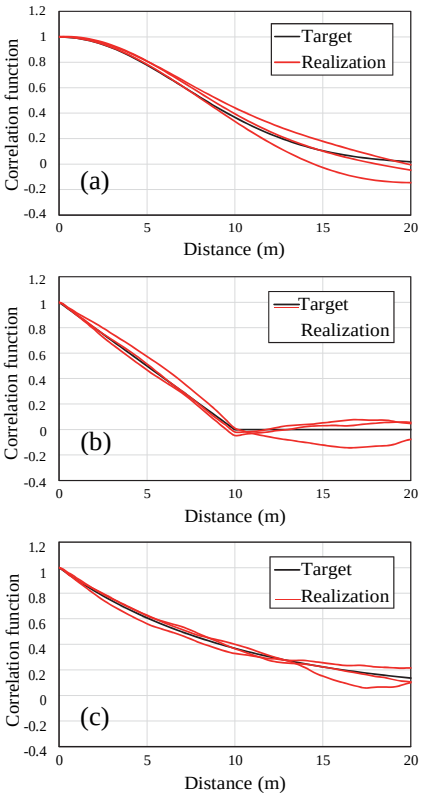

Figure 3. Correlation function for N_1 value: (a) Gaussian, (b) Triangular, (c) Exponential

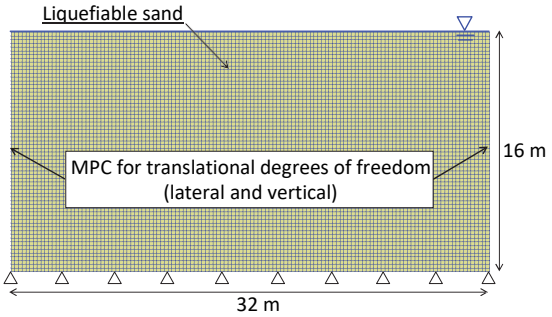

Figure 4. Finite element mesh of horizontally layered liquefiable ground

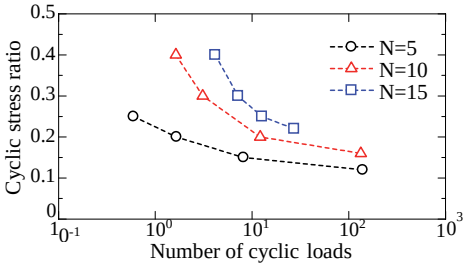

Figure 5. Liquefaction resistance curve

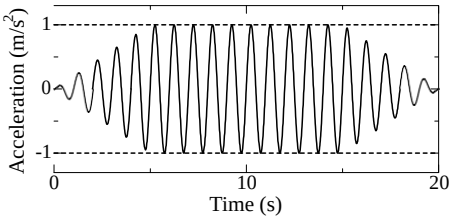

Figure 6. Input ground motion

4 Analysis Results

4.1 Maximum Lateral Displacement

The variations of maximum lateral displacement at the right (or left) boundary with depth are shown in Figure 7 with the results of three uniform (i.e. deterministic) models. For each stochastic model, an averaged profile over three realizations is depicted. When the SPT N_1 value is treated as a stochastic variable (see Figures 1 through 3), a similar profile is obtained regardless of the type of stochastic fields in Figure 7(a). The surface displacements for these stochastic realizations are comparable to that for a uniform model with N_1 value between the 20th and 50th percentiles, although the distribution of shear strains, which can be calculated from the displacement profile, are different between the uniform and stochastic models. The discrepancy may be because the contrast between looser and denser zones is much more vivid in the stochastic models than that in the uniform model (as shown in Figure 10 later) and the difference affects the shear strain distribution. Figure 7(a) also indicates that the 20th percentile (i.e. N_1=3.3) results in smaller surface displacement than the 80th percentile (i.e. N_1=6.6) and the trend is different from the results for a gently sloping ground [3]. This may be because acceleration and shear stress decay, particularly in the shallower layers, due to very severe liquefaction in both ground conditions, but no driving force for lateral movement does not accumulate shear strain in the horizontally layered ground.

When the shear wave velocity and internal friction angle are treated as a stochastic variable, the difference in the type of stochastic fields has no significant effect on the displacement profiles (Figure 7(b)(c)) as is the case with the SPT N_1 value. Figure 7(c) indicates that the surface displacements for the stochastic realizations are closest to that for a uniform model with an internal friction angle of the 20th percentile (ϕ_f=31.2 degree), but the precise representative ϕ_f value is currently hard to be specified because whether less percentile values give a closer profile to the stochastic cases was not tested. The smallest surface displacement for the 20th percentile may be attributed to the reason mentioned in the previous paragraph. In contrast, the 20th percentile

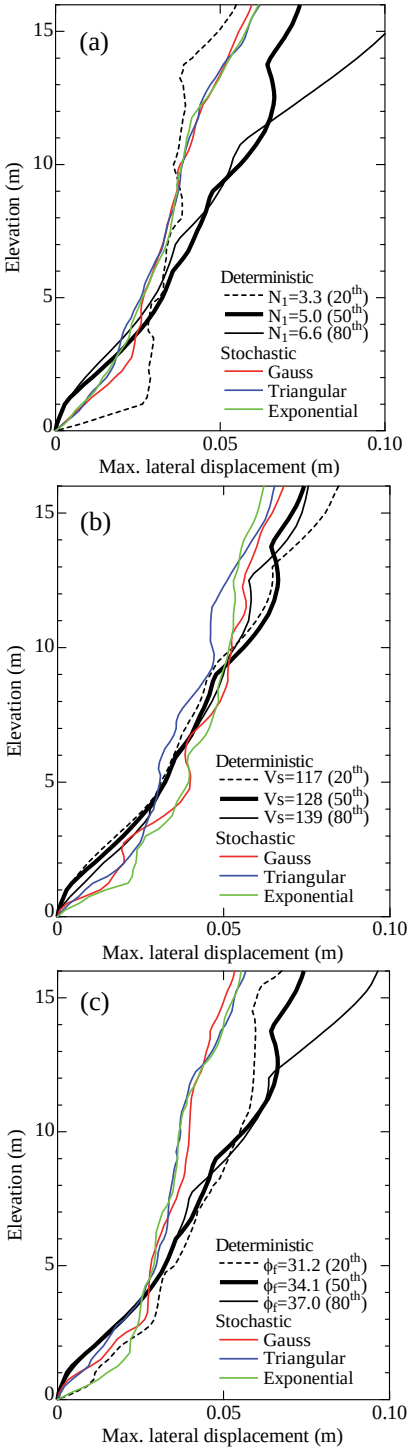

Figure 7. Maximum lateral displacement profiles: the case of variable (a) SPT N_1 value, (b) shear wave velocity, (c) internal friction angle

results in the largest displacement and the 50th percentile is closest to the stochastic models in Figure 7(b) focusing on the ground surface response. However, the discrepancy among the three uniform models is not

so large. Thus, the heterogeneity of shear wave velocity (or initial shear modulus) is considered to have no significant effect on lateral displacement profiles.

4.2 Excess Pore Water Pressure Ratio

Time history of simulated EPWP ratio is shown in Figures 8 and 9. Figure 8 shows the largest value (P_{max}) among 8,192 soil elements while Figure 9 does the average value (P_{ave}) over the elements. The difference between P_{max} and P_{ave} is considered to indicate the magnitude in the simulated EPWP variation in location. When the SPT N_1 value is treated as a stochastic variable, a similar response is observed regardless of the type of stochastic fields in Figures 8(a) and 9(a) as is the case with the lateral displacement profiles. P_{max} eventually results in the same value (=0.97) after shaking between the uniform and stochastic models, although the build-up process is different during shaking (Figure 8(a)). In contrast, a final value of P_{ave} in the stochastic models is about 0.1 smaller than that in the uniform models of the 50th and 80th percentiles (Figure 9(a)). The loosest case (i.e. the 20th percentile) happens to give the same P_{ave} after shaking as the stochastic models, which indicates that the use of over-conservative parameters may lead to an unrealistic prediction of pore water pressure as pointed out [1].

The comparison of the time history of EPWP ratio for stochastic and deterministic models in Figures 8(a) and 9(a) with the lateral displacement profiles in Figure 7 illustrate how the representative N_1 value depends on the specific response measure and the timing of concern. Different from the value (between the 20th and 50th percentiles) for the lateral displacement profiles, the representative N_1 value is almost the same as the mean N_1 value (i.e. the 50th percentile) during and after shaking if P_{max} is the response measure of concern. In contrast, the representative N_1 value varies depending on the timing if P_{ave} is the response measure of concern. More specifically, the representative value is the mean N_1 during shaking, whereas the 20th percentile becomes the representative value after shaking. However, the simulated EPWP ratio using the 20th percentile may be unrealistic, and thus further studies are required.

When the shear wave velocity is treated as a stochastic variable, no significant difference is recognized among the uniform and stochastic models for both P_{max} and P_{ave} shown in Figures 8(b) and 9(b), respectively, as is the case with the lateral displacement profiles (Figure 7(b)). This is because the variation of shear wave velocity (or initial shear modulus) may only affect linear elastic behavior within a small strain range, whereas a strength parameter (e.g. internal friction angle, undrained shear strength at steady state) is thought to exercise a dominant influence on nonlinear behavior such as liquefaction.

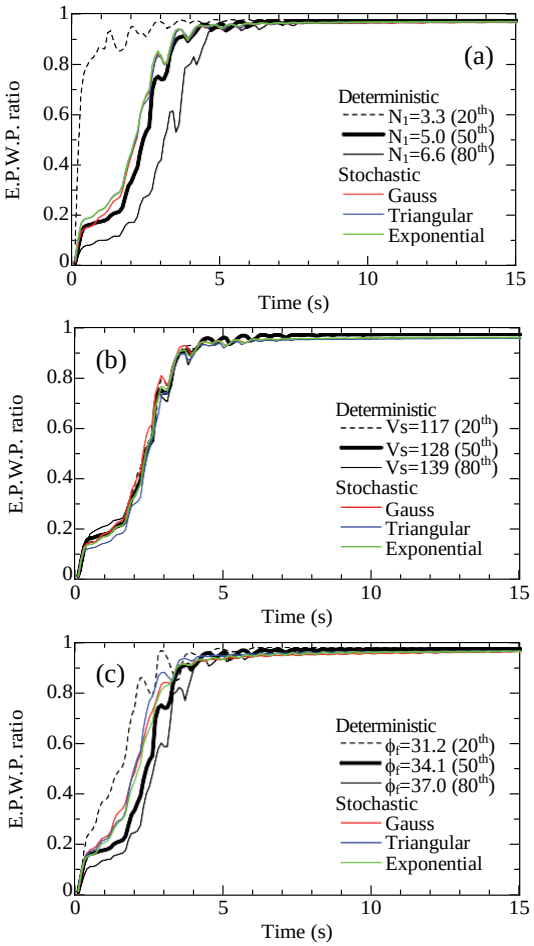

Figure 8. Time history of maximum EPWP ratio: the case of variable (a) SPT N_1 value, (b) shear wave velocity, (c) internal friction angle

Figures 8(c) and 9(c) show the time history of EPWP ratio obtained from stochastic simulations in which the variability of internal friction angle is considered. The overall trend is similar to the case of SPT N_1 value being a stochastic variable (Figures 8(a) and 9(a)), except for the response of the 20th percentile (i.e. N_1=3.3). As described in a former paragraph, the representative ϕ_f value depends on the specific response measure and the timing of concern. The ϕ_f value is between the 20th and 50th percentiles during shaking and almost the same as the mean N_1 value after shaking if P_{max} is the response measure of concern. In contrast, no difference is observed before 3 s among the three uniform and three stochastic models when P_{ave} is the concern. The difference of the uniform and stochastic models becomes larger and larger between 3 and 5 s, and is kept constant after 5 s up to the end of shaking. The final difference of P_{ave} is between 0.15 and 0.2, which are larger than that in the case of SPT N_1 value being a stochastic variable (Figure 9(a)).

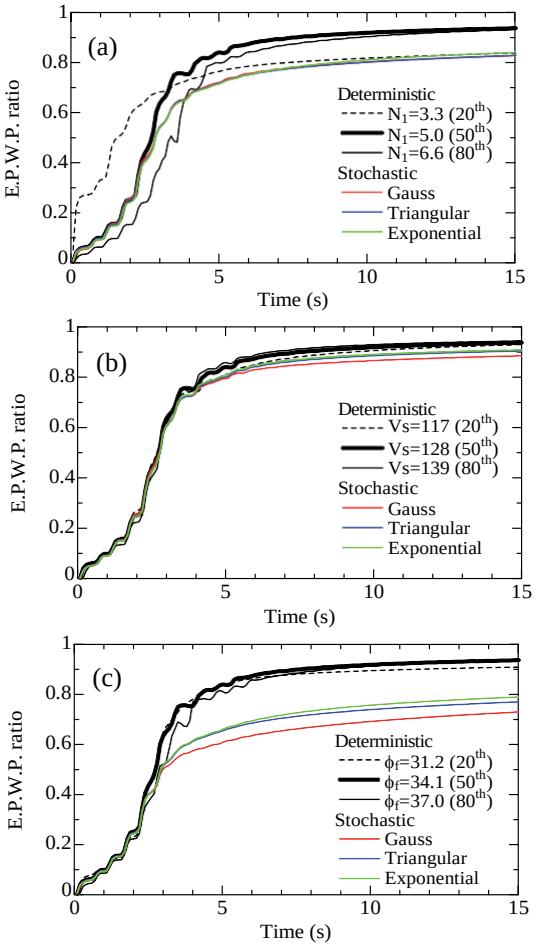

Figure 9. Time history of averaged EPWP ratio: the case of variable (a) SPT N_1 value, (b) shear wave velocity, (c) internal friction angle

Figure 10 shows some examples of the distribution of EPWP ratio after shaking when the SPT N_1 value is treated as a stochastic variable. Each figure corresponds to the counterpart in Figure 1 (e.g. the left figure in Figure 10(a) was obtained using the spatial distribution located on the left side of Figure 1(a)). Whereas uniform distribution of EPWP ratio (=0.97) is obtained except for the bottom layer of the analytical domain in the deterministic model, the contrast between looser (i.e. higher EPWP ratio) and denser zones (i.e. lower EPWP ratio) is clearly recognized in the stochastic models. The difference among the three types of stochastic fields in Figure 10 has a superficial similarity to that of the spatial distribution of SPT N_1 value shown in Figure 1. Therefore, the distribution of EPWP ratio after shaking is considered to be affected by the spatial variability of input soil parameters. The reason EPWP is locally hard to build up in the case of stochastic models may be that liquefaction of locally looser zones (see Figure 1) decreases the amount of shear stress (or acceleration) on surrounding denser zones essentially having higher resistance to liquefaction. This interpretation may hold only in the given condition (e.g. soil properties such as SPT N_1 value, model geometry, input motions), and further studies are required in order to clarify whether deterministic models are more prone to liquefaction than stochastic ones under other conditions.

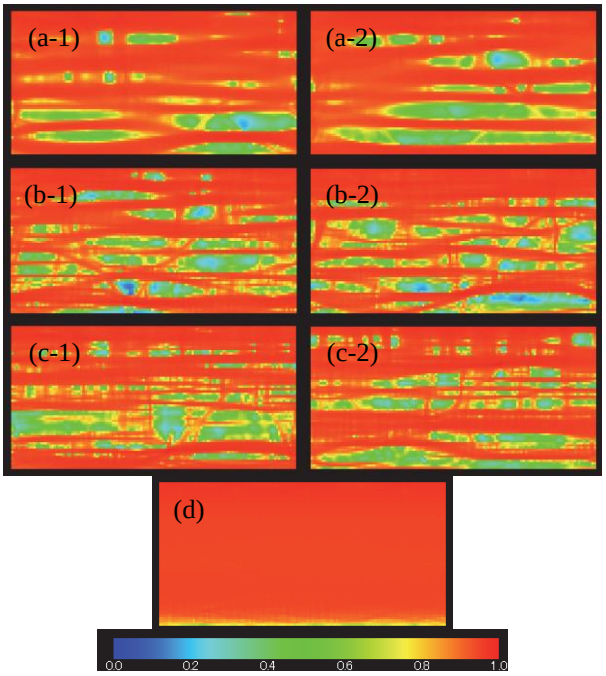

Figure 10. Distribution of EPWP ratio after shaking: (a) Gaussian, (b) Triangular, (c) Exponential, (d) Deterministic model (N_1=5)

4.3 Effect of Mean N_1 Value and Input Motion

The effect of varying the mean SPT N_1 value was investigated by performing simulations with a mean N_1=15 and twice the acceleration amplitude of the input motion shown in Figure 6. The amplitude was determined to obtain almost the same liquefaction condition (i.e. EPWP ratio after shaking) as the case of N_1=5 for deterministic models. In the simulations, the N_1 value was treated as a stochastic variable. The variations of maximum lateral displacement at the right (or left) boundary with depth are shown in Figure 11(a) with the results of three uniform models. Different from Figure 7(a) with a mean N_1=5, the displacement profiles are widely different between the Gaussian and the other two realizations. The reason has not yet been confirmed, but may be related to the fact the level of shear strain (or material nonlinearity), which corresponds to the inclination of the displacement profiles, is two or three times of that shown in Figure 7(a). The surface

displacement for the Gaussian stochastic realization is comparable to that for a uniform model with N_1 value of the 20th percentile as is the case with a mean N_1=5, whereas the displacement for the other stochastic realizations is smaller than that for the three uniform models. At the elevation between 0 and 5 m, no significant difference is recognized among the deterministic and stochastic models.

The time history of maximum EPWP ratio (P_{max}) and average one (P_{ave}) is depicted in Figures 11(b) and (c), respectively. The difference among the stochastic realizations seems slightly larger than that in Figures 8 and 9. As mentioned in the section 4.2, the representative N_1 value depends on the specific response measure and the timing of concern. When P_{max} is the response measure of concern, no difference is observed after 6 s among the three uniform and three stochastic models, although EPWP is more likely to build up in the stochastic models before the time as reported by Popescu et al. [1]. In contrast, if P_{ave} is the response measure of concern, the representative N_1 value is between the 20th and 50th percentiles during the build-up process of EPWP and the final EPWP values for the stochastic models are less than those for the uniform models. Comparison among the stochastic realizations in Figure 11(c) indicates the Gaussian is less prone to the buildup of EPWP all over the analysis domain than the other two stochastic fields in this study, but further studies are required to reach a definitive conclusion.

Figure 12 shows some examples of the distribution of EPWP ratio after shaking. Whereas uniform distribution of EPWP ratio (=0.97) is obtained in the deterministic model, the contrast between looser and denser zones is clearly recognized in the stochastic models as is the case with a mean N_1=5 (Figure 10). The difference among the three types of stochastic fields may be influenced by spatial variability of input N_1 values. As described in the section 4.2, EPWP is locally hard to build up in the stochastic models because liquefaction of locally looser zones may reduce the shear stress that acts on surrounding denser zones. Comparison of Figures 10 and 12 indicates the contrast between looser and denser zones (i.e. the difference between the upper and lower limits of EPWP ratio) is more vivid in Figure 12. This may be because medium dense sand (e.g. N_1=15) has a higher tendency to show positive (or dilative) dilatancy, which results in the local decrease of EPWP, than loose sand (e.g. N_1=5) in which negative (or contractive) dilatancy is dominant.

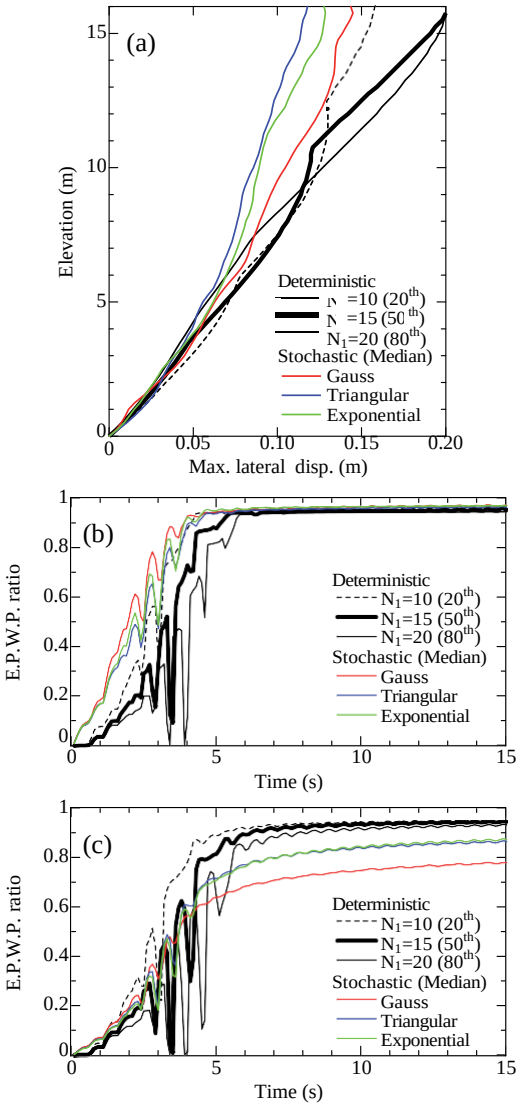

Figure 11. The case of variable SPT N_1 value: (a) Maximum lateral displacement profiles, (b) Time history of maximum EPWP ratio, (c) Time history of averaged EPWP ratio

5 Conclusions

The effects of soil heterogeneity on the liquefaction potential and dynamic response of stochastically heterogeneous soil deposits was examined using two-dimensional nonlinear seismic response analyses. Three types of sample functions (i.e. Gaussian, triangular, and exponential) of discretized stochastic fields were used for the spatial distribution of the SPT N_1 value, shear wave velocity, and internal friction angle in the liquefiable deposits.

The analyses has revealed that the heterogeneity of shear modulus has no significant effect on the maximum lateral displacement profiles and the distribution of EPWP ratio if other parameters remain constant. In contrast, the results were influenced by the spatial variability in SPT N_1 value and internal friction angle. The average value of EPWP ratio for the stochastic models became less than that for the deterministic

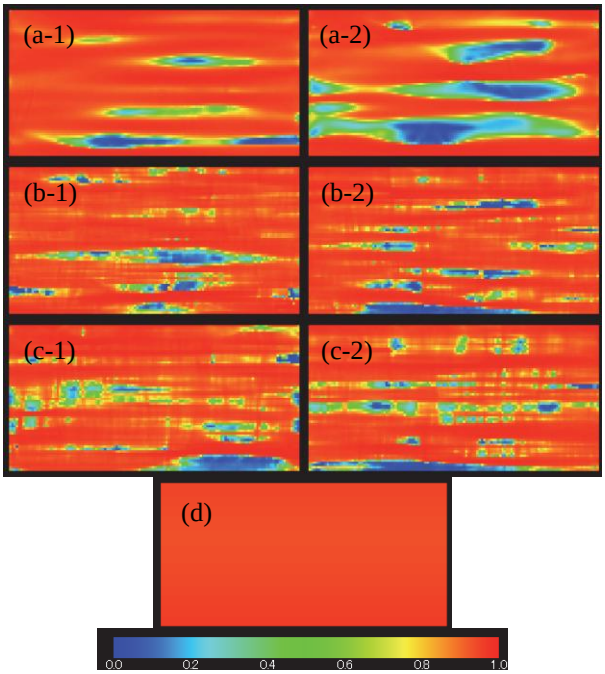

Figure 12. Distribution of EPWP ratio after shaking: (a) Gaussian, (b) Triangular, (c) Exponential, (d) Deterministic model (N_1=15)

models. In particular, the heterogeneity of internal friction angle has been recognized to reduce the average value to about 80% of that in the case of homogeneity. This is because the variation of shear wave velocity may only affect linear elastic behavior, whereas a strength parameter (e.g. internal friction angle) is considered to exercise a dominant influence on nonlinear behavior.

Comparison of the stochastic with deterministic models has illustrated how the representative value depends on the specific response measure and the timing of concern. When SPT N_1 value was treated as a stochastic variable for loose sandy ground, the representative N_1 value to be used in uniform models for estimating the median value of the lateral displacement on the ground surface obtained from stochastic models range from the 20th to 50th percentile. In contrast, the lateral displacements for the stochastic realizations were out of the range when the internal friction angle was treated as a stochastic variable.

With regard to the time history of EPWP ratio, the representative N_1 value was almost the same as a mean N_1 value (i.e. the 50th percentile) for both loose and medium dense sandy ground if the maximum value of EPWP ratio after shaking was the response measure of concern. During shaking, EPWP was more likely to build up in stochastic models in the case of medium dense ground, whereas a mean N_1 value was also applicable for loose ground as the representative value. In contrast, the representative value has been confirmed to vary depending on the timing if the average value of EPWP ratio is the response measure of concern.

The consequence obtained from this study may hold only in the given analytical conditions. Thus, further studies are required in order to clarify whether stochastic models are more prone to liquefaction than deterministic ones under other conditions.

References

[1] Popescu, R., Prevost, J. H. and Deodatis, G. Effects of Spatial Variability on Soil Liquefaction: Some Design Recommendations, *Geotechnique*, 47(5): 1019-1036, 1997.

[2] Popescu, R., Prevost, J. H. and Deodatis, G. 3D Effects in Seismic Liquefaction of Stochastically Variable Soil Deposits, *Geotechnique*, 55(1): 21-31, 2005.

[3] Montgomery, J. and Boulanger, R. W. Effects of Spatial Variability on Liquefaction-Induced Settlement and Lateral Spreading, *Journal of Geotechnical and Geoenvironmental Engineering*, 143(1): 1-15, 2017.

[4] Iai, S., Matsunaga, Y. and Kameoka, T. Space Plasticity Model for Cyclic Mobility, *Soils and Foundations*, 32(2): 1-15, 1992.

[5] Kanda, K. and Motosaka, M. The Evaluation of Effects of Spatial Variability of Soil Properties, Surface Topography and Spatial Coherency of Incident Wave on Ground Motion Amplification – The Case of Kushiro J.M.A. Site–, *J. Struct. Constr. Eng.*, AIJ, 476: 85-94, 1995 (in Japanese).

[6] Andrus, R. D. and Stokoe II, K. H. Liquefaction resistance of soils from shear-wave velocity. *Journal of Geotechnical and Geoenvironmental Engineering*, 126(11): 1015-1025, 2000.

[7] Mikami, T., Ozutsumi, O., Nakahara, T., Iai, S., Ichii, K. and Kawasaki, T. Easy method for setting parameters of liquefaction analysis program FLIP, In *Proceedings of the 46th Japan National Conference on Geotechnical Engineering*, Kobe, Japan: 1627-1628, 2011 (in Japanese).

[8] Vanmarcke, E. *Random Fields*, MIT Press, Cambridge, MA, USA, 1984.

[9] Nadim, F., Einstein, H. and RoBerds, W. Probabilistic Stability Analysis for Individual Slope in Soil and Rock, In *Proceedings of Int. Conf. on Landslide Risk Management*: 63-98, 2005.

[10] Shinozuka, M. and Deodatis, G. Simulation of Multi-dimensional Gaussian Fields by Spectral Representation, *Applied Mechanics Reviews*, ASME, 49(1): 29-53, 1996.

[11] Phoon, K. K. and Kulhawy, F. H. Characterization of Geotechnical Variability, *Canadian Geotechnical Journal*, 36(4): 612-624, 1999.

An Index on the Appropriateness of Parameter Determinatinon for Analysis considering Liquefaction

Koji Ichii[a] and Toshiki Murakami[b]

[a]Faculty of Societal Safety Science, Kansai University, Japan
[b]School of Engineering, Hiroshima University, Japan
E-mail: ichiik@kansai-u.ac.jp, b132690@hiroshima-u.ac.jp

Abstract –

Dynamic analysis to obtain the seismic indeuced deformation on the sturucture is a key issue in performance-based design. The appropriateness of the results from dynamic analysis depends on the appropriateness of the input parameters. In this study, an index to represent the degree of the parameter appropriateness is discussed. Indexes of the similarity in the liquefaction resistance curves both from tests and numerical simulations are proposed. Then, the relationship between the differences in the FEM analysis results with various parameters and the indexes of these various input parameters are examined. The proposed indexes are expected as a reference in the parameter determination in effective stress analysis.

Keywords –

Liquefaction; Effective stress analysis; FEM; Parameter determination; Performance based design;

1 Introduction

Effective stress analysis is a tool of seismic performance verification in PBD. There are various types of constitutive models (i.e., Dafalias and Manzari 2004[1]; Boulanger and Ziotopoulou 2015[2], Fukutake 1990[3]; Iai et al. 2011[4]), and some of them are implemented in 2D or 3D / FEM or FDM. However, one of the difficulties in the application of these advanced models in practice is the parameter identification.

The parameters for the effective stress analysis are often given by the trial-and-error calibration analysis on liquefaction tests. However, the results of these trial-and-error scheme strongly depends on the engineers experiences. Especially, for the dynamic analysis considering liquefaction, the determination of parameters for dilatancy is quite difficult and residual errors in the soil behavior in analysis is inevitable to a certain extent. The difference in determined paramters in analysis by different engineers may result in inconsistency in computed results.

In this paper, a trial to proposed an index to evaluate the appropriateness of determined paramters are conducted. As an example of effective stress analysis program, FLIP ROSE (strain space multi-spring model) (Iai et al., 1992) [5] was used. Several sets of parameters are determined to fit liquefaction test resutls, and the validation of the obtained parameter sets were examined.

2 Model and Paramter Determination

2.1 Strain-space Multi-spring Model

The process of parameter determination can be dependent on the characteristics of constitutive model. Therefore, the authors want to explain the model briefly.

As the first step of the study, a simple strain-space multi-spring model (Iai et al., 1992) [5] was used. Note the model was improved as the latest "Cocktail-glass model" (Iai et al. 2011) [4], however, the old type model was used for the simplicity.

In the strain-space multi-spring model, the pore water pressure generation (decrease in effective stress) is modeled by the accumulated plastic shear work as shown in Figure 1. In Figure 1, liquefaction front parameter S_0 is the index representing the effective stress ratio of the soil under no shear stress condition. Although the stress state of the soil depends on the current shear stress level due to the effect of dilatancy (cyclic mobility), the effective stress in case of no shear stress decreases with increase in plastic shear work. The effective stress reduction rate is controlled by parameter p_1 (for the first half phase) and p_2 (for the last half phase), while overall liquefaction resistance is controlled by w_1. Here, parameter w_1 is given as the total plastic shear work to reach the stress state so that 40 % of initial effective confining stress remained. The parameter S_1 is given as the ultimate value in the model, introducing small value of residual effective stress to maintain the numerical stability even in the extensive liquefaction.

Althogh the concept of these parameters are clear, explicit determination of these parameters are quite difficult. For example, Figure 2 shows the observed effective stress reduction in a cyclic shear test and a calibrated curve by least square method. The fluctuations in pore water pressure ratio are quite large, and it make it difficult to give a unique value for the parameters.

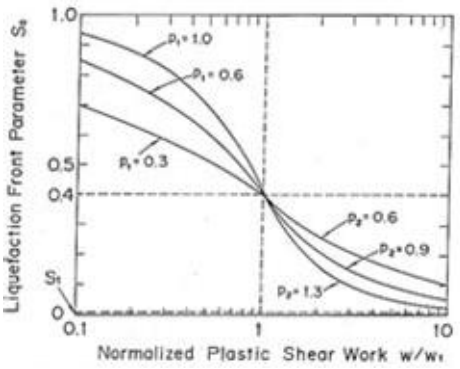

Figure. 1 The reduction of effective stress based on plastic shear work (Iai et al. 1992) [5]

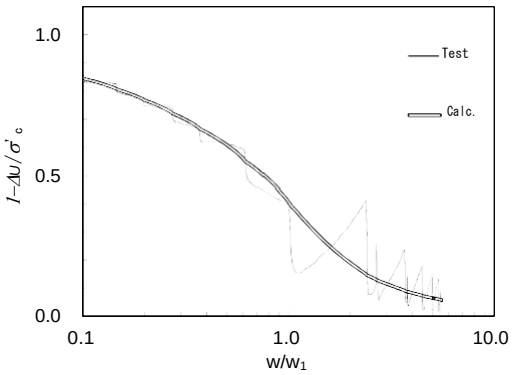

Figure 2. Comparizon of the observed effective stress and the model with calbrated paremeter[6]

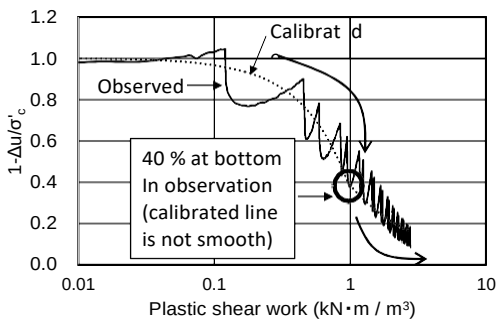

Figure 3. Inappropriate parameters to represent the observed effective stress reduction [6]

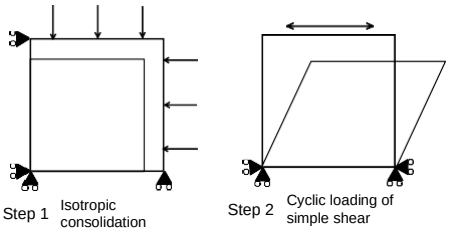

Figure 4. The scheme of element test simulation

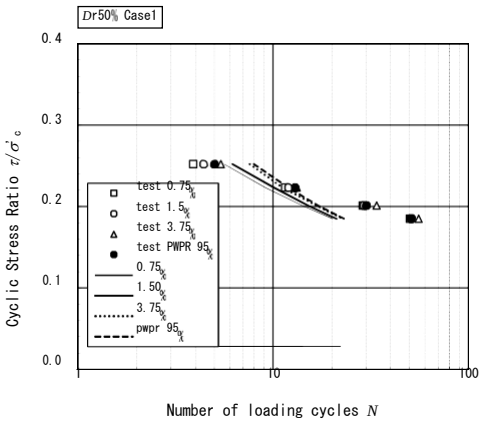

Figure 5. Example of the comparizon of cyclic shear test results and computed results[6]

An Extreme example of parameter determination is shown in Figure 3. Here, w_1 is given as the value corresponding to residual effective stress ratio of 40 %. However, due to the fluctuation of effective stress under shear loading, lines detemined by p_1 and p_2 are inconsistent in slope at the point of connection with the calibrated value of w_1.

Therefore, in many cases, parameters are given to successfully simulate the cyclic shear test result. Figure 4 shows the numerical scheme to conduct the simulation of the cyclic shear test (often called as "the element test simulation"). Although only one element is modeled, the observed behavior of soil specimen under cyclic loading can be simulated. The relationship between the number of loadings and observed shear strain are summarized as the liquefaction resistance curve, and the experiment results and simulation results are carefully compared as shown in Figure 5. Note the various level of strain shall be considered to model the soil behavior appropriately.

Complete agreement of the simulation results and test results is impossible. For example, in Figure 5, liquefaction resistance of CSR of 0.21 to 0.22 may be O.K. However, there is a larger discrepancy on the liquefaction resistance of CSR under 0.21.

2.2 Parameter Calibration Process

In order to minimize the diffrence between computed results and test results, trial-and-error process is often conducted. With a small change of parameters, computed results also change. The parameters are varied to an adequate value so that the tests are successfully simulated. For example, Figure 6 is a summary on how the liquefaction resistance curve can be changed with the variation of parameters.

In this scheme, one of the serious problem in practice is how we can define "successfull" in simulation. The perfect agreement on the computed results and test results is impossible, and the extent of agreement significanlty depends on the engineering judgement in practice.

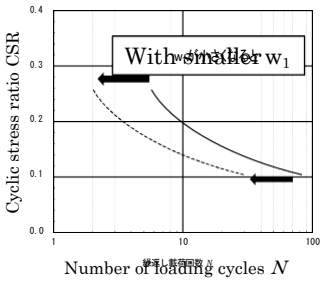

(a) Effect of the paraemter w_1

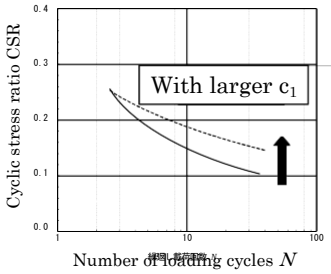

(b) Effect of the paraemter c_1

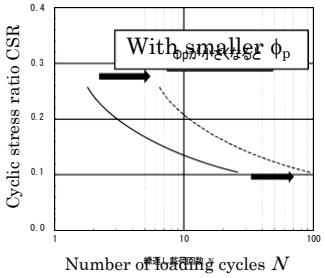

(c) Effect of the paraemter ϕ_p

Figure 6. Typical variation of liquefaction resitance curves by the variation of parameters

3 Proposal of an Index

3.1 Liquefaction Resistance Curves

In order to define the extent of "successful" simulation of element test, the authors propose an index. This index is to express the extent of the agreement between the liquefaction test results and the computed results of the element test. However, the index can be regarded as the index of appropriateness of the determined parameters.

As the first step, we approximate the liquefction test results by using the following formulra [7].

$$R = \frac{a}{\overline{N^c}} + b \tag{1}$$

Here, R: cyclic stress ratio, N: number of loading cycles, a,b,c: constants.

The agreement of the fomura to the liquefaction test results are quite good. Figure 7 shows some example of the approximation lines by Eq.(1) for Toyoura sand with relative density Dr = 50 % and 80 %.

3.2 Fitting Level Index

Once the liqufaction resistance curves are given as continuous formula defined in Eq.(1), we can calcurate the area below the liqefaction resistance curve as shown in Figure 8. We define the area below the target liquefction rsistance curve as A. Note the range of loading cycle numbers are quite important to discuss the index. However, as the first step, we define the area as 10 cycles of loading to 100 cycles of loading.

As same as the area A, we define the area E as the difference of target liquefaction resistance curve and computed liquefaction resistance curve, as shown in Figure 9. The range of loading cycles are same with the area A: 10 to 100 cycles so far. Both positive and negative discrepancy of the 2 curves are considered.

Then, we difine the fitting level index: K as follows.

$$K = (1 - \frac{E}{A}) \times 100 \qquad (\text{For } A > E) \tag{2}$$

$$K = 0 \qquad (\text{For } A < E) \tag{3}$$

In the case of complete agreement of the target curve and computed curve, the index will be 100 (%) since E is 0. To avoid the negative value of the index, if the area A is smaller than the area E, the index is given as 0 (%).

In this definition, the number of loading cycles are plotted in log scale. The index with the combination of curves defined by various strain levels is remained for

future study, and only the curve for 3.75 % strain is forcused in this paper.

Note the appropriate range for the number of loading cycles depends on the characteristics of input motions. However, it is also remained for future study.

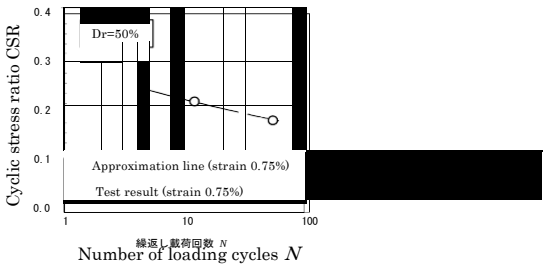

(a) Dr = 50 %, strain level of 0.75 %

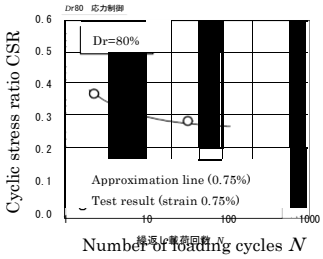

(b) Dr = 80 %, strain level of 0.75 %

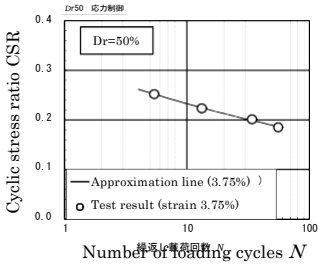

(a) Dr = 50 %, strain level of 3.75 %

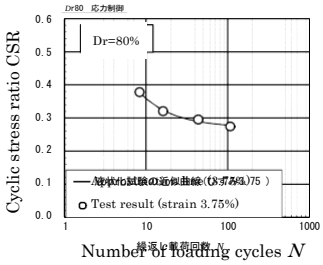

(d) Dr = 80 %, strain level of 3.75 %

Figure 7. Agreement of the approximation lines for the test results

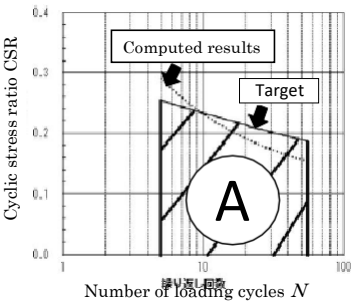

Figure 8. *A* :Area below the target liquefaction resitance curve (10 to 100 cycles)

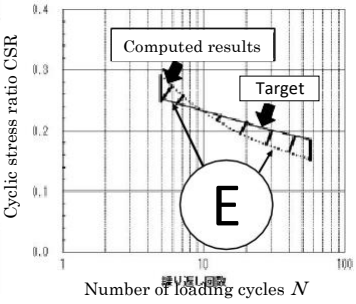

Figure 9. *E* :Area of the difference between the target curve and the computed curve (10 to 100 cycles)

4 Performance of the Proposed Index

4.1 2D FEM Analysis

In practice, the computed results on the earthquake induced defomration is the key issue to be focuesed. Therefore, 2 dimensional FEM is often used.

As one of the most typical practice, computation of a gravity type quay wall (caisson type quay wall) is forcused. Figure 10 is the FEM model and the deformation at the rop of the caisson is focused.

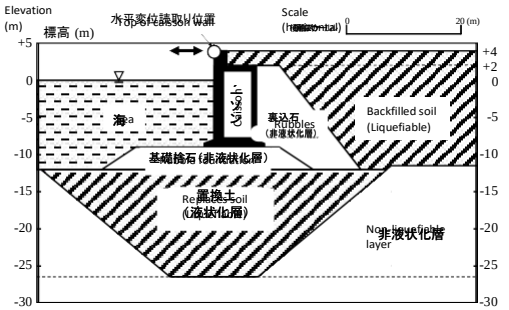

Figure 10. Target gravity-type quay wall

As the liquefiable soil layers, backfilled soil and replaced soil below the caisson wall are focused. The soil conditions of the Toyoura sand of *D*r = 50 % (Case 1) and 80 % (Case 2) are used for the target liquefaction resistance. Various level of paraemter fitting are considered as shown in Table 1. For Case 1, 6 types of parameter sets with 86 to 99 % of fitting level index are prepared. For Case 2, fitting was quite difficult, and 6 types of parameter sets with 0 to 87 % of fitting level index are prepared. Some example of the liquefaction resistance curves are shown in Figure 11.

Table 1. Parameter sets with various level of fitting level indexes

Index(%)	W_1	ϕf	C_1
Case 1			
99	8.43	28.5	2.21
98	6.58	26.7	2.17
95	8.43	28.5	2.04
92	7.52	26.7	1.84
89	12.04	28.5	1.40
86	9.14	26.7	1.32
Case 2			
87	7.56	28.9	2.32
69	4.57	28.0	2.23
58	12.61	28.0	1.42
19	4.57	23.0	1.83
0	11.88	23.0	1.31
0	25.21	28.9	1.29

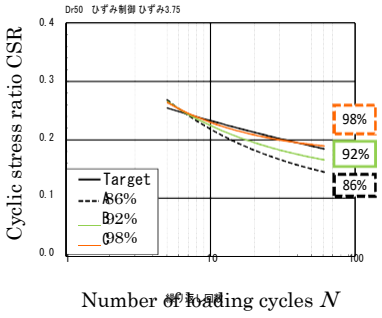

(a) Case 1

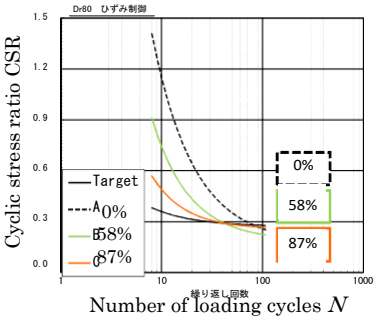

(b) Case 2

Figure 11. Examples of calibrated curves

As the input motion, the Kobe earthquake motion shown in Figure 12 was used. Figure 13 is an example of the computed deformation of the quay wall. The deformation pattern agree with the observation at 1995 Kobe earthquake disaster.

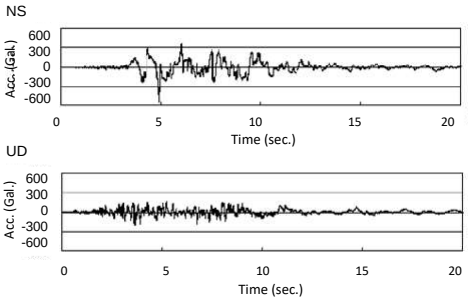

Figure 12. Input motions (NS and UD direction)

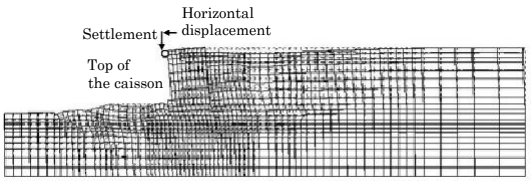

Figure 13. Example of the computed deformation

4.2 Relationship between the Index and 2D FEM Results

Since we assume the liquefable soil layer as Toyoura sand of *D*r = 50 % or 80 %, there are no exact solution. Therefore, the authors assumes the computed result of the case with highest value of the proposed index as the most probable value d_m. Then, the error e at the case i can be defined as,

$$e = \left| \frac{d_m - d_i}{d_m} \right| \times 100 \tag{4}$$

where, d_i is the deformation at case i.

The relationship between the value of the proposed index and errors in the computed results are summarized in Figures 14 and 15. Figure 14 shows the results of all cases, and Figure 15 shows the close up on the cases with higher index values.

As shown in Figure 14, even for some cases with low index values, the observed errors are only around 10 %. This results implies the accuracy is not strongly dependent on the liquefaction resistance defined at the 3.75 % strain. However, the objective of the study is to define the extent of "successful" simulation of element test, and the discussion on the cases with low agreement

of the target curve is out of the scope. In other word, even if the error is quite small with the cases with low value of the proposed index, it is just luckey and no necessary to discuss in detail. The author believe it is important to focus on the close up of the results shown in Figure 15.

In figure 15, with increase of the index, the observed error decrease. The observed tendency is not so different in horizontal displacement and settlement. Thus, we can discuss the minimum level of the agreement to be called "successful" from the proposed index. For example, if the requested accuracy of the computation is less than 10 % of errors, the agreement of the element test results shall be more than 94 % of the proposed index to be called as "successful" simulation of element test.

Thus, the proposed index is quite usuful to discuss the appropriate level of the parameter determination. However, this estimation result just come from this limited case, and more case studies are necesary to propose accurate value to discuss the "successful" level.

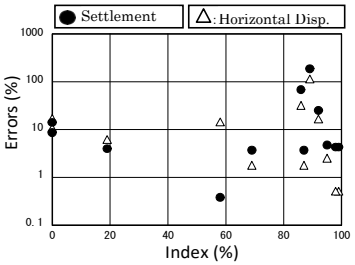

Figure 14. Relationship between the index and errors of computed results (all cases)

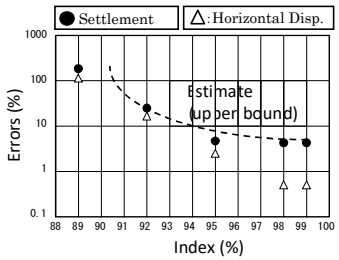

Figure 15. Relationship between the index and errors of computed results (close up)

5 Conclusions

An index to represent the degree of the parameter appropriateness is discussed in this paper. The follwing conclusions are obtained in this study.

(1) Indexes of the similarity in the liquefaction resistance curves both from tests and numerical simulations are proposed.

(2) The relationship between the differences in the FEM analysis results with various parameters and the indexes of these various input parameters are examined. The results indicate that the proposed indexes are expected as a reference in the parameter determination in effective stress analysis.

(3) Although it is just come from the limited case shown here, 94 % of the proposed index is necessary to obtain the result of within 10 % error of the computed deformation, in case of gravity type quay wall.

Acknowledgement

We used the liquefaction test data by Dr. Mikami, Maeda Co. Ltd. The research is supported by JSPS Kakenhi. The aurhos sincrely appriciate these supports.

References

[1] Dafalias, Y. F., and Manzari, M. T. Simple plasticity sand model accounting for fabric change effects, *Journal of Engineering Mechanics*, ASCE, 130(6):622-634, 2004.

[2] Boulanger, R. W., and Ziotopoulou, K. PM4SAND (version 3): *A sand plasticity plane-strain model for earthquake engineering applications*, Report No. UCD/CGM-15-01, Center for Geotechnical Modeling, Department of Civil and Environmental Engineering, University of California, Davis, CA, 2015.

[3] Fukutake, K., Ohtsuki, A., Sato, M., and Shamoto, Y. Analysis of saturated dense sand-structure system and comparison with results from shaking table test, *Earthquake Engineering and Structural Dynamics*, 19(7):977-992, 1990.

[4] Iai, S., Matsunaga, Y., and Kameoka, T. Strain space plasticity model for cyclic mobility, *Soils and Foundations*, 32(2):1-15, 1992.

[5] Iai, S., Tobita, T., Ozutsumi, O., and Ueda, K. Dilatancy of granular materials in a strain space multiple mechanism model. *International Journal for Numerical and Analytical Methods in Geomechanics*, 35(3):360-392, 2011.

[6] Ichii, K., Murakami, T., and Mikami, T. Parameter identification for effective stress analysis from a multi-stage cyclic loading test, *Proceedings of PBD-III*, Vancouver, Canada, 2017.(in Printing)

[7] Nukui, Y., Yanagishita, F., and Shiomi, T. Improvement of the accuracy of soil profile setting in the simplified liquefaction analysis using cumurative damage theory, *AIJ proceedings*, pages 529-530, 2005. (in Japanese)

Effective Stress Analysis for Landslide on Gentle Slopes

Tetsuo Tobita[a], Kei Kashiwagi[a], Masahiro Chigira[b] and Susumu Iai[b]

[a]Department of Civil, Environmental and Applied System Engineering, Kansai university, Japan

[b]Disaster Prevention Research Institute, Kyoto university, Japan

E-mail: tobita@kansai-u.ac.jp, k651087@kansai-u.ac.jp, chigira@slope.dpri.kyoto-u.ac.jp, iai.susumu@flip.or.jp

Abstract –

Earthquake-induced landslides of collapsible soils, such as volcanic cohesive soil, have caused tremendous damage to human society. They are highly mobile and their runout distance is long. What is worse, since they typically occur on gentle slopes which is not designated as a steep slope area in danger of failure, it is incomprehensible even to residents nearby. Characteristics of such a landslide have been studied by many researchers. However, failure mechanism, especially under dynamic condition, is yet unknown. Based on the field investigation and laboratory test results, the slope of Hanokidaira in Fukushima Pref., Japan, where this type of landslide occurred in the 2011 Tohoku Earthquake, is modeled as one-dimensional FEM model to elucidate the failure mechanism and improve quality of landslide hazard warning by combining the numerical analysis with conventional method.

Keywords –

Landslides; Effective stress analysis; Hazard mapping; Dynamic; Numerical analysis

1 Introduction

Earthquake-induced landslides of pyroclastic fall deposit typically occur on gentle slopes, nevertheless they are highly mobile and their travel distance is quite long. Field investigation after those landslides revealed that the material of the sliding surface is composed of weathered cohesive soil originating from pyroclastic fall deposit [1, 2]. They typically form slope-parallel bedding and have interlayering weathered and weak beds, which may give preferable condition to earthquake-induced landslides with long runout distance [4]. This type of landslides, also called slide-avalanche, have been reported in many countries/earthquakes (e.g., [3-6]).

Although such events are thought to be rare, once it occurred they may cause tremendous damage to human society. For example, landslides of pyroclastic fall deposit occurred in the 2011 off the Pacific coast of Tohoku, Japan, earthquake took 13 lives in Hanokidaira in Fukushima Prefecture [2, 7, and 8]. In 2016 Kumamoto, Japan, earthquake, many earthquake-induced landslides of pyroclastic fall deposit occurred on the slopes of Aso-Caldera which forms one of the largest volcanos in Japan [9]. One of them hit residential houses located in the middle of a slope and took 5 lives [9].

To mitigate such a disaster, landslide-prone areas need to be designated as hazardous zone. As a current practice in Japan, those areas with slope angle more than 30 degrees are designated as such by the law. Although field investigations such as mentioned above indicate that landslides composed of volcanic soil tend to occur on gentle slopes, typically 15 to 20 degrees, these areas are excluded from the designation. The fact clearly indicates the necessity of designation of landslide-prone area based not only on the slope angle, but also on their material compositions.

Using the so-called pseudo-static method, Ishihara and Nagao [10] studied the landslide observed in the 1978 Izu-Oshima-Kinkai, Japan, Earthquake. They studied failure mechanism of the landslide and reported such a landslide typically occurred with soil blocks separate one after another from their slope toe. They pointed out that strength parameters of soil determined under dynamic condition must be used to achieve a reasonable degree of accuracy in the assessment of the stability of slopes during earthquakes.

Base on the field and laboratory investigations, Chigira [11, 12] showed that material of the sliding surface contains a clay mineral called “halloysite” which might be weak against shaking. Chigira and Suzuki [13] reported landslide in Hanokidaira whose sliding surface is also halloysite-rich. They deduce that halloysite might play an important role on the occurrence of the landslide particularly under dynamic conditions. However, dynamic behavior of the halloysite-rich clay is not well understood and needs further study.

1.1 Safety factors

Safety factor approach for slope stability, so-called limiting equilibrium method, has been conventionally used in practice. The safety factor, F_s', is defined by Equation (1) under the equilibrium between the maximum shear resistance force of sliding layer to a driving force due to a gravity acting on an assumed sliding block.

$$F_S' = \frac{c + W'\cos\theta\tan\phi}{W\sin\theta} \quad (1)$$

where c is cohesion, ϕ is internal friction angle, θ is slope angle, W is weight of a sliding block, W' is effective weight corresponds to W without influence of pore water pressure. Here, $W\sin\theta$ and $W'\cos\theta$ are, respectively, equivalent to the shear and vertical forces exerted on the sliding surface.

Effect of earthquake can be included in the safety factor of the infinite slope stability by the method so-called pseudo-static method (Equation (2)), in which the maximum shear resistance force is reduced and driving force is added by the fraction of horizontal inertial force due to an earthquake acting on the sliding block.

$$F_S' = \frac{c + (W'\cos\theta - k_h \cdot W'\sin\theta)\tan\phi}{W\sin\theta + kW\cos\theta} \quad (2)$$

$$k_h = a_{max}/g \quad (3)$$

where k_h is the horizontal seismic coefficient which is expressed by the ratio of the maximum horizontal acceleration of earthquake a_{max} to the acceleration due to gravity, g. Here, for simplicity, the vertical component of an earthquake motion is not considered.

Another possible approach to estimating stability of natural slopes is numerical modeling, such as, to name a few, FEM, DEM, and SPH. Those methods have been intensively developed as the advancement of computer technologies from scores of years ago. To elucidate failure mechanism of a landslide and to improve quality of landslide hazard warning those tools may become useful soon. At present, however, they have so far rarely been applied to the analysis of a slope stability of natural slopes because of the complexity of natural conditions and requirements for a 3D analysis as well as development of proper constitutive models to simulate landslides.

For natural slopes, requirements to carry out numerical analysis are not simple compared with the case of man-made slopes. One must know at least a soil profile of an area, and preferably a longitudinal cross section of a slope. Also, mechanical and physical properties of the material in a slope should be investigated by taking a soil sample to a laboratory. With these at hand, numerical stability analysis in 2D can be barely carried out. However, it is very difficult to evaluate and validate results obtained in 2D analysis. Nature of a landslide depends not only on its material properties but also on geological and topographic conditions. In this sense, therefore, 3D analysis must be carried out.

In this paper, not directly jumping into a numerical analysis in 3D, possibility of a 1D effective stress analysis is investigated by utilizing material parameters obtained from the site. Factor of safety with parameters computed by the numerical analysis is compared with those derived by the conventional stability analysis.

Purpose of the paper is to apply the effective stress analysis to stability of infinite slopes assuming slope-parallel bedding of pyroclastic fall deposit. Novelty lies on; (1) proposing a safety factor considering the anisotropy of an initial static stress state in a sliding surface; (2) comparison of the safety factor derived by the numerical method to that of conventional method; and (3) pointing out a limitation of the conventional method. The methodology presented in the study can be utilized to develop landslide hazard warning system of gently slopes.

2 1D modeling of an infinite slope

In this study, the slope of Hanokidaira in Fukushima Prefecture is chosen as a target by assuming the actual slope being infinite. It is modeled as one-dimensional column (Figure 1). The effective stress finite element analysis method proposed by Iai et al [14] is employed. Material parameters are determined by the laboratory tests with undisturbed samples taken from the site (Table 1 and 2) [15].

As shown in Figure 1, the model slope is composed of 40 elements and 82 nodes and separated into 3 layers; “surface,” “slide,” and “bottom” layers. In this study, one element at the depth of 7 to 8 m, is assigned as the sliding surface.

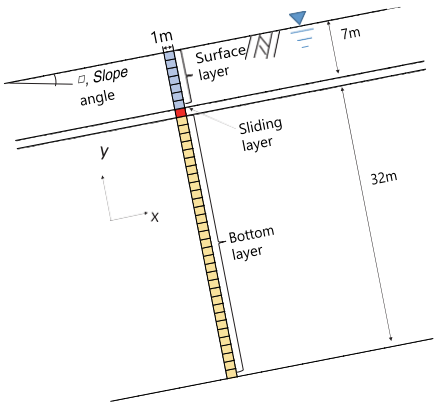

Figure 1. 1D FEM model implemented in the present study for infinite slope stability.

These nodes are given two degree of freedom in x and y directions. The ground water table is located at the ground surface by assuming the material of a slope is fully saturated. This assumption was given merely for simplicity. Thus, in what follows, normal stresses denoted with σ_x and σ_y are effective. A coordinate system and a slope angle are taken as shown in Figure 1. The x-axis is taken in the upslope direction. In computation, accelerations are decomposed into both directions.

Table 1. Parameters for the model ground [15]

	Unit	Layer		
		Surface	Slide	Bottom
SPT N-value	-	5	8	-
Initial shear modulus, G_0	GPa	34,406	47,066	6,000
Initial bulk modulus, K_0	GPa	89,725	122,742	15,647
Effective mean stress, p_{m0}	kPa	98	98	98
Pressure dependent coefficient, m_G/n_κ	-	0.5	0.5	0.5
Density, ρ	g/cm^3	1.8	2	1.5
Porosity, n	-	0.45	0.45	0.7
Cohesion, c	kPa	0	0	0
Internal friction angle, ϕ	Degree	34.09	35.28	33
Max. damping constant, h_{max}	-	0.24	0.24	0.24

Table 2. Dilatancy parameters for the sliding surface [15]

ε_d^{cm}	0.50	l_k	2.00
$r_{\varepsilon_d}^{C}$	0.23	r_k	0.50
$r_{\varepsilon d}$	0.20	c1	1.00
q_1	1.00	q_{us}	35.00
q_2	1.50	S_1	0.005

3 Static analysis

3.1 Static stress state in the sliding surface

Prior to the dynamic analysis, the static analysis is carried out by applying the gravitational force statically to the inclined 1D model to define the initial anisotropic stress state. Then, factor of safety derived from the computed initial stress state is defined and is compared with the one derived by Equation (1).

In the static analysis, the soil element is confined by the overburden effective stress due to gravity. For example, Figure 2 shows profile of computed stresses for slope angle of 27 deg. As expected, triangular distribution of stresses with depth are observed, where σ_x and σ_y are the normal stresses acting on the side of each element in x and y direction, respectively, and τ_{xy} is the shear stress. As shown, at the slope angle of 27 deg., σ_y is slightly larger than σ_x, i.e, anisotorpic stress state is simulated.

Now, to see how the anisotropic stress state varys, let us focus on stresses in the sliding surface. Figure 3(a) shows variation of those stresses with slope angles. As slope angle increases, normal and shear stresses increase. However, the deviator stress defined by $(\sigma_y - \sigma_x)/2$, decreases with the increase of the slope angle. This indicates that, as slope angle increases, stress state approaches to isotropic state.

Figure 3(b) depicts stresses in terms of mean effective stress which is equivalent to the center of a Mohr's circle and the stress corresponding to the radius of a Mohr's circle defined by,

$$l_1 = \sqrt{\tau_{xy}^2 + \{(\sigma_x - \sigma_y)/2\}^2} \tag{4}$$

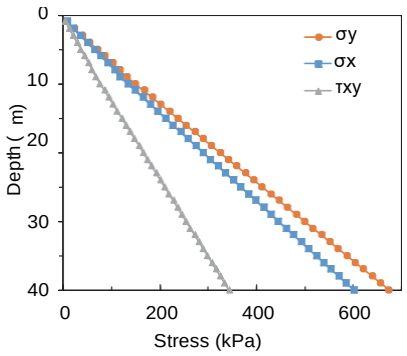

Figure 2. Vertical profiles of stresses after the static analysis at slope angle of 27 deg.

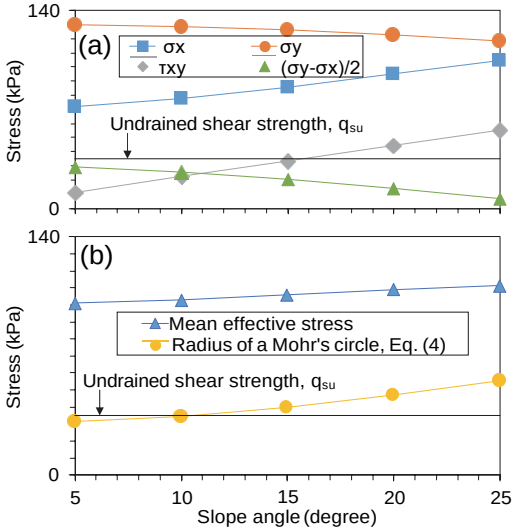

Figure 3. Stress versus slope angle in the sliding surface after static analyses; (a) various stresses, (b) mean effective stress and stress corresponding to the radius of a Mohr's circle.

From Figure 3(b), compared with the mean effective stress, the stress corresponds to the radius of the Mohr's circle increases slightly rapidly with the increase of the slope angle.

Figure 3(b) can be transferred into a set of Mohr's stress circles (Figure 4). In Figure 4, as slope angle increases, the circle become larger and approaches to the Mohr-Coulomb's yield criterion. Also, in Figure 4, stress states of the sliding surface indicated by solid circles on each Mohr's circle indicate that, as slope angle increases, the normal stress, σ_x and σ_y, approaches each other toward the value of the mean effective stress, i.e., toward isotropic stress state.

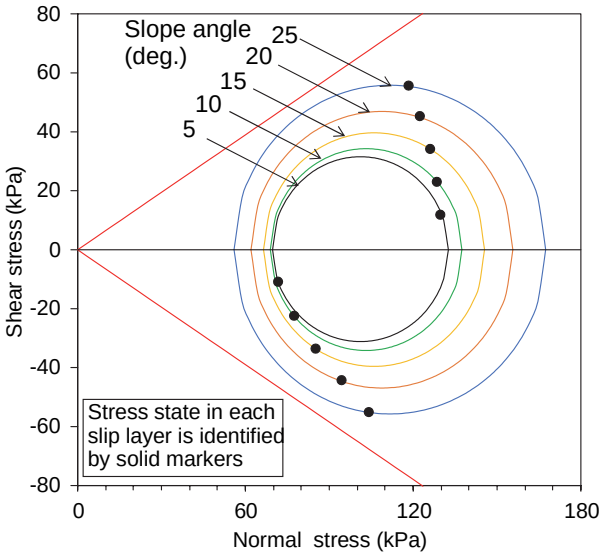

Figure 4. Mohr's stress circles drawn after the static analysis of various slope angles.

3.2 Comparison of the safety factors

For various slope angles, the safety factors by Equation (1) and the one with computed stresses by the effective stress analysis are compared. With the weight of the surface layer, *W*, which can be simply computed from the given model parameters (Table 1) and the area of a sliding soil block, a conventional safety factor can be computed by Equation (1).

Next, let us define the safety factor to include stresses derived by the effective stress analysis. The radius l_1 of Mohr's stress circle is given by Equation (4). Distance l_2 from the center of Mohr's stress circle to the point on the Mohr-Coulomb's yield criterion is expressed by,

$$l_2 = c \cdot \cos\phi + \frac{\sigma_x + \sigma_y}{2} \sin\phi \qquad (5)$$

These l_1 and l_2 are indicated in Figure 5. If soil is at failure, then l_1 and l_2 coincide. Hence, with l_1 and l_2, the safety factor F_s can be defined by,

$$F_s = \frac{l_2}{l_1} = \frac{c \cdot \cos\phi + \{(\sigma_x + \sigma_y)/2\} \sin\phi}{\sqrt{\tau_{xy}^2 + \{(\sigma_y - \sigma_x)/2\}^2}} \qquad (6)$$

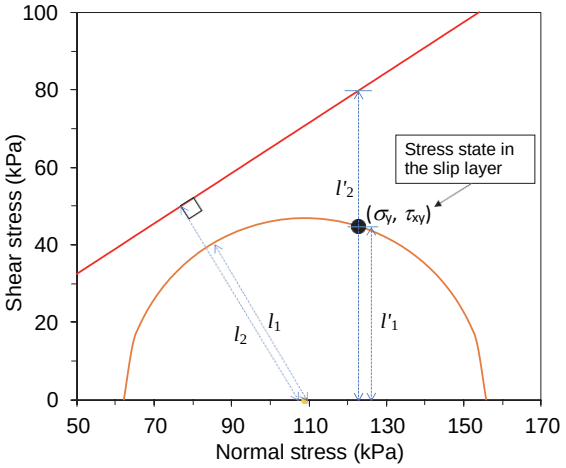

Figure 5. Mohr's stress circle and definition of the proposed safety factor by Equation (6), $F_s=l_2/l_1$.

The safety factors of the infinite slope stability by Equation (1) and (6) are compared in Figure 6. Effective stress analysis diverged at the slope angle over 27 deg. In Figure 6, compared with the safety factor derived by Equation (6), Equation (1) gives larger values when the slope angle is smaller than 10 deg. Because landslides of volcanic cohesive soil under earthquake tend to occur on gentle slopes, the conventional safety factor (Equation (1)) might cause underestimation of landslide hazards.

The difference on the safety factors at small slope angle is investigated by plotting the safety factors of Equation (1) and the one only with the shear stresses τ_{xy} (Equation (7)) and the other only with $(\sigma_y - \sigma_x)/2$ (Equation (8)) contained in the denominator of Equation (6).

$$F_{S1} = \frac{c \cdot \cos\phi + \{(\sigma_x + \sigma_y)/2\} \sin\phi}{\tau_{xy}} \qquad (7)$$

$$F_{S2} = \frac{c \cdot \cos\phi + \{(\sigma_x + \sigma_y)/2\} \sin\phi}{(\sigma_y - \sigma_x)/2} \qquad (8)$$

From Figure 7(a), shapes and the values of the curve derived only with shear stress, τ_{xy} (Equation (7)) and the one by Equation (1) are similar. Contrary, the curve derived only with $(\sigma_y - \sigma_x)/2$ (Equation (8)) sharply increases with the increase of slope angle. This clearly indicates that cause of small safety factor at gentle slopes are due to the stress component expressed with

$(\sigma_y - \sigma_x)/2$ in Equation (6). This component is responsible for the anistoropic stress state at rest.

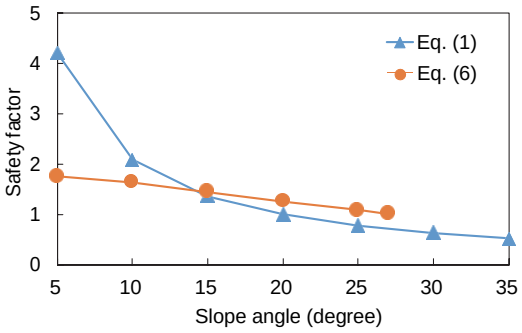

Figure 6. Comparison of the safety factors derived by Equation (1) and Equation (6).

Next, similarity between Equation (1) and (7) shown in Figure 7(a) is investigated by replacing $W\sin\theta$ and $W'\cos\theta$ in Equation (1) with computed stresses τ_{xy} and σ_y, respectively, which may correspond to the parameters inplemented in Equation (1). Thus, with c=0, Equation (1) can be rewritten as,

$$F_S' = \frac{c + W'\cos\theta\tan\phi}{W\sin\theta} = \frac{\sigma_y \tan\phi\left(l_2'\right)}{\tau_{xy}\left(l_1'\right)} \qquad (1')$$

Here, l_1' and l_2' correspond to the vertical lengths indicated in Figure 5. Figure 7(b) compares those curves expressed by Equation (1) and (1'). They draw similar curves for the safety factor of an infinite slope stability in which anisotropic stress state is not considered.

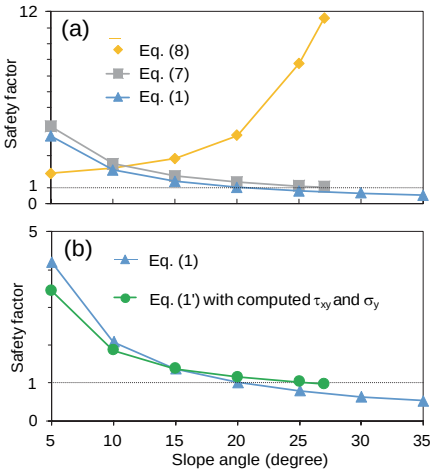

Figure 7. Variation of safety factors against slope angles: (a) Equation (1), (7) and (8), and (b) Eq. (1) and Eq. (1') with computed τ_{xy} and σ_y.

Thus, it can be said that the effect of stress anisotropy in the static stress state should be considered in the safety factor of infinite slope stability of gentle slopes.

4 Dynamic analysis

4.1 Results of the dynamic analysis

Dynamic analysis is conducted consecutively after the static analysis with the recorded ground accelerations; the 2011 off the Pacific Coast of Tohoku, Japan, Earthquake (K-Net, FKS016) (Fig 8(a)) and the 2016 Kumamoto, Japan, Earthquake (K-Net, KMM005) (Fig 8(b)). These acceleration records are decomposed into *x* and *y* directions and input at the base of the model ground shown in Fig. 1.

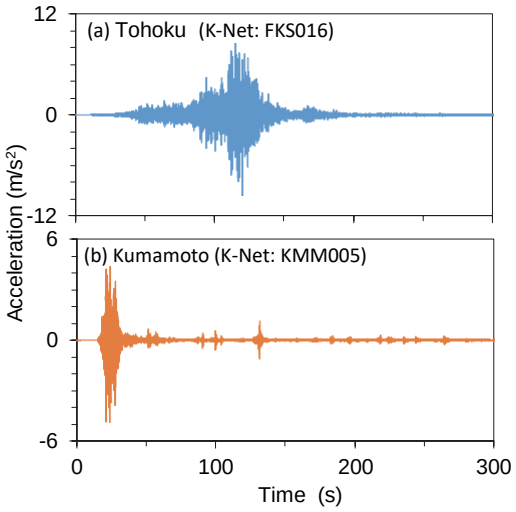

Figure 8. Input acceleration; (a) the 2011 off the Pacific coast of Tohoku, Japan, Earthquake (K-Net, FKS016), (b) the 2016 Kumamoto, Japan, earthquake (K-Net, KMM005).

To see variation of acceleration with slope angle, simulated accelerations at the lower node of the sliding surface are plotted in Figure 9. As shown, those accelerations at the slope angle of 5 deg. have not much difference with the input motion. In Fig. 9(b), as the slope and become large at 20 deg., the maximum amplitude becomes about half of their input motions. However, the shapes of the waves are kept like the input motion.

The simulated accelerations passing through the sliding surface are plotted in Figure 10. Compared with Figure 9, amplitudes are attenuated reflecting the failure of softening of the soil element. For Tohoku motion (Figure 10(a)), a packet of large amplitude at around 120 s appeared in the input motion is disappeared. For larger slope angle (Figure 10(b)), amplitudes become very small indicating the failure of soil.

Figure 11 shows time histories of the shear strain

exerted in the sliding surface. As shaking starts, the shear strain increases. For slope angle of 5 deg., the shear stain reaches to 0.2 to 0.3 and are kept constant after shaking for both Tohoku and Kumamoto motions, while for the slope angle of 20 deg., the shear strain continuously increases even after shaking. This can be regarded as occurrence of a landslide in the computation.

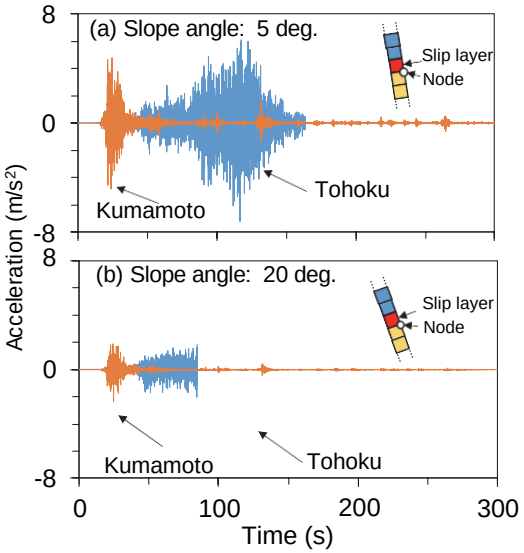

Figure 9. Computed acceleration at the bottom node of the weak layer, (a) slope angle at 5 deg., and (b) 20 deg.

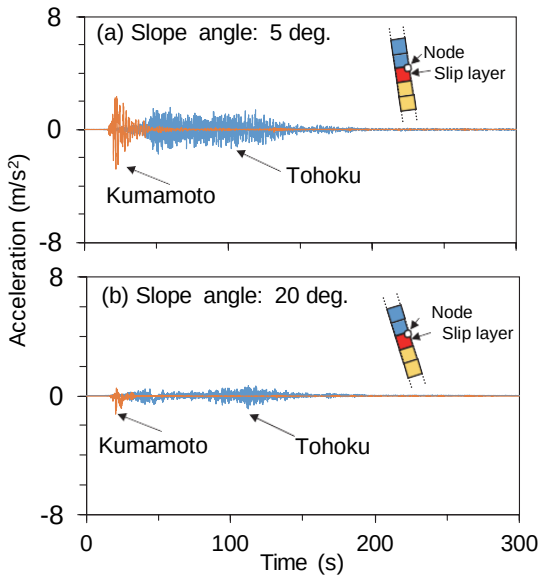

Figure 10. Computed acceleration at the top node of the weak layer, (a) slope angle at 5 deg., and (b) 20 deg.

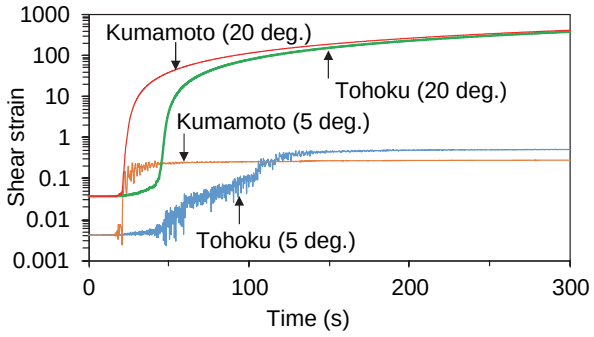

Figure 11. Time histories of the shear strain in the sliding surface.

Effective stress paths for the sliding surface is plotted in Fig. 12. The vertical axis is equivalent to the deviator stress expressed by Equation (4). When the slope angle is at 20 deg., the curves start from the mean effective stress of 110 kPa and the deviator stress of 45kPa. Then, as shaking continues, the mean effective stress decreases. The shapes of the curves are concave down and reach the failure line. On the other hand, for the slope angle of 5 deg., both the mean effective stress and the deviator stress start from smaller values than those of 20 deg., as expected, and the shapes of the curves are concave up, and they approach but do not reach the failure line.

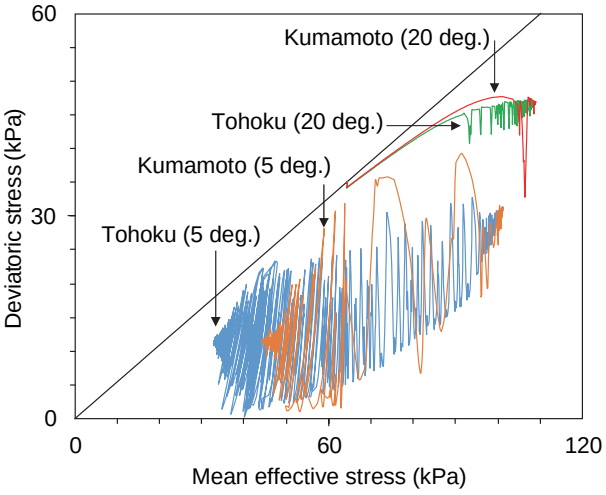

Figure 12. Computed effective stress paths in the sliding surface

To investigate the characteristics of the sliding surface against shear deformation, time histories of the deviator stress, $(\sigma_y - \sigma_x)/2$ (Figure 13), and the pure shear, τ_{xy} (Figure 14) are plotted. For curves of the deviator stress shown in Figure 13, all of them decrease during shaking and approach to zero or slightly negative values as shaking continues. On the other hand, behaviour of the pure shear τ_{xy} varies depending on the

slope angle. As shown in Figure 14, initial values of the pure shear stresses depend on the static analysis. During shaking, if the slope angle is 5 deg., the value of τ_{xy} fluctuates around the initial values and the final value return to the initial value. When the slope angle is 20 deg., the values of shear stress decrease and become constant at 35 (kPa), which is the undrained shear strength q_{us} of the sliding surface given in Table 2.

In summary, when an initial value of a pure shear stress τ_{xy} is smaller than the shear strength, a deviator stress expressed by Equation (4) converges to the initial value of the pure shear stress computed by the static analysis and the effective stress path does not reach the failure line. While the initial value of the pure shear stress is larger than the shear strength, deviator stress converges to shear strength, i.e., a stress path reaches a failure line which corresponds to an occurrence of a landslide. Thus, if the in-situ value of the pure shear stress and shear strength of the sliding surface can be estimated properly, it may be possible to evaluate the stability of a slope due to an earthquake without conducting dynamic analyses.

From the above discussion, the stability of a slope strongly depends on the initial stress state, or slope angle, and the level of an undrained shear strength of the sliding surface, and depends less on types of input motions.

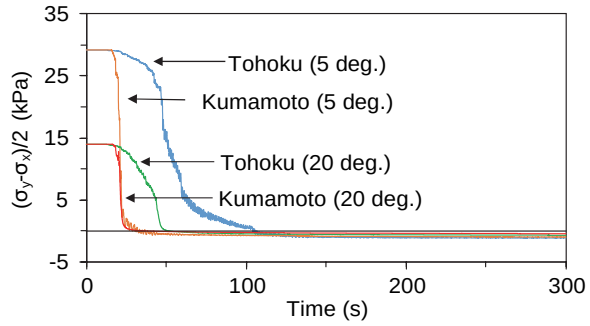

Figure 13. Computed time histories of the deviator stress, $(\sigma_y - \sigma_x)/2$ in the sliding surface.

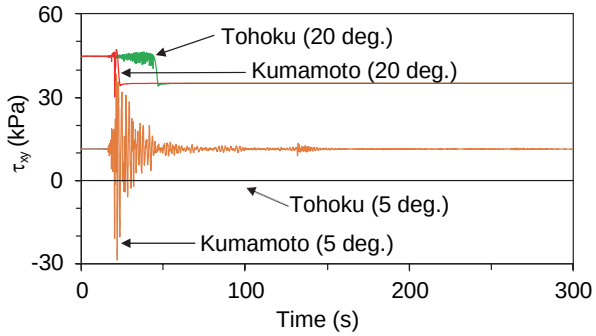

Figure 14. Computed time histories of the pure shear stress, τ_{xy} in the sliding surface.

5 Conclusions

Earthquake-induced landslides of pyroclastic fall deposit typically occur on gentle slopes, nevertheless they are highly mobile and their runout distance is quite long. In this paper, possibility of a 1D effective stress analysis of infinite slopes assuming slope-parallel bedding of pyroclastic fall deposit is investigated by utilizing material parameters obtained from the site. A new definition of the factor of safety with parameters computed by the numerical analysis is compared with those derived by the conventional stability analysis.

Compared with a proposed approach, a conventional safety factor tends to give larger safety factor in a range of slope angles less than 15 degrees. This is because, in the conventional approach, only the pure shear stress exerted in the sliding surface is considered and the deviator stress, i.e., anisotropic stress state, is not considered. Hence, it is likely that a conventional safety factor overestimates the safety factor, particularly when the slope angle is less than 15 degrees. From the comparison, for the case of a gentle slope, the importance to consider the effect of stress anisotropy in the static stress state was pointed out.

Dynamic analysis showed that behavior of the slope strongly depends on the initial stress state and the level of the undrained shear strength, and depends less on types of input motions.

The methodology presented in the study can be utilized to improve landslide hazard warning of gentle slopes.

Acknowledgements

This study is supported by the Ministry of Education, Science, Sports and Culture, Grand-in-Aid for Scientific Research (B), No. 26282102. Strong motion data used in this study was provided by the digital strong-motion seismograph network, K-Net, National Research Institute for Earth Science and Disaster Resilience (NIED). The numerical analysis code FLIP was provided by the FLIP Consortium (http://www.flip.or.jp/).

References

[1] Chigira, M., Dry debris flow pyroclastic fall deposits triggered by the 1978 Izu-Oshima-Kinkai Earthquake: The "collapsing" landslide at Nanamawari, Mitaka-Iriya, southern Izu peninsula, *Journal of Natural Disaster Science*, 4(2): 1-32, 1982.

[2] Nakamura, S., Wakai, A., Umemura, J., Sugimoto, *H.* and Takeshi, T., Earthquake-induced landslides: Distribution, motion and mechanisms, *Soils and Foundations*, 54(4): 544-559, 2014. 10.1016/j.sandf.2014.06.001.

[3] Hirano, M., Ishii, T., Fujita, T. and Okuda, S., Geomorphological and geological characteristics of 1984 landslide hazard in Ohtaki village, Nagano Prefecture, Japan, *Annuals of Disaster Prevention Research Institute, Kyoto Uiversity*, 28: 519-532, 1985.

[4] Hsu, K. J., Catastrophic debris streams (sturzstroms) generated by rockfalls, *Geological Society of America Bulletin*, 86: 129-140, 1975.

[5] Inoue, Y., Honsho, S., Matsushima, M. and Esashi, Y., Geological and soil mechanical studies on the slides occurred during the 1968 Tokachioki earthquake in southeastern area of Aomori Prefecture, *Bulletin of the Central Research Institute of Electric Power Industry*, 1970.

[6] Jibson, R. W., Crone, A. J., Harp, E. L., Baum, R. L., Major, J. J., Pullinger, C. R., Escobar, C. D., Martinez, M. and Smith, M. E., Landslides triggered by the 13 January and 13 February 2001 earthquakes in El Salvador, *Geological Society of America Special Papers*, 375: 69-88, 2004. 10.1130/0-8137-2375-2.69.

[7] Sugimoto, H., Toshiya, T., Uto, T. and Honma, H., Geomorphic and geologic features of landslides induced by the 2011 Off the Pacific Coast of Tohoku Earthquake, in Shirakawa Hills, Fukushima Prefecture, *Earthquake induced landslides, K. Ugai, H. Yagi, A. Wakai (Eds.), Springer-Verlag, Tokyo*: 189-201, 2012. 10.1007/978-3-642-32238-9_20.

[8] Wang, G., Suemine, A., Zhang, F., Hata, Y., Fukuoka, H. and Kamai, T., Some fluidized landslides triggered by the 2011 Tohoku Earthquake (Mw 9.0), Japan, *Geomorphology*, 208: 11-21, 2014. 10.1016/j.geomorph.2013.11.009.

[9] Kiyota, T., Ikeda, T., Konagai, K. and Shiga, M., Geotechnical Damage Caused by the 2016 Kumamoto Earthquake, Japan, *International Journal of Geoengineering Case Histories*, 4(2): 78-95, 2017. 10.4417/IJGCH-04-02-01.

[10] Ishihara, K. and Nagao, A., Analysis of landslides during the 1976 Izu-Oshima-Kinkai earthquake, *Soil and Foundations*, 23(1): 19-37, 1983.

[11] Chigira, M., Geological and geomorphological features of deep-seated catastrophic landslides in tectonically active regions of Asia and implications for hazard mapping, *Episodes*, 37: 284-294, 2014.

[12] Yoshida, M. and Chigira, M., The relation between weathering of pyroclastic fall deposits and the collapses caused by the 1968 Tokachi oki Earthquake, *Journal of the Japan Society of Engineering Geology*, 52(6): 213-221, 2012.

[13] Chigira, M. and Suzuki, T., Prediction of earthquake-induced landslides of pyroclastic fall deposits, *Aversa et al. (ed.) Landslides and Engineered Slopes. Experience, Theory and Practice. Associone geotecnica Italiana, Rome*: 93-100, 2016.

[14] Iai, S., Matsunaga, Y. and Kameoka, T., Strain space plasticity model for cyclic mobility, *Soils and Foundations*, 32(2): 1- 15, 1992.

[15] Kawahara, T., Ueda, K., Iai, S., Chigira, M. and Tobita, T., Numerical analysis of landslides of pyroclastic fall deposits, *1st International Conference on Natural Hazards & Infrastructure, ICONHIC2016*, 65, 2015.

Typhoon-induced settlement of caisson breakwater on granular material

Gi-Chun Kang[a], Woong-Ki Hwang[b], and Tae-Hyung Kim[b]

[a]Department of Civil Engineering, ERI, Gyeongsang National University, 501 Jinju-daero, Jinju, Gyeongsangnam-do 52828, Republic of Korea
[b]Department of Civil Engineering, Korea Maritime and Ocean University, 727 Taejong-ro, Yeongdo-gu, Busan 49112, Republic of Korea
E-mail: gkang@gnu.ac.kr, wkhwang@kmou.ac.kr, kth67399@kmou.ac.kr

Abstract –

Breakwater settlement studies have been conducted primarily through numerical model tests and laboratory wave tank tests using scaled models. No studies have been conducted on the settlement measured in an actual breakwater structure because most breakwaters are located in places where measuring is difficult. The study presented in this paper analyzed settlement data measured in an actual caisson breakwater over a long period of time, and the characteristics and causes of wave-induced settlement in the caisson (including beneath the ground), were examined qualitatively. The analysis revealed that waves clearly affect the settlement in breakwater, especially under high wave conditions, such as typhoons. Breakwater settlement is caused by ground liquefaction, which occurs due to the increase in excess pore pressure, the combination of oscillatory and residual excess pore pressures, and the solidification process of ground caused by the dissipation of the accumulated excess pore pressure. Solidified ground is not likely to experience liquefaction under such wave conditions, thus reducing the possibility of settlement.

Keywords –

Wave-induced settlement; Caisson breakwater; Excess pore pressure

1 Introduction

When constructing a caisson breakwater (Fig. 1(a) non-perforated caisson), its stability must be judged; thus, establishing a plan to measure its settlement is important. Figure 1(b) shows the non-perforated caisson's settlement (#6) data measured in the west breakwater of the Jeju Outer Harbor from January 2003 to October 2006. The settlement was measured at four edges, numbered from one to four starting from the seaward edge of the caisson.

In this location, the seabed is mainly sandy ground, with no clay. Thus, the immediate settlement that commonly occurs in sand has been observed after caisson installation due to the weight and water pressure (Fig. 1(b)). This is because, unlike clay, sandy soil tends to settle immediately. Increased weight on saturated sandy soil increases the pore water pressure. Due to the high permeability of sandy soil, the pore pressure dissipates immediately as it increases, which decreases the ground volume. This results in immediate ground settlement.

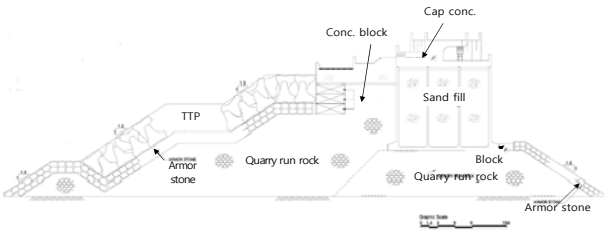

(a) Plan view of non-perforated caisson #6 used in west breakwater

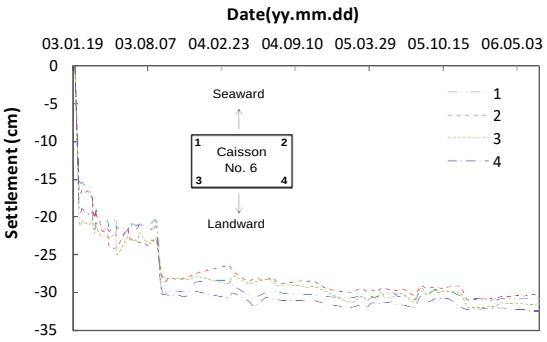

(b) Settlement data of the caisson #6 in west breakwater

Figure 1. Plan view of non-perforated caisson #6 used in west breakwater, Jeju Outer Harbor and its settlement data

Date-settlement curve (Fig. 1(b)) indicates that settlement continues long after the immediate settlement. Cho [1] investigated this phenomenon, finding that the carbonate sand formed by fish bones and shellfish caused this creep settlement. In the area investigated in the current study, approximately half of the sand is carbonate sand. The cracking of carbonate sand and the rearrangement of sand particles under caisson loading conditions cause this creep settlement. Grain size analysis and compression tests have confirmed that the degree of cracking is higher in carbonate sand than in silica-type sand under the same loading conditions [2].

The measurements depicted in Fig. 1(b) also show that, in addition to the immediate settlement and the creep settlement caused by carbonate sand, another form of settlement occurred rapidly. It is unlikely that this rapid settlement was caused by carbonate sand because it occurred very quickly in a short period of time and had a completely different form than the creep settlement.

The settlement trend of #6 caisson in west breakwater of Jeju Outer Harbor can be schematically depicted as Fig. 2. Three types of settlement is involved; immediate, and creep, and rapid settlements. This rapid settlement (marked A and B in figure) may be caused by waves because it occurred at the same time as a big wave attack.

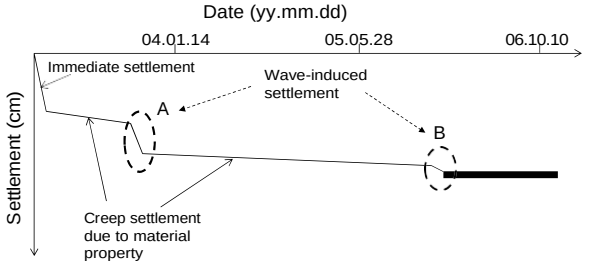

Figure 2. Schematic diagram of settlement of the caisson #6 in west breakwater of Jeju Outer Harbor

Many coastal researchers have discovered that coastal structures and the seabed lying around and underneath them are situated such that they experience repetitive loading by waves, thereby exhibiting quite different behavior than other land structures [3, 4, 5, 6]. These studies have focused mainly on the combination of oscillatory excess pore pressure [7, 8], as well as residual excess pore pressure [9].

Many numerical studies have been conducted on the dynamic behavior of excess pore pressure in the seabed where coastal structures, such as breakwaters, have been installed. Li and Jeng [10] and Ye et al. [11] used 2D or 3D numerical wave fields based on the consolidation equation proposed by Biot [12] to evaluate the possibility of liquefaction, the dynamic response of oscillatory and residual excess pore pressure, and the effective stress of the seabed grounds near and underneath breakwater areas.

Experimental breakwater studies have been conducted in laboratory wave tanks, such as those undertaken by Zen and Yamazaki [13, 14] and Kudella et al. [15]. Through a model experiment that used a device that generates vertical oscillatory pressure in sand, Zen and Yamazaki [13, 14] stressed that structure settlement can occur due to the liquefaction caused by oscillatory excess pore pressure. Kudella et al. [15] experimentally proved the mechanism of excess pore pressure in caisson foundations.

Thus far, previous breakwater research has focused mainly on numerical model tests and scale model tests in laboratory wave tanks to verify the effect of waves on the behavior of coastal structures and the surrounding seabed. No studies have used measurement data obtained from actual breakwater structures to prove the wave-induced settlement because taking measurements in these locations is difficult. Thus, in this study, the settlement data measured in actual caisson breakwaters over a long period of time, more than 5 years, were analyzed to determine the characteristics and causes of wave-induced settlement in caisson breakwater (including underneath the ground). The data obtained from caissons used to build the west breakwater at the Jeju Outer Harbor were selected for use in this study.

2 Site description

2.1 Characteristics of the soil and wave at the site

The results of a boring investigation conducted at the west breakwater construction site in the Jeju Outer Harbor indicate a seabed ground level of DL (-) 12.78 ~ (-) 22.62 m. The bedding in this region consists of marine alluvial deposit, weathered bedrock deposit, and soft rock from the face of the seabed surface. The marine alluvial deposit, the main subject of this study, consists of fine to medium sand (SP) and silty sand (SM), based on USCS classification guidelines. It has been transported by waves and distributed between 0.3 and 17.5 m, with an average of approximately 10 m. This sediment sand contains a significant amount of carbonate sand formed by fish bones and shellfish. Varying based on the location and depth, the N value of the standard penetration test ranged from 9 to 25, which indicates a generally dense or very dense relative density. Interestingly, according to the soil profile in Fig. 3, no soft clay layer exists in this area.

2.2 Characteristics of wave

A self-recording wave gauge was installed to observe the height and direction of the waves at the west breakwater construction site. The impact of wave reflection due to the structure of the caisson body was minimized because the measuring point was 500 m from the front of the breakwater (see Fig. 5). This space between the gauge and the breakwater was big enough to eliminate the wave reflection effect.

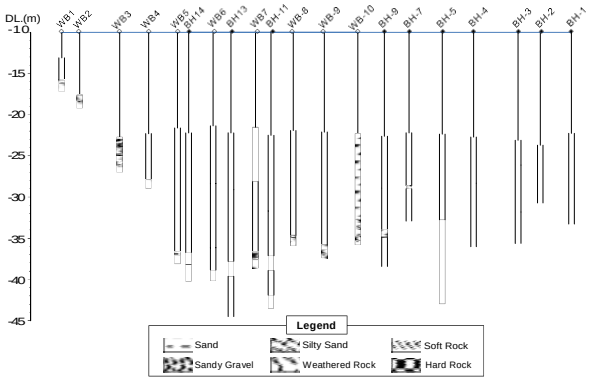

Figure 3. Boring location and soil profile at west breakwater construction site in Juju Outer Harbor

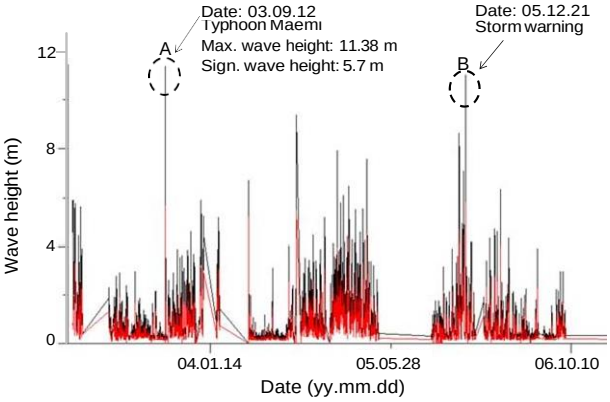

Figure 4. Recorded wave height during the construction of breakwater in Jeju Outer Harbor

Figure 4 shows a recorded wave height during the construction of breakwater. During the monitoring period, one mega typhoon (Maemi) occurred. Maemi produced waves with a maximum height of 11.38 m (maximum significant weight height of 5.7 m), and with a maximum wave period of 7.8 sec (maximum significant wave period of 8.4 sec). The time occurring the rapid settlement in Fig. 1(b) (also marked A in Fig. 2) exactly corresponds to the Maemi attack. Table 1 summarizes the observation of waves over 5 m from 2002 to 2006. After Typhoon Maemi, more than 14 times the average number of waves over 5 m in height passed this area. On December 21, 2005, a storm hit this area, producing waves with a maximum height of 11.01 m, and with a maximum wave period of 9.7 sec.

Table 1. Data recorded by wave gauge installed in front of the west breakwater in Jeju Outer Harbor

Date (y.m.d)	Time	Max. wave height (m)	Max. wave period (s)	Sign. wave height (m)	Sign. wave period (s)	Vel. (m/s)	Flow Dir.	Wave Dir.	Temp. (°C)
02.12.30	0:00	5.91	5.6	0.80	4.5	0.05	NNW	SW	16.0
03.01.05	8:00	5.76	7.3	3.12	7.0	0.07	NW	NNW	14.7
03.01.20	18:00	5.63	9.3	2.55	6.4	0.13	N	NNW	14.5
03.09.12[1)]	18:00	11.38	7.8	5.70	8.4	0.08	WSW	N	21.2
03.12.19	12:00	5.90	6.5	3.01	6.6	0.06	N	NNW	15.3
03.12.26	20:00	5.23	5.8	2.61	6.5	0.07	NNE	NW	15.8
04.02.05	4:00	5.18	6.7	3.03	7.2	0.11	N	NNW	14.0
04.11.26	18:00	5.20	8	3.08	7.7	0.12	NW	NW	18.7
04.12.31	20:00	7.91	8	3.97	8.5	0.11	NNW	NW	15.3
05.01.16	8:00	6.10	17.2	2.88	6.8	0.23	N	NW	15.0
05.02.01	2:00	6.49	8.2	4.30	8.6	0.02	N	NW	14.7
05.02.19	18:00	5.53	6.3	3.02	7.2	0.06	NW	NW	13.4
05.03.12	6:00	5.56	5.9	3.09	7.1	0.15	NNW	NW	13.1
05.03.24	18:00	7.57	7.1	4.51	8.9	0.08	WNW	NW	13.3
05.12.04	18:00	8.64	11.6	4.60	9.9	0.11	WNW	NW	18.7
05.12.17	20:00	7.07	9.1	4.46	9.3	0.16	WSW	NW	15.5
05.12.21[2)]	22:00	11.01	9.7	5.50	10.4	0.07	WNW	NW	16.3
06.03.28	16:00	6.35	7.2	4.00	7.7	0.05	NW	NW	15.3

Note: [1)] Typhoon Maemi, [2)] Storm

3 Measurement of caisson settlement

3.1 Measurement method Type Style and Spacing

To obtain an accurate measurement, a settlement gauge must be installed underneath the caisson to measure the ground settlement, accompanied by level measurement at the top of the caisson. However, in the case of the Jeju Outer Harbor, only level measurement was conducted because no settlement gauge was installed underneath the caisson.

Figure 5 shows the site survey location provided by the National Oceanographic Administration. Jeju TBM (No. 7) was used as a reference point. The caisson's settlement was recorded after its installation at the

reference point. The settlement was measured at four edges, numbered from one to four starting from the seaward edge of the caisson (Fig. 1 (b)). In this study, for convenience, the average settlement was used for the analysis.

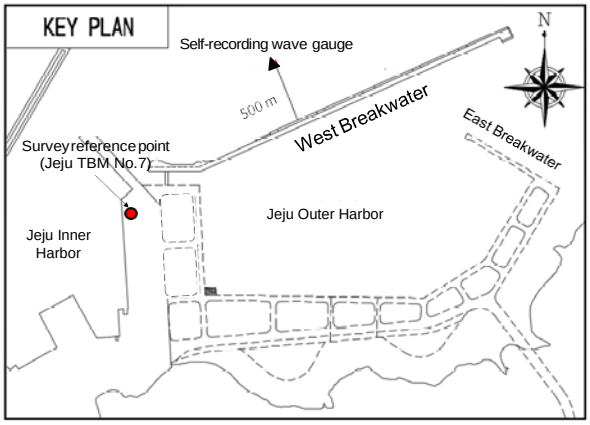

Figure 5. Plane view of west breakwater, including settlement survey point and installation point of self-recording wave gauge

3.2 Caisson installation

A total of 84 caissons were installed at the west breakwater in Jeju Outer harbor. Caisson #5 was the first to be installed, followed by #1, 2, 3 and 4, which were installed to connect to #5. From caisson #6, they were installed to the eastbound direction in sequence. The caissons installed in the west breakwater can be classified into four groups: non-perforated, curved slit, enlarged slit and different shapes curved slit.

Based on the caisson type, the first 19 non-perforated caissons (see Fig. 1(a)) were installed in the westbound direction, followed by enlarged slit caissons #20 and #21. The curved slit caissons, #22 ~ #31, were installed, followed by the enlarged slit caissons, #32 and #33. Then, curved slit caissons #34 ~ -#43, 47 ~ 56, 59 ~ 68, and 71 ~ 78 were installed. Enlarged slit caissons #44, 45, 46, 57, 58, 69 and 70 were installed between the curved sleet caissons. Lastly, different shapes curved slit caissons #79 ~ #84 were installed to complete the round shape of the end of the eastbound part of the breakwater. In summary, a total of 84 caissons (19 non-perforated, 48 curved slit, 11 enlarged slit and 6 different shapes curved slit) were installed in the west breakwater of the Jeju Outer Harbor (Fig. 6).

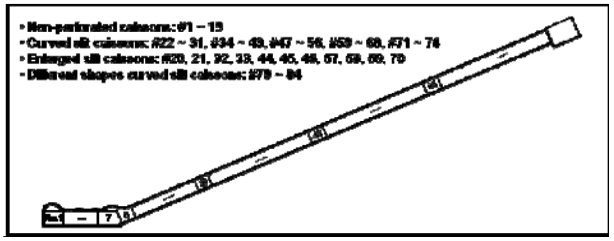

Figure 6. Schematic diagram of installed caissons in west breakwater

3.3 Results of settlement measurement

Figures 7, 8, and 9 show the selected caisson settlement data of the 84 total caissons installed in the west breakwater. These selected caissons were installed from approximately 2003 through 2005 and had experienced wave actions. The vertical dotted lines in Figs. represent the date of the occurrence of a high wave that could have affected the caisson's settlement.

Figures 7 and 8 show the settlements of non-perforated caissons. Figure 7 shows the caissons #4, 5, 7, 8, and 9 installed before Typhoon Maemi attacked on September 12, 2003. Figure 8 depicts caissons #11, 13, 14, and 16 installed after Typhoon Maemi.

As shown in Fig. 7, the final settlement varied for each caisson, but the settlement trend was very similar across caissons. The initial immediate settlement occurred after the installation of the caisson due to its weight. Then, creep settlement occurred steadily due to the properties of the sand in this area. Then, on particular dates, such as September 12, 2003, a significant amount of settlement occurred rapidly. It is unlikely that this rapid, significant settlement was caused by the material properties of the sand because the settlement progressed greatly in a short period of time. Rather, this settlement may have been induced by wave actions. The settlement occurred at the same time that a big wave hit. This wave-induced settlement is discussed in more detail in Section 4.

As Fig. 8 illustrates, the caissons installed after Typhoon Maemi exhibits continual settlement behavior, and on particular dates, such as in March and December of 2005, rapid settlement occurred. This tendency was similar to that depicted in Fig. 7.

Figure 9 shows the settlement histories of curved slit caissons #22, 25 and 26. They were installed from September 2004 to March 2005. Each caisson exhibited different final settlement characteristics but a similar settlement trend, such as that depicted in Figs. 7 and 8, which involved initial immediate settlement after the installation of the caisson, a steady creep settlement, and a significant amount of rapid settlement due to wave loading.

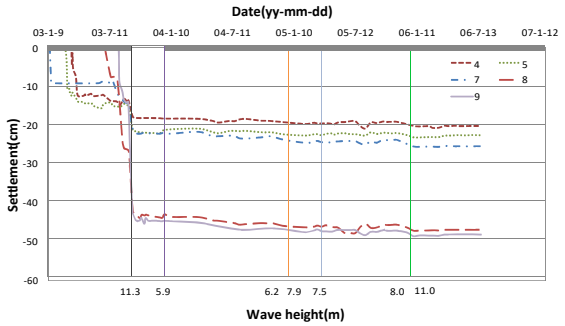

Figure 7. Settlement histories of caissons with wave occurrence for non-perforated caissons #4, 5, 7, 8 and 9

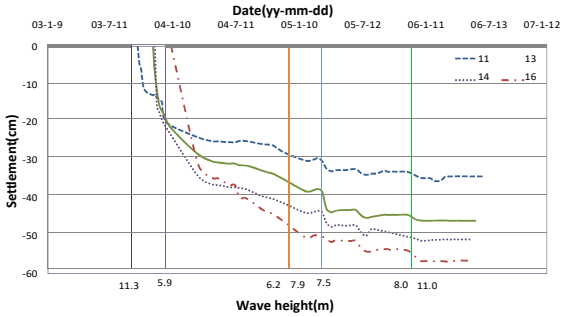

Figure 8. Settlement histories of caissons with wave occurrence for non-perforated caissons #11, 13, 14, and 16

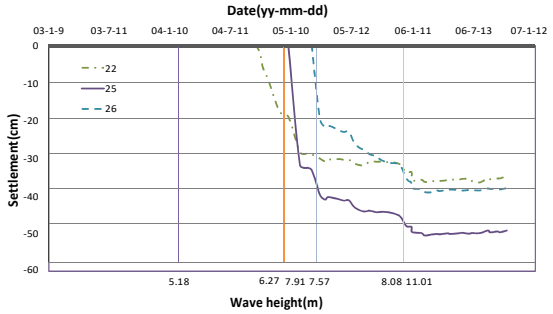

Figure 9. Settlement histories of caissons with wave occurrence for curved slit caisson #22, 25, and 26

4 Analysis of settlement results in caisson breakwater

The results from the non-perforated caissons, which had the longest measurement period, clearly show the effect of waves on caisson settlement. As Fig. 7 illustrates, significant settlement occurred when Typhoon Maemi attacked; the highest recorded wave height of this typhoon was 11.38 m. The settlement of caisson #8, which was installed just three months before the typhoon, increased from 26 cm to 42 cm after the typhoon. The settlement of caisson #9, which was installed just one month before the typhoon, increased greatly from 14 cm to 45 cm after the typhoon. Other caissons also exhibited a significant amount of wave-induced settlement, though of a lesser magnitude than caisson #9 because they were installed much earlier.

After Typhoon Maemi, several instances of waves exceeding 5 m in height occurred at this site (see Table 1 and Fig. 7). Interestingly, they produced no significant settlement occurrence that could have been considered wave-induced settlement. Only slight rapid settlement occurred on December 21, 2005, during a storm that produced waves as high as 11.01 m. It shall be explained why does this happen at section 4.3.

Figure 8 shows the settlement data of the non-perforated caissons installed after Typhoon Maemi. They followed a similar settlement trend, even though the exact amount of settlement of each caisson differed. Significant settlement occurred when the 7.57 m wave hit on March 24, 2005. Then, another instance of rapid settlement occurred in July 2005; unfortunately, the wave height was not recorded because the wave gauge was missing. However, this settlement certainly occurred due to the force of a wave. Another instance of settlement considered to have been wave-induced occurred around December 2005, when wave heights reached 8.64 m and 11.01 m. Figure 9 shows data obtained from other types of caissons indicating a similar relationship between waves and settlement.

Based on the measured settlement data, the characteristics of wave-induced settlement that occurred in the caissons can be categorized into two groups: 1) significant, rapid settlement when big waves hit, such as during a typhoon, ii) very slight, if any, settlement when smaller waves hit. The first type of settlement characteristic is related to the full (or partial) liquefaction caused by the buildup of oscillatory and residual excess pore pressure. The seabed surrounding coastal structures may experience large excess pore pressure buildup during high wave loading. This excess pore pressure can reduce the strength of the soil and potentially induce the full (or partial) liquefaction of a particular layer of the seabed. The second settlement characteristic is related to the ground compaction resulting from the solidification process (dissipation of excess pore pressure) occurring in the seabed.

5 Conclusions

This study was conducted to characterize wave-

induced settlement in the caisson breakwater by analyzing the settlement data measured in actual breakwaters over a long period of time, more than 5 years. To determine the effect of waves on seabed settlement, the wave history recorded during the same construction period also was analyzed. Waves clearly influence the settlement of caisson breakwaters. Wave-induced settlement in breakwaters becomes very significant and rapid when big wave attack, such as during a typhoon. Meanwhile, if a subsequent wave is similar to or less than the previous wave in terms of magnitude, its effect on the settlement of the caisson will be insignificant. Settlement in caisson breakwaters is induced by full (or partial) liquefaction of the seabed ground resulting from the increase of excess pore pressure and the solidification process of seabed grounds, which occurs due to the dissipation of excess pore pressure.

Acknowledgements

This work was supported by the National Research Foundation of Korea Grant funded by the Korean Government (MSIP) (2017R1C1B5017461).

References

[1] S.-H Cho, *A Study on the Characteristics of Cheju Island's Beach Sands*, Cheju National University, Master Thesis, 2007.

[2] T.-H. Kim., J.-M. Nam, L. Ge and K.-I. Lee, Settlement Characteristic of Beach Sands and Its Evaluation, *Marine Georesources & Geotechnology*, 26(2):67–85, 2008.

[3] J.R.C., Hsu and D.S. Jeng, Wave-induced Soil Response in an Unsaturated Anisotropic Seabed of Finite Thickness, *Intl. J. for Numerical Analytical Methods in Geomechanics*, 18(11):785–807, 1994.

[4] H. Sekiguchi, K. Kita and O. Okamoto, Response of Pore-elastoplastic Beds to Standing Waves, *Soils and Foundations*, 35(3):31–42, 1995.

[5] J. Miyamoto, S. Sassa and H. Sekiguchi, Progressive Solidification of a Liquefied Sand Layer during Continued Wave Loading, *Geotechnique*, 54(10): 617–629, 2004.

[6] S. Sassa and H. Sekiguchi, Analysis of Wave-induced Liquefaction of Beds of Sand in Centrifuge, *Geotechnique*, 49(5):621–638, 1999.

[7] O.S. Madsen, Wave-induced Pore Pressure and Effective Stresses in a Porous Bed, *Geotechniqu*e, 28:377–393, 1978.

[8] T. Yamamoto, H. Koning, H. Sllmejjer and E. Van Hijum, On the Response of a Poroelastic Bed to Water Waves, *Journal of Fluid Mechanics*, 87:193–206, 1978.

[9] B.M. Sumer and J. Fredsøe, *The Mechanics of Scour in the Marine Environment*, World Scientific, 2002.

[10] J. Li and D.S. Jeng, Response of a Porous Seabed Around Breakwater Heads, *Ocean Eng*., 35:864–886, 2008.

[11] J. Ye, D. Jeng, P.L.-F. Liu, A.H.C. Chan, W. Ren and Z. Changqi, Breaking Wave-induced Response of Composite Breakwater and Liquefaction in Seabed Foundation, *Coastal Eng*., 85:72–86, 2014.

[12] M.A. Biot, General theory of three-dimensional consolidation, *Journal of Applied Physics*, 12:155–165, 1941.

[13] K. Zen and H. Yamazaki, Mechanism of Wave-induced Liquefaction and Densification in Seabed, *Soils and Foundations*, 304:90–04, 1990.

[14] K. Zen and H. Yamazaki, Oscillatory Pore Pressure and Liquefaction in Seabed Induced by Ocean Waves, *Soils and Foundations*, 304 :147–61, 1990.

[15] M. Kudella, H. Oumeraci, M.B. de Groot and P. Meijers, Large-Scale Experiments on Pore Pressure Generation underneath a Caisson Breakwater, *Journal of Waterway, Port, Coastal, and Ocean Engineering*, 132(4):310–324, 2006.

A Study on the Development of Maintenance System for Tunnel with Freezing-Thawing Damage

K.H. Park[a], J.W. An[b], S.H. Park[c] and T. G. Yoon[d]

[abcd] Korea Infrastructure Safety & Technology Corporation, Jinju-City, Gyeongsangnam-Do, Korea
E-mail: pkh2989@kistec.or.kr, jwan@kistec.or.kr, icewind98@kistec.or.kr, yoon7647@kistec.or.kr

Abstract –

South Korea is a country where consists of about 64% mountainous. Due to these geographical characteristics, a number of tunnels are constantly increasing and it is inevitable with national land development. Especially, many problems in the winter season such as water leaks, icicles, etc. have been occurred by freezing phenomenon at the road tunnels. Therefore, in order to reduce property damage caused by cold environment, it is necessary to establish a mechanism of freezing-thawing of tunnel structures.

The maintenance of the tunnel is essential because tunnel exposed in cold region exists as possibility of collapse. Additionally, it can seriously damage the national economy and people. Hence, the development of the new concept of technique and evaluation method is needed to deal with the freezing problem and to keep the tunnel durability performance continuously. Based on freezing-thawing day(F), repair/reinforcement process and maintenance strategy system(plan) of tunnel were suggested in this study.

Keywords –

"Water leaks", "Freezing-thawing day(F)", "Tunnel durability performance"

1 Introduction

About 64 % of South Korea's land is mountainous area, and there are a large number of mountain tunnels constructed since the 1970s. In particular, the Gangwon area is in a situation where cannot but inevitably increase the maintenance cost used for repair and reinforcement due to the deterioration of rocks and tunnel linings caused by the repetition of freezing-thawing because of its topographical and climatic characteristics. Accordingly, a reasonable durability level assessment is needed for efficiently utilizing the maintenance cost as the demand for repair and reinforcement of the tunnels in the cold zone of Gangwon area is on the rise.

In particular, the tunnels, which have been used for a lot of public use years after building by a conventional construction method, cause frequent water leaks because the waterproof effect of structures is reduced in a condition where the concrete lining quality is degraded. In addition, the sections influenced by external temperature variation have a poorer quality than the sections not influenced by external temperature because there are delamination and exfoliation of concrete caused by the rebar corrosion, netlike cracks due to dew condensation and the repeated freezing-thawing etc. As a result of investigating entrances and exits for the tunnels in Gangwon area as an example, their construction quality such as linings is relatively poorer than other sections due to adverse environmental conditions of freezing-thawing, and they have a characteristic of frequently causing water leak in a vicious circle as well as accelerating defects due to internal and external temperature variations. In other words, the repair and reinforcement of cold tunnels should select proper materials and construction methods in accordance with the environmentally required performance of facilities, and carry out experimental examination if necessary, or evaluate the performance of construction methods from the test construction and construction results.

Consequently, a reasonable repair and reinforcement should fundamentally remove the cause of deformation rather than structural reinforcement first, repair defects to carry out repair and reinforcement for the purpose of preventing rebar corrosion (carbonation, salt injury etc.), and then observe progress for deformation in the management process.

This study carried out Delphi analysis for a group of experts in the tunnel field in order to derive a performance index for evaluating the durability of cold tunnels, and developed a repair and reinforcement process and a performance checklist corresponding to environmental characteristics of cold zones for the derived performance index.

2 Research Method

In general, the construction management of concrete lining during its hardening process is often negligent from the construction for the mountain tunnels with rapid changes in external temperature. In other words, defects such as tunnel deformation including cracks could occur in a certain section such as pit heads or ventilating holes under the influence of external temperature or temperature variation. Particularly, the kinds of defects and degradation occurred mostly at the entrance and exit of a tunnel under the influence of internal and external temperature variation could include cracks (netlike cracks), freezing damage, delamination and exfoliation caused by freezing and thawing of influent water and water leaks, rebar corrosion caused by dew condensation, and vegetation of mosses etc.

Table 1. Delphi Survey Process

Steps of the Survey	Contents
Primary Survey	○ Documentary Survey ○ Categorization & Classification of the preliminary Performance Indexes
Select Survey Participants	○ Organization the Survey Participants(Expert Panels)
1st Survey	○ Making the Survey Questions
Analysis of the Result of the 1st Survey	○ Evaluating the CVR & making the Performance Index Pool
2nd Survey	○ Revaluating the 1st Survey Items & statistical Analysis ○ Evaluating the additional Items ○ Using the 7-point Likert Scale
Analysis of the Result of the 2nd Survey	○ Calculating the Media, interquartile Range ○ Analysis of Frequency
3rd Survey	○ Revaluating the 2nd Survey Items & statistical Analysis ○ Using the 7-point Likert Scale
Analysis of the Result of the 3rd Survey	○ Evaluating the CVR & Verifying the Reliability
Final Analysis	○ Analysis of Frequency about the Order of Priority and the Agreement Degree of Importance of Performance Indexes

Therefore, Delphi technique was utilized by making use of experts to derive an evaluation index related to the detailed elements influencing the durability performance of tunnels from diverse deformation causes.

Delphi technique has an advantage in that different opinions derives an agreement as the number of times being surveyed is repeated by carrying out repetitive surveys for the same panel and sharing the result derived from respective panels. This study carried out a total of three Delphi surveys to derive an agreed result of the panel composed of experts in tunnel field.

In order to utilize Delphi technique, a preliminary evaluation index was derived through the existing precedent studies and literature search, and the first Delphi survey with a mixture of open and closed types was carried out to collect various opinions of experts. The second and third Delphi surveys analyzed the expert group's opinions about the importance between respective performance indexes through closed type questions to derive the final performance evaluation index. The Delphi survey process carried out in this study is as Table 1.

For a Delphi survey, expertise and sincerity etc. were considered to organize an expert panel, and there is no definite rule on the number of a panel which is a expert group, but there is a functional relation between the Delphi research's reliability and the size of a Delphi panel. In general, if the number of a panel for Delphi analysis is 13 or more, the process reliability between before and after questionnaires never becomes a problem, and it shows a high correlation of 0.80 or more on average (Na, 1999). In order to maximize the reliability of Delphi analysis, the number of a panel should be 10 or more at least (Ewing, 1992), and a panel of just only 10~15 persons could obtain useful results (Ziglio, 1996).

Table 2. Personnel organization for delphi research

Field	Research Institute	Academia	Industry
Personnel organization	10	2	2

Table 3. Career of the panel

Career	10~15 years	Over 15 years
Personnel organization	4	10

This study organized an expert panel of a total of 14 experts in tunnel field who are engaged in a research institute, academia and industry etc. Experts were 10 in research institute, 2 in academia and 2 in industry, and because the expert's qualification is a very important factor (Kwon, 2008) in a Delphi survey, the panel's career was considered to organize with four experts of 10 to 15 years experience in the related field and ten experts of 15 or more years experience in the related field as Table 2 and 3.

The first Delphi questionnaire was prepared with a

mixture of open and closed types. The open-type questions tried to collect additional opinions of experts for the evaluation index, and the closed-type questions were organized to assess whether the evaluation index derived from the literature data review corresponded to the index for performance evaluation. The expert opinions by the first Delphi survey were organized as closed types when preparing the second and third questionnaires to carry out the surveys. The expert opinions of the closed type questionnaire were reflected to select the first performance evaluation index and verify the content validity for reflecting in the second Delphi survey. The content validity is verified by using the content validity ratio (CVR). A CVR value suggests the minimum value according to the number of panels, and it is determined that there is content validity on experts' opinions when it becomes above the minimum value. The content validity is calculated by the following equation (1) (Lawshe, 1975).

$$CVR = \frac{n_e - \frac{N}{2}}{\frac{N}{2}} \quad (1)$$

where, n_e is the number of panels who responded as valid, and N means the number of the entire Delphi panels participating in the study. If the number of panels who responded as an evaluation index being valid for performance evaluation is 100%, 50% and less than 50%, the CVR value is represented as 1.0, 0 and a negative number, respectively. In other words, if the number of panels who responded as valid is 50~100%, the CVR value is located on 0~1.0, and such a CVR value could determine the minimum value as Table 4 according to the number of panels with the data presented by Schipper (Lawshe, 1975).

Table 4. Minimum CVR by respondents

Respondents	CVR	Respondents	CVR
10	0.62	20	0.42
11	0.59	25	0.37
12	0.56	30	0.33
13	0.54	35	0.31
14	0.51	40	0.29
15	0.49	-	-

Average, standard deviation, median, mode and CVR values were calculated for the second Delphi analysis, and the agreement was evaluated to assess the items' validity and whether the panel's opinions converge or not. The agreement is a method that verifies how much agreement is reached between respondents by using quartile deviation and median to schematize a value between Q3 and Q1, and it is said that the ratio of inter-quartile range and median is 0.3 if the agreement is 0.7, which means that the interval of intermediate 50% respondents exists in the range of 0.3×median around the median.

If the agreement of A is 0.9, it means intermediate 50% respondents exist in the range of 0.1×median, which could be determined that 0.9 has responses of the people surveyed being more agreed than 0.7. The agreement is calculated by the following equation (2) (Kim, 2015).

$$1 - \frac{Q_3 - Q_1}{M_d} \quad (2)$$

where, Q3, Q1 and Md are 3/4 fractile, 1/4 fractile and median, respectively. Interquartile (IQR) is calculated by equation (3) which is a measure representing the deviation of panel responses around the median, and it is generally considered that agreement is reached if it is 1.0 or less (Upton, 1996).

$$IQR = Q_3 - Q_1 \quad (3)$$

The third Delphi survey included the statistical analysis result for the second survey result, that is, feedback on the panel's group trends. In order to re-evaluate the importance for each evaluation index, the median and interquartile range for the second survey result were indicated to refer to other panel's opinions. And if advisory opinions were different from majority opinions, it was requested to present the opinions. The results were compiled to derive the final performance evaluation index.

3 Developing the Performance evaluation Index for Cold Tunnels

3.1.1 Deriving the Durability Index for Tunnels

Do In order to derive a preliminary evaluation items for each tunnel's performance, it was investigated and analyzed domestic and foreign tunnel evaluation guides, guidelines, standards and research cases etc.

In Korea, the safety of tunnels is evaluated through the 「Detailed Guide on Safety Check and Precision

Safety Diagnosis 」, and according to the Ministry of Construction and Transportation (2001), tunnels are evaluated through various evaluation indexes in several countries such as「Road and Rail Tunnel Standards」in Japan, 「 Maintenance Standards for Concrete Structures 」 in the U.S., and 「 Classification and Management Standards for Segment Damages 」 in Austria.

As a result of analyzing domestic and foreign literature materials carried out in advance, a total of 47 preliminary performance evaluation indexes were derived. Performance items are classified into safety, durability and service performance, and of them, the safety evaluation index was analyzed as 25 items, and the durability and service performance evaluation indexes are as 11, respectively.

In this study, a panel of 14 persons had responded to the survey, and the resulting content validity (CVR value) was based on 0.51 and more. As previously explained, the first Delphi survey was organized by mixing closed and open type questions for 47 preliminary evaluation items derived through literature analysis, and as a result of carrying out the survey, it was represented a total of 7 indexes in durability satisfied the content validity as Table 5. Additionally, as 19 additional evaluation items were derived as Table 6 in the open type survey result, a closed type survey was carried out for a total of 57 preliminary evaluation items in the second Delphi survey.

As a result of carrying out the second Delphi analysis for 57 preliminary evaluation indexes selected through the first Delphi survey, 7 items satisfied the content validity, and for the agreement, the panel's opinions were agreed in 8 items.

In order to re-evaluate the importance of each evaluation index, it was requested that the median and interquartile range for the second survey result were represented to refer to other panels' opinions, and if an advisory opinion was different from the majority opinion, the opinion was presented.

Table 5. Results of 1st Delphi-Survey

Performance	Primary Category	Subcategory	CVR
Durability	Concrete Lining	(1) Strength	0.86
		(2) Carbonation	0.86
		(3) Chloride Content	0.86
	Timber	(4) Strength	0.29
	Ground	(5) Weathering	0.43
		(6) Rock Strength	0.29
	Circumstance	(7) Salt Stress Circumstance	0.86
		(8) Carbonation Circumstance	0.86
		(9) Freezing Damage Circumstance	0.86
		(10) Quality of Water	0.29
		(11) Carbon Dioxide Concent	0.57

As a result, the evaluation indexes satisfying the content validity were 9 items, and two items were more increased than the second evaluation result. Also for the agreement, as 44 evaluation indexes were agreed, 7 items were more increased than the second evaluation result. The results of three evaluations are as Table 7.

Table 6. Additional Index by Open Questions

Performance	Additional Index
Durability	(1) Reinforced Coating
	(2) Lining Thickness
	(3) Timbering Standard
	(4) Tunnel Potal Slope

Table 7. Results of 3rd Delphi-Survey

Performance Assessment			CVR	agreement (less than1)
Performance	Primary Category	Subcategory		
Durability	Concrete Lining	Strength	1.00	1.00
		Carbonation	1.00	1.00
		Chloride Content	0.43	1.75
		Cover Thickness	1.00	1.00
		Lining Thickness	1.00	2.00
	Timber	Timbering Standard	0.71	1.00
	Ground	Tunnel Potal Slope	1.00	2.00
	Circumstance	Salt Stress Circumstance	0.86	1.00
		Carbonation Circumstance	1.00	1.00
		Freezing Damage Circumstance	1.00	1.00
		Carbon Dioxide Concent	0.14	1.00

As a result of carrying out a total of three Delphi surveys to select the performance evaluation index for tunnels, 9 durability evaluation indexes were selected. The selected performance evaluation index went through an expert joint meeting of three persons in research institute, four safety diagnosis practitioners and two in industry to undergo a process that modifies and complements the index, where some redundancy existed and investigation was practically impossible, to select the final performance evaluation index. The finally selected durability performance evaluation index is as Table 8.

Table 8. Results of 3rd Delphi-Survey

Performance Assessment		
Performance	**Primary Category**	**Subcategory**
Durability	Plain Concrete Lining	Strength
		Freezing Damage Circumstance
	Reinforced Concrete Lining	Strength
		Salt Stress Circumstance
		Carbonation
		Chloride Content
		Freezing Damage Circumstance

3.2 Durability Index Analysis Considering Environmental Characteristics of Cold Zones

As a result of analyzing content validity (CVR value) by the performance evaluation index, of the durability indexes that could consider special environmental characteristics of tunnels in cold zone, salt injury, carbonation and freezing were selected as major indexes. As the following derived durability index for tunnels (Table 9), among salt injury, carbonation and freezing environment factors of major index items, particularly for mountain tunnels in Gangwon area, progressive crack is extended by the repeated mechanism of freezing-thawing, and damages also occur inevitably by secondary damage from salt injury caused by salt water and calcium chloride etc. frequently sprayed due to the cold zone's characteristics in addition to the extended cracks.

Table 9. Final performance assessment and evaluation method

Performance Assessment		
Primary Category	**Subcategory**	**Assessment Methods**
Plain Concrete Lining	Strength	- Nondestructive strength
	Freezing Damage Circumstance	- Freeze-thaw cycles(day)
Reinforced Concrete Lining	Strength	- Nondestructive strength
	Salt Stress Circumstance	- Coastal distance measurement
	Carbonation	- Carbonation depth
	Chloride Content	- Amount of chloride & Permeability
	Freezing Damage Circumstance	- Freeze-thaw cycles(day) - Number of snowfall - Spraying of snow remover

In addition, the number of repeated freezing-thawing days, snowfall frequency and scattering deicing agent or not were selected as assessment methods for the durability evaluation index of the freezing-thawing environment, and in particular, for the tunnels which have been used for a lot of public use years after building by a conventional construction method, water leak frequently occurs because the concrete lining's quality was low in general and the waterproof effect of the tunnel structures is reduced.

Gangwon area, which is the subject of this study, has about 10% of all tunnels in Korea as the following Fig. 1, and most of them are mountain tunnels due to the regional characteristics. Therefore, for the tunnels located on the cold zone like Gangwon, an environmental condition, in which deterioration and deformation of tunnels cannot but more occur inevitably due to repetitive freezing-thawing compared to other regions, exists.

In particular, major damage cases of the existing tunnels built in cold zone lead to blocking tunnel drainage caused by icing or freezing of ground water around tunnels etc., and as a result, it is applied as repetitive stress extruding-releasing tunnel linings toward the inside cavity by base surface freezing of the lining back face in a poor tunnel drainage condition.

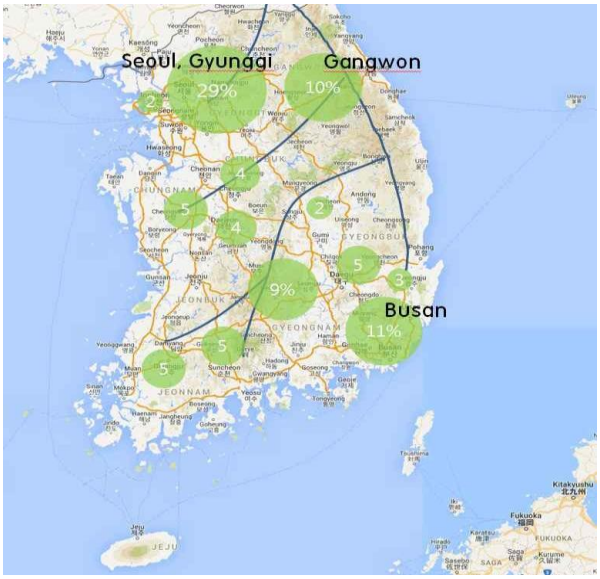

Figure 1. Status of 1. 2 domestic tunnels Tables

According to a domestic tunnel freezing case study related to freezing-thawing of cold zones (Kim, 2013), for the area like Daegwallyeong (Gangwon), it was generally observed the phenomenon where drain pipes had frozen if daily mean temperature remains below about -7℃ for 2~3 days, and it was reported that the phenomenon, where icicles melt down, occurs repeatedly if ambient air becomes above 0℃ after icicles form by ascending from the sidewall floor of construction joints to the ceiling in particular.

Table 10. The grading system of freeze-thaw cycle(F)

Grade	Freeze-thaw cycle(F)	Explanation
A	F < 3	Best condition without freeze-thawing
B	3 ≤ F < 15	No significant impact but exiting minor influence on auxiliary member due to freezing-thawing
C	15 ≤ F < 30	Simple maintenance and reinforcement are necessary because of prevention for durability degradation with freeze-thawing
D	30 ≤ F < 50	Need to repair and reinforcement of urgent heat insulation degradation with freeze-thawing
E	50 ≤ F	Need to do maintenance techniques such as heat etc.for tunnel with freeze-thawing

※ If the relative elastodynamic coefficient is above 90% based on 300 repeated days of freezing-thawing, the freezing damage environment assessment could be omitted. The freezing-thawing repeated days are calculated based on the Meteorological Administration's data to uses for the evaluation, and relative elastodynamic coefficient is measured by KS F 2456 (A law).

※ Relative elastodynamic coefficient: A criterion to determine the freezing damage resistance, which represents the ratio of elastodynamic coefficients before and after being influenced by freezing-thawing as a percentage (freezing damage resistance is larger as relative elastodynamic coefficient is higher).

Therefore, this study proposed that the number of freezing-thawing repeated days(F) is derived and then ranked for practical performance evaluation corresponding to regional and environmental characteristics and follow-up action(repair and reinforcement) to derived tunnel durability performance index, and the calculation referred to the freezing-thawing test standard of Ireland(freezing: two days or more at -7℃, thawing: three days or more at 6℃.

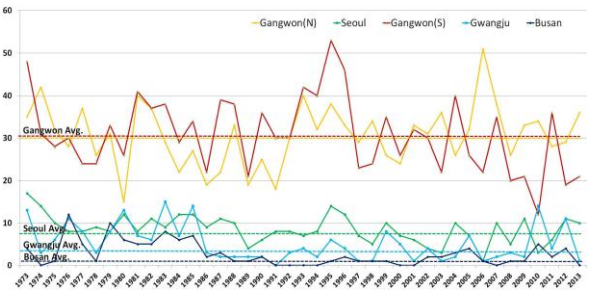

Figure 2. Comparison of freeze-thaw cycle(F) for 40 years with regions in S. Korea

In order to calculate the freezing damage environment standard, the evaluation method referred to the performance-focused evaluation manual by facility type(2016) to analyze the effects of freezing-thawing based on the Korea Meteorological Administration's data of Gangwon(Wonju, Daegwallyeong), Seoul, Busan and Gwangju areas in winter season(November 1 ~ March 31) over the past 40 years.

As a result of analyzing with the number of freezing-thawing repeated days as the following Fig2 and Table10, Gangwon area was a D region, which was classified into a region where had the greatest number of freezing-thawing repeated days(F) compared to Seoul, Busan and Gwangju areas. In other words, as Fig. 2 of the result that calculated the number of freezing-thawing repeated days(F) to plot, the number of freezing-thawing repeated days(F) in Gangwon area was calculated more than about 2~3 times compared to other

areas in Korea, and the class was mostly C~E, which should be classified into cold tunnels rather than general tunnels, and it is judged that repair and reinforcement for improving tunnel durability should also prepare a maintenance system considering cold area's environmental characteristics corresponding to regional environment characteristics.

4 Developing a Repair and Reinforcement Process and Maintenance Strategy System for Tunnels in Cold Area

Currently, many tunnels are used in Gangwon area where mountains are widely distributed, and it is known that temperature is usually about -5℃ lower than the tunnel inside because of low sunshine amount at tunnel's entrance and exit and shadows produced by nearby slopes in particular. Then, the ground water flowed in from nearby valleys or the melted snow flowed down into a pit head to freeze the road surface which temperature in winter season is low to cause user damages (slippiness) or road freezing if not quickly removing snow accumulated on the road due to heavy snowfall.

In addition, if the leaked ground water is frozen due to temperature drop inside the tunnel, it causes secondary damage by tunnel structure's durability reduction and falling ice to users driving the road. The tunnel structure affected by cold area's freezing damage would continue to accelerate durability reduction of the structure rather than one-time damage, and the degree recently becomes more severe because of climate change. For development and application of maintenance technology for the structures affected by freezing damages, as its introduction timing is earlier, it could decrease the structure's durability reduction speed, and secure safety of road users in cold area.

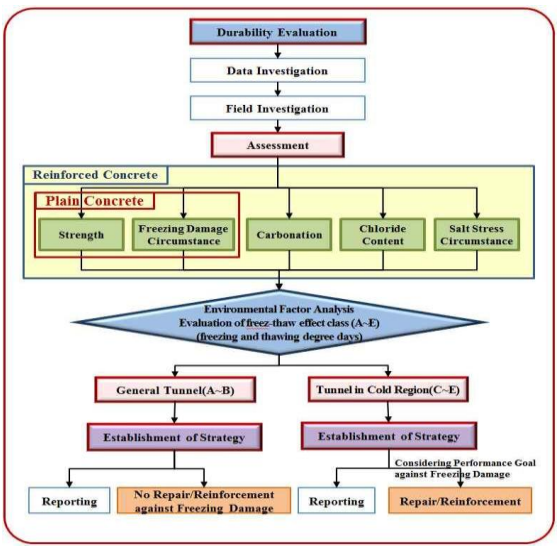

Figure 3 Maintenance and reinforcement process

Accordingly, it is important to develop and apply a proper blocking technology to prevent damages that could arise because the ground water of valleys near tunnel's entrance and exit, snow accumulated on the road due to heavy snowfall, or snow melted during the thaw is flowed in the road to freeze, and a systematic maintenance plan should be established for reasonable blocking and repair·reinforcement depending on tunnel's ambient air by classifying general/cold tunnels corresponding to environmental elements based on the developed durability evaluation index.

This study proposed a repair·reinforcement process and maintenance strategy system (proposal) as the following Fig. 3 and Table11 based on tunnel's regular and precision safety diagnosis, durability index, and the number of freezing-thawing repeated days (F) related to cold tunnel's repair·reinforcement.

Table 11. Maintenance and reinforcement management strategy detailed-items

Target Freezing Damage Reduction Method		Required Performance
▢ Road Tunnel Lining Part Insulation Performance Improvement Method	Environmental Factors	○ Reach the target heating temperature even under extreme conditions such as ambient temperature and humidity
		○ Keep the reaching and duration time of the target heating temperature
		○ No damage harmful to structures due to heating
		○ Material itself should be applied to extreme environment not to be damaged and to be preserved and kept
	Material Factors	○ Secure heating, maximum heat reaching time and duration time of CNT (or moisture absorption heating fiber)
		○ There should be no excessive deformation after installing on the lining
		○ It should be easy to attach and install to the lining, and have durability
		○ It should be easy to combine between CNT materials and system components
		○ Efficiency of power (energy) consumption

		○ Corrosion resistance, minimize malfunction over time
		○ Also secure durability of not only CNT but also component materials (covering material etc.)
▢ Road Tunnel Lining Part Leakage Prevention Method	Environmental Factors	○ Keep the drainage system's drain function
		○ Prevent freezing caused by outflow water retention in the drainage system (drain board and pipe)
		○ Function to prevent the water leak spread of drain board's attached material (Hotty Gel)
		○ Durability of drainage system itself for low temperature environment
	Material Factors	○ Drain boards should keep the prescribed strength even under severe cold conditions
		○ Drain boards should be easy to assemble, process and attach
		○ The drain board and guided drain pipe product itself should have great resistance to freezing when contacting the inflow water
		○ Hotty Gel should be materials that formability and bondability continues to keep in a four-season condition to attach between two materials (concrete lining - drainage board) not to spread water leaks.
▢ Freezing Prevention Method for Road Surfaces at Road Tunnel's Entrance and Exit	Environmental Factors	○ Reach the target heating temperature even under an extreme condition such as ambient temperature and humidity
		○ Keep the target heating temperature reaching and duration time
		○ There should be no damage harmful to structures due to heating
		○ Material itself should be applied to extreme environment not to be damaged and to be preserved and kept
		○ Keep performance and functions even in the vehicle driving environment
	Material Factors	○ Secure heating, maximum heat reaching time and duration time of CNT (or moisture absorption heating fiber)
		○ There should be no excessive deformation after installing on the lining
		○ It should be easy to attach and install to the lining, and have durability
		○ It should be easy to combine between CNT materials and system components,
		○ Efficiency of power (energy) consumption
		○ Corrosion resistance, minimize malfunction over time
		○ Also secure durability of not only CNT but also component materials (covering material etc.)

5 Conclusion

In general, because the tunnel's freezing-thawing arises from moisture (water leak), proper drainage of ground water in the tunnel's back side is most important, and a proper complementary method such as insulation and leakage prevention should be applied for the existing tunnels constructed.

This study derived major evaluation indexes for tunnel's durability performance and classified into general/cold tunnels by regional environment characteristics to prepare a reasonable maintenance system based on the tunnel's durability index, and prepared a reasonable repair·reinforcement and maintenance system corresponding to it.

As a result of analyzing the related literature and precedent studies for this purpose, a total of 47 preliminary evaluation indexes were derived, and in order to derive the final index for performance-focused evaluation, three Delphi surveys were carried out for 14 experts engaged in research institute, academia and industry and the final agreement was derived.

Based on the durability evaluation index derived in this study, it could be utilized to support a reasonable decision making and management system when establishing a durability performance focused repair·reinforcement and maintenance system for tunnel structures in cold area, and if detailed items for each repair·reinforcement(maintenance) method are modified and complemented through a future trial application, a more reasonable performance-focused(durability) maintenance system would be able to prepare.

Acknowledgements

This research was supported by a grant(17RDRP-B066780) from Regional Development Research Program funded by Ministry of Land, Infrastructure and Transport of Korean government

References

[1] ASCE, 2013, Report Card for america's infrastructure
[2] Ewing, D.M, 1992, Future Competencies Needed in the Preparation of Secretaries in the State of Illinois Using the Delphi Technique, Ph. D. Dissertatio, University of Iowa
[3] Federal Highway Administration, 2004, Highway and Rail Transit Tunnel Maintenance and Rehabilitation Manual
[4] ISO, 2010, Bases for design of structures—Assessment of existing structures(ISO 13822)
[5] KISTEC, 2002, The manual of tunnel maintenance(in Korea)
[6] KISTEC, 2013, Development of the performance assessment criteria and maintenance manual for the shield-TBM tunnel(in Korea)
[7] KTA, 2009, The Manual of the tunnel design standard(in Korea)
[8] Kwon, T.I., 2009, Study on drawing priority of the influence factors of tourist resort remodeling business : Delphi technic & analytic hierarchy process,the graduate school of sejong university(in Korea)
[9] Lawshe,1975, A Quantitative approach to content validity. Personnel Psychology, 28(4), pp563~575.
[10] Waheed Uddin, W.Ronald Hudson & Ralph Haas, 2014, Public Infrastructure Asset Management 2nd edition,McGrawHillEducation,pp.203~204
[11] Ziglio, 1996, The Delphi method and its contribution to decision-making. M. Adler & E. Ziglio(Eds). Gazing into the oracle: the Delphi method and its application to social policy and public health, pp3-33. London, Jessica Kingsley Publishers
[12] Kim. 2013 A study on the freezing case of 2 arch tunnel

Risk Assessment of Landslide by using Fragility Curves - A Case Study in Shenmu, Taiwan

Chen-Yang Lee[a], Bing-Jean Lee[b], Yi-Min Huang*[c], Tsu-Chiang Lei [d], Meng-Hsun Hsieh[b], Hsin-Ping Wang[d], Yao-Min Fang[c], Hsiao-Yuan Yin[a]

[a]Soil and Water Conservation Bureau, Concil of Agriculture, Executive Yuan, Taiwan, R.O.C.
[b]Dept. of Civil Engineering, Feng Chia University, Taiwan, R.O.C.
[c]GIS Research Center, Feng Chia University, Taiwan, R.O.C.
[d]Dept. of Urban Planning and Spatial Information, Feng Chia University, Taiwan, R.O.C.
*E-mail: niner@gis.tw

Abstract –

About three fourth area of Taiwan is a hillside. In these areas, the steep topography and geological vulnerability make the landslides more likely to occur during torrential rainfall and typhoons. In recent years, because of the increasing torrential rainfall and typhoons, the rainfall-induced landslide has become more common in Taiwan. Therefore, risk assessment of rainfall-triggered shallow landslides has become important, and an empirical model for landslide risk assessment was proposed in this paper. The bi-factor model of using historical rainfall data (the hazard factor) and the landslide fragility curves (the vulnerability factor) was included in the proposed risk assessment method. The estimation of influence of rainfall and the fragility of shallow landslides were addressed in the paper. The use of the critical hazard potential (H_c) and critical fragility potential (F_c) were described by a case study of Shenmu Village in the Chen-Yu-Lan Watershed in Taiwan. The events of Typhoon Sinlaku (Sep. 2008) and Typhoon Morakot (Aug. 2009) were used in the case. This empirical model can express the probability of exceeding a damage state of landslides under certain conditions of rainfall intensity and accumulated rainfall. The results of this study indicated that the proposed method of risk assessment for landslide can be considered as a warning model in practice for disaster preparation and response.

Keywords –

Landslide; Fragility Curves; Risk Analysis; Hazard Analysis

1 Introduction

Taiwan is on the path of Western-Pacific Tyhpoon Path, and on the Cirum-Pacific Earthquakes Belt, indicating Taiwan suffered from two or more naural disasters, which was the highest in the world [1]. Besides, most of the land in Taiwan, about 70% of total area, is hillside. Given the conditions of increasing impacts of climate change and extream weathers, the rainfall-induced landslide has become a serious issue in Taiwan.

Most researches about the landslide used the landslide susceptibility analysis (LSA) to develop landslide evaluation model [2]. The LSA models basically use factors and observed data to construct the description of landslides. The common models developed for landslide hazard or landslide evaluation are usually deterministic analysis [2]. Recently, a novel concept of applying probability to landslide evaluation had been proposed. The fragility curves, which is commonly used in the earthquake-induced structure analysis, had been adopted to represent the probability of landslide [3][4].

In this study, the Landslide Fragility Curve (LFC) model used in the previous research [2][3] was improved. The spatial statistics and geographic information systems (GIS) for data processing were performed on the slope-unit base. The newly improved LFC model introduced the Landslide Fragility Surface (LSF) by considering the influence of both rainfall intensity and accumulation at the same time. The risk assessment of landslide then was analyzed by the LFC model associated with the rainfall hazard potential. The Shemu area of Chen-Yu-Lan Watershed was selected as the study area and historical cases were used to illustrate the application of LFS model.

2 Study Area and Environment Database

The Shenmu area locates in the watershed of Chen-Yu-Lan River. Chen-Yu-Lan watershed is at the central part of Taiwan, as shown in Figure 1. The Chen-Yu-Lan River originates from the north peak of Yu Mountain and is one of the upper rivers of the Zhuoshui River system, which is the largest river system in Taiwan. Chen-Yu-Lan River has a length of 42.4 km with an average declination slope of 5 %, and its watershed area is about

45,000 hectares. This area was fragile after Chi–Chi Earthquake (occurred on September 21, 1999).

The Shenmu area is a location where debris flows frequently occurred [5]. The local village is adjacent to the confluence of three streams: Aiyuzi Stream (DF226), Huosa Stream (DF227) and Chushuei Stream (DF199). In Shenmu, the debris flows usually occurred at the Aiyuzi Stream due to its shorter length and large landslide area (Table 1) in its upstream [5]. Figure 2 shows the terrain of three streams.

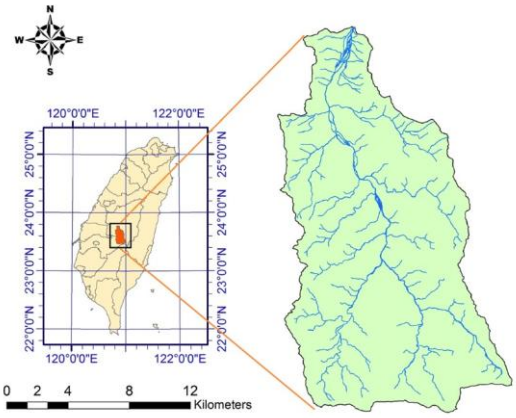

Figure 1. Chen-Yu-Lan Watershed (after [2])

Table 1. The landslide area in Shenmu after 2009 [5].

Debris Flow No.	Stream	Length (km)	Catchment Area (ha)	Landslide Area (ha)
DF199	Chusuei Stream	7.16	861.56	33.29
DF227	Huosa Stream	17.66	2,620	149.32
DF226	Aiyuzi Stream	3.30	400.64	99.85

In addition to the basic terrain data of Shemu area, the hydrologic and geographic factors are needed in modeling [2][3]. To obtain these factors, an environment database of Chen-Yu-Lan watershed was prepared. Among the data collection, the landslide increment (i.e., new landslides) after a rainfall event was also obtained by imagem processing method in this study.

To develop the LFC model, the local environmental data was collected for the study area, and GIS was used to process the data. The environemt database includes data of geology, geological layers, rock property, slope and slope aspects, and DEM, as shown in Figure 3. The new landslide areas (Figure 4) were identified by using pre- and post-events satellite images of Tyhpoon Sinlaku in 2008 and Typhoon Morakot in 2009. These landslide areas were used for later LFC model analysis. Another important factor in the LFC model is the vegetation conditions. The information of vegentation status was also obtained by image processing the same as the determination of new landslides.

In addition to the hydrologic and geographic data , the landslide triggering factors were also considered in data preparation. This study focused on the rainfall-induced landslides. The rainfall data of 10 years (2004~2014) in Shenmu area was collected to compute rainfall indices in the model.

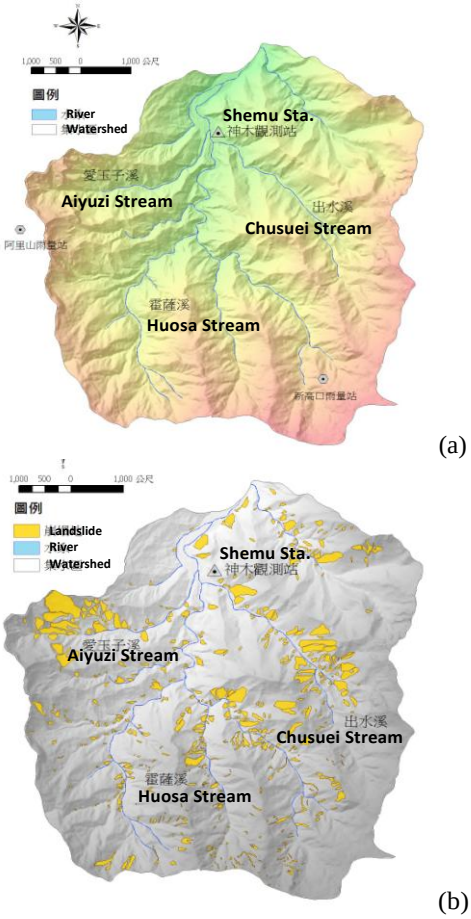

(a)

(b)

Figure 2. The terrain (a) and landslide areas (b) of Shenmu area.

3 LFC Model and Risk Assessment

The risk assessment of landslide considers the hazard potential, the vulnerability, and exposure (target), as expressed in Equation (1). In this study, the hazard was referred to the rainfall hazard, and the vulnerability was represented by the LFC model. The last component in Equation (1) was defined as the protected village, i.e., the Shemu Village in this study.

$$Risk = Hazard \times Vulnerability \times Exposure \quad (1)$$

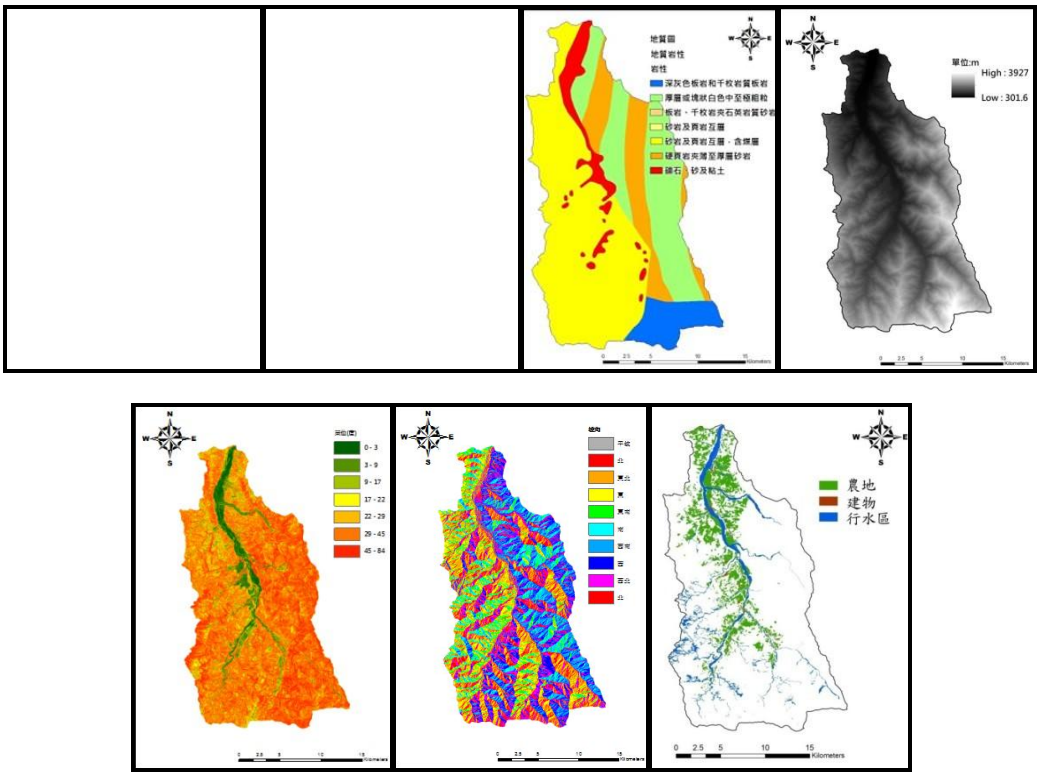

Figure 3. The maps of environment database of Chen-Yu-Lan watershed: (from top left) geologic time, geologic layers, rock property, 5-m DEM, slope, slope aspect, and land use.

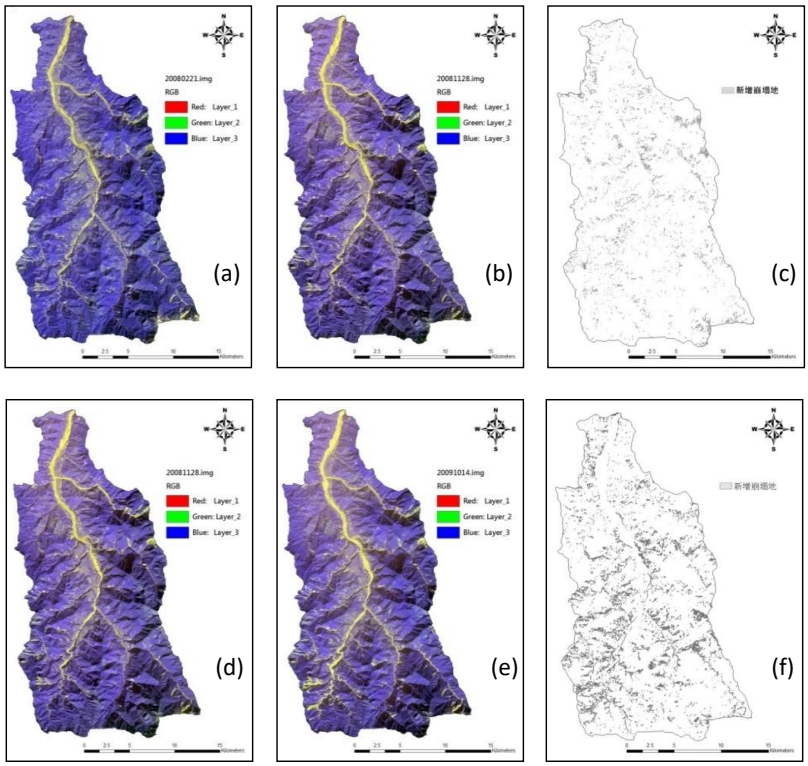

Figure 4. Satellite images of pre- and post-events and the new landslide areas in Chen-Yu-Lan watershed: Typhoon Sinlaku (a) (b) (c); Typhoon Morakot (d) (e) (f).

In the risk assessment of landslides, probability functions were assumed and applied to address rainfall hazard (the potential estimation) and the fragility of landslides. The assessment model was then applied to determine the critical values of rainfall hazard and fragility of landslide based on the landslide case histories.

3.1 Slope Unit

To establish the LFC model, the landslide area was first calculated on the basis of slope units. A slope unit is defined as in Figure 5. The idea of using slope unit as the analysis basis was to properly and physically represent the local conditions, not like the grid cell methods which cannot describe the terrain features properly [3]. Figure 6 shows the slope units of Shenmu area. The number of slope unit of Shenmu area was determined based on the locations of protected targets (houses, roads, and facilities).

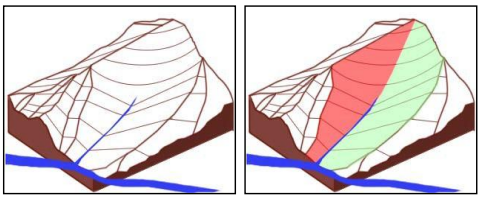

Figure 5. Slope unit delineation.

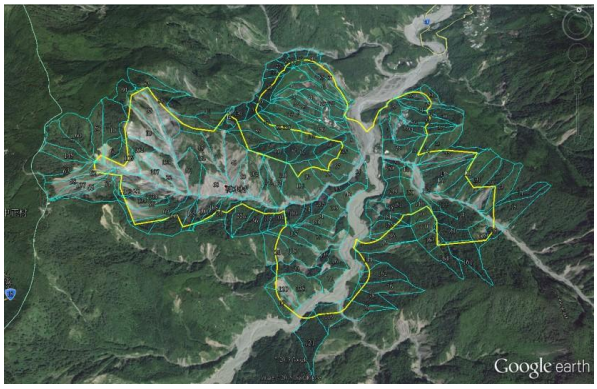

Figure 6. The slope units of Shenmu area.

3.2 Rainfall Hazard Estimation

The 10-year rainfall data of Shenmu area was processed in terms of rainfall events and rainfall indices. The rainfall indices of maximum hourly rainfall (I_{max}) and effective accumulated rainfall (R_{te}, see Equation (2)), as explained in Figure 7, were used for rainfall hazard estimatioin.

$$R_{te} = \sum_{i=1}^{n} \alpha^{i} R_{i}, \text{ where } \alpha = 0.7 \qquad (2)$$

The lognormal standard probability distribution was assumed to construct the probabilitiy model of rainfall hazards. Joint probability mass function (JPMF) and Joint Cumulative Distribution Function (JCDF) were used, in association with the rain patterns, to develop a 3D-like probability distribution of rainfall hazard (Figure 8). The probability distribution in Figure 8 was projected onto a 2D plane, and the correspondent distributioin was expressed as a probability contour map. Figure 9 illustrates the rainfall hazard probability contour map of Shame area. This figure was later applied to determine Shemu's critical probability (H_c) of rainfall hazard when given hazard histories.

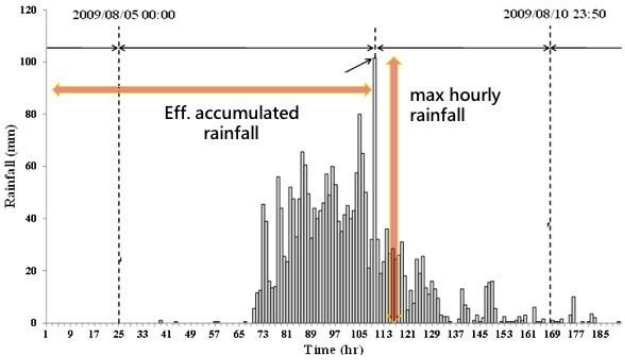

Figure 7. The definition of ranfall indices.

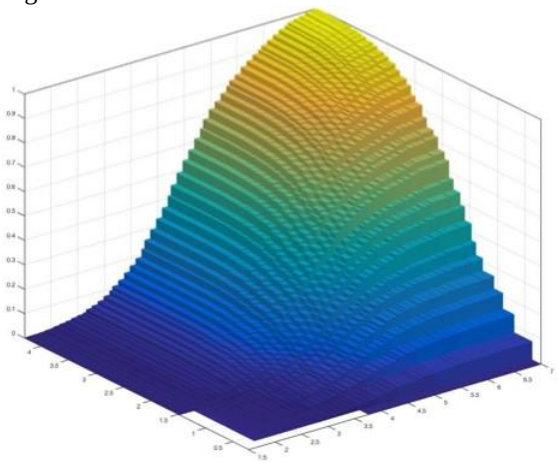

Figure 8. The 3D probability distribution of ranfall hazard.

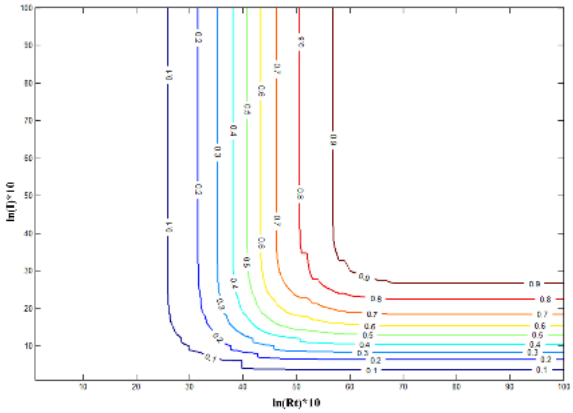

Figure 9. The rainfall hazard probability contour lines (R vs. I) of Shenmu area.

3.3 LFC and LFS model

Based on the available environmental data, 2 triggering factors and 8 environmental factors were chosen to develop LFC model. These factors were max. hourly rainfall (I_{max}), effective accumulated rainfall (R_{te}), geology (G), slope (S), distance to rivers (R), normalized difference vegetation index (N), and slope aspects (A), as shown in Figure 10. Each environmental factors were further divided into levels to classify slope units. There were at most 48 classifications [3][4]. Due to the sparce number of landslide cases, samples of certain classifiations were combined together to improve the model optimization.

Similar to the rainfall hazard estimation, the lognormal probability distribution was assumed to develop LFC model. The maximum likelihood estimation (MLE) was used in the computation to match the results for model optimization. A 3D-like distribution was obtained in terms of I_{max} and R_{te}, as shown in Figure 11. The landslide fragility surface was projected onto a 2D plane and a probability contour map was generated. The landslide fragility curves of Shemu was obtained as in Figure 12.

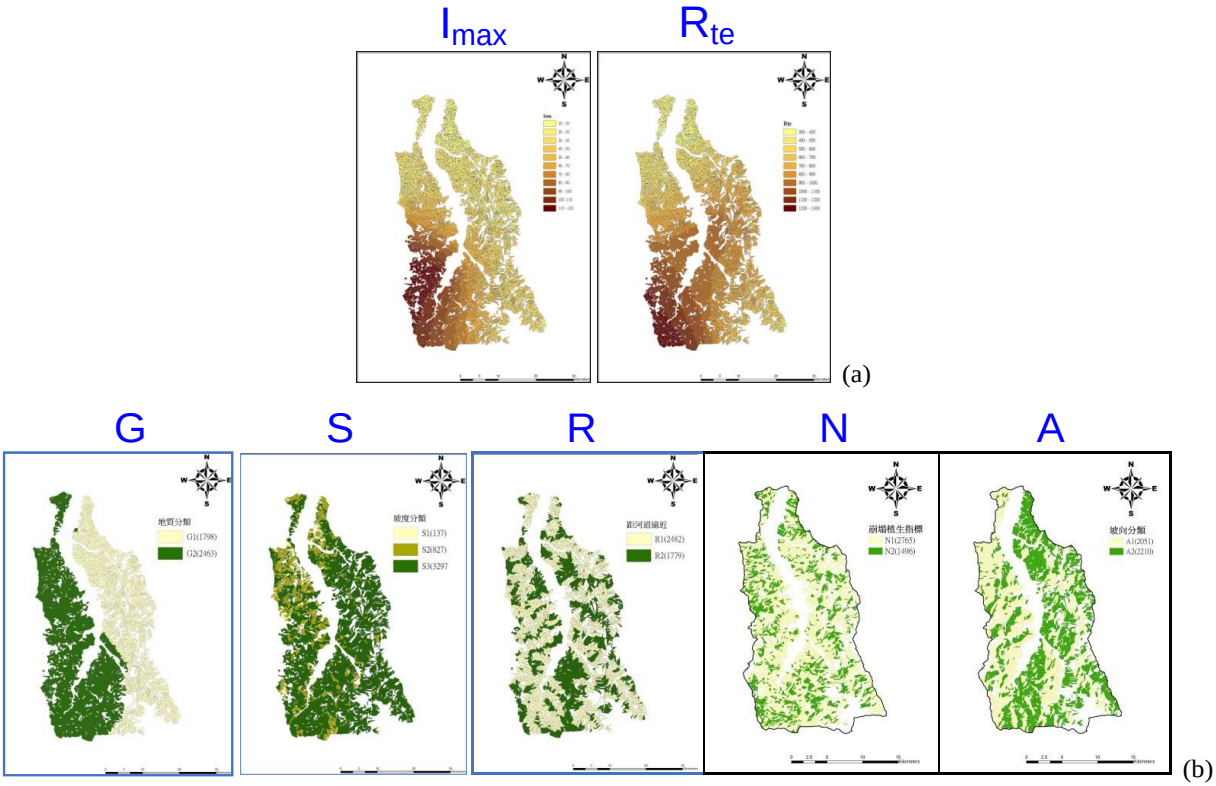

Figure 10. The factors used for developing landslide fragility curve model. (a) triggering factors: rainfall intensity (I_{max}) and effective accumulated rainfall (R_{te}) (b) environmental factors: geology (G), slope (S), distance to river (R), vegetation NDVI (N), and slope aspect (A).

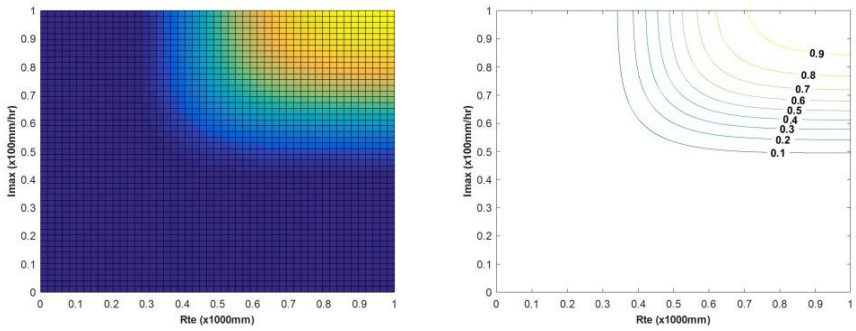

(a) classification: G2S1A1R1N1

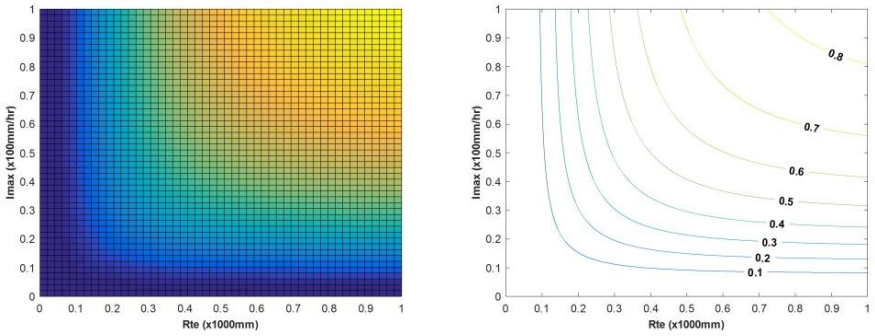

(b) classification: G2S3A2R2N2

Figure 11. Examples of the landslide fragility surface.

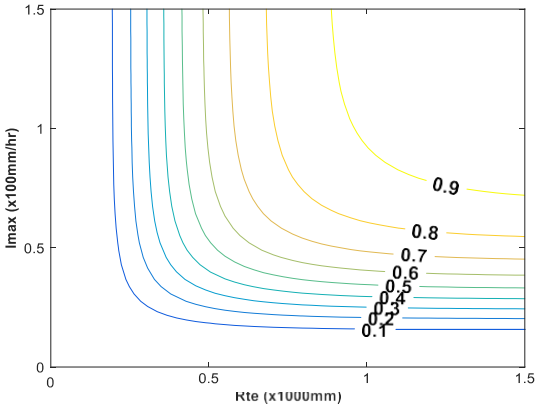

Figure 12. The landslide fragility curves of Shenmu.

4 Case Studies and Results

The risk of landlside was demonstrated by using the critical values of rainfall hazard and landslide fragility. The concept of landslide warning was adopted in this study, and by combining both H_c and F_c, the warning status includes safe stage and unsafe stages, as illustrated in Figure 13. It should be noted that there are two stages of unsafe status, Red I and Red II. Red I stage indicates that the situation has pass H_c and a rainfall hazard could occur. Red II stage implies the most serious condition that in addition to the rainfall hazard, a landslide could occur as well. Both stages are determined with a probability when given a rainfall condition. The procedure of determining safe stage was designed to match the needs of disaster preparation and prediction of government.

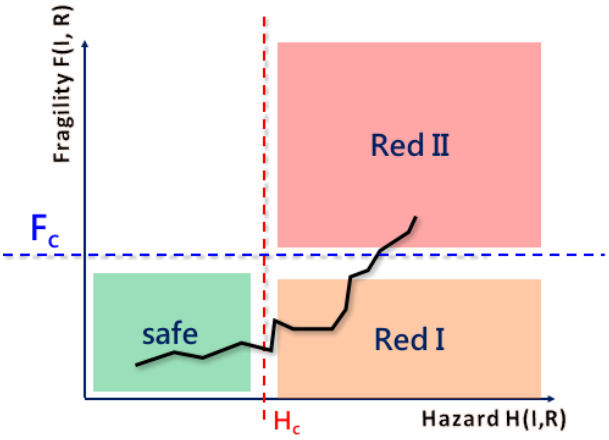

Figure 13. The warning conditions based on landslide fragility (F_c) and rainfall hazard (H_c).

Cases of landslides and debris flows in Shemu were collected from the disaster notices issued by Soil and Water Conservation Bureau of Taiwan. As shown in Figure 14, total of 7 cases were used to determine the critical values of H_c (=0.91) and F_c (=0.23) of Shemu.

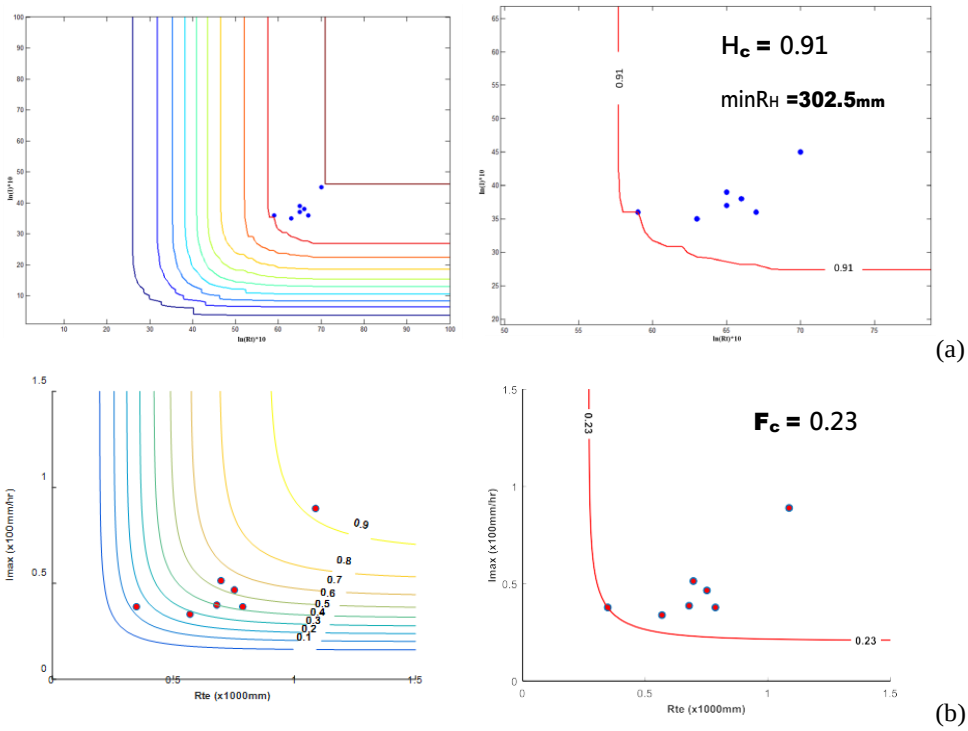

Figure 14. The probability thresholds of rainfall hazard and landslide fragility in Shemu area. (a) rainfall warning threshold (b) landslide warning threshold.

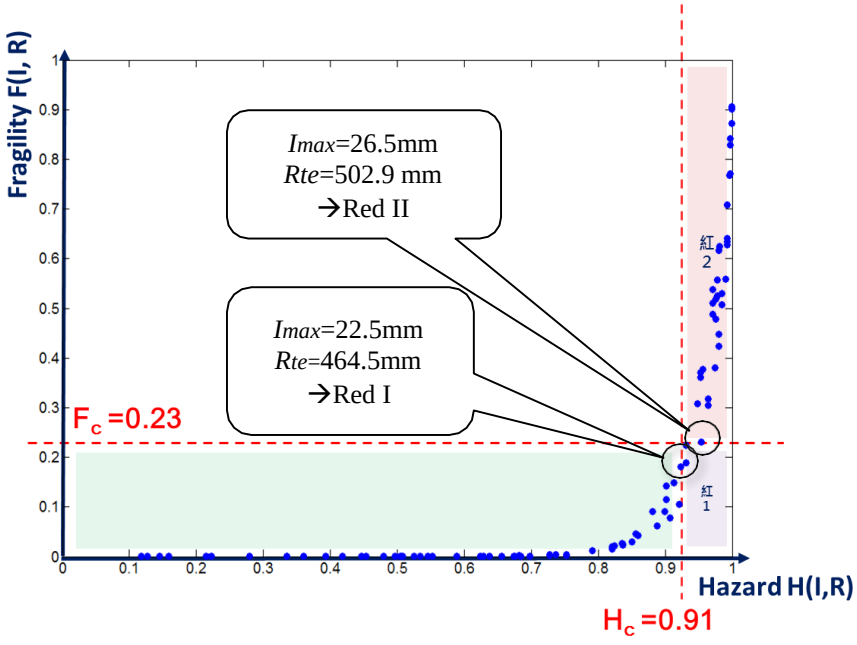

Figure 15. The change of probability during Typhoon Morakot (2009) event in Shenmu area.

The rainfall history of Typhoon Morakot in 2009 was used to evaluate the landslide risk assessment in Shemu. Figure 15 shows the results of event and the dots in the figure represent the rainfall condition (hourly rainfall and cumulative rainfall) and the probability of hazard. It was noted that the dots behaved like a "snake" line going from

Safe stage to Red I and Red II stages. Also, the snake line stayed shortly at Red I stage, and passed to Red II in a jump. This condition implied that when the situation was beyond the H_c line, the landslide hazard was very likely to occur since the rainfall conditions were within Red II zone, not stayed in Red I zone. The results comformed to the records of Typhoon Morakot. Severe landslides occurred at the upper stream areas in Shemu during the typhoon. Therfore, the proposed risk assessment and warning stages of landslide were reasonably useful in this case.

5 Conclusion

This study proposed landslide risk assessment using rainfall hazard potential and landslide fragility curves, and concluded findings as follows.

1. The factors in models were considerably important and essential to evaluate landslide potential.
2. Adoption of slope unit was physically proper in modeling landslide locations.
3. For landslide risk assessment, the impact of rainfall hazard was well described using probability model associated with the historical rain patterns.
4. The proposed landslide fragility curves was derived by considering both rainfall intensity and accumulated rainfall together. The 3D-like probability model was useful for practice if coverted onto a 2D contour lines.
5. The classifications of slope unit can be applied to different areas, and the fragility curve of each classification can be used directly.
6. The procedure of risk assessment was useful for practical landslide disaster preparation and prediction.
7. More cases were needed in order to understand the change of “snake” line under different rainfall conditions and environment.

Acknowledgement

This research was partly supported by the Soil and Water Conservation Bureau, Council of Agriculture, Executive Yuan, Taiwan. Thanks to all people providing help on this study.

References

[1] Dilley M, Chen RS, Deichmann U, Lerner-Lam AL, Arnold M, Natural disaster hotspots. *World Bank report*, 2005, ISBN: 9780821359303

[2] Lei, T.-C., Huang, Y.-M., Lee, B.-J., Hsieh, M.-H., Lin, K.-T. Development of an Empirical Model for Rainfall-induced Hillside Vulnerability Assessment- A Case Study on Chen-Yu-Lan Watershed, Nantou, Taiwan, *Natural Hazards*, 74(2), pp. 341-373, 2014

[3] Lee B.J. et al. 2015 Application of Landslide Fragility Curves in Landslide Risk and Warning Criteria, *Project Report*, Soil and Water Conservation Bureau, 341 (in Chinese), 2016.

[4] Lee B.J. et al. 2016 Application of Landslide Fragility Curves in Landslide Risk and Warning Criteria, *Project Report*, Soil and Water Conservation Bureau, 224 (in Chinese), 2017.

[5] Huang Y.M., Chen W.C., Fang Y.M., Lee B.J., Chou T.Y., Yin H.Y. Debris Flow Monitoring – A Case Study of Shenmu Area in Taiwan, *Disaster Advances*, 6(11), 1-9, 2013.

[6] Yi-Min Huang, Chung-Ray Chu, Yao-Min Fang, Ming-Chang Tsai, Bing-Jean Lee, Tien Yin Chou, Chen-Yang Lee, Chen-Yu Chen, and Hsiao-Yuan Yin. Characteristics of debris flow vibration signals in Shenmu, Taiwan, In *Proceedings of Interpraevent International Symposium 2016*, Lucerne, Switzerland, 2016.

The Vibration Signal Analysis of Debris Flow in Taiwan

Yi-Min Huang* [a], Yao-Min Fang [a], Tien-Yin Chou [a], Chen-Yang Lee[b], Hsiao-Yuan Yin [b]

[a]GIS Research Center, Feng Chia University, Taiwan, R.O.C.
[b]Soil and Water Conservation Bureau, Concil of Agriculture, Executive Yuan, Taiwan, R.O.C.
*E-mail: niner@gis.tw

Abstract –

Debris flow has become a common disaster in Taiwan in recent years since the impacts of extreme weathers has been aggravated. To protect people from the debris flow disasters, a monitoring and warning system was developed by Soil and Water Conservation Bureau (SWCB). There are two types of sensors in the monitoring system: direct and indirect options. The rain gauge, which is an indirect option, measures rainfall in a monitoring station, and used as a debris flow warning factor in the disaster response. In contrast, the geophones (short period seismograph) and broadband seismographs are direct options of debris flow monitoring, and they were used to record the vibration signals generated by debris flows. In this paper, the signal analysis of debris flows was performed by applying FFT, wavelet transform, and Gabor transform. The comparison of the analysis results indicated the characteristic signal of a debris flow was evident in the frequency range of 10~40 Hz, and the signal of front end of debris flow was identified in the lower frequency range of 0~10 Hz. The possibility of applying geophones and broadband seismographs to debris flow warnings was also discussed in this paper.

Keywords –

Debris Flow; Vibration Signal Analysis; Geophone; Broadband Seismograph

1 Introduction

Debris flow has become a common disaster in Taiwan in the past decade [1][2]. In order to protect people and their property from debris flow disasters, the Soil and Water Conservation Bureau (SWCB) of Taiwan worked with universities to develop the debris flow monitoring system and network since 2002. The debris flow monitoring network includes 19 on-site monitoring stations in Taiwan, 3 mobile stations, and 17 portable units. Most of on-site stations are located at the central part of Taiwan. Mobile and portable monitoring stations are used to support monitoring network in an event-driven manner. Most of the warning systems or models of debris flow are rainfall-based options [3][4][5]. Rainfall is considerably easier to measure than other debris flow-related factors. However, rainfall measurement by rain gauges is an indirect option in terms of debris flow detection [2]. False alarms are usually issued in these rainfall-based warning models. In contrast, using direct option in the debris flow monitoring may improve the warning efficiency [2]. The geophone (short period seismograph) and broadband seismograph ([6][7]) are direct options of debris flow monitoring, and they are used to record the vibration signals generated by debris flows. The vibration signals of several debris flow events in Shenmu, Taiwan, were used in this paper to analyze the lower frequency (<30 Hz) characteristics and the signal energy. Disscussion about the using vibration signals for debris flow waring was also addressed in this paper.

2 Study Area and Monitoring Options

The events used in this study are the debris flow disasters occurred in Shenmu Village, Shenmu, Taiwan. The Shenmu area is located in the central Taiwan, where debris flows frequently occurred [8]. A monitoring station was built in 2002, and the village are close to three high-potential debris flow torrents: Aiyuzi Stream (DF226), Huosa Stream (DF227) and Chushuei Stream (DF199). The environmental conditions of Shemu are summarized in Table 1. Based on the case histories, debris flows usually occurred at the Aiyuzi Stream, due to its shorter length and large landslide area in its upstream [1].The debris flow events occurred at Aiyuzi Stream in the past six years are listed in Table 2. There are total of 7 events and no debris flows in Shemu area after 2014.

The monitoring options of debris flow are classified into two types: indirect and direct sensors [1]. The indirect sensor is simply referred to the rain gauge. The direct sensors are wire sensors, geophones, and broadband seismographs. Geophones and broadband seismographs are sensors installed along the river banks to detect ground surface vibration which comes from the movement of debris in the channel.

Theese sensors were installed in the Shenmu

Monitoring Station. The layout of monitoring sensors is shown in Figure 1. There are one geophone and two broadband seismographs installed in the Aiyuzi Stream area. The geophone of GS-20 DX made by Geospace Tech. was used, which has clean band pass of 250 Hz and intrinsic sensitivity of 0.7 V/in/sec. The broadband of Yardbird DF-2, made by Institute of Earth Science, Academia Sinica Taiwan, was used with frequency measurement of 0.13~200 Hz, intrinsic sensitivity of 150 V/m/s, and 24 bit digital resolution [2]. The vibration signals of vertical direction (z-axis) were collected from events and used in the study.

Table 1. Environment of Shenmu Station [1]

Location	Shenmu Village, Nantou County	**Debris Flow No.**	DF199, DF227, DF226
Catchment	Zhuoshui River	**Streams**	Chusuei, Huosa, Aiyuzi
Debris Flow Warning Threshold	250 mm	**Hazard Type**	Channelized debris flow
Monitored Length	5.518 km	**Catchment Area**	7,216.45 ha (Shenmu)
Geology	neogene sedimentary rock	**Slope at Source**	30~50°
Landslide area	Large, 1%≦ landslide ratio ≦5%	**Sediment**	Average debris material size: 3”-12”
Vegetation	Natural woods, medium sparse	**Damaged by**	debris, overflow
Engineering Practice	None	**Priority of Mitigation**	High
Station Elevation	1,187 m	**Coordinate (TWD97)**	X: 235367 Y: 2602749
Protected Targets	**Residents**	**Facility**	**Transportation**
	> 5 households	school	roads, bridges

Table 2. Debris flow hazard history of Aiyuzi Stream, Shenmu (after [2])

Date	Event	Occurrence	Geophone Warning*	Hazard Type
2011/7/13	-	14:33	No	debris flow
2011/7/19	0719 Rainfall	3:19	No	debris flow
2011/11/10	-	13:17	Yes 13:18 (Nov 10)	debris flow
2012/5/4	-	15:56 16:09	No	debris flow
2012/5/20	-	8:15	No	flood
2012/6/10	0610 Rainfall	10:34 15:14	NA (unstable communication)	debris flow
2013/5/17	0517 Rainfall	7:02 (May 19)	No	flood
2013/7/13	Typhoon Saulik	6:54 (July 13)	Yes 6:47 (July 13)	debris flow
2013/8/21	Typhoon Trami	22:41 (Aug. 21)	NA (under repair)	flood
2014/5/20	0520 Rainfall	12:53 (May 20)	NA (unstable communication)	debris flow

*: the warning was issued when the max. accumulated wavelet energy was 5 times the background wavelet energy.

Figure 1. The monitoring layout of Shenmu Station [2].

3 Vibration Signals of Debris Flow

The vibration signals captured by geophones and broadband seismographs are recorded in a time sequence of velocity. The signal is first converted into frequency domain using Fast Fourier Transform (FFT), and then the Haar wavelet transform [9] is used in the signal analysis for geophone data, as well as to estimate the wavelet energy. Based on the previous study, the signal strength has peaks when a debris flow is approaching, and the singal at lower frequency range, i.e., 0~31.25 Hz, shows more clear strength in time sequence [2]. Figure 2 shows typical geophone signals of a debris flow event occurred on July 13, 2011 at Aiyuzi Stream. The debris flow was captured at around 14:33, and the peaks of velocity were observed in the graph. The peaks were also noted in the energy of wavelets.

Similar observation and anlaysis results were found in other debris flow events, as shown in Figure 3 and Figure 4. The singal processing indicates that (1) velocity peaks will occur when a debris flow is approaching; (2) the vibration from a debris flow is majorly within the freancy range of 0~30 Hz; (3) the energy of vibration signals also reflects the peak-manner in the records. It is also noted that stronger amplitudes of frequency usually occurred at frequency less 20 Hz, even less than 10 Hz. Signals from broadband seismogrphs (Figure 4) supports this findings.

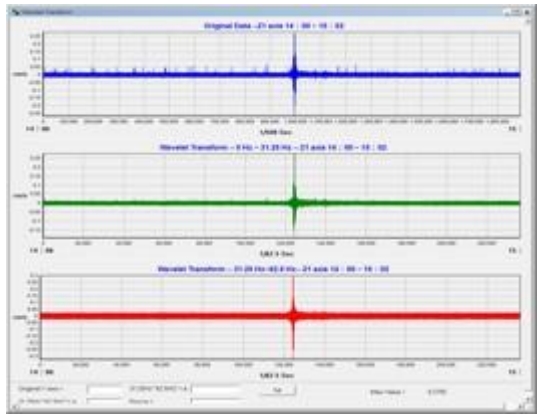

(a) wavelet transform

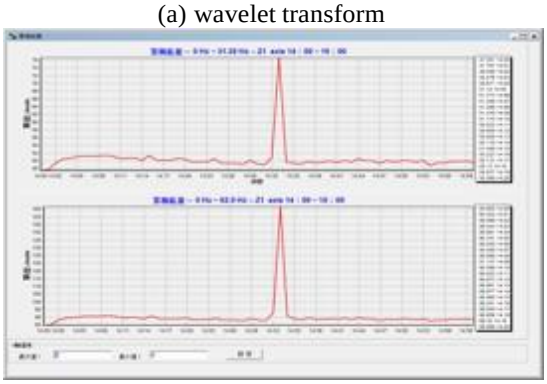

(b) energy of wavelets

Figure 2. The vibration signals of debris flow event on July 13, 2011.

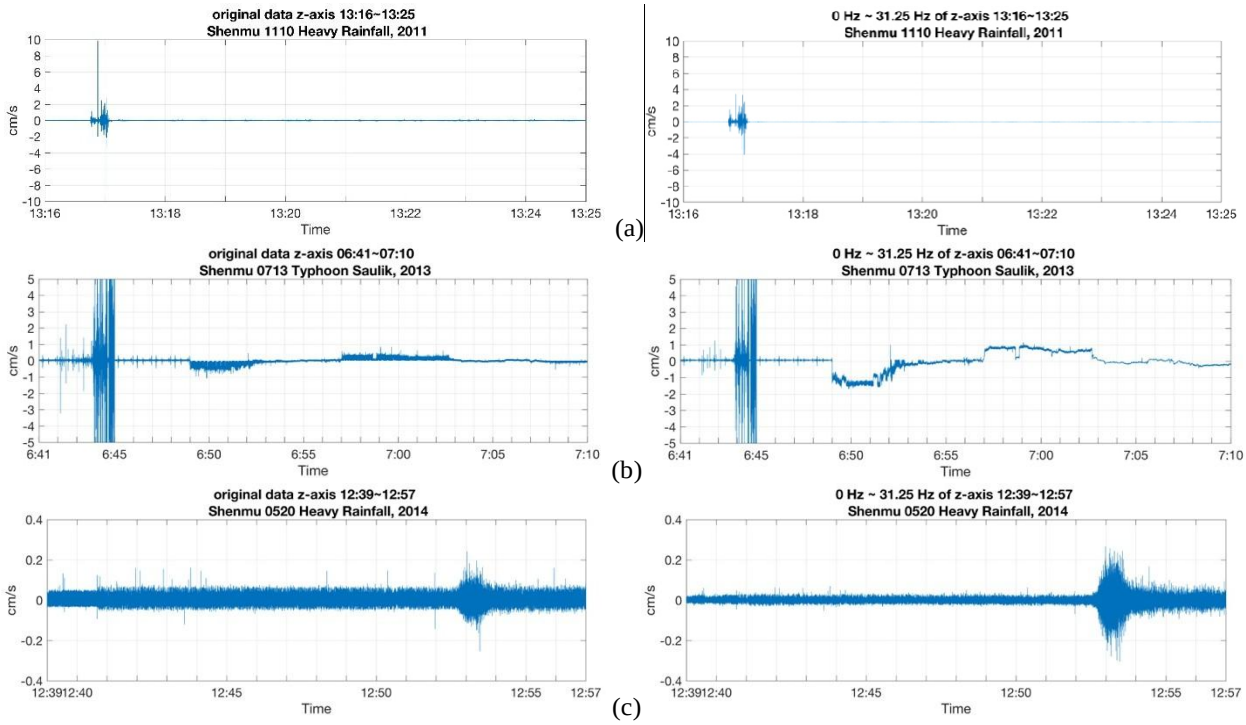

Figure 3. Comaprison of original (left) and 0~31.25 Hz (right) signals of geophone. (a) Nov. 10, 2011 (b) Typhoon Saulik (c) 0520 Rainfall (after [2]).

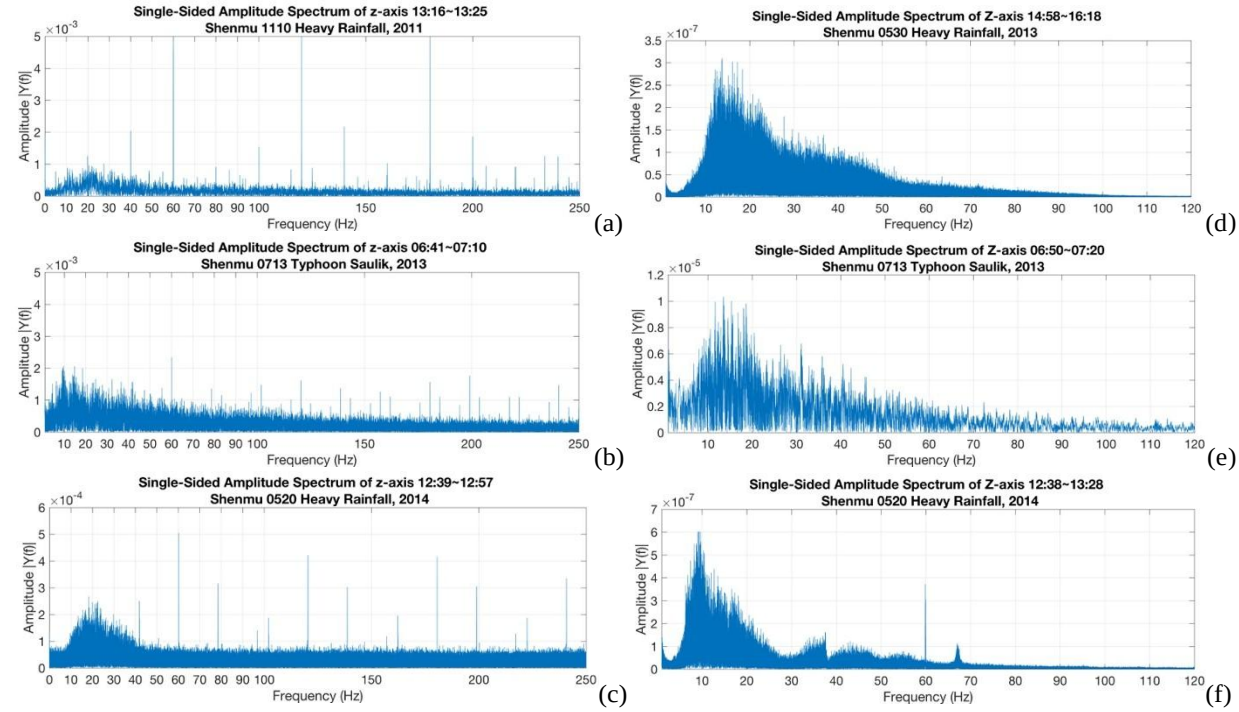

Figure 4. FFT of study cases: geophone (a) Nov. 10, 2011 (b) Typhoon Saulik (c) 0520 Rainfall; broadband seismograph (d) May 30, 2013 (e) Typhoon Saulik (f) 0520 Rainfall.

4 Case Studies and Results

From Table 2, three debris flow events were selected for signal processing and analysis. Since the broadband seismographs were installed in 2013, only the signals of two events of Typhoon Saulik in 2013 and 0520 Rainfall in 2014 were used for comparsion.

The lower frequency range (0~20 Hz) is the main focus of this study. To study the lower range of frequencies, spectrogram was applied to enhance the color of the range. Figure 5 shows the spectrograms of the selected cases. Both signals from geophones and broadband seismographs indicate the early initiation of apparent signal strength at frequency of 0~10 Hz, and even at 0~5 Hz in some cases (e.g., Figure 5 (d) (e)). This behavior implied that the debris flow was captured slightly earlier than the peak signal (the dark red color in the figure) if watching lower frequency signals. Furthermore, the constitution of frequency with time was analyzed by Short-Time Fourier Transform (STFT) to evaluate the strength change of certain frequencies. STFT applies sreening window and separate the signals into sections, and FFT is performed at each section. The Gaussian Window was applied in the STFT, and Figure 6 shows the results. The brighter color in Figure 6 represents stronger intensity of a specific frequency.

It was noted that the stronger frequency was observed in the range of 0~10 Hz, and usually was few mintures earlier than the occurrence of debris flow. This characteristic provides an indication of debris flow occurrence. However, the detection of low frequency range (0~10 Hz) requires higher resolution sensor, and the low-frequency signal may not be clear enough to be identified. Therefore, other option is needed to assist the evaluation.

The energy of vibration signals was used as another factor to evaluate the occurrence of a debris flow. The energy per second, converted from velocity data, of three debris flow events was illustrated in Figure 7. Take Figure 7 (a) for explanation. The first graph shows the energy of signals (denoted as E), in unit of Joule/sec, and the second graph is the cumulative energy (denoted as E_c). The third graph is the slope (= dE_c/sec) of cumulative line, and the last graph is the change of slope (=$(E_{c,i}-E_{c,1})/dt$). It was clear to find a jump in the cumulative energy before the peak velocity, and the timeing of change was clearly determined by comparing both the slope of cumulative energy and the change of slope. When the slope increased from roughly 1.0 to a greater value, or the change of slope jumped up over 1.0, the signal at this moment indicated the upcoming of debris flow. The transition time period in the energy graphs conformed to the period of initiation of low frequency in the seismographs and STFT results.

From these results, the low frequency signal was observed minutes before the arrival of debris flow, and the signal energy was an useful indicator to help determine the status of debris flow occurrence. Both low frequency signal and signal energy can be taken into consideration together in the monitoring system.

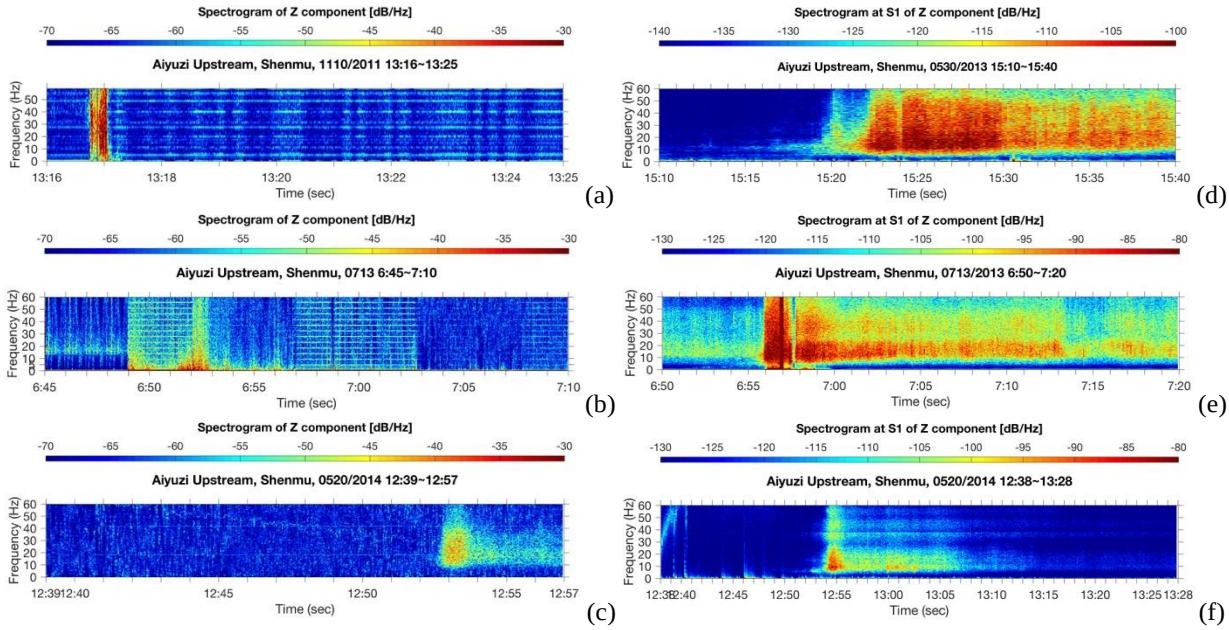

Figure 5. Spectrograms of study cases: geophone (a) Nov. 10, 2011 (b) Typhoon Saulik (c) 0520 Rainfall; broadband seismograph (d) May 30, 2013 (e) Typhoon Saulik (f) 0520 Rainfall.

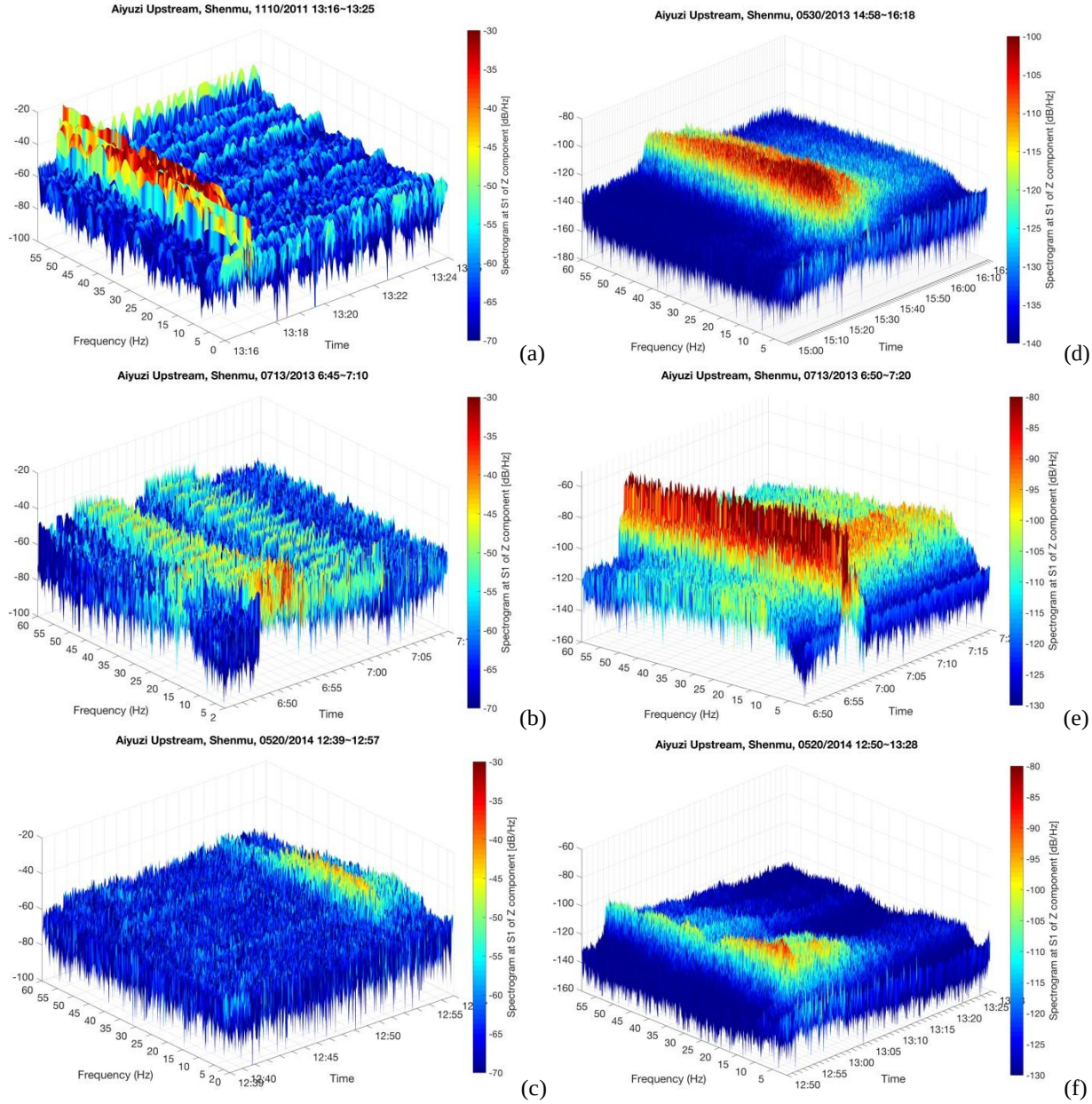

Figure 6. STFT (Gussian wondow) of study cases: geophone (a) Nov. 10, 2011 (b) Typhoon Saulik (c) 0520 Rainfall; broadband seismograph (d) May 30, 2013 (e) Typhoon Saulik (f) 0520 Rainfall.

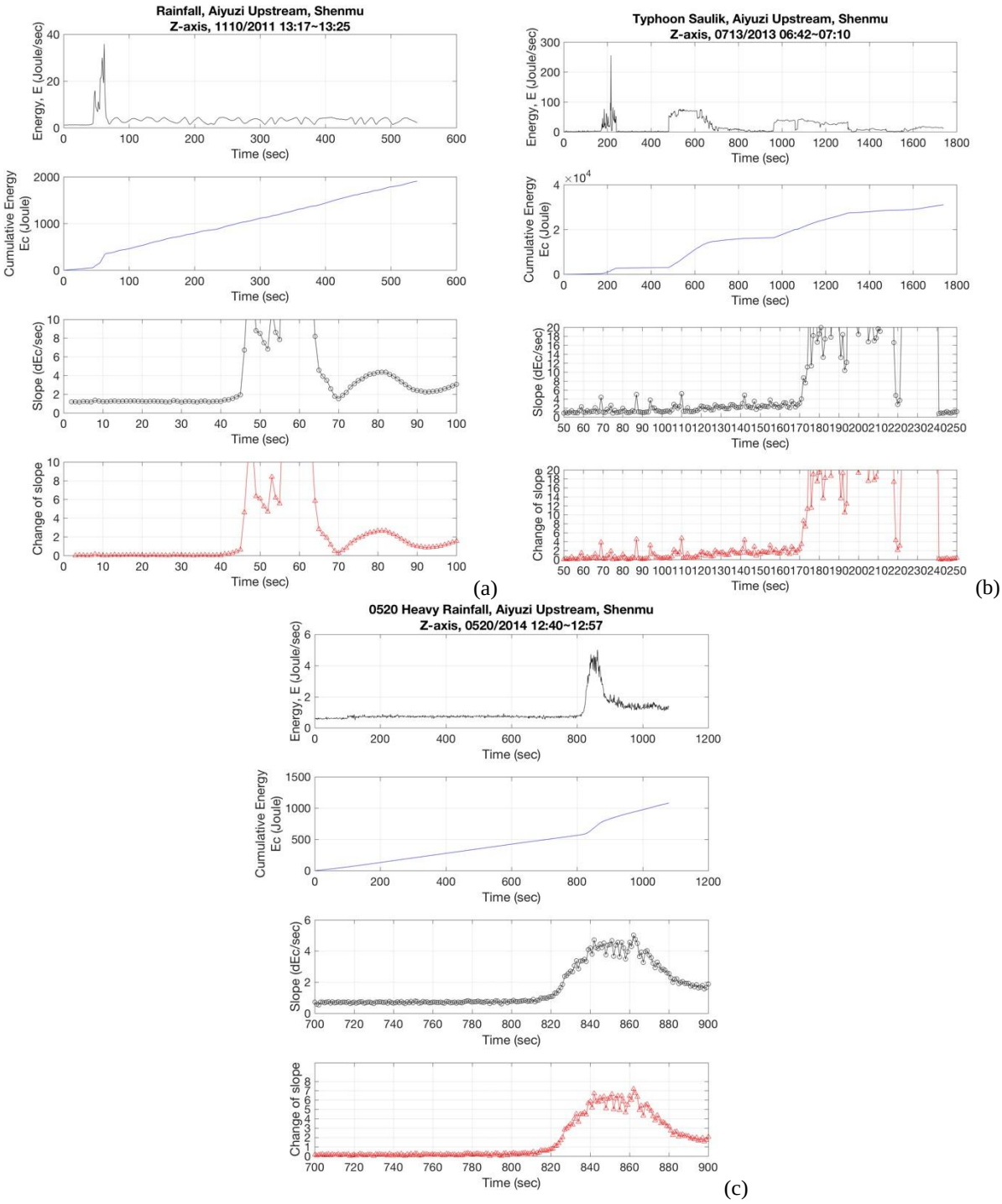

Figure 7. The energy of vibrational signals (geophones) of cases (a) Nov. 11, 2011 (b) Typhoon Saulik (c) 0520 Rainfall.

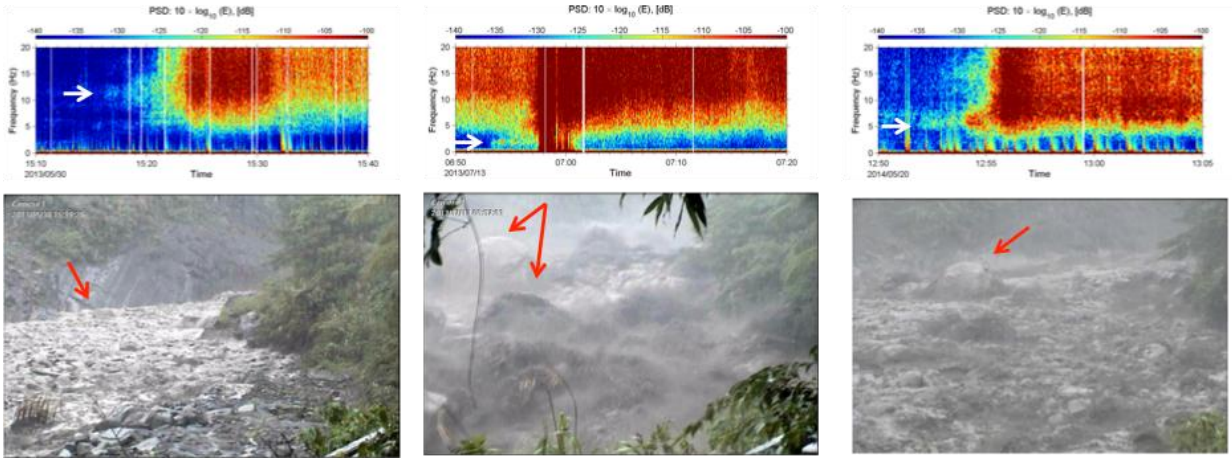

Figure 8. The front-end signals and the video images of debris flows (a) May 30, 2013 (b) Typhoon Saulik (c) 0520 Rainfall.

The lower-frequency signals implied the longer-period vibration waves, which were usually caused by the movement of large boulders or rocks in a debris flow. These longer-period signals were captured as the front-end frequency of a debris flow. Figure 8 shows the comparison of front-end signal and the real-time CCD images. The rocks shown in the images was at the front-end of debris flow, and the main current of debris flow arrived later. Therefore, the low-frequency content of signals represented the a part of front-end of a debris flow, and the earlier arrival time of these signals can help on debris flow detection.

Since the vibration signals of a debris flow was used as the direct monitoring option, the layout of geophones or broadband seismographs can be designed in a sequence along the stream to create a time window for warning. Figure 9 shows an example of applying both geophones and broadband seismographs in Aiyuzi Stream during Typhoon Saulik event. By layout these sensors at upper- and downstream sections, a time window of 3 to 7 minutes was created for warning. Although the time window was small in this case, the layout of vibration signal sensors still helped issue debris flow warning to people living at downstream areas.

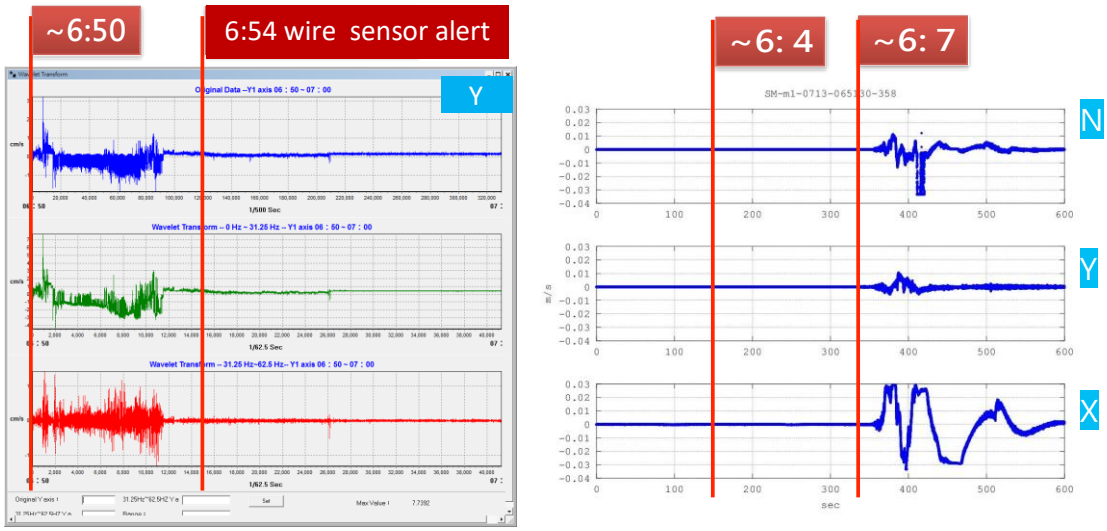

(a) the geophone signals at the upper stream (b) the broadband signals at the downstream

Figure 9. The time window of signals at Aiyuzi Stream in the event of Typoon Saulik on July 13, 2013.

5 Conclusion

This study evaluated the vibration signals of debris flows and concluded findings as follows.

1. The frequency range of 0~35 Hz was suitable for debris flow detection, and 0~10 Hz was potentially good for debris flow warning.
2. The seismographs and STFT were useful to process vibration signals, in order to evaluate the contribution of frequency with time.
3. It was noted that energy of signals was helpful in determining the transition period before a debris flow to arrive.
4. By desgining an appoper layout of vibration signal sensors, a time window can be created to issue debris flow warning for those living at the downstream areas.
5. A method of considerting both front-end frequency and signal energy transition is suggested to be included in the debris flow warning system.
6. Overall, the study showed that the direct method of geophones and broadband seismograph was practically promising for debris flow monitoring.

Acknowledgement

This research was partly supported by the Soil and Water Conservation Bureau, Council of Agriculture, Executive Yuan, Taiwan. Thanks to all people providing help on this study.

References

[1] Huang Y.M., Chen W.C., Fang Y.M., Lee B.J., Chou T.Y., Yin H.Y. Debris Flow Monitoring – A Case Study of Shenmu Area in Taiwan, *Disaster Advances*, 6(11), 1-9, 2013.

[2] Yi-Min Huang, Chung-Ray Chu, Yao-Min Fang, Ming-Chang Tsai, Bing-Jean Lee, Tien Yin Chou, Chen-Yang Lee, Chen-Yu Chen, and Hsiao-Yuan Yin. Characteristics of debris flow vibration signals in Shenmu, Taiwan, In *Proceedings of Interpraevent International Symposium 2016*, Lucerne, Switzerland, 2016.

[3] Jan C.D., Lee M.H., Huang T.H. Effect of Rainfall on Debris Flows in Taiwan, In *Proceedings of the International Conference on Slope Engineering*, Hong Kong, 2, 741-751, 2003.

[4] Jan C.D. and Lee M.H. A Debris-Flow Rainfall-Based Warning Model, *Journal of Chinese Soil and Water Conservation*, CSWCS, 35(3), 275-285 (in Chinese), 2004.

[5] Lee M.H. (2006) A Rainfall-Based Debris Flow Warning Analysis and Its Application, *Ph.D. Thesis*, National Cheng Kung University, Taiwan, (in Chinese), 2006.

[6] Chu C.-R., Huang C.-J., Lin C.-R., Wang C.-C., Kuo B.-Y., Yin H.-Y. The Time-Frequency Signatures of Advanced Seismic Signals Generated by Debris Flows, *Abstract* NH51B-3853 presented at 2014 Fall Meeting, AGU, San Francisco, Calif., 15-19 Dec., 2014.

[7] Huang C.-J., Chu C.-R., Tien T.-M., Yin H.-Y., and Chen P.-S. Calibration and deployment of a fiber-optic sensing system for monitoring debris flows, *Sensors*, 12(5), 5835-5849, 2012.

[8] Lee B.J. et al. (2015) The 2015 On-site Data gathering and Monitoring Station Maintenance Program, *Project Report*, Soil and Water Conservation Bureau, 476 (in Chinese), 2015.

[9] Fang Y.M. et al., Analysis of Debris Flow Underground Sound by Wavelet Transform-A Case Study of Events in Aiyuzih River, *Journal of Chinese Soil and Water Conservation*, CSWCS, 39(1), 27-44, 2008.

A Study on Developing the Evaluation System for Maintenance of Road Tunnels

J.W. An[a] , K.H. Park[b], M.H. Jung[c] and J.H. Sung[d]

[abcd] Korea Infrastructure Safety & Technology Corporation, Jinju-City, Gyeongsangnam-Do, Korea
E-mail: jwan@kistec.or.kr, pkh2989@kistec.or.kr, mhjung@kistec.or.kr, bluehill@kistec.or.kr

Abstract –

In Korea, the condition of road tunnels has been evaluated for the maintenance the road tunnels by investigation or safety inspection based on the operation period. The result of the condition evaluation is used for accident preventive maintenance such as repairing the defects or damaged parts and performing reinforcement satisfying design criteria.

The causes of defects at tunnel lining and road surface could be classified into structural causes and non-structural causes such as freezing and thawing, carbonation and drying shrinkage in cold regions. These defects could have a bad affect to the safety of tunnels and users who use the tunnels and maintenance managers.

However, since the existing maintenance system is a safety-based system, it does not take into consideration the evaluation to predict the deterioration of tunnel lining and road surface performance or usability for aspect of users and managers. Therefore, we intend to derive a new evaluation index for the development of a new concept of maintenance system considering the environmental, geographical and material aspects as well as users and manager's point of view.

In this study, for the development of a new maintenance system for the road tunnels, we selected the indices to evaluate the safety, durability and usability of tunnels based on the literature reviews and expert opinions. Then, the final evaluation indices have been derived from the Delphi survey. In addition, for the quantitative evaluation, the AHP analysis which can calculate the weights for each index was conducted to develop an evaluation table to assessment road tunnels.

Keywords –

Road Tunnels; Freezing and Thawing; Cold Region; Maintenance; Delphi Survey

1 Introduction

For Korea's SOC facilities, because they were built on a large scale by the construction revival actually started since the 1970s and their public use years are currently elapsed over 30 years, the facilities entered an aging period are increasing rapidly. Infrastructure (SOC) is a key measure estimating national competitiveness, and the deterioration of infrastructure could greatly damage the national economy and public safety, so there is a need to actively cope with it.

In Korea, there was the collapse of the Seongsu Bridge which caused a total of 49 casualties including 32 deaths in 1994, and in the next year, 1995, the collapse of the Sampoong Department Store due to faulty construction made loss of 1,445 lives including 502 deaths. Consequently, Korea had enacted a special law for facilities' safety management in 1995 to continuously perform facilities' maintenance until now according to the relevant law.

The existing maintenance system is managed by an accident preventive safety-oriented maintenance method such as repair of defects and damaged areas or reinforcement to satisfy the design standard. Because such a maintenance system has a limit in performing economical and strategic maintenance, it is needed to prepare a performance-focused maintenance system that could predict facilities' performance degradation and invest a budget in a proper time and location.

For the road tunnels located in Korea's Gangwon area, they are exposed to poor freezing environment such as average snowfall days and cold wave due to climatic properties. This leads to serious freezing damages on the lining of tunnel's entrance and exit and the road surface, and the damage of lives and property caused by traffic accidents increases, so proper maintenance for it is needed.

Accordingly, this study would like to secure structural safety and evaluate durability performance and service level at the same time to efficiently utilize the limited maintenance cost and prepare a performance -focused evaluation system to comprehensively evaluate

Table 1. Summary of Infrastructure Assessment Report

Classification	Infrastructure	Factors
U. S. A	Aviation, Dam, Drinking Water, Wastewater, Energy, Hazardous Waste, Solid Waste, Inland Waterways, Levees, Ports, Rail, Roads, Bridges, Schools, Transit	Capacity, Condition, Funding, Future need, Operation & Maintenance, Public Safety, Resilience
Canada	Drinking Water, Wastewater, Rainwater, Roads	Condition, Management Status, Capacity
Australia	Roads, Rail, Aviation, Ports, Drinking Water, Wastewater, Rainwater, Irrigation, Electricity, Gas, Telecommunications	Condition, Safety, Sustainability(Economic, Environmental, Social Issues), Resilience
U. K	Energy, Transit, Regional Transit, Drinking Water, Wastewater, Flood, Waste, Resource	Condition, Capacity, Resilience, Sustainability, Prediction next 5 years, Impact of fiscal cuts
Republic of South Africa	Water, Sanitation, Solid waste, Roads, Aviation, Ports, Rail, Electricity, Health facilities, Schools	Condition, Maintenance Level, Capacity, Preparation to the Emergencies

facilities' performance considering it.

Recently, there have been many presentations that continuous investment should be made in infrastructure for national economy growth, and studies for evaluating infrastructures' performance are continuously conducted in several countries including the U.S., Canada and Australia.

In the U.S., ASCE (American Society of Civil Engineers) publishes the infrastructure evaluation report card every year, and continuously promotes national level interest and investment for maintenance of SOC facilities through the relevant reports[1]. Kang et al. (2013) carried out comparison • analysis of the infrastructure evaluation system of respective countries for the countries publishing the infrastructure evaluation report card to suggest direction of introduction into Korea, and according to the relevant report, it could been confirmed that the evaluation index to evaluate performance is different depending on the purpose and use environment[2].

Table 2. Delphi Survey Process

Order	Contents
Pretest	Literature survey about a tunnel evaluation method and related research
Panel Selection	Composition of experts panel(Academia, Industry, Research Institute)
Primary Survey	Consists of the open and closed questions
Primary Analysis	Obtain the preliminary evaluation indexes by assessment of CVR(Content Validity Ratio) and open survey
Secondary Survey	Revaluation of the primary research index Add the performance evaluation indexes
Secondary Analysis	Calculation of Median, quartile(IQR) and frequency analysis
Third Survey	Revaluation of the Secondary research index
Third Analysis	Review for CVR and agreement Obtain of final performance evaluation indexes for AHP analysis

for each country. Therefore, it is desirable to derive a performance evaluation index suitable for Korea's situation.

This study carried out Delphi analysis for experts in tunnel field to determine performance evaluation items and derive performance indexes for each item to conduct performance-focused maintenance considering the perspective of users and managers, Korea's environmental, geographical and material aspects around road tunnels, and conducted AHP analysis for each derived performance index to derive the importance by performance index.

2 Research Meathod

Delphi technique was utilized to derive tunnel's evaluation indexes for each performance item. Delphi technique has an advantage in that different opinions derives an agreement as the number of times being surveyed is repeated by carrying out repetitive surveys for the same panel and sharing the result derived from respective panels.

This study carried out a total of three Delphi surveys to derive an agreement of the panel composed of experts in tunnel field. In order to utilize Delphi technique, a preliminary evaluation index was derived through the existing precedent studies and literature search, and the first Delphi survey with a mixture of open and closed types was carried out to collect various opinions of experts.

The second and third Delphi surveys analyzed the expert group's opinions about the importance between respective performance indexes through closed type questions to derive the final performance evaluation index. The Delphi survey process carried out in this study is as Table 2.

For a Delphi survey, expertise and sincerity etc. were considered to organize an expert panel. In order to maximize the reliability of Delphi analysis, the number of panel should be 10 or more at least (Ewing, 1992), and a panel of just only 10~15 persons could obtain useful results (Ziglio, 1996)[3][4].

The first Delphi questionnaire was prepared with a mixture of open and closed types. The open-type questions tried to collect additional opinions of experts for the evaluation index, and the closed-type questions were organized to assess whether the evaluation index derived from the literature data review corresponded to the index for performance evaluation. The expert opinions by the first Delphi survey were organized as closed types when preparing the second and third questionnaires to carry out the surveys.

The expert opinions of the closed type questionnaire were reflected to select the first performance evaluation index and verify the content validity for reflecting in the second Delphi survey.

The content validity is verified by using the content validity ratio (CVR). A CVR value suggests the minimum value according to the number of panels, and it is determined that there is content validity on experts' opinions when it becomes absove the minimum value. The content validity is calculated by the following equation (1) (Lawshe, 1975).

$$\mathrm{CVR} = \frac{n_e - \frac{N}{2}}{\frac{N}{2}} \tag{1}$$

where, $n_e$is the number of panels who responded as valid, and N means the number of the entire Delphi panels participating in the study. If the number of panels who responded as an evaluation index being valid for performance evaluation is 100%, 50% and less than 50%, the CVR value is represented as 1.0, 0 and a negative number, respectively.

In other words, if the number of panels who responded as valid is 50~100%, the CVR value is located on 0~1.0, and such a CVR value could determine the minimum value as Table 3 according to the number of panels with the data presented by Schipper (Lawshe, 1975)[5].

Average, standard deviation, median, mode and CVR values were calculated for the second Delphi analysis, and the agreement was evaluated to assess the items' validity and whether the panel's opinions converge or not. The agreement is a method that verifies how much agreement is reached between respondents by using quartile deviation and median to schematize a value between Q3 and Q1, and it is said that the ratio of inter-quartile range and median is 0.3 if the agreement is 0.7, which means that the interval of intermediate 50% respondents exists in the range of 0.3×median around the median.

Table 3. Minimum CVR by Responders

Respondents	CVR
10	0.62
11	0.59
12	0.56
13	0.54
14	0.51
15	0.49
20	0.42
25	0.37
30	0.33
35	0.31
40	0.29

If the agreement of A is 0.9, it means intermediate 50% respondents exist in the range of 0.1 × median, which could be determined that 0.9 has responses of the people surveyed being more agreed than 0.7. The agreement is calculated by the following equation (2) (Kim, 2015)[6].

$$1 - \frac{Q_3 - Q_1}{M_d} \tag{2}$$

where, Q_3, Q_1 and Md are 3/4 fractile, 1/4 fractile and median, respectively. Interquartile (IQR) is calculated by equation (3) which is a measure representing the deviation of panel responses around the median, and it is generally considered that agreement is reached if it is 1.0 or less (Upton, 1996)[7].

$$\mathrm{IQR} = Q_3 - Q_1 \tag{3}$$

The third Delphi survey included the statistical analysis result for the second survey result, that is, feedback on the panel's group trends. In order to re-evaluate the importance for each evaluation index, the median and interquartile range for the second survey result were indicated to refer to other panel's opinions. And if an advisory opinion was different from majority opinions, it was requested to present the opinion. The results were compiled to derive the final performance evaluation index.

The performance evaluation indexes derived through

Delphi surveys were classified suitable for the types and characteristics of road tunnels, and AHP (Analytic Hierarchy Process) surveys were carried out around the state safety evaluation index to select the importance for each performance evaluation index.

The most important member forming a road tunnel is lining, and the lining constructed is different depending on the construction method. If tunnels are classified by the purpose and construction method of a tunnel and the lining's material, it is as Figure. 1.

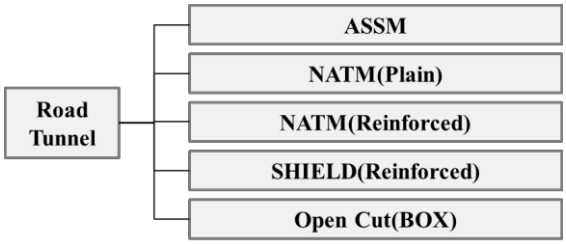

Figure 1. Classification of the Road Tunnel by Material

The characteristic of the AHP analysis is to hierarchize a complex problem, and derive the importance through pairwise comparison between elements organizing the hierarchical structure. Examining the related literature, Sung et al. (2013) analyzed maintenance systems of the existing domestic and foreign tunnels to develop the performance evaluation standard and maintenance manual of the shield TBM tunnel, and utilized the AHP analysis to suggest evaluation scores by evaluation item of the shield TBM tunnel[8].

In addition, Kimura et al. (2012) proposed a performance-focused evaluation method for the railway tunnel in public use, and the proposed evaluation method classified the tunnel-related performance into a total of 7 categories (user safety, usability, structural safety, durability, manageability, maintainability, and peripheral influence), and utilized the AHP technique to determine weights of respective performance's evaluation elements[9].

The AHP survey was carried out for 15 domestic experts in tunnel field, and the expert group was composed of experts who have more than 15 years of experience in tunnel field.

For the safety class, the lowest performance class would be finally selected as a safety class by comparing the evaluation results of state safety and structural safety. For the structural safety, because its class was determined depending on analytical results such as safety factor or allowable stress, displacement, the weight calculation through AHP would apply only to the state safety evaluation index.

3 Deriving the Evaluation Index

In order to derive a preliminary evaluation items for each tunnel's performance, it was investigated and analyzed domestic and foreign tunnel evaluation guides, guidelines, standards and research cases etc. In Korea, the safety of tunnels is evaluated through the「Detailed Guide on Safety Check and Precision Safety Diagnosis」, and according to the Ministry of Construction and Transportation (2001), tunnels are evaluated through various evaluation indexes in several countries such as「Road and Rail Tunnel Standards」in Japan,「Maintenance Standards for Concrete Structures」in the U.S., and「Classification and Management Standards for Segment Damages」in Austria[10][11].

As a result of analyzing domestic and foreign literature materials carried out in advance, a total of 47 preliminary performance evaluation indexes were derived. Performance items are classified into safety, durability and service performance, and of them, the number of safety evaluation indexes was 25, in which the greatest number of items were derived, and it was analyzed the durability and service performance evaluation indexes were as 11, respectively.

For the durability evaluation index, it was added an evaluation for the deterioration environment not used in the current maintenance system. For road tunnels, performance degradation and serious damage occurs over time due to the freezing damage. In the existing maintenance system, such a environmental effect is not considered. In Japan, it is presented the freezing prevention measures suitable for regional situation, and Norway's road association establishes measures considering tunnel cross section and freezing index etc. to prevent freezing, and the use of freezing prevention PE (polyethylene foam) is recently defined in the specification.

In this study, a panel of 14 persons had responded to the survey, and the resulting content validity (CVR value) was based on 0.51 and more. As previously explained, the first Delphi survey was organized by mixing closed and open type questions for 47 preliminary evaluation items derived through literature analysis, and as a result of carrying out the survey, it was represented that a total of 38 indexes satisfied the content validity as Table 4. Additionally, as 19 additional evaluation items were derived as Table 5 in the open type survey result, a closed type survey was carried out for a total of 57 preliminary evaluation items in the second Delphi survey.

As a result of carrying out the second Delphi analysis for 57 preliminary evaluation indexes selected through the first Delphi survey, 42 items satisfied the content validity, and for the agreement, the panel's opinions were agreed in 37 items.

Table 4. Results of 1st Delphi-Survey

Performance	Primary Category	Subcategory		CVR
Safety	Tunnel Inside	Crack		1.00
		Deterioration of a Sealing		1.00
		Leakage		1.00
		Icicle		0.71
		Exfoliation		1.00
		Spalling		1.00
		Efflorescence		1.00
		Rebar Exposure		1.00
		Breakage		1.00
		Rear Side Cavity		0.86
		Inner Section Reduction		0.86
	Tunnel Outside	Weathering		0.43
		Uniaxial Compressive Strength		0.14
		R. Q. D		0.14
		Weathering Degeneration		0.14
		Fragmental Zone of Fault		0.71
		Drainage Condition		1.00
		Sediment Condition		1.00
		Pipe Utility Conduit Condition		1.00
	Structural Safety	Normal	Factor of Safety	0.86
			Displacement	1.00
			Stress	1.00
		Earthquake	Factor of Safety	0.86
			Displacement	1.00
			Stress	1.00
Durability	Concrete Lining	Strength		0.86
		Carbonation		0.86
		Chloride Content		0.86
	Timber	Strength		0.29
	Ground	Weathering		0.43
		Rock Strength		0.29
	Circumstance	Salt Stress Circumstance		0.86
		Carbonation Circumstance		0.86
		Freezing Damage Circumstance		0.86
		Quality of Water		0.29
		Carbon Dioxide Content		0.57
Serviceability	Construction Gauge			0.86
	Subsidiary Facilities Condition			1.00
	Damage Prevention Facilities Condition			0.86
	Maintainability			0.71
	Vibration & Noise Condition			1.00
	Traffic ability			0.71
	Detour			0.86
	Illumination			0.86
	Quality of Air			1.00
	Degree of the ringing in Ears			0.71

Table 5. Additional Index by Open Questions

Performance	Additional Index
Safety	1) Invert Condition
	2) Swelling of Roadbed
	3) Pavement Condition
	4) Sub-ballast
	5) Railway
	6) Track
	7) RMR
	8) Geological Characteristics
	9) Drainage Canal Condition
Durability	1) Reinforced Coating
	2) Lining Thickness
	3) Timbering Standard
	4) Tunnel Portal Slope
Serviceability	1) Traffic ability
	2) Road Surface Condition
	3) Pavement
	4) Car-Clearance
	5) Water Treatment
	6) Luminance

In order to re-evaluate the importance of each evaluation index, it was requested that the median and interquartile range for the second survey result were represented to refer to other panels' opinions, and if anadvisory opinion was different from the majority opinion, it was requested to present the opinion. As a result, the evaluation indexes satisfying the content validity were 44 items, and two items were more increased than the second evaluation result. Also for the agreement, as 44 evaluation indexes were agreed, 7 items were more increased than the second evaluation result. The result of three evaluations is as Table 6.

Table 6. Results of 3rd Delphi-Survey

Performance	Primary Category	Subcategory	CVR	Aggrement (less than 1)
Safety	Tunnel Inside	Crack	1.00	1.00
		Deterioration of a Sealing	0.71	1.00
		Leakage	1.00	1.00
		Icicle	0.71	1.00
		Exfoliation	0.71	1.75
		Spalling	1.00	1.00
		Efflorescence	0.43	1.75
		Rebar Exposure	1.00	1.00
		Breakage	1.00	1.00
		Rear Side Cavity	1.00	1.00
		Invert Condition	0.43	1.50
		Swelling of Radbes	0.86	1.00
		Pavement	0.14	1.00
		Sub-ballsast	0.14	1.00
		Railway	0.43	1.50

		Track		0.43	1.50
		Inner Section Reduction		1.00	1.00
	Tunnel Outside	RMR		0.71	1.00
		Geological Characteristics		1.00	1.00
		Fragmental Zone of Fault		1.00	0.75
		Drainage Condition		1.00	1.75
		Sediment Condition		0.86	1.00
		Drainage Canal Condition		0.29	1.00
		Pipe Utility Conduit Condition		0.57	1.00
	Structural Safety	Normal	Factor of Safety	1.00	1.00
			Displacement	1.00	1.00
			Stress	1.00	1.00
		Earthquake	Factor of Safety	1.00	1.75
			Displacement	1.00	1.00
			Stress	1.00	1.00
Durability	Concrete Lining	Strength		1.00	1.00
		Carbonation		1.00	1.00
		Chloride Content		0.43	1.75
		Cover Thickness		1.00	1.00
		Lining Thickness		1.00	2.00
	Timber	Timbering Standard		0.71	1.00
	Ground	Tunnel Portal Slope		1.00	2.00
	Circumstance	Salt Stress Circumstance		0.86	1.00
		Carbonation Circumstance		1.00	1.00
		Freezing Damage Circumstance		1.00	1.00
		Carbon Dioxide Content		0.14	1.00
Serviceability	Construction Gauge			0.57	1.00
	Subsidiary Facilities Condition			0.14	1.00
	Damage Prevention Facilities Condition			1.00	1.00
	Maintainability			0.71	1.00
	Vibration & Noise Condition			0.57	0.75
	Detour			0.14	2.00
	Trafficability			0.57	1.00
	Road Surface Condition			0.57	1.00
	Pavement Condition			0.57	1.00
	Car-Clearance			0.86	1.75
	Water Treatment			0.00	1.00
	Illumination			0.71	1.00
	Luminance			0.86	1.00
	Quality of Air			0.86	1.00
	Degree of the ringing in Ears			0.71	1.00

As a result of carrying out a total of three Delphi surveys to select the performance evaluation index for tunnels, 17 safety evaluation indexes, 9 durability evaluation indexes and 12 service performance evaluation indexes were selected. The selected performance evaluation indexes went through an expert joint meeting of three persons in research institute, four safety diagnosis practitioners and two in industry to undergo a process that modifies and complements the indexes, where some redundancy existed and investigation was practically impossible, to select the final performance evaluation indexes. The finally selected performance evaluation indexes are as Table 7.

Table 7. Final Result of Delphi-Survey

Performance Assessment			
Performance	Primary Category	Subcategory	
Safety	Tunnel Inside	Crack	
		Deterioration of a Sealing	
		Leakage	
		Exfoliation	
		Spalling	
		Rebar Exposure	
		Breakage	
		Segregation	
		Rear Side Cavity	
		Inner Section Reduction	
	Tunnel Outside	Ground Condition	
		Drainage Condition	
		Pipe Utility Conduit Condition	
		Special Conditions	
	Structural Safety	Normal	Factor of Safety
			Displacement
			Stress
		Earthquake	Factor of Safety
			Displacement
			Stress
Durability	Plain Concrete Lining	Strength	
		Freezing Damage Circumstance	
	Reinforced Concrete Lining	Strength	
		Salt Stress Circumstance	
		Carbonation	
		Chloride Content	
		Freezing Damage Circumstance	
Serviceability	Road Tunnel	Road Surface Condition	
		Illumination	
		Damage Prevention Facilities Condition	
		Emergency Evacuation Time	
		Mechanical and Electrical Equipment	
		Subsidiary Facilities Condition	
		Traffic ability	
	Railway Tunnel	Luminance	
		Damage Prevention Facilities Condition	
		Emergency Evacuation Time	
		Mechanical and Electrical Equipment	
		Traffic ability	

4 Selecting Weights for the Evaluation Indexes

In order to analyze the importance of state safety evaluation index for a total of 15 experts in tunnel field, the AHP survey was carried out and the result is summarized as Table 12. As a result, it was represented that the evaluation indexes with high importance in the

Table 8. Results of AHP Analysis(Road Tunnel)

Performance		Assessment Index	ASSM (Plain)	NATM (Plain)	NATM (Reinforced)	SHIELD (Reinforced)	Open Cut
			Importance/Ranking				
Safety	Tunnel Inside	Crack	0.1201/2	1.222/2	0.1022/2	1.1131/2	0.1332/2
		Leakage	0.1075/3	1.1115/3	0.0923/4	1.1000/3	0.1062/3
		Breakage	0.0828/6	0.0797/6	0.0718/7	0.0861/4	0.0809/5
		Exfoliation	0.0347/11	0.0333/10	0.0308/12	0.0357/11	0.0361/11
		Spalling	0.0560/9	0.0499/9	0.0525/9	0.0570/9	0.0553/8
		Segregation	0.0405/10	0.0315/12	0.0310/11	0.0343/12	0.0360/12
		Rebar Exposure	-	-	0.0855/6	0.0832/6	0.0951/4
	Tunnel Outside	Drainage Condition	0.0755/7	0.0755/7	0.0665/8	0.0640/8	0.0673/7
		Pipe Utility Conduit Condition	0.0313/12	0.0320/11	0.0272/13	0.0282/13	0.0315/13
		Ground Condition	0.1065/4	0.0898/5	0.0897/5	0.0853/5	0.0719/6
		Inner Section Reduction	0.1888/1	0.2125/1	0.2013/1	0.1921/1	0.1837/1
		Rear Side Cavity	0.0948/5	0.1049/4	0.1000/9	0.0723/7	0.0553/9
		Special Conditions	0.0615/8	0.0572/8	0.0492/10	0.0487/10	0.0475/10
Durability	Deterioration Progress	Strength Carbonation Chloride Content	Lowest Rating				
	Deterioration Circumstance	Freezing Damage Circumstance	-	-	-	-	-
		Salt Stress Circumstance	-	-	-	-	-
Serviceability	Usability	Road Surface Condition	0.182/3	0.182/3	0.182/3	0.182/3	0.182/3
		Illumination	0.139/6	0.139/6	0.139/6	0.139/6	0.139/6
		Damage Prevention Facilities Condition	0.187/1	0.187/1	0.187/1	0.187/1	0.187/1
		Emergency Evacuation Time	0.184/2	0.184/2	0.184/2	0.184/2	0.184/2
	Functionality	Mechanical and Electrical Equipment	0.144/5	0.144/5	0.144/5	0.144/5	0.144/5
		Traffic ability	0.164/4	0.164/4	0.164/4	0.164/4	0.164/4

road tunnel's state safety evaluation indexes were the reduction or not of inside cavity's cross section, cracks, water leak, ground state and rear side cavity or not etc., and the evaluation indexes with relatively low importance were the pipe utility conduit state, delamination and material segregation etc. The durability item considers the index's characteristic to evaluate by the lowest class, so the weight by index was not selected. For the deterioration progress of the durability evaluation, it was judged that it is difficult to divide into sections to evaluate and if any part of a road tunnel has a poor durability performance it could affect the entire facility. In addition, the deterioration environment evaluation is one for the environment where respective facility is placed, which is evaluated depending on the environment of respective facility.

It could be confirmed that the importance by evaluation index was different depending on the type of a tunnel and construction method. In the evaluation index of NATM tunnels, the rear side cavity or not was selected as a relatively important evaluation index, but in the shield tunnels, its importance was represented as relatively small.

Such a result is judged because there is high probability of deformation caused by the rear side cavity in a NATM tunnel.

The importance acquired through the AHP analysis is planned to utilize as a weight of the evaluation index to use in calculating evaluation scores of every evaluation index. If an evaluation score is given for each evaluation index, it is judged that the performance class of a tunnel could be presented quantitatively.

5 Conclusion

In this study, the evaluation indexes were derived to prepare the performance-focused evaluation system for road tunnels, and the importance between respective evaluation indexes was calculated. As a result of analyzing the related literature and precedent studies for this purpose, a total of 47 preliminary evaluation indexes were derived. In order to derive the final index for performance-focused evaluation, it was derived a total of 44 final evaluation indexes composed of 20 safety evaluation indexes, 7 durability evaluation indexes and 14 service performance evaluation indexes as a result of carrying out three Delphi surveys for 14 experts engaged in research institute, academia and industry and deriving the final agreement.

In order to evaluate respective importance for each derived performance evaluation index, the AHP analysis was conducted, and it is judged that respective

importance could be utilized in calculating evaluation scores by evaluation index to use in evaluating the tunnel's performance quantitatively.

The improvement in the current maintenance system is securing structural safety as well as evaluating safety and performance together such as durability and service performance.

It is a system that could evaluate the durability reduction of linings caused by freezing-thawing and the service performance degradation caused by road surface freezing etc. like the road tunnels located in cold area, which could maintain facilities more reasonably.

The performance evaluation indexes and importance by index derived in this study could be utilized to support rational decision making when establishing a performance-focused maintenance system for tunnel facilities, it is needed to prepare a repair and reinforcement method and a management system considering the freezing and salt damage environment to improve durability and service performance for establishing a maintenance plan by the performance evaluation in the future.

Acknowledgements

This research was supported by a grant(17RDRP-B066780) from Regional Development Research Program funded by Ministry of Land, Infrastructure and Transport of Korean government

References

[1] American Society of Civil Engineers. 2013 Report Card for America's Infrastructure. American Society of Civil Engineers, 113-128, 2013

[2] S.H. Kang. and Y.H. Lee. Understanding the Infrastructure Assessment System in Developed Countries and Introduction Plan. Construction & Economy Research Institute of Korea, 49, 2013

[3] D.M. Ewing. Future Competencies Needed in the Preparation of Secretaries in the State of Illinois Using the Delphi Technique. Ph. D. Dissertation University of Iowa, 1992

[4] E. Ziglio and M. Adler. The Delphi method and its contribution to decision-making. Gazing into the oracle : the Delphi method and its application to social policy and public health, Jessica Kingsley Publishers, 1996

[5] Lawshe. A Quantitative approach to content validity. Personnel Psychology. Content Validity, 563-575, 1975

[6] B.W. Kim. Delphi analysis Method. Kims information, 2015

[7] Upton and Graham. Understanding Statistics. Oxford Press, 55, 1996

[8] J.H. Sung. A special tunnel excavation(shield tunnel) performance criteria and maintenance manual development, Korea Infrastructure Safety and Health, 2013

[9] S. Kimura, T. Kitani and A. Koizumi. Development of Performance-Based Tunnel Evaluation. Journal of Transportation Technologies, 119-128, 2012

[10] Ministry of Land. Transport and Maritime Affairs. Guideline of Safety and in-depth Safety Inspection, 2011

[11] Ministry of Construction and Transportation. Establishment of standards for evaluating the condition of facilities(Tunnels), 2001

Assessment of the liquefaction susceptibility by means of different damage severity indices: A case study of 2012 Emilia Romagna earthquake

D.C. Lo Presti[a], M. Francesconi[a], M.G. Persichillo[b], C. Meisina[b]

[a]Department of Civil Engineering, University of Pisa, Pisa, Italy
[b] Department of Earth and Environmental Sciences, University of Pavia, Pavia, Italy
E-mail: d.lopresti@ing.unipi.it , m.francesconi7@gmail.com , mariagiuseppin.persichillo01@universitadipavia.it , claudia.meisina@unipv.it

Abstract -

Since mid-May 2012, a seismic sequence has affected a wide sector of the Po River Plain (Northern Italy). The sequence has been dominated by two main events: Mw = 5.9 occurred on May 20th and Mw=5.8 occurred on May 29th. The earthquake sequence triggered widespread liquefaction through a vast area of the Emilia-Romagna region (northern Italy). Moreover, it was noticed that the presence of drainage and fluvial landforms strongly influenced and favoured the occurrence of liquefaction phenomena. Cone penetration test CPT and CPTu have been carried out before and after the two main shocks and some of them are located close to the sites where liquefaction effects have been observed.

The main aim of this work was to exploit this database to deeply investigate the liquefaction potential over the area affected by the 2012 earthquake. Two damage potential indices, the Liquefaction Potential Index (LPI) and the Liquefaction Severity Number (LSN), were applied and compared. The available CPT and CPTu were divided in relationship with the morphological and lithological location. After that, the LPI and the LSN were computed by comparing the prediction with the liquefaction effects inventory. Some differences were identified by the application of different potential indexes. In particular the LSN showed an underestimation of the results respect to the LPI.

The results allowed identifying the most suitable index for the correct characterization of the liquefaction potential of the investigated area, giving useful advices for land use planning and risk assessment.

Keywords –

Liquefaction susceptibility; liquefaction potential indices; 2012 Emilia Romagna earthquake

1 Introduction

The 2010-2011 Canterbury Earthquake Sequence (CES) has raised a renewed interest in soil – liquefaction studies and many lessons have been learned from the study of that seismic sequence. In particular, [1] state that the earthquake shakings of such a sequence triggered localized-to-widespread minor-to-severe liquefaction especially in the Central Business District of Cristchurch (NZ). [2], [3] and [4], thanks to an accurate study of the induced damages to structures and infrastructures, have proposed different liquefaction-severity-classification-criteria. In particular the proposed criteria consider: a) damages to residential dwelling foundation system, b) extension of ejecta and its impact on lifelines and infrastructures, c) lateral spreading. On the Authors knowledge, the above mentioned papers represent excellent examples that classify liquefaction related phoenomena from an "engineering" point of view and do not consider them as pure naturalistic events.

On the other hand, the liquefaction hazard assessment can be pursued by different methods:

1. classical geological approach [5][6];
2. statistical, Artificial Neural Network, Support Vector Machine [7];
3. simplified empirical (or semi – empirical) procedures [8][9].

Simplified procedures evaluate the liquefaction potential of soils computing the factor of safety (FS_L) against liquefaction at a given depth in the soil profile and consist of two steps: 1) to evaluate the earthquake-induced shear stress through an estimate of the cyclic stress ratio (CSR) [8] and 2) to evaluate the soil strength to liquefaction usually accomplished through an estimate of the cyclic resistance ratio (CRR). Because of the difficulty of sampling, CRR is generally determined via in situ tests, such as standard penetration test (SPT) (e.g., [8] [10]), cone penetration test (CPT) (e.g., [11] [12]),

shear wave velocity (Vs), flat dilatometer tests (DMTs), and self-boring pressure meter (SBPT).

Once the safety factor against liquefaction has been computed at various depths, numerical indicators or qualitative criteria to define the liquefaction severity at ground level can be used. The oldest and most popular numerical indicator is the index proposed by [13]. Such a method requires the assessment of the FS_L according to [8]. Triggering of liquefaction by the [8] approach is extended down to 20 m depth. After that the Liquefaction Potential Index (LPI) is computed as the integral of the safety factor against liquefaction along depth [13], LPI quantifies liquefaction hazard in terms of liquefaction occurrence, which may not completely correlate to liquefaction manifestation [4].

The LPI assumes that liquefaction severity increases as FS_L decreases, the thickness of the liquefiable layers increases and the depth of the liquefiable layers decreases. On the other hand, it is assumed that the occurrence of liquefaction at depth greater than 20 m has negligible or nil effects at the ground surface. It is possible to state that, according to these criteria, if LPI<5, minor or nil effects of liquefaction could be expected at the ground surface while if LPI>15, very severe effects are expected.

[14] introduced the Liquefaction Severity Number (LSN), which represents intensity of liquefaction using volumetric densification strain as a proxy, with depth weighting by a hyperbolic (1/z) rather than a linear reduction. The intent was that the LSN should more heavily weight the contribution to ground surface damage from soil layers which liquefy closer to the ground surface compared to those layers that liquefy at greater depths.

In a different way, [15] suggests that in the case of a non –liquefiable cap (shallow layer) of given thickness (H1), overlying a liquefiable layer of thickness (H2) the liquefaction effects are negligible at the ground surface if H1 > H2.

LPI and LSN have been used extensively by researchers and practitioners to assess the liquefaction hazard, nevertheless their applicability are thus uncertain [16]. The potential effects of using different Liquefaction Evaluation Procedures (LEPs) on the threshold values (i.e. Iwasaki criteria) have been analyzed by [4]. Other researchers have proposed to modify/calibrate the LPI [17] or have introduced new vulnerability parameters.

The threshold - values of LPI that have been proposed by [13] are based on data from 55 liquefaction sites in Japan and there is a need to calibrate LPI in different geological and seismological contexts.

Most of the studies used the procedure from [11] to compute FS_L against the liquefaction in conjunction with LPI, there is thus a need to evaluate how other procedures affect the liquefaction hazard assessment.

Nowadays CPT-based simplified methods are the most common used approach to determine the liquefaction hazard. Several authors have already verified the applicability of them, but their use in evaluating liquefaction hazards is a rather challenging task. For example for the Emilia Romagna case study some papers state that the estimated liquefaction potential is not in complete agreement with the liquefaction evidences mapped in post event field surveys and generally an underestimation of liquefaction potential is highlighted [18][19].

2 Study area

2.1 Gelogical and seismological aspects

The study area corresponds to the southern sector of the central Po Plain, where the most evident and widespread liquefaction effects induced by the 2012 seismic sequence occurred [20][21]. Figure 1 shows the location (stars) of the shakings with M > 5. Moreover, some locations where liquefaction – related phenomena occurred are also shown.

This portion of the Apennines is characterized by N- and NE-verging thrusts and folds, formed as a consequence of Cenozoic collision between the European and the Adria (African) plates [22]. This involved both the terrigeneous sedimentary cover and the carbonate Mesozoic sequences resulting from the late Oligocene-Quaternary compressional tectonic phases [23]. The geomorphologic framework is characterized by complex drainage and ancient drainage patterns of the Po, Secchia, Panaro and Reno Rivers, strongly influenced by climate, tectonic and man-made interventions consisting in land reclamation and artificial embankment construction. The shallow alluvial deposits are Holocene in age. Their particle-size distribution is mainly silt and clay with sand levels in correspondence with ancient riverbeds and crevasse splays. Their thickness is variable from hundreds of meters to thousands of meters, depending on the local depth of the Apennine buried structures [23]. These deposits are due to fluvial aggradation of both the Po and its Apennine tributaries. The grain-size distribution is extremely variable from place to place, due to frequent changes of path that affected the rivers and creeks in the past and, consequently, the hydraulic conductivity is extremely variable. The seismic sequence that occurred in the 2012 was characterized by two main shocks. The first occurred on 20th May at 02:03 UTC with MW = 5.9. The epicenter was located at coordinates 44.89° (Latitude) and 11.23° (Longitude), while, the depth of the hypocenter was estimated at 6.3 km. The second main shock occurred on 29th May at 07:00 UTC with a MW = 5.8 (ISIDe Database 2012), 12 km southwest of the previous main shock and at a depth of 10.2 km [24].

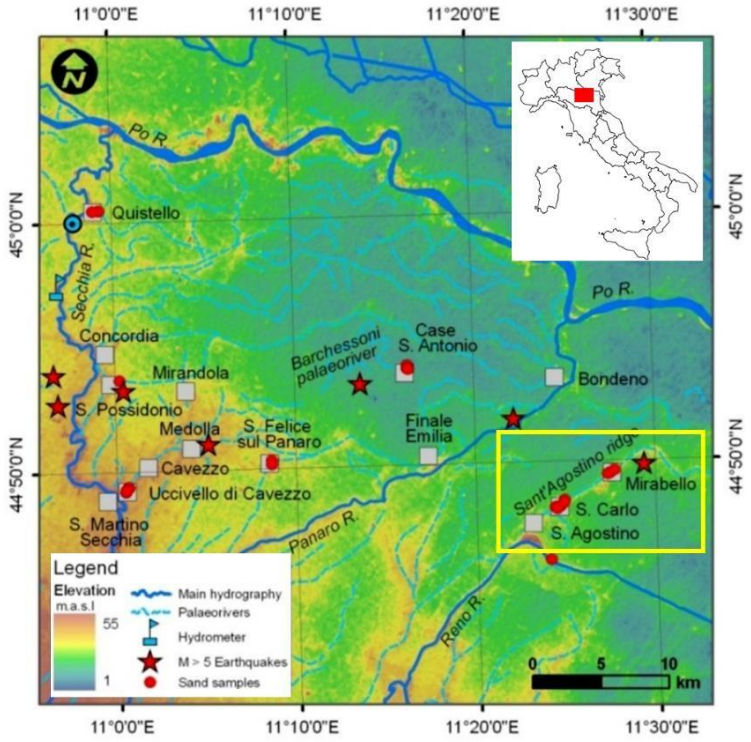

Figure 1. SRTM (Shuttle Radar Topography Mission; ~90 m cell size). Most of the "liquefaction" sites are located on elevated fluvial ridges. Red dots represent the location of sand samples collected at the sites where liquefaction phenomena occurred [20]. In the yellow rectangle are indicated the study area site.

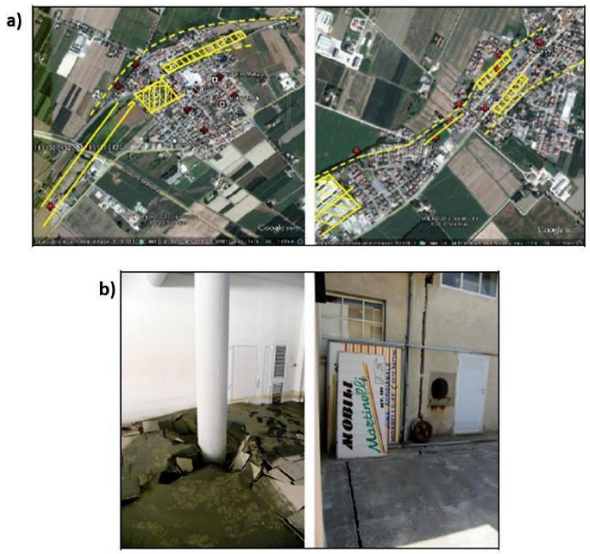

Figure 2. (a) Satellite photos of San Carlo (left) and Mirabello (right). Areas affected by damages to the foundation systems are evidenced. (b) Examples of damages to the foundation systems [21][24].

The liquefaction phenomena have been described in a number of papers (see as an example [20][24]). As a whole, 1362 sites with geologic co-seismic effects were identified over more than 1200 km2; 768 were classified as fracture/liquefaction, 485 as liquefaction, and 109 as fracture [24]. Liquefaction events were not randomly distributed, but appeared to be concentrated along alignments that follow the abandoned riverbeds (Secchia, Reno, Panaro and Po rivers). In the area affected by liquefaction, the structural damage was generally modest. A peculiar high density of observations is located between Mirabello and Sant'Agostino villages, where the interactions of liquefaction effects with man-made structures was particularly strong; many buildings, roads, fenced walls and lifelines were severely affected and damaged by liquefaction phenomena (Figure 2).

2.2 Database

Four different sites were analyzed in the area of the 2012 Emilia Earthquake:

1. San Carlo-Sant'Agostino, Mirabello in SE sector: the liquefaction effects occurred during the 20 May shock, A peculiar high density of observations is located between Mirabello and Sant'Agostino villages. The interactions of liquefaction effects with man-made structures was particularly strong , many buildings, roads, fenced walls and lifelines were severely affected and damaged by liquefaction phenomena;

2. Cavezzo in SW sector: the liquefaction effects occurred during the 29 May shock. Observations are concentrated near the main canal with light interaction with infrastructures;
3. Bondeno in NE sector: the liquefaction effects occurred during the 20 May shock. The zone mainly crosses agricultural fields
4. Quistello in NW sector: the liquefaction effects occurred during the 29 May shock, low density of coseismic effects and light interaction with infrastructures.

Available stratigraphic logs of the upper 20-30 m provided by the Emilia Romagna Region (http://ambiente.regione.emilia-romagna.it/geologia/cartografia/webgis-banchedati/sezioni-geologiche-prove-geognostiche-pianura) , as obtained from existing boreholes in the area interested by liquefaction effects, were preliminarily examined. Grainsize distributions of liquefied sands that came out from the surface during the earthquake and retrieved from the sites located in Figure 1 were also analyzed. This information was used to calibrate the CPT and CPTU test results as far as the assessment of soil stratigraphy is concerned.

Before using penetration test results for liquefaction potential analyses, a very time consuming procedure was implemented in order to assess the quality and reliability of each test result. The selection of the tests was carried out according to the following criteria:

a) Test location: The most part of the tests were selected at a relative short distance from the liquefaction phenomena. For comparison purposes some tests were also selected in correspondence of non-liquefied sites. In few cases, penetration tests are located at very short distance from the areas where liquefaction phenomena occurred.
b) Presence of continuous records in the penetrometric tests: in some cases the test have not continuous measurements and they have been discarded;
c) Period of test execution: generally pre-earthquake data were used; only in the case those data were not available, results from tests performed after the seismic sequence have been used. In very few cases both pre and post earthquake data are available, in this case a comparison between the liquefaction potential obtained was carried out in order to observe the effects of soil liquefaction.

At the end of the selection 627 mechanical CPT e 30 CPTu were selected for the analysis.

3 Method

The selected penetrometic tests were used to evaluate the factors of safety against liquefaction, according to the procedures proposed by [12][25][26]. The CPT-based simplified methods allow to derive the FS_L against liquefaction, at a given depth in the soil profile, evaluating:

- the resistance of a soil to triggering of liquefaction, usually accomplished through an estimate of the cyclic resistance ratio (CRR);
- the loading to a soil caused by an earthquake through an estimate of the cyclic stress ratio (CSR) [8].

Liquefaction at a given location and depth occurs if $FS_L \leq 1$.

The liquefaction severity at the ground surface, which more directly correlates to damage potential, was evaluated by means of the liquefaction potential index LPI [13], and the Liquefaction Severity Number LSN [14].

LPI was computed as:

$$LPI = \int_0^{20} F_1 * W(z) * dz \qquad (2)$$

Where: F1 =1 - FS_L for $FS_L \leq 1$ and F1 = 0 for $FS_L > 1$; W(z) is a depth weighting function given by W(z) = 10 - 0.5z; and z is depth in metres below the ground surface.

LPI can range from 0 to a maximum of 100 (i.e. where FS_L is zero over the entire 20 m depth). Analysing SPT data from 55 sites in Japan, [13] proposed that severe liquefaction should be expected for sites where LPI > 15 but not where LPI < 5.

The Liquefaction Severity Number (LSN) was computed following the method of [14]:

$$LSN = 1000 \int_z \frac{\varepsilon_v}{} dz \qquad (3)$$

Where: ε_v is the calculated volumetric consolidation strain in the layer and z is the depth below the ground surface.

For the assessment of FS_L, LPI and LSN, in addition to the CPT results the following data were also necessary:

- soil unit weight;
- water table depth;
- PGA (peak ground horizontal acceleration);
- Mw (moment magnitude).

An estimate of the unit weight (γ) was obtained from laboratory tests on specimens collected after the earthquake in San Carlo [27]. In particular the following estimate was adopted for computations: γ =19.0 kN/m3.

Ground water table depth (GWT) was supposed to be at the ground level at the moment of the earthquake. Indeed, post – earthquake evidences indicates a water table depth mainly at about 1.0 m below ground level.

The CSR was inferred from an estimate of PGA (Peak Ground acceleration) and Mw (moment magnitude).

The Mw = 5.9 (20th May event) and Mw = 5.8 (29th

May event) were used in order to estimate the FS_Lover the study area.

[28] Lai et al. (2012) inferred a PGA = 0.215g in the case of the M = 5.9 earthquake of May 20 2012 by using the GMPE [29].

During the analysis the measured sleeve friction (fs) from mechanical CPT was corrected in the following way:

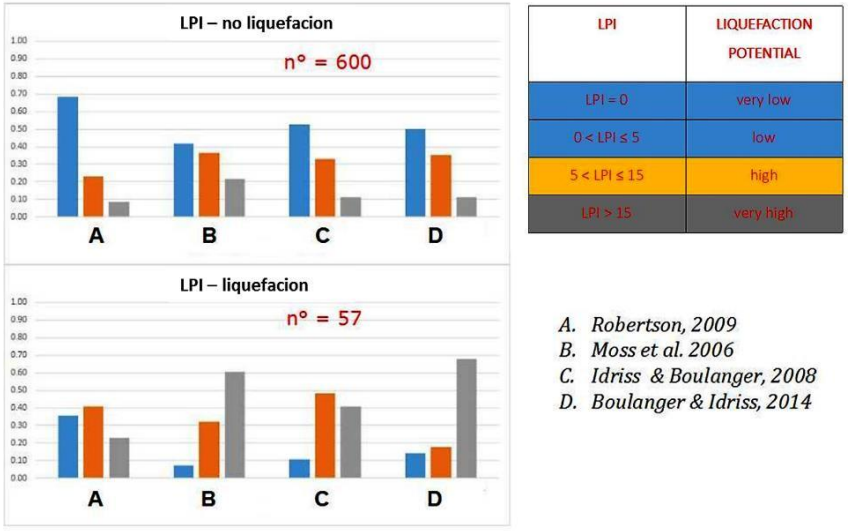

Figure 3. Percentages of success for LPI and various LEPs

$$f_s(CPTu) = [0.0797 * f_s CPTm]^{2.504}$$
$$\text{If } f_s(CPTm) < 65KPa \qquad (4)$$

$$f_s(CPTu) = f_s(CPTm)$$
$$\text{If } f_s(CPTm) \geq 65KPa \qquad (5)$$

4 Results

In order to assess the capability of LPI and LSN parameters in evaluating the liquefaction risks the investigation database was split into two categories:

1. Cases wherein surface manifestations of liquefaction were observed (57 liquefaction cases) in a radius of 50 meters;
2. Cases wherein surface manifestations of liquefaction were not observed (600 no liquefaction cases) in a radius of 50 meters.

Moreover, different LEPs were used to estimate the liquefaction safety factor. Figure 3 shows (upper part) the number of successful predictions of the absence of liquefaction. The criterion is to have LPI ≤ 5. The best LEP seems to be that proposed by [25] with about 70 % of true predictions and only 30 % of false predictions. The lower part of Figure 3 refers to the cases where liquefaction occurred. [25] has again 64 % of success (LPI > 5).

Other considered LEPs exhibit very high percentages of success when predicting the occurrence of liquefaction (LPI > 5). In particular [26] obtain 93% of success; [12] 89%; [9] 86%. On the other hand the predictive capability for those cases where liquefaction did not occur is very low. These last three LEPs respectively obtain the percentages of 42, 53 and 50% for LPI ≤ 5.

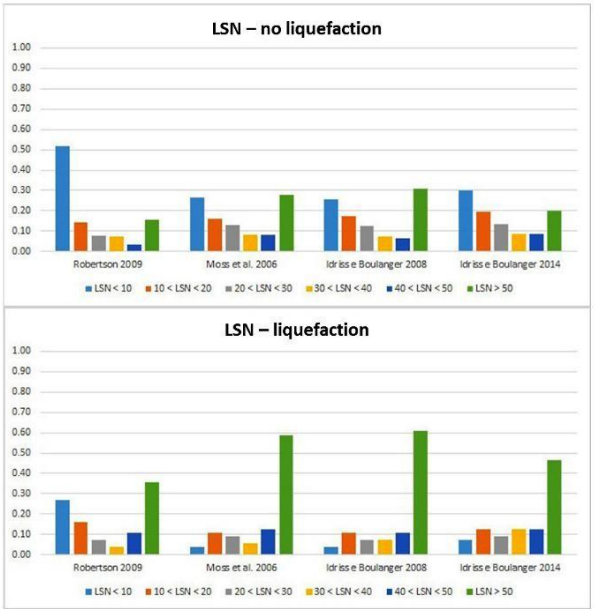

Figure 4. Percentages of success for LSN and various LEPs

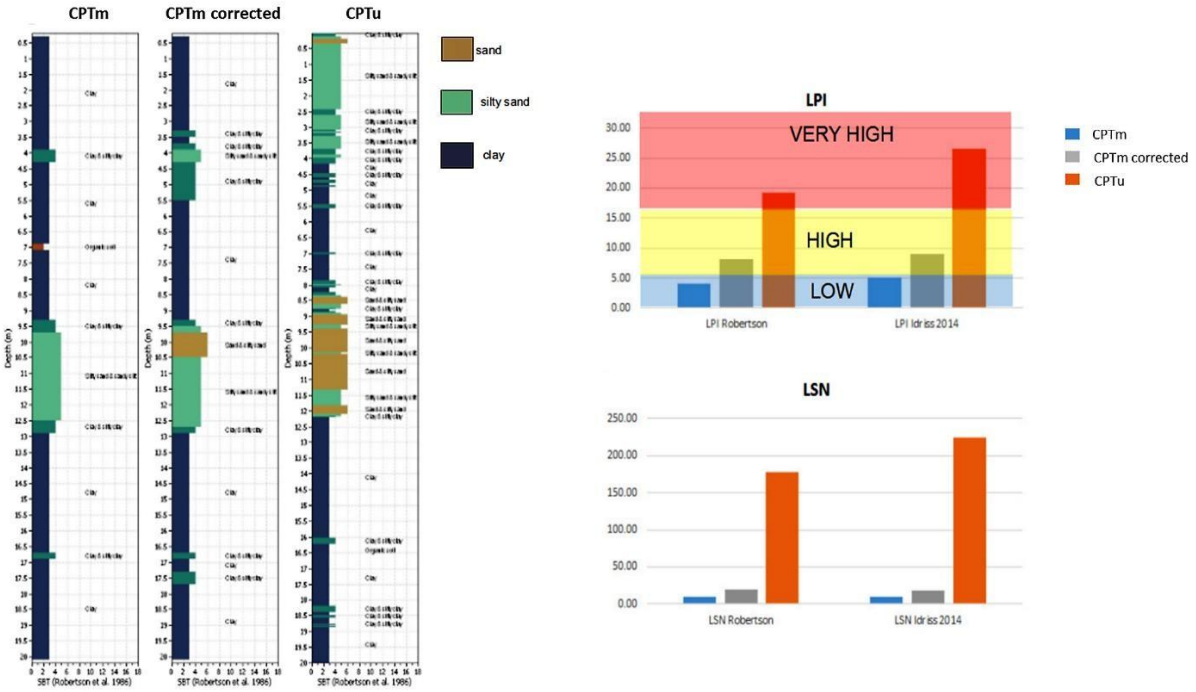

Figure 5. Comparison of SBT, LPI and LSN from CPTm, CPTm corrected and CPTu

Similar comments apply when using LSN parameter and various LEPs (Figure 4). [25] again obtains the highest percentage of true predictions (about 50 %) of the absence of liquefaction (LSN < 10). The considered LEPs exhibit LSN values generally greater than 50 for those cases where liquefaction occurs (Figure 4, lower part). The prediction of a very high liquefaction risk in almost all the cases, when using LSN parameter is not consistent with the observed liquefaction phoenomena and induced damages.

In conclusion, the method by [25] seems the most accurate for the study case, while the other appears more conservative. At the same time the LPI index give reasonable estimate of the liquefaction risk, whilst LSN tends to largely overestimate this risk. The predictive capability of the four LEPs was already discussed [2][14] on the basis of the Canterbury earthquake sequence. They found consistent results among the different methods and indicated slightly higher level of accuracy as far as the [12] method is concerned.

More generally, the high rate of false predictions of the absence of liquefaction, for the present case study, can have a twofold explanation:

- the considered LEPs implicitly contain conservative criteria;
- the considered LEPs cannot correctly take into account the beneficial effects of the presence of a non liquefied crust.

Indeed there are various evidences [14][15] that a non liquefied crust at the ground surface and inter-layered silty soils in the top 5-6 m reduces the effects of liquefaction at ground surface. This could be the cause of the high percentage of test with
high LPI and LSN without liquefaction manifestations in a radius of 50 m.

The results from CPTm lead to different estimate of the liquefaction risk with respect to the predictions inferred from CPTu. This fact is well-known. More specifically, the liquefiable horizons do not coincide and generally, using CPTm, it is not possible to detect all the liquefiable layers that on the contrary are found when using CPTu. In conclusion, use of CPTm leads to an underestimate of LPI and LSN values and consequently to an underestimate of the liquefaction risk. The Authors believe that this is mainly a consequence of the differences in measuring the sleeve friction. At depth higher than 5 m, the fs(CPTm) is sistematically higher than fs (CPTu), while the qc are similar.

Indeed after the application of the proposed correction, the predictive capability of liquefiable layers by using CPTm approaches that based on CPTu (Figure 5).

More details about the proposed correction and of its positive effects are given in another paper under review process.

5 Conclusions

CPT based simplified methods, developed generally from data measured with electrical tip or piezocone, may lead to relevant non-conservative estimate of liquefaction potential. The liquefaction hazard assessment, through simplified procedures based on CPT, appears to be affect by mistake due to the failure to identify silty-sand or sand. This is mainly due to the overestimation of the fs parameter of CPTm test in respect to the test CPTu. The fs has a significant influence on soil classification in terms of SBT and liquefaction potential. In consequence, CPTm underestimates the grain size of loose soils (silts and sands) with respect to CPTu. This underestimation is of great importance for the evaluation of the liquefaction susceptibility, since the loose soils are those that experience the phenomenon. Therefore, the application of two simplified methods (LPI and LSN) give different results using CPTm or CPTu tests. The proposed correction of the measured sleeve friction from CPTm enabled us to use a large database of CPTm for assessing the liquefaction risk in the area hit by the 2012 Emilia Romagna Sequence. The comparison with the evaluations inferred from CPTu seems to confirm the usefulness of such a correction.

The LEP by [30] seems, among the considered approaches, the most accurate as for the study area. Other LEPs are certainly more conservative.

The LPI parameter turns out to be a useful index for the estimate of the liquefaction potential.

Finally, we must emphasize that the proposed procedure, based on the LPI parameter, various LEPs and a large database, cannot give practical indications the scale of the single building, but rather an estimate of the liquefaction risk at urban level.

Assessment of the liquefaction risk for a given structure requires specific testing and analysis because of the extreme variability of soil deposits that can experience liquefaction phoenomena.

The LSN parameter, as proposed by [14], is not reliable for the assessment of liquefaction in the study area. This is probably due to its excessive sensitivity to the value of G.W.T earthquake (depth to groundwater during the earthquake) entered to perform processing.

References

[1] Bray J.D. et al. CPT-based liquefaction assessments in Christchurch, New Zealand. *Papers of the 3rd International Symposium on Cone Penetration Testing*, Las Vegas, Nevada, 2014.

[2] Green R.A., Cubrinovski M., Cox B., Wood C., Wotherspoon L., Bradley B. and Maurer B. Select Liquefaction Case Histories from the 2010–2011 Canterbury Earthquake Sequence. *Earthquake Spectra*, 30(1): 131–153, 2014.

[3] van Ballegooy S. et al. Methods for characterizing effects of liquefaction in terms of damage severity. *Proceedings of The 15th World Conference on Earthquake Engineering*, Lisboa, Portugal, 2012.

[4] Maurer B. et al. Assessment of CPT-Based Methods for Liquefaction Evaluation in a Liquefaction Potential Index (LPI) Framework. *Géotechnique*, Vol. 65, p. 328-336, 2015.

[5] Knudsen K. L., Sowers J. M., Witter R. C., Wentworth C. M., and Helley E. J. Description of mapping of quaternary deposits and liquefaction susceptibility, nine-county San Francisco Bay Region, California. *Rep. No. United States Geologic Survey Open-File Report 00–444*, United States Geologic Survey, Reston, Va, 2000.

[6] Stanciucu M. A brief method for evaluation of the liquefaction susceptibility in Bucharest area, 1183-1186, 5, G. Lollino et al. (eds.) *Engineering Geology for Society and Territory*, 2015.

[7] Xue X, Yang X. Seismic liquefaction potential assessed by support vector machines approaches. *Bull. Eng. Geol. Environ*, 75, 153-162, 2016.

[8] Seed H.B. and Idriss I.M. Simplified Procedure for Evaluating Soil Liquefaction Potential. *J. Soil Mechanics and Foundations Div.* ASC E 97 (SM9), 1249–1273pp, 1971.

[9] Boulanger R.W. and Idriss I.M. CPT and SPT Based Liquefaction Triggering Procedures. *Report No. UCD/CMG–14/01, Dept. of Civil & Environmental Engineering*, University of California at Davis, 2014.

[10] Youd et al. Liquefaction Resistance of Soils: Summary Report from 1996 NC EER and 1998 NC EER/ NSF Workshops on Evaluation of Liquefaction Resistance of Soils, *Journal of Geotechnical and Geoenvironmental Engineering*, 127 (10), 817–833pp, 2000.

[11] Robertson P.K., and Wride C.E. Evaluating cyclic liquefaction potential using the cone penetration test. *Canadian Geotechnical J.* 35 (3), pp. 442-59, 1998.

[12] Idriss I.M. e Boulanger R.W. Soil Liquefaction during Earthquakes. *Earthquake Engineering Research Institute*, 2008.

[13] Iwasaki, T, Tatsuoka, F., Tokida, K, and Yasuda, S. A Practical Method for Assessing Soil Liquefaction Potential Based on Case Studies at Various Sites in Japan. *2nd International Conference on Microzonation for Safer Construction Research and Application*, pp. 885-896, 1978.

[14] Tonkin and Taylor Liquefaction vulnerability study, Tonkin and Taylor Report 52020.0200. February 2013. *Report for New Zealand Earthquake Commission.*

http://www.eqc.govt.nz/sites/public_files/documents/liquefaction-vulnerability-study-final.pdf, 2013.

[15] Ishihara K. Stability of Natural Deposits during Earthquakes. Theme lecture, Proc. 11th Int. *Conf. on Soil Mechanics and Foundation Engineering*, San Francisco, 2, 321–376pp, 1985.

[16] Maurer B.W., Green R.A., Cubrinovski M. and Bradley B.A. Evaluation of the Liquefaction Potential Index for Assessing Liquefaction Hazard in Christchurch, New Zealand. *Geotechnical Special Publication* 75, 580–613pp, 2014.

[17] Sonmez H. Modification to the liquefaction potential index and liquefaction susceptibility mapping for a liquefaction-prone area (Inegol-Turkey). *Environmental Geology*, Vol. 44, p. 862-871, 2003.

[18] Facciorusso J., Madiai C., Vannucchi G. The 2012 Emilia earthquake (Italy): Geotechnical characterization and ground response analyses of the paleo-Reno river levees. *Soil Dynamics and Earthquake Engineering*, 86 (2016) 71–88, 2016.

[19] Papathanassiou G., Mantovani A., Tarabusi G., Rapti D., Caputo R. Assessment of liquefaction potential for two liquefaction prone areas considering the May 20, 2012 Emilia (Italy) earthquake. *Engineering Geology* ,189, 1–16, 2015.

[20] Lo Presti D. and Sassu M., Luzzi L. and Pacor F., Castaldini D. and Tosatti G., Meisina C., Zizioli D. and Zucca F., Rossi G., Saccorotti G. and Piccinini D. A report on the 2012 seismic sequence in Emilia (Northern Italy)". *7th International Conference on Case Histories in Geotechnical Engineering*, 29 April – 4 May, 2013, Chicago, 2013.

[21] Fioravanti V. et al. Earthquake Geotechnical Engineering Aspects OF the 2012 Emilia-Romagna Earthquake (Italy). *Proceedings of the 7th International Conference on Case Histories in Geotechnical Engineering*, Chicago, U.S., 2013.

[22] Boccaletti M. et al. (1985) - "Considerations on the seismotectonics of the Northern Apennines" – Tectonophysics, Vol. 117, p. 7-38.

[23] Pieri M. and Groppi G. Subsurface geological structure of the Po Plain (Italy). *C.N.R., Prog. Fin. Geodinamica*, pubblicazione n. 414, p. 1-13, 1981.

[24] Emergeo Working Group Liquefaction phenomena associated with the Emilia earthquake sequence of May-June 2012 (Northern Italy). *Natural Hazards Earth System Sciences*, Vol. 13, p. 935-947, 2013.

[25] Robertson P.K. Interpretation of cone penetration tests – A unified approach. *Canadian Geotechnical Journal*, Vol. 46, p. 1337-1355, 2009.

[26] Moss R.E.S, Seed R.B., Kayen R.E., Stewart J.P., Der Kiureghian A., and Cetin K.O. CPT-based Probabilistic and Deterministic Assessment of in situ Seismic Soil Liquefaction Potential. *Journal of Geotechnical and Geoenvironmental Engineering*, ASC E, 132(8), 1032–1051, 2006.

[27] Romeo R.W. Terremoto dell'Emilia del 20 Maggio 2012 (M5.9): insoliti fenomeni di liquefazione. *Italian Journal of Engineering Geology and Environment*, Vol. 2, p. 75-84, 2012.

[28] Lai C., Bozzoni F., Mangriotis M.D., Martinelli M., Scandella L. and Decarro F. Geotechnical aspects of May 20th, 2012 M5.9 Emilia Earthquake, Italy. July 13 2012. EUCENTRE, Pavia, Italy, 2012.

[29] Cauzzi C. and Faccioli E. Broadband (0.05 to 20s) prediction of displacement response spectra based on worldwide digital records. *Journal of Seismology*, 12, p 453-475, 2008.

[30] Robertson P.K. Soil Classification Using the Cone Penetration Test. *Canadian Geotechnical Journal*, Vol. 27, p. 151-158, 1990.

Evaluation of the degree of compaction of levees by a CPT-based method

B. Cosanti, N. Squeglia, D. Lo Presti

Department of of Civil and Industrial Engineering, School of Engineering, University of Pisa, Italy
E-mail: barbara.cosanti@gmail.com, squeglia@ing.unipi.it, d.lopresti@ing.unipi.it

Abstract –

Permeability and strength parameters of compacted soils may be correlated to their degree of compaction. Unfortunately, the use of conventional and recent testing methods for the assessment of density and water content of earthworks under construction cannot be applied to existing levees. Therefore, the development of an expeditious and accurate method for the assessment of the degree of compaction of existing and new levees, after their completion, appears extremely useful. The purpose of this research is to develop a simple tool for the assessment of the degree of compaction of "compacted", partially saturated, fine grained soils. The proposed method combines in situ testing like electric CPT or CPTu with laboratory penetration testing performed with a mini–cone in a calibration chamber.

Keywords –

Compacted soils; Partially saturated soils; In situ testing; Calibration chamber

1 Introduction

Nowadays adverse weather conditions are more and more frequent because of global climatic changes. Particularly adverse climatic conditions such as repeated floods, very prolonged rain periods and very intense rainfalls can lead to an almost complete saturation of the levees and cause their failures [1]; [2]; [3]; [4]. Since budgets for levees refurbishments are limited, priority lists become mandatory.

The assessment of the safety factor against possible Ultimate Limit States of existing levees requires, at least, the knowledge of strength and permeability parameters and it is well recognized that these parameters mainly depend on the degree of compaction and the degree of saturation [5]. Therefore, the assessment of soil density and water content can contribute to a correct estimate of the required parameters. The use of both conventional and recent testing methods for the assessment of density and water content of earthworks, under construction, cannot be applied to existing levees. The Rubber Balloon Method [6], the Sand Cone Method [7], the Time Domain Reflectometry [8] and the Nuclear Methods [9] are only applicable at shallow depths. On the other hand, the use of specially equipped piezocones for electrical resistivity measurements [10]; [11], is not very popular and its application is restricted to fully saturated soils. Also nuclear density probes ([12]; [13]) are not very popular.

Therefore, an expeditious and accurate method for the assessment of the degree of compaction of existing and new levees appears extremely useful.

The proposed method combines in situ testing like electric CPT or CPTu with penetration testing with a mini–cone in a calibration chamber (CC).

2 Hypotheses

In the literature, many calibration chamber were designed for different purposes and very advanced mini-cones were realized. On the contrary, the purpose of this research is that of developing the simplest tool for the assessment of the degree of compaction of "compacted", partially saturated, fine grained soils.

A reference tip resistance, q_{cLAB}, is inferred from laboratory tests in a mini CC using a mini CPT. q_{cLAB} is expressed as a function of the expected dry density and of the relevant influential factors. Such an empirical relationship is obtained by carrying out a number of repeated tests in the CC at given densities and different values of the influential factors. A comparison between q_{cLAB} and the tip resistance inferred from in situ CPT gives the possibility of assessing the dry density of existing embankments, while, for new embankments, the method defines the expected in situ tip resistance for a given target dry density.

A similar procedure is described in the technical standards by AFNOR [14] and [15]. This procedure is applied to coarse grained soils and requires the construction of a trial embankment (physical soil model) and the performance of dynamic penetration tests. As a results a reference "penetrogramme" (i.e. displacement per blow vs. depth) is obtained from the experiments.

The standards also state the criteria for the acceptance of the in situ controls in comparison to the design "penetrogramme". According to Setra–Lcpc [16], [17], this methodology should be applied to the control of the compaction degree of trenches.

The proposed method is based on the following considerations and assumptions:

1. The tip resistances of a standard cone (d = 35.7 mm) and a mini–cone (dC = 8 mm) are the same irrespective of the cone diameter when carried out in the same soil under the same conditions. This hypothesis involves two different aspects. The first one is related to the ratio between the cone diameter and the grain size of the soil and is discussed with the fourth hypothesis. The second aspect is related to the normalized penetration rate ([18]; [19]):

(1)

where V = normalized penetration rate; d = cone diameter, v = penetration rate, c_v = coefficient of consolidation.

It is evident that for the mini-cone penetration occurs at a lower normalized penetration rate since the mini cone has a normalized velocity four times smaller than that of a standard cone. According to many researchers, higher tip resistances should be measured at lower normalized penetration rates, especially in the case of saturated silty clay ([20]; [21]; [22]). For the soils under consideration, unsaturated silt mixture, the correctness of the hypothesis, has been experimentally verified by performing, in situ, at close distances 4 standard and 4 mini cone tests in the Calendasco site (Piacenza, Italy) [1]. Since the obtained tip resistance profiles are very similar and do not show systematic differences it is possible to conclude that in the case of unsaturated silt mixtures standard and mini–cone give very similar tip resistances. It is worth noticing that the silt mixtures that were tested in this research are similar to the Calendasco soil in terms of texture.

2. Tip resistance in pluviated dry sand, can be expressed by the following equations ([23]; [24]; [25]; [26], [27]):

(2)

(2bis)

where: Q_c = tip resistance; C_0, C_1, C_2, C_3 = experimental constants; σ'_{v0}, σ'_{h0} = vertical and horizontal effective stress respectively; D_R = relative density as a fraction of 1 and σ'_m = mean effective stress. It is widely accepted that for dry or saturated clean sands the tip resistance is mainly controlled by relative density, soil type and stress state. As for the stress state, other equations are also available in literature.

In the case of silt mixtures, compacted at a given water content, the boundary stresses are no more representative of the effective stress state which depends on suction (i.e. saturation degree or water content during formation). Moreover, the compaction energy is also a relevant parameter because of the pre-stressing (or pre-straining) of the compacted soil. Tatsuoka [28] suggests that the degree of compaction, defined for certain compaction energy, is more appropriate than the relative density for the evaluation of the compacted state of soil including a large amount of fines content. Therefore, the influence of the effective stress state in the case of compacted silt mixtures should be defined in a different way.

3. A ratio between the calibration chamber diameter (D_{CC}) and that of the cone (d_C) equal to 40 is considered acceptable in order to consider the CC as an infinite medium. There is evidence in literature that this type of size effect in sands depends on the boundary conditions and soil dry density ([29]; [30]; [31]; [25]; [26], [27]). Even if, for very dense sands and zero lateral strain, higher value of the D_{CC}/d_C ratio are necessary in case of silt mixtures this assumption seems acceptable. In fact, a number of Cone Penetration Tests (CPTs) were carried out in a recently constructed levee at increasing horizontal distances from a Marchetti Flat Dilatometer Test (DMT) blade [32]. The blade was used as a cell pressure: it was maintained at a given fixed depth and continuously monitored. The tests show that when the horizontal distance between the DMT and the CPT is 20 times that of the cone diameter the DMT is no longer sensitive to the passage of the cone.

4. It is considered acceptable that the ratio of the cone diameter to the mean grain size be equal to or greater than 300 ([33]; [34]; [35]; [36]).

This assumption is necessary to perform tests using a cone having a diameter of only 8 mm in the case of silt mixtures. This hypothesis is not verified for the Ticino sand. It is worth noticing that it is not verified even in the case of standard CPT in Ticino sand. The ratio is about 70 for standard cone and only 16 for the mini–cone.

3 Laboratory procedure

The equipment consists of a cylindrical aluminum mold with an inner diameter of 320 mm and a height of 210 mm . Lattice membranes are located at the bottom of the mold and all around the internal lateral surface. Air pressure can be inflated inside the membranes in order to apply horizontal and vertical stresses to the sample: there are manual air pressure regulators for the vertical and horizontal stresses. The mold is housed in a stainless steel frame with a lower and upper plate that

are connected to each other by means of four stainless steel rods. A locking system is located in the lower plate in order to push up the mold and put it in contact with the upper plate. Therefore, the bottom and lateral surfaces of the CC are flexible boundaries, while the top is rigid. A nozzle is located in the upper plate for the passage of the mini–cone. The mini–cone (8 mm in diameter) has an external sleeve along its full length and the tip resistance is measured by means of a load cell located above the cone. Since the external sleeve is not in contact with the load cell the sleeve friction is not measured. An electric step motor is used to drive the mini-cone at a constant rate of 20 mm/s. The system uses proximity transducers to automatically stop the penetration when the cone is close to the bottom (30 mm above the base).

Ticino sand, and four different silt mixtures (classified as A4 to A6 according to [37]) were used for the testing program. Table 1 summarizes the main characteristics of the silt mixtures (FR, PC, DD, TC).

Tests on the well known Ticino sand were carried out only for a preliminary check of the equipment.

Ticino sand samples were reconstituted by dry pluviation. In practice the sand was poured into the mold using a funnel that moved over the entire mold surface. This method gave a repeatable relative density of about 40%. The mold was also subject to slight vibrations. This method gave a repeatable relative density of about 60%. Moist tamping would be more appropriate to simulate the behavior of compacted sand fills but tests on Ticino sand samples were carried out only to validate the equipment, by comparison of the results obtained with the mini-cone in the mini-CC with those available in literature [27].

The silt mixtures were used for the construction of new levees and for the refurbishment of existing structures. The soils were sieved in order to eliminate the fraction with a diameter greater than 2 mm.

Samples of fine grained soil were reconstituted in four layers (each 52.5 mm high) using a stainless steel mold with an internal diameter of 310 mm (smaller than that of the CC). The soil was prepared at a given water content and compacted to a given density by applying a vertical pressure to the upper surface of the sample via a loading piston and an upper plate of 300 mm in diameter (i.e. under K_0 conditions). Each layer was compressed to the desired density by applying a static pressure on the upper surface of the layer. Since the applied force (pressure) and the associated displacement were measured, it was possible to compute the compaction energy per unit volume of soil for each layer and for the whole sample:

$$\frac{-}{\qquad\qquad} \tag{3}$$

where: F_i = force applied for each layer; δ_i = displacement caused by each applied force; V_i = soil volume of each layer.

After the sample had been reconstituted, it was transferred into the CC. There was a gap between the sample and the lateral membrane. The CC was then put inside the frame and the locking system was used to push up the CC and put the upper surface of the soil in contact with the upper aluminum plate.

The consolidation stresses were applied to the sample in two steps: first the isotropic component of horizontal and vertical boundary stresses was simultaneously applied and after that, the deviatoric component of the consolidation stresses was imposed.

The penetration test was carried out few minutes after the application of the consolidation stresses.

All the tests were performed under constant boundary stresses (Boundary Condition 1: BC1).

Table 1. Main characteristics of the tested fine grained soils: FR, PC, DD, TC.

Soil	γ_{dmax} kg/m^3	w_{opt} %	e_{opt}	$(Sr)_{opt}$ %	LL	PL	PI	AASHTO M 145	Gs	d_{50} mm
FR	2047	9.43	0.33	78	26÷31	18÷24	7÷10	A4÷A6	2.72	0.002÷0.025
PC	1950	10.7	0.39	74	25	19	6	A4	2.71	0.085
DD	1820	13.1	0.49	73	31.5	23.5	8	A4	2.71	0.01
TC	1895	12	0.42	77	25	6	19	A6	2.69	0.02

4 Test results

Table 2 sums up test results for Ticino sand. It reports boundary stresses (σ'_v, σ'_h), estimated relative density (D_R), measured average tip resistance (Q_c) and that evaluated by means of equation 2bis. A single Ticino sand sample was reconstituted in the laboratory. Indeed, moving the CC in the horizontal plane of about 40 mm in various directions it is possible to perform at least six penetration tests on the same sample. Therefore, a single relative density of about 40% was considered and different boundary stresses were applied on the same sample. In a first phase, the vertical stress was kept constant while the horizontal stress took different

values.

Table 2. Test conditions and results for Ticino dry sand samples.

σ'_v (kPa)	σ'_h (kPa)	Q_c (kPa)	Q_c by eq. 2 (kPa)	D_R
50	50	4277	5071	39.7
50	100	6560	6791	39.9
50	150	8269	8272	40.2
50	50	4377	5147	40.2
100	50	4501	6047	40.2
150	50	5772	6851	40.2

After that, a second set of stresses was applied by keeping the horizontal stress constant and applying different values of the vertical stress. When the initial boundary stresses of 50 kPa were restored for the second set of tests, the measured average tip resistance was very close to the first measurement. The agreement between measured and computed (eq. 2bis) tip resistances seems acceptable, even though a certain scatter is observed (Table 2). The low ratio between cone and grains diameters could be a reason for the observed scatter. The following parameters were used to compute the tip resistance by means of eq. 2bis [27]: C_0 = 23.19; C_1 = 0.56 and C_2 = 2.97. From a multiple – variable linear regression analysis of experimental data, the following values of the parameters of eq. 2 were obtained: C_0 = 52.4; C_1 = 0.22 and C_2 = 0.61. C_3 constant could not be assessed as the data referred to a single relative density. Therefore it was assumed C_3 = 2.97 [25]. The exponent C_2 is greater than C_1, i.e. the effect on Q_c of the horizontal stress is greater than that of the vertical one and this result is qualitatively in agreement with the results of a numerical simulations carried out by Arroyo *et al.* [38] and with experimental evidences ([26], [27]).

Table 3 sums up test results for the fine-grained soils. It reports soil type; boundary stresses (σ_v, σ_h); sample dry unit weight (γ_d); maximum dry unit weight (Modified Proctor), γdmax; sample water content (w), optimum water content (Modified Proctor), w_{opt}, compaction energy per unit volume (E); maximum vertical stress applied during sample formation (σ'_{pmax}) and average tip resistance (Q_c).

Samples of fine grained soils were reconstituted at densities in between 80 and 92% of the maximum (Modified Proctor) with a water content approximately corresponding to the optimum value. For the FR samples a value of the water content higher than the optimum (9.43%) was used and a test series at constant density (equal to 80% of the optimum) and variable water content (4, 8 and 12%) was also performed. Therefore, these samples were produced by moist-compaction as in the field compaction. After testing, measurements of sample heights and diameters were performed by means of calipers. The maximum vertical strain (in the centre of the sample) was of less than 4 %. Since the after testing evaluation of current sample volume was not considered too much accurate, the dry densities reported in the tables refer to the values just after formation.

For the fine–grained soils, it has been observed that, for a given soil and a given water content a correlation exists between:

- the dry density (γ_d) and the compaction energy per unit volume (E) as shown by Figure 1. FR soil shows a certain scatter especially at higher densities. This scatter could be a consequence of the fact that various batches of FR soil were used and the various batches exhibit small differences.
- the average tip resistance (Q_c) and the compaction energy per unit volume (E) as shown by Figure 2.
- the dry density (γ_d) and the average tip resistance (Q_c) as shown by Figure 3.

Table 3. Test conditions and results for fine grained soils.

Soil	σ_v [kPa]	σ_h [kPa]	γ_d [kN/m^3]	γ_{dmax} [kN/m^3]	γ_d/γ_{dmax}	W [%]	w_{opt} [%]	E [MJ/m^3]	σ'_{pmax} [kPa]	Qc [MPa]
DD	30	30	14.56	17.85	0.82	13.2	13.1	0.395	8224	2.807
DD	50	50	14.56	17.85	0.82	13.2		0.238	6157	1.786
DD	80	80	14.56	17.85	0.82	13.2		0.299	6752	1.512
DD	30	30	16.38	17.85	0.92	13.2		1.324	24474	4.751
DD	50	50	16.38	17.85	0.92	13.2		1.413	24523	4.063
DD	80	80	16.38	17.85	0.92	13.2		1.501	24523	4.990
PC	30	30	15.60	19.13	0.82	10.8	10.7	0.62	13731	3.274
PC	50	50	15.60	19.13	0.82	10.8		0.697	14712	3.648
PC	80	80	15.60	19.13	0.82	10.8		0.545	13731	3.850
PC	30	30	17.55	19.13	0.92	10.8		2.407	39627	7.191

PC	50	50	17.55	19.13	0.92	10.8		2.76	40707	7.877
PC	80	80	17.55	19.13	0.92	10.8		2.211	36979	7.603
FR	30	30	18.50	2.05	0.92	12.0		4.123	46864	6.533
FR	30	30	18.50	2.05	0.92	12.0		3.315	43136	6.535
FR	30	30	18.50	2.05	0.92	12.0		2.938	37465	6.767
FR	30	30	18.00	2.05	0.90	12.0		1.735	22730	3.254
FR	30	30	18.00	2.05	0.90	12.0		1.735	24005	3.568
FR	30	30	18.00	2.05	0.90	12.0		1.828	24400	4.056
FR	30	30	16.00	2.05	0.80	12.0		0.511	8608	1.843
					0.80	12.0	9.43	0.463	8313	1.736
					0.80	12.0		0.475	7823	2.022
					0.80	4.0		0.26	10103	2.036
					0.80	4.0		0.307	9809	1.479
					0.80	4.0		0.346	10790	1.827
					0.80	8.0		0.579	15990	3.077
					0.80	8.0		0.622	15891	2.533
					0.80	8.0		0.564	15303	2.455

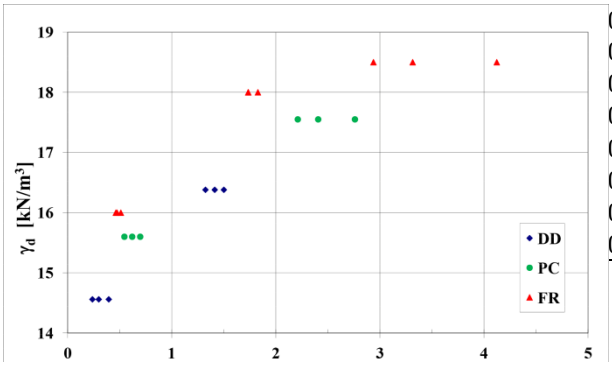

Figure 1. Partially saturated fine grained soils: correlation between dry density (γ_d) and compaction energy per unit volume (E).

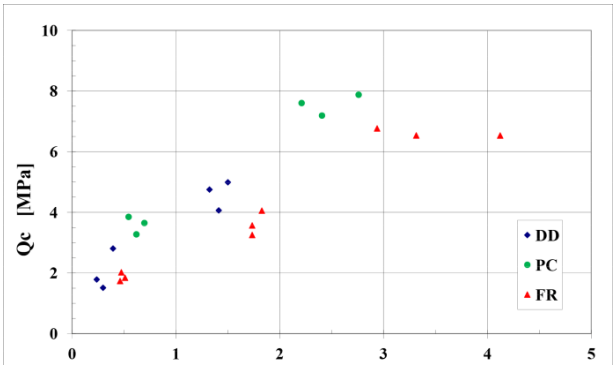

Figure 2. Partially saturated fine grained soils: correlation between average tip resistance (Q_c) and compaction energy per unit volume (E) for a given water content and a given soil.

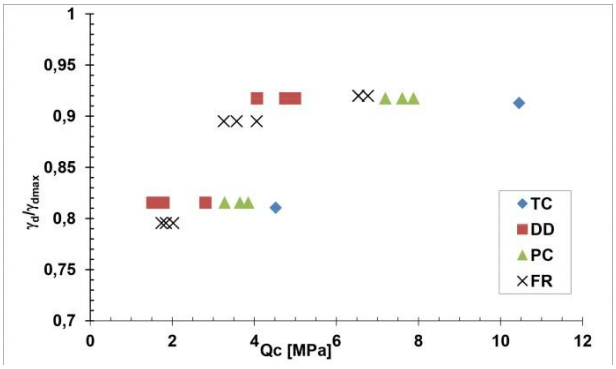

Figure 3. Partially saturated fine grained soils: correlation between dry density (γ_d) and average tip resistance (Q_c) for a given water content (w_{opt}) and a given soil.

The effect of boundary stresses seems negligible. This is supposed to be a consequence of two facts:

- effective stresses are mainly controlled by the suction;
- the compaction stresses, applied during sample formation, are several hundreds of times greater than the applied boundary stresses.

Therefore, it is possible to predict the dry density from the measured tip resistance irrespective of the boundary stresses. The water content during earthwork formation may be also an influent parameter. The use of compaction equipment measuring the compaction energy represents an alternative to infer the in situ density after an appropriate calibration. Moreover, the control of the compaction process in the laboratory offers a quantitative evaluation of the soil workability.

In fact, Table 3 and Figure 1 show that some soils are more workable than others. For example, for FR soil, the maximum compaction pressure or the compaction energy per unit volume that is necessary to obtain a given percentage of the optimum dry density is smaller in comparison with that required in order to compact the PC and DD soils.

5 Water content after sample formation and elapsed time effects

In order to study in the laboratory, the tip resistance variation with water content after the sample formation a sample of soil was prepared at the optimum water content and a dry density equal to 90% of the optimum value and several penetration tests were repeated on the same sample. In fact, it was observed that it is possible to horizontally move the CC of about 40 mm along all directions and to repeat the penetration tests along different verticals at least 6 times for the same sample. The possibility of performing repeated tests on the same sample was preliminary checked several times. The tests were carried out at different dates and water contents. The water content decreased with time because of evaporation and was increased by adding water to the sample. Water was sprayed on the top surface in several steps. For each step the water content was increased of about 2.5%. The penetration test was performed after seven days. Figure 4 shows the Qc (average value between 6 and 15 cm depth) vs. the water content for all the fine grained soils. While for the PC soil the experimental results (Table 5) show that the tip resistance linearly increases with a decrease of the water content and the phenomenon seems perfectly reversible, in the case of DD soil, the data (Table 6) show that the tip resistance also increases with time and not only with a water content decrease. In this case the phenomenon is not fully reversible.

Therefore, the effect of the elapsed time after sample formation was experimentally studied by performing repeated penetration tests, in the CC, on the same sample over a period of 2 months. The sample water contained remained constant over the time. The same testing program was repeated using two different material, TR and PE soil samples, in order to compare the results. The two soil samples were reconstituted at a water content equal to the optimum water content and at a dry density approximately corresponding to the 80% of the maximum value (Modified Proctor). Tables 8 and 9 sum up, for each soil, the average tip resistance values measured at different dates.

As TR soil is concerned, Table 8 reports, in the last column, the mass of the CC and of the sample. Measurements of such a mass were taken after each penetration tests. The reported values include 31 kg of CC. The only variations concern the water mass. For PE soil, the water mass variation over a period of time of two months was of 0.205kg.

Test results show an almost linear increase of the resistance with the time for both soils (Figure 5). From the regression analysis of the whole data it is possible to assume an increase of about 40% of the tip resistance per log cycle of time.

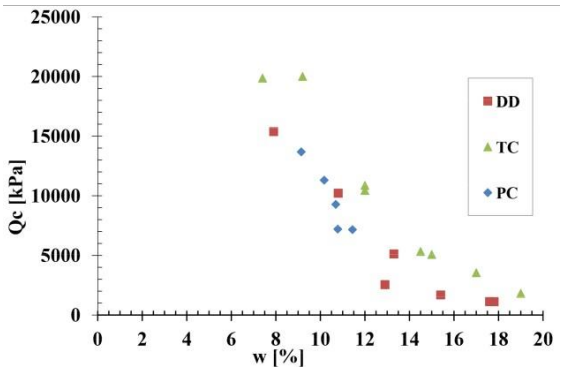

Figure 4. CC tests at variable water content: average tip resistance vs. water content for all the fine grained soils.

Table 5. CC tests on a PC soil sample: average tip resistance measured for the same sample (Qc), along different verticals, at different dates and water contents (w).

Test	Date	Time days	w %	Qc kPa
1	22/07/2014	0	10.78	7206
2	07/08/2014	15	10.69	9278
3	05/09/2014	45	10.17	11307
4	19/09/2014	59	9.14	13680
5	02/10/2014	72	11.44	7163

Note: Soil sample: PC; $\gamma_d = 0.9\gamma_{dmax}$

Table 6. CC tests on a DD soil sample: average tip resistance measured for the same sample (Q_c), along different verticals, at different dates and water contents (w).

Test	Date	Time days	w %	Qc kPa
1	16/10/2014	0	12.9	2548
2	27/10/2014	11	15.4	1685
3	03/11/2014	18	17.6	1124
4	10/11/2014	25	17.8	1120
5	21/11/2014	36	13.3	5125
6	05/12/2014	50	10.8	10216
7	22/12/2014	67	7.9	15377

Note: Soil sample: DD; $\gamma_d = 0.9\gamma_{dmax}$

Table 8. TR soil sample: average tip resistance values measured at different dates.

Test	Time [Days]	Qc [kPa]	Mass (kg)
1	7	4253	58.740
2	14	5738	58.730
3	21	5413	58.725
4	28	6461	58.685
5	39	6570	58.650
6	57	6597	58.605

Table 9. PE soil sample: average tip resistance values measured at different dates.

Test	Time [Days]	Qc [kPa]
1	4	4211
2	16	4451
3	28	5492
4	38	5784
5	50	5908
6	60	6044

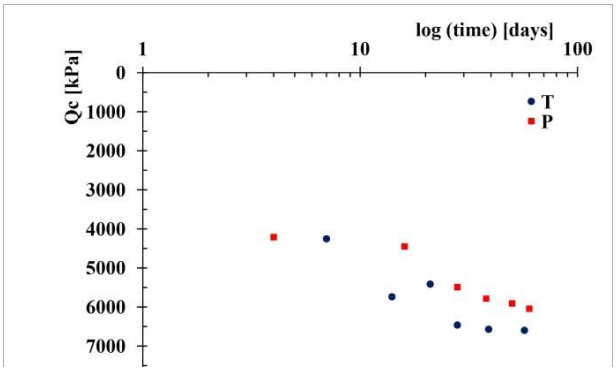

Figure 5. Average tip resistance versus time for TR and PE soils.

6 Conclusions and further research

The tests on the compacted partially saturated fine-grained soil samples suggest that the tip resistance mainly depends on the compaction degree and water content after sample formation. The total boundary stresses are not influent probably because the effective stress state, in this case, mainly depends on suction and pre-stressing during compaction.

The water content during sample formation has a lesser influence.

For practical application of this method, it is suggested to define, for a given soil, a design compaction degree. Therefore, it is possible to experimentally determine, for the given compaction degree, the design tip resistance vs. the water content after sample formation. For the experimental determination of this design curve it is sufficient to reconstitute a sample of a given soil at a given dry density and water content. On this sample it is possible to repeat the tests with variable water contents after sample formation.

The effect of the elapsed time since the sample formation has a great effect and also this aspect deserves further research. While for new earthworks, it is suggested to proceed with controls immediately after the work completion, for earthworks realized centuries ago it would be interesting to understand how this indication should be applied to.

References

[1] Cosanti, B. Guidelines for the geotechnical design, upgrading and rehabilitation of river embankments. *PhD Thesis.* Doctoral School of Engineering "Leonardo da Vinci". University of Pisa. Italy, 2014.

[2] Cosanti B., Squeglia N., Lo Presti D. Analysis of existing levee systems: the Serchio river case. *Rivista Italiana di Geotecnica*. (4)14: 47-65, 2014.

[3] Cosanti, B.; Squeglia, N.; Lo Presti, D. Geotechnical Characterization of the Flood Plain Embankments of the Serchio River (Tuscany, Italy). *7th International Conference on Case Histories in Geotechnical Engineering and Symposium in Honor of Clyde Baker*. April 29-May 4, 2013. Chicago, IL, 2013.

[4] Squeglia, N, Cosanti, B, Lo Presti, DCF (2013). Stability Analysis of the Serchio River Flood Plain Embankments (Tuscany, Italy). *7th International Conference on Case Histories in Geotechnical Engineering and Symposium in Honor of Clyde Baker*. April 29-May 4, 2013. Chicago, IL.

[5] Tatsuoka, F. Compaction Characteristics and Physical Properties of Compacted Soils Controlled by the Degree of Saturation. *Proc. Of the Sixth International Symposium on Deformation Characteristics of Geomaterials*. IS Buenos Aires, 15-18 November, 2015.

[6] ASTM D2167-15, Standard Test Method for Density and Unit Weight of Soil in Place by the Rubber Balloon Method, ASTM International, West Conshohocken, PA, 2015.

[7] ASTM D1556/D1556M-15e1, Standard Test Method for Density and Unit Weight of Soil in Place by Sand-Cone Method, ASTM International, West Conshohocken, PA, 2015.

[8] ASTM D6780/D6780M-12, Standard Test Method for Water Content and Density of Soil In situ by Time Domain Reflectometry (TDR), ASTM International, West Conshohocken, PA, 2012.

[9] ASTM D6938-15, Standard Test Methods for In-Place Density and Water Content of Soil and Soil-Aggregate by Nuclear Methods (Shallow Depth), ASTM International, West Conshohocken, PA, 2015.

[10] De Graaf H. C. Van and Zuidberg H. M. (1985). Field Investigations. *The Netherlands Commemorative*,Vol. XI ICSMFE 29-52, 1985.

[11] Campanella R.G and Kokan M. J. A New Approach to Measuring Dilatancy in Saturated Sands. *Geotechnical testing Journal*, ASTM, 16(4): 485-495, 1993.

[12] Nieuwenhuis J. K. and Smits F. P. The Development of a Nuclear Density Probe in a Cone Penetrometer. *Proc. ESOPT II*, Balkema 2: 745-749, 1982.

[13] Tjelta T. I.; Tieges A.W.W.; Smits F.P.; Geise J.M.; Lunne T. In-Situ Density Measurements by Nuclear Backscatter for an Offshore Soil Investigation. *Proc. Offshore Technology Conference*, Richardson Texas, Paper No 40917, 1985.

[14] AFNOR (1997) XP P 94-063. Controle de la qualité du compactage-methode au penetrometre dynamique a energie constante.

[15] AFNOR (2000) XP P 94-105. Controle de la qualité du compactage-methode au penetrometre dynamique a energie variable.

[16] SETRA – LCPC. Remblelayage des tranchées et réfection des chaussées – Guide Technique. Setra/LCPC, D9441, 1994.

[17] SETRA – LCPC. Remblelayage des tranchées et réfection des chaussées – Compléments. Setra/LCPC, 117, 2007.

[18] Chung, S.F., Randolph, M.F. And Schneider, J.A. Effect of Penetration Rate on Penetrometer Resistance in Clay. *J. Geotech. Geoenviron. Eng.* 132:1188-1196, 2006.

[19] Whittle, A. J., Sutabutr, T., Germaine, J. T. & Varney, A. Prediction and interpretation of pore pressure dissipation for a tapered piezoprobe. *Géotechnique* 51(7): 601-617, 2001.

[20] Bemben, S.M. and Myers, H.J. The influence of rate of penetration on static cone resistance in Connecticut river valley varved clay. *Proceedings of the European Symposium on Penetration Testing*, ESOPT, Stockholm, 2.2, 33-34, 1974.

[21] Roy, M., Tremblay, M., Tavenas, F. and Rochelle, P. L. Development of pore pressure in quasi-static penetration tests in sensitive clay. *Canadian Geotechnical Journal*, 19(1): 124-138, 1982.

[22] Lunne, T., Robertson, P.K. and Powell, J.J.M. Cone Penetration Testing in Geotechnical Practice. EF Spon/Blackie Academic, Routledge Publishers, London, 312, 1997.

[23] Baldi, G., Bellotti, R., Ghionna, V., Jamiolkowski, M. and Pasqualini, E. Interpretation of CPT's and CPTU's. 2nd Part: Drained Penetration. *Proceeding 4th International Geotechnical Seminar*, Singapore, 143-156, 1986.

[24] Jamiolkowski, M., Ghionna, V.N., Lancellotta, R. and Pasqualini, E. New correlations of penetration tests for design practice. *Proc., Penetration Testing 1988, ISOPT 1*, Orlando, Florida, J. De Ruiter ed., Vol. 1: 263-296, 1988.

[25] Garizio, G.M. Determinazione dei parametri geotecnici e in particolare di K0 da prove penetrometriche. M.Sc. Thesis, Department of Structural Engineering, Politecnico di Torino (In Italian), 1997.

[26] Jamiolkowski, M., Lo Presti, D.C.F. and Garizio, G.M. Correlation between Relative Density and Cone Resistance for Silica Sands. *75th Anniversary of Karl Terzagni's ERDBAU*, 2000.

[27] Jamiolkowski, M., Lo Presti, D.C.F. and Manassero, M. (2001). Evaluation of Relative Density and Shear Strength of Sands from CPT and DMT, *Invited Lecture Ladd Symposium*, GSP No. 119, ASCE, 201-238, 2001.

[28] Tatsuoka, F. Laboratory stress-strain tests for the development of geotechnical theories and practice. *Bishop Lecture, Proc. 5th International Conference on Deformation Characteristics of Geomaterials*, Seoul, Korea, Sept., 3-50, 2011.

[29] Fioravante V, Jamiolkowski M., Tanizawa F. and Tatsuoka F. Results of CPT's in Toyoura Quartz Sand. *Proceedings of the First International Symposium on Calibration Chamber Testing – ISOCCT1*, Postdam, New York, 28-29 June 1991, 135-145. Elsevier New York, 1991.

[30] Mayne, P. W. and Kulhawy, F. H. (1991). Calibration chamber database and boundary effects correction for CPT data. *In Calibration chamber Testing*. New York, Elsevier, 257-264, 1991.

[31] Tanizawa F. Correlations between cone resistance and mechanical properties of uniform clean sand. *Internal Report ENEL – CRIS*, Milan, 1992.

[32] Marchetti, S. and Crapps, D.K. Flat Dilatometer Manual. *Internal Report of G.P.E. Inc*, 1981.

[33] Baldi, G. and O'Neill, D.A. Developments in penetration technology for geotechnical and environmental applications. *International*

Symposium on Cone Penetration Testing, Linkoping, Sweden, 1995.

[34] Parkin, A.K. The calibration of cone penetrometers. *Proceedings of the First International Symposium on Penetration Testing, ISOPT-1*, Balkema, Rotterdam, The Netherlands, Orlando, Florida, De Ruiter (Ed.) 221-243, 1988.

[35] Salgado, R. The mechanics of cone penetration: contributions from experimental and theoretical studies. In: Coutinho, R.Q., Mayne, P.W. (Eds.), Geotechnical and Geophysical Site Characterization 4, ISC4. CRC Press, Boca Raton, FL, USA, 131-153, 2013.

[36] Schmertmann, J.H., Guidelines for cone penetration test: performance and design. Federal Highway Administration, Washington, D.C., 1978.

[37] AASHTO M 145 1991. (R1995) (R2000). Standard Specification for Classification of Soils and Soil-Aggregate Mixtures for Highway Construction Purposes. HM-22: PART IA.

[38] Arroyo, M., Butlanska, J., Gens, A., Calvetti, F. and Jamiolkowski, M. Cone penetration tests in a virtual calibration chamber. *Géotechnique*, 61(6), 525–531, 2011.

EVALUATION OF SHEAR MODULUS OF SAND-CLAY MIXTURES WITH VARIOUS FINES CONTENT

Taichi HYODO[a], Yang Wu[b], Masayuki HYODO[b], Yoshiaki KIKUCHI[a] and Yoshimichi TSUKAMOTO[a]

[a]Department of Civil Engineering, Tokyo University of Science, JAPAN
[b]Department of Civil and Environmental Engineering, Yamaguchi University, JAPAN
E-mail: t.hyodo@rs.tus.ac.jp, yangwuuu0226@hotmail.com

Abstract

The soil is generally categorized into sand or clay using different evaluation methods in design practice. However, the medium soils composed of sand and clay are widely distributed in natural systems. The appropriate approach to classify the sand-clay mixture is still insufficient. Natural soils are composed of the grains with various grading curves and different particle characteristics. The unified evaluation method is required to examine the mechanical properties of soil mixtures of sand and fines. Specimens were prepared with natural clay and silica sand with different proportions by weight using the tamping energy method. A series of bending element tests were performed on sand-clay mixture specimens to investigate the influence of fines on the shear modulus.

Keywords –

bender element test; sand-clay mixtures; fines content; shear modulus; equivalent granular void ratio

1 Introduction

The numerical analysis on the vibration characteristics and deformation behaviour of ground foundation during earthquake loadings plays an important role in seismic design of structure[1)2)]. The equivalent shear modulus and damping ratio are the dynamic deformation coefficients and regarded as the important input parameters for the earthquake response analysis. The determination of the dynamic deformation coefficients of ground foundation are significantly important for the stability and response characteristics of foundation subjected to earthquake loading.

The naturals soils are generally divided into the sand and clay in according to the grain size of soil grains existing in ground. The mechanical properties of sand and clay are largely different. For example, the friction resistance angle is considered for sand and the cohesion is selected for clay with regard to the associated strength decision in design. The gap exists in the basic design concept for sand and clay under both of static and dynamic conditions. Currently, different approaches are employed to evaluate the dynamic deformation coefficients for ground foundations composed of sand or clay, separately. The establishment of quantitative evaluation method are required to understand the dynamic deformation characteristics of naturals soils varying from sand to clay with different component proportions.

Plenty of studies were performed to examine the dynamic deformation characteristics. Some equations were proposed to estimate the dynamic deformation coefficients in consideration of grain shape, void ratio and confining pressure [3)~6)]. However, these estimation expressions were obtained based on the measured results of clay without sands. Such equations are inapplicable for the sand-clay mixtures containing fines or clay with various characteristics.

This study presents the bender element test results on the tamped mixtures specimens of marine clay containing various fines content and silica sand. This study intends to clarify the influences of the skeleton structure of sand-clay mixtures and elastic shear modulus at smaller strain levels on the water content in clay. Besides, the water content is adjusted to the twice of liquid limit for sand-clay mixture specimens dominated by the clay with the fines exceeding some certain value. The bender element tests were conducted on the specimens prepared by the pre-consolidation method and the shear modulus are calculated.

2 Materials tested

2.1 Physical properties of specimens

The specimens employed in this study are composed of marine sediment and silica sand with different composition proportions and varying grading curves. Table 1 shows the physical properties of the materials

Table 1 Physical properties of specimen

	Gs	Ip	e_{max}	e_{min}	Fc(%)
配合珪砂	2.652	NP	0.850	0.524	0
IC5	2.650	NP			4.9
IC10	2.648	NP			9.8
IC15	2.646	NP			14.7
IC20	2.643	20.71			19.6
IC30	2.639	18.67			29.4

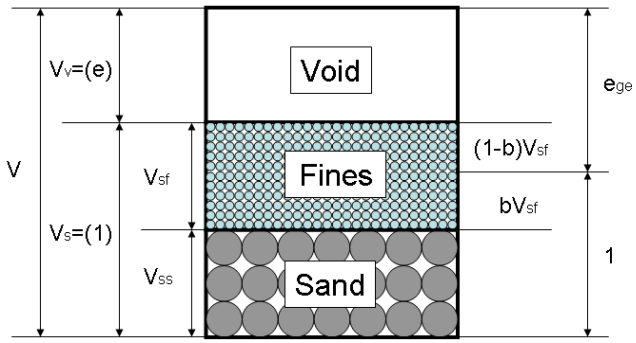

Figure 1 The composition model of soil

tested. The coarse sand grains are slightly adjusted to possess a smooth grading curve. The Iwakuni clay is selected as the fines in this study (F_C=98%, liquid limit w_L=77.34%, plastic index I_P=47.5). Particles with grain size over 0.425 mm in Iwakuni clay is removed in specimen preparation process. The sand and clay are uniformly mixed. The specimens are produced by five layers and each layer is tamped under a designated energy using rammer from the target height. The specimen is 5 cm in diameter and 10 cm in height.

2.2 Skeleton structure of sand-clay mixtures

The receiver bender element (BE) and sender BE are placed on the top and bottom of the triaxial shearing test apparatus. The receiver BE is 4.4 mm in height, 12.0 mm in width and 1.4 mm in length. The sender BE is 4.1 mm in height, 12.0 mm in width and 1.2 mm in length. The height of BE is equal the insertion length of BE into the specimens. The voltage induced by the deformation of the sender BE is obtained as the input voltage.

2.3 Specimen preparation method

The mixtures are composed of the silica sand as coarse matrix and the Iwakuni clay as the fine matrix. The granular void ratio e_g and the equivalent granular void ratio e_{ge} are employed to evaluate the state of mixtures. The granular void ratio e_g are generally employed as the parameter to evaluate the mechanical properties of sand-clay mixtures [7)~9)]. The fines exit in the pore space between sand grains in the sand-clay mixtures. The mechanical behaviour of sand-clay mixtures are solely dominated by the sand skeleton and this is the basic concept granular void ratio. Figure 1 expresses the granular void ratio e_g using the three phases model in saturation state.

$$e_g = \frac{V_V + V_{Sf}}{V_{Ss}} \tag{1}$$

where V_v is the volume of air, V_{Sf} is the volume of fines and V_{Ss} is the volume of coarse grain.

The equivalent granular material e_{ge} is the extension concept of granular void ratio and dose not completely neglect the volume of fines. Some proportion of fines plays the similar role to ture specimens is obtained irrespective of the amount of fines.

The density of coarse sand and fines particles are assumed to be the identical value as ρ_s. The fines content can be expressed using Eq. (1). The equivalent granular void ratio e_{ge} is the function of void ratio e, fines content Fc and contribution ratio b. The contribution ratio b represents the proportion of fines which plays the similar role to that of sand skeleton and it varies between 0 and 1.

$$Fc = \frac{V_{Sf}}{V_S} \tag{2}$$

$$e_{ge} = \frac{e + (1-b)Fc}{1-(1-b)Fc} \tag{3}$$

From Eq. (3), the equivalent granular void ratio e_{ge} is equal to the void ratio e when the contribution ratio b=1 and comes back to the granular void ratio e_g when the contribution ratio b=0. The most suitable contribution ratio b is searched under the conditions that the relation between the shear modulus sand equivalent granular void ratio of the sand-clay mixtures containing F_C=10~30% is the same to that of sand-only specimens. The most suitable b value is adopted in the relevant examinations.

Table-2 Adjustment method of tamped specimens

Tamping energy E_c (kJ/m^3)	Number of dropping per a layer					Dropping height of a rammer (m)
	1st layer	2nd layer	3rd layer	4th layer	5th layer	
22	5	10	15	25	30	0.050
504	60	80	100	120	140	0.184

3 Bender element test

3.1 Test apparatus

The receiver bender element (BE) and sender BE are placed on the top and bottom of the triaxial shearing test apparatus. The receiver BE is 4.4 mm in height, 12.0 mm in width and 1.4 mm in length. The sender BE is 4.1 mm in height, 12.0 mm in width and 1.2 mm in length. The height of BE is equal the insertion length of BE into the specimens. The voltage induced by the deformation of the sender BE is obtained as the input voltage.

3.2 Specimen preparation method

The specimen with initial water content w=10% was produced by two levels of the tamping energy[11] Ec = 22 and 504 kJ/m^3. The specimen was 5 cm in diameter and 10 cm in height. The specimen was prepared in mold by five layers. Each layer was tamped using the specific energy Ec. The tamping energy Ec is determined using the following equation[12)~14)].

$$E_c = \frac{W_R \cdot H \cdot N_L \cdot N_B}{V} \qquad (4)$$

Here, W_R is the weight of rammer, H is the drop height of rammer, N_L is the number of layer (five layers), N_B is the amount of blows for each layer, V is the volume of mold. The weight of rammer W_R and is the number of layer N_L are the same for a specimen. The tamping number N_B and the drop height for each layer H are adjusted to attain the target tamping energy E_c. Table 2 shows the required drop height of rammer H and tamping number for one layer N_B for the specific tamping energy Ec applied on the specimens. The tamping number for on layer is different and determined by the density of specimens which is designated in advance of testing. The drop heights of rammer H for Ec=22 kJ/m^3 and 504 kJ/m^3 are 0.05 m and 0.184 m.

The specimens cannot be prepared using the method described above. The clay and sand specimens mixed with different proportions of 20:80, 30:70 by the dry weight are adopted without the pre-consolidation process. The water content in the reconstituted specimens is increased to be twice of the liquid limit. The specimens are consolidated under one-dimensional loading with the maximum vertical load σ_{vc}=50 kPa after the initial load σ_{vc}=10, 20 kP for one entire day.

3.3 Specimen preparation method

The specimens were first soaked in de-aired water to replace the air in void by the CO_2 at an effective confining pressure σ_c'=20 kPa. All samples were saturated to a B value larger than 0.95 after the back pressure was increased to 100 kPa. The specimens were isotropically consolidated to different pressures of 50 kPa, 100 kPa, 200 kPa and 400 kPa. A series of BE tests were conducted at various confining pressures.

In BE test, the sinusoid wave is employed as the sending wave with the oscillation starting voltage V=20 V. The frequency varies as f=2.5，5，10，15，20，25，30 kHz to make the receive wave record the time. The distance between the sending wave and receiving wave L are is regarded as the necessary transmission length to compute the elastic shear velocity Vs. The transmission time Δt is decided by the start-to-start method.

The elastic shear velocity V_S and elastic shear coefficient G can be expressed using Eqs. (5) and (6).

$$V_S = \frac{L}{\Delta t} \qquad (5)$$

$$G = \rho_t \cdot V_S^2 \qquad (6)$$

Herein, Δt is the wet density of specimen.

4 Evaluation of shear characteristics based on equivalent granular void ratio

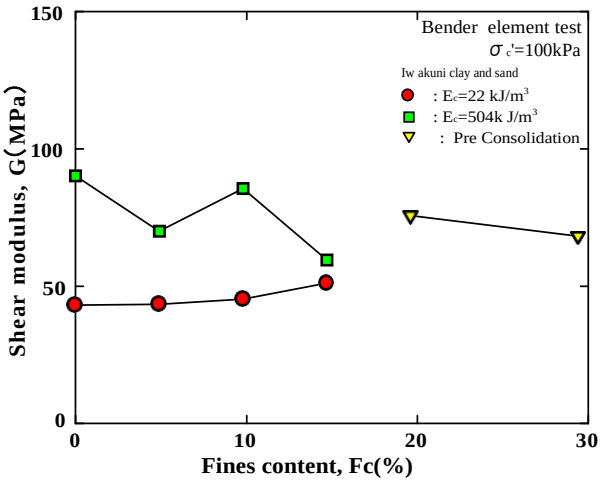

Figure 2 Relationship between shear modulus and fines content

Figure 2 shows the shear modulus plotted against the fines content of specimens at an effective confining pressure σ_c'=100 kPa. It is well accepted that the shear modulus of soil increases with the reduction in void ratio. However, the addition of clay into the sand to increase the fines content and reduce the void ratio is not a prerequisite for a rise in shear modulus. It is seen that the shear modulus of specimens with *E*c=22 kJ/m3 increases with the level of fines content. The relation between the shear modulus and fine content for specimens with *E*c=504 kJ/m3 becomes less clear. The shear modulus of specimens with two levels of *E*c approach to the similar value when the fines content is around 15%. The shear modulus decreases with the increasing fines content as the fines content exceeds 20%. A bigger difference in the shear modulus at the boundary of sand side and clay side and it is originated from the preparation method for specimens whose behaviour is dominated by the sand and clay. The specimen alike sand is prepared by tamping method and the specimen alike clay is prepared by the pre-consolidation method. For specimen with behaviour alike sand, the clay with high water content enter into the skeleton of sand. For specimen with behaviour alike clay, the water content of clay as the matrix is reduced due to the pre-consolidation and this reduction reversely enhances the shear modulus. results of sample containing *F*c=0% with *E*c=113 kJ/m^3 is also included.

Figure 3 (a) also shows the fitting curve in accordance with the previous work by Hardin and Richar15) on Ottawa sand.

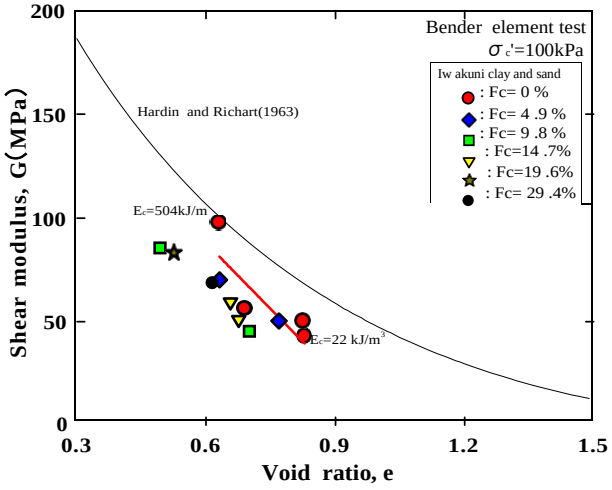

(a) b=1,（e_{ge}=e）

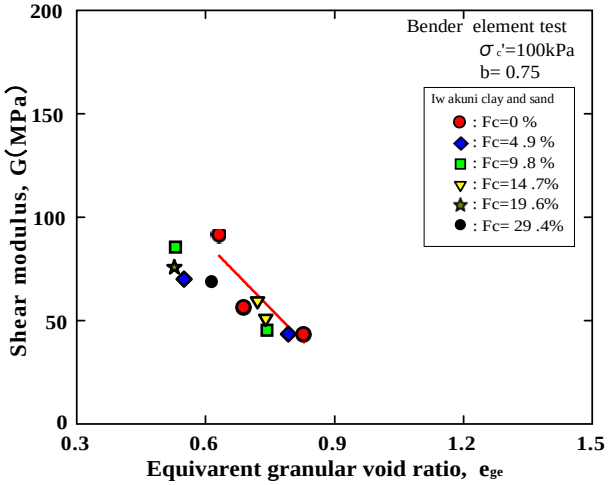

(b) b=0.75

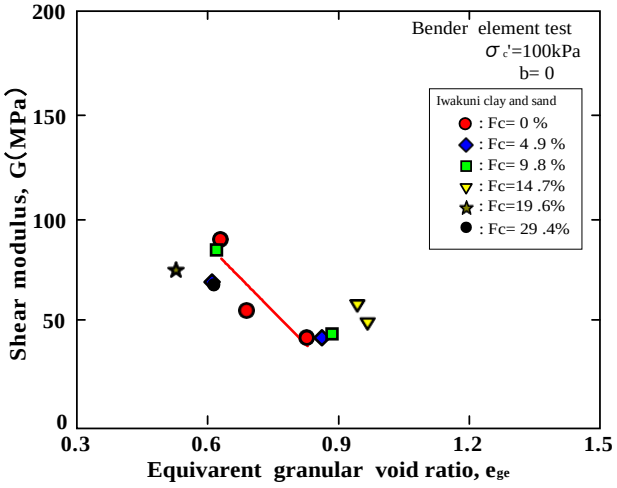

(c) b=0,（e_{ge}=e_g）

Figure 3 Relationship between shear modulus and equiv alent granular void ratio e_{ge}

$$G = 6930 \frac{(2.17 - e)^2}{1 + e} (\sigma_m')^{0.5} \qquad (7)$$

The shear modulus of sand-clay mixture specimen containing *F*c=0% is close to but lower than the estimation value by the Hardin and Richart [15] method. Additionally, good correlation between the measured shear modulus of specimens containing various of fines content and the fitting line could be watched. A larger tamping energy applied for preparing the specimens containing the same fines content leads to a smaller void ratio and a higher shear modulus.

Figure 3 (b) shows the shear modulus plotted against the equivalent granular void ratio decided by Eq. (3) with *b*=0.75. For the specimens prepared by the pre-consolidation method with *b*=1, the void ratio is directly plotted. A better correlation between the shear modulus and equivalent granular void ratio could be obtained compared to the relationship displayed in Fig. 3(a). The distribution of the plots for the sand-clay mixtures containing various fines content is better than the fitting line for specimens containing *F*c=0%.

Figure 3 (c) shows the shear modulus plotted against the equivalent granular void ratio decided by Eq. (3) with *b*=0. For the specimens prepared by the pre-consolidation method with b=1, the void ratio is directly plotted. The better correlation between the shear modulus and equivalent granular ratio could be confirmed. However, it is clearly noticed that the plots of specimens containing various fines content slightly diverge from the fitting curve for specious containing *F*c=0% compared to the results in Figs. 3(a) and 3(b).

Varying *b* value from 0 to 1 are input into the Eq. (3) to examine the correlation between shear modulus. The best correlation is obtained when *b* is equal to 0.75.

The specific evaluation equation is expected to be proposed in further work. The good correlation between the shear modulus and equivalent granular void ratio of specimens prepared using the tamping method and pre-consolidation method is acquired. More test data are necessary to establish the evaluation equation. Besides, the influence of water content on the clay behaviour in the evaluation equation[16] should also be considered.

5 Conclusions

This study presents the bender element test performed in the triaxial cell on the sand-clay mixtures containing various fines content. The unified evaluation method is employed to examine the shear modulus of clay-sand mixtures. The main findings of this study are shown as follows.

1. The correlation between the shear modulus and fines content could not be obtained for sand-clay mixtures prepared by tamping energy method.
2. The equivalent granular void ratio is employed to evaluate the mechanical properties at small strain levels. The best correlation between the shear modulus and equivalent granular void ratio could be acquired when *b*=0.75 based on the concept of equivalent granular void ratio.
3. In exception of fines content, the influence of water content on the shear modulus of clay-sand mixtures should also be considered in further study.

References

[1] Arakawa N. , Tuneta K. et.al, “EARTHQUAKE RESPONSE CHARACTERISTICS –SHAKE : DERSA”. *Report of PWRI*,Vol.1778:1982. (in Japanese)

[2] Zen K. , Yamazaki H. and Umehara Y. “Experimental Study on Shear Mosulus and Damping Ratio of Natural Deposits for Seismic response Analisys”, *Report of P.H.R.I.*, Vol.26, No.1, 1987. (in Japanese)

[3] Seed, H.B.： “Evaluation of soil liquefaction effects on level ground during earthquakes”, State-of-Art Repot, Preprint of ASCE Annual Convention and Exposition on Liquefaction Problems in Geotechnical Engineering, Philadelphia, 1976

[4] Ishihara, K., F. Tatsuoka and S. Yasuda：“Undrained deformation and liquefaction of sand under cyclic stress”, Soils and Foundations, Vol.15, No.1, pp.29~44, 1975

[5] Hardin, B.O. and F.E. Richart Jr.：“Elastic wave velocities in granular soils”, Jour. Of SMF Div., Proc. ASCE, Vol.89, No.SM1, Proc. Paper 3407, Feb., pp.33~65, 1963

[6] Iwasaki, T., F. Tatsuoka and Y. Takagi：“Shear moduli of sands under cyclic torsional shear loading”, Soils and Foundations, Vol.18, No.1, pp.39~59, 1978

[7] Omine K. and Ochiai H. , “STRESS-STRAIN RELATIONSHIP OF MIXTURES WITH TWO DIFFERENT MATERIALS AND ITS APPLICATION TO ONE-DIMENTIONAL COMPRESSION PROPERTY OF SAND-CLAY MIXED SOILS”, *Journal of Japan Society of Civil Engineers, Ser. C (Geosphere Engineering)*, No.448/III-19, pp.121-130, 1992 (in Japanese)

[8] Ito S. , Hyodo M. , Fuji T. , Yamamoto Y. and Taniguchi T. , “UNDRAINED MONOTONIC AND CYCLIC SHEAR CHARACTERISTICS OF SAND, CLAY AND INTERMEDIATE SOILS”, *Journal of Japan Society of Civil Engineers, Ser. C (Geosphere Engineering)*, No. 680 P 233-243,

2001 (in Japanese)

[9] Hyodo M. , Kim J. , Fukumoto K. , Yamada S. and Yoshimoto N. , "UNDRAINED CYCLIC SHEAR BEHAVIOR OF SAND AND CLAY MIXTURE SUBJECTED TO INITIAL STATIC SHEAR STRESS", *Journal of Japan Society of Civil Engineers, Ser. C (Geosphere Engineering)*, Vol.62, No.1, pp.240-245, 2006 (in Japanese)

[10] Thevanayagam, S., Shenthan, T, Mohan, S. and Liang, J.: Undrained fragility of clean sands, silty sands, and sandy silts, Journal of Geotechnical and Geoenvironmental Engineering Vol. 128, No.10, pp.849-859, 2002.

[11] Ni, Q., Tan, T.S., Dasari, G.R. & Hight, D.W. : Contribution of fines to the compressive strength of mixed soils, Geotechnique 54, No.9, pp.561-569, 2004.

[12] Naeini, S. A., Baziar, M. H.: Effect of fines content on steady-state strength of mixed and layered samples of a sand, Soil dynamics and earthquake engineering 24, pp. 181-187, 2004.

[13] Adachi M. , Yasuhara K. and Shimabukuro A. , "Influences of the Sample Preparation Method on Behaviour of Non-plastic Silts in Undrained Monotonic and Cyclic Triaxial Tests", *Soil mechanics and foundation engineering*, vol.48, pp.24-27, 2000 (in Japanese)

[14] Ladd, R.S.: Preparing test specimens using undercompac-tion, Geotechnical Testing Journal,1(1), pp.39-49, 1978.

[15] Hardin, B.O. and Richart Jr. F.E.: Elastic wave velocities in granular soils, Proc. ASCE., Vol.89, SM1, pp.33-65, 1963.

[16] Kaneko T. , Hyodo M . , Tatebe S, Yamada S. , Nakata Y. nad Yoshimoto N., "INITIAL SHEAR STIFFNESS OF SAND AND CLAY MIXTURES WITH VARIOUS WATER CONTENTS", *Journal of Japan Society of Civil Engineers, Ser. C (Geosphere Engineering)*, Vol. 68 (2012) No. 1 P 188-198, 2012 (in Japanese)

Utilisation of Compound Tyre Chips-Incinerator Bottom Ash as Low-Cost Earthquake Buffer

P. Promputthangkoon[a], D. Chuphan[b], and A. Lukjan[a]

[a]Department of Civil Engineering, Rajamangala University of Technology Srivijaya, Thailand
[b]College of Industrial Technology and Management, Rajamangala University of Technology Srivijaya, Thailand
E-mail: panu_pptk@hotmail.com, dusit65@yahoo.com, federun9@gmail.com

Abstract

In the past solid wastes were simply dumped in open areas. Then, landfills were utilised. Nontheless, the wastes have been growing to the point that burying is unpractical. Hence, incinerators have been employed. This leaves another waste called incinator ash that also requires treatment. Since the invention of a motor car decades ago the number of car sales is still going strong. This, as well, results in the huge amount of discarded tyres required to be properly managed. This study attempted to make use of those two wastes as foundation soil to buffer the ground vibration tramsmitted to superstructures. It was done by first constructing a 50 cm thick sand layer in a 120 cm diameter steel chamber. During the construction an explosive detonator was installed at 10 cm from the bottom. Overlying the sand was 25 cm thick compound incinerator bottom ash-tyre chips (IBA-TC) having the by-weight IBA to TC ratios of 100:0, 95:5, 90:10: 75:25, 40:60, and 0:100. A total of three accelemeters were installed: one on the ground (G1) and the other two over the roofs of one- and two-storey houses (G2 and G3, respectively). Note that the sand was prepared to be two states: dry (DS) and saturated (SS). After the set-up completed the detonator was ignited; the ground acceleration as well as the accelerations induced on the houses were monitored and recorded. The results showed that, for the DS the acceleration is virtually increased with increasing TC. This, however, was contrary to that of the SS as the ground acceleration gradually decreases with the increase of TC. Furthermore, it was found that the percentage reductions for G2 and G3 with repect to G1 for the case of SS is quite higher than those for the case of DS. These findings suggest that both wastes may be employed as foundation soil to buffer the vibration transmitted to superstructures.

Keywords

Incinerator bottom ash; Tyre chips; Earthquake; Sesmic isolator

1 Introduction

When a major earthquake strikes, even though not quite often, a number of injuries and deaths as well as scores of damaged built environment are expected. Note that there are several causes that can initiate an earthquake; the continuing movement of the earth's crust is believed to be the main cause though. One of the most important aspects of the crust is that it comprises several plates interconnected. Essentially, it is the continuous movement of molten rock underneath that is driving the crust; and, this has been called convection. In addition, the flowing of the molten rock is one of the causes triggering volcano activities along the boundary between plates. Hence, it also continuously drives the plates thereby causing them to move either against each other or away from other plates. This movement is one of the causes triggering major earthquakes. Note that each year approximately 10,000 people die from the earthquake [1]. Unfortunately, even with current technology and knowledge, we still unable to precisely predict an earthquake incident concerning where, when, and magnitude.

Countries around the world are increasingly facing environmental problems concerning the accumulated numbers of discarded tyres. For example, huge amounts of used tyres disposed in open areas are susceptable to fire, whether by accidents or intensions. When this has happened, it would be very difficult to cease the fire quickly because they are very good for burning. Then, there would be consequences such as the groundwater may be contaminated when the burnt tyres are brought into underground by rainfalls. Consequently, the contaminated groundwater would require several decades to become clean again. It is therefore essential for them to sensibly consider this problem.

For those reasons, in the future countries should have some kinds of regulation or law concerning the management for those wastes. It should be noted herein that the USA and Europe have been imposing the laws concerning these wastes for some times. For example,

since 2003 disposing of whole used tyres in the EU have been prohibited. In case of tyres required to be thrown away, they must be undergone some processes first, e.g., be shredded to have smaller size. Nonetheless, this process must be carried out by authorised privates [2].

Solid wastes are mostly leftover materials generated from households as well as industries. In the past landfills were normally employed. As the world's population has been dramatically increasing, however, areas for the landfills are scarce. This resultes in the application of incinerators. For instance, an incinerator having a burning capacity of 250 tonnes per day could eliminate around 85.90% of the waste, resulting in approximately 10% ashes by volume. it can be seen that some work is still required to manage those ashes [3].

Incinerator bottom ashes (IBA) are the waste generated from burning solid wastes. They have a grey colour, porous- and rough particle, and quite big size compared with soil. When the ashes just coming out from a burning chamber, they are first cooled by means of water. Then, they are stored in order to be transported for further actions. There have been attempts to utilise the IBA. For example, Alhassan and Tanko collected the IBA from Kano Municipal, Nigeria, in order to study general properties. They reported that its specific gravity is in the range of 1.86 - 2.37. There was about 5.07 - 10% of organic materials mixed with. In addition, some silicon and metals were also found. The classification test revealed that it has a well-graded particle distribution. According to the AASHTO soil classification, it was found that it is equivalent to A-3, showing a very good quality for road construction [4].

EA investigated and surveyed the materials left from incinerators in England and Wales during 1996-2000. They found that each year there are approximately 28 million tonnes ashes generated from 11 incinerators. They stated that the ashes can be categorially classified as bottom ash and fly ash. The problem is the latter can easily be blown away in the air. When one takes a breath with such polluted air the ashes might be kept in lungs for good. They also reported that from a total of 23 million tonnes of ashes a total of 2.5 million tonnes are landfilled. Another 2 million tonnes were recycled in the following manners: research and re-burning. [5]

This research attempted to utilise tyre chips (TC) and IBA as low-cost earthquake buffer. It was achieved by first mixing them; and, employed them as earthquake buffer. These mixtures were employed as foundation soil located underneath structures in order to absorb earthquake-induced vibration. This would somewhat reduce the vibration transmitted to superstructures thereby softening the damage. The benefits are that both wastes could be utilised instead of just throwing away. In addition, overall construction would be decreased as the wastes can be obtained with virtually no cost.

2 Test materials

This research was mainly about investingating whether the mixtures of tyre chips and incinerator bottom ash placed as foundation soil could reduce the earthquake shaking transmitted to a superstructure. The foundation soil comprised compound IBA-TC overlying sand layer. During preparing the foundation soil explosive charge was buried to produce underground vibration when ignited. Over the surface two model houses, one- and two- storey, having an accelerometer attached on the roof was installed. All of the materials employed are described in the following sections.

2.1 Sand

Medium river sand, shown in the background of Figure 1 (a), typically found in the South of Thailand was chosen as foundation soil. It was brown, medium sand having the specific gravity of 2.65. The values for D_{10}, D_{30}, and D_{60}, were 0.30, 0.96, and 1.10 mm, respectively. These corresponded to the coefficients of uniformity and gradation of 3.67 and 0.85, respectively, as shown in Figure 3 (a). It was found that the average particle size is 0.96 mm. According to the Unified Soil Classification System (USCS), it was classified as SP, poorly-graded sand.

2.2 Incinerator bottom ash

The incinerator bottom ash was obtained from Phuket Municipal Solid Waste Incineration Plant, located in Phuket Island, Southern Thailand. It was light grey and medium coarse, as shown in Figure 2 (a). Note that ashes obtained from an incineration plant normally consist of particles having a wide range of sizes. In this case, the particles bigger than number 4 sieve were discarded because it would be problematic when mixed with tyre chips. Its size distribution charactieristics are shown in Figure 3 (b). Its specific gravity was 2.62. According to the USCS, it may be classified as SW.

2.3 Tyre chips

The tyre chips used in this study were commercially obtained from a waste management company located in Nakhonpathom, Middle Thailand. It had an average size of 0.54 mm, as shown in Figure 2 (b). Comparing this value to the D_{50} of IBA of 1.10 mm, this means that they may reduce the void ratio of the compound IBA-TC. The sieve analysis result is illustrated by Figure 3 (c). Note that according to ASTM [6], recycled tyres can be classified based on their sizes as granulated, ground rubber, powder, rough shred, tyre chips, and tyre shreds, with respect to smaller to bigger particle size. The specific gravity was found to be 1.02, which was quite smaller than those studied by Edil and Bosscher [7]

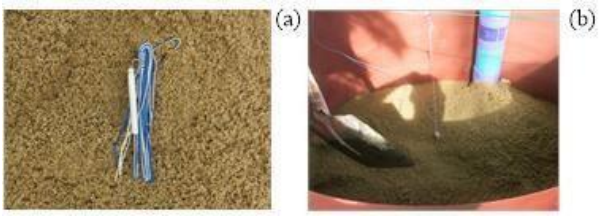

Figure 1. Detonator employed in this study (a) the detonator being installed (b)

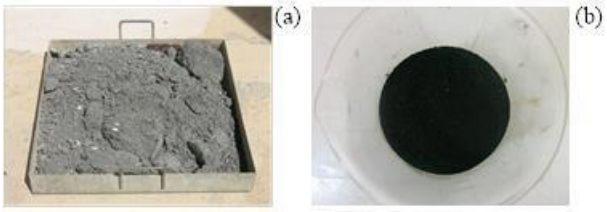

Figure 2. Incinerator bottom ashes (a) tyre chips (b)

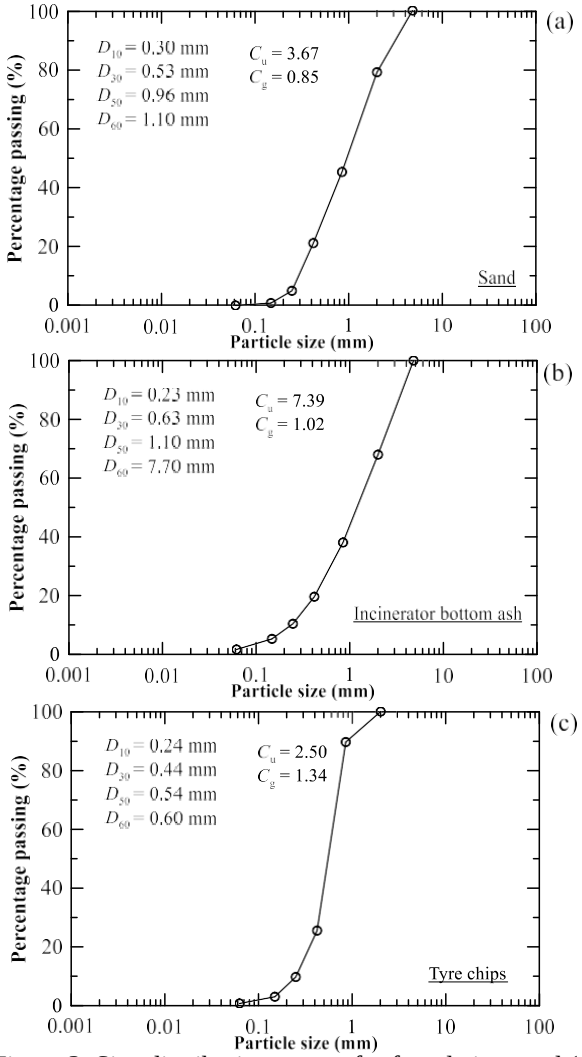

Figure 3. Size distribution curves for foundation sand (a) tyre chips (b) and incinerator bottom ashes

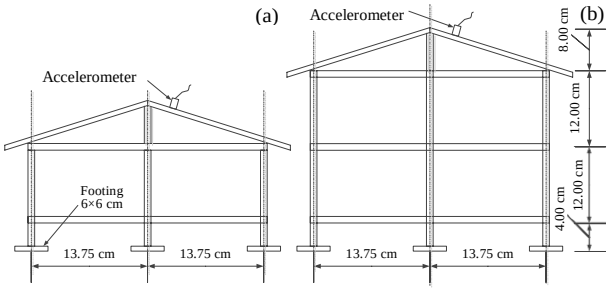

Figure 4. Model houses with accelerometer installed: one-storey house (a) two-storey house (b)

2.4 Explosive

Explosive employed in this study was by means of a detonator having 0.16 g of charge. This was because such small amount of explosive is more than enough for producing simulated earthquake vibration in a steel chamber with 120 cm diameter. Figure 1 displays the denonator being installed (buried) into the sand layer.

2.5 Model houses

A total of two model houses, one- and two-storey, were constructed in order to be placed over the foundation soil. They were entirely made from balsa wood having the dimensions of 27.5 by 27.5 cm, corresponding to 8.25 by 8.25 m by the scale of 1:30. They were constructed to have such structural members that are the same as a real house, comprising footings, pillars, columns, beams, slabs, walls, and roofs, as illustrated by Figuer 4. These were done so in the hope that the model houses constructed could mimic the transmited-vibration behaviour induced in the real house.

3 Study methods and procedures

In this study, the very first step was to construct a sand layer having the thickness of 50 cm, acting as supporting soil. During the construction, however, a detonator having the charge of 0.16 g was also installed within the sand at 10 cm from the bottom. It should be noted that a steel chamber having the diameter and height of 120 and 75 cm, respectively, was employed to house the model foundation soil because it could withstand the explosion.

Then, overlying the sand layer was the 25 cm thick layer of the mixtures between the IBA and the TC. These materials were meant to be investigated their effectiveness in terms of softening the vibration caused by the explosion transmitted to the model houses. The IBA to TC proportions by weight were 100:0, 95:5, 90:10, 75:25, 40:60, and 0:100.

After the foundation soil was completed, both model houses were installed according the test configuration

displayed in Figure 5. Over the roof of the houses an accelerometer was attached in order to measure the explosive-induced vibration transmited from the ground. Another accelerometer was also installed on the ground; but, to directly measure the ground vibration. These arrangements would provide data that could be analysed later on in order to evaluate the effectiveness of the mixtures in terms of reducing the vibration transmitted from the ground to the superstructures. In the other words, by comparing the ground acceleration and the accelerations measured on the roofs, either the decrease or the increase of acceleration could be obtained.

It should be noted that all of the accelerometers were connected to a data acquisition system (DAQ) obtained from National Instruments, comprising the cDAQ-9174 chasis and the NI-9234 module. The DAQ was then connected to a computer that has a monitoring and recording signal software installed.

When the test set-up described above finished, the detonator was ignited using a car battery directly connected to the detonator's wire. This created an instantaneously extreme impact underground thereby producing the vibration that sent stress waves travelling across the ground; Eventually, they were transmitted to the superstructers. In the same time, the accelerometers sensed the vibration, both on the ground and structures. Figure 6 displays the setting up for this experiment, showing all three accelrometers: (1) G1 installed on the ground, (2) G2 installed over the roof of one-storey house, and (3) G2 installed over the roof of two-storey house.

It should be noted herein that the presence of the groundwater near the surface is not unsual in most parts of the world. As such, it was also interesting to observe the ground shaking behaviour when saturated. Therefore, the sand layer was prepared such that it had two states, completely dry and saturated. This resulted in a total of 12 different test configurations, as explained in Table1.

Table 1 List of all test configuration

Number	Fondation material	Sand layer state	Mixture proportion (%)	
			IBA	TC
1	D-A100	Dry	100	0
2	D-A95	Dry	95	5
3	D-A90	Dry	90	10
4	D-A75	Dry	75	25
5	D-A40	Dry	40	60
6	D-A0	Dry	0	100
7	W-A100	Saturated	100	0
8	W-A95	Saturated	95	5
9	W-A90	Saturated	90	10
10	W-A75	Saturated	75	25
11	W-A40	Saturated	40	60
12	W-A0	Saturated	0	100

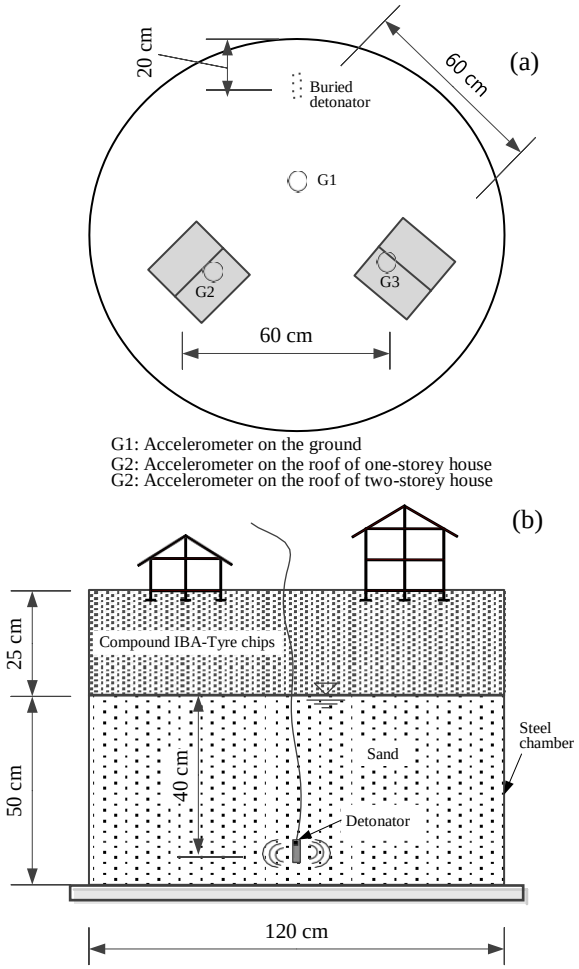

Figure 5. Test set-up and measurement arrangement: top view (a) sectional view (b)

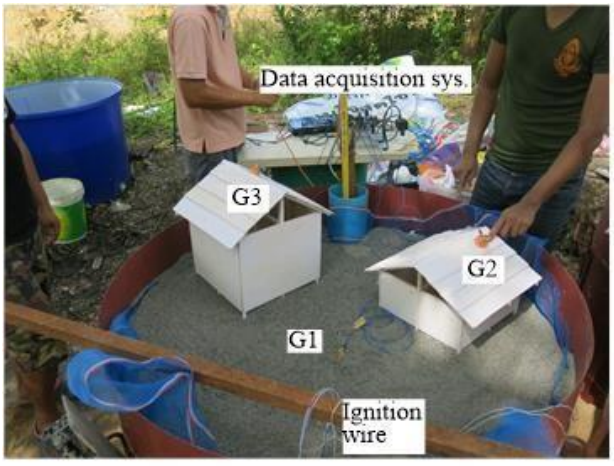

Figure 6. Accelerometers being installed and connected to the data acquisition system

Table 2 Maximum accelerations for the dry conditions

Fondation material	Max. measured acceleration (g)			Percentage diff. with respect to G1	
	G1	G2	G3	G2	G3
D-A100	2.18	0.52	0.76	-76	-65
D-A95	2.86	0.57	0.84	-80	-71
D-A90	2.98	0.55	1.09	-82	-63
D-A75	5.03	0.81	1.26	-84	-75
D-A40	3.50	0.86	1.55	-76	-56
D-A0	4.99	0.84	1.15	-83	-77
			Average	-80	-68

Table 3 Maximum accelerations for the wet conditions

Fondation material	Max. measured acceleration (g)			Percentage diff. with respect to G1	
	G1	G2	G3	G2	G3
W-A100	50.3	6.73	7.31	-87	-85
W-A95	50.3	3.76	4.30	-93	-91
W-A90	22.3	2.29	2.60	-90	-88
W-A75	29.1	2.05	2.71	-93	-91
W-A40	34.8	2.89	3.07	-92	-91
W-A0	17.7	2.24	2.07	-87	-88
			Average	-90	-89

4 Results and discussion

The results obtained from this study were chiefly maximum acccelerations measured on the ground and over the roofs of both model houses, designated as G1, G2, and G3, with respect to the valuess on the ground and over the roofs of one- and two- storey houses, respectively. The testing results for the dry sand were summarised and shown in Table 2; while Table 3 displays the results for the saturated sand. Also shown in both tables are the percentage differences of the accelerations for G2 and G3, with respect to G1. Examples of acceleration versus time for the dry sand are illustrated by Figure 7; while Figure 8 displays some measured accelerations obtained from the saturated sand. Overall, it was found that the accelerations obtained from the saturated sand are much greater than those obtained from the dry sand. This may be because the pore water acted as the blockage of travelling stress waves thereby increasing the ground vibration. In case of the dry sand, however, the stress waves probably were more freely to travel and radiate within the foundation soil.

Considering the accelerations obtained from G1, it was observed that for the dry sand the maximum acceleration is gradually increased with the increase of TC from 0 to 25%. After that it slightly decreased when the TC was 60%; and, increased again when the TC was 100%. This is quite contrary to the case of saturated sand: the maximum acceleration was progressively decreased with the increase of TC.

The difference between the maximum measured accelerations obtained from the dry- and saturated sands can be clearly seen when considering Figures 7 and 8, corresponding to the mixtures D-A75 and W-A75, respectively. Note that both mixtures had the IBA and TC of 75% and 25%, respectively. In case of the ground acceleration (G1), it was found that the maximum acceleration for W-A75 is almost 29.1 g; while it was only just 5.03 g for D-A75. This clearly confirms that the presence of pore water in the sand layer caused the dramatic increase of ground vibration.

When considering the acceleration induced on both model houses, however, the maximum accelerations obtained from G2s with respect to D-A75 and W-A75 were approximatley 0.81 g and 2.05 g. Comparing these values to their corresponding G1s, it was observed that the transmitted accelerations for D-A75 and W-A75 are 84% and 93% lower. This demonstrates that when the sand saturated, even though the ground acceleration is much greater than that of the dry sand, the vibration transmitted to the house is much lower compared to the ground acceleration.

Figures 9 and 10 display the maximum measured accelerations versus tyre chip contents with respect to the sand layer being dry and saturated, respectively. To be able to analyse the effects of the compound IBA-TC on the acceleration transmitted to the superstructures, the percentage differences of maximum measured accelerations of G2 and G3 with respect to G1 for both sands were plotted and shown in Figure 11.

It revealed that the behaviours of both G2 and G3 for the dry sand is quite different to those for the saturated sand. For instance, the maximum measured acceleration induced on the houses was gradually increased with the increase of tyre chip contents, as seen in Figure 9. In addition, it was maximum when the mixture having the TC of 60%. Contrary to the dry sand, the accelerations obtained from G2 and G3 for the saturated sand was gradually decreased with the increase of TC from 0 up to 25%. When the TC was greater, however, the accelerations were virtually constant, as illustrated by Figure 10.

Another point should be noted is that the difference of accelerations between G2 and G3 for the dry sand is quite greater than that for the saturated sand. These findings strengthen the idea that the presence of pore water in the sand layer could: (1) amplify the ground acceleration and (2) soften the acceleration transmitted to the superstructure, as can be clearly seen in Figure 11.

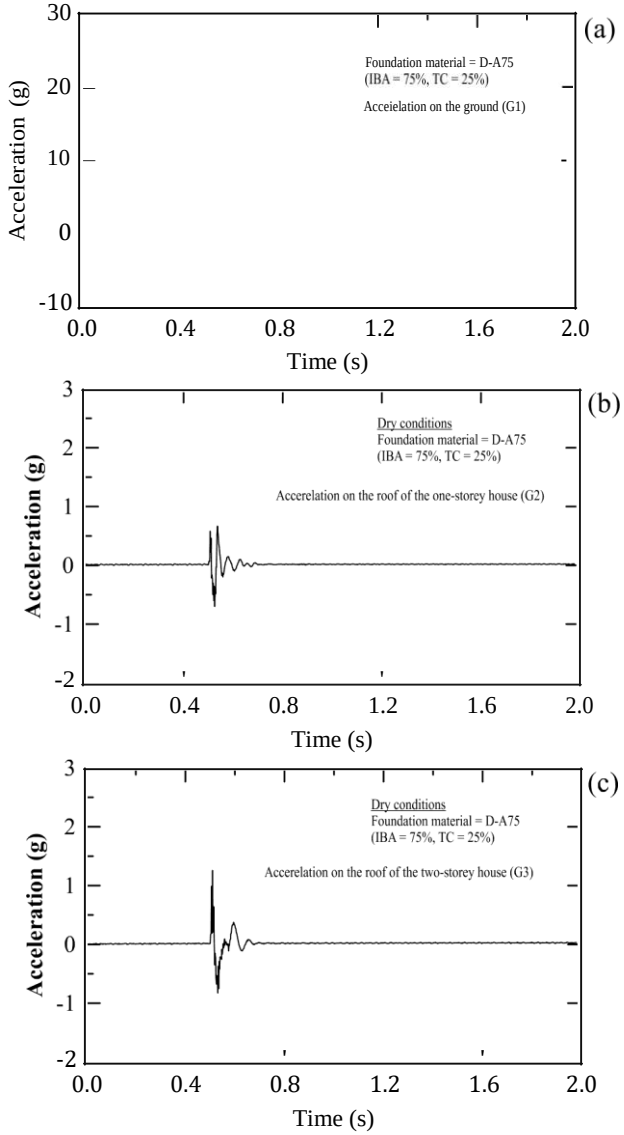

Figure 7. Acceleration signals for dry conditions: G1 (a) G2 (b) and G3 (c)

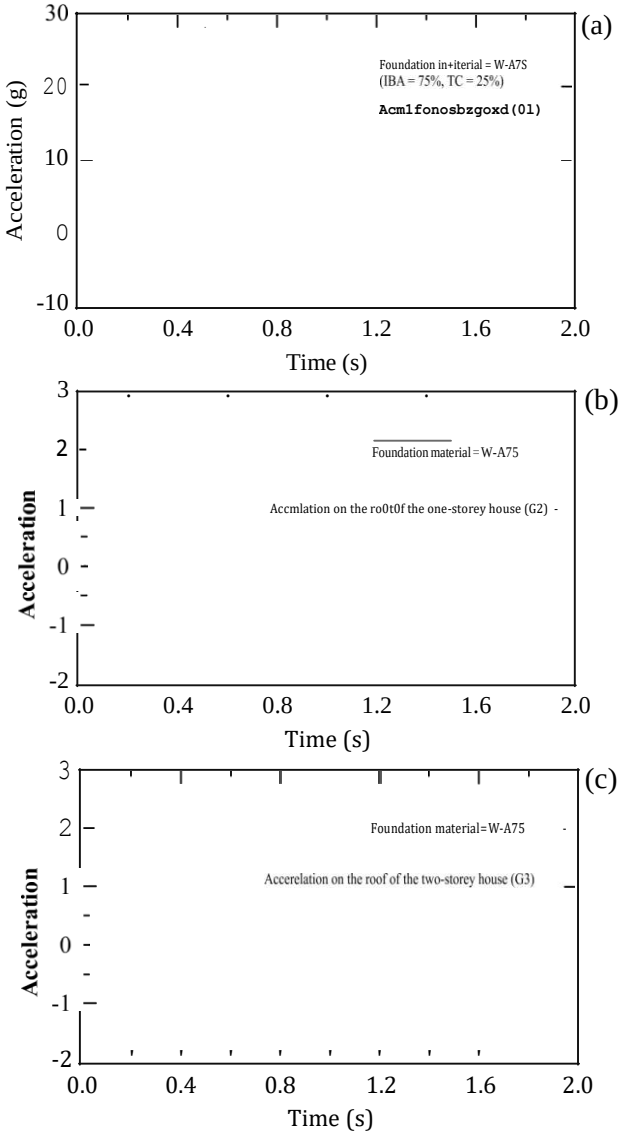

Figure 8. Acceleration signals for wet conditions: G1 (a) G2 (b) and G3 (c)

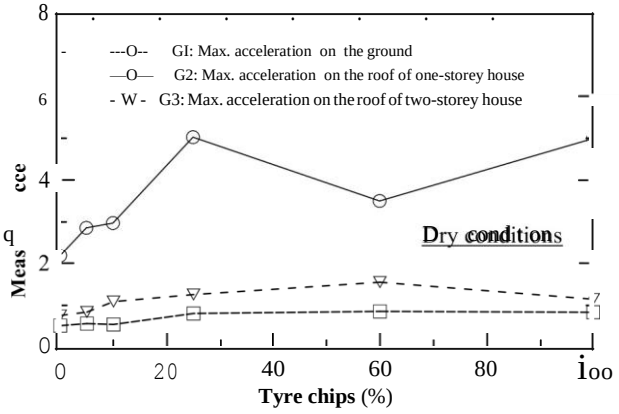

Figure 9. Maximum measured accelerations versus percentage tyre chips for the dry conditions

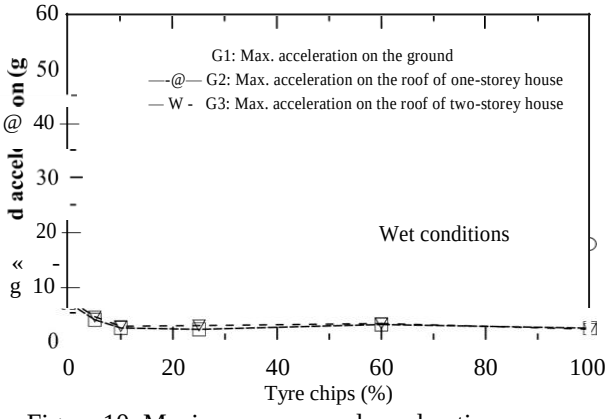

Figure 10. Maximum measured accelerations versus percentage tyre chips for the wet conditions

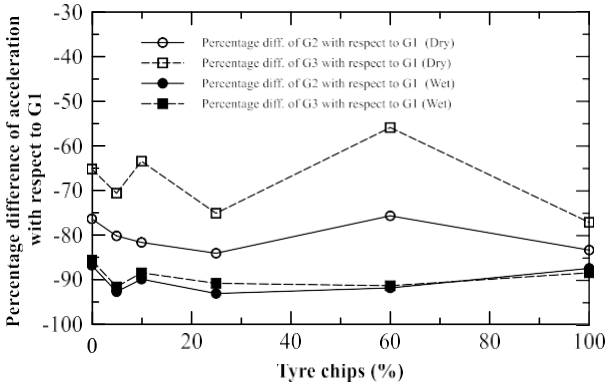

Figure 11. Percentage differences of max. accelerations of G2 and G3 with respect to G1

5 Conclusions

In this study, incinerator bottom ash were mixed with recycled tyre chips in order to be employed as foundation soil. The main purpose was to investigate their effectiveness in terms of reducing the vibration transmitted from the ground to superstructures. It was achieved by first construction a 50 cm thick sand layer in a steel chamber having the diameter of 120 cm. During the sand layer construction an explosive detonator was installed at 10 cm from the bottom. Then, the compound IBA-TC having varied mixes was placed over the sand. The ratios of IBA to TC were 100:0, 95:5, 90:10, 75:25, 40:60, and 0:100, by weight.

After the completion of the foundation material construction two model houses, one- and two-storey, were placed over the ground. A total of three accelerometers were then installed: one on the ground and the other two over the roof of the two houses. This set-up was followed by the immediate ignition of the explosive already installed thereby generating the vibration under the ground. Eventally, the ground vibration was transmitted to the model houses. In the mean time the accelerations on the ground as well as on the roofs were monitored and recorded for further analysis. It shoud be emphasised that the sand layer was prepared to be two states, dry and saturated. This was intended for investigating the effects of the presence of pore water in the sand layer on the transmission of acceleration from the ground to superstructures. Based on the experiment conducted, the following conclusions have been drawn:

(1) Overall, the ground vibration in the case of dry sand is progressively increased with the gradual increase of TC from 0 to 25%; then, it decreases when the TC is 60%. It increases again when the mixture has no IBA.

(2) For the saturated sand, the ground vibration dramatically decreases when the TC is 10%; then, it gradually increases when the TC contents are from 25 to 60%. However, the ground vibration is dramatically decreased again when the mixture has no IBA.

(3) In the case of dry sand, the vibrations measured on the two-storey house are quite greater than those occurred on the one-storey house. This is not the case for the saturated sand because the accelerations for the both houses are virtually similar.

(4) From the findings, it may be concluded that in the case of water table is near the ground surface employing compound IBA-TC as foundation soil could reduce the vibration transmitted to superstructures. This could benefit many ways. For example, both IBA and TC, regarded as waste, could be used as construction material thereby reducing overall construction cost somewhat as well as preserve the environment.

6 Acknowledgement

The authors wish to thank Rajamangala University of Technology Srivijaya, Thailand, for financial aid as well as support throughout this study. In addition, we are sincerely appreciative for the help and support obtained from Faculty of Engineering and Research and Development Institute, RMUTSV.

References

[1] Elnashai, A. S., and Sarno. L. D. *Fundamentals of earthquake engineering*, John Wiley & Sons, West Sussex, 2008.

[2] Khalid, H. A., and Artamendi, I. Mechanical properties of used tyre rubber, Engineering Sustainability, *Proceedings of the Institution of Civil Engineers*, Vol. 157, Issue 1, 37-43, 2004.

[3] Boonpan, S., Promputthangkoon, P., Anusiri, M., and Choosilp, N. The Utilisation of Incineration Bottom Ash as Construction Material for Roadways, *Preceedings of the 19th National Convention on Civil Engineering*, Khonkaen, Thailand, 1758-1763, 2014. (in Thai)

[4] Alhassan, H. M., and Tanko, A.M. Characterization of Solid Waste Incinerator Bottom Ash and the Potential for its Use, *International J. of Engineering Research and Application*, 2(4): 516-522, 2012.

[5] EA. *Solid residues from municipal waste incinerators in England and Wales*, Environmental Agency, UK, 2002.

[6] ASTM. Standard practice for use of scrap tires in civil engineering, *American Society for Testing and Materials*, ASTM D6270-98, 1998.

[7] Edil, T. B., and Bosscher, P. J. Engineering properties of tire chips and soil mixtures, *Geotechnical Testing Jounal*, ASTM, 17(4): 453-464, 1994.

Site Response at a Location Affected by Soil Softening and Liquefaction during the 2011 Tōhoku Earthquake

M. Davi[a], L. Kingdom[b] and M. Redaelli[c]

[a] State & Local Governments Sector, CH2M, United Kingdom
[b] Golder Associates, United Kingdom
[c] State & Local Governments Sector, CH2M and School of Earth & Environment, University of Leeds, United Kingdom
E-mail: Manuela.Davi@ch2m.com, LKingdom@golder.com, Marco.Redaelli@ch2m.com

Abstract –

Although the influence of liquefaction on seismic shaking at ground surface has been identified more than a decade ago, the number of quantitative studies on the induced changes in spectral acceleration is still limited. Japan's KiK-net offers abundant data that can be used to study this influence, as its stations are equipped not only with seismometers at ground surface but also with instruments installed down a borehole drilled in the bedrock. This paper focuses on one of the KiK-net stations which experienced liquefaction during the 2011 Tōhoku earthquake. Spectral accelerations were calculated by propagating the shaking at bedrock level through the softer shallow layers with a linear-equivalent analysis that neglects the influence of liquefaction. By comparing this prediction with the spectral acceleration actually recorded at ground surface the effect of liquefaction on ground shaking at the surface is quantified. In summary, liquefaction reduces the spectral accelerations for periods shorter than 0.5s. For periods longer than 0.5s the spectral accelerations are amplified, particularly up to 1.3s.

Keywords –

Seismic site response; Liquefaction; Cyclic softening; Spectral acceleration; Tohoku earthquake

1 Introduction

1.1 Background

The influence of cyclic softening and soil liquefaction on spectral acceleration has been clearly acknowledged more than a decade ago [1], [2]. To date, however, the number of available case histories is still limited and very little guidance on how to incorporate these effects in design is available in the current building codes. Therefore, the analysis of well-documented cases is of great interest.

This paper investigates the site response at the Iwase station (IBHRH11), which is part of the Japanese strong-motion seismometer network known as KiK-net (Kiban Kyoshin network), consisting of pairs of strong-motion sensors installed in a borehole and at ground surface [3]. Evidence of liquefaction at this site during the 2011 Tohoku earthquake is presented by Cox and co-workers [4]; geotechnical and geophysical information are available from NIED (Japan's National Research Institute for Earth Science and Disaster Resilience).

In order to quantify the effect of soil softening and liquefaction triggered by the Tōhoku earthquake of 11 March 2011 (M_w = 9.0), the ground shaking recorded at ground surface is compared with the ground shaking calculated through a linear-equivalent site response analysis based on the unsoftened and unliquefied soil properties. In this site response analysis, the horizontal components of the acceleration time history recorded in the bedrock propagated through the 1D column of weathered rock and sediments using the software EERA (Equivalent linear Earthquake site Response Analyses) [5].

The comparison of the observed and predicted ground motion at surface suggests that the liquefaction induced a reduction of the peak ground acceleration. For periods T < 0.5s the effect of liquefaction is to reduce the spectral acceleration compared the values that would be calculated with a linear-equivalent site response analysis. However, for periods 0.5s < T < 1.3s the effect of liquefaction is to amplify the spectral acceleration compared to predictions. By performing site response analysis of selected time windows the liquefaction initiation time is estimated.

1.2 Previous studies

Several authors have investigated the influence of cyclic softening and nonlinear soil behavior on local ground response during earthquakes. Trifunac and co-workers studied the effect of soil softening on peak accelerations and induced damage during the 1994 earthquake in Northridge, California (USA) [6]. In particular, they noticed reduction of peak acceleration on softening affected sites, compared with stiffer sites. Moreover, they noted a shift of Fourier spectra peaks toward longer periods.

Yang & Satoh [1] used records from downhole array to identify soil liquefaction. Youd & Carter [2] developed a comprehensive study of five sites and, in addition to the effects observes by Trifunac and his colleagues, they were able to detect the influence of the time of liquefaction onset. In summary, they demonstrated that where softening occurs early in the strong ground motion the main effect is reduction of spectral accelerations at short periods (indicatively $T <$ 1s); where the softening occurs late in the sequence this reduction is small or negligible. In both cases there is potential for spectral acceleration at longer periods (indicatively $T >$ 1s).

Kramer and his colleagues proposed a method to predict site response in liquefiable deposits [7]. Bonilla provided a review of site response across KiK-net and K-net, which is another NIED network (with surface seismometers only), in the aftermath of the 2011 Tōhoku earthquake [8].

Satoh and his coauthors carried out a detailed study of soil nonlinearity at the Iwase station IBRH11 [9]. More precisely they inverted the structure from the seismic bedrock to the surface in the linear regime was inverted from (i) array records of microtremors using Rayleigh-wave inversion, (ii) surface-to-borehole spectral ratios of weak motions using S-wave inversion based on the 1D wave propagation theory, and (iii) horizontal-to-vertical spectral ratios of weak motions using the inversion based on the diffuse-field theory for plane waves. Their work identified a strong impedance contrast at 30m depth as the main cause for the large ground motions observed in 2011. In addition they demonstrated the key role of nonlinearity of the shallow layers behavior in reducing the peak accelerations at ground level.

This study contributes to the expansion of the results about the influence of liquefaction and cyclic softening on ground motion by applying the technique developed by Youd & Carter [2] to the response at the Iwase station IBRH11 during the Tōhoku earthquake. In doings so it adds new considerations to the extensive work of Satho and co-workers [9].

2 Factual evidence

2.1 KiK-net

The Kiban Kyoshin network, often shortened in KiK-net, is an interconnected system of strong motion instruments managed by the Japanese National Research Institute for Earth Science and Disaster Prevention (NIED).

The network comprises almost 700 sites across Japan and, at each station, instruments have been installed both at the ground surface and down a borehole in the bedrock. The depth of the instruments down the borehole varies from station to station depending on local topography and geological conditions; however most deep sensors are located past 100m below ground level to avoid surface noise [3].

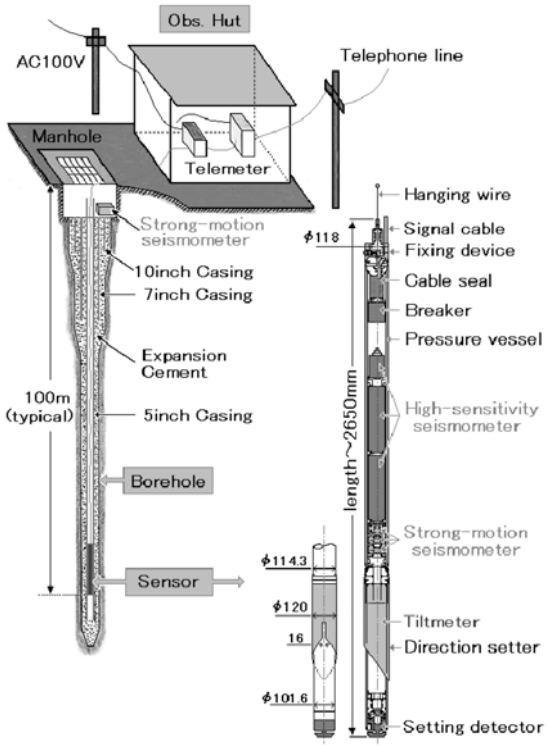

Figure 1. Typical configuration of a KiK-net station [3].

The typical arrangement of an observation station is shown Figure 1. A strong motion seismometer, measuring three components of acceleration, is located at ground surface (generally in a protected location in a manhole). A composite sensor is located down the borehole; its key components being another strong-motion seismometer and a high sensitivity seismometer. The observed strong-motion data are widely available to the public through the internet from a

dedicated web site (http://www.kyoshin.bosai.go.jp). The data provided by NIED include three components of acceleration time histories recorded at depth (UD1, NS1, EW1) and three components recorded at ground surface (UD2, NS2, EW2). The geological and geophysical data derived from the boreholes at KiK-net stations are also available.

2.2 The 2011 Tōhoku earthquake

On March 11th 2011, at 14:46 local time, which is 5:46 Coordinated Universal Time (UTC), a fault rupture in the zone where the Pacific Plate is subducting under the Okhotsk Plate resulted in an earthquake of moment magnitude Mw = 9.0. The epicenter was located off the coast of Japan, approximately 70km east of the Oshika Peninsula, in the Tōhoku region. The hypocenter was estimated at approximately 30km below the seafloor.

Very high surface peak ground accelerations (PGA) were recorded across Japan, with the maximum recorded value being 2.7*g* in the Miyagi Prefecture (Figure 2).

2.3 Iwase Station IBRH11

The KiKnet station IBRH11 in Iwase, Sakuragawa city, Ibaraki prefecture, has a distance of 310 km from the Tohoku earthquake hypocenter. It experienced, during the main event, large horizontal peak ground accelerations (PGAs) and peak ground velocities (PGVs), exceeding 800 cm/s2 and nearly 60 cm/s, respectively.

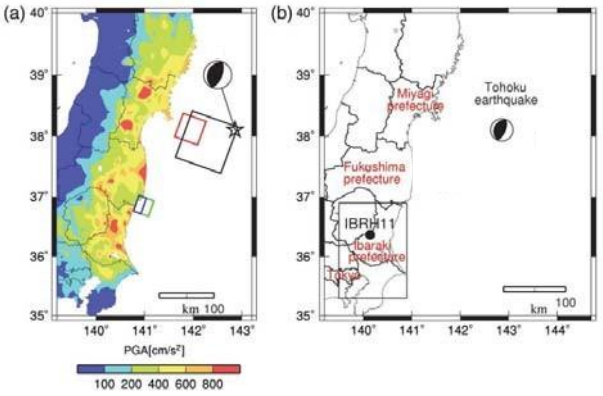

Figure 2. (a) PGA, epicenter and centroid moment tensor for the 11th March 2011 Tōhoku earthquake; (b) location of the IBRH11 KiK-net station (modified after [9]).

The site was affected by liquefaction, as confirmed by Cox and coauthors [4]. The availability of acceleration time histories recorded in the bedrock, at 103m depth, as well as at ground surface, make it an ideal location to investigate the effect of soil liquefaction and softening on the site response.

The borehole log available for IBRH11 shows deposits and residual soils from rock weathering approximately for the first 30m below ground surface. At greater depth fresher rocks, for the Tertiary or older periods, is encountered. A simplified soil column is presented in Figure 3; the ground profile is summarized in Table 1

Table 1 Ground profile at IBRH11

Layer	From (mBGL)	Thickness (m)
Surface soil I	0.0	2.5
Surface soil II	2.5	5.0
Weathered Granit	7.5	2.5
Gravel	10.0	6.0
Gravelly Clay	16.0	4.0
Weathered Granit	20.0	10.0
Granit	30.0	2.0
Sandstone	32.0	38.0
Granit	70.0	26.3
Sandstone/Shale	96.3	> 6.7

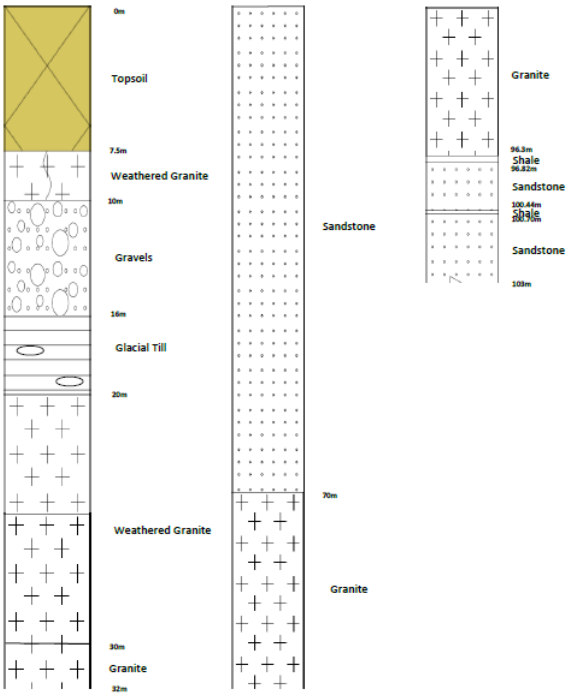

Figure 3. Ground profile at the Iwase station IBRH11.

3 Method of investigation

In order to assess the impact of liquefaction and soil softening on local ground response, the strong motion

ground shaking recorded at station IBRH11 was analyzed. In particular, the records from the deeper instruments, beneath the liquefiable layers, were used to predict the ground motion at surface that would have occurred in absence of liquefaction and soil softening. This prediction was then compared with the actual ground motion recorded by the shallower instruments at ground surface, in presence of liquefaction. The differences between prediction (without liquefaction) and observation (with liquefaction) is used here to discuss the influence of liquefaction and soil softening on ground motion, with a special focus on spectral acceleration.

After minimal pre-processing of the acceleration time-histories at depth, the predicted time-histories at ground surface in absence of liquefaction were calculated through a linear-equivalent site response analysis with the software EERA [5].

Both the observed and predicted time histories at ground surface were translated into response spectra to facilitate the comparison of ground motions, with and without impact of liquefaction, in the frequency domain.

The computer program SeismoSignal [10] was used to pre-process the time histories at depth and to translate the time histories at surface into response spectra.

4 Site Response Analysis

Besides the geological classification discussed in Section 2, seismic waves velocity form suspension logging in the borehole are available for the layers encounters at the Iwase station. Average values for each layer are reported in Table 2.

Table 2 Seismic waves velocity at IBRH11

Layer	From (mBGL)	V_s (m/s)	V_p (m/s)
Surface soil I	0.0	130	500
Surface soil II	2.5	180	500
Weathered Granit	7.5	180	500
Gravel	10.0	240	1500
Gravelly Clay	16.0	240	1500
Weathered Granit	20.0	450	2000
Tertiary or older bedrock	30.0	2100	4700

Considering the geological description of the fresher rock below 30m depth and, more importantly, the shear wave velocity in these layers, it can be concluded that the subsoil between 103m depth (seismometer location) and 30m depth (base of softer layers) is entirely constituted of competent bedrock. Therefore the seismic shaking is not expected to change significantly when propagating across these layers due to absence of sharp contrasts in mechanical properties, in particular small-strain stiffness. For this reason, the site response analysis was conducted applying the time histories recorded at 103m depth to the sequence of layers comprised between 30m depth and ground surface.

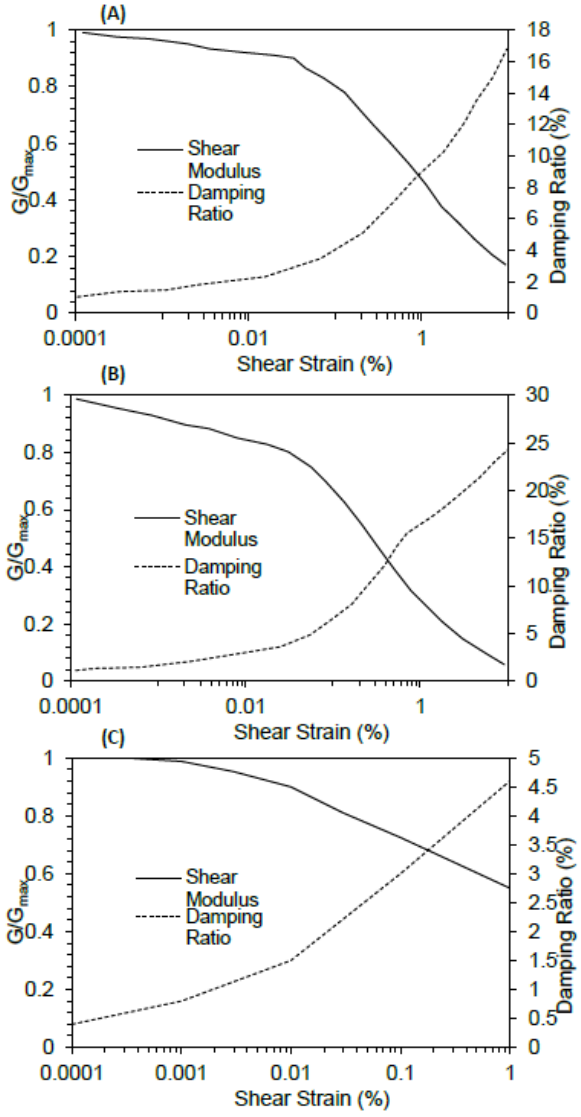

Figure 4. Stiffness degradation and damping curves adopted in the linear-equivalent site response analysis.

The idealized soil column shown in Figure 5 was used in the site linear equivalent response analysis with EERA. The adopted shear modulus degradation curves and damping ratio curves are shown in Figure 4. Curves (A) and (B) are based on the empirical relations for soils by Yasuda and Yamaguchi [11]; curves (C) for soft rock are based on the work by Bardet and coworkers [5]. The degradation and damping curves selection is summarized in Table 3, which also lists the estimated

density of the materials.

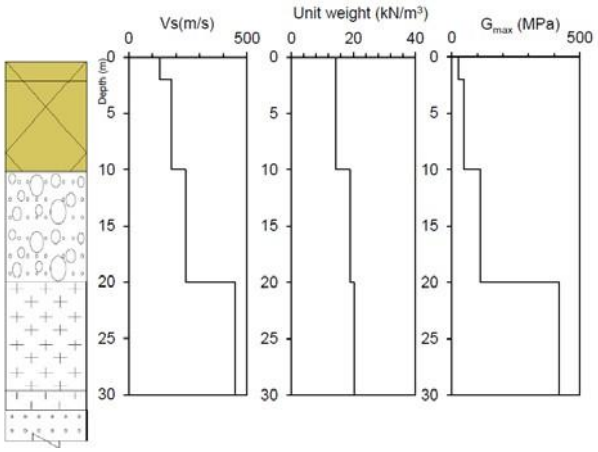

Figure 5. Ground model used in the site response analysis.

Table 3 Density and degradation curves

Layer	ρ (g/cm³)	Curves type
1-Surface soil I	1.45	A
2-Surface soil II	1.47	A
3-Weathered Granit	1.50	C
4-Gravel	1.95	B
5-Gravelly Clay	1.90	B
6-Weathered Granit	2.07	C

5 Results

5.1 Time histories

The comparison between actual acceleration time history form recording at ground surface and predicted time history is shown in Figure 6. It should be noted that the plotted record includes also some pre-shaking data and the shear waves velocity arrival can be recognized at approximately t = 40s in this reference system.

The actual PGA is reached about 75s after shaking imitation, for both NS and EW component, and it amounts to 0.83g and 0.84g, respectively. The predicted PGA is obtained slightly later, by approximately 3s and is significantly higher: 1.24g for NS component and 0.93g for EW. Therefore, a conventional liner-equivalent analysis, overestimates the PGA by 49% and 11% respectively. Figure 7 focuses on a smaller time window, which still contains all the largest amplitudes, between 70s and 90s from initiation (110s < *t* < 130s in the pictured reference system), to enable a better visual comparison of the results. It is interesting to observe that, in the time domain, the predicted accelerations exceed in amplitude the actual observations only between approximately 73s and 85s from initiation (113s < *t* < 125s in the pictured reference system). The opposite is true for the rest of the signal, before and after this time interval.

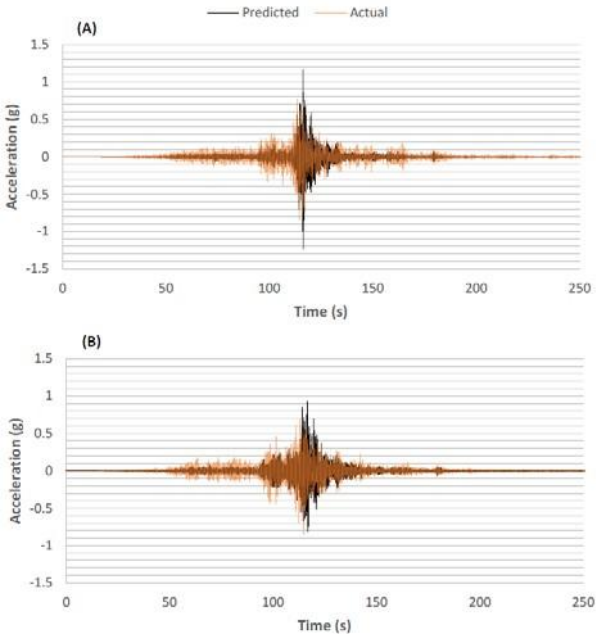

Figure 6. NS (A) and EW (B) ground motion at surface – comparison between predicted and actual acceleration time histories.

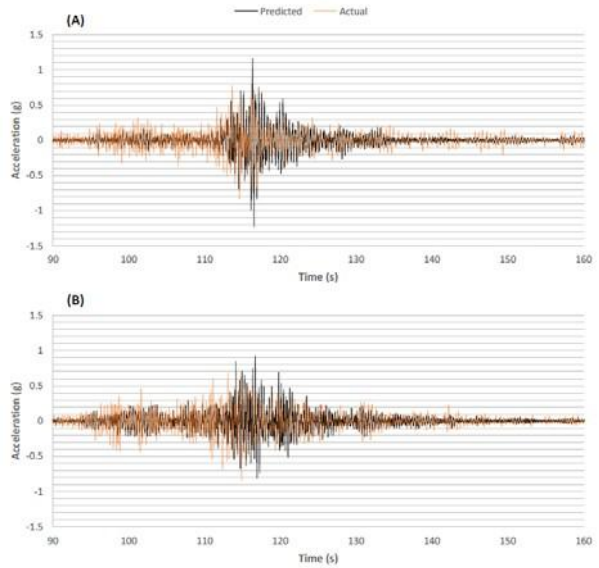

Figure 7. NS (A) and EW (B) ground motion at surface – comparison between predicted and actual acceleration time histories over a reduced time window.

5.2 Response spectra

The predicted and actual response spectra with 5% damping are shown in Figure 8. For the NS component, the spectral acceleration S_a has a single peak, in excess of 5g, at a period of T = 0.4s, The actual spectral acceleration, instead, has two much smaller peaks that could be reasonably enveloped by a plateau with S_a = 0.29g between 0.25 and 0.65s.

For the EW component, the spectral acceleration S_a has a single peak, in excess of 5g, at a period of T = 0.4s, The actual spectral acceleration, instead, has two much smaller peaks that could be reasonably enveloped by a plateau with S_a = 0.29g between 0.25 and 0.65s.

For both components, for periods larger than 0.5s the actual spectral acceleration is larger than the prediction. This difference remains detectable for periods up to 1.3s, after which it becomes small and almost negligible. The underestimation of actual spectral acceleration by the prediction is at its maximum around T = 0.6s. For this period, in fact, the prediction is about 1.4g lower in the NS direction (1.5g from site response analysis vs. 2.9g observed), and 2.1g lower in the EW direction (0.7g calculated vs. 2.8g observed).

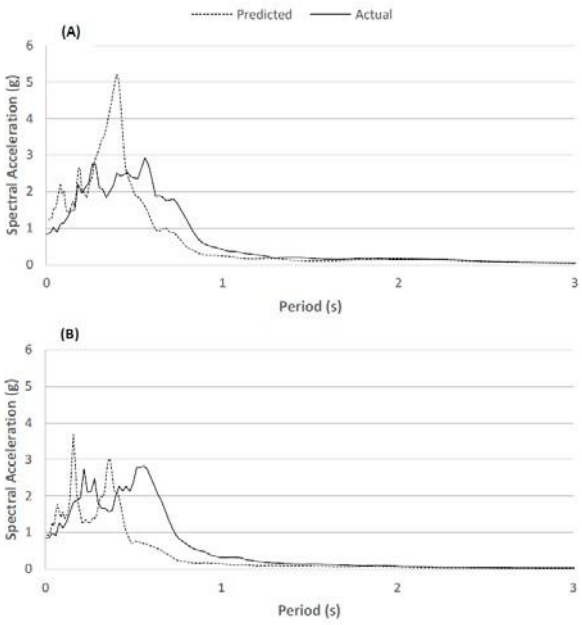

Figure 8. NS (A) and EW (B) ground motion at surface – comparison between predicted and actual response spectra with 5% damping.

5.3 Time windows

In order to explore the timing of different phenomena and check when short-period motions were attenuated and when long-period motions amplified response spectra were compared for three different time windows:

- the first 70.0s after initiation, which is before the most intense shaking took place;
- the first 76.6s, which includes the time histories up to peak acceleration;
- the first 90.0s, which includes the entire portion of time histories with the most intense shaking.

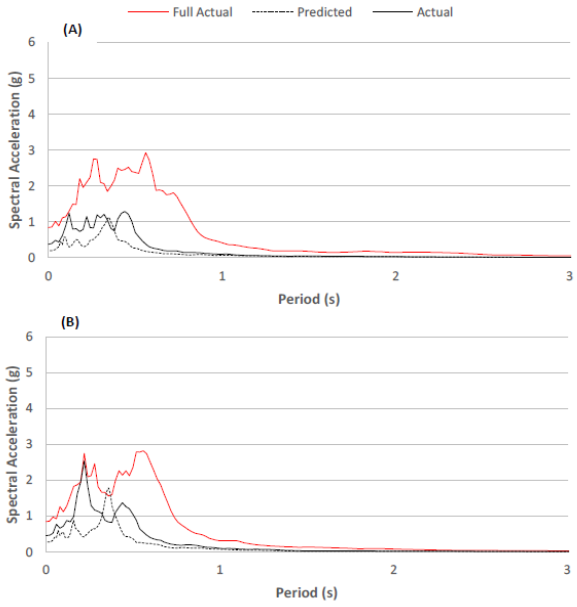

Figure 9. NS (A) and EW (B) spectral acceleration – predicted and actual response spectra for the first 70.0s of ground shaking.

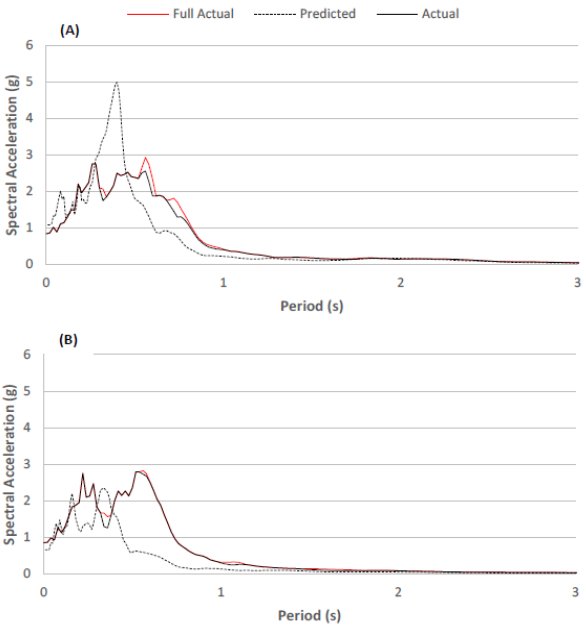

Figure 10. NS (A) and EW (B) spectral acceleration – predicted and actual response spectra for the first 76.6s of ground shaking.

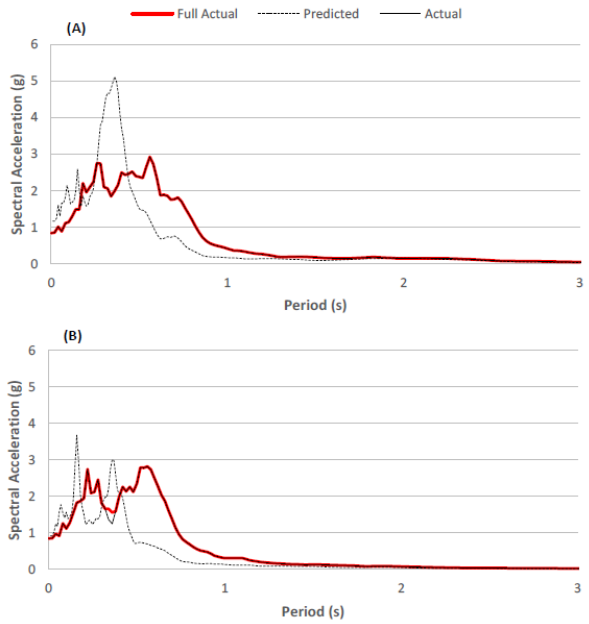

Figure 11. NS (A) and EW (B) spectral acceleration – predicted and actual response spectra for the first 90.0s of ground shaking.

In the first time window the prediction returns lower spectral accelerations than the actual records for periods up to 0.3s. As softening and liquefaction are known to reduce spectral acceleration at short periods, it seems unlikely that these processes developed during the first 70s of ground motion.

In the second time window a marked reduction of S_a for periods between 0.3 and 0.5s can be observed for the NS component (prediction far exceeds the observed values). The EW component does not exhibit such a marked reduction. However, the actual spectrum shows a clear shift of the two peaks toward longer periods, which is also a typical feature of liquefied sites. In summary, there are indications that soil softening and liquefaction took place between 70 and 77s of ground motion.

Finally, in the third time window, the window-specific spectra, both predicted and actual, essentially coincide with the full spectra. This implies that the signal composition in the frequency domain does not change significantly after 90s of shaking.

6 Conclusions

This paper discusses the influence of soil softening and liquefaction on ground motion at the KiK-net Iwase station IBRH11 during the 2011 Tōhoku earthquake.

To obtain a hypothetical ground motion in absence of liquefaction, spectral accelerations were calculated by propagating the shaking at bedrock level through the softer shallow layers with a linear-equivalent analysis. By comparing this prediction with the spectral acceleration actually recorded at ground surface the effect of liquefaction on ground shaking at the surface is quantified.

It was found that liquefaction reduces the spectral accelerations for periods shorter than 0.5s. In particular the conventional linear-equivalent analysis produced a peak, in proximity of 0.4s that greatly overestimates the actual response of the liquefied site (approximately 70% overestimate of S_a for the NS component).

For periods longer than 0.5s the actual spectral accelerations are larger than the prediction in absence of liquefaction and softening. In particular, for periods near to 0.6s this difference is at its maximum, with the linear-equivalent analysis retuning a spectral acceleration that is only in the range of 25% of the observed one for the EW component and in the range of 50% for the NS component.

The difference between prediction and observation becomes small for periods beyond 1.3s. Therefore, in this specific case, soil softening and liquefaction have little influence on periods longer than 1.3s and there is no evidence of large-amplitude/low-frequency oscillations observed in many other sites which experienced liquefaction [2].

The analysis of different time windows indicates that soil softening and liquefaction begins to show its influence approximately 70s after the imitation of ground motion.

References

[1] Yang, J. and Sato, T. Identification of soil liquefaction using downhole array records. In *Proceedings of the 12th World Conference on Earthquake Engineering*, Auckland, New Zealand, 2000.

[2] Youd, T. L. and Carter, B. L. Influence of soil softening and liquefaction on spectral acceleration. *Journal of Geotechnical and Geoenvironmental Engineering*, ASCE, 131: 811-825, 2005.

[3] NIED, Strong-motion Seismograph Networks (K-net, KiK-net) On-line: http://www.kyoshin.bosai.go.jp/

[4] Cox B.R., Boulanger R.W., Tokimatsu K., Wood C.M., Abe A., Ashford S., Donahue J., Ishihara K., Kayen R., Katsumata K., Kishida T., Kokusho T., Mason H.B., Moss R., Stewart J.P., Tohyama K. and Zekkos D.. Liquefaction at strong motion stations and in Urayasu City during the 2011 Tohoku-Oki earthquake. *Earthquake Spectra,* 29: S55-S80, 2013

[5] Bardet J. P., Ichii K. And Lin C. H. *EERA A Computer Program for Equivalent-linear*

Earthquake site Response Analyses of Layered Soil Deposits. Department of Civil Engineering, University of Southern California, Los Angeles, USA.

[6] Trifunac M.D. and Todorovska M.I. Nonlinear soil response - 1994 Northridge, California, earthquake, *J. Geotech. Engrg*, ASCE, 122 (9): 725-735.

[7] Kramer S.L., Hartvigsen A.J., Sideras S.S. and Ozener P.T. Site response modelling in liquefiable soil deposits. In *Proceedings of the Fourth IASPEI/IAEE International Symposium on the Effects of Surface Geology on Seismic Motion*, University of California, Santa Barbara, USA, 2011.

[8] Bonilla F.K. Preliminary analysis of site response K-NET and KiK-net records from the Mw 9 Tohoku earthquake. *Earth, Planets and Space*, 63: 785-789.

[9] Satoh T., Hayakawa T., Oshima M., Kawase H., Matsushima S., Nagashima, F. and Tobita K. Site effects on large ground motions at KiK-net Iwase station IBRH11 during the 2011 Tohoku Earthquake. *Bulletin of the Seismological Society of America*, 104: 653-668, 2014.

[10] SeismoSignal, computer program by Sesismosoft, Pavia, Italy, 2014.

[11] Yasuda, S., and I. Yamaguchi (1985). Dynamic soil properties of undisturbed samples In *Proc. of the 20th Annual Convention of Japanese Society of Soil Mechanics and Foundation Engineering*, Nagoya, Japan, 10–13 June 1985, 539–542 (in Japanese).

Large-scale field tests on blast-induced liquefaction in saturated sand site

Y.M. Chen[a,b], H.L. Liu[a,b,c], W.G. Wang[d] and W.W. Li[a,b]

[a]Institute of Engineering Safety and Disaster Prevention, Hohai University, Nanjing, 210098, China
[b]Key Laboratory of Geomechanics and Embankments Dam Engineering, Hohai University, Nanjing 210098, China
[c]Key Laboratory of New Technology for Construction of Cities in Mountain Area, Chongqing University, Chongqing 400045, China
[d]Ningbo Traffic Construction Project Testing and Inspection Center Co., Ltd, Ningbo 315124, China
E-mail: ymch@hhu.edu.cn, hliuhhu@163.com, 2008hmily@163.com, lwwgeo@hotmail.com

Abstract –

Vibration induced liquefaction of soils is a hot-topic in geotechnical earthquake engineering. Building collapse and embankment burst caused by vibration or liquefaction are fatal for loss of lives and properties of human beings. A series of blasting tests including single blast and multiple underground blasts with millisecond delays were conducted on a large scale controlled field test site with saturated sand. The aim of this paper is to study the liquefaction mechanism produced by single shallow-buried detonations and multiple blasts with millisecond delays in saturated sand, and the influence factors on blast-induced liquefaction. Based on the results, the methods to produce a large area of liquefaction condition were determined. Stability of a refinforced concrete structure and a soil embankment were studied finally on the liquefaction site induced by multiple blasts with millisecond delays. The results can provide a reference to produce a large artificial liquefaction environment, and the basis for design and reinforcement of structures and soil-embankment on the sand foundation with a high water pressure.

Keywords –

Blast-induced liquefaction; Soil embankment; Large-scale field test; Saturated sand

1 Introduction

Saturated soil liquefaction is a hot topic in the field of geotechnical engineering. Saturated cohesionless soils are susceptible to be liquefied under earthquake, impact or blast loadings. Although earthquake-induced pore water pressure increases and soil liquefaction have been studied in great detail[1]–[5], comparatively little attention is given to the more intense and shorter duration ground motions generated by explosives. During the past decades, increasing blasting disaster from terrorist attacks and accidents have led to greater scrutiny of the design of structures, but little to liquefaction or the secondary disasters caused by blast-induced liquefaction. Blast-induced liquefaction is defined as a condition when the excess pore water pressure increase equals to the initial vertical effective stress of a cohesionless soil because of blast loading[6]. Blast-induced liquefaction and the resulting loss of shear strength can lead to landslide or collapse of embankments and port structures, loss of bearing supports of piles, floating of underground pipelines, and asymmetry settlement of foundations. In 1935, the Swir-III concrete filling dam in the former Soviet Union was destoryed shortly after the completion of the blasts at the upstream. At the same time of the moment of blasting operation, the dam body and the dam foundation liquefied, and resulted in the dam landslide, with the dam slope from the original 1:2 down to 1:10[7].

Similar to the earthquake action, the saturated foundation under the action of explosion can also produce serious foundation liquefaction damage, such as sand blasting water, large deformation and subsidence. Ashford et al.[8], Rollins et al.[9] adopted a multi-point millisecond explosions to manufacture an artificial vibration liquefaction environment, the development law of excess pore water pressure in soil was analyzed, and the dynamic response of pile and underground pipeline in the liquefied site and the performance of vertical drainage system were studied. Wang et al.[10] carried out an explosion liquefaction tests in a saturated lose site, and confirmed the objective existence of loess liquefaction.

For blast-induced pore water pressure response, three stages of interest can be described as follows: the millisecond transient response directly associated with the detonation, the accumulation of excess pore water pressure shortly after the passage of the stress wave, and the longer term dissipation of the pore water pressure. Some cases of blast-induced excess pore water pressure

increases or liquefaction have been reported [11], [12] to study the blast-induced liquefaction possibility. And majority of these tests were conducted in the specific sites, with the great variation of soil properties in different zones inevitably.

In this study, a pilot test with three blasts in the backfilled water-saturated sand which had successfully been conducted is described. Based on the field of large scale explosion liquefaction test, a single point and multi point micro-difference explosion liquefaction tests were carried out to determine the conditions of homogeneous explosion liquefaction in the site. The experimental study on the effect of explosion liquefaction on the stability of reinforced concrete (RC) structure and soil embankment were carried out. Applicability of the results of this investigation may provide guidance to predict the pore water pressure or extent of liquefaction induced by blast loading, particularly for safety of embankments and underground pipelines in the following full-scale liquefaction tests.

2 Experimental Setup

A series of single explosion tests and multiple underground blasts with millisecond delays aiming to evaluate the liquefaction effect were performed in the large outdoor test site. The explosion liquefaction test site is located on a farm in Wuhan City, China.

2.1 Site characteristics

The test site shown in Figure 1 was a circular-section manmade pit, with a radius of 9.5 m and 8.0 m for top and bottom sections, respectively. The poorly graded backfilled sand extended to a depth of 3 m below the ground surface without compaction. The artificially-deposited sand in the tests has an average fines content of 2% with additional information provided in Table 2. Water content for the backfilled sand is about 6~8%. Grain-size distribution for backfilled material is shown in Figure 2. Cone penetration test (CPT) was performed in the test pit before the blast testing. The relative density D_R (%) plotted in Figure 3 is estimated from the cone tip resistance q_t (kPa) normalized by the in situ vertical effective stress σ'_{v0} (kPa), which is provided in equation (1)[13].

$$D_R = 1.8\sqrt{\frac{q_t}{\sqrt{\sigma'_{v0}\cdot \mathrm{kPa}}}} \quad (1)$$

CPT measurements indicated that the initial in situ relative density for the sand layer was about 25~30% before blasting, categorizing the sand as very loose.

Table 1 Soil conditions for the backfilled sand material

ρ (kg/m^3)	D_{60} (mm)	D_{50} (mm)	D_{10} (mm)	C_u	G_s
1 440	0.21	0.18	0.10	2.10	2.63

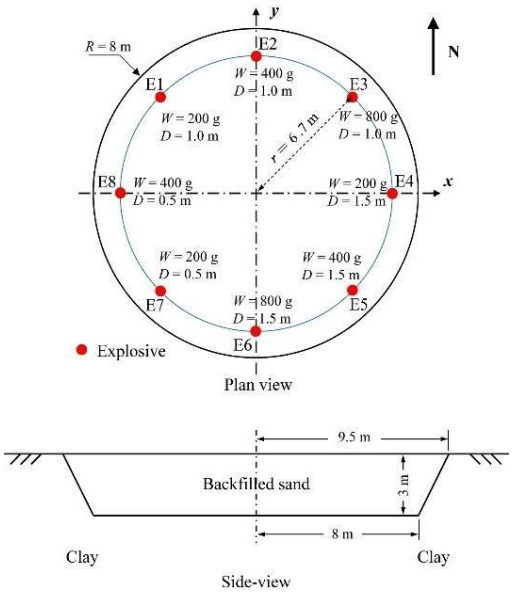

Figure 1 Blasting layout of the test site

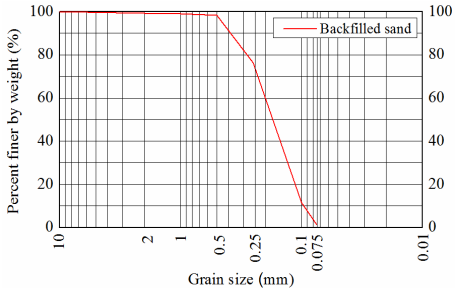

Figure 2 Grain-size distribution for backfilled sand

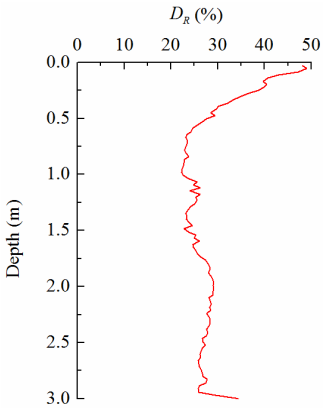

Figure 3 Typical profiles of relative density

2.2 Blast design

Charge weight and buried depth have the decisive effect on blast-effect of soil material. Boreholes in the test program are all presented in the schematic diagram of Figure 1. Emulsion explosives adopted in this study, have the excellent detonation performances in mining and blasting demolition. The detonation velocity of the explosive is tested to be greater than 3 600 m/s. Density of the explosive is about 1.0~1.1 g/cm^3. eight single explosives arranged on a circle with the radius of 6.7 m were detonated successively with the changes of charge weight and buried depth. The blast interval of any two blasts is 30 minutes. PVC hard plastic tube was used to drill borehole and placed around the hole to prevent contamination in the drilling mud until the transducer could be pushed into the ground, as shown in Figure 4(a). After the transducer was pushed into a specified depth, the borehole was filled with dry drilling sand.

The charge weight and corresponding buried depth for each borehole are presented in Table 3. In the tests, ground vibration was recorded as well. Figure 4(b) shows the planting process of the vibration meter. Embedding depth of the vibrometer was 0.25 m below the ground surface. Detail information about the vibrometer is shown in Table 2.

Figure 4 Borehole drilling and vibrometer embedding before the tests: (a) borehole drilling; (b) vibrometer embedding

Table 2 Weight and buried depth for each borehole

Borehole No.	Charge weight /g	Buried depth /m	Horizontal distance for vibrometer /m		
			#6	#2	#1
E 1	200	1.0	4	7	9
E 2	400	1.0	4	7	8.8
E 3	800	1.0	4.4	7.1	10
E 4	200	1.5	2.7	6.1	11.7
E 5	400	1.5	2.5	5.65	11.2
E 6	800	1.5	2.3	5.7	9.7
E 7	200	0.5	3.2	6.2	8.7
E 8	400	0.5	3.8	6.5	7.3

The test elements and instruments involved in the test include the special pore water pressure sensor and the acceleration sensor, the high speed dynamic strain collection system and the high speed photographic instrument, as shown in Figure 5.

The method of burying the pore water pressure sensor in soil according to the following steps:

(1) After the site has been formed, the rigid PVC polymer pipe with a diameter of 75 mm was used to penetrate the design depth above 10~15 cm with rotational soil or hydraulic impact method, the nozzle is then protected;

(2) The site consolidated after checking tube depth, the pore water pressure sensor attached to the scale of the fine wood inserted into the soil to the design depth of the buried after the fixed;

(3) The PVC pipe was pulled up side to the pipe backfill sand and tamping;

(4) Check the depth of a wood plated embedded in the soil layer and record the actual burial depth of the pore water pressure transducer.

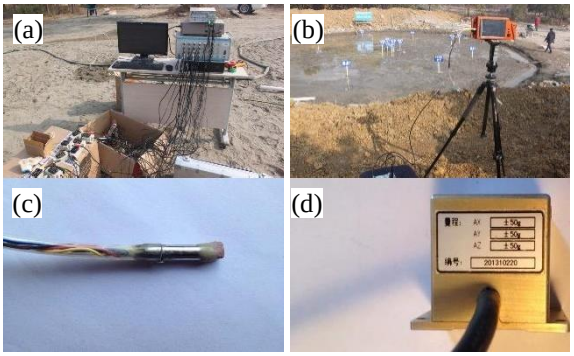

Figure 5 Sensors and instruments: (a)high-speed strain collection system; (b) high-speed photographic instrument; (c) The pore Water Pressure sensor (d) three-direction accelerometer

3 Single Blast Tests

Six single blast tests was designed based on different weight and buried depths of charge. The charge weights range from 200 g to 400 g, and the correspongding scaled buried depths (ratio of buried depth to the cube root of charge's TNT equivalence) range from 1.21 m/kg$^{1/3}$ to 2.49 m/kg$^{1/3}$. The time interval between two tests was 60 min. Nine pore water pressure transducers were used in the test to record the time histotys of excess pore pressure at different locations.

The layout of the test site are shown in Figure 6. The tests includes the following steps:

(1) Level the test site and locate the position of borehole, then drill hole and bury the pipe;

(2) Pour water to saturate the test site and keep the site static for three weeks;

(3) Pump out extra water to ensure water level is the same as ground level;

(4) Check the depth of buried pipe, bury transducers

into the pipe, and keep the site static for 24 hours.

(5) Bury the charge and detonator, and then conduct the single blast tests.

Figure 6 Layout of single shallow-buried detonation tests

The charge weight buried in E5 was 400 g and the burid depth was 0.93 m (scaled buried depth was 1.36 m/kg$^{1/3}$). The pore pressure transducer which has the shortest distance from E5 was P9 with a buried depth of 1.60 m. The time history of excess pore pressure measured at P9 is shown in Figure 7.

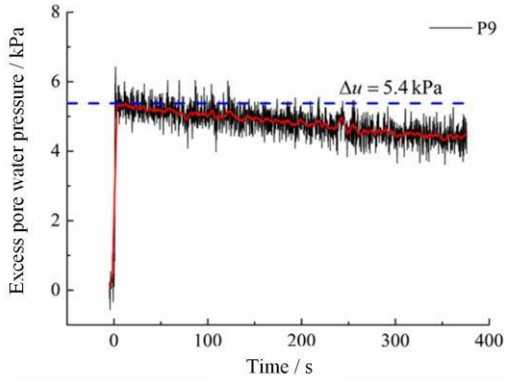

Figure 7 Time-history of excess pore water pressure of P9

The scaled distance of P9 (ratio of the distance from E5 to the cube root of charge's TNT equivalence) was 4.723 m/kg$^{1/3}$. The initial vertiacal effective stress ($\sigma_{v0}^{'}$) was 13.1 kPa, and the excess pore pressure (Δu) was 5.4 kPa. The excess pore pressure ratio (Ru) can be defined as the riatio of Δu to $\sigma_{v0}^{'}$, therefore the maximum excess pore pressure ratio was 0.412. Besides, no obvious liquefaction characteristics were observed in the test site. This result indicated that test site didn't reach liquefaction. The reason for this phonomennon was that the charge weight and buried depth were too small, which leads to a great propotion of energy generated by explosion dissipating through the ground surface.

The influence of charge's buried depth on observed Ru is shown in Figure 8. The scaled buried deptj of charge at E4 and E5 were 1.97 and 1.36 m/kg$^{1/3}$, respectively.

As can be seen in Figure 8, the buried depth of charge has significant influence on the development of excess pore pressure with scaled disctance. Due to the ground surface, shallow-buried charge's explosion had little influence on the development of excess pore pressure. With the increase of scaled buried depth, the development of excess pore pressure at the same sacled distance from explosion point become more significant. Therefore, the buried depth of charge shoud reach or be close to the critical value of closed explosion so that the energy generater by explosion can fully apply to the development of excess pore pressure.

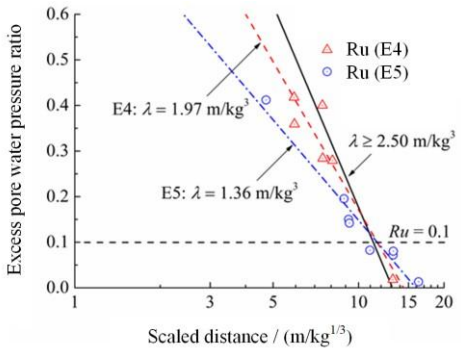

Figure 8 The influence of charge's buried depth on observed Ru

4 Multiple Blast Tests with Millisecond Delays

The layout of test site for multiple blasts with millisecond delays tests is shown in Figure 9. The charge weights were all 3*600 g. The buried depth of charge was 2.0 m. A circular array was used for the blasting layout, with all charges buried on the circle with a radius of 6m. And detonations of the charges were spaced at a very small interval of 110 milliseconds.

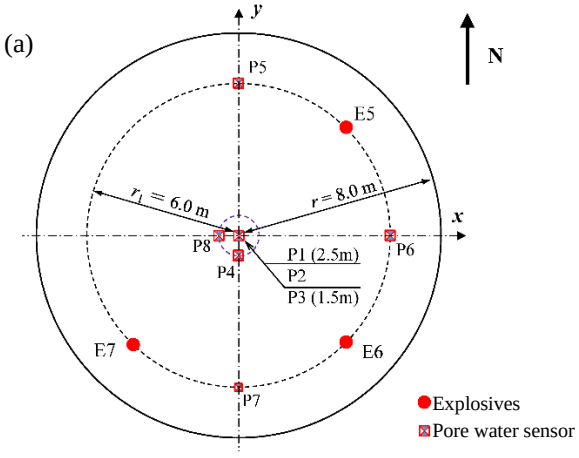

Figure 9 Layout for three-blast liquefaction test: (a) Layout of charge of transducers; Test site before blast

The time histories of excess pore pressure ratio measured at the depth of 2.5m (P1) and 1.5m (P3) were shown in Figure 10. As presented in Figure 10, the excess pore pressure ratio measured at P1 and P3 reached 0.83 and 0.95, respectively. Alough the excess pore pressure ratios didn't reach the theoretical value of liquefaction, sand boilings lasted for more than 10 min were observed at several locations which are 2~3 m distance from the blast point. The sand boiling locations are shown in Figure 11. This phenonmenon indicated that the shallow ground in test site had basically liquefied. However, no obvious liquefaction was observed at the centre of test site, where the superposition effect of multiple blasts was the most significant. The reason could be that the charge weight was small, the distance between charges were too large and the millisecond delay was not rational.

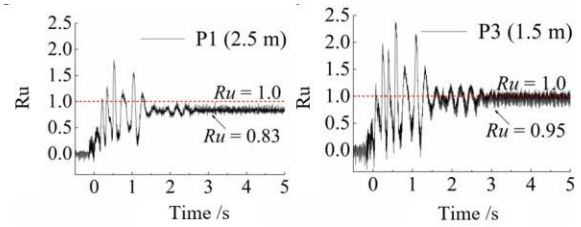

Figure 10 Time-histories of Ru for P1 and P3 at the center of the test site

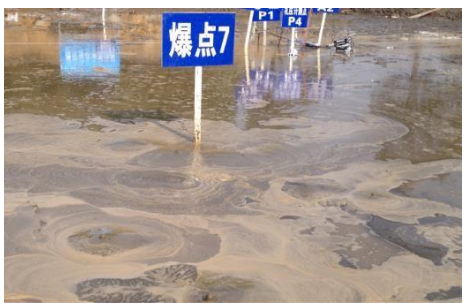

Figure 11 Sand boiling at the ground surface near the blast

5 Deformation Test of RC Structure and Embankment

Based on the results of aforementioned tests, 8 600g-weight charges were adopted in this test. The charges were placed on a circle with a radius of 6.0 m. The buried depth was 2.0 m. Detonations of the charges were spaced at a very small interval of 310 milliseconds.

The RC structure was casted one-time, with 1.6 m in height and 1.1 m in both length and width. The bottom 0.4 m of RC structure was buried into ground. The embankment was divided into three parts, including: 1) part S1 consisted of clay and sand, and was enforced with geogrids and eotextiles at the depth of 0.1, 0.3 and 0.5 m below the ground.; 2) part S2 consisted of gravel, clay and sand without any reinforcement.; 3) part S3 consisted of clay and sand without emforcement. The height of embankment was 0.5 m. Each part of the embankment was 1.2m in length and 1.6 m in width. Figure 12 shows the layout of RC structure and embankment in test site.

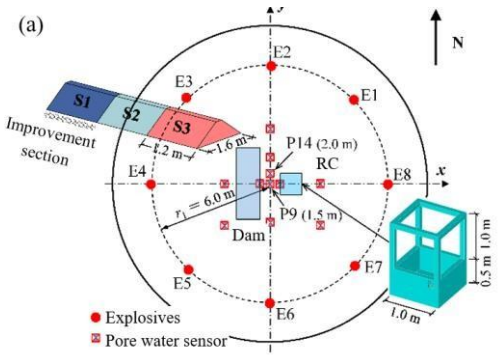

Figure 12 Layout of RC structure and embankment in the blast-induced liquefaction test: (a) Layout of RC structure and embankment in test site; (b) RC structure and embankment before blast

Sand boiling and water spraying were observed in the whole range of test site, whih is shown in Figure 13. The time histories of excess pore pressure measured at point P9 and P14 are presented inFigure 14. The buried depths of transducers placed at point P9 and P14 were 1.5 m and

2.0 m, respectively. The measured maximum excess pore pressures were 16.2 and 16.8 kPa. Therefore, the excess pore pressure ratio at P9 and P14 reached 1.0 and 0.95. It can be concluded that the whole test site was liquefied after the blast.

Figure 13 Large area of sand boils in the test site

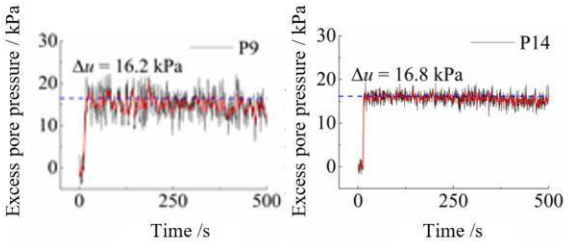

Figure 14 Time-histories of excess pore water pressure near the center

Figure 15 presents the deformation of RC structure and embankment after blast-induced liquefaction. Due to significant cpmpression settlement of liquefied sand in short time after blast, obvious settlement and offset of RC structure were observed. Figure 16 shows the settlement and north-south offset of RC structure measured in two hours after the blast. Most of settlement and offset developed within 30 min after blast.Two hours after blast, the lateral displacement of RC structure reached 11.5 cm and the vetical settlement of beam AD and BC reached 14.9 cm and 12.6 cm, which accouts for 10% of the structure' height.

Figure 15 Lateral offset of RC structure produced by blast-induced liquefaction: (a) Before blast; (b) 3 min after blast

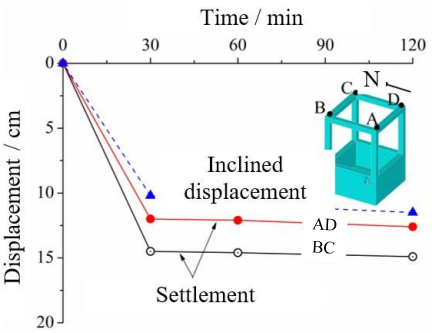

Figure 16 Settlement and north-south offset of RC structure after blasting

The deformation and settlement of embankment shows a hysteresis effect. Due to the weight of gravel adopted in Part S2 of embankment, the settlement of Part S2 is obviously larger than other's settlement. The reinforcement method combing three layers of geogrids and geotextiles provided better liquefaction resistance for Part S1, therefore the liquefaction-induced settlement of Part S1 was smaller than that of Part S3 (shown in Figure 17). The settlement measured at the top of the embankment is shown inFigure 18. Similarly, most of the settlement of embankment developed during the first 30 min after blast. Two hours after the blast, average settlement of reinforced part (S1) reached 16 cm, while average settlement of part without reinforcement (S3) reached 21 cm. This results suggest that the reinforcement combining geogrids and geotextiles can reduce liquefaction-induced settlement by 30%.

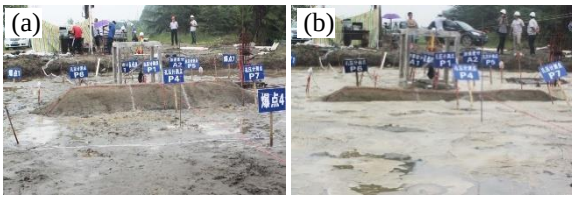

Figure 17 Differential settlement of embankment on the liquefaction site: (a) before blasting; (b) 30 min after blasting.

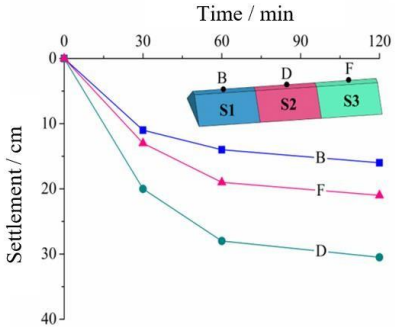

Figure 18 Differential settlement of embankment on the liquefaction site

6 Conclusions

A pilot test program for studying the susceptibility of liquefaction due to the detonation of multiple buried explosives in water-saturated sand was designed, based upon evaluating of the existing experimental data and empirical models for predicting excess porewater pressure response. The method of realizing large scaled liquefaction environment with multiple blasts of millisecond delays has the advantages of rapid economy and long duration of liquefaction. It provides a feasible method for experimental research on displacement of a RC structure and soil embankment in the large-scale liquefaction environment.

References

[1] K. Ishihara, "Liquefaction and flow failure during earthquakes," *Géotechnique*, vol. 43, no. 3, pp. 351–451, 1993.

[2] R. Rasouli, I. Towhata, and T. Hayashida, "Mitigation of seismic settlement of light surface structures by installation of sheet-pile walls around the foundation," *Soil Dyn. Earthq. Eng.*, vol. 72, pp. 108–118, 2015.

[3] S. Yasuda, K. Harada, K. Ishikawa, and Y. Kanemaru, "Characteristics of liquefaction in Tokyo Bay area by the 2011 Great East Japan Earthquake," *Soils Found.*, vol. 52, no. 5, pp. 793–810, 2012.

[4] S. M. Haeri, A. Kavand, I. Rahmani, and H. Torabi, "Response of a group of piles to liquefaction-induced lateral spreading by large scale shake table testing," *Soil Dyn. Earthq. Eng.*, vol. 38, pp. 25–45, Jul. 2012.

[5] J. ZHANG, "Transient shear strength of saturated sand under cyclic loading considering strain-rate effect," *Soils Found.*, vol. 34, no. 4, pp. 51–65, 1994.

[6] W. A. Charlie, G. E. Veyera, D. S. Durnford, and D. O. Doehring, "Porewater pressure increases in soil and rock from underground chemical and nuclear explosions," *Eng. Geol.*, vol. 43, no. 4, pp. 225–236, 1996.

[7] S. A. S. A. Ashford, K. M. K. M. Rollins, and J. D. D. Lane, "Blast-induced liquefaction for full-scale foundation testing," *J. Geotech. Geoenvironmental Eng.*, vol. 130, no. 8, pp. 798–806, 2004.

[8] S. A. Ashford, K. M. Rollins, and J. D. Lane, "Blast-Induced Liquefaction for Full-Scale Foundation Testing," *Journal of Geotechnical and Geoenvironmental Engineering*, vol. 130, no. 8. pp. 798–806, 2004.

[9] S. a. Ashford, K. M. Rollins, and J. I. Baez, "Comparison of deep foundation performance in improved and non-improved ground using blast-induced liquefaction," *Soil Dyn. Liq.*, pp. 20–34, 2000.

[10] L. Wang, K. He, Y. Shi, and J. Wang, "Study on liquefaction of saturated loess by in-situ explosion test," *Earthquake Engineering and Engineering Vibration*, vol. 1. pp. 50–56, 2002.

[11] W. A. Charlie, T. E. Bretz, L. A. Schure, and D. O. Doehring, "Blast-induced pore pressure and liquefaction of saturateds sand," *J. Geotech. Geoenvironmental Eng.*, vol. 139, no. 8, pp. 1308–1319, 2013.

[12] W. A. Charlie, W. A. Lewis, and D. O. Doehring, "Explosive Induced Pore Pressure in a Sandfill Dam," *Geotech. Test. J.*, no. 1948, pp. 391–400, 2012.

[13] F. H. Kulhawy and P. . W. Mayne, "Manual on estimating soil properties for foundation design," 1990.

Case Study on a Dip Slope Influenced by Riverbank Erosion and Highway Construction

YaChu Chiu[1a], BaiChiao Lo[2a], Wei Lo[3a], TienChien Chen[4b] and TaiTien Wang[5a]

[a]Institute of Mineral Resources Engineering, National Taipei University of Technology, Taiwan
[b]Department of Soil and Water Conservation, National Pingtung University of Science & Technology, Taiwan
E-mail: clarice.chiou@gmail.com, www90251@gmail.com, lowei93@ntut.edu.tw, tcchen@mail.npust.edu.tw, ttwang@ntut.edu.ttw

Abstract –

A highway slope along Ailiao Creek is stroke by Typhoon Morakot in 2009. Based on multi-temporal aerial photos, digital elevation model and field investigations, several dip slope failure were confirmed in the past 70 years. The sliding masses of dip slope were formed by bedding surface and two joints. Before sliding occurr, gullies along joint direction developed. Under long-term gravitational effect, dip slope failure then triggered by daylight produced after bank erotion or highway construction. Investigation shows that dip slope failure presents various features such as deformation, buckling and sliding of rock mass according to their relative height on the slope. In response to their deformation or failure feature, the two highway passing through case slope were repaired with different engineering measures, which were proved effective after 8 years.

Keywords –

Dip slope; Riverbank erosion; Highway maintenance; Daylight; Slope deformation

1 Introduction

Deformation reduces the stability of slope, thus the deformation feature of rock mass is one of the crucial information needed to mitigate geological disaster. The ineractions between factors inducing slope instability are intricate. Inner factors generally included geological structure, geological structure movement and underground water, as exterior factors contain topography, envinronment and human activity. Part of the slope with landslide potential have remarkable amount of displacement on sliding surface before failure. The deformation pattern and progess of a slope is highly connected with oncoming failure and worth investment in order to maintain the safety of the slope.

Kvapil and Clews [1] distinguish active and passive zones from the topographic feature of dip slope. Severe deformation, swell and facture may occurred near slope toe. Huang [2] investigate many large-scale landslides in China, and conclude several geomechanical models. Among these models, a general pattern for dip slope is creep-bending-shearing mode. Failure of a slope is related to its material and type of movement. For example, brittle failure develop after long-term gravitational deformation, and that the extent of brittle failure is constrained by the topographical condition around.

In example of a slope in southern Taiwan, this study observe the unlike deformation patterns on different heights, the landform variation from multi-temporal aerial photos generated digital elevation models and field geological investigation. The movement process of the case slope is recognized and the response measures to highways and the appropriateness of existing engineering structures is discussed.

2 Geography and Geology

The case slope is located in Sandimen Township, Pingtung County (Figure 1), at Sta. 29k+000 - 30k+000 on Tai-24 highway. The slope dips to southeast, the slope degree is 20°-30° in the upper part and 30°-40° in the lower part. The altitude of the slope is between 225-900 m. Ailiao Creek passes through the slope and takes a sudden turn to southwest, producing cut bank at the toe of the case slope. Two highway, Tai-24 and Ping-31, went through the slope in altitude 420 m and 650 m, respectively. Ping-31 seperate into Ping-31O and Ping-31E at the section damaged during Typhoon Morakot in 2009. Ping-31O, at altitude 660 m, is the substitute roadway when constructing Ping-31E. Tai-24 is the primary highway connecting Sandimen and Wutai Township, both are popular scenic spots in Pingtung County.

The outcrops around case slope are the Miocene stratum Chaochou Fomation, formed by slate, argillite and alterations of metasandstone and slate. The bedding attitude is N40-50°E/30°S, and the foliation attitude is

N40-50°E/30°S. Since bedding and foliation are parallel with slope direction, the case is a dip slope. No nearby geological strcutures are discovered [3-4].

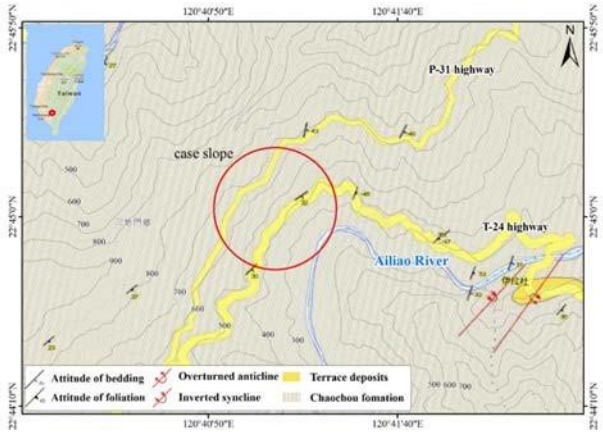

Figure 1. Geological map of the case slope [3-4].

3 Movement Progress and Characteristics of the Case Slope

Serious landslides took place after Typhoon Morakot in August 2009, as shown in Figure 2. To suggest engineering mitigation strategy on sliding mechanism, this research collect aerial photos of the surrounding from 1948 to 2016 (Figuer 3). By observing the feature of bare rock after landslide, the evolution of gullies, and the landform variation of case slope on images as well as digital elevation model produced from those images, the movement progress and deformation mechanism of rock mass is discussed herein.

3.1 Interpreation of Multi-temporal Aerial Photos

Interpretation of aerial photos shows that gullies parallel with slope direction developed at 1948, when there is no obvious sign for large-scale landslide. In 1948, only one highway passed through case slope (Figure 3(a)), which is the former road before Ping-31. Gullies sparsely distributed on slope surface. Strings and irregular landslides can be found along the road and gullies. Collapses near the highway are mostly small-scale debris flow formed by weathered rocks (green circle in Figure 3(a)). Below the highway there are strings of bare and well-developed landslides (yellow circle in Figure 3(a)). Agricultural activities were found on the upper part of the slope in 1952 (Figure 3(b). The feature of landslide in this year is similar with that in 1948, present string figures with Y shaped gullies. From 1992 to 2005， landslide stripes appear piecemeal above and below highways， and along gullies (Figure 3).

The serious damages in 2009 creates many bare rock surfaces where discontinuities can be identified, as delineated with magenta lines in Figure 2(b). Those well-developed discontinuities which intersect parallel or perpendicularly with the slope surface exist long before landslide occurred. Three spots favorable for landslide were identitied as follows.

(a)

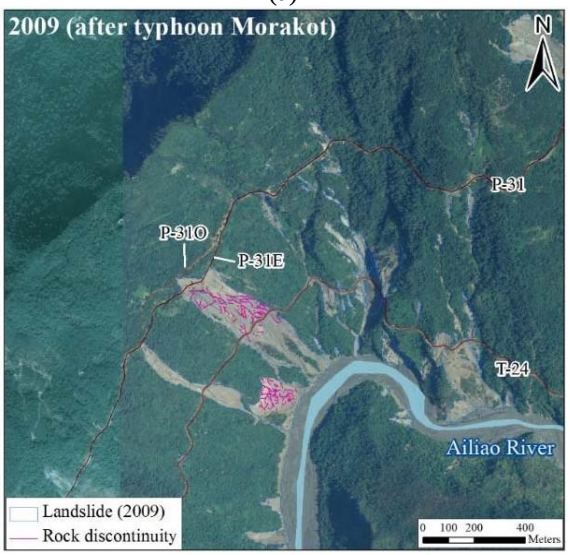

(b)

Figure 2. Orthopohtos of the case slope (a) before and (b) after Typhoon Morakot. Multiple sets of discontinuities were observed on the bare rock surface after sliding, as depicted by magenta lines.

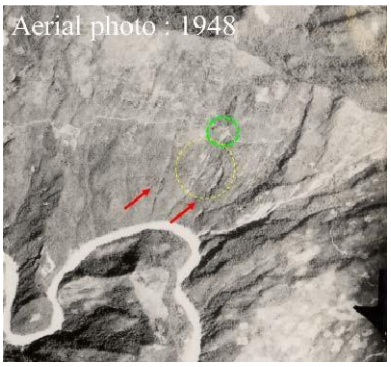

(a)

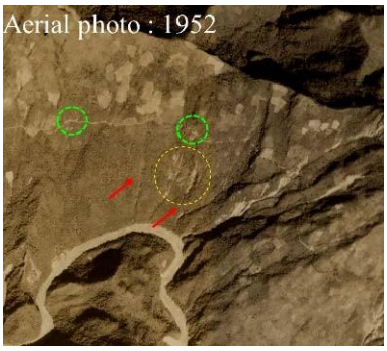

(b)

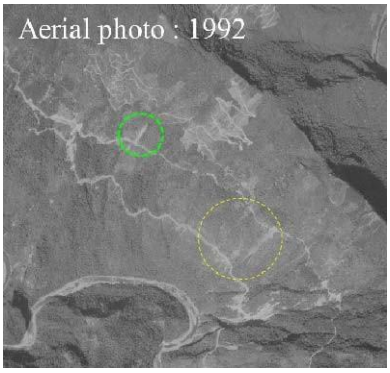

(c)

(d)

Figure 3. Aerial photos of the case slope taken in (a) 1948, (b) 1952, (c) 1992 and (d) 2005. Circles denote the landslide areas, and arrows indicate gullies.

1. From slope belly to slope toe: The largest one is 657 m long and 180 m wide, at altitude 690 m. This type of landslide is related to the development of gullies, either debris flow or dip slope movement.

2. At slope toe: The landslide after Typhoon Morakot (Figure 2(b)) is 150 m long and 180 m wide, mainly composed of debris.

3. Along the sides of gullies: Reach up to altitude 640 m, creating water channel for rainfall and fissure water, and transit debris to Ailiao Creek.

Comparing aerial photos and orthophotos, it is found that a set of well-developed discontinuity perpendicular with slope direction prevails over the slope, dominate gully evlolution and become the boundaries of dip slope movement.

3.2 Landform Variation before and after Typhoon Morakot

This research acquired the digital elevation model of the case slope in 2009, and produced the models in 2005 and 2013. Two profiles at locations with distinct geographic variation, A-A' and B-B' (Figure 4), were used to analyze the change before and after Typhoon Morakot. Daylight is observed at highway and slope toe along profile A-A' (Figure 4(b)), where the landform is cut by highway construction and bank erosion. The sliding surface at the slope toe is as deep as 16 m. Landform varies along profile A-A' and B-B', where the color of the slope map transforms from bright to dark, i.e., gentle to deep slope (Figure 4). Slope map also reveals three main lineations. The most obvious one is parallel to slope direction. Secondly, bedding creates surfaces perpendicular with slope direction. There is another discontituity conjugate with the slope direction.

3.3 Field Investigation and Deformation Mechanism of Rock Mass

A geological investigation containing surface condition and attitude of discontinuity, and rock mass deformation is carried out along the highway. Combined with interpretation of aerial photos and digital elevation models, a hypothesis on failure mechanism of case slope is built. The content is described below:

In 2015, outcrop of slate at upper slope has weathered to brown. A set of discontinuity parallel with the slope direction (yellow dash line in Figure 5(a)) is cut by another two sets of discontinuities (on of them is the magenta line in Figure 5(a)), extending stepwise downward. The scarp of the westmost boundary of the largest landslide occurred in 2009 (Figure 5(c)) is the heritage of a former developing gully. Between highway Tai-24 and Ping-31 (Figure 5(d)) there are two well-developed discontinuities, one parallel (magenta line) and the other is oblique (green line) with the slope

direction. Water seepage is identified along the slope direction. A the toe of slope (Figure 5(e), (f)), the remaining sliding surface after landslide is distinctly lower than adjacent slope surface. Some discontinuities on sliding surface opened (Figure 5(e)). Outside the landslide area, gravity and geographic constraint together lead to rock mass deformation and buckle (Figure 5(d)).

Aerial photos, digital elevation model and field investigation shows that multiple dip slope sliding and debris flow had occurred on case slope. The moving mass of dip slope sliding is bounded by bedding and two discontinuities. Debris flow is the collapse of weathered rock or colluvium. Former sliding produced the various thickness and stepwise appearance.

In a process of landslide, gullies developed along three main lineations, the slope direction, the ones oblique with slope direction and perpendicular with slope direction. As gullies grow, debris fall on two sides of a gully, and gullies expand. Gullies and bedding with daylight may together compose a sliding mass that is triggered by gravity, bank erosion or highway construction. Presetly the remains of the sliding mass after Typhoon Morakot can still be found on the slope. Discontituities on the sliding surface near slope toe has cracked. The rock mass around deformed and swell (Figure 6(a)), and is very likely to facture and initiate another dip slope sliding. Bank erosion accelerate the process. The same feature also exists elsewhere on the slope.

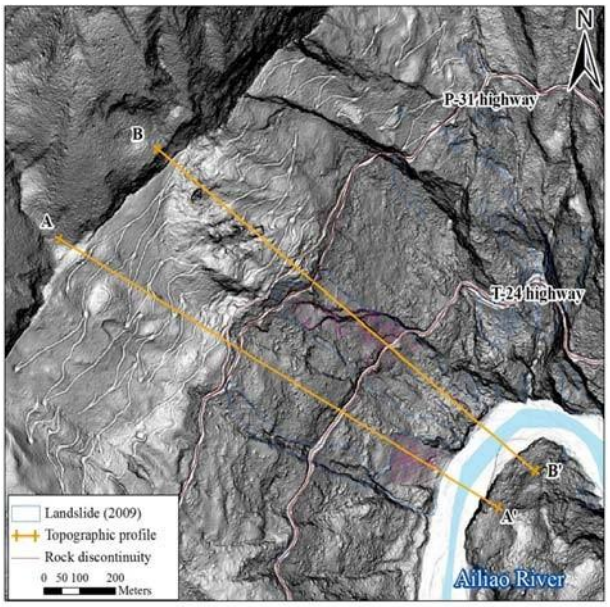

(a)

Figure 4. (a) Slope map of the case slope generated from digital elevation model in 2009.

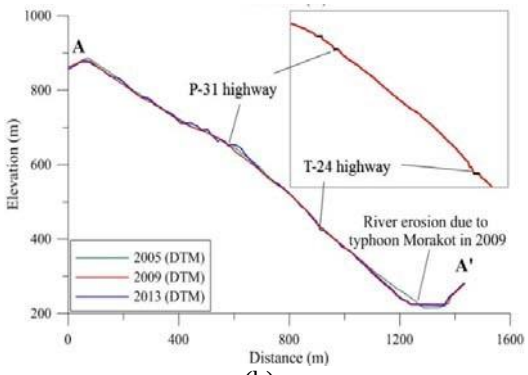

(b)

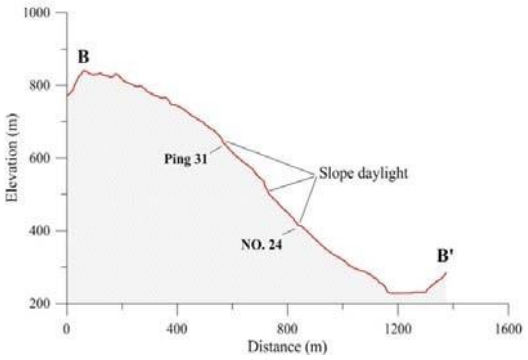

(c)

Figure 4(cont.). (b) Elevation along A-A' profile and (c) B-B' profile, before and after Typhoon Morakot, respectively.

4 Discussion on Engineering Measures of Highway Slope

The case slope contain two types of failure, dip slope sliding and debris flow. The landslide process can be summarized as gully development-deformation-fracture-sliding. Therefore, this research suggest that that the following principles be adopted on highway slope: 1). Retard gully development. 2). Restrain slope deformation. 3). Reduce the influence of dip slope sliding on highway. 4). Prevent debris flow from damaging highway.

Highway Tai-24 and Ping-31 were damaged to different extent in 2009 (Figure 2(a)). Crown of the largest landslide passes through Ping-31 (between (b)-(c) in Figure 5), where upper and lower slope is constrained with anchor and retaining walls. Gullies were protected with shotcrete to prevent further erosion. Fences were constructed on retaining walls to block falling debris. Tai-24 passes through the central slope, thus is vulnerable to dip slope sliding. Two rock sheds were built, with anchor on both upper and lower slope (Figure 5(d)). Bore hole records show that the anchor length is longer than rock mass deformation range, thus is sufficient to maintain highway operation.

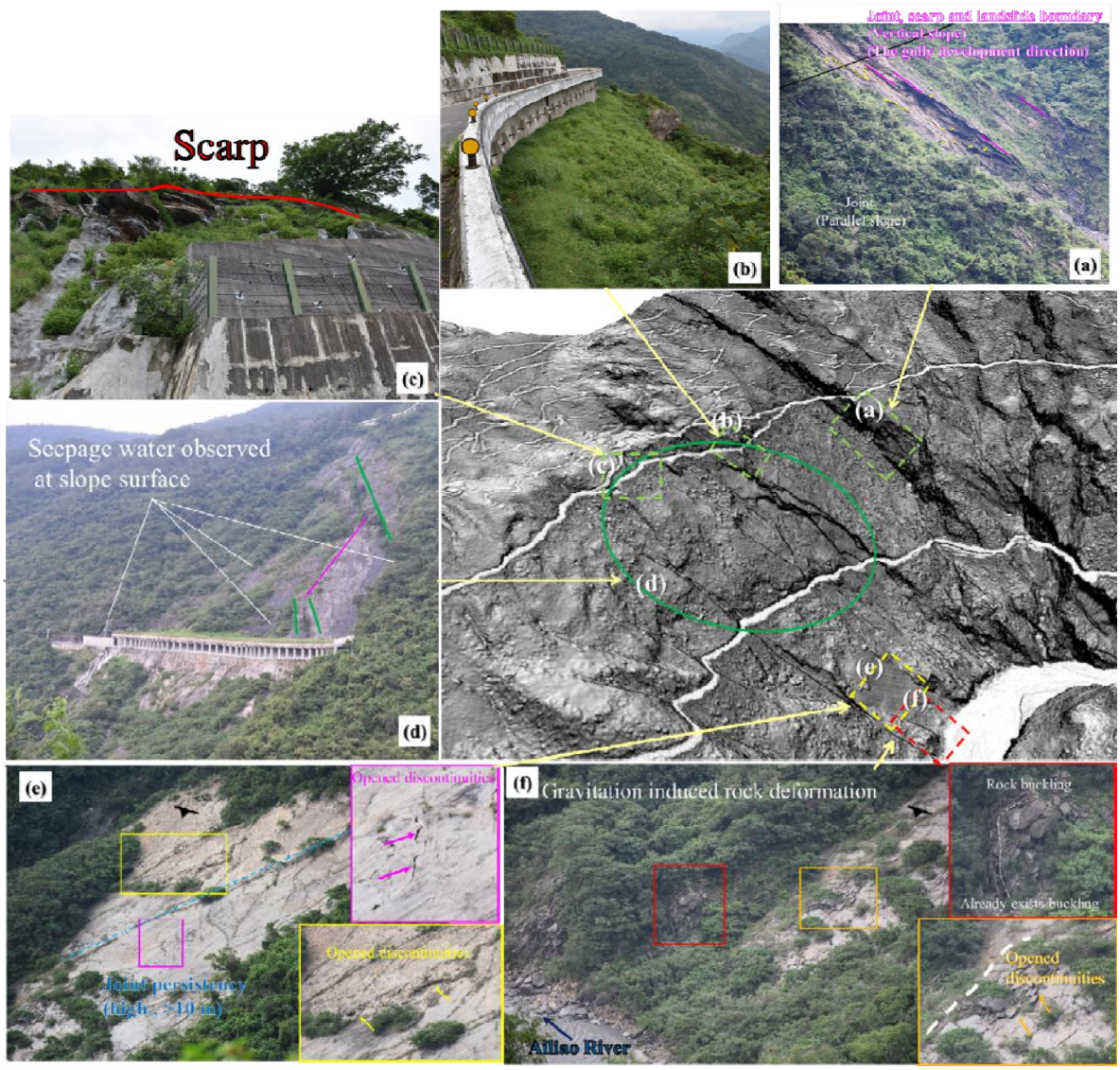

Figure 5. Engineeing facilities and rock mass deformation of the case slope in 2015.

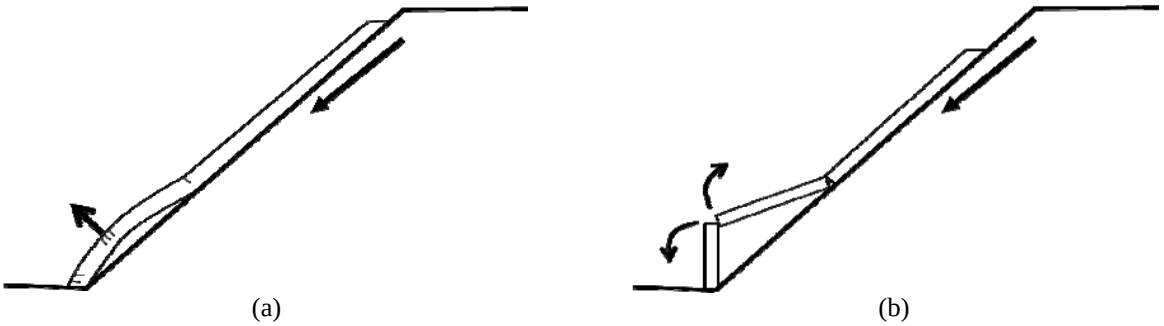

(a) (b)

Figure 6. A simplified model elucidating the mechanism of landslide at slope toe. (a) Rock mass deformed and the lower part rise. Cracks can be found on slope surface. (b) Constrained by slope toe and rock strata, landslide takes place as the rock mass fracture and buckle.

5 Conclusions

This research utilized aerial photos, digital elevation model, field ovservation and discontinuity investigation to acquire landform variation, rock mass doformation and mechanical parameters of rock mass. It is found that 1). The development of gullies not only influence slope stability, but also affect the boundary of developing landslide; 2). Daylight caused by highway construction or riverbank erosion reduce slope stability; 3). The deformation of rock mass due to gravity concentrate on slope toe; 4). The movement evolution and deformation mechanism of the case slope is known and measures of follow-up repair engineering facilities is suggested. The design of the reinforcing works afer Typhoon Morakot had considered and took actions regarding potential types of slope failure. The present engineering facilities ensure the safety of slope to the extent of current knowledge.

References

[1] Kvapil R. and Clews K.M. An examination of the Prandtl mechanism in large-dimension slope failures. *Transactions of the Institution of Mining and Metallurgy: Section A: Mining Industry*, 88:A1–A5, 1979.

[2] Huang, R. Large-scale landslides and their sliding mechanisms in China since the 20th century. *Chinese Journal of Rock Mechanics and Engineering*, 26 (3):433-454, 2007.

[3] Lin C.W., Lin, W.H. and Kao M.C. *Geological map of Taiwan scale 1:50,000-Chaozhou*, Central Geological Survey, MOEA, Taipei, 2011.

[4] Lin C.W. and Hong G.T. *Geological map of Taiwan scale 1:50,000-Meinong*, Central Geological Survey, MOEA, Taipei, 2012.

The Case Study for Evaluation of Landslides Volume and Moving Paths of Single Falling Rock

Feng-Chi Huang[a] Yi-Hsuan Lee[a] Jiun-Ting Lin[b] Kuo-Wei Chen[a] Chen-Yu Chen[a] Kuo-Lung Wang[b]

[a] Research Technology Development Team, Soil and Water Conservation Bureau Council of Agriculture, Executive Yuan, Taiwan (R.O.C)
[b]Department of Civil Engineering, University of National Chi Nan, Taiwan (R.O.C)
E-mail: fchuang@mail.swcb.gov.tw, limermaidyam@gail.com, nokilin@gmail.com, ckw@mail.swcb.gov.tw, cychen59@gmail.com, kuolung@gmail.com

Abstract –

Landslides are natural evolution of topography. Since human behavior started reaching to mountain area, landslide disasters often occur and threaten people. The study uses the case of typhoon-Meranti-induced Hongye landslide in Taiwan on September 15th, 2016 to determine the landslide terrain feature, geological conditions, and disaster impact area by surveying the site for investigate and using the unmanned aerial vehicle (UAV) for monitoring. The UAV's aerial photos are used to build the 3D model, orthophoto and digital surface model (DSM). The landslide area can be drawn with the area orthophoto. Compare the digital terrain model before and after the landslide to evaluate the terrain change of slope and landslide volume. While surveying the site of Hongye landslide, we found there is a risk of rock fall. To assess the motion track and form of the rock on slope, this study uses RocScience Rocfall 5.0 to conduct stability analysis to analyze the potential path and risk of the rock.

Keywords –

UAV; DTM; Landslide volume evaluate; RocScience

1 Introduction

Landslides are important type of natural disaster worldwide, and can cause major hazard in mountain area, costing human casualties and economic losses. Landslides can be triggered by intense rainfall, earthquakes or human activities. Take rainfall-induced landslide as example, a landslide dam was formed in Taiwan by 0610 heavy rainfall event, and was just collapsed few hours later (Kuo-Lung Wang et al., 2016) ; In Brazil, heavy thunderstorms occurred and triggered thousands of landslides on steep slopes with trees and block rich debris materials converged into the river channels, hence avalanches down valley (André S. Avelar et al., 2013). To avoid human casualties and economic losses, there is a mission not only to understand the landslide process but also the landslide-triggered mechanisms. Analysis of historical records of landslide and reliable monitoring methods seems important.

The use of remote-sensing technology for mapping and monitoring landslide has improved a lot since the last decade, including the (airborne or terrestrial) laser scanning or unmanned aerial vehicles (UAV). This paper focuses on the research of UAVs landslide monitor, analysis and application. Unmanned Aerial Vehicles (UAVs) are an inexpensive, low- labor costs, effective, user-friendly and new remote sensing tool (Mark A. Fonstad et al.,2013； J. Travelletti et al.,2012； M.J. Westoby et al.,2012), which can acquire high resolution spatial data. (Darren Turner et al., 2012 ； Mark A. Fonstad et al., 2013). Development of UAV platforms requires broad technical skills covering platform development, data post-processing, and image analysis (Joshua Kelcey et al., 2012). Therefore, Structure from Motion (SfM) computer vision techniques were applied to derive ultra-high resolution 3D models from multi-view aerial photography (Arko Lucieera et al., 2014). SfM is a flexible approach to capturing complex topography (M.J. Westoby et al., 2012). Then, the imagery can be used to produce dense point clouds using multi-view stereopsis techniques (MVS) combining computer vision and photogrammetry (Steve Harwin et al., 2012). Therefore, UAV application is a capability of producing 3D model, orthophoto and digital terrain model (DTM). Furthermore, comparing a laser scanner survey of the same site, SfM-MVS produced comparable data and reduced data collection time by 80% (M. R. James et al., 2012).

UAVs are ideal tools to map and monitor features at the Earth surface. For instance, chalk sea cliffs in UK (John Barlow et al., 2017) ； Italy mapping discontinuities within a marble quarry (Riccardo Salvini

et al., 2016) ; changing snow and polar vegetation of Antarctic moss beds (Arko Lucieera et al., 2014), etc. Now, UAVs have been used to monitor landslides (Kuo-Lung Wang et al., 2016; U. Niethammer et al., 2012 ; Arko Lucieer et al., 2014). UAV ' s aerial photos can be used to produce a high-resolution ortho-mosaic of the entire landslide, 3D models and digital terrain models (DTMs) of several regions, that more geological formation can be discovered from (Kuo-Lung Wang et al.,2016; U. Niethammer et al.,2012; Mariella Danzi et al.,2012). An environmental remote sensing application using a UAV is specifically aimed to reducing the data gap between field scale and satellite scale in soil erosion monitoring (Sebastiand' Oleire-Oltmanns et al., 2012).

High resolution digital terrain models produced by UAV' s collected data should be based on the real-world and accuracy coordinate system in order to measure distance, observe elevation changing or analysis slope. However, Khairul has evaluated the accuracy of slope mapping results from different altitudes at semi-undulated area and undulated area and found altitudes did have an influence on the slope accuracy (Khairul Nizam Tahar, 2015). Therefore, during the process producing digital terrain models, the point clouds are in an arbitrary coordinate system and need to be georeferenced. The point clouds are transformed into a real-world coordinate system using either a direct georeferencing technique that uses estimated camera positions (the UAV's log file) or via a Ground Control Point (GCP) technique that uses automatically identified GCPs within the point cloud (Sebastiand'Oleire-Oltmanns et al., 2012 ; Darren Turner et al., 2012; Mark A. Fonstad et al., 2013; SteveHarwin et al., 2012). The models fitted the ground control network are able be within a standard error with horizontal and vertical precision in the centimeter range (John Barlow et al., 2016 ; Mark A. Fonstad et al., 2013).

The UAV has demonstrated its capability for producing valuable landslide data, imaging fissures and displacements on the landslide surface (U. Niethammer et al., 2012). Also, UAV can evaluate landslide failure volume through volumetric analysis, a comparison of sequential models (John Barlow et al., 2016).

Data capture through UAV photogrammetry can provide useful terrain information, including slope condition, discontinuities, slope geometry or unattainable measurements, for slope numerical modeling of stability or kinematic analysis (Riccardo Salvini et al., 2016 ; John Barlow et al., 2017 ; Mariella Danzi et al., 2012 ; Kuo-Lung Wang et al.,2016). Cross sections and joint system data were obtained from DTM and used as input parameters for the slope stability analyses (Á kos Török et al., 2017). For instance, John Barlow used the method to analyze over sea cliffs and coast (John Barlow et al., 2017); Á kos Török modelled the rocky slope by 2D FEM (Finite Element Method) software and identified potential hazards such as planar failure, wedge failure and toppling (Á kos Török et al., 2017). By geological analysis and correlation between soil properties and geotechnical behavior can explain the catastrophic slope movement mechanisms and processes (André S. Avelar et al., 2013).

2 Research Preparation

2.1 Geological setting

The landslide located only 4.3 km away from the Luye fault, which is a north-south directional reverse fault. The region geological, aged about Eocene or earlier, is Pilushan Formotion (Ep). The main lithology is Slate and Phyllite, but in the layer there is the thicker Meta-Sandstone layer, including Calcareous, Arkose (Figure 1). On September 15th, 2016, typhoon Meranti occurred, with the rainfall of 513.5mm accumulated rain and 19mm/hr rainfall intensity, inducing the first landslide that ranged about 5.62 hectares.

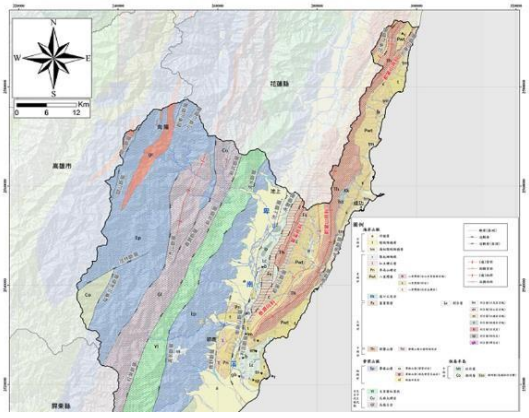

Figure 1. The regional geological map in the research case

2.2 Numerical Model Analysis

2.2.1 Soil material

Marinos presents a quick and easy method to estimate the engineering parameters of rock mass (Marinos and Hoek, 2000). This method considers three main parameters as follows: the uniaxial compressive strength (σ_{ci}), a material constant (m_i) related to the frictional properties of the rock, and the Geological Strength Index (GSI) that response to the geological joint condition of rock. The two constant, (σ_{ci}) and (m_i), can be obtained from laboratory test, but both of the

value still can be estimated if there is no test data. Then, the engineering parameters of rock, including friction angle (φ) and cohesive strength (c) can be determined with Figure 2 and Figure 3 according to the estimated value. This study assesses the corresponding parameters of the above description, shown in Table 1.

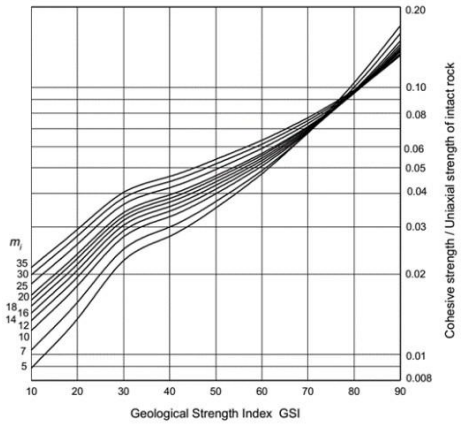

Figure2 Relationship between ratio of cohesive strength to uniaxial compressive strength of intact rock (c/σ_{ci}) and GSI for different (m_i) values (Marinos and Hoek,2000)

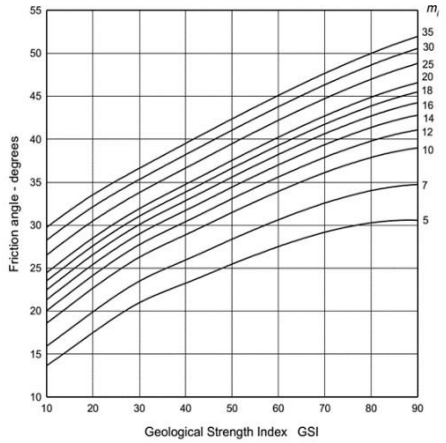

Figure3 Friction angle φ for different GSI and mi values(Marinos and Hoek,2000)

Table1 Field estimates of rock mass properties by Marinos and Hoek,2000

Grade	Uniaxial Comp. Strength (σ_{ci}) MPa	Values of the constant (m_i)	Geological strength index (GSI)	Cohesive strength / Uniaxial etrength of intact rock (c/σ_{ci})	Cohesive strength (C) KPa	Friction angle (φ°)
R1	1-5	7-11	10-15	0.011-0.015	11-15	17-21

2.2.2 Rockfall Model

This study adopts the rockfall analysis in RocScience Rocfall 5.0.This statistical analysis program can assess the energy, velocity, bounce-height and location of rock endpoints of the process of motion rock over the slope, and uses the Monte Carlo techniques to do the risk level statistics. This program needs to be defined with the slope and the rock geometry and material properties, including dynamic friction, rolling friction coefficient, rock density, rock mass and the slope terrain elevation and so on.

3 Research procedures

3.1 Landslide terrain change and volume evaluate

3.1.1 Aerial survey mission and 3D model

This study uses remote-controlled UAV Phantom 3 Professional equipped with digital camera and GPS to acquire airborne digital photographs on September 16, 2016 and March 24, 2017. The images recorded in 2016 is in emergency mission, the image resolution ranges between 0.042m to 0.370m, and did not set the ground control point. UAV mission in 2017 took different elevation as Aerial survey route (Figure 4) to raise the image resolution which ranges between 0.036m to 0.190m, and 10 ground control points were set around the landslide area to calibrate the elevation (Figure 5).

This study uses Bentley Context Capture version 4.0 to feature the points of the aerial photos by aerotriangulation and produce the three-dimensional model. The 2016 and 2017 orthophoto and the digital surface model (DSM) were also be obtained. The DSM grid size is 0.140m of 2016 and 0.093m of 2017.

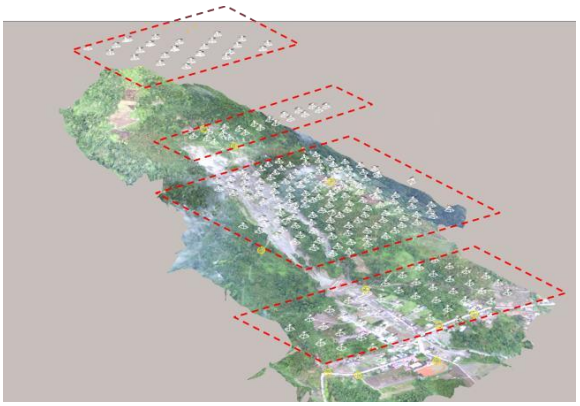

Figure 4 UAV aerial survey route

Figure 5 Ground control points

3.1.2 Terrain change tracking and volume evaluation

This study uses the orthophotos made from aerial images after the landslide to plot the range of the exposed and landslide area. Aerial survey had done again in the following year to track the changes of the landslide area. Comparing orthophotos between 2016 and 2017 can find that the part of the vegetation in the landslide area has been recovered, but the upper edge of the landslide seems to be expanded, and the new tension cracks can be discovered (Figure 6).

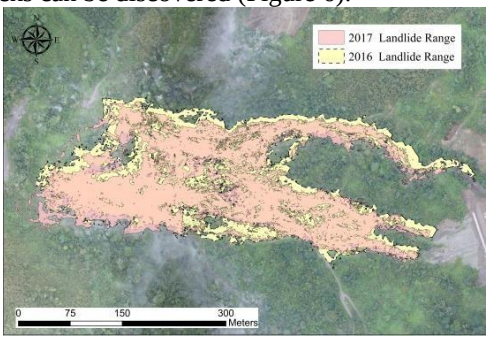

Figure 6 Orthophotos comparison between 2016 and 2017

This study compares the DSM before and after the landslide, determines the elevation difference after landslide and evaluates the landslide volume. The results show that the landslide area is about 56,194 m^2, and the mean elevation difference of the landslide area is 2.70 m, including the deepest erosion of 13.48 m and the highest accumulation of 21.25m (Figure 7). The landslide area is divided 56,194 grids of single 1m^2, including 14,609m^2 of the accumulation area, 41,585m^2 of the erosion area that defined as five levels according to the erosion depth (Table 2). After the statistics of the landslide erosion area, the landslide volume 211,466 m^3 is evaluated.

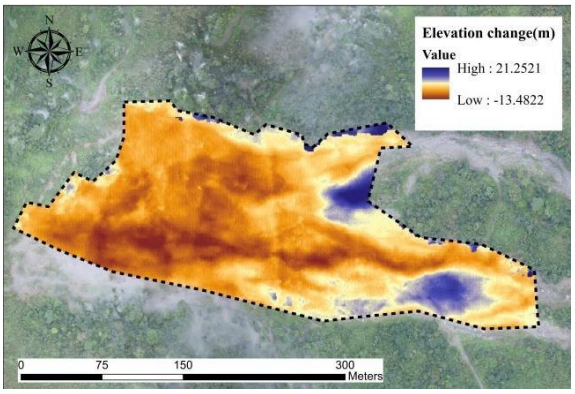

Figure 7 Terrain change after landslide

Table 2 Landslide area for five levels according to erosion depth

Depth(m)	Number of Grid (m^2)
0~2.5	9415
2.5~5.0	12175
5.0~7.5	10715
7.5~10	7316
10~13.48	1964

3.2 Numerical Analysis of Rockfall

3.2.1 Material parameters and analysis assumptions

According to the surface model of 2017, the risk of dangerous rock of the landslide is estimated. The length, width and height of the rock is 9.20m, 5.70m and 3.60m respectively. The rock volume is about 65.22m^3. Through the investigation, the rock is considered as the sandstone with unit weight of 2.70 (T / m^3), and the rock is about 176,094 kg. In addition, the surface of the slope after the landslide is extremely weathering erosion, assessed the friction angle of the slope is 21 °. This study assumes the rock is moved by the influence of the foundation loss and earthquake.

According to the terrain slope and the shadow map, the four tracks of the motion rock are decided (Fig. 8), and the rock is located on intersection points of each path. Two erosion depth : 3.60m (rock height) and 13.48 m (maximum erosion depth) were analyzed and also the seismic acceleration 400 gal. Considered the possible aggravation, every condition of the analysis tests 100 times, and statistics of the end location and the probability of occurrence.

Table 3 Surface-erosion impact rock stability anlyisis

track	Rock displacement and occurrence probability					Highest probability and Rock displacement	
	Erosion Depth	Max Displacement(m) **(A)**	Percentage (%)	Min Displacement (m)	Percentage (%)	Percentage (%)	Highest probability displacement (m) **(B)**
1	3.6	47.09	100	-	-	100	47.09
	13.48	110.49	1	47.09	87	87	47.09
2	3.6	54.52	100	-	-	100	54.52
	13.48	81.78	1	54.52	96	96	54.52
3	3.6	58.53	83	45.91	17	83	58.53
	13.48	109.02	1	45.91	21	74	58.53
4	3.6	51.08	100	-	-	100	51.08
	13.48	51.08	100	-	-	100	51.08

Table 4 The earthquake-acceleration impact rock stability anlyisis

track	Rock displacement and occurrence probability					Highest probability and Rock displacement	
	Erosion Depth	Max Displacement(m) **(C)**	Percentage (%)	Min Displacement (m)	Percentage (%)	Percentage (%)	Highest probability displacement (m) **(D)**
1	0	47.09	100	-	-	100	47.09
	3.6	82.31	1	47.09	93	93	47.09
	13.48	138.66	1	47.09	86	86	47.09
2	0	54.52	100	-	-	100	54.52
	3.6	209.02	1	54.52	98	98	54.52
	13.48	336.26	1	54.52	72	72	54.52
3	0	58.53	85	15	45.91	85	58.53
	3.6	109.02	1	45.91	17	75	58.53
	13.48	109.02	5	45.91	12	33	58.53
4	0	51.0	100	-	-	100	51.0
	3.6	68.29	1	51.08	95	95	51.08
	13.48	68.29	2	51.08	95	95	51.08

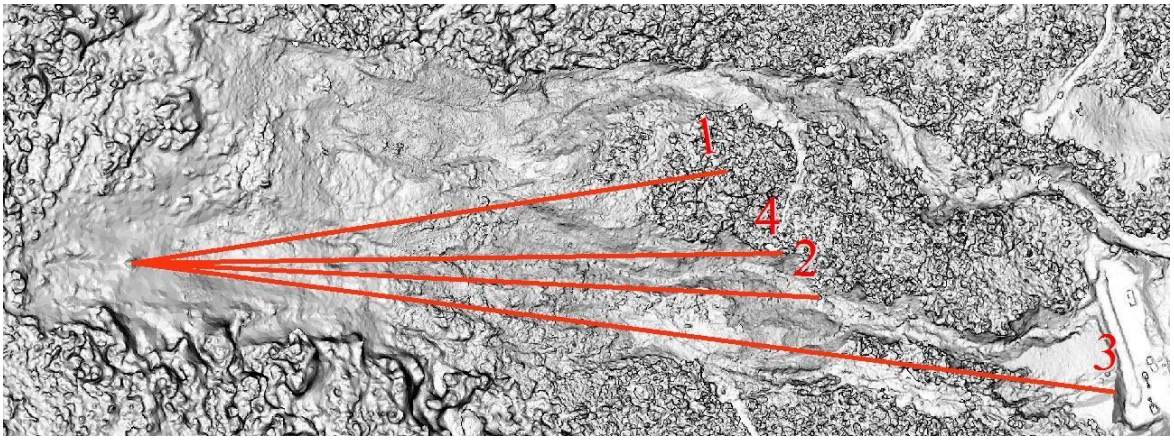

Figure 8 Moving paths of single falling rock

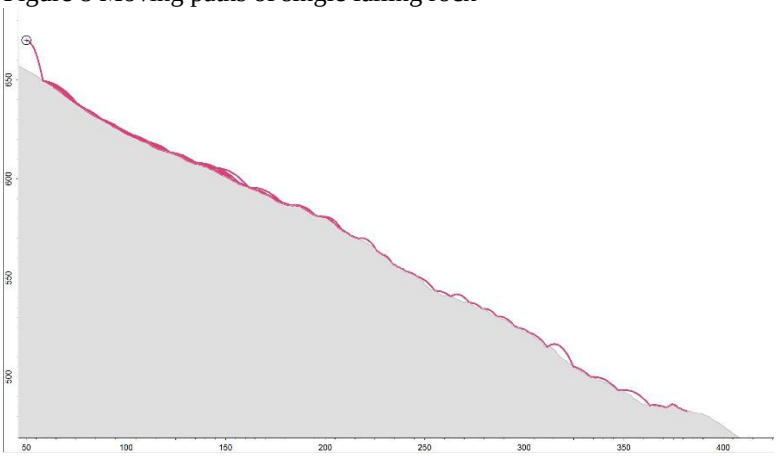

Figure 9 Moving path of track 2

3.2.2 Results and discussion

According to the results, this study shows that with only the terrain erosion without earthquake impact; the rock lost support would fall and slide (Table 3). Erosion of depth 3.60m, the motion of the displacement the value A and B seems the same. Erosion of depth 13.48m, the motion paths are almost the same except for track 4, which the maximum probability of occurrence and the maximum displacement distance is not the same. Considering the acceleration of earthquake, the value C and D are the same of the nonerosion slope.

In addition, when the slope occurs erosion, the probability of maximum displacement and the highest occurrence for each erosion depth are different (Table 4). The path 2 in the erosion depth of 13.48m, the displacement of the rock is 336.26m, which is the maximum displacement of all paths . The track of path 2 may have the factors of terrain that leads the rock to the bounce, nonstop at the gentle area and keeps moving on. So, this path is the highest risky path of all (Figure 9).

4 Conclusions

1. Using UAV to record images for a wide-range area tracking and ground control points improves the measurement accuracy. The details of the landslide region can be presented more accurate, such as this study survey investigate found that above the original landslide exists the tension cracks, and scope of the landslide tend to be expanded.
2. Using the orthophoto to plot the range of landslide which is considered as a basis for the terrain surface elevation difference comparison of before and after the landslide, the surface elevation difference is the landslide volume. The concept of this calculus is that when the landslide happens, the surface of the area is exposed without vegetation, so the digital surface model elevation of the area is equal to the digital terrain model, therefore, it presents the exact terrain elevation, and the comparison between the pre-disaster (DEM) and after-disaster (DSM) of the landslide area elevation is determined.
3. This study uses the numerical analysis program RocFall to conduct the rock motion track analysis.

According to the gradient of the slope, 4 possible motion paths are predicted and of which two factors of the loss of the foundation support and the earthquake effect are assumed. The rockfall stability analysis is carried out to evaluate the fall end of each path and the probability of occurrence and to presume the most possible occurrence and damage possible rock motion path.

5 References

[1] Á kos Török, Á rpád Barsi, Gyula Bögöly, Tamás Lovas, Á rpád Somogyi and Péter Görög. Slope stability and rock fall hazard assessment of volcanic tuffs using RPAS and TLS with 2D FEM slope modelling. Natural Hazards and Earth System Sciences :56-85, 2017.

[2] Avelar AS, Coelho Netto AL, Lacerda WA, et al. Mechanisms of the recent catastrophic landslides in the mountainous range of Rio de Janeiro, Brazil. In: Margottini C, Canuti P, and Sassa K (eds) Landslide Science and Practice. Volume 4: Global Environmental Change. Berlin: Springer, 265–270, 2013.

[3] d'Oleire-Oltmanns S, Marzolff I, Peter K, et al. Unmanned aerial vehicle (UAV) for monitoring soil erosion in Morocco. Remote Sensing 4: 3390–3416, 2012.

[4] Fonstad MA, Dietrich JT, Courville BC, et al. Topographic structure from motion: A new development in photogrammetric measurement. Earth Surface Processes and Landforms 38(4): 421–430, 2013.

[5] Guzzetti F, Mondini AC, Cardinali M, et al. Landslide inventory maps: New tools for an old problem. Earth-Science Reviews 112: 42–66, 2012.

[6] Harwin S and Lucieer A . Assessing the accuracy of georeferenced point clouds produced via multi-view stereopsis from unmanned aerial vehicle (UAV) imagery Remote Sensing 4: 1573–1599, 2012.

[7] James MR and Robson S Straightforward reconstruction of 3d surfaces and topography with a camera: Accuracy and geoscience application. Journal of Geophysical Research 117: F03017, 2012.

[8] John Barlow and Jamie Gilham. Stability analysis of chalk sea cliffs using UAV photogrammetry.19th EGU General Assembly, 2017.

[9] John Barlow, Jamie Gilham & Ignacio Ibarra Cofrã. Kinematic analysis of sea cliff stability using UAV photogrammetry. International Journal of Remote Sensing, 38:2464–2479, 2017.

[10] Kelcey J and Lucieer A. Sensor correction of a 6-band multispectral imaging sensor for UAV remote sensing. Remote Sensing 4: 1462–1493, 2012.

[11] Khairul Nizam Tahar. Multi rotor UAV at different altitudes for slope mapping studies. The International Archives of the Photogrammetry, Remote Sensing and Spatial Information Sciences, XL-1/W4, 2015.

[12] Kuo-Lung Wang and Zhi-Jie Huang. Discover failure mechanism of a landslide dam using UAV. Proceedings of the 16th International Conference on Computing in Civil and Building Engineering (ICCCBE 2016). MOST 103-2625-M-260-001, 2016.

[13] Lucieer A, Turner D, King DH, et al. Using an Unmanned Aerial Vehicle (UAV) to capture microtopography of Antarctic moss beds. International Journal of Applied Earth Observation and Geoinformation. 27 (Part A): 53–62, 2014.

[14] Marinos, P. and Hoek, E. GSI: A geologically friendly tool for rock mass strength estimation: Proceedings, GeoEng 2000, Melbourne, Australia, 2000.

[15] Mariella Danzi, Giuseppe Di Crescenzo, Massimo Ramondini & Antonio Santo. Use of unmanned aerial vehicles (UAVs) for photogrammetric surveys in rockfall instability studies. Società Geologica Italiana, 2012.

[16] Niethammer U, James MR, Rothmund S, et al. UAV-based remote sensing of the Super-Sauze landslide:Evaluation and results. Engineering Geology 128: 2–11, 2012.

[17] Riccardo Salvini, Giovanni Mastrorocco, Marcello Seddaiu, Damiano Rossi and Claudio Vanneschi. The use of an unmanned aerial vehicle for fracture mapping within a marble quarry Carrara Italy photogrammetry and discrete fracture network modelling. Geomatics, Natural Hazards and Risk, 2016.

[18] Travelletti J, Delacourt C, Allemand P, et al. Correlation of multi-temporal ground-based optical images for landslide monitoring: Application, potential and limitations. ISPRS Journal of Photogrammetry and Remote Sensing 70: 39–55, 2012.

[19] Turner D, Lucieer A and Watson C. An automated technique for generating georectified mosaics from ultra-high resolution Unmanned Aerial Vehicle (UAV) imagery, based on Structure from Motion (SfM) point clouds. Remote Sensing 4: 1392–1410, 2012.

[20] Westoby M, Brasington J, Glasser N, et al. 'structure- from-motion' photogrammetry: A low-cost, effective tool for geoscience applications. Geomorphology 179: 300–314, 2012.

Factors Affecting Roadbed Subsidence in Mountain Area : Example of Kenanguan Section of Highway No. 14A

Meng-Chen Tsao[a], Rou-Fei Chen[b] and Tai-Tien Wang[a]

[a] Institute of Mineral Resources Engineering, National Taipei University of Technology, Taiwan
[b] Department of Geology, Chinese Culture University, Taiwan
E-mail: niko_cabi_money@hotmail.com, roufei@earth.sinica.edu.tw, taitienwang@gmail.com

Abstract –

Using the Kenanguan section of No. 14A Highway which zigzagged along the source mountain area of the Tacijili River as an example, through collecting the results of aerial photogrammetry, light detection and ranging and interferometric synthetic aperture radar technology, and analyzing the variation of topography and geomorphy to figure out that the service capability of highway and geotechnical facilities near the study area were affected by the shallow debris slide caused from headward erosion. Field investigation can find the geomorphological features of gravitational slope deformation and regional scale normal fault, such as reverse scarplets, multiple ridge, linear depressions and echeloned scarps. However, the influence extent of all factors still need more precise technique with monitoring to provide references to facilities management and maintenance.

Keywords –

Highway in Mountain, Roadbed Subsidence, Headward Erosion, Deep-seated Gravitational Slope Deformation

1 Introduction

Highway in mountain area is the main artery to connect two districts, so that the management and maintenance of the highway is more important. Several factors will affect the service capability of highway, including environmental factor (rock fall, headward erosion, gravitational deformation and geological structure process) and landslide factor (heavy rain and earthquake). Knowing the characteristic of different section, the stability of the road and the factors affect the service capability to provide important information of the maintenance management decision is the key issue about the mountain area highway respond accordingly to the modernization in sustainable development of infrastructure.

Kenanguan section of No. 14A Highway in central Taiwan is a highway which passed through the crest line formed by several mountain peaks in 3000 meters. Since 1980, roadbed drain and subsidence, retaining wall dislocation and pavement cleavage have occurred many times and caused roadbed be backfilled about 10 meters (Figure 1) so that the management and maintenance have suffered challenge. This paper is a case study of using multitemporal remote sensing images interpretation, digital terrain model production and field investigation to discuss the suspected factors affected the service capability of highway.

2 Study Area

The Kenanguan section of No. 14A Highway locates northwest of the Mt. Shimen, one of the Top 100 Mountains of Taiwan (mountain with its peak over 3,000 m in height), has an elevation of 3,200 m approximately. This section got its name in the middle of 1950s since the No. 14A Highway cut the ridge that connects the main peak (3,237 m) and the north peak (3,275 m) of Mt. Shimen(Figure 2) and formed a precipitous notch. The highway zigzagged along the source area of the Tacijili River, the upstream of Liwu River in eastern Taiwan, and has been reported with roadbed emptied, subsidence, retaining wall dislocation and pavement cracking since 2005. Thereafter, the roadbed has been backfilled more than 10 m to maintain a smooth vertical profile for the highway(Figure 1)

The Miocene Dayuling formation and Lushan formation are the major strata exposed. The former composes of slate, phyllite, metasandstone and marble, and the latter are mainly slate and the interbedded of slate and thin sandstone layer (Figure 3). Slate is the major lithology that exposes along the Kenanguan section of No. 14A Highway. The slate has its cleavage dip to southeast with dip angles of 36˚-66˚. The cleavage of the slate are obviously disturbed, resulted that the rock mass nearby are fractured. The Tacijili River suffers from headward erosion in evidence, with fault gauge exposed on its bare slope.

(a)

(b)

Figure 1. Photos about the (a)northern part and (b)southern part of the downhill slope at Kenanguan section. Multiple measures such as piles, retaining wall with anchors have been applied to mitigate the roadbed subsidence problem.

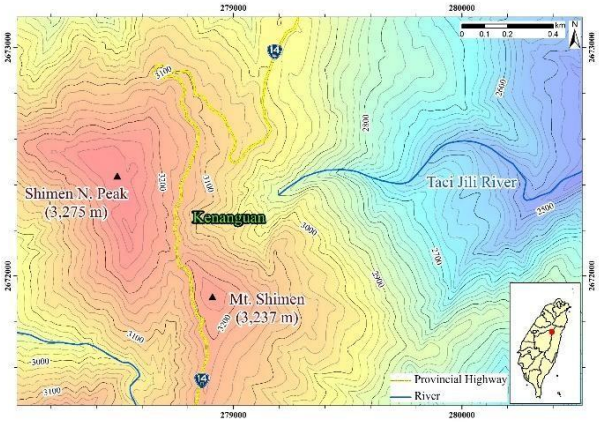

Figure 2. Effect of iron concentration on the amount of precipitate found during hydrolytic precipitation from waste processing solution

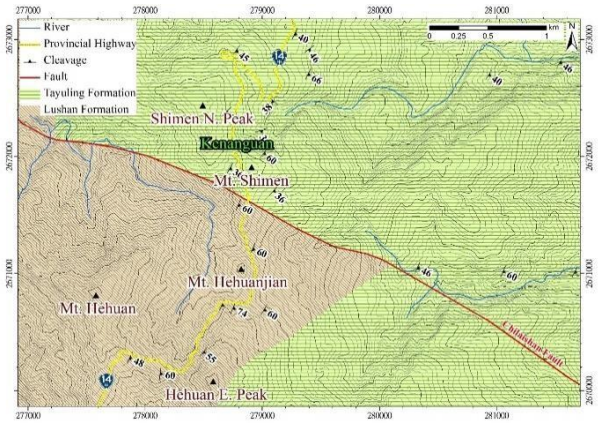

Figure 3. Geological map near Kenanguan area.

3 Investigation and Results

3.1 Aerial Photographs

Figure 4 shows that existed landslides and obvious headward erosion near the Kenanguan area can be interpreted from the aerial photo taken five years (1951) before the construction of the highway. The highway was built west of the top of the landslide area in 1956. In the subsequent decades the gullies nearby have strongly developed, and adjacent slopes have continued collapsed, forcing that the highway has to be moved westward to lease the roadbed lose problem.

In the 2014 aerial image several scarps can be interpreted nearby the north peak of the Mt. Shimen, which distribute along contours west of topographic ridge and cave in westward intermittently. Scarps and linear depressions that distribute echeloned are also interpreted east of the ridge with several reverse scarplets, seemed multi-ridges (Figure 5 and Figure 6).

(a)

(b)

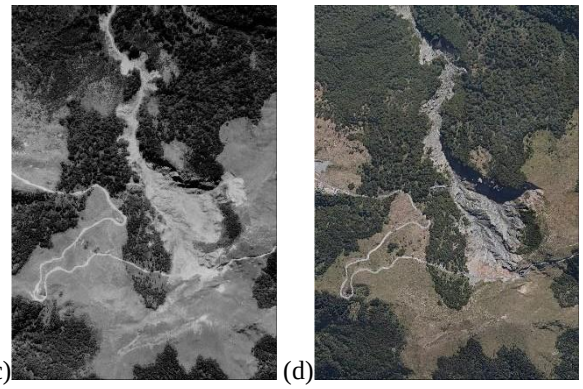

(c) (d)

Figure 4. Historical aerial photos/images taken in (a)1951, (b)1969, (c)1980 and (d)2014.

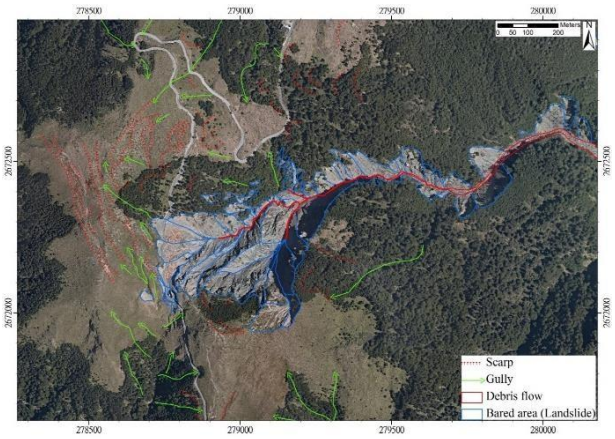

Figure 5. Interpreted scarps, gullies and landslides using aerial image taken in 2014. Note the scarps and linear depressions appear in both sides of the ridge near the north peak of Mt. Shimen.

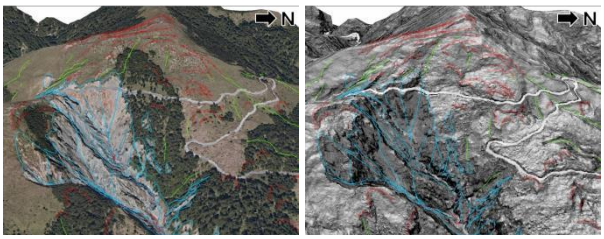

Figure 6. Three dimensional aerial view of the interpreted scarps, gullies and landslides near Kenanguan section. Digital elevation model are produced using point cloud scanned by air-bone based LiDAR (DEM by courtesy of the Fourth Maintenance Office, Directorate General of Highways).

3.2 Topographic Variation Revealed by DEM and TCP-InSAR

Digital elevation model are produced using temporal arieal photographies and point cloud scanned by air-bone based LiDAR. Temporarily Coherent Point SAR Interferometry (TCP-InSAR) technology is also utilized to determine the topographic variation near the study area.

Comparing with 1980, highway have been moved westwards about 10 meters in 2014. However, the scarp of the landslide has significantly developed upward and gone 50 m beyond the uphill (west) side of the highway. Results of DTM and TCP-InSAR analyses show that erosion and deposition let topography changed strongly and frequently. From 1980 to 2014, River was incised over 20 meters on the source of gully and deposited downstream over 10 meters. The site of highway in 1980 have already subsided and existed no more in 2014, the maximum of elevation difference between 1980 and 2014 was about 10 meters. The slope collapsed cliffs have a maximum elevation difference of 5 meters and become range-facing scarp, just like multiple ridge (Figure 7. Variation of elevation near Kenanguan area between 1980and 2014.

to Figure 9. Profiles in Figure 7 and Figure 8. Arrows in profiles (a) A-A' and (b) B-B' indicate locations where gullies and scrap are interpreted.).

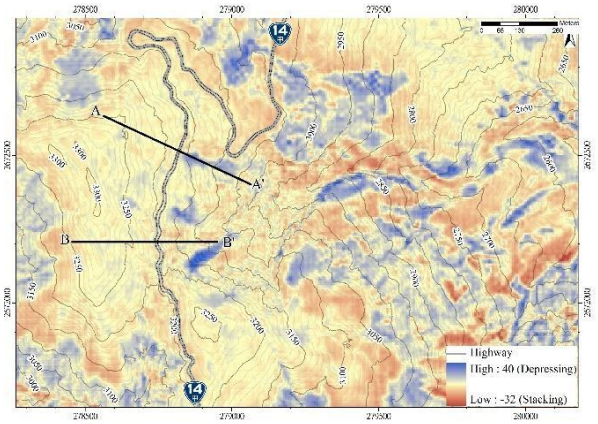

Figure 7. Variation of elevation near Kenanguan area between 1980and 2014.

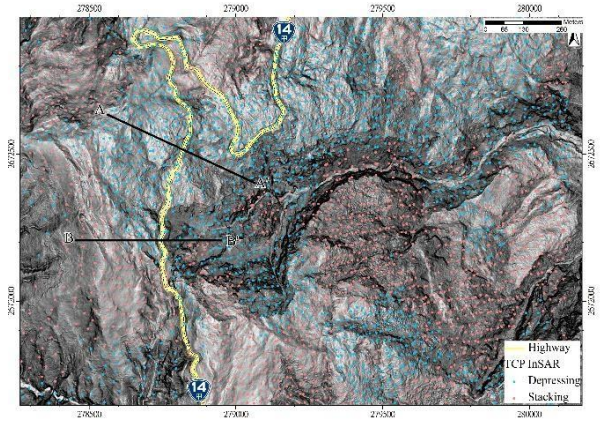

Figure 8. The surface displacement obtained from the TCP-InSAR solution from 2007 to 2011.

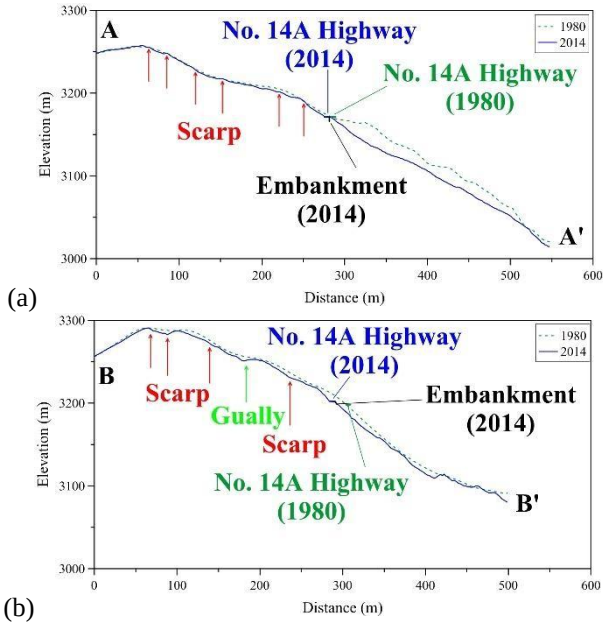

Figure 9. Profiles in Figure 7 and Figure 8. Arrows in profiles (a) A-A' and (b) B-B' indicate locations where gullies and scrap are interpreted.

3.3 Discussion

The headward erosion of the Tacijili River erodes the downhill slope of the highway, resulting in continuous debris avalanche of the slope and persistent deterioration of roadbed. The linear depressions and reverse scarplets (Figure 10 and Figure 11) in the uphill slope of the highway might reveal the signs for a gravitational slope deformation. And the echeloned scarps (Figure 12) in the vicinity of the north peak of Mt. Shimen looks as if one of the suspected topography of a regional scale normal fault. However, the possible influence of the latter two facts on the roadbed subsidence of the Kenanguan section remains unclear and needs further study.

Figure 10. The photo of linear depressions and reverse scarplets in the uphill slope.

Figure 11. The photo of reverse scarplets in the uphill slope near the north peak of Mt. Shimen. The Kenanguan section is located at the cove.

Figure 12. The photo of echeloned scarps in the vicinity of the north peak of Mt. Shimen.

4 Conclusion

This study analyzed the variation of topography and geomorphy near the Kenanguan section of No. 14A Highway by collecting the results of aerial photogrammetry, air-bone based LiDAR and TCP-InSAR technology. The study results show that the gullies near the study area develop strongly in last 35 years, the scarps expand to the top of slope more than 50 meters, the highway and geotechnical facilities nearby subside so that the backfilled is about 10 meters, and the main factor affected the service capability of highway is the shallow debris slide caused by the headward erosion. Field investigation can find the geomorphological features of gravitational slope deformation and regional scale normal fault, such as reverse scarplets, multiple ridge, linear depressions and echeloned scarps. However, the influence extent of all factors still need more precise technique with monitoring to provide references to facilities management and maintenance.

References

[1] Jaboyedoff, M., Oppikofer, T., Abellán, A., Derron, M.H., Loye, A., Metzger, R. and Pedrazzini, A. (2012). Use of LIDAR in landslide investigations: A review. Natural Hazards, 61, 5-28.

[2] Lillesand T., Kiefer, R.W. and Chipman, J. (2015). Remote sensing and image interpretation. 7th Edition, John Wiley & Sons.

[3] Zhang, L., Ding, X. and Lu, Z., (2011). Modeling PSInSAR time series without phase unwrapping. IEEE Transactions on Geoscience and Remote Sensing, 49(1), 547-556.

[4] Zhang, L., Lu, Z., Ding, X., Jung, H.-S., Feng, G. and Lee, C.-W., (2012). Mapping ground surface deformation using temporarily coherent point SAR interferometry : Application to Los Angeles Basin. Remote Sensing of Environment, Vol.117, 429-439.

[5] Lo, W., (1993). Geological map of Taiwan scale 1:50,000 – Tayuling. Published by Central Geological Survey.

Ground-Motion Simulation for Guiding Ground-Motion Prediction Equation Input Parameters Setting and Evaluation in PSHA

Y.T. Yen[a*], M.C. Hsieh[a], P.S. Lin[a] and S.Y. Chi[a]

[a]Disaster Prevention Technology Research Center, Sinotech Engineering Consultants, Inc., Taipei, Taiwan

E-mail: ytyen@sinotech.org.tw, mchsieh@sinotech.org.tw, person@sinotech.org.tw, sychi@sinotech.org.tw

Abstract

Ground-motion prediction equation (GMPE), which is an efficient way in predicting earthquake-induced ground motions by giving simple input parameters of source geometry, attenuation of wave propagation and specific site condition, is a key component and widely implemented in probabilistic seismic hazard analysis (PSHA) process. However, for the complex fault rupture cases like listric fault and insufficient information like the site is located at the subduction-zone edge, ground motion prediction by GMPE faces difficulties to set input parameters for implementing to seismic hazard analysis due to the simplification of input parameters. Fortunately, by introducing ground-motion-simulation techniques, complex source geometry and wave propagation in media can be physically modeled. Furthermore, overall characteristics of ground motion at a specific site of interest can also be delineated throughout multiple earthquake-scenario cases. In this study, we firstly present the application of ground-motion simulation to evaluate and adjust GMPE input parameters for the listric-fault case. Therefore, quantitatively comparing the resulting ground motions from GMPE prediction and simulated data is feasible for guiding the setting of input parameters for GMPEs. In addition to the evaluations of ground motion characterization of the listric-fault cases, retrieving the scaling relationship between along-rupture and off-end sites with respect to subduction-source fault geometry is also a rigorous issue for the use of subduction-zone type GMPEs in seismic hazard analysis. Our results show that simulated response spectra of the along-rupture sites reveal higher ground motions with respect to off-end sites in the subduction-zone case. A maximum reduction of ~14% and a mean reduction of ~10% can be found on the sites which are located off the end of the subduction zone.

Keywords –

ground motion simulation, listric fault, subduction zone, GMPE, PSHA

1 Introduction

In general, a comprehensively probabilistic seismic hazard analysis (PSHA) was utilized to develop the design specification of ground motion level (i.e. design spectrum, peak ground acceleration etc.) or understanding the seismic hazard for a specific site. A simplified flowchart shows the scheme of PSHA can be seen in Figure 1. Due to robustness and reliability of GMPE models as well as easy to implement. GMPEs are still a general tool for hazard analyses[1]. In PSHA, prediction of ground motion is a key component for the final hazard level. Handling the uncertainties of ground motion prediction by selecting and weighting GMPEs used in PSHA become a critical issue.

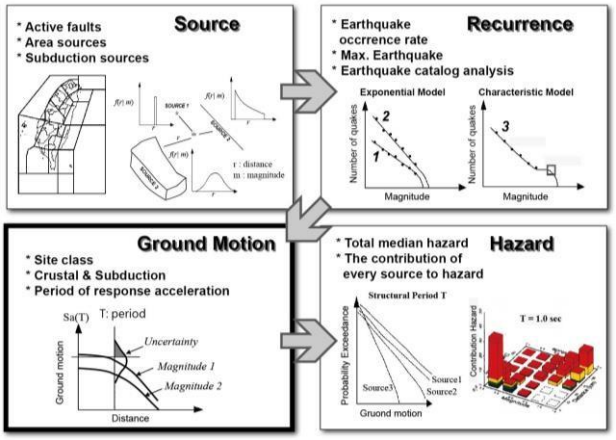

Figure 1. Flow chart of probabilistic seismic hazard analysis.

The "Seismic Reevaluation of Nuclear Facilities" project launched by Taiwan Power Company (TPC) in Taiwan follows the Level 3 study defined by Senior

Seismic Hazard Analysis Committee (SSHAC Level 3)[2] for seismic hazard assessment. The Ground Motion Characterization (GMC) shall be built with Technical Defensible Interpretation (TDI) and documented with foreign and local GMPEs in the SSHAC Level 3 project scope. The results from ground motion simulations are supplemented for the evaluation and integration of final logic tree establishment.

Applications to adjust GMPE input parameters and add additional adjustment of prediction ground motion from performing ground motion simulations are described in this study. In general, GMPE is suitable for the use of evaluating ground motions from fault sources having single dipping angle in the seismic hazard analysis panel. However, for complex fault rupture cases of listric fault that having at least two dipping angles, ground motion prediction by GMPE faces difficulties to be implemented to seismic hazard analysis due to the nature of the functional form. Therefore, comparing the resulting ground motions from GMPE prediction and simulated data is a sufficient way for adjusting the use of GMPE in seismic hazard analysis. In addition to the listric-fault case, retrieving the scaling relationship between along-rupture and off-end sites with respect to subduction-source fault geometry is also a rigorous issue for the use of subduction-zone-type GMPE in seismic hazard analysis. Thus, in this study, applications of ground motion simulation are described for two objectives: (1) exploring the applicability of GMPEs for listric faulting; and (2) evaluating the difference of ground motion level at sites off the end of subduction zone.

2 Application of ground motion simulation for adjusting GMPEs

2.1 Ground motion simulation method of EXSIM

In this study, we selected EXSIM for ground motion simulation. EXSIM is a stochastic-based finite-fault simulation algorithm (e.g. [3]) that accounts for site amplification function and generates time histories for earthquakes. In EXSIM, a fault plane defined, having a specified size according to its seismic moment, is divided into a matrix of subsources, each of which is treated as a point source. Time series from the subsources are modeled using the point-source stochastic model. The ground motion from each subsource is treated as the random Gaussian noise of a specified duration, having an underlying spectrum as given by Brune point-source model for shear radiation. The Brune model specifies the Fourier spectrum at the source by seismic moment and stress parameter and is attenuated in the frequency domain according to an empirical attenuation model. The time series from the subsources are summed in the time domain, with appropriate time delays for the propagation of the rupture front. EXSIM is a representative stochastic ground motion simulation method, and it has been verified by Southern California Earthquake Center (SCEC) and validated by crustal and subduction-zone earthquakes.

For a given fault geometry, rupture models were generated by a number of random slip distributions, each of them was treated as an individual realization of simulation. The regional shear wave velocity was set to 3.7 km/s. The rupture velocity was assumed to 2.96 km/s (80% of the shear wave velocity). The stress drop was assumed to 150 bars. These parameters were common parameters having not been adjusted for the regional difference. If the regional difference is considered, a stochastic model of the region of interest for ground motion simulation should be developed. Thus, we took the ratio of ground level between two simulation cases to be the index for adjusting GMPE input parameters.

2.2 Applicability of GMPEs for listric fault

According to geological survey, well logging, and seismic profiles, the fault geometries of Shanchiao Fault structure in northern Taiwan are delineated and have two dipping angles, namely the listric-fault system, and several combinations of dipping angle and fault width are recommended to be considered in ground motion prediction with respect to uncertainty of seismogenic depth in northern Taiwan. According to the prescribed fault geometry, sites for analyzing are located on the hanging wall. We further focused on the major hazard contribution of the major fault with respect to study sites. Henceforth, ground motion evaluation of listric-fault case at the site 5 km away from the fault source was delicately operated for the use of GMPEs in seismic hazard analysis.

We selected the upper segment with its dipping angle of the Shanchiao Fault as a reference case (shown in Figure 2, Ref. case), and a two-dipping-angle fault model was proposed as a control case. The scaling relationship derived from the reference and the control cases were able to evaluate whether GMPE can be used in calculating reasonable ground motions from listric faults. In Figure 2, cases of A1, A2 and A3 are fault models having (1) a dipping angle from the upper segment; (2) a dipping angle from the lower segment; (3) a dipping angle from averaging dips of the upper and lower segments, and applied to GMPEs. Each individual case was taken as an approach for GMPE. Therefore, Approaches 1, 2 and 3 were for cases A1, A2, and A3,

respectively. Furthermore, according to the SWUS (Southwestern United States) Project[4], the SRSS(Square Root of the Sum of the Squares) approach was also used, and the resulting response spectra from the upper and lower portions were used to compute a single response spectrum (Case D).

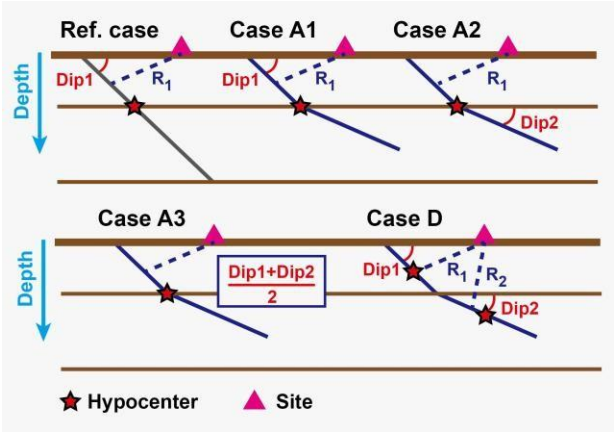

Figure 2. Schematic diagram of listric-fault models for simulation

A total of 30 ground motion realizations of each case were carried out for fault models with (1) two dipping angles of the upper and lower segments and (2) a single dipping angle of the upper segment. An averaged response spectrum was calculated by the 30 realizations. The scaling relationship was determined by calculating spectral ratios of two-dipping-angle and single-dipping-angle cases, i.e. simulation/simulation_ref, shown in Figure 3. For the calculation of response spectrum, we used the approaches of 1, 2 and 3 and the SRSS approach for cases A1, A2, A3, and D, respectively. Thus, spectra from the 4 approaches were compared with simulated spectra in order to determine an appropriate GMPE input parameters for ground motion prediction in the sense of listric-fault.

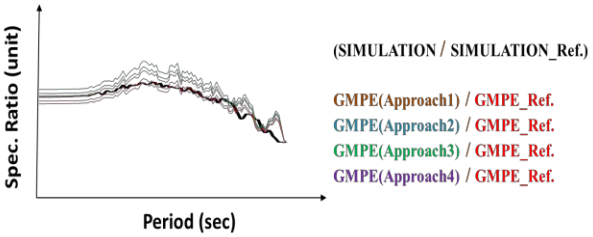

Figure 3. Example of comparison between simulated and GMPE-predicted ratio of mean response spectra

Schematic plot of listric-fault cases which practically implemented in simulation analyses is shown in Figure 4. Two dipping angles of 60° and 70° of the upper segment and a single dipping angle of 25° of the lower segment were proposed. Furthermore, three seismogenic depths of 10, 15 and 20 km were also considered for ground motion simulations. Thus, a total of 6 groups for ground motion simulation were proposed and displayed in Table 1: M(70,25,10), M(70,25,15), M(70,25,20), M(60,25,10), M(60,25,15) and M(60,25,20) (the first two variables of each bracket represent dipping angles; and the rest one is for seismogenic depth). We selected 4 GMPEs, which accounted for fault-dip in their functional forms, from the NGA-West2 Project [5]: ASK14 [6], BSSA14 [7], CB14 [8] and CY14 [9].

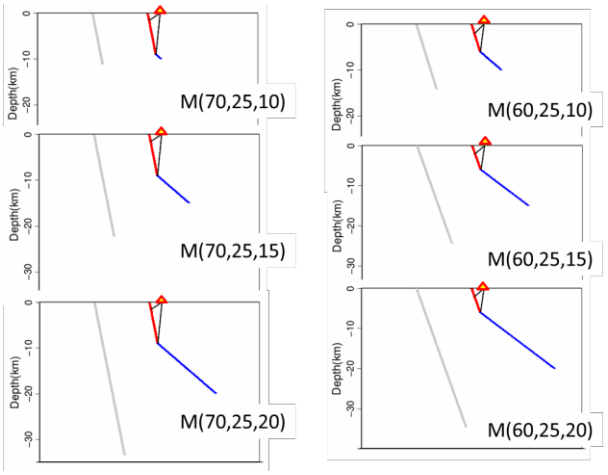

Figure 4. Cases of listric faults for ground motion simulation. The triangles represent the fictitious station, and grey lines are for the reference case. Red and blue lines show the upper and lower segments of the listric-fault model, respectively.

Table 1. Magnitude list for cases of listric fault model

Seismogenic Depth (km)	Ref. Case (Mw)	Shallow segment (Mw)	Deep segment (Mw)
Model for combination of 70 degree/ 25 degree			
10	6.68	6.68	6.07
15	6.95	6.68	6.85
20	7.14	6.68	7.11
Model for combination of 60 degree/ 25 degree			
10	6.78	6.54	6.68
15	7.04	6.54	7.03
20	7.21	6.54	7.22

Figure 5 is an example indicating spectral ratios of M(70,25,10) case. The results are categorized into two groups according to dipping-angle pairs. Our results show that the M(70,25,10) case, which has a magnitude difference larger than 0.5 from the upper and lower segments, has a better agreement with GMPEs using the dip of upper segments. For cases of M(70,25,15) and

M(70,25,20), of which turning depths are deeper (> 9 km) and have larger magnitudes of lower segments, the use of averaged dips from upper and lower segments to GMPEs displays better fittings. Furthermore, for cases of M(60,25,10), M(60,25,15) and M(60,25,20), of which turning depths are shallower (< 9 km) and have larger magnitudes of lower segments, the use of dips from lower segments to GMPEs displays better fittings. The R_{jb} based GMPE of BSSA14 is not suitable for ground motion simulation of listric faults from these comparisons.

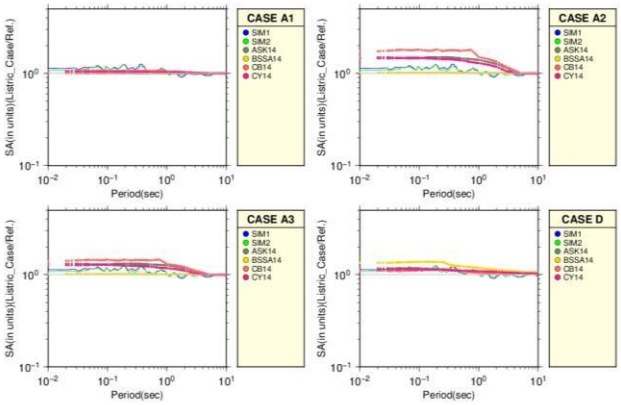

Figure 5. Comparison between simulated and GMPE-predicted response spectra of the M(70,25,10) case

2.3 Edge effect from off-end subduction-zone earthquakes in large magnitude

In order to discuss the off-end ground motion factor for subduction-zone-earthquakes in large magnitude to study sites (Coded to be as NPP1, NPP2, and NPP4), we considered the megathrust case of Ryukyu Trench. The fault length (F_L) and width (F_W) were assumed to 190 and 56 km, the upper and bottom depths of fault plane were set to 8 and 30 km, and the dipping angle was set to 25°. By the setting of geometry, the resulting moment magnitude was 8.0. To consider different locations for hypocenter, we divided the fault plane along the strike direction into four equal parts, and three hypocenters are assumed at 1/4, 1/2, 3/4 of F_L, and 1/2 of F_W. Rupture distance (R_{RUP}) was calculated according to the presumed fault plane to a certain NPP site. Therefore, R_{RUP} were 74.5, 63.9, 303.4 and 38.5 km for NPP1, NPP2, NPP3, and NPP4, respectively. For each site, a total of 13 fictitious stations were assumed. R_{RUP} for these fictitious stations were equal to the R_{RUP} from a specific NPP to the fault plane. Among the 13 fictitious stations, 11 stations were equidistantly distributed along R_Y direction, and all R_X were equal. The other two stations were located at (R_X, F_L+R_X) and (R_X, -R_X). Thus, these fictitious stations were used to calculated spectral acceleration ratio for a specific NPP site to evaluate the edge effect of the subduction zone. Figure 6 shows the presumed fault geometry and station distribution in this section. As previously described, 30 stochastic simulations were performed at each hypocenter, so a total of 90 stochastic simulations were performed and used to calculated average response spectrum for NPP (Nuclear power plant) sites and fictitious stations. Figure 7 are the comparisons on average response spectrum for NPP4 and fictitious stations (blue lines are for NPP sites; gray lines are for fictitious stations). The results show that the spectral accelerations for all NPP sites are smaller than the fictitious stations for all period samples.

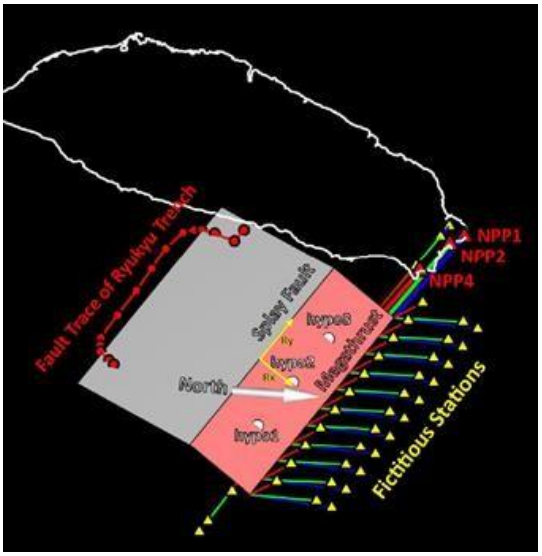

Figure 6. Fault geometry and station distribution for discussing edge effect of subduction zone

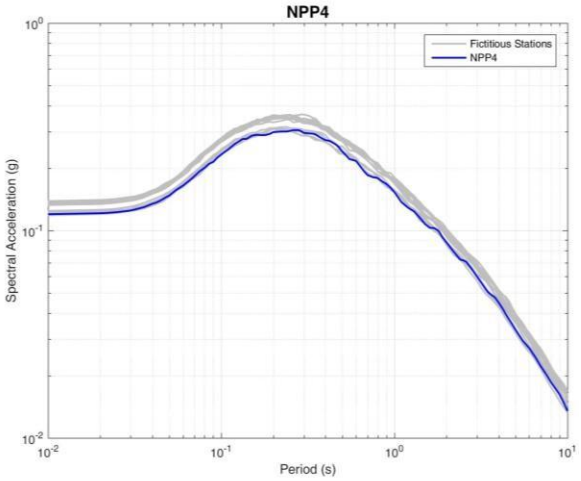

Figure 7. Averaged response spectra for NPP4

In order to quantitatively compare the difference of SA(acceleration spectrum) at different periods, the SA

ratio at each period between a specific site and one of its corresponding fictitious stations is computed by

$$SpectralRatio_j(T_i) = \frac{RSP^{mean}_{NPPsite}(T_i)}{RSP^{mean}_{j^{th}station}(T_i)} \quad (1)$$

where i is the ith period sample and j is the jth fictitious station. The results are shown in Figure 8. The variation of SA ratios is small in shorter period range (about 0.01 to 0.2 s) whereas the variation is large in longer period range (about 0.2 to 10 s). Generally, the SA ratios are from 0.86 to 0.97 indicating that the NPP sites located at the edge of subduction zone have smaller SA values than stations are distributed along rupture. Furthermore, the average ratios of NPP1, NPP2, and NPP4 are 0.89, 0.91 and 0.91, respectively.

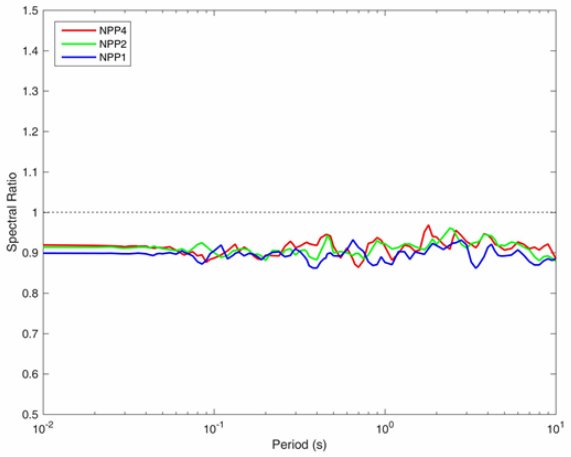

Figure 8. Spectral ratios of NPP1, NPP2, and NPP4.

The comparison between the simulation results and subduction-type GMPEs are also addressed. A total of 6 subduction-type GMPEs for rock site were used in the comparison: LL08 [10], BC HydroSubV3 [11], Gregor06 [12], Kanno06 [13], Youngs97 [14] and AB03Haz [15]. An example of NPP4 is shown in Figure 9. All the GMPEs at three analyzed sites show quite consistent characteristics. The SA predictions of LL08 show good agreement in shorter period range. However, the predictions in the longer period are slightly smaller than the simulation results, and the discrepancy is larger as the period is longer. These characteristics can also be seen in Youngs97 and AB03Haz ground motion models. The ground motion predictions from BC HydroSubV3 are larger than the simulated values for periods less than 2 s, but the predictions for a longer period (>2 s) are quite smaller than the simulated values. For Gregor06 and Kanno06, the predictions are larger than the simulated values for all periods.

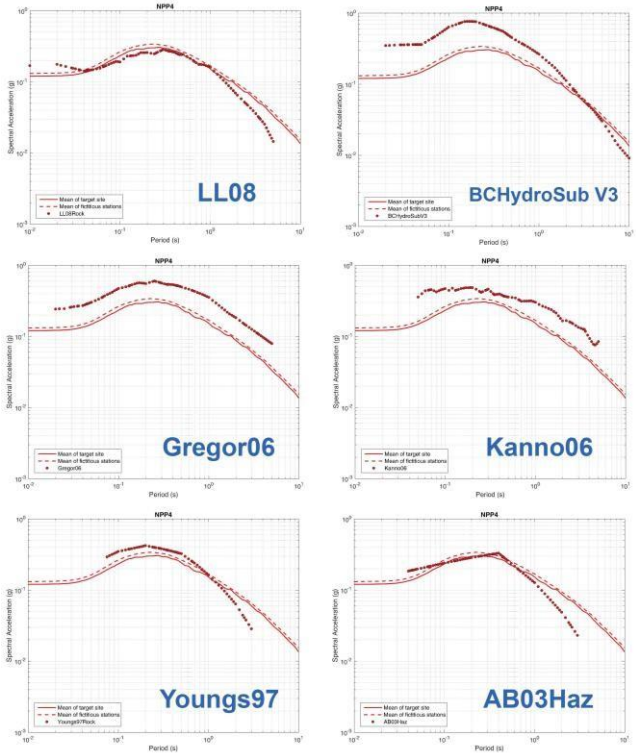

Figure 9. Response spectrum comparisons between subduction-zone-type-GMPE predictions and simulation results (NPP4).

3 Discussion and conclusion

Physics-based ground motion simulation is a powerfully alternative way to help to figure out what trend of ground motion is when we have no enough data to identify how large of ground motion is. However, due to a lack of high resolution of velocity structure and site factor for correction of ground motion simulation, we can not precisely capture the minimum uncertainty range. We thus adopt the relative value to express the correction factor of ground motion. Usually, it is very useful for the extended applicability of simulation. For instance, in this study, we have dealt with the problem of correction of ground motion level for listric fault and edge fact of subduction zone source.

We carried out ground motion simulations to justify GMPEs for the uses of seismic hazard assessment. Two important issues of (1) implementation of listric-fault to GMPEs and (2) edge effect from off-end subduction-zone earthquakes in large magnitude are addressed.

In summary, for listric-fault cases, the following items are suggestions for implementing and adjusting GMPEs in the seismic hazard analysis panel.

1. A single dipping angle of the upper segment can be implemented to GMPEs for listric-fault cases, of which magnitude of upper segment is larger and the

magnitude difference is larger than 0.5.

2. An averaged dipping angle from upper and lower segments can be implemented to GMPEs for listric-fault cases, of which magnitude of lower segment is larger and turning depth is deeper (> 9 km).

3. A single dipping angle of the lower segment can be implemented to GMPEs for listric-fault cases, of which magnitude of lower segment is larger and turning depth is shallower (< 9 km).

4. GMPEs, which are independent of dipping angle or account for R_{jb} distance in their functional forms, might not be applied to listric-fault cases.

For the edge effect subduction-zone, simulated response spectra of the fictitious stations show higher ground motions with respect to all NPP sites. A maximum reduction of ~14% and a mean reduction of ~10% can be found for NPP sites which are located off the end of the subduction zone. The comparison between the simulation results and subduction-type GMPEs are also addressed for identifying for these specified GMPEs in order to discuss how to evaluate the large discrepancies between GMPEs for subduction-zone earthquakes.

Due to the significant improvements in techniques, knowledge, experience and computing power, physics-based ground motion simulation methods can provide time-histories, ground motion value (peak ground acceleration, velocity, displacement) and response spectra which are necessary for studies requiring engineering analyses. However, GMPEs are still a useful and easy tool for ground motion prediction and hazard analysis. An alternative way to balance the advantage and disadvantage of both of empirical and theoretical methods can contribute to achieving efficient implementation in practical projects.

References

[1] Douglas J. and Edwards B. Recent and future developments in earthquake ground motion estimation. *Earth-Science Reviews*, 160, 203-219, 2016.

[2] U.S. NRC. *Practical Implementation Guidelines for SSHAC Level 3 and 4 Hazard Studies: Washington D.C.*, US Nuclear Regulatory Commission, NUREG 2117, 2012.

[3] Atkinson G. M and Assatourians K. Implementation and validation of EXSIM (a stochastic finite-fault ground-motion simulation algorithm) on the SCEC broadband platform. *Seismological Research Letters*, 86(1):48–60, doi: 10.1785/0220140097, 2015.

[4] GeoPantech Southwestern United States Ground Motion Characterization SSHAC Level 3, Technical Report, Rev. 2., 2015.

[5] Bozorgnia Y., Abrahamson N. A., Atik, L. A., Ancheta T. D., Atkinson G. M., Baker J. W., Baltay A., Boore D. M., Campbell K. W., Chiou B. S. J., Darragh R., Day S., Donahue J., Graves R. W., Gregor N., Hanks T., Idriss I. M., Kamai R., Kishida T., Kottke A., Mahin S. A., Rezaeian S., Rowshandel B., Seyhan E., Shahi S., Shantz T., Silva W., Spudich P., Stewart J. P., Watson-Lamprey J., Wooddell K., and Youngs R. NGA-West 2 research project, *Earthquake Spectra*, 30: 973–987, 2014.

[6] Abrahamson N. A., Silva W. J., and Kamai R. Summary of the AKS14 ground-motion relation for active crustal regions. *Earthquake Spectra*, 30(3):1025–1055, doi: 10.1193/070913EQS198M, 2014.

[7] Boore D. M., Stewart J. P., Seyhan E., and Atkinson G. M. NGA-West 2 equations for predicting PGA, PGV, and 5%-damped PSA for shallow crustal earthquakes. *Earthquake Spectra*, 30(3):1057–1085, doi: 10.1193/070113EQS184M, 2014.

[8] Chiou B. S. J. and Youngs R. R. Update of the Chiou and Youngs NGA model for the average horizontal component of peak ground motion and response spectra, *Earthquake Spectra*, 30(3):1117–1153, doi: 10.1193/072813EQS219M, 2014.

[9] Campbell K. W. and Bozorgnia Y. NGA-West2 ground motion model for the average horizontal components of PGA, PGV, and 5%-damped linear acceleration response spectra, *Earthquake Spectra*, 30(3): 1087–1115, doi: 10.1193/062913EQS175M, 2014.

[10] Lin P. and Lee C. Ground-motion attenuation relationships for subduction-zone earthquakes in northeastern Taiwan, *Bulletin of the Seismological Society of America*, 98(1):220–240, doi:10.1785/0120060002, 2008.

[11] BC Hydro. *Probabilistic seismic hazard analysis (PSHA) model: ground motion characterization (GMC) model*. British Columbia Hydro and Power Authority, BC Hydro Report No. E658(3), British Columbia (B.C.), Canada, 2012.

[12] Gregor N., Silva W., Wong I., and Youngs R. Updated response spectral attenuation relationship for Cascadia subduction zone megathrust earthquake, *Seismological Research Letters*, 77(2):325–326, 2006.

[13] Kanno T., Narita A., Morikawa N., Fujiwara H., and Fukushima Y. A new attenuation relation for strong ground motion in Japan based on recorded data, *Bulletin of the Seismological Society of America*, 96(3): 879–897, doi:10.1785/ 0120050138, 2006.

[14] Youngs R., Chiou S. J., Silva W. J., and Humphrey J. R. Strong ground motion attenuation

relationships for subduction zone earthquakes. Seismological Research Letters, 68(1):58–73, doi:10.1785/gssrl.68.1.58, 1997.

[15] Atkinson G. and Boore D. M. Empirical ground-motion relations for subduction-zone earthquakes and their application to Cascadia and other regions, *Bulletin of the Seismological Society of America*, 93(4):1703–1729, 2003.

Predictive susceptibility analysis of typhoon induced landslides in Central Taiwan

Keh-Jian Shou[a] and Zora Lin[a]

[a]Department of Civil Engineering, National Chung-Hsing University, Taiwan
E-mail: kjshou@dragon.nchu.edu.tw, zoradcrc@gmail.com

Abstract

Climate change caused by global warming affects Taiwan significantly for the past decade. The increasing frequency of extreme rainfall events, in which concentrated and intensive rainfalls generally cause geohazards including landslides and debris flows. The extraordinary, such as 2004 Mindulle and 2009 Morakot, hit Taiwan and induced serious flooding and landslides.

This study employs rainfall frequency analysis together with the atmospheric general circulation model (AGCM) downscaling estimation to understand the temporal rainfall trends, distributions, and intensities in the adopted Wu River watershed in Central Taiwan. To assess the spatial hazard of the landslides, landslide susceptibility analysis was also applied. Different types of rainfall factors were tested in the susceptibility models for a better accuracy. In addition, the routes of typhoons were also considered in the predictive analysis. The results of predictive analysis can be applied for risk prevention and management in the study area.

Keywords –

Landslide hazard; Climate change; Mountain highway, Landslide susceptibility

1 Introduction

The climate change affects Taiwan significantly by an increasing frequency of extreme rainfall events, in which induced large scale landslides. Considering the existence of various types of large scale landslides and the protection targets, this study aims to analyze the landslide susceptibility along the Nantou County Road # 89 of Taiwan (see Fig.1). For the predictive analysis of landslide susceptibility, this study employed AGCM downscaling estimation. For the adopted large scale landslides (see Fig. 2), based on the information from boreholes, the temporal behavior and the complex mechanism of large scale landslides were analyzed in local scale. Based on the results, the pros and cons of the analysis in both scale were discussed, which could be applied for the risk assessment and management.

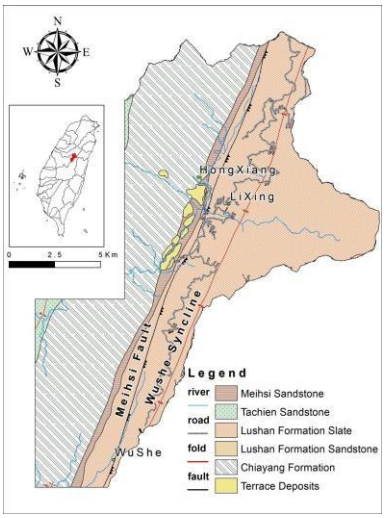

Figure 1. Geology of the study area

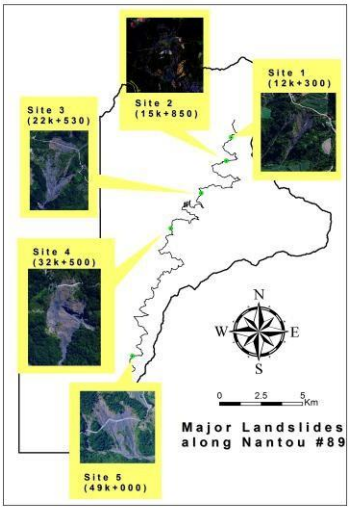

Figure 2. Large landslide along the Nantou County Road # 89

2 Methodologies

Landslide inventories, SPOT satellite images, borehole data were collected in the study area, including 5 major deep-seated landslides along the County Road #89. In addition, mobile laser ranging was performed along the road to obtain the 0.1 LiDAR data. The obtain information and data were used for the shallow and deep-seated landslides in different scale.

2.1 Landslides intepretation

This study adopts the NDVI-slope angel criterion, in which the normalized differential vegetation index (NDVI) is from satellite images and the slope angle is from digital elevation model (DEM). And improving the accuracy of landslide identification in shadow areas with different screening indexes, including brightness (BRI, Hsieh et al 2011), greenness (GI, Liu et al 2012; Lin et al 2013), and vegetation mask (Beumier and Idrissa 2014). The compare of landslides interpretation in different indexes as Table 1. A1 is the number of landslide cells interpreted as landslide, A3 is the number of landslide cells not interpreted as landslide, A2 is the number of non-landslide cells interpreted as non-landslide, A4 is the number of non-landslide cells interpreted as landslide.

Table 1. Comparison of the Criteria for Automatic Landslide Interpretation.

Criterion	Accuracy of Landslide Cells A1/ (A1+A3)	Accuracy of Non-landslide Cells A4/ (A2+A4)	Accuracy of Total Cells (A1+A4)/ (A1+A2+ A3+A4)
Slope=20%, NDVI=0, BRI=40	6.60	99.63	98.49
Slope=20%, NDVI=0, GI=0.25	7.11	99.62	98.49
Slope=20%, NDVI=0.2	21.02	97.79	96.86
Slope=20%, NDVI=0.2, BRI=40	18.81	97.87	96.90
Slope=20%, NDVI=0.2, GI=0.25	20.40	97.92	97.00
Slope=20%, NDVI=0.2, BRI=60	7.04	98.46	97.34

2.2 Landslide-rainfall index (Id)

For a specific typhoon event, by the overlapping function of GIS, the accumulated rainfall and rainfall intensity data at the landslide locations can be extracted and plotted in graph of accumulated rainfall and rainfall intensity (see Fig. 3).The landslide-rainfall index (Id) is defined by the distances d1 and d2 from the unknown point to the linear thresholds as d2/(d1+d2) (Shou et al, 2015).

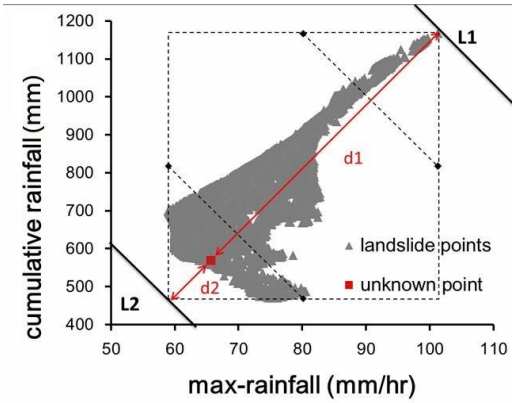

Figure 3. The landslide-rainfall index (Id) is defined as d2/(d1+d2).

It ranges between 0 and 1. As Id approaches 1, the slope becomes increasingly susceptible to rainfall-induced landslide. On the contrary, as the point of the rainfall of potential landslide approaches the lower threshold, or as Id approaches 0, the slope becomes less susceptible to landslide.

2.3 Landslide susceptibility models

This study adopts the In Logistic Regression Method for the landslide susceptibility analysis. Its performance was compared for the analyses of 2004 Mindulle, 2009 Morakot, and 2012 Saola. Based on the training samples, which comprised a group of data points or data locations, categorized as landslide and non-landslide. The data layer of each factor was then placed upon the landslide and non-landslide layers, and the correlation between each factor and landslides was used to conduct binary logistic regression. For the susceptibility model obtained by logistic regression, this study employed the eceiver operating characteristic (ROC) curve (Swets 1988), in which the area under the curve (AUC) of the ROC curve was used to evaluate the prediction accuracy. Generally, the larger the AUC values the better. As the area approaches 0.5, the result may not necessarily be superior to that of a random selection. AUC values of less than 0.5 are not worth employing.

3 Landslide Susceptibility Analysis

This study adopts the Logistic Regression Method for the landslide susceptibility analysis. The model based on 2004 Mindulle can be expressed as

$$P=0.663F1+0.055F2-0.317F3-0.062F4-0.301F5-0.216F6-0.093F7+0.081F8-2.451F9+0.295 \quad (1)$$

where P is the logistic function, F1 is the slope angle, F2 is the elevation, F3 is the aspect, F4 is the distance to fault, F5 is the distance to river, F6 is the distance to road, F7 is the dip slope index (Ids), F8 is the landslide-rainfall index (Id), and F9 is the normalized differential

vegetation index (NDVI). Eq. (1) can be used to calculate the landslide susceptibility based on the predicted rainfalls, including various extreme weather scenarios as below.

By using Eq. (1), we can estimate the landslide susceptibility of 2009 Morakot and 2012 Saola based on their specific rainfalls. The ROC curves for these estimations shows the AUC values are 0.806 for 2009 Morakot and 0.717 for 2012 Saola, which also reveal an acceptable performance of the 2004 Mindulle model.

For the predictive analysis, the rainfall in the future was estimated by the climate change model introduced as below. The Taiwan Climate Change Projection and Information Platform Project (TCCIP), analyzes the results from the assessment reports of the United Nations Intergovernmental Panel on Climate Change (IPCC), results of 2004Mindulle and Top1 Typhoon show as Figs. 4~5, and compare of cells number as Table 2.

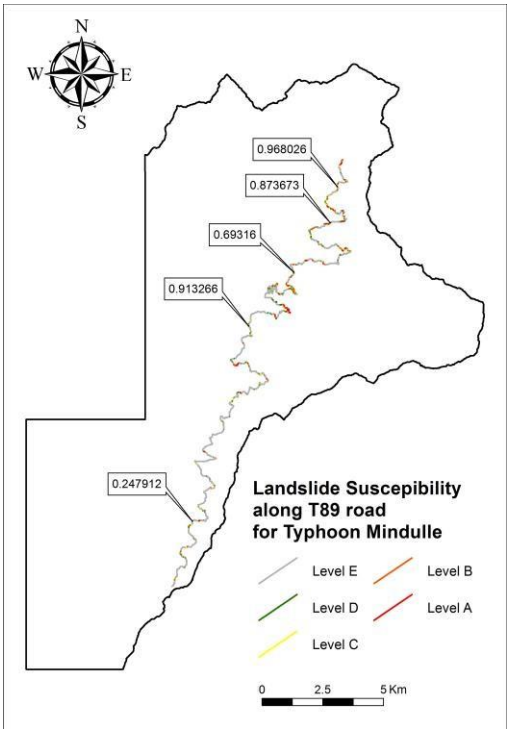

Figure 4. The landslide susceptibility along Nantou County Road #89 estimated by 2004 Mindulle model

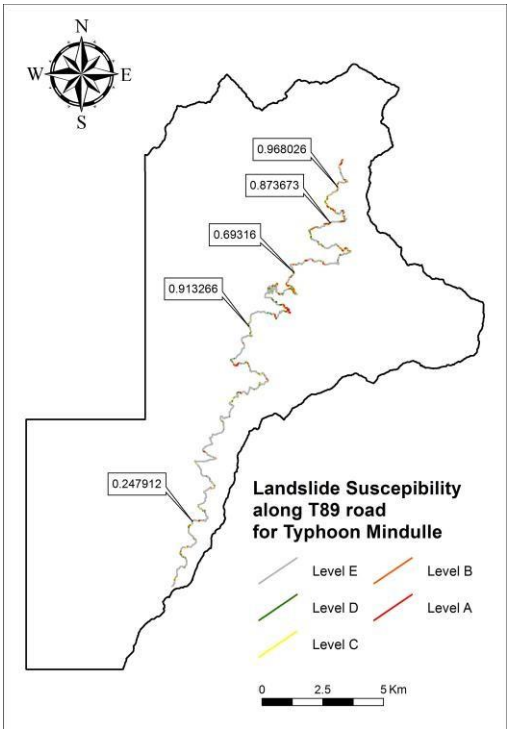

Figure 5. The landslide susceptibility along Nantou County Road #89 estimated by the TCCIP Top1 Typhoon

Table 2 Comparison of the Landslide Susceptibility and Risk Ranking of the Large Scale Landslides

Site	Mindulle Landslide Susceptibility		Predict Top1 Typhoon(2075-2099) Landslide Susceptibility	
	Value	Ranking	Value	Ranking
12k+300	0.968026	1	0.966557	1
15k+850	0.873673	3	0.8683	3
22k+530	0.69316	4	0.688009	4
32k+500	0.913266	2	0.914724	2
49k+000	0.247912	5	0.271284	5

4 Analysis of Major Large Scale Landslides

For the adopted large scale landslides (see Fig. 2), based on the information from boreholes, the temporal behavior and the complex mechanism of large scale landslides were analyzed in local scale. Fig. 6 shows locations of the 5 studied major profile. In this study, the limit equilibrium analyses software Slide 6.0 (Rocscience 2015) was applied.

In the analyses, three types of geo-material were assumed, i.e., highly weathered slate in the boundary

layer, medium weathered slate in the middle layer, and fresh slate in the bottom. Their material properties were determined based on the report of exploration (Xie-Sheng Engineering Consulting, 2014). For a better comparison, this study considered three different groundwater conditions, i.e., dry (no groundwater), 1/2 ground water level, and full ground water level. The results of equilibrium analyses were summarized in Table 3.

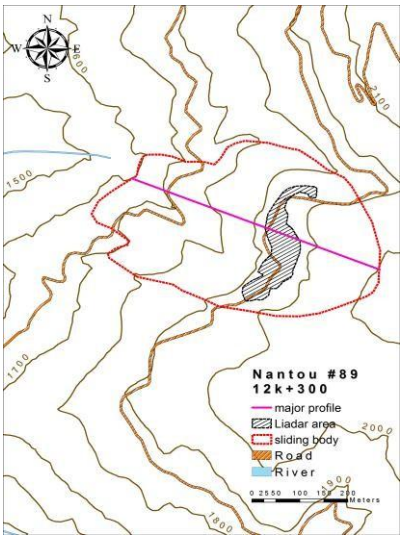

Figure 6. The profiles of the large scale landslides (a) 12k+300

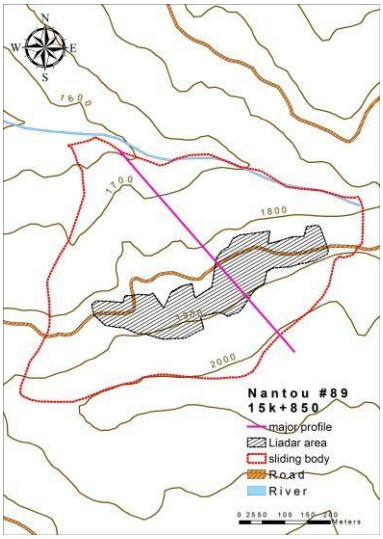

Figure 6. The profiles of the large scale landslides (b) 15k+850

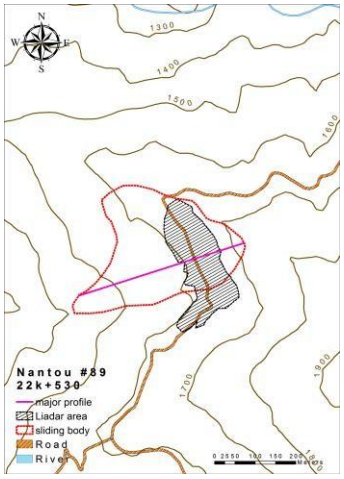

Figure 6. The profiles of the large scale landslides (c) 22k+530

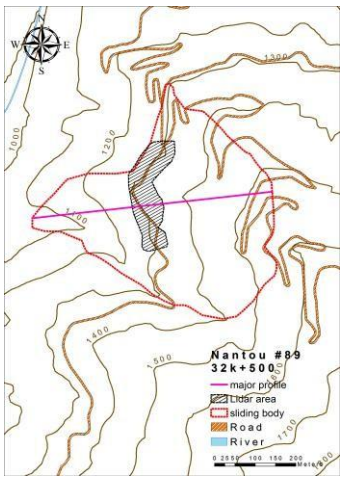

Figure 6. The profiles of the large scale landslides (d) 32k+500

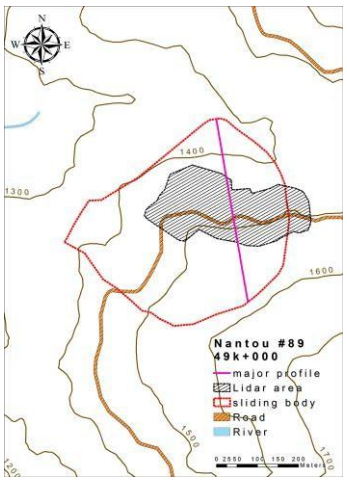

Figure 6. The profiles of the large scale

landslides (e) 49k+000

Table 3. Comparison of the Safety Factors and Risk Ranking of the Large Scale Landslides

Site	No Groundwater		1/2 Groundwater		Full Groundwater	
	FS,min	Rank	FS,min	Rank	FS,min	Rank
12k+300	0.700 (toe)	2	0.594 (toe)	2	0.456 (toe)	2
15k+850	0.659 (whole)	1	0.539 (head)	1	0.384 (head)	1
22k+530	1.058 (head)	4	0.841 (head)	4	0.577 (head)	3
32k+500	1.082 (middle)	5	0.877 (middle)	5	0.61 (middle)	5
49k+000	0.978 (whole)	3	0.796 (whole)	3	0.603 (whole)	4

5 Conclusion

In this study, rainfall frequency analysis and the atmospheric general circulation model (AGCM) downscaling estimation were applied to understand the temporal rainfall trends and distributions in the study area. The susceptibility analysis in catchment scale and local scale were performed for the hazard assessment of the mountain highway, i.e., Nantou County Road # 89 in Central Taiwan. The hazard of the major landslides can be ranked to prioritize the hazard mitigation. It is worth noting that the results of local scale analysis also suggest a similar hazard ranking of these landslides, i.e. the sites 15k+850 and 12k+300 are the most dangerous.

6 Acknowledgements

This research was made possible by the financial support of the National Science Council (Project No. 102-2625-M-005-001-MY2) of Taiwan. We also deeply appreciate the databases and support from the research groups conducting the Central Geological Survey project (Project No. 97-5826901000-05).

References

[1] Beumier, C. and Idrissa, M. Building detection with multi-view colour infrared imagery. EARSeL eProceedings 13:77-84, 2014.

[2] Hsieh, Y.T., Wu, S.T., Liao, C.S., Yui, Y.G., Chen, J.C., and Chung, Y.L. Automatic extraction of shadow and non-shadow landslide area from ADS40 image by stratified classification. Geoscience and remote sensing, IEEE International symposium – IGARSS: 3050-3053, 2011.

[3] Lin, E.J., Liu, C.C., Chang, C.H., Cheng, I.F., and Ko, M.H. Using the FORMOSAT-2 high spatial and temporal resolution multispectral image for analysis and interpretation of landslide disasters in Taiwan. Journal of Photogrammetry and Remote Sensing 17(1):31-51, 2013.

[4] Liu, J.K., Hsiao, K.H., and Shih, T.Y. A geomorphological model for landslide detection using airborne LIDAR data. Journal of Marine Science and Technology 20(6):629-638, 2012.

[5] Rocscience Inc. *User manual of Slide 6.0 – 2D limit equilibrium analysis of slope stability*, 2015.

[6] Shou, K.J. and Yang, C.M. Predictive analysis of landslide susceptibility under climate change conditions – a Study on the Chingshui River Watershed of Taiwan. Engineering Geology 192:46-62, 2015.

[7] Swets, J.A. Measuring the accuracy of diagnostic systems. Science 240: 1285-1293, 1988.

[8] Xie-Sheng Engineering Consulting. Minitoring of Major Landslides along the Nantou County Road #89 after 2012 Typhoon Talim. Report to the Nantou County Government, 2014

Effects of Stress Path on the Compression Characteristics of South China Sea Calcareous Sand

Yang Shen[a] , Hua-yang Ge[a] , Han-long Liu[a,b] , Xue Shen[a]

[a] Key Laboratory of Geomechanics and Embankment Engineering of Ministry of Education, Hohai University, China
[b] School of Civil Engineering, Chongqing University, China
E-mail: shenyang1998@163.com, ghy812025127@163.com

Abstract –

South China Sea has important strategic and economic significance for China. In order to ensure the safety of shipping routes, a large number of hydraulic fill projects of coral reefs have been carried out. Calcareous sand is the main material of hydraulic fill ground. Based on 1-D compression tests on calcareous sand taken from Nansha Islands under different stress paths, this paper analyses effects of different stress paths on the compression and rebound characteristics of calcareous sand, and explains effect mechanism combined with particle shape analysis of calcareous sand. The results show that calcareous sand particles have more rich edges and corners and more irregular shapes than quartz sand particles, their shape characteristics are markedly different at three perpendicular directions, these special characteristics influence their compression characteristics; the increase of loading ratio leads to the increase of compressibility under the same stress, with the increase of stress, the effect becomes more evident; particle breakage may result in different compressibilities of calcareous sand in 1-D rebound and re-compression tests with different unloading stress. Above conclusions have reference value for the treatment of hydraulic fill ground and settlement calculation in practical engineering.

Keywords –

calcareous sand; stress path; compression characteristics; particle shape analysis

1 Introduction

Calcareous sand is a kind of marine biogenic sand in which calcium carbonate content exceeds 50%, mostly distributes between south latitude 30 degree and north latitude 30 degree. The sand has high internal friction angle, high void ratio, high compressibility and high breakability[1-4]. Calcareous sand in the South China sea is mainly coral debris and its calcium carbonate content mostly exceeds 90%[5]. Due to national defense and economic construction, China has been carrying out hydraulic fill projects of coral reefs. As the main material of hydraulic fill ground, calcareous sand has a crucial influence on the ground stability of hydraulic fill island. Therefore based on 1-D compression tests and particle shape analysis, this paper analyses effccts of stress path on the compression characteristics of calcareous sand and explains effect mechanism, in order to provide reference for the treatment of hydraulic fill ground.

2 Experimental material and procedures

2.1 Experimental material

The calcareous sand used in this experiment is taken from a reef in Spratly Islands. This batch of calcareous sand is uncemented loose particles，mainly consisted of coral debris and marine organism skeletal bodies. Its particle shape is extremely irregular and its major colour is white, dark red rare.

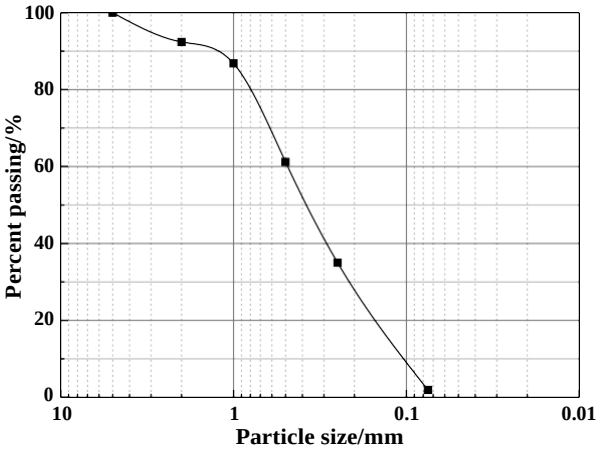

Figure 1. Grading curve for calcareous sand

We wash away the salt from the calcareous sand, dry calcareous sand and then sieve them. The sieving result shows that the proportion of particles with size greater than 5mm is very small. Considering the size of 1-D compression test sample, calcareous sand with particle size greater than 5mm should be eliminated, in order to reduce the error caused by large particles. After eliminating the large particles, the grading curve for calcareous sand is shown in Figure 1. Table 1 gives main physical properties of calcareous sand.

Table 1. Main physical properties of calcareous sand

C_u	C_c	G_s	e_{min}	e_{max}
4.8	0.9	2.69	0.799	1.186

2.2 1-D compression test procedures

In order to study effect of stress path on the compression and rebound characteristics of calcareous sand, a series of 1-D compression tests with different loading ratios, 1-D compression tests with constant stress increment, 1-D rebound and re-compression tests with different unloading stresses are conducted respectively. Concrete test procedures are given in Table 2.

Table 2. 1-D compression test procedures

No.	loading and unloading ratio	constant stress increment /kPa	loading and unloading/kPa
①	1	/	1—12.5—25—50—100—200—400—800—1600—3200
②	3	/	1—12.5—50—200—800—3200
③	15	/	1—12.5—200—3200
④	255	/	1—12.5—3200
⑤	/	25	1—25—50—⋯—200
⑥	1	/	1—12.5—25—50—100—200—100—50—100—200—400—800—1600—3200
⑦	1	/	1—12.5—⋯—400—200—100—50—100—⋯—3200
⑧	1	/	1—12.5—⋯—800—400—200—100—50—100—⋯—3200

1-D compression tests are conducted on the single lever type high pressure consolidometer. It is pressurized with weights, and the highest axial stress is 4000kPa. The sample is 61.8mm in diameter and 20mm in high. Its axial strain is measured by the dialgauge which has 10mm of range and 0.01mm of division value. The standard of compressive stability is that the axial strain of the sample doesn't exceed 0.005mm per hour.

2.3 Particle shape analysis procedures

Calcareous sand particles have extremely irregular shapes, rich edges and corners, rich void(including inner void) and low strength[6]. The edges and corners of calcareous sand particles are easily broken when loaded. Therefore the particle shape of calcareous sand is closely related to its compression and filling characteristics.

In the previous research on the particle shape, the microscope can only photograph the particle shape in one direction, and it can't fully reflect the particle shape characteristics of calcareous sand. Therefore we invent a method for photographing the particle shape from three perpendicular directions. We use epoxy resin and cubic molds to make calcareous sand particle into transparent cubic specimen, as shown in Figure 2. By rotating the specimen under the microscope, researchers are able to photograph the particle shape from three perpendicular directions.

In order to study particle shape characteristics of calcareous sand, we respectively select 30 representative particles from particle groups of 5-2mm, 2-1mm, 1-0.5mm, 0.5-0.25mm to make transparent cubic specimens and take photographs. Moreover we select quartz sand particles from the same particle groups to conduct the comparison experiments. For being convenient to study, the three perpendicular directions are denoted as *x*, *y* and *z* respectively in this paper.

Figure 2. Calcareous sand particle cubic specimen

After photographing the particle profiles of *x*, *y* and *z* directions by microscope, we conduct two valued processing for the profile photographs, as shown in Figure 3. The geometric parameters of sand particles of *x*, *y* and *z* directions can be obtained by using Image J software to analyze the particle shape.

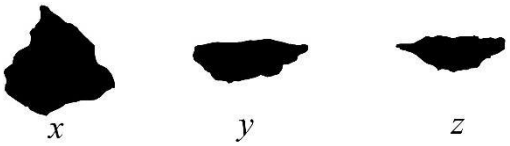

Figure 3. The particle profiles of *x*, *y* and *z* directions after two valued processing

3 Results of particle shape analysis

According to the previous research[7], the shape parameter *S* calculated from projection area *A* and projection perimeter *P* of the particle profile can well reflect the shape characteristics of particle materials. This paper analyzes the shape characteristics of calcareous sand particles according to the shape parameter *S* and their axial ratio *T* of *x*, *y* and *z* directions, and compare them with quartz sand.

The expressions for shape parameter *S* and axial ratio *T* are shown as follows:

$$S = \frac{2\sqrt{\pi A}}{P} \quad (1)$$

$$T = \frac{L}{B} \quad (2)$$

where *L* is particle length, namely the maximum outer tangent parallel distance of the particle profile, and *B* is particle width, namely the minimum outer tangent parallel distance of the particle profile.

The shape parameter *S* (value range from 0 to 1) reflects the edges and corners of sand particles. The smaller the value, the richer the edges and corners of sand particles, ans *S*=1 represents a circular particle. The axial ratio *T* (value greater than or equal to 1) is the ratio of the longest axis to the shortest axis. The greater the value, the closer the sand particles to branch shape.

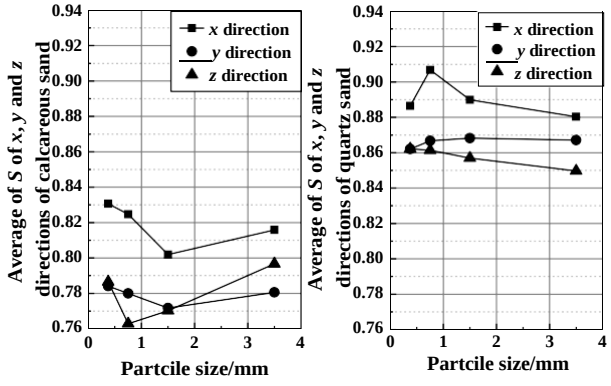

Figure 4. Average of *S* of *x*, *y* and *z* directions of each calcareous sand particle group and quartz sand particle group

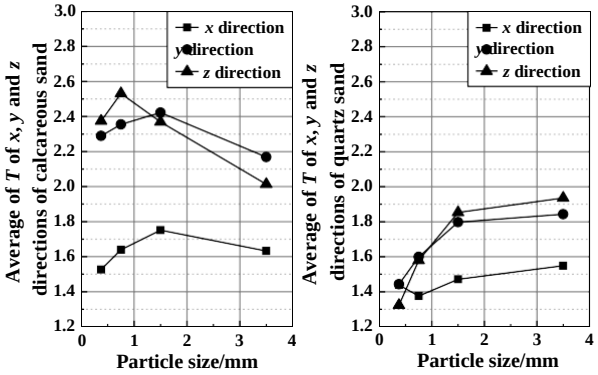

Figure 5. Average of *T* of *x*, *y* and *z* directions of each calcareous sand particle group and quartz sand particle group

After obtaining the particle geometric parameters of calcareous sand and quartz sand by Image J software, *S* and *T* of *x*, *y* and *z* directions and their averages can be calculated respectively. Figure 4 gives average of *S* of *x*, *y* and *z* directions of calcareous sand and quartz sand, Figure 5 gives average of *T* of *x*, *y* and *z* directions of calcareous sand and quartz sand (each particle group is represented by its median size on the abscissa).

Left figures of Figure 4 and Figure 5 show that, *S* of *x* direction of calcareous sand is evidently greater than that of *y* and *z* directions, and *T* of *x* direction is far smaller than that of *y* and *z* directions. It illustrates that calcareous sand particles have more rich edges and corners and more irregular shapes in *x* direction than that in *y* and *z* directions. The principal reason is that *x* direction shows the profile projections of calcareous sand particles at rest under the action of gravity, therefore the shape of *x* direction is more regular. This is also reflected in quartz sand particles (as shown in right figures of Figure 4 and Figure 5). When researchers studied the shape characteristics of sand particles in the past, they usually placed sand particles on the microscope stage naturally to photograph, the particle profile was basically the same as that in *x* direction. As a result, the irregularity of particle shape was conservative, and it couldn't fully reflect the shape characteristics of sand particles. Calcareous sand is one of the typical examples.

As shown in Figure 4 and Figure 5, with the increase of particle size, *S* decreases at first and then increases, and *T* increases at first and then decreases. It illustrates that the particle shape of medium grained calcareous sand (0.5-2mm) is the most irregular. Compared with quartz sand, the particle shape of calcareous sand tends to branch shape, and the edges and corners are richer. The special particle shape characteristics have effcct on the compression characteristics of calcareous sand.

4 Results of 1-D compression tests

4.1 1-D compression tests with different loading ratios and 1-D compression tests with constant stress increment

①, ②, ③, ④ represent 1-D compression tests with loading ratios of 1, 3, 15 and 255 respectively, and all of their final stress is 3200kPa. Figure 6 shows their *e*-lg*p* curves.

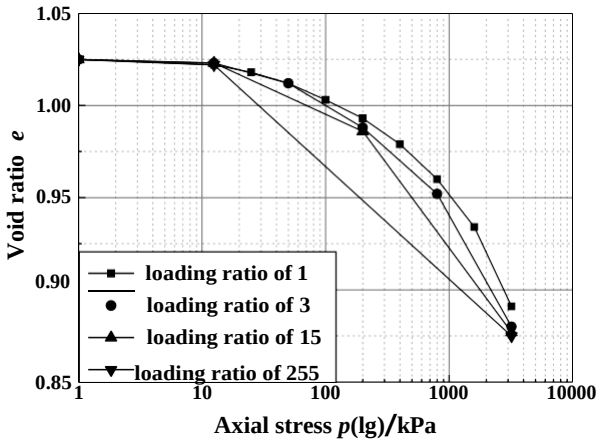

Figure 6. *e*-lg*p* curves of 1-D compression tests with different loading ratios

As shown in Figure 6, loading ratio has effcct on the compression characteristics of calcareous sand. The increase of loading ratio leads to the increase of compressibility under the same stress.With the increase of stress, the effect becomes more evident. The reason may be that the greater the loading ratio, the greater the stress change of the calcareous sand particles at each stage of loading, the more easily the edges and corners of particles are fractured and the more particles are broken[8]. The broken particles are filled into the pores, so that the void ratio becomes smaller.

At the same time, 1-D compression tests with constant stress increment (the number is ⑤) are conducted. The stress increment of each stage is 25kPa, and the final stress is 200 kPa. In order to show the effects of stress path on the compression characteristics intuitively, volume strain of each sample under axial stress of 200kPa and 3200kPa is shown in Figure 7. As shown in Figure 7, under axial stress of 200kPa, volume strain of ⑤ is smaller than that of ② and ③, but greater than that of ①. The reason may be that in tset ⑤, the small stress increment result in the small frictional resistance increment between calcareous sand particles. Therefore, compared with test ①, the particles are more easily to slip, adjust positions and rearrange in tset ⑤, and the volume strain of ⑤ is greater.

Under axial stress of 3200kPa, volume strain of ② is 8.6% greater than that of ①. This value is much greater than that of common sand (2.6%)[9]. It illustrates that effect of loading ratio on the compression characteristics of calcareous sand is more evident than that of common sand, which may be due to the special particle shape characteristics of calcareous sand.

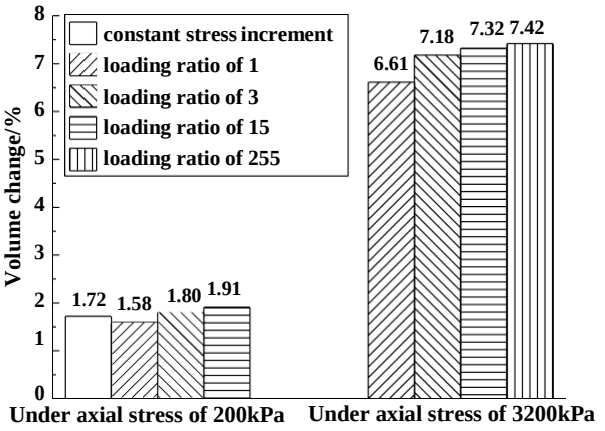

Figure 7. volume strain of each sample under axial stress of 200kPa and 3200kPa

4.2 1-D rebound and re-compression tests with different unloading stresses

① , ⑥ , ⑦ , ⑧ represent 1-D rebound and re-compression tests with loading ratio and unloading ratio of 1 and final stress of 3200kPa. Thereinto ① isn't unloading, ⑥, ⑦, ⑧ is unloading from 200kPa, 400kPa, 800kPa to 50kPa and then reloading respectively. Figure 8 shows their *e*-lg*p* curves.

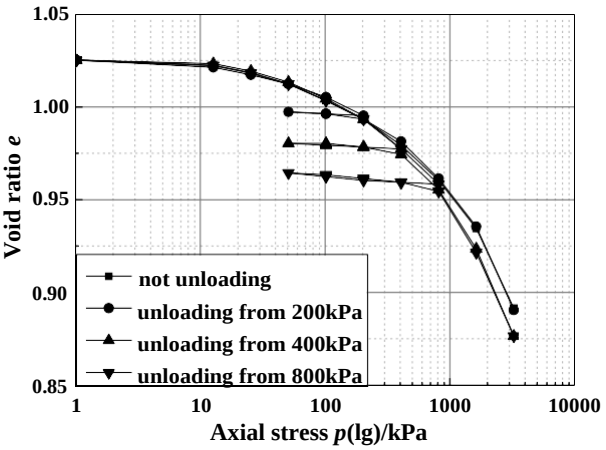

Figure 8. *e*-lg*p* curves of 1-D rebound and re-compression tests with different unloading stresses

As shown in Figure 8, the unloading rebound of calcareous sand is very small. It illustrates that the deformation of calcareous sand during the compression process is mainly no-recoverable plastic deformation. Volume strains of ① and ⑥ are approximately equal, but evidently smaller than that of ⑦ and ⑧. Under axial stress of 3200kPa, volume strains of ①, ⑥, ⑦ and ⑧ are 6.61%、6.66%、7.36%and 7.34% respectively. The reason may be when the axial stress reaches 200-400kPa, calcareous sand particles break more easily. Unloading makes the broken particles no longer contact closly, and reloading makes the broken particles easier to slip and dislocation. As a result, the volume strains increase evidently. Figure 8 shows when ⑦ and ⑧reloading to 400kPa and 800kPa respectively, their void ratios are evidently smaller than the void ratios when unloading. This phenomenon can prove the above conjecture.

5 Conclusions

1. Compared with quartz sand, calcareous sand particles have more rich edges and corners and more irregular shapes, and tend to branch shape. The special particle shape characteristics have effcct on the compression characteristics of calcareous sand.
2. The particle shape characteristics of calcareous sand in three perpendicular directions are evidently different. Therefore the particle shape in one direction can't fully reflect the particle shape characteristics of calcareous sand.
3. Loading ratio has effcct on the compression characteristics of calcareous sand. The increase of loading ratio leads to the increase of compressibility under the same stress. With the increase of stress, the effect becomes more evident, which may be due to particle breakage.
4. When the axial stress reaches 200-400kPa, calcareous sand particles may break more easily. As a result, compressibilities of calcareous sand in rebound and re-compression tests with different unloading stresses are evidently different.

Acknowledgements

The authors would like to acknowledge the financial support of the 111 Project（B13024）and Fundamental Research Funds for the Central Universities (2015B17114).

References

[1] COOP.M.R. The mechanics of uncemented carbonate sands. *Geoteehnique*, 40(4):607–626, 1990.

[2] LIU Chong-quan, YANG Zhi-qiang, WANG Ren. The present condition and development in studies of mechanical properties of calcareous soils. *Rock and Soil Mechanics*, 16(4):74–83, 1995.

[3] Yasser Dehnavi, Habib Shahnazari, Hossein Salehzadeh and Reza Rezvani. Compressibility and Undrained Behavior of Hormuz Calcareous Sand. *Electronic Journal of Geotechnical Engineering*, 15: 1684–1702, 2010.

[4] Toshiya SHINJO and Mayumi SHIMAKAWA. Particle breakage of calcareous sands under vertical stress in one−dimensional compression. *The science bulletin of the College of Agriculture, University of Ryukyus*, 45:141–148, 1998.

[5] LIU Chong-quan, WANG Ren. Preliminary research on physical and mechanical properties of calcareous sand. *Rock and Soil Mechanics*, 19(1):32–37, 1998.

[6] CHEN Hai-yang, WANG Ren, LI Jian-guo, ZHANG Jia-ming. Grain shape analysis of calcareous soil. *Rock and Soil Mechanics*, 26(9):1389–1392, 2005.

[7] TU Xin-bin, WANG Si-jing. Particle shape descriptor in digital image analysis. *Chinese Journal of Geotechnical Engineering*, 26(5):659–662, 2004.

[8] QIN Yue, YAO Ting, WANG Ren, ZHU Chang-qi, MENG Qing-shan. Particle breakage-based analysis of deformation law of calcareous sediments under high-pressure consolidation. *Rock and Soil Mechanics*, 35(11):3123–3128, 2014.

[9] WANG Hui-min, ZHANG Yun, HE Jia-jia. Creep of Saturated Sand under One-dimensional Compression. *Chinese Journal of Underground Space and Engineering*, 5:1580–1584, 2009.

Alternative Designs of the Super Levee to Protect Below-sea-level Area of Tokyo (BAT) from Flooding

H. Ohta[a], T. Aoyama[b], S. Ochi[c], T. Shimizu[d], S. Hamada[b] and M. Nakamura[b]

[a]Research and Development Initiative, Chuo University, Japan
[b]Construction Industry Engineers Center, Japan
[c] Foundation of River & Basin Integrated Communications
[d] Research Institute of Construction and Economy
E-mail: Ohta@tamacc.chuo-u.ac.jp, aoyama@cezaidan.or.jp, s-ochi@river.or.jp, shimizu-to66@rice.or.jp, hamada@cezaidan.or.jp, nakamura@cezaidan.or.jp

Abstract –

Below-sea-level Area of Tokyo (BAT) is the area in and around Tokyo of which the ground level is lower than the mean sea water level of high tides. The area is as large as 116 km^2 and inhabited by 1.74 million people. BAT is naturally under threat of tsunamis and storm tidal surges.

The authors believe that development of super levees along the entire coast of BAT is highly reliable measures to protect the area against storm tidal surges and tsunamis. The super levee is an extensively wide riverbank levee with a gentle slope in the hinterland area. The basement of the super levee is as wide as 30 meters multiplied by height of the levee (W=30 x H m).

Shared public understanding on imminence and risks of flood disasters in BAT is a must to promote development of super levees as it requires consent of hundreds of landowners and other stakeholders. Public trust and expectations for disaster management authorities should be raised in accelerated manners. Different design alternatives of levees should also be developed so that they can be applied to various conditions of subject areas.

Development of super levees in BAT is steady but slow. This paper proposes action alternatives to enable development of super levees in BAT in accelerated manners.

Keywords –

Floods; Earthquakes; Storm tidal surges

1 Introduction

How much will Japan have to pay as indemnity if it is forced to cancel Tokyo Olympic Games in 2020 due to disasters? This may be an instinctive, absurd question to many but pressing, real one for the authors (who have discussed risks of disasters in Tokyo Metropolitan Area [1]).

Tokyo Inland Earthquake is feared to happen with 70% probability in the next 30 years. The expected damage can be as severe as that of Hanshin-Awaji Earthquake in 1997. If the capital area is hit and devastated by a mega-earthquake, so will be the Olympic facilities, which will result in the cancelation of the Olympic Games. Stakeholders of Olympic Games can give up compensation as force majeure clause may apply. However, what happens if the Olympic facilities survive but not the access facilities? Cases like this may have not been surmised. However, the possibility of such case is increasing. If they do, the effect will be far graver than compensating for cancellation of Olympic Games.

Hurricane Sandy (October, 2012) that landed on State of New Jersey had a direct impact on the City of New York. Metropolitan Transport Authority of the city suspended operation of all the subway lines one day before the inundation. Although prevention measures such as placing sand bags had been implemented, flood water of storm surges intruded in tunnels through emergency exits and other unexpected water routes. Eight subway lines including eight stations were submerged under sea water. The relief and response works were swift. Immediate drainage and rehabilitation works enabled recommission of 57% of the submerged subway lines in a week and that of 97% in 9 days. The system was back in service impressively fast. This was possible because non-water-proof equipment such as electronic machinery and motors of switches had been moved to higher areas or were sealed against water. Stand-by machines were also available [2].

Typhoon Nari was born in North East of Taiwan in September, 2001. It landed on Sandiaojiao in the north of Taiwan and moved through the south of Taiwan Straight from Tainananping and brought heavy storms in inland areas. The typhoon moved very slowly and

stayed over the main island of Taiwan for 49 hours. It caused severe flooding and slope failures over all prefectures of Taiwan, which resulted in 94 fatalities, 10 missing people, and 19,000 flooded houses.

Flood water brought by the typhoon flowed into subway system of Taipei City. Jieyuntaibei, Zhongshan, Taidayiyuan, Zhongshanjiniantang and Shuanglian Stations along with 12 kilometers of tunnels were flooded. Operation of Zhonghexinlu, Songshanxindian, Danshuixinyi, and Bannan lines were suspended, which seriously affected city transportation and economy. 1.2 million tons of flood water flooded subway tunnels. It took 15 days to drain the flood water out of the tunnels by numerous pumps including those of Navy. It took 3 months to resume full operation of the subway system [3].

Damage estimation and countermeasures of large-scale flooding in Arakawa River with focus on evacuation of affected people are described in detailed and comprehensive manners in a series of papers by Ikeuchi et al. [4,5,6]. Ikeuchi et al. [5] refered to flood incidents of subways in Chicago (1992), Boston (1996), Seoul (1998), Fukuoka (1999 and 2003), Nagoya (2000), Taipei (2001), Prague (2002) and Azabujuban Station of Tokyo Metro Subway System (2004), and described damage estimation and mitigation measures when flood water of Arakawa River intruded the subway system of Tokyo.

Quick and thoughtful response to the intrusion of sea water into the subway system prevented cascading problems in the city of New York. Although we hope appropriate and quick response actions will be taken when a similar disaster happens in Tokyo, more pessimistic scenario comes up to the mind of the authors.

2 Expected Damage in Below-sea-level Area of Tokyo (BAT)

Although lowlands of Koto Delta Area (KDA) were deeply affected by Kanto Earthquake in 1923, total submersion of KDA did not occur as the ground level was higher than the sea water level. Excessive deep-well pumping of the ground water caused progressive land subsidence in the subsequent period. 4.5 meters of settlement was observed in some areas of KDA. Since some of the settled areas became lower than the sea-water-level as shown in Fig. 1, flood protection facilities such as levees, gates, and inland locks were constructed. Below-sea-level Area of Tokyo (BAT) is protected by these facilities. The area would quickly submerge under water if the existing large-scale drainage pumps cease their operation.

Figure 1. Below-sea-level Area of Tokyo (BAT)

Flooding in coastal areas of Tokyo Bay has been witnessed for a few times since the beginning of Meiji Period in 1868. The population in the area is concentrated in the lowlands. Tokyo Big Flood in 1910, Storm surge disaster in 1916 (which was then misunderstood as a tsunami) and Flooding due to Catherine Typhoon in 1945 were the top three of the major water-related disasters in the area. These disasters occurred because of not only the geographical situation but also the change of industrial structure in the upper watersheds. Mitigation measures were planned and implemented after the major disasters. These included 1) construction of Arakawa Floodway to protect rapidly urbanized downstream areas; 2) construction of levees and water gates; and 3) construction of multi-purpose dams. These were ex-post measures which were planned to prevent recurrence of disasters of a similar nature and scale rather than carefully designed ex-ante schemes.

Widely-spread land subsidennce due to the over-withdrawal of ground water is the core of the current problems. Land subsidence as deep as four meters gave birth to BAT. If sea water is let into BAT, the area in which 2 million people reside will be four meters below the water surface. The submerged towns will include subways, underground streets, and basement floors of buildings. Storm tidal surges behave as if tsunamis do. It is known that they form high waves that can break concrete seawalls when they arrive in seacoasts as witnessed in Tidal Wave in 1916 and Ise Bay Typhoon in 1959. The high waves devastated levees and houses in those disasters. Storm tidal surges are the most dangerous when their arrival coincides with full tide of the day. Probability of such coincidence is becoming higher than those of mega-earthquakes because of the climate change, etc.

If a large-scale earthquake hits Kanto Metropolitan area, some of hundreds of flood gates and levees in Tokyo can be left to malfunction due to liquefaction. Mega flood disasters are feared if storm tidal surges occur before the repair works of those facilities are

completed. Maximum height of storm surge caused by a Typhoon of Ise Bay-class could be 5 meters. Even if the height of the storm surge is lower, large-scale flooding will occur if it happens before the rehabilitation works are completed. That could give not only grave human impact but also global economic impact.

1.8 kilometers of the left bank settled due to liquefaction when Hanshin-Awaji Earthquake hit Yodo River. The settlement was as deep as 3 meters at maximum, lowering the levee top to just 1.3 meters above the high tide water level. Rehabilitation works were fortunately finished before typhoon season that came six months after the earthquake. Flooding of Osaka City was avoided by a sheer luck.

Figure 2. A flood gate under the aseismic reinforcing work

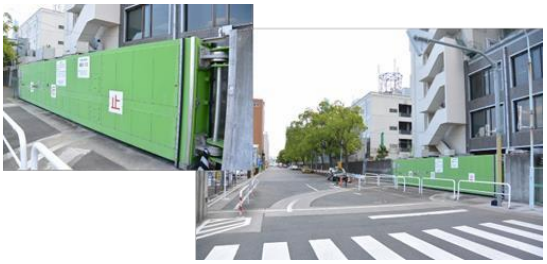

Figure 3. Floodwall gate at Harumi

Figure 4. Seawall at Tenozu

Figures 2, 3 and 4 show protecting fascilities such as flood gate, floodwall gate and seawall. They are being systematically strengthend by aseismic reinforcing works that are still on the way and not yet fully completed.

Japan will literally collapse if the lower areas of Below-sea-level Area of Tokyo (BAT), i.e., areas of Sumida, Koto, Katsushika, and Edogawa Wards currently below low tide water level as well as areas of Adachi, Kita, Arakawa, and Taito Wards below high tide water level, become four meters below sea water level although we hope it is just our hypothetical nightmare. Stock prices of Japanese companies may plummet to almost nil. Submersion of subways will cause this nightmare. Most workers will be unable to commute to their offices if the subway system is stopped. Machines and computers will come to standstill due to lack of operators. Japanese production systems, which are based on division of labor, depend largely on small and medium sized companies. Most manufacturers will have to suspend their operation as their supply chains are broken. Rehabilitation of subway system will take years if it is submerged under water due to lack of appropriate and timely pre-disaster measures. Companies without workers and production lines will inevitably go bankrupt.

Income of workers who are unable to commute to their offices will soon be substantially reduced. They will be unable to repay their housing loans. They will have to migrate to local areas. Housing loans of millions of people will become bad debt. Mortgaged houses will lose their values. Companies will move their factories away from capital areas. They will have to prioritize their funding for the transfer of production base over repayment to banks. Banks will be burdened by shrunken cash flow and increase of insolvent houses and lands. Some of them may go under if a run on a bank happens.

Damages in Great East Japan Earthquake, Hanshin-Awaji Earthquake, and Kumamoto Earthquake gave significant but localized impact. Submersion of subways in Tokyo will give a nation-wide impact. Most of 100 million Japanese people will find it hard to make a living. Oversea media argues that Great Tonankai Trough Earthquake will cause graver global economic crisis than Lehman Shock. The authors fear that Japanese economy will be unable to recover when BAT is submerged under water as deep as four meters even if all the people survive thanks to perfect ex-post measures.

3 How Can We Prevent Submersion of Below-sea-level Area of Tokyo (BAT)?

Numbers of people have warned that the situation as described in the previous section may happen. Many also have proposed ways to prevent it. Current Below-sea-level Areas of Tokyo (BAT) is protected by facilities such as levees, tidal embankment, seawalls, flood gates, and floodwall gates. However, large scale disasters such as mega-earthquakes, super typhoons, and extremely heavy rains may paralyze the facilities. If one of the tidal locks is attacked by terrorists, BAT will be under water by the next high tide of the day. Subway lines in Tokyo are mutually connected at certain points. BAT submersion may lead to submersion of the entire subway system.

Super levee is an effective measure to prevent the devastation. Construction cost of the super levees is much lower than national economic loss caused by submersion of BAT.

We have described a picture of Tokyo when a mega-flooding hits the area. Land subsidence of Tokyo areas that has already happened made the scenario likely. It is a matter of not if but when. Just pre-empting recurrence of experienced disasters will not work. If a disaster as described happens, not only Tokyo but Japan will not survive. A dark future is before us. A disaster management policy that principally aims to prevent recurrence of experienced disasters does not properly address submersion of BAT. Paradigm shift in disaster management policy is needed. The shift should be from "preventing recurrence of experienced disasters" to "anticipating and preempting disasters that have not been experienced in the past". General public may vaguely recognize this. However, sense of urgency is lacking. It seems that they do not understand that structural measures such as water-proofing of subway entrances and super levees are urgently needed.

Only governments or political leaders can deal with an issue of such grave magnitude as this. Although the authors who are non-governmental individuals can make only a small contribution, we started an initiative to build public trust in order to help addressing the issue. One of our actions is an outreach to citizens through PR activities of scientific society. There is a "Committee on Geotechnical Research of Historical Heritages" under Kanto Branch of Japanese Geotechnical Society. Sub-committee on Historical Research of Flood Disasters in Tone and Arakawa Rivers was established under the Committee. It is chaired by Ochi, the third author of this paper. One of the objectives of the sub-committee is to publicize outcomes of research on historical disasters through a workshop co-sponsored by municipalities. We intend to make known historical records of large-scale disasters and national economic impact of mega-flooding in which BAT will be submerged under as deep water as 4 meters.

4 Anti-Seismic Capability of Grounds within Below-sea-level Area of Tokyo (BAT)

Sub-committee on Historical Research of Flood Disasters in Tone and Arakawa Rivers under Committee on Geotechnical Research of Historical Heritages will conduct a research to investigate historical floods through geotechnical lens. It aims to identify possible relations between the experienced disasters and the geotechnical weakness of the area. The findings will be shared with citizens of the area. Research group to estimate anti-seismic characteristics of grounds within BAT was established under the sub-committee.

Let us reiterate that we were just lucky in 1923. Submersion of Koto Delta Area (KDA) did not happen at the mega-earthquake in 1923 because Japanese industrial boom was yet to come. Progress of land subsidence as deep as 4.5 meter at maximum since 1923 made Below-sea-level Area of Tokyo (BAT) more vulnerable to water-related disasters. BAT is protected by advanced facilities. However, damage would be more severe and extensive than in 1923 once the protection line is broken through by an earthquake, storm tidal surge, or the combination of the both. This is the situation the authors fear the most.

To what extent will liquefaction of grounds of BAT happen when an earthquake of a certain magnitude hits the area? The research group has started to work to answer this question. Steps of works towards the answer are as follows:

Ohta, the first author, conducted a simulation analysis of ground movement of Kasai Coastal Park while the construction works of the park was in progress. A computer software called DACSAR [7] was used for the simulation. Ohta et al. [8] found through assimilating process of the model that the ground movement during the construction period of the park was not properly reproduced without feeding in the model initial mechanical conditions of the ground that had experienced the land subsidence caused by excessive deep-well pumping of the ground water. The conditions were obtained through detailed simulation of land subsidence process caused by the continuous withdrawal of ground water since 1890's in Meiji Period.

The authors will take the following steps that reflect empirical findings described as above: Sample sites of

which monitoring records of the withdrawal of groundwater level and land subsidence are available will be selected; Mechanical conditions of the grounds will be obtained through simulation that reflect historical data of groundwater withdrawal and progress of settlement; The simulation results will be verified with expectation that it is consistent with the actual data of ground settlement for the past 100 years since Meiji Period.

Kanto Earthquake occurred in 1923 when land subsidence had not progressed much yet. As the mechanical condition of grounds at the time of Kanto Earthquake is known (from the simulation of land susidence), the ground movement and acceleration of grounds at the time of Kanto Earthquake can and will be dynamically simulated by DACSAR-I model [9]. Seismic record of Kanto Earthquake may not be accurate enough vis-a-vis the present standard. However, it is possible to compare acceleration of the earthquake assumed from historical records and damage profiles with the simulation output. We expect that the model, after a few test-run with trials and errors, will produce fairly accurate analytical output on dynamic behavior of grounds during Kanto Earthquake.

Seismic movement data at Great East Japan Earthquake (GEJE) are available at a few sites. Seismic response of the grounds to the earthquake will be obtained through simulation analysis by DASCAR-I using the data. Since GEJE happened after deep-well pumping of groundwater was rigorously restricted by law, seismic response after termination of settlement should be analyzed fairly accurately. Silt layers should have been hardened as water was squeezed out of the layer when the ground subsided as deeply as 4.5 meters. As a result, attenuation characteristics of seismic waves that are transmitted from foundation to ground surface is changed, which leads to change of frequency characteristics of seismic waves at ground surface. Accordingly, susceptible buildings to earthquake will be different before and after land subsidence.

If the both Kanto Earthquake and GEJE can be analyzed with appropriate accuracy using the identical set of soil parameters, seismic response of grounds to a hypothetical mega-earthquake will be obtained fairly accurately through the same analytical method. The authors expect that the result will be more convincing to the public.

The authors intend to confirm the appropriateness of both the parameters (needed in the Sekiguchi-Ohta's constitutive model [10]) of foundation and analytical software (DASCAR-I) by conducting multiple calibrations taking into account land subsidence by withdrawal of groundwater as well as different data sets of Kanto Earthquake and GEJE. After the confirmation, we intend to conduct analysis using a few seismic waves of hypothetical earthquakes that may happen in the future. We expect that the analysis will produce variety of seismic behavior of foundation and accruing variety of damages such as liquefaction.

The authors are confident that we can conduct the analysis successfully although there is no 100% assurance at this moment. After sample analysis in some points of BAT is conducted successfully, we intend to conduct holistic seismic response analysis covering the entire BAT, which will require super large software. We would like to use Integrated Earthquake Simulation (IES) software which is uploaded on Supercomputer "K". IES was built by Hori (Earthquake Research Center of Tokyo University and RIKEN Advanced Institute of Computation Science)[11, 12]. Takeyama and Iizuka [13] are currently conducting earthquake disaster simulation of the entire network of Hanshin Expressway that covers the cities of Osaka, Kobe and surrounding areas by means of IES together with DACSAR-I already uploaded on Supercomputer "K".

Analysis result can be shown by motion picture if holistic seismic response analysis of BAT is conducted using "K". Video showing the simulation result of Kobe City and a part of Tokyo already exists. The video is overwhelmingly comprehensive and detailed. Individual buildings with various natural periods are swaying differently in the video picture. Intrusion of sea water into land is shown vividly as if the scene is captured from a helicopter. We hope that we can show such video to the public. Each of the citizens can literally see what will happen in his/her house, flat or office building through the video.

5 Alternative Measures to Strengthen Tidal Protection Function of Riverbanks in Tokyo Waterfront

Cross section of a super levee project in BAT is shown in Fig.5. Coordination of rights among numbers of stakeholders has been time-consuming, which led to slow progress of the project.

A picture of seawalls at Kachidoki is shown in Fig.6. Use of coastal structures for tidal protection can be considered in case as large area as shown in Fig 6. When more limited area is only available, Chicago's Cross Walk [14] is a good example of such case. Buildings under highways can be used for shopping malls cum protection walls. Riparian buildings can be used for protection against tidal waves. Steep concrete slopes of 45 degrees can be built along river banks.

They can be used for pedestrian decks with sitting places, amphitheaters, and concert stages.

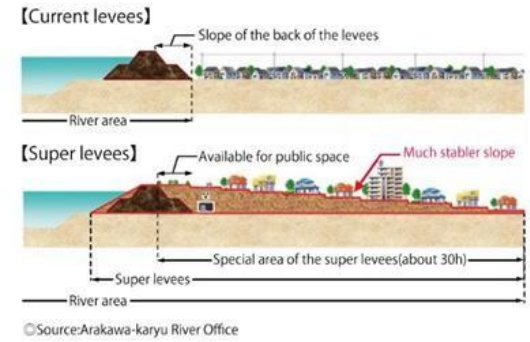

Figure 5. Typical cross section of Super levee

Figure 6. Seawalls at Kachidoki

Deregulation of Japanese river management policy is required to realize proposals as mentioned above. Practical ways of deregulation include the followings:

Private buildings along rivers should be legally treated, under certain conditions, as part of a levee by designating them as "dual-use structure". Only public facilities such as roads have been so far designated as "dual-use structure" (meaning the structure serves dually as, e.g., a road and a levee). The flexible designation allows for installing private houses as a part of levee in a river area where building any structure was rigorously restricted under River Law.

A legislative system called "three-dimensional river area" should be used to legally allow for use of lower part of private buildings as river facilities, thereby enabling houses to be built within a river area as a part of levee. The legal system was originally created to mainly allow for private use of space above artificial underground rivers.

Paradigm shift of the river management policy towards closer collaboration between public and private sectors is needed to make these changes to happen. Proactive use of private facilities, coordination with multi-stakeholders, and deregulation are the keys to realize the shift.

Acknowledements

The authors wish to express their gratitude to Dr. Kenzo Hiroki (High-level Experts and Leaders Panel on Water and Disasters), Prof. Susumu Iai (Kyoto University), Prof. Meei-Ling Lin (National Taiwan University) and Prof. Kuo-Lung Wang (National Chi Nan University) for their generous support.

This work was supported by JSPS Grant-in-Aid for Scientific Research (No. 26282103, 26420486).

References

[1] Ohta H., Aoyama T., Shimizu T., Hamada S. and Nakamura M. Chapter 8 Possibility of 4m-deep flooding in densely populated low-land area of Tokyo. *Developments in Earthquake Geotecnics*. 2017 (in print).

[2] Study Report on Hurricane Sandy in the USA (2nd edition), Joint Study Team of Ministry of Land, Infrastructure, Transport and Tourism (MLIT) and Academic Societies on Disaster Management, 2013.

[3] Chen A. S., Hsu M. H., Chen T. S. and Chang T. J. An integrated inundation model for highly developed urban areas. *Water Science and Technology*, 51(2):221-229, 2005.

[4] Ikeuchi K., Ochi S., Yasuda G., Okamura J. and Aono M. Estimates of the number of stranded persons and the rescue waiting time in case of large-scale floods with effectiveness analysis of the mitigatory operations, *Journal of Japan Society of Civil Engineers*, Ser. B1 (Hydraulic Engineering)

67(3):145-154, 2011.

[5] Ikeuchi K., Ochi S., Yasuda G., Okamura J. and Aono M. Estimates of inundation of subways due to due to large-scale floods and an analysis of effectiveness of mitigation measures, *Journal of Japan Society of Civil Engineers*, Ser. B1 (Hydraulic Engineering) 68(3):136-147, 2012.

[6] Ikeuchi K., Ochi S., Fujiyama H., Yasuda G., Okamura J. and Aono M. Estimates of the number of fatalities in case of large-scale floods with effectiveness analysis of the mitigatory operations, *Journal of Japan Society of Civil Engineers*, Ser. B1 (Hydraulic Engineering) 69(4):I_1651-I_1656, 2013.

[7] Iizuka A. and Ohta H. A determination procedure of input parameters in elasto-viscoplastic finite element analysis. *Soils and Foundations*, 27(3):71-86, 1987

[8] Ohta H., Matsumoto K. and Kobayashi A. Estimation of in-situ initial effective stresses in soft ground in Tokyo, *Proc. JSCE*, 487/III-26:217-226, 1994.

[9] Takeyama T., Tachibana S. and Furukawa A. A finite element method to describe the cyclic behavior of saturated soil, *International Journal of Material Science and Engineering*, 2(1):20-25, 2015.

[10] Sekiguchi H. and Ohta H. Induced anisotropy and time dependency in clays, *Constitutive Equation of Soils, Proc. Specialty Session 9, 9th Int. Conf. Soil Mech. And Found. Engrg, Tokyo*:306-315, 1977.

[11] Hori M. Introduction to computational earthquake engineering. *Imperial College Press*, London (2nd edition in 2011):2007.

[12] Hori M., Ichimura T. Current state of integrated earthquake simulation for earthquake hazard and disaster. *J Seismol* 12(2):307–321, 2008.

[13] Takeyama T. and Iizuka A. Information about an on-going research project introduced through personal correspondence, 2017

[14] Hellenthal M. F. and Gross D. M. Rooms with a view, *Civil Engineering, The Magazine of the American Society of Civil Engineers ASCE*, Dec.:56-77, 2016.

Estimation of the Residual Shear Strength of Clay Shale from Laboratory Tests for Case of Slope Failure at Semarang-Bawen Toll Road, Central Java, Indonesia

Idrus M. Alatas[a], Masyhur Irsyam[b] and Pintor T. Simatupang[c]

[a]Department of Civil Engineering, Institut Sains dan Teknologi Nasional (ISTN), Jakarta, Indonesia
[b] Department of Civil Engineering, Institut Teknologi Bandung (ITB), Bandung, Indonesia
[c]Department of Civil Engineering, Universitas Mercu Buana (UMB), Jakarta, Indonesia
E-mail: hb_idrus@yahoo.com, masyhur.irsyam@yahoo.co.id, pintorsimatupang@gmail.com

Abstract -

This study presents a laboratory testing method to predict residual shear strength of clay shale. To obtain an accurate prediction, the laboratory testing method should considered important inherent property of clay shale. The most important property of clay shale is significantly degradation of shear strength due to wheathering process. To capture the weathering condition, the testing was done by using triaxial multistage. Residual shear strength of clay shale resulted from this proposed method then compared to back analysis method both the Limit Equilibrium Method (LEM) and Finite Element Method (FEM). Both the laboratory testing and numerical method show the agreement results. However, the accurate prediction of residual shear strength of clay shale is necessary to design carefully slope reinforcement due to slope failured especially in the location of Semarang-Bawen toll road. At this location, in the back analysis by FEM, for Factor of Safety, FS = 1.0 was obtained the shear strength parameters of residual cohesion c_r range of 13.5 - 24.7 kN/m^2 and residual internal angle friction ϕ_r range of 9.3° - 16.1°, where the ground water level was average. Back analysis by LEM showed residual cohesion c_r range of 12 - 50 kN/m^2 in case of lower water level and range of 9 - 25 kN/m^2 in case of higher water level. While residual internal angle friction ϕ_r was range of 8.6° - 16° in case of lower water level and range of 9° - 13.6° in case of higher water level. Identical result was shown by laboratory testing method of triaxial multistage at stress release. This condition of clay shale was weathered condition which reached by cycles of wetting and drying in the range of time 8 to 16 days where wetting was done about 5 minutes every 4 days. It is concluded that residual shear strength of clay shale obtained by laboratory testing is an accurate prediction to use on slope reinforcement analysis.

Keywords -

clay shale, finite element method, limit equilibrium method, residual shear strength

1 Introduction

Back analysis is very often used to determine the shear strength that occur at sliding surface of slope failure. Back analysis can be done through Finite Element Methods (FEM) or Limit Equilibrium Methods (LEM) [6], [8], [11-12], [15]. For example, a case of slope failure at Cipularang toll road STA 97+500 [12]. Shear strength determined from back analysis is residual shear strength which used for slope stability analysis. Slope failure on clay shale deposit is generally occured due to excavation work. During the excavation, clay shale deposit was exposed by atmosphere and hydrosphere directly, therefore clay shale quickly happened weathering which causes degradation of the shear strength [4], [13]. Degradation of shear strength is also includes the residual shear strength [5].

2 Residual Shear Strength of Clay Shale

Residual shear strength occurs after soils achieve peak stress, where soil deformation continues happening [16-17], and [19]. Fig. 1 presents a correlation of drained residual friction angle and soil index properties, at effective normal stress of 100, 400, and 700 kPa. It can be seen there is a relationship between the secant residual friction angle and both liquid limit and clay-size fraction. The higher liquid limit and clay-size fraction the lower the secant residual friction angle [21]. Fig. 2 exhibits the change of clay shale shear strength due to weathering process which measured by "Weathering Grade" [9].

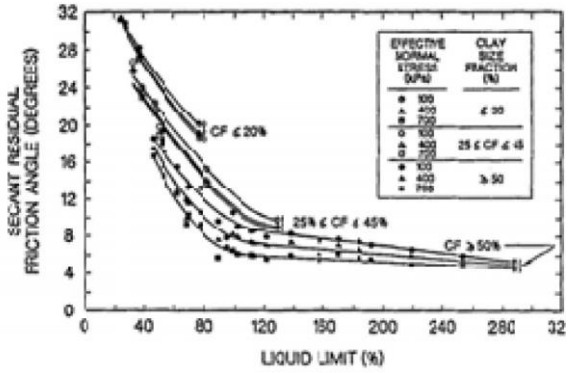

Figure 1. Relationship between drained residual friction angle and liquit limit [21]

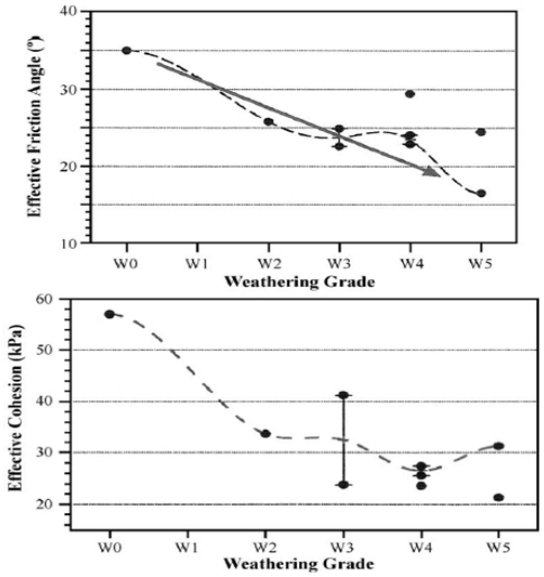

Figure 2. The effect of weathering grade to degradate shear strength of clay shale [9]

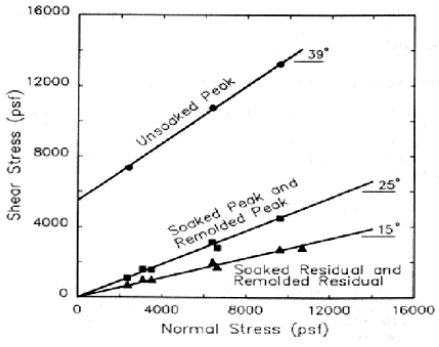

Figure 3. The change of shear strength from peak to residual stresses. [9]

Degradation of residual shear strength from the peak strength of clay shale was investigated by [20] as shown at Fig. 3.

Several previous studies showed that residual cohesion for clay was generally zero. This is because at residual strength state, clay sample was ruptured completely, where sliding surface was formed at clay deposit [8], [10], [14], [17], [22]. However, the other researcher determined residual cohesion c_r more than zero. This case is assumed due to failure surface is not formed clearly, because the surface is not separated clay deposit completely and there is still a cohesive part. Therefore, shear strength testing at laboratory resulted non zero residual cohesion [7], [11-14], [18], [23-24].

3 Residual Shear Strength Caused by Stress Release

For slope with clay shale deposit which failure surface occured, the shear strength parameters used to calculate factor of safety is its residual shear strength. Residual shear strength may without stress release, such as shown on Fig. 4. However, if the slope is excavated, then stress release occurs at failure surface. The shear strength on failure surface is residual shear strength with stress release, as shown at Fig. 5 [3].

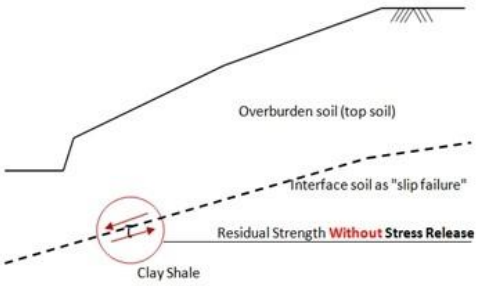

Figure 4. Residual shear strength without stress release. [3]

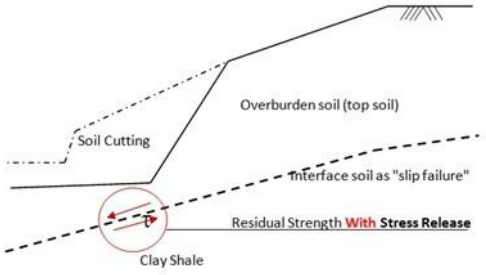

Figure 5. Residual shear strength with stress release. [3]

4 Determination Residual Shear Strength of Clay Shale at Laboratory

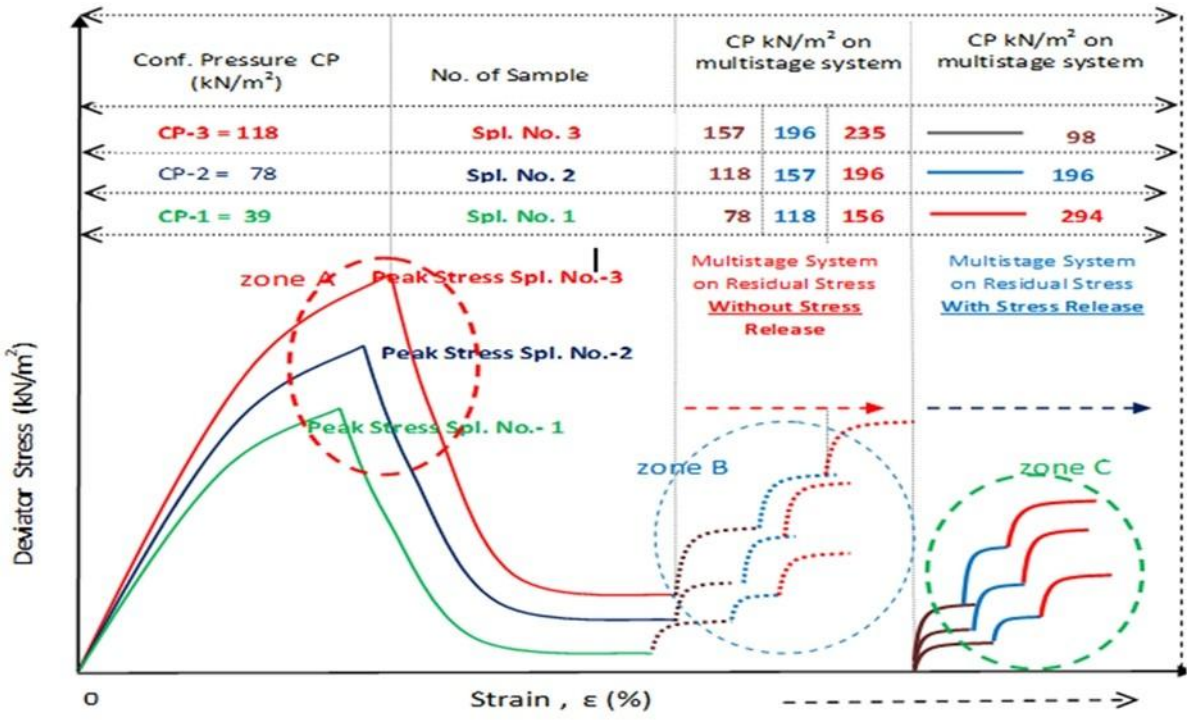

Figure 6. Multistage Triaxial UU test to obtain residual shear strength without stress release and with stress release

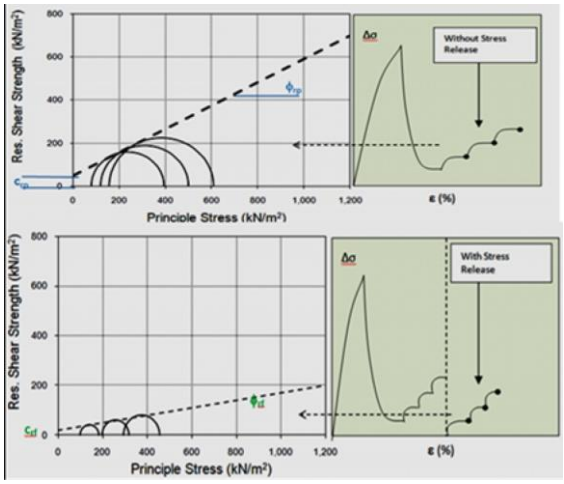

Figure 7. Residual shear strength without stress release and residual shear strength with stress release [5].

Residual shear strength of clay shale is determined by using multistage triaxial test. Prior to shearing, clay shale sample is prepared to have the effect of weathering process. Weathering at laboratory can be modeled by two steps, i.e. drying process up to 80 days and then wetting and drying cycles up to 24 days [5]. On Figs. 6 and 7 show stress strain process which resulted by multistage triaxial test, esidual shear strength without stress release (Zone B) and with stress release (Zone C).

Table 1 Degradation unsaturated peak shear strength and residual shear strength [5]

Semarang Bawen

DRYING TIME	PEAK STRESS		RESIDUAL STRESS			
	UnSaturated		UnSaturated			
	Total Stress		Res. Stress without Stress Release		Res. Stress with Stress Release	
	c (kN/m²)	ϕ°	C_{cb} (kN/m²)	ϕ_{cb}(°)	C_{cf} (kN/m²)	ϕ_{cf}(°)
0	700.0	59.4	285.0	46.0	26.7	4.9
4	370.0	60.9	360.0	29.4	3.7	22.5
8	150.0	72.0	79.0	13.0	11.3	4.3
16	260.0	73.0	211.5	13.9	7.5	6.7
24	250.0	70.8	225.7	18.2	41.0	17.2
32	270.0	70.4	207.0	25.8	9.0	5.1
40	290.0	68.1	137.5	42.9	16.5	15.0
48	280.0	61.3	145.0	37.2	3.0	4.4
64	240.0	47.1	59.0	18.3	11.7	7.0
80	220.0	38.4	29.0	8.9	5.0	3.1

Clay shale sample from a location at STA 19+250 Semarang-Bawen toll road was tested by multistage triaxial UU test where drying process was done for 80 days. The results of test are shown on Table 1 for

unsaturated clay shale sample and Table 2 for saturated clay shale sample. Both results exhibit that residual shear strength (cohesion and internal angle friction) are reduced until finishing of drying time (80 days).

Table 2 Degradation saturated peak shear strength and residual shear strength [5]

Semarang Bawen

DRYING TIME	PEAK STRESS			
	Saturated			
	Total Stress		Effective Sress	
	c_t (kN/m²)	ϕ_t (°)	c' (kN/m²)	ϕ' (°)
0	300.0	53.2	300.0	53.2
4	182.0	31.5	182.0	31.5
8	79.0	36.2	78.0	36.4
16	165.0	33.8	165.0	33.8
24	156.0	25.2	156.0	25.2
32	110.0	21.8	110.0	21.8
40	105.0	15.7	107.0	15.3
48	60.0	26.6	65.0	25.7
64	80.0	23.4	78.5	23.7
80	79.0	19.4	79.0	19.4

Semarang Bawen

DRYING TIME	RESIDUAL STRESS							
	Saturated							
	Total Stress without Stress Release		Eff. Stress without Stress Release		Total Stress with Stres Release		Eff. Stress with Stress Release	
	c_{rst} (kN/m²)	ϕ_{rst} (°)	c_{rs}' (kN/m²)	ϕ_{rs}'	c_{rft} (kN/m²)	ϕ_{rft} (°)	c_{rf}' (kN/m²)	ϕ_{rf}' (°)
0	172.0	27.4	170.0	28.1	8.0	6.1	7.0	6.3
4	170.0	23.5	169.0	23.5	4	4.29	4	4.29
8	70.0	26.1	70.0	26.1	25.3	23.4	19.7	25.2
16	150.0	20.8	152.0	21.0	9.7	19.7	8.3	20.2
24	132.0	18.3	130.0	18.725	35.3	14.1	34.3	14.6
32	102.0	18.7	102.0	18.680	34.0	4.9	33.0	5.2
40	95.0	17.8	93.0	18.1	10.7	13.2	9.0	14.4
48	46.0	18.8	50.0	18.8	21.0	11.0	20.7	11.2
64	38.0	11.8	38.0	12.1	0.0	7.7	0.0	7.7
80	35.0	10.9	36.5	10.3	4.7	4.6	8.3	4.6

Table 3 Shear strength degradation of Semarang-Bawen clay shale due to cycles of wetting and drying process with 5 minutes soaked every 4 days

Wetting and drying time	Peak Stress		Residual Stress			
			Without Stress Release		With Stress Release	
	c_u (kN/m^2)	ϕ_u (°)	c_{urp} (kN/m^2)	ϕ_{urp} (°)	c_{urf} (kN/m^2)	ϕ_{urf} (°)
0	700	59	285	46	27	24
8	342	58	197	27	22	13
16	230	55	145	25	16	14
24	150	49	85	20	6	9
32	After 24 days of wetting drying cycles, all remaining sample were destroyed befote the test was done					

The wetting and drying cycles for Semarang-Bawen clay shale sample was done up to 24 days where wetting every 4 days. After 24 days, clay shale sample could not tested anymore because sample was broken. The results of testing clay shale for shear strength degradation due to wetting and drying cycles is shown in Table 3. The reducing of shear strength after wetting and drying cycles is faster than drying process in same duration [5].

5 Back Analysis of Slope Failure at the case of Semarang-Bawen Toll Road

Slope failure at STA 19+250 Semarang-Bawen toll road occured during construction on September 2010. The failure was triggered by high slope excavation to satisfy road elevation in design. The excavation work caused clay shale deposit underlying of tuff breccia to be opened [2]. Fig. 8 exhibits slope failure at STA 19+250, where failure surface was formed fracture plane in tuff breccia layer which is occured previously. The interface between tuff breccia deposit and clay shale is called as interface fracture, as shown in Fig. 9 [10].

Figure 8. Residual shear strength without stress release and residual shear strength with stress release [5].

Back analysis is intended to determine residual shear strength during failure occured. By aasuming that residual shear strength still contains cohesion, then residual shear strength contains residual cohesion and internal friction angle. Thus, there are several possibilities for pair of cohesion and internal friction angle give an unity factor of safety (SF). Finite Element Method of Plaxis Program resulted residual shear

strength for factor of safety, FS = 1 as shown in Fig. 10. If residual cohesion increases, then internal friction angle decreases, as shown in Fig. 11.

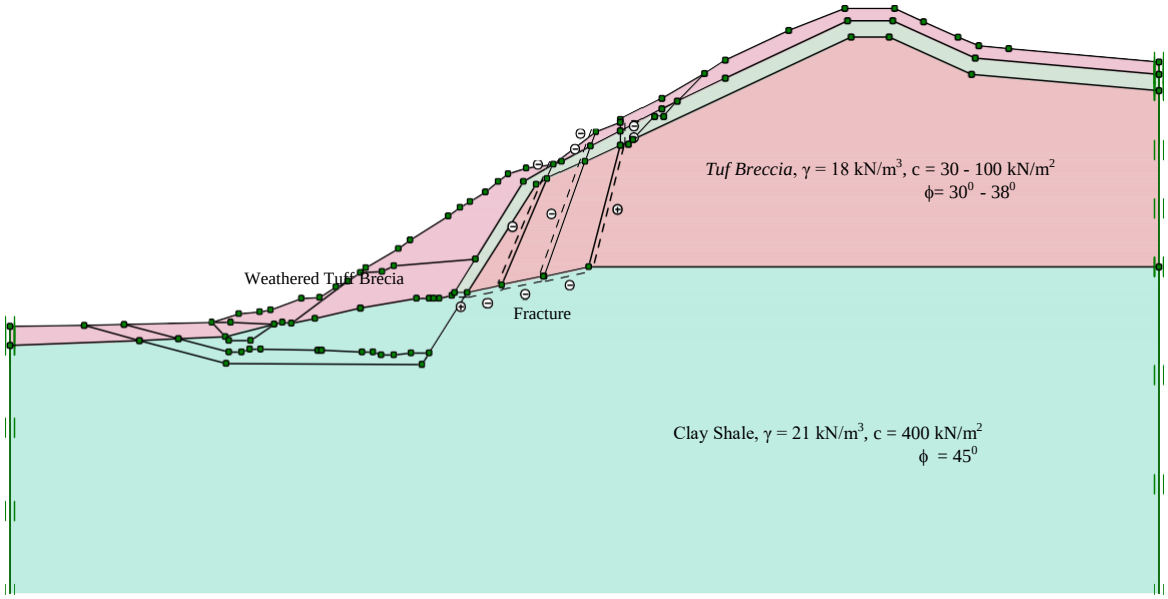

Figure 9. Cross section of slope before failure with some fracture zone

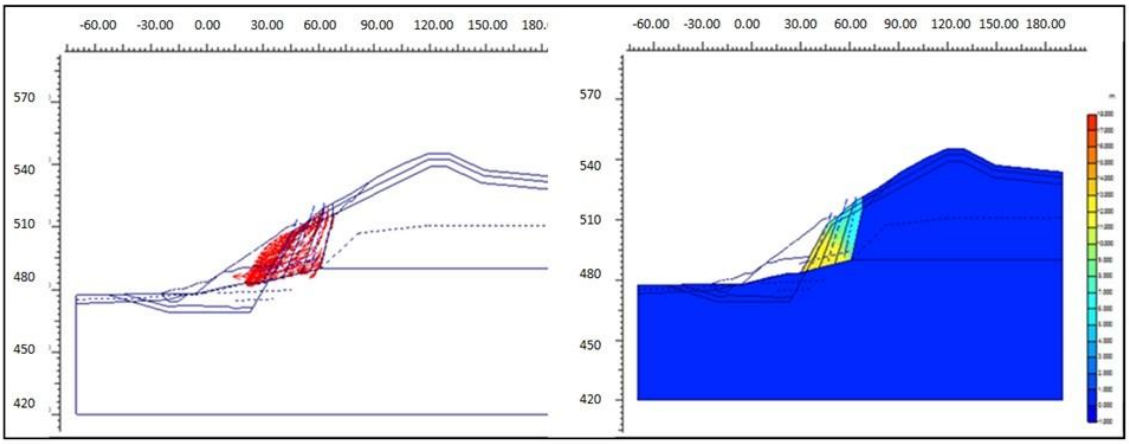

Figure 10. FEM analysis output

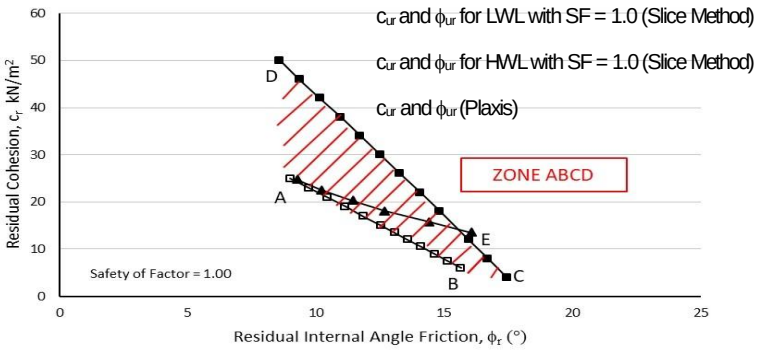

Figure 11. The acting residual shear strength of clay shale that caused slope failure SF =1 using FEM and LEM

Fig 11 shows back analysis results by using FEM and LEM. On the figure, there is a zone of ABCD which denoted that residual shear strength on the zone causes slope failure, safety factor SF = 1.

6 Results of Shear Strength from Laboratory Test

The results of multistage triaxial UU test which done to Semarang-Bawen clay shale sample after given the effect of weathering for both drying and wetting and drying cycles are plotted together with results from Fig. 11. It shown that some residual shear strengths are dropped in zone ABCD, as shown in Figs. 12 and 13. From the figures, it can be understood that shear strength values lying above of zone ABCD means no failure of slope or SF > 1. However, if the values are located under zone ABCD, then it means slope failure occur or SF < 1. The shear strength values include in zone ABCD means slope failure will occur or SF = 1.

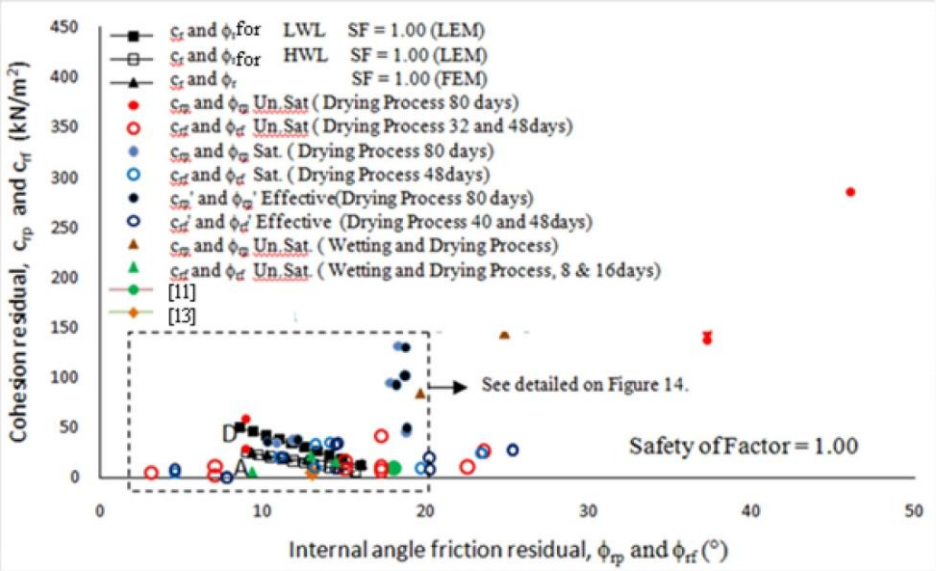

Figure 12. Combination of residual shear strength that caused slope failure SF=1 from laboratory testing and back analysis [1]

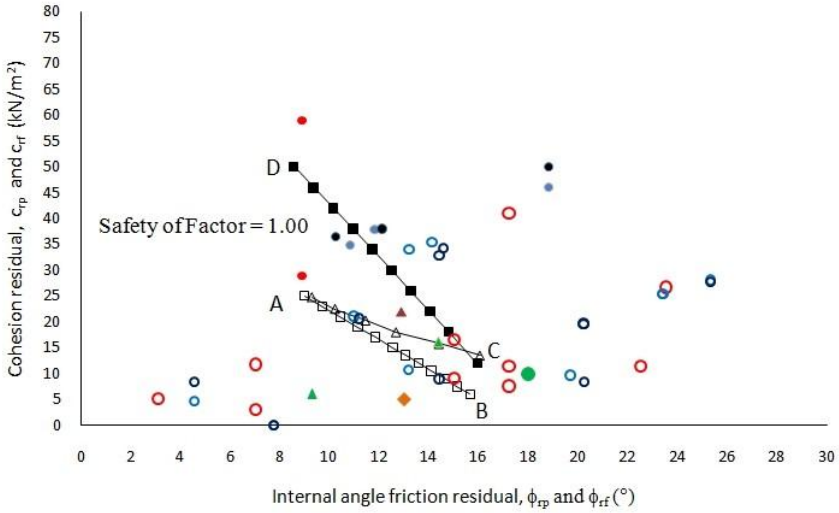

Figure 13. Detailed of Figure 11 [1]

From Fig. 13 it can be seen clearly that not all values of residual shear strength of clay shale from laboratory test caused slope failures. There are 9 data of shear strength values exist on zone ABCD, as summarized on

Table 4. It is well known that behaviour of fresh clay shale is indicated by high shear strength, nevertheles the shear strength will be reduce sifnificantly after weathering due to interaction of clay shale deposit with atmospher and hydrosphere. The effect of wetting and drying cycles to model tropical area make weathering process more quicker, therefore reducing shear strength of clay shale is also more faster. From 9 data include in zone ABCD, i.e., SF = 1 as shown in Fig. 13, all data are affected by weathering process. In the drying process, it was needed time from 32 days to 80 days at least to achieve the necessary residual shear strength which cause slope failure at STA 19+250 Semarang-Bawen toll road. However, for weathering due to wetting and drying cycles in once of 4 days wetting for 5 minutes, the process needs only 8 to 16 days. It is clearly seen that time more faster than drying process.

Table 4 Type of weathering and clay shale sample condition which led to lab test results in accordance with back analysis

Time of Weathering	Weathering Process		Triaxial Sample Type	Residual Shear Strength	
	DP	WD		Without Stress Release	With Stress Release
80	✓		Un. Sat	✓	---
80	✓		Saturation	✓	---
80	✓		Saturation	✓(effective)	---
48	✓		Un. Sat	---	✓
48	✓		Saturation	---	✓ (effective)
40	✓		Saturation	---	✓
32	✓		Un. Sat	---	✓
8		✓	Un. Sat	---	✓
16		✓	Un. Sat	---	✓

DP is Drying Process and WD is Wetting and Drying Process

7 Conclusions

From previous discussion, some conclusions can be drawn as following :

1. The weathering process with the wetting and drying cycles of clay shale in the laboratory accelerates the decrease in shear strength of clay shale.
2. To get a good and correct analysis on the slope of clay shale, the study to obtain information on the existence of the existing failure surface on the slope becomes very important
3. The residual shear strength of clay shale can be obtained in the laboratory for slope stability design with regard to whether there are excavation works during construction. Excavation work causes a reduction of shear strength at failure surface.
4. Multistage triaxial UU testing is best to use for determine residual shear strength for both without and with stress releases.
5. The weathering process carried out with wetting and drying cycles on 8 to 16 days, is the fastest weathering time, where residual shear strength results with stress release is accordance with back-analysis results through the FEM and LEM methods.

References

[1] Alatas, I.M., Kesan Luluhawa Terhadap Kekuatan Ricih Syal Lempung Dalam Penentuan Parameter Kestabilan Cerun., Razak School of Engineering and Advanced Technology, Universiti Teknologi Malaysia, Kuala Lumpur, 2016.

[2] Alatas, I.M., Irsyam, M., Himawan, A., Nawir, H. and Wiriodinoto, I. D., Instability of a High Cut Slope of Volcanic Breccia Laid on Clay Shale at KM 31+875 in Central Java, Indonesia. Paper presented at Proceedings of the 16th Conference on Current Researches in Geotechnical Engineering in Taiwan at Kaohsiung, Taiwan, September 2-4, 2015.

[3] Alatas, I.M., Irsyam, M., Ramli, N., Samira, A. K. and Himawan, A., Perilaku dan Kinerja Kuat Geser Clay Shale Semarang-Bawen Pada Perencanaan Stabilitas Lereng. Paper presented at PIT ke 2, Ikatan Ahli Kebencanaan Indonesia, at Yogyakarta, 26 - 28 Mei 2015.

[4] Alatas, I.M., Samira, A. K., Ramli, N. and Irsyam, M., Effect Of The Weathering On Disintegration And Shear Strength Reduction Of Clay Shale Paper presented at The Manuscript Paper For : "Geotropika 2016", The 10th International Conference of Geotechnical and Transportation Engineering, at Kuala Lumpur, Malaysia, 16 - 17 February 2016.

[5] Alatas, I.M., Samira, A. K., Ramli, N., Irsyam, M. and Himawan, A., Shear Strength Degradation of Semarang-Bawen Clayshale Due To Weathering Process. *Jurnal Teknologi (Sciences and Engineering) Special Edition, acceptance September 2015*.

[6] Alekhya, K.K., 2D and 3D Back Analysis of the Forest City Landslide (South Dakota), Iowa State University, 2013.

[7] Binod, T., Thomas. L. B., Hideaki, M. and Gyanu, R. T., Comparison of Residual Shear Strengths from Back Analysis and Ring Shear Tests on Undisturbed and Remolded Specimens. *Journal of Geotechnical and Geoenvironmental Engineering, Vol. 131, No. 9, September 1, 2005*.

[8] Duncan J.M, Timothy D.S., Soil Strength from back analysis of slope failure. *Stability and performance of slopes and embankments II Proceeding GT Div*, 1992.

[9] Emberhardt E, T.K., Luginbueh M., Slope Instability Mechanisms in dipping interbedded conglomerates and weathered marls- The 99 Rufi landslide Switzerland. *Elsevier*, 2004.

[10] Gartung E, H.-G.R., Toolkit Landfill Technology ; Priciples of Bottom Barrier System. *Technical Committee Landfill Technology*, 2009.

[11] Himawan A., Alternatif Mitigasi Kelongsoran dan

Perkuatan Lereng Galian Tower SUTT STA 19+255 Pembangunan Jalan Tol Semarang - Solo Tahap I Ruas Ungaran - Bawen Paket V Tinalun - Lemah Ireng STA 18+000 - 21+825 In *Technical Report* LAPI ITB PT, 2013.

[12] Irsyam M, Endra.S., Himawan A., Slope Failure of an Embankment on Clay Shale KM 97+500 Of The Cipularang Toll Road and The Selected Solution : A Case Of Slope Failure Due To Strength Degradation Of Clay Shale. *Proceeding of The Geotechnical International Symposium in Bangkok 6-7 Decemebr, 2007*.

[13] Irsyam M, Jayaputra.A.A., Himawan A, Kartawiria A., Kasus-Kasus Kelongsoran Pada Tanah Clay Shale dan Alternatif Penanggulangannya. *Proceeding of the 9th Indonesian Society for Geotechnical Engineers Conference and 15th Yearly Scientific Meeting, Jakarta .December, 2011*.

[14] Liew S. S, G.S.S., Liong C. H., Geotechnical Investigation and Monitoring Results of a Landslide Failure at Southern Peninsular Malaysia (Part 2: Back Analyses of Shear Strength and Remedial Works). In *Technical Report Gue & Partners Sdn Bhd, Malaysia*, 2003.

[15] Matasovic N, C.C., Witthoeft A.F, Stern A, Hamou T.H., Back Analysis of Landslide Deposit Basal Failure Plane Residual Shear Strength. In *IACGE 2013*.

[16] Mesri G, Capeda,D. A. F., Residual shear strength of clays and shales. *University of Illinois at Urbana-Champaign*, 1986.

[17] Mesri G, Huvaj-Sarihan N., Residual Shear Strength Measured by Laboratory Tests and Mobilized in Landslides. *Journal of Geotechnical and Geoenvironmental Engineering, Vol. 138, No. 5, May 1, 2012*.

[18] Singh K., Back Analysis studies of the quarry heights road landslide. Dicipline of Geological Science University of Kwazulu-Natal, Durban, South Africa, 2012.

[19] Skempton A.W., Residual strength of clays in landslides, folded strata and the laboratory. *Géotechnique ISSN 0016-8505 | E-ISSN 1751-7656*. Volume 35 Issue 1, March 1985, pp. 3-18, 1985.

[20] Timothy D.S, Duncan M., Mechanisms of strength loss in stiff clays. *Journal of Geotechnical Engineering*. 117 (1), 139-154, 1991.

[21] Timothy D.S, Hisyam.E. Drained residual strength of cohesive soils. *Journal of Geotechnical Engineering*. 120 (5), 856-871, 1994.

[22] Timothy D.S, Hisyam.T.E. Comparison of field and laboratory residual strength. *Stability and performance of slopes and embankments II Proceeding GT Div*, 1992.

[23] Watry S.M, Lade P.V. Residual Shear Strengths of Bentonites on Palos Verdes Peninsula, California. In *Slope Stability 2000*.

[24] Yang H, Xiao J., Wang S., Zuo W., Study on the Determination of Residual Shear Strength for Expansive Soil. *Recent Advancement in Soil Behavior, in Situ Test Methods, Pile Foundations, and Tunneling*, 49-54, 2009.

Debris as Resources utilized for Wild Creeks Remedial Work after Morakot Typhoon

Su Miau-Bin[a] Chen Jun-Yang[b] Ho Hsueh-Chen[c] Lin Yu-Shu[d]

a.b.c.d Department of Civil Engineering, National Chung Hsing University, Taiwan

Corresponding author: Su Miau-Bin, PhD, Professor,

E-mail: mbsu@dragon.nchu.edu.tw

Abstract

In recent years, especially after typhoon Morakot, extreme torrential rain has resulted in large amounts of landslides in Taiwan. Debris that accumulated downslope blocked the drainage way and induced debris flow afterward. The large amount of debris transported to downstream may caused elevated riverbeds and channel siltation. All nearby villages and utilities are threatened. Cleanout work for aggregated debris is of great priority afterward. In processing the cleanout work for wildcreek, debris should be treated as useful resources. This is very important in the watershed management and rehabilitation work.

In solving the debris blockage problem, cleanout of debris so as to recover the drainage capability of watershed and at the same time, used the debris material to form the protecting measures. Cleanout of the debris can be used in filling low-lying land in the upstream catchment area. By applying feasible methods to improve its engineering properties, the debris can be used to make a variety of protective measures, to recover the loss of land, roads, damaged buildings and other issues. In planning, the first is to consider the location and the protected object. It can be planned to establish of embankment, bank protection, slope protection, and berms construction.

Keywords –

Wildcreek, Cleanout, Debris Resources, In-situ Reuse

1. Introduction

After typhoons and torrential rain, wild creeks are often filled with debris due to upstream landslides. If nothing is done to remedy this situation, it will become a source of debris flow when the next period of heavy rain occurs. The transported debris often has a serious impact on the environment. However, regarding the practice of trafficking the debris, if the quality is poor, no user are willing to purchase it. The public often thinks that the Government implements cleanup plans poorly. Faced with this difficult situation, the implementation will of organizations can get lower and lower, causing a vicious cycle in which everyone is a victim.

Wild creek cleanouts tend to be urgent matters that must be completed before the next typhoon or period of torrential rain. Otherwise, the lack of dredging will result in the silting of the riverbed or overflowing from the sides. During cleanup, if the construction steps can be simplified, the efficiency of construction can be enhanced, and the construction period can be shortened, this will be a great help for wild creek cleanout work. In addition, the recovered material can be effectively reused in-situ. It can be used for filling the low-lying land, constructing slopes, and riverbank protection. This is an effective way to solve the above-mentioned problems.

2. In-situ reuse

The methods of adding cement for the in-situ use of debris, according to the characteristics of the production process, are shown in Figure 1. Comparison of engineering methods of debris use in Table 1. It can be regarded as cement concrete, using debris as the source of the concrete aggregate in accordance with the graded concrete material standards and the requirements for cement mixing methods, such as the accuracy of the scales in the ready-mix plant and the performance of the batching machine.

Another use of the material is for ground improvement, in which the aggregate requirements and the mixing requirements are not so strictly as those for cement concrete. Bulldozers are often used to compact

the concrete after it is poured. The main mechanisms of cement to stabilize soil are the Pozzolanic reaction and the hardening effect. In other words, the calcium ion of the lime contained in the cement and the silicate and aluminum acid salt of the minerals in the soil generate a cemented reaction to form CSH and CAH; such colloids can help to promote the bonding of particles and the filling of the pores of the soil to considerably promote strength and reduce permeability. Moreover, it is generally believed that the changes of the engineering properties of cement are mainly caused by the hardening of the cement. When the cement hardening occurs, the cement particles and the surrounding soil particles will bind to form discontinuous strong and hard aggregate around the soil particles. The aggregates can be regarded as the fillings of the pores in the soil (Chen, 2008).

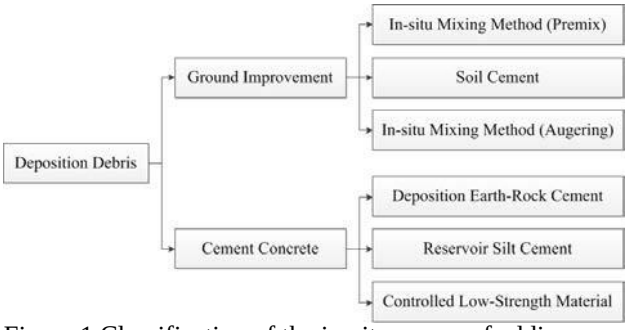

Figure 1 Classification of the in-situ reuses of adding cement to debris

2.1 Soil Cement

According to the definition of soil cement in Chapter 02715 of the Public Works Construction Program Standards, soil cement is made in the following process: first according to the design descriptions, pound and smash the soil; then, spread cement on the soil and blend by in-situ mixing or other mixing methods; finally, make compact the mixture using rolling pressure. The standards suggest that the aggregate particle size should be no more than 75mm, and that at least 55% of the particles should be able to pass through a 4.75mm sieve. Such soil cement is suitable for road bases and bottom layers.

2.2 In situ mixing method

The in situ mixing method, which uses cement to solidify in-site stone and soil, was developed in 1992 in Japan. On the construction site, cement, water and a mixing agent are mixed according to a mixing ratio into a cement slurry. This is delivered to a mixing machine installed at the front of an excavator and is directly mixed with earth and stones that have a particle size below 300mm, which is then excavated in-situ and selected to produce a base or structural body similar to cement of a certain strength. The equipment configuration is as shown in Figure 2 (Japan, ISM Engineering Method Research InstituteWebsite, 2011).

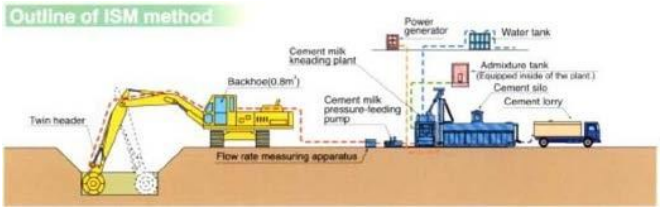

Figure 2 ISM engineering method in-situ equipment configuration (Source: ISM Engineering Research Institute Website)

2.3 Deposition earth-rock cement

According to Chen (2008), the deposited stone material sized above 5cm can be separated using a mechanical hand with a hopper (known as large filling materials, a self-propelled pounding machine can be used to grind them into stone materials with a particle size below 5cm). Adding cement to the smaller filling materials (with a particle size below 5cm) will comply with the cement aggregate provisions of CNS (to adjust the proportions of improper earth and stone contents). In-situ self-propelled mixing machines and other machinery can be used to produce deposition earth-rock cement with a design strength of 210 kg/cm2 and a slump degree of 12.5cm ± 4.5cm. According to the cost estimation and in consideration of the material, machinery and testing fees, this process has no economic benefits, unless the usage is over a certain level.

2.4 Reservoir silt cement

After a typhoon or torrential rain, the earth and stones carried by floods often cause reservoir silting. This reduces the effective capacity of the reservoir and poses a threat to the safety of the reservoir. The excavation of dry silt during the dry season for effective reuse is a good countermeasure to this threat. According to the definition of reservoir silt cement in Chapter 03081 of the Public Works Construction Program Standards, reservoir silt can replace some of the fine aggregate to make pure cement or low strength steel reinforced cement for secondary structures. The recommended ratio design strengths are of two types: 175 kg/cm2 and 210 kg/cm2.

2.5 CLSM (Controlled low-strength material)

CLSM has the properties of self-fulfillment and high flow, similar to high performance cement, and it therefore does not require rolling or vibration for compaction. CLSM is suitable for the backing of underground pipelines by replacing traditional earth and stone backfilling. According to the CLSM provisions in Chapter 03377 of the Public Works Construction Program Standards, CLSM can be produced by the in-situ excavation of earthworks and recycled materials, in addition to using clean aggregates for general cement in the ready-mix plant. At present, most of the ready-mix plants in the market use clean aggregates that have controllable quality but also have relatively higher prices. However, in-situ excavated earthworks are an acceptable replacement for aggregate. Despite their lower prices (60-80% of clean aggregates, according to the Public Works Engineering Price Database, 2011, and Construction Material Prices, Issue 81), the in-situ excavated earth and soil still have to be delivered to the ready-mix plant by the construction unit, resulting in higher costs.

3. In-situ Mixing Method

3.1 Literature Review amd Ratio design

According to the literature, after blending the in-situ cement and soil evenly by the in-situ mixing method or by other methods, and after full compaction, the soil will classified as GW, GP, GM, or GC. The recommended usage of cement for in-situ mixing is around 3%~9%, as shown in Table 1, and the compression strength is roughly 66 kgf/cm2 (6.5MN/mm2), as shown in Table 2.

The purpose of this study was to find the optimal balance between engineering economic benefits, and energy savings and carbon reduction. Therefore, this study selected the common ratios for construction engineering to design the engineering ratios in various testing areas. This could speed up the promotion of in-situ mixing as well as facilitate engineering personnel in using the in-situ mixing of cement.

Therefore, the in-situ mixing method can be defined as a method for soil improvement. The principle of improvement is similar to that of soil cement, namely, mix the in-situ excavated earth and stone with the cement for ready use. The aggregates are not separated in-situ. By adding water into the aggregates and mixing evenly, the produced material can be directly used in backfilling as a composite material for erosion resistance, with improved structural safety and in-situ strength. With the in-situ mixing method, the cement content can be as high as 7%~8%. To simplify the construction procedure, if the in-situ earth and rock belong to Class G of the USCS classification, the weight ratio of the cement and silt is recommended to be 1:12 (the cement usage is 7.7%). In other words, each cubic meter of in-situ mixing material will use 165 kg of cement. In addition, the silt debris is a composite material made up of mud, earth, sand and stone, which may have different water absorption rates. The water content of the in-situ earth may also be different due to the depth of excavation or the distance from the river channel. In practice, water usage should be gradually added in-situ until all the materials have been evenly mixed.

In consideration of the minimum economic costs, the minimum amount of cement was used. With a ratio of 1:4:8, the lowest strength was at least 33kgf/cm2. In order to reduce project costs and use the least amount of cement required to maintain a certain level of strength and a higher level of compression strength, this study implemented in-situ mixing in Hewang and Hongxian using a ratio of 1:3:6.

Table 1 Typical cement requirements for various soil types [after Anon 1990, State of the art report on Soil-cement, ACI 87(4)]

Unified soil classification	Typical range of cement requirement,* (% by wt)	Typical cement content for moisture-density test (AMST D 558),+ (% by wt)	Typical cement contents for durability tests (ASTM D 559 and D 506),☆ (% by wt)
GW, GP, GM, SW, SP, SM	3-5	5	3-5-7
GM, GP, SM, SP	5-8	6	4-6-8
GM, GC, SM, SC	5-9	7	5-7-9
SP	7-11	9	7-9-11
CL, ML	7-12	10	8-10-12
ML, MH, CH	8-13	10	8-10-12
CL, CH	9-15	12	10-12-14
MH, CH	10-16	13	11-13-15
* Does not include organic or poorly reacting soils. Also, additional cement may be required for severe exposure conditions such as slope protection.			
+ ASTMD558(1992) Standard Test Method for Moisture-Density Relations of Soil-Cement Mixtures, American Society for testing Materials, Philadelphia.			
☆ ASTMD559(1982) Standard Methods for Wetting and Drying Tests of Compacted Soil-cement Methods for Freezing and Thawing Tests of Compacted Soil-Cement Mixtures, American Society for Testing Materials, Philadelphia.			
Source:F.G.Bell (1993), "Engineering Treatment of Soils", E & FN SPON, an imprint of Chapman & Hall, London.			

Table 2 Typical average properties of soil-cement and soil-lime mixtures[after Ingles and Metcalf, 1972]

Typical ment* properties of soil-cement+						
Soil type (Unified classification)	Compressive strength (MN/m^2)	Young's Modulus, E(MN/m^2)	CBR	Permeability (m/s)	shrinkage	Comments
GW, GP, GM, GC, SW	6.5	2×10^4	>600	Decreases ($\cong 2\times10^{-7}$)	Negligible	Too strong; liable to wide spaced cracks☆
SM, SC	2.5	1×10^4	600	Decreases	Small	Good material
SP, ML, CL	1.2	5×10^3	200	Decreases	Low	Fair material
ML, CL, MH, VH	0.6	2.5×10^3	<100	Increases	Moderate	Poor material
CH, OL, OH, Pt	<0.6	1×10^3	<50	Increases ($\cong 1\times20^{-11}$)	High	Difficult to mix; needs excessive cement
* Variations of approximately 50% around the mean may be expected.						
+ Values shown are at 10% cement content						
☆ Good material if less cement is used						
Source：F.G.Bell (1993), Engineering Treatment of Soils , E & FN SPON, an imprint of Chapman & Hall, London						

3.2 Laboratory mixing simulation test

This study used a 1:12 cement to silt (coarse and fine aggregate mixture) ratio to conduct a simulation test. To support the Hewang River de-silting project, this study took samples from the Hewang River in Ren-ai Township, Nantou County, and conducted a test using a 1:12 cement to silt ratio. The water usage referred to the general settings of cement preparation: the water/cement ratios were set at W/C=1.82 and W/C=1.98 for a slump of 15 cm and 20 cm, respectively. The mixing ratio referred to CNS 1174 by removing rocks sized at or above 37.5mm to make cylindrical specimens that were 15 cm in diameter and 30 cm in height. The strength testing results are shown in Figure 10. For a slump of 15cm and 20cm, the strength of the 28-day cement was 39kgf/cm2 and 36kgf/cm2, respectively, which was lower than the lowest strength found at a mixing ratio of 1:4:8, as mentioned in the previous section. This could have been caused by the relatively higher W/C ratio of the simulation test in the laboratory.

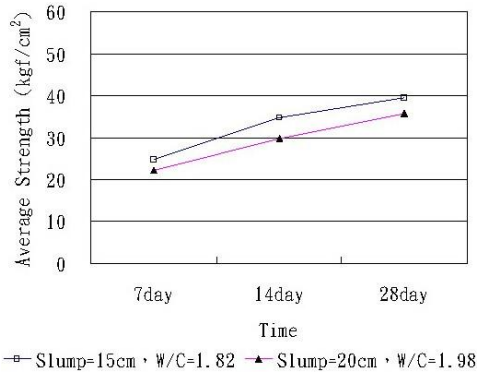

Figure 3 Indoor Strength Testing Results

3.3 Application of in-situ mixing method

The Hewang area in Nantou was hit by three typhoons in 2008: Kalmaegi, Sinlaku, and Jangmi, all of which caused a large amount of earth and sand to flow into the river channel. The floods damaged the riverside lands and buildings, and the debris accumulated in the channel of Hewang River, resulting in an insufficient cross section of the river channel. The slopes collapsed under the impact of the river floods, and a number of roads were damaged. Reconstruction was seriously needed, and thus, the de-silting project of Hewang River and a nameless bridge commenced.

During the de-silting project, the silt materials obtained in-situ were modified according to their properties. Coupled with the planned protection measures, the in-situ mixing method was promoted. Hence, along Hewang River, the mixing for ground improvement engineering method was applied in various places to achieve the designed purpose. In Nantou County's Hewang River and Honghsiang Tribe, troughs were excavated along the river channel. The troughs were filled with the in-situ mixture, which formed an underground protection structure between the river channel and the objects under protection, as shown in Figure 8. In normal times without flooding, the river channel will run left and right due to landforms, rainfall and other factors. The channel will gradually erode and remove the fine aggregates, leaving the coarse aggregate with its pseudo stability to temporarily support the soil. Once too much sand and stone have been carried away, or when the river water's scouring force becomes greater, the structure will be damaged and there will be in soil erosion. If the eroded area has gabions or stone deposits on the top, the bottom will become depleted, ultimately damaging the gabions and the slope. On the contrary, the mixing land improvement engineering work will improve the level of resistance to the scouring of river water. However, the erosion resistance capability must be higher than that of the unmodified silt. When the river channel is close to the improved structure, this method can prevent or at least delay the earth and stone from being eroded or scoured.

Application of the mixing land improvement engineering method along Hewang River:

1. Riverbank at the toe of the collapsed slope.
2. Riverbank at the toe of the slope in the area of earth and rock backfilling.
3. Attack riverbank.
4. Riverbank at the toe of the slope of the agricultural land base.
5. Riverbank at the toe of the slope below the agricultural land.

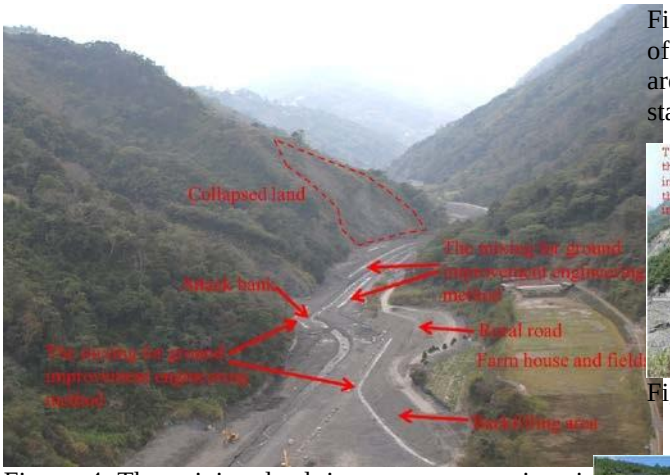

Figure 4 The mixing land improvement engineerin method improvement structure, showing th objects to be protected

The purpose of this study was to find the optim balance between engineering economic benefits, an energy savings and carbon reduction in wildcre cleanout process. Therefore, this study selected t common ratios for construction engineering to design the engineering ratios in various testing areas. This could speed up the promotion of in-situ mixing as well as facilitate engineering personnel in using the in-situ mixing of cement. As show in Figure 9.

Figure 5 The process of In-situ Mixing Method (Premix)

3.4 Compression results of the mixing ground improvement engineering method

Regarding the de-silting project in Hewang River and Honghsiang Tribe of Nantou County, according to the in-situ characteristics and protection requirements, this study applied the mixing ground improvement engineering method using the ratio from CNS 1174 by removing pebbles sized at and above 37.5mm to make cylindrical specimens with a diameter of 15 cm and a height of 30 cm. The land improvement compression strength of 28 kgf/cm2 was about 20% that of general concrete (140 kgf/cm2), which provided resistance to lateral erosion, improved structural safety and in-situ strength considerations to protect objects, as shown in Figures 11~12. The compression strength testing results of the cylindrical specimens in Hewang and Honghsiang are shown in Figure 13. The results indicated that the standard of 28 kgf/cm2 had been met in both cases.

Figure 6 Hewang mixing land improvement engineering method used to protect against slided land

Figure 7 Honghsiang mixing land improvement engineering method used to protect against slided land

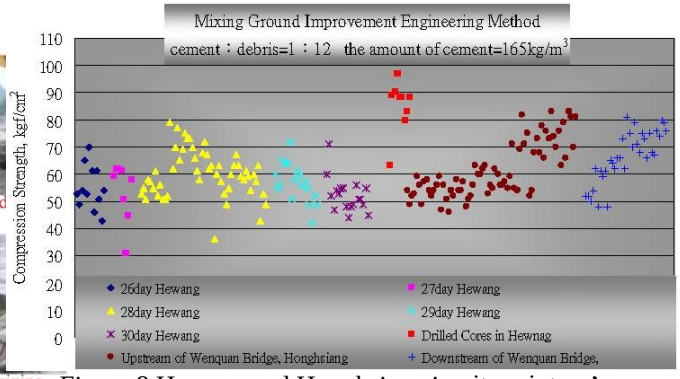

Figure 8 Hewang and Honghsiang in-situ mixture's compression strength

4. Statistics and promotions of using in-situ debris

4.1 Statistics of using in-situ debris

In the overall improvement plan implementation, In processing the cleanout work for wild creek, debris should be treated as useful resources. In solving the debris blockage problem, cleanout of debris so as to recover the drainage capability of watershed and at the same time, using the earth material to form the protecting measures can meet the carbon reduction requirement. By applying feasible methods to improving engineering properties of the debris can be

used to make a variety of protective measures, to resolve the loss of land, roads, damaged buildings and other issues. Soil and Water Conservation Bureau carried out debris reuse about 12.37 million Cubic meters and created 313 hectares from Morakot Typhoon to 2013.

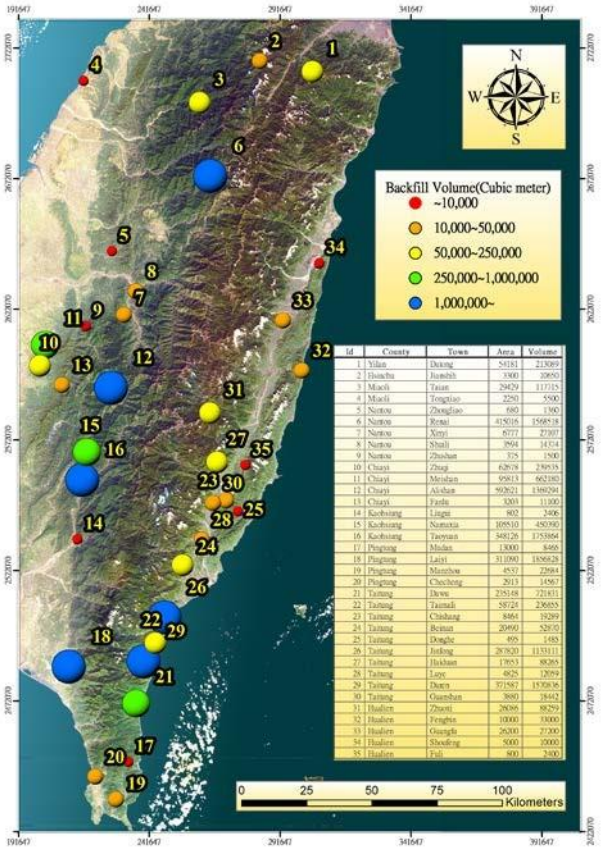

Figure 9 Statistics of in-situ debris reused by SWCB between 1999~2013

4.2 Promotions of in-situ use of debris

Upstream areas of Choushui River due to its steep slope and poor geological conditions, plus climatic anomalies and rainfall strength increment in recent years, resulted in the area of landslide increase heavily. In order to protect the safety of embankment, farmer's livelihoods and energy saving. The 4th River Management office used in-situ debris mixing materials develop low-water regulation work in WanFeng area of Nantou County which showed suitable to solve problem in upstream areas of Choushui River.

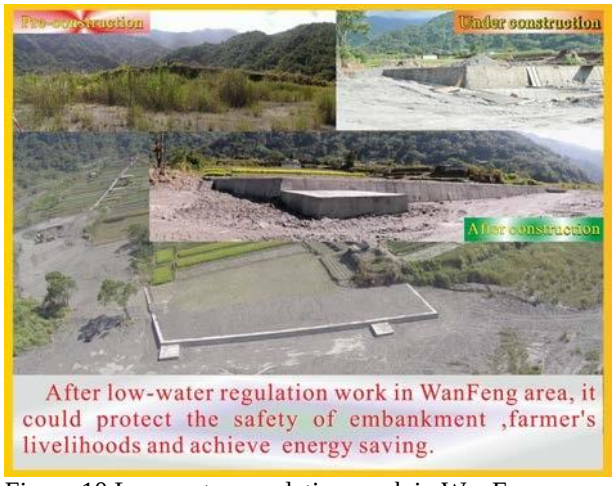

Figure 10 Low-water regulation work in WanFeng area

4.3 Assessment of using field debris

After investigating the sediment spatial variation of the catchment area, overall management planning and implementation can proceed. It can complement each other with the dredging operations and handled overall conservation management plan. In the overall improvement plan implementation, In processing the cleanout work for wild creek, debris should be treated as useful resources. This is very important in the watershed management and rehabilitation work. In solving the debris blockage problem, cleanout of debris so as to recover the drainage capability of watershed and at the same time, using the earth material to form the protecting measures can meet the carbon reduction requirement. By applying feasible methods to improving engineering properties of the debris can be used to make a variety of protective measures, to resolve the loss of land, roads, damaged buildings and other issues.

1. Strategy

(1) Wildcreek debris deposition, can cause loss of agricultural land, roadbed destroyed, River erosion. Overall problem is serious in Taiwan.

(2) Upstream area need it dredging operations as soon as possible, and it will plan the place of stacked debris.

(3) In the dredging operations, and the debris as usable resources is considered. In the field, according to requirement of the repairing and protection work. Debris is treated to from the structures. It use the earth material to form the protecting devices which can meet the carbon reduction requirement.

2. Evaluation process

According to the material properties of dredged debris, and it will add the cement and using in-situ mixing method to build the structure. According to needs of repair and protection in-situ, and it can use in restoring the loss of agricultural land, low-lying land

backfill, subgrade embankment protection, slope protection and bank protection as shown in Figure 7.

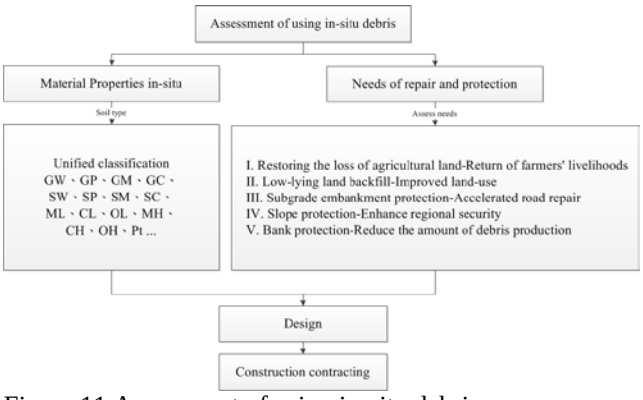

Figure 11 Assessment of using in-situ debris

Assessment I: Restoring the loss of agricultural land-Return of farmers' livelihoods.

Agricultural land near the river which were destroyed and lost. Because of wildcreek debris transport needs restoration. It should be proceed when wildcreek dredging operations at the same time, restore its lost parts and increase its elevation.

Assessment II: Low-lying land backfill to improve land-use.

The low-lying land near river, which are impact by wild creek debris transport and flood. Backfill ground and increase their elevation can improve the conditions of land use, and achieve improved results.

Assessment III: Subgrade embankment protection to accelerate road repair.

Bank road suffered floods erosion, "in situ mixing method" can be used to improve roadbed and the bottom of the embankment site. In particular, there have erosion loss in-situ and causing some uncovered rock. By "in situ mixing method" as the preferred carrier layer protection. It can also avoid the loss of follow-up, and speed up the repair of roads.

Assessment IV: Slope protection-Enhance regional security.

Slope damage due to the loss and erosion of the Foundation. In the wildcreek dredging process together with slope toe protection, can from a whole considerations. If the slope toe can stabilize , it can speed up the subsequent recovery of the overall slope and enhance regional security.

Assessment V: Bank protection-Reduce the amount of debris production.

The wildcreek dredging work can improve the riverbed cross section for where riverbank suffering erosion and avalanche phenomenon. In the process of dredging, riverbank or embankment protection can effectively improved and the subsequent production of sediment.

5. Conclusion

In recent years, typhoons and torrential rain have caused slope landslides to silt river channels, causing serious floods disaster in Taiwan. The de-silting of rivers and rivers regulation should be done immediately and without delay. It is recommended to dig deep troughs to river channels at a minimum cost in the shortest time. The excavated silt can be reused. According to the in-situ restoration and protection requirements, with the help of the in-situ mixing engineering method, riverbank land improvements can be carried out. This engineering method is fast, easy to apply and has a low cost, making it economically effective and environmentally conscious, as it can save energy and reduce carbon emissions.

The mixing land improvement engineering method is a method that requires a more even mixing, as compared with soil cement. The product can be used directly in backfilling to provide resistance to lateral erosion and scouring, improved structural safety and in-situ strength. As far as the compression strength of the in-situ engineering method is concerned, it was found to be 70 kgf/cm2, or 50% of that for general concrete (140 kgf/cm2); for land improvement, it was 28 kgf/cm2, or 20% of the standard for general concrete.

Protection factors should be taken into consideration during the de-silting process, including the filling of low-lying land and the in-situ mixing ground improvement method. Promotions of in-situ use of debris is worth to conduct in the future.

References

[1] Public Construction Commission, Executive Yuan, Public Works Construction Outline and Regulations webpage data (2011)http://pcces.archnowledge.com/csinew/Default.aspx?FunID=Fun_9_3&SearchType=B.

[2]Public Construction Commission, Executive Yuan, Public Works Pricing Database webpage data (2011) http://pcces.archnowledge.com/csinew/Default.aspx?FunID=Fun_11_2&SearchType=D.

[3]Ren-ai Township Office Nantou County (2010). “Ho-wang Stream Wu-ming Bridge Upperstream 0K+950~1K+500 Emergency Dredging Works” unit price analysis table. Ren-ai Township Office Nantou County.

[4]Taiwan Construction Research Institute (2011). Construction Quotes. Issue 81. Taiwan Construction Research Institute.

[5]Chen, C. C. (2008). Siltation Debris Land Utilization Research and Counseled Pilot Project Works. Taiwan Construction Research Institute. Soil and Water Conservation Bureau, Council of

Agriculture, Executive Yuan.
[6]Official website webpage data from the "ISM Method Society," Japan. (2011) http://www.ism-method.jp/.
[7]Chinese National Standard (2009), Bureau of Standards, Metrology & Inspection, M. O. E. A..
[8]ASTM Stands, American Society for Testing and Materials(1998) (ASTM D2487)
[9]F.G.Bell (1993), "Engineering Treatment of Soils", E & FN SPON, an imprint of Chapman & Hall, London

Quantifying the Temporal Variations and Spatial Distribution in Landslide-Driven Sediment Production by Using Decision Tree at Watershed Scale

Yu-Wen Lin [a], Li-Sheng Chou [a], Che-Wei Shen [a], Yu-Jia Chiu [b], Kang-Tsung Chang [c]

[a] Disaster Prevention Technology Research Center, Sinotech Engineering Consultants Inc.
[b]Hydrotech Research Institute, National Taiwan University
[c]Department of Geography, National Taiwan University

E-mail: ywlin@sinotech.org.tw, lschou@sinotech.org.tw, cwshen@sinotech.org.tw, yujiachiu@ntu.edu.tw, ktchang@ntu.edu.tw

Abstract –

This research contains 2 parts. First, the study has so far collected 11 annually nationwide landslide inventories from 2004 to 2014. Geographic information system analysis and visualization software Tableau were conducted to analyze the long term trend of landslide ratio (LSR) and to visualize preferred characteristic factors of each basin area in Taiwan. In the decade of 2004 to 2014, the LSR of 10 largest basins in Taiwan generally tend to ascend from less than 1% to more than 2%. While focus on the Kaoping River watershed, where heavily striken by Typhoon Morakot in 2009, the LSR before 2009 was slightly ascending and sharply rose at 2009, then the trend of LSR appears to recovering from high spot until now and indicated the natural LSR recovering period is about 9 to 10 years. Second, this research conduct decision tree (J48) method analyzed 11 event-based landslide inventories from 2001 to 2010 and each 20m raster grid of Kaoping River watershed in southern Taiwan. Decision tree method induct the rules of landslide potential and calculate the sediment volume of each slope unit. With automatic metadata analysis and visualization method, this research provides the authorities intuitive and interactive panel to management real-time probability of landslide and sediment producing of each sub-basin.

Keywords –

Visualization; Landslide Ratio; Decision Tree; Landslide Potential, Sediment Production

1 Introduction

Taiwan is an island of 36,000 km^2 and is situated in the active subduction-collision region between the Eurasian Continent and the Philippine Sea plates (Huang et al., 1997), with frequent large earthquakes. About 70% of the island is either hilly or mountainous.

The topography is characterized by small drainage basins, fractured rock formations, high relief, and steep stream gradients. Taiwan is also located on the major tracks of typhoons (tropical cyclones) in the northwest Pacific region, with an average of four typhoons per year (Wu and Kuo, 1999). Landslides triggered by typhoons and earthquakes act as major sources of both coarse and fine sediments in channels and rivers in Taiwan. These sediments are then transported and deposited in dams and reservoirs, reducing their storage capacity for drinking water and/or electricity production. Estimates of long-term average landslide erosion rates are therefore needed for sediment budget calculations as well as for the general purpose of watershed management in Taiwan.

It was indicated that in 1980 to 2010, accumulative rainfall increased 85.25 mm per decade in average (NCDR, 2011) and the days with rainfall decreased 4 days per decade in average. Overall, the intensity of rainfall in Taiwan is steadily increasing in the past few decades to extreme rainfall condition. The extreme rainfall induced landslides will contribute to debris flows, landslide dam, and etc. Multi-hazard causes serious threats to people and properties in southern Taiwan. To prevent catastrophic disaster, landslide potential and sediment management will be the main topic we have to concern about.

In this study, we established open format database from Soil and Water Conservation Bureau (SWCB) and analyzed nationwide LSR trend and characteristic factors in the decade of 2004 to 2014. Also conduct Tableau software to visualize LSR trends and preferred factors of each sub-basin in Taiwan.

Second, this study conduct Waikato Environment for Knowledge Analysis (WEKA) decision tree analysis

which inducted 11 rainfall event-based landslide factors of 20m raster grids of Kaoping River watershed. WEKA is an open source freeware and supports Hadoop Distributed File System (HDFS) in Hadoop/Spark metadata analysis frameworks which is based on MapReduce algorithm model. This study constructed open format HDFS and Hadoop framework to analyze landslide characteristics with J48 decision tree method in order to connect the Application Programming Interface (API) of government released open data such as predicted rainfall (QPESUMS, etc.) to establish automatically real-time computing landslide potential model and sediment management platform in the next stage.

2 Study Area

The Kaoping River watershed, located on the south-western side of the Central Mountain Range of Taiwan, was selected as the study area (Figure 1). The watershed has a drainage area of 2868 km^2, with elevations ranging from 22 to 3872.7m and an average slope of 26.4° derived from a 20-m digital elevation model (DEM). The lithology is composed of metamorphosed and deformed rocks, including black and green schist, phyllite, and argillite, terrace deposits, and alluvium. About 76% of the study area is primary indigenous forest, with cultivated fields and built-up areas accounting for the remaining 24%. The suspended sediment discharge is about 49 Mt per year, mainly produced by typhoon and earthquake-triggered landslides (Dadson et al., 2003).

Annual rainfall in the Kaoping River watershed ranges from 2300 mm in the downstream area to 4500 mm on the south-eastern side of the headwater area. Rainfall distribution is extremely uneven, with 90% of annual rainfall falling during the wet season of May to September (Water Resource Agency, 2015).

Rainfall during the wet season is mainly induced by typhoons. When a typhoon crosses northern Taiwan, it can bring heavy rainfall in southern Taiwan, including our study area, due to south-westerly wind flows (Wu and Kuo, 1999). The extreme event Typhoon Morakot had 548 to 1,448mm rainfall in Kaoping River watershed and 998mm in average. Compare to the extreme event, 100yr reoccurrence rainfall of study watershed is 554 to 1,108mm and 831mm in average.

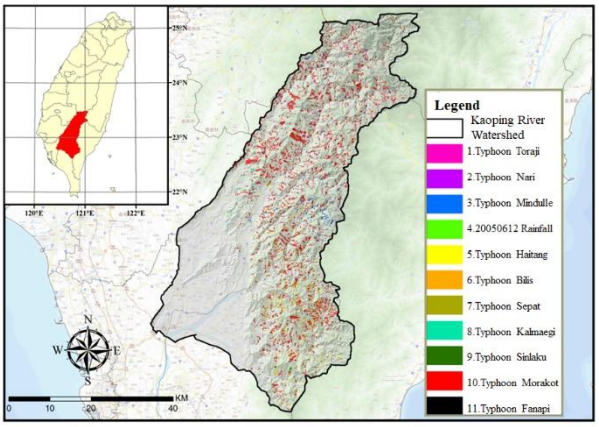

Figure 1. The Kaoping River watershed and the multi-temporal, event-based landslide inventory from 2001 to 2009. The color polygons show new landslides triggered by rainfall events in the Kaoping River watershed.

3 Methods and materials

This study followed the work flow in Figure 2. It analyzed nationwide annually and event-based landslide inventories separately.

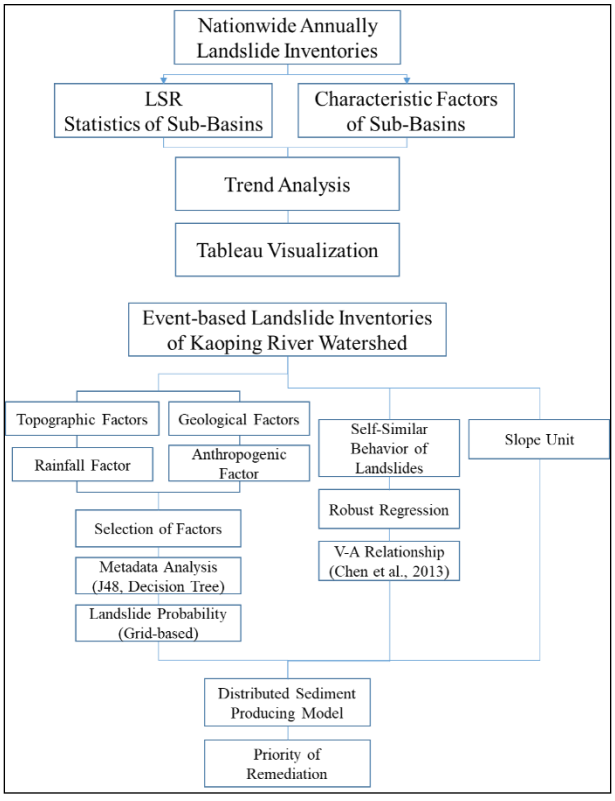

Figure 2. Work flow of this research.

3.1 Trend of LSR in Taiwan

This research collected annually landslide inventories from 2004 to 2014 and factors as slopes, aspects (reproduced from 5m resolution DEM), rainfall (max 24 hrs accumulative rainfall each year), and geology.

LSR is calculated as the proportion of newly added landslide area over hillside area (area of slope over 5%) of sub-basin or watershed. LSR of each watershed in 2004 to 2014 is calculated in Figure 3 and the trend of LSR in Taiwan is shown as steadily rising from under 2% to over 2% except only 1 watershed. Watersheds in southern Taiwan were apparently affected by Typhoon Morakot and LSR of these watersheds sharply increase to more than 5%. Kaoping River and Linbian River watershed recovered from extreme event and LSR gradually decrease from 5% in 2009 to 2.5% in 2014 while LSR of other watersheds affected by Typhoon Morakot were fluctuating during this period.

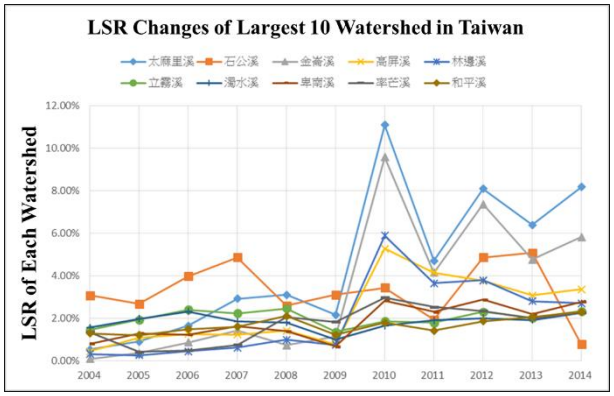

Figure 3. The LSR trend in the decade from 2004 to 2014 which is steadily increasing from 0~2% to over 2% in 2014.

Due to the LSR recovering phenomenon of Kaoping River watershed, this research focus on it to analyze the trend changes. The LSR of the largest 15 sub-basins of Kaoping River watershed are shown in Figure 4. The figure displays different slope of LSR trend. Before the extreme event in 2009, the LSR trend increases slightly as well as the trend of 10 largest watershed in Taiwan. However, the trend after 2009 shows recovering LSR and probably meet the trend before 2009 at the period between 2018/2019. The figure indicates the recovering period of extreme event is about 9 to 10 years in Kaoping River watershed. Figure 4 also implies the possible LSR from 6% to 16% of sub-basin under extreme rainfall condition (about 1,000mm accumulative rainfall in single event).

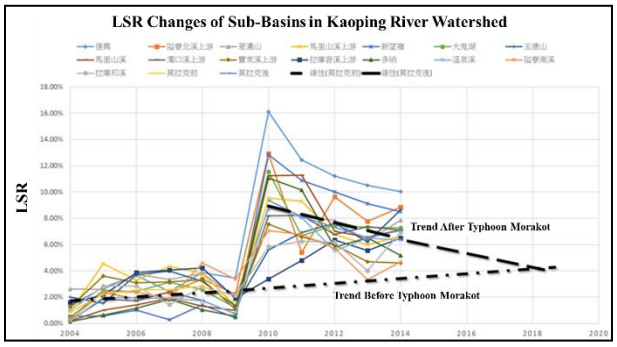

Figure 4. The LSR changes of sub-basins in Kaoping River watershed indicate that 9~10 years are needed to recover from strike of an extreme event (Typhoon Morakot).

To integrate LSR curves of watersheds in Taiwan depend on time and preferred factors, this study conducted Tableau software to visualize LSR trends and characteristic factors in 1 interactive graph as shown in Figure 5. The figure can be interactive clicked to display characteristic factors of certain watershed as Figure 6 shown. In Figure 6, Kaoping River watershed is highlighted with the graphs of LSR versus each preferred factor on the right-hand side. The preferred factors of high LSR in Kaoping River watershed are also highlighted that slopes are concentrated in 55% to 100% as 6th grade slope (7 grades of slope level classified by SWCB), aspects distributed in southeastern, southern, eastern, and southwestern. Rainfall is mostly over 500mm and are mainly placed in Chaochow, Pilushan, and Changchihkeng geological zone.

In this visualization method, data is integrated and the new landslides' characteristics of a watershed will be distinct in the graph while clicked by user. The graph also supports interacting via browser to display changes of LSR and mainly preferred factors. The graph provide an intuitive way for authorities to understand the input budgets and the problems in the past years of each watershed.

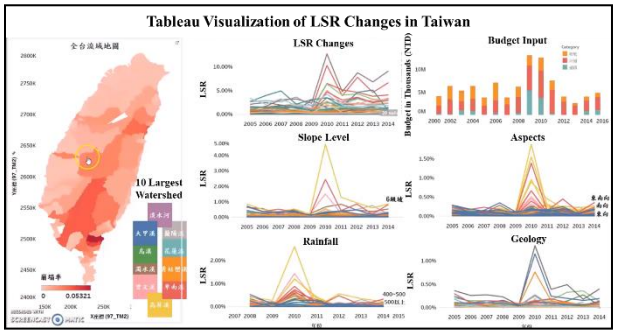

Figure 5. The integrated interactive LSR changes

of watersheds in Taiwan with preferred factors including slope level, aspects, rainfall, and geology.

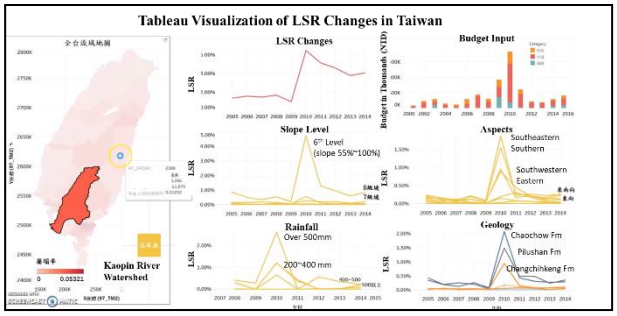

Figure 6. Kaoping River watershed is selected in interactive LSR graph. Preferred factors of high LSR are highlighted that slopes are concentrated in 55% to 100%, aspects in southeastern and southern, rainfall over 500mm and are mainly placed in Chaochow, Pilushan, and Changchihkeng geological formation.

3.2 J48 Decision Tree Analysis

J48 decision tree algorithm, also known as C4.5 decision tree algorithm (Quinlan, 1993), is a model to classify training data into branches and generate rules of classifying. This research analyzed 20m resolution raster grids of Kaoping River watershed with 14 factors and 11 event-based landslide inventories, therefore, metadata analysis method is necessary in this study. J48 decision tree algorithm is well known as an efficient analyzing tool of metadata mining (Patil and Sherekar. 2013) and is a purely inductive analyzing method without model.

3.2.1 Principles of J48 Decision Tree

In J48 decision tree algorithm (Dai and Wei, 2014), data is classified by the Gain Ratio of data which is shown as Equation (1). Where S is attributes and T is training data set.

$$GainRatio(S,T) = \frac{Gain(S,T)}{SplitInfo(S,T)} \quad (1)$$

Gain(S,T) is the information gain defined as the difference between information of attributes which is calculated by *Entropy* of data features as shown in Equation (2). Where *Values*(T_S) is the set of values of S in T, T_s is the subset of T induced by S, and T_s,v is the subset of T in which attribute S has a value of v.

$$Gain(S,T) = Entropy(S) - \sum_{v \in value(T_S)} \frac{|T_{S,v}|}{|T_S|} Entropy(S_v) \quad (2)$$

The entropy of data attribute S means the uncertainty or the amount of disorder of information which calculate by Equation (3) where C denote the number of classes, j is one certain value of attribute S and $p(S,j)$ is the proportion of instances in S that are assigned to j-*th* class.

$$Entropy(S) = -\sum_{j=1}^{C} p(S,j) \times log_2(p(S,j)) \quad (3)$$

And Splitinfo(S,T) is calculated as Equation (4).

$$SplitInfo(S,T) = -\sum_{j=1}^{v} p(T_S, T_{S,v}) \times log_2(p(T_S, T_{S,v})) \quad (4)$$

Decision tree is composed of *internal nodes*, *edges*, and *leaf nodes*. Each internal node (decision node) stands for a test on an attribute or a subset of attributes and has edges at internal node. Each edge is labeled with certain value or range of value to separate data from internal node to next depth. The leaf node is the terminal node of the tree with a class label. Figure 7 shows the structure of decision tree.

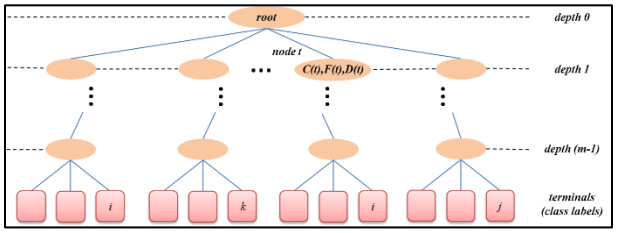

Figure 7. Structure of decision tree. Each elicpse is internal node with branches (edges) and rectangles are leaf nodes.

With the open source metadata analysis tool **WEKA**, which includes J48 decision tree method, data is classified into various class label and gives rules of classification of each leaf node (terminal node) such as following example:

if *(Accumulative Rainfall in 24 hrs < 500mm) and (Elevation < 500m)*

then *Landslide Prediction* = ***Yes***

3.2.2 Data Format and Analyzing Structure

The original data from SWCB are IMG or SHP geographic information system (GIS) formats. This research established python process to automatically and real-time transformed to 20m ASCII files (open format) and are saved in Hadoop Distributed File System (HDFS). The process is shown in Figure 8.

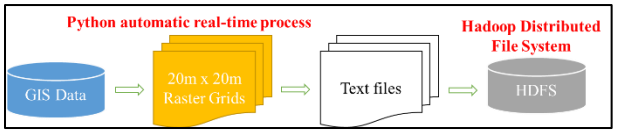

Figure 8. The Python-based automatic real-time process of data format transformation.

The structure of metadata analysis combines Linux OS and Hadoop framework to compute simultaneously on slaves and master HDFS clusters.

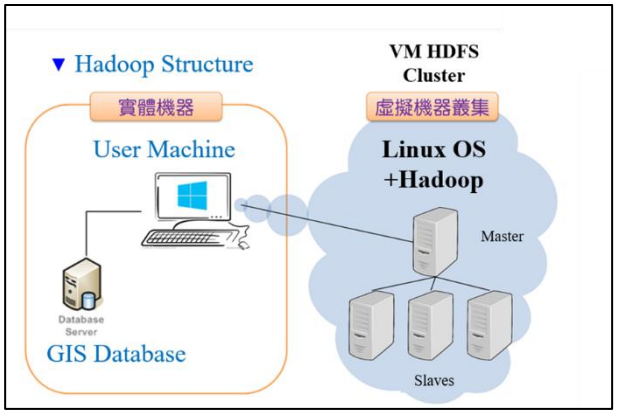

Figure 9. The analysis structure of Hadoop metadata analysis. It includes several virtual HDFS cluster computing collaborated and displays results on user's machine.

3.2.3 Factors and Event-Based Inventories

Factors of Kaoping River watershed in this research were collected from SWCB and Government Open Data of R.O.C., Taiwan. Selected factors and the range of values are shown in Table 1.

Table 1. Selected factors for J48 decision tree analysis

Factors	Unit	Range	Mean
Elevation	m	22~3,872.7	1,974.4
Slope	%	0~3,245.6	49.64
Asp_sin/Asp_cos	Rad	-1~1	0.0
Curvature	1/m	-1,057~696	-180.6
Topographic Index, TI	m	1.9~16.5	9.2
Roughness	m	0~130.5	65.3
Roughness of Slope	%	0~559.4	279.7
Relief	m	0~123.8	61.9
*Dist_Fault	m	0~22,931.9	11,466
*Dist_River	m	0~2,352.9	1,176.5
*Dist_Ridge	m	0~2,251.1	1,125.6
*Dist_Road	m	0~10,043.0	5,021.5
Geology	Type	15 Types	-
Dip Slope	Binary	0 / 1	-
Rainfall of Morakot	mm	548~1,448	998
Rainfall of 100yr Reoccurence	mm	554~1,108	831

*Distance from faults, rivers, ridge lines, and roads

There are 11 event-based landslide inventories collected in J48 decision tree analysis and the first 10 events are training sample while the 11th event as validation sample. Landslide inventories are shown in Table 2.

Table 2. Event-based landslide inventories collected in this study

No.	Typhoon Event	New Added LS Area(km2)
1	Typhoon Toraji	2.515
2	Typhoon Nari	0.306
3	Typhoon Mindulle	6.598
4	20050612 Rainfall	0.533
5	Typhoon Haitang	12.312
6	Typhoon Bilis	1.945
7	Typhoon Sepat	0.949
8	Typhoon Kalmaegi	2.238
9	Typhoon Sinlaku	0.384
10	Typhoon Morakot	116.368
***11**	Typhoon Fanapi	0.460

*The 11th event Typhoon Fanapi is the validation sample

3.2.4 Decision Tree of Kaoping River Watershed

Give factors in Table 1 and event samples in Table 2 as input of WEKA, the first and second depth of output decision tree result is shown in Figure 10. The decision tree can be separated into 3 basins of Kaoping River watershed and it indicates charateristics of each basin.

In the Ailiao basin, landslides are mainly controlled by natural condition of geological, topographic and hydrological factors due to rare human developments and activities in the upstream area. The geological condition in Ailiao basin is Pilushan Formation where landslides triggered frequently.

In the largest Laonong River basin, the characteristic factor is rainfall and related to location of slope of landslide. Rainfall, location, and topographic condtion control the landslide potential in Laonong River basin.

The distinguished result of decision tree is Chishang River basin, the first node is distance from road and no rainfall factor is preferred in this basin area. Chishang River basin has lower average elevation distribution and human activities are prospering.

The first and second depth nodes of WEKA decision tree properly reflect various charateristics of basins in Kaoping River watershed.

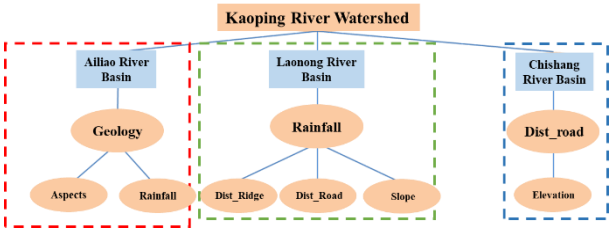

Figure 10. J48 Decision Tree results of Kaoping River Watershed and 3 basins contain different characteristic factors on the first and second depth of tree. 1) Landslides in Ailiao River basin are mainly controlled by geological condition, and also related to aspects and rainfall. 2) Landslides in Laonong River are controlled by rainfall and related to distance from ridge, road, and slope angle. 3) Landslide potential in Chishang River basin is controlled by human factor and related to elevation.

3.2.5 Preferred Landslide Rules of Kaoping River

To summarize the decision tree results, the preferred characteristics and rules of landslides are aggregated into tables as Table 3 to Table 5. The node order is the depth of node and also implys the importance of factors. The first order factors will dominate the regional characteristic of each basin. In addition, the nodes of preferred rules can be interpreted as conditional probability of landslides which are listed below the table. The combinatorics of factors in the following tables indicate certain rule and probability of landslide.

Table 3. Preferred Rules of Ailiao River Basin

Node Order	Factors	Favorite Charateristics
1	Geology	Pilushan Fm. Lushan Fm.
2	Aspects	NE/E/SE/S
3	Rainfall (mm)	300~400 Over 500
4	Elevation (m)	500~1,500
Else	Slope (%)	5 to 7 grade (>40%)
	Roughness of Slope (m)	13.16~30.7
	Roughness (%)	3.98~8.95

e.g. if *Geology = Pilushan* & *Rainfall > 300 mm*
then **Landslide** = ***Yes***

Table 4. Preferred Rules of Laonong River Basin

Node Order	Factors	Favorite Charateristics
1	Rainfall (mm)	Over 200
2	Dist_Ridge (m)	Over 200
3	Dist_Road (m)	Over 200
4	Slope (%)	6 to 7 grade (>55%)
Else	Relief (m)	2.8~4.54
	Aspects	E/SE/S

e.g. if *Rainfall < 200 mm*
then **Landslide** = ***No***
e.g. if *300 < Rainfall < 400 mm* & *Dist_Road > 200*
then **Landslide** = ***Yes*** and probability rises while roughness increases

Table 5. Preferred Rules of Chishan River Basin

Node Order	Factors	Favorite Charateristics
1	Dist_Road (m)	Over 200
2	Elevation (m)	500~2,000
Else	Rainfall (mm)	Over 400
	Dist_Fault	Over 200

3.3 Sediment Production

The sediment production is one of the causes of multi-hazard of debris flow, landslide dam, and basin sediment disaster to hydrologic infrastructures. Therefore, this research establishs the connection between landslide potential and sediment production with distributed estimation method. The relations of volume and area (Chen et al., 2012) are conducted in this part.

3.3.1 Relations of Volume and Area

Chen et al.(2012) collected multi-temporal inventory covered landslides triggered by 12 typhoons volumes of landslide samples in Kaoping River watershed. And one heavy storm that occurred between 2001 and 2009 and the heavy storm in June 2005, which had a cumulative rainfall of 545 mm in 47 hours in Kaoping, because it was comparable to a typhoon event in terms of triggering landslides. Chen et al.(2012) indicate that newly added landslides of Kaoping River watershed fit power-law relationship bewtween landslide volume (V) and area (A) as the following Equation (5).

$$V_L = \varepsilon \times {A_L}^{\alpha} \quad (5)$$

where V_L (in m^3) is landslide volume, A_L (in m^2) is landslide area, and ε and α are calibrated parameters.

3.3.2 Robust Regression of V-A Relation in Kaoping River Watershed

With Robust regression analysis and measured volume of landslides in field collected in Kaoping River watershed, Chen et al. (2012) estimated the volume and area relation of Kaoping River as Equation 6 and Figure 11.

$$V_L = 0.202 \times A_L^{1.268} \ (r^2 = 0.78, n = 153) \qquad (6)$$

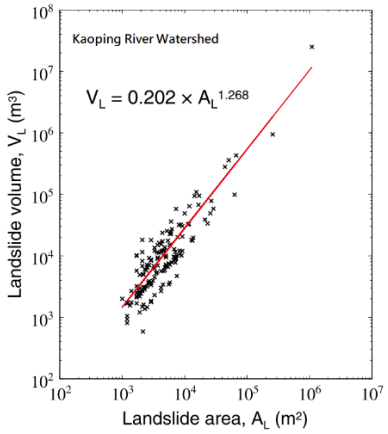

Figure 11. The Robust regression analysis result of Kaoping River watershed with 153 volume and area samples of newly added landslides. (Chen et al., 2012)

3.3.3 Distributed Sediment Production Model

This research combined J48 decision tree results and relation of volume and area in Kaoping River watershed to estimate sediment production of each raster grid. It is set as landslide grid if the probability is over 50% under a rule and will be calculated by volume and area relation. The analyzing method is shown in Figure 12.

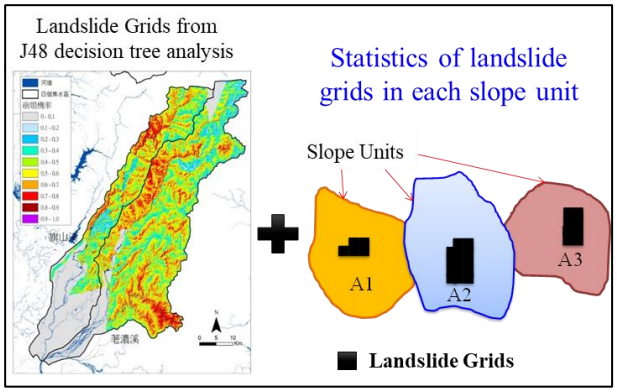

Figure 12. Sediment estimation of distributed sediment production model. Landslide grids are dicided by the probability of J48 decision tree results which is over 50% and calculate by V-A relation of Kaoping River watershed.

4 Results

4.1.1 J48 Decision Tree

Due to the difficulties of interpretation of the complicate decision tree rules and preferred factors, this research conduct D3.js language to automatically visualize decision tree as tree graph and landslide rules as sunburst graph. As the tree shown in Figure 13, each branch represents one rule of landslide potential. Every nodes can fold up or extend to display nodes or edges on the next depth. While it encounters the leaf node (terminal node), the probability of landslide is shown behind it and is calculate by the samples from 10 event-based inventories under each rule.

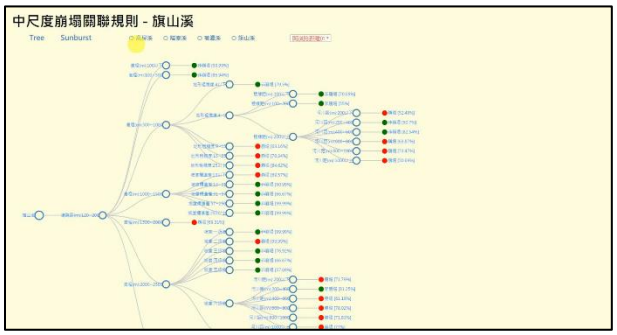

Figure 13. D3.js tree graph visualization of decision tree. Each node can fold up/extend the branches by click. The red/green colors show the probability of landslide (Y/N) under certain rule which is calculated by training samples of 10 event-based landslide inventories.

To summarize the grids (samples) of each rule and the probability of landslide, sunburst graph is conducted to visualize the proportion of samples and J48 results of rules. Take one of the rules from J48 analysis with rainfall condition of Typhoon Mindulle as an example in Figure 14, the place where cursor point to indicate a rule as following factors:

Dist_Road > 200 m & *Elevation: 1,500 ~ 2,000 m* & *Dist_Fault > 1,000 m* & *Rainfall: 600 ~ 700 mm* & *Dist_River < 200 m*

There are 17,890 grids match this particular rule and 93.57% of 17,890 grids are landslide samples. Therefore, the rule tends to landslide. The first ring is the most important factor (node on first depth) in decision tree and the arc length of circle ring indicates grids proportion of upper node.

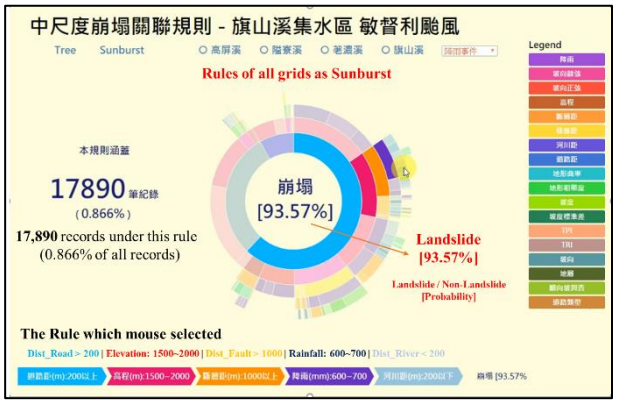

Figure 14. The J48 decision tree analysis results with rainfall condition of Typhoon Mindulle. The left-hand side shows amount of grids under the rule which cursor picked and is shown below the graph. The percentage means the probability of landslide under the rule and also the grids proportion of landslide samples.

4.1.2 Validation of J48 Decision Tree Analysis

The analysis result of J48 decision tree classifier is tested by 4 events and validated by Typhoon Fanapi and shows the correct rate in Table 6. The correct rates are calculated by the proportion of correctly predicted LS/non-LS grids over total LS/non-LS grids.

The average correct rates of all grids in Kaoping River watershed distributed from 70% to 84%. Table 6 indicates no significant differences of correct rate between general typhoon events and severe events. It implys that decision tree gives consistent accuracy on events with various rainfall condition.

Table 6. Correct rate of J48 decision tree analysis

	Typhoon Event	Correct Rate of Non-LS	Correct Rate of LS	Avg. Correct Rate
Test	**Nari**	75.1%	69.4%	**72.3%**
	Sinlaku	81.7%	85.7%	**83.7%**
	***Haitang**	74.2%	75.3%	**74.8%**
	***Morakot**	61.5%	79.7%	**70.6%**
Vali-dation	**Fanapi**	73.6%	74.4%	**74%**

*Severe events

4.1.3 Distributed Sediment Production Model

Take 100yrs reoccurrence rainfall condition as an example, which is calculated by decision tree analysis results of landslide probability and V-A relation (Chen et al., 2012). The sediment production map is shown in .

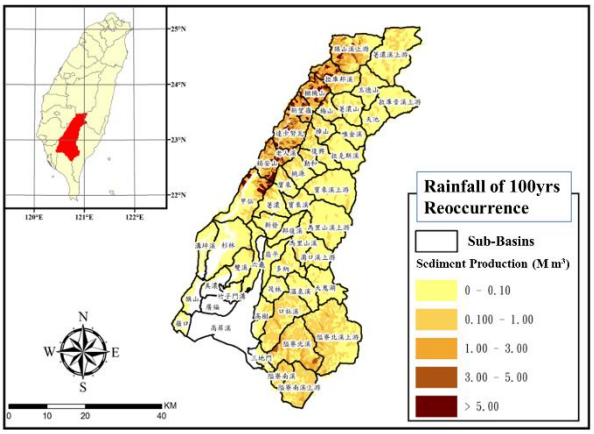

Figure 15. The sediment production under 100yrs reoccurrence rainfall condition. The Chishan River basin have the main proportion of sediment production in this rainfall case.

5 Discussion

In the first part, LSR of each watersheds in Taiwan shows steadily increasing trend to more than 2% until 2014 of each watershed. While we focus on Kaoping River watershed, the LSR of sub-basins fluctuated by Typhoon Morakot and have opposite trend slope at the cutoff point at 2009. The slope after Typhoon Morakot shows recovering trend and it is estimated to intersect the rising trend before 2009 on 2019/2020. The trends indicate recovering period from extreme event of a watershed in Taiwan takes 9 to 10 years. To visualize the LSR and characteristic factors of each watershed in Taiwan, this research conduct Tableau to integrate time series data of LSR, budgets, slopes, aspects, geology, and rainfall into single graph which is interactive to highlight preferred factors of selected watershed.

In the second part of this research, J48 decision tree method in WEKA open source freeware is condutcted to analyze 20m raster grids in Kaoping River watershed including 15 factors and 11 event-based landslide inventories in open format ASCII file which saved in HDFS system and analyzed in Hadoop framework. The conditional probability of landslides can be classified into rules consist of factors. The results of J48 decision tree analysis are tested and validated by landslide grid samples and get correct rates over 70% in average.

This research established automatically J48 decision tree analysis and connected landslide probability to distributed sediment production model via V-A relation. The process of this research can analyze landslide probability and sediment production in real-time scale while instantaneous rainfall is connected to this model. With visualization tools such as Tableau and D3.js, the model displays interactive and intuitive tree graph and

sunburst graph to provide decision making information to authorities.

Acknowledgement

A part of data analyzed in this research was provided by Soil and Water Conservation Bureau (SWCB), Taiwan, R.O.C. Thanks to SWCB for their kindly assistance.

References

[1] Chen, Y.C.,Chang, K.T.,Chiu, Y.J.,Lau, S.M., Lee, H.Y., 2013. *Quantifying rainfall controls on catchment-scale landslide erosion in Taiwan.* Earth Surf. Process. Landf. 38, 372–382.

[2] Dadson, S.J.,Hovius, N., Chen, H., Dade, W.B.,Hsieh, M.L.,Willett, S.D.,Hu, J.C.,Horng, M.J.,Chen, M.C.,Stark, C.P.,Lague, D.,Lin, J.C., 2003. Links between erosion, runoff variability and seismicity in the Taiwan orogen. Nature 426, 648–651.

[3] Huang, C.Y., Wu, W.Y.,Chang, C.P., Tsao, S., Yuan, P.B., Lin, C.W., Xia, K.Y., 1997. Tectonic evolution of accretionary prism in the arc-continent collision terrane of Taiwan. Tectonophysics 281, 31–51.

[4] National Science and Technology Center (NCDR), 2011. *Taiwan Climate Change Report.* National Science and Technology Center of Ministry of Science and Technology, R.O.C.

[5] Quinlan, J.R., 1993. C4.5: programs for machine learning. Morgan Kaufmann Publishers Inc.

[6] Tina R. Patil and Mrs. S. S. Sherekar, 2013. *Performance Analysis of Naive Bayes and J48 Classification Algorithm for Data Classification.* National Conference on Advances in Computing & Networking, Vol. 6, No.2, Apr 2013.

[7] Water Resource Agency, 2015. *Hydrological Yearbook 2015, Taiwan, Republic of China, Part I—Rainfall.* Water Resource Agency of Ministry of Economic Affair, Taipei.

[8] Wei, D., Wei, J., 2014. A MapReduce Implementation of C4.5 Decision Tree Algorithm. International Journal of Database Theory and Application. Vol. 7, No.1, 49-60

[9] Wu, C.C.,Kuo, Y.H., 1999. Typhoons affecting Taiwan: current understanding and future challenges. Am. Meteorol. Soc. Bull. 80, 67–80.

Case Study for Sustainability of Reservoir in Taiwan

Bin-Ru Tsai[a], Yan-Jhih Lin[b], Te-Fu Chiu[c] and Min-Chen Lee[d]

[a] Northern Region Water Resources Office, WRA, MOEA, Taiwan, R.O.C.
[bcd] Geotechical Department, Sinotech Engineering Consultants LTD, Taiwan, R.O.C.
E-mail: fcjooyclin@mail.sinotech.com.tw

Abstract

Earthquake and typhoon are two major natural hazards in Taiwan. Earthquake-triggered landslide in mountainous areas accompany with torrential rainfall supply large amount of sediment to river basin and cause sediment accumulation of reservoir. Considering strategies can be used to reduce sediment delivery or prevent sediment deposition, hydraulic desilting has proven to be the most effective and economical method. Thus desilting tunnels have been implanted to release sediment of reservoirs in Taiwan recently.

For Shimen Reservoir, after 53 years of operation, the most challenging issue is severe siltation. According to the siltation survey, 33% of the storage volume was occupied by silt. To solve the siltation problem, the Water Resources Agency (WRA) determined to construct a desilting tunnel with intake structure situated at Amuping area, which is 7 km upstream from the dam. After completion, the tunnel could carry silt as well as coarse and fine sand to the outlet structure. The desilting tunnel is expected to discharge silt and enhance flood-discharging capability as well.

Keywords –

Shimen Reservoir; Sediment; Desilting tunnel

1 Introduction

In recent year, abnormal hydrologic activities caused by climate change trigger frequent and extreme rainfalls. The tendency of reducing rainfall duration and increasing rainfall intensity becomes more and more obvious. The difference of annual precipitation is significant. Referring to Figure 1, the annual precipitation reaches 3,568 mm in wet years is over two times of those in dry years (1,572 mm). Climate changes in the last couple of years, Taiwan has suffered the continuous drought in year 2014, 2015 and 2017.

Moreover, heavy rainfall and landslide had caused reservoir to lose capacity rapidly. For example, Aere typhoon in 2004 and Morakot typhoon in 2009, each caused Shimen, Zengwen and Nanhau reservoirs to lose capacity about 9% to 12% of its original storage volume (Table 1). Especially for Aere typhoon, the flood-induced high sediment concentration more than 200,000 Nephelometric Turbidity Unit (NTU) in Shimen Reservoir and water supply cut-off for 18 days.

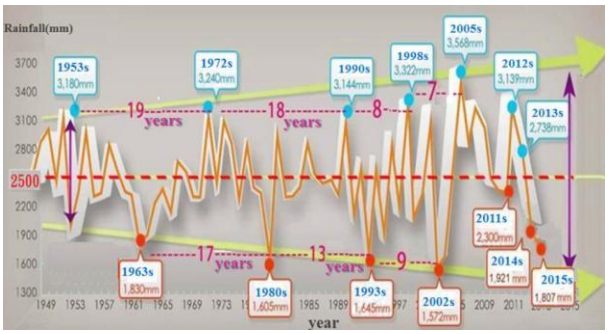

Figure 1. Annual precipitation in Taiwan

Table 1. Typhoon events cause reservoirs lose capacity

Reservoir	Typhoon (Year)	Original storage (10^6M^3)	Siltation (10^6M^3)	Ratio
Shimen	Arre (2004)	309.12	27.88	9%
Zengwen	Morakot (2009)	748.40	91.08	12%
Nanhau	Morakot (2009)	158.05	17.06	11%

2 Strategies against sedimentation

In general, three different strategies are considered for reservoir sediment management:

- Reduce sediment delivery (catchment management)
- Prevent sediment deposition (route sediments through or around storage)
- Increase or recover volume (removal of deposited sediments)

Figure 2 shows a variety of sediment management techniques proposed by Kondolf *et al.* (2014) including the three strategies. A combination of several measures

from the above categories is necessary to maintain reservoir capacity and achieve reservoir sustainability. In overall, hydraulic desilting is the most effective and economical method to release sediment out of reservoir.

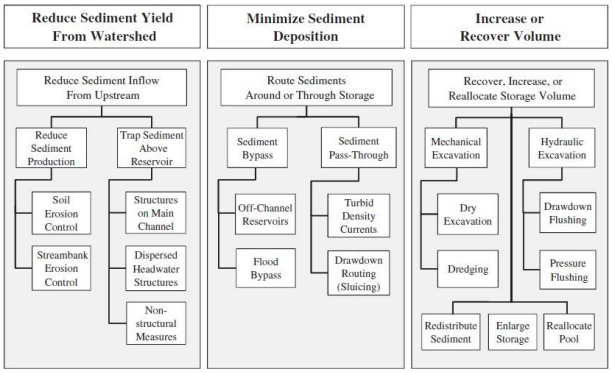

Figure 2. Diagram of sediment management options for reservoir sustainability (Kondolf *et al.*2014)

Based on the consideration, hydraulic desilting projects have been implanted for many reservoirs in Taiwan (Figure 3). For example, a rehabilitation program of Agongdian reservoir was completed in 2005 which practices empty flushing sediment in flood season ever year. Sluicing tunnels are under construction for Zengwen and Nanhau reservoirs to discharge the high turbidity water during flood period. Furthermore, a desilting tunnel is under design and a sluicing tunnel is under planning for Shimen reservoir,.

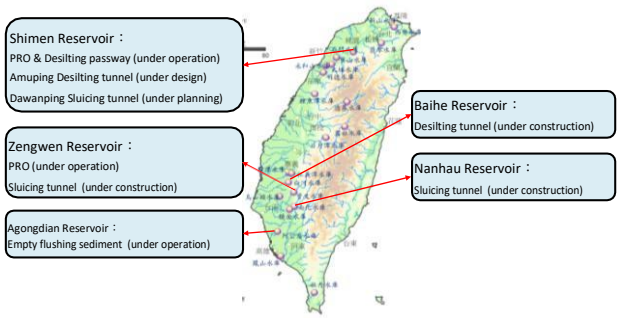

Figure 3. Hydraulic desilting project in major reservoir

Shimen Reservoir is a unique case in all of the reservoirs. In order to solve the problem of severe siltation, WRA proposed a integrated desiltation strategies as shown in Figure 4. By the combination of mechanical removal, dredging, and hydraulic discharge, the sediment discharge amount is up to $2.07\times10^6 m^3/yr$. It should be especially noted for the hydraulic desilting passway, which is reconstructed from existing penstock in 2012 and works as a bottom outlet for the dam with a discharge capacity of 300 m^3/s, has been desilt 3.1 million m^3 of sediment during the typhoon period in 2013-2016.

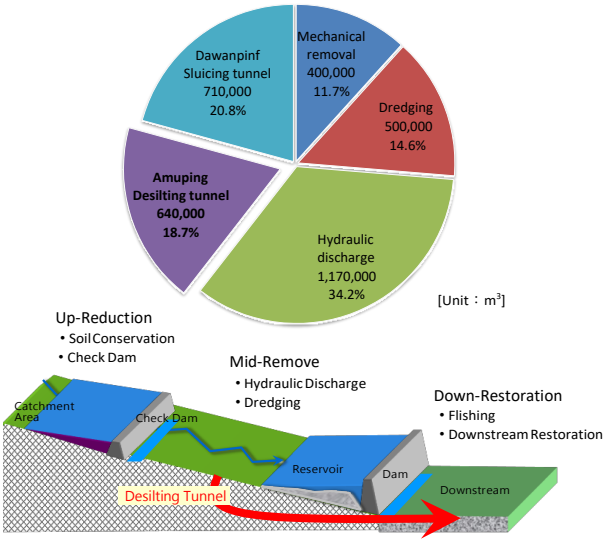

Figure 4. Integrated desiltation strategies for Shimen Reservoir

After the installation of the hydraulic desilting passway, the ratio of desilting during a typhoon event could reaches to about 30% in average in Shimen Reservoir (Table 2).

Table 2 Comparison of desilting in Shimen

	Year	Typhoon	Ratio of desilting
Without desilting passway	2008	Fung-wong	12.9%
	2008	Sinlaku	26.5%
	2008	Jangmei	17.9%
	2009	Morakot	14.3%
	2010	Fanapi	3.0%
	2011	Saola	15.0%
With desilting passway	2013	Soulik	34.3%
	2013	Trami	37.2%
	2015	Soudelor	36.7%
	2015	Djuan	37.4%
	2016	Megi	21.1%

In addition to Figure 4, WRA determined to build a desilting tunnel, which is a bypass tunnel with the intake structure at river section 19－about 7 km upstream from the dam and discharge coarse sand and fine sand directly. The desilting tunnel is expected to deal with sever siltation and enhance the flood-discharge capacity. The details of desilting tunnel for Shimen Reservoir will be introduced as follows.

3 Desilting Tunnel of Shimen Reservoir

Shimen Reservoir is the main water conservation facility in northern Taiwan, which has the function of irrigation, electric power generation, water supply, flood prevention and tourism. The Shimen Reservoir dam impounds the water from Dahan River with the catchment area of 763.4 km^2. The designed storage volume is 3.09 $\times$ $10^8 m^3$ and the assumed sediment discharge is $3.42 \times 10^6 m^3$/yr. The location of Shimen Reservoir is shown in Figure 5.

Because of the climate change today, heavy rainfall have occurred frequently which causes large amount of sediment flushing into the reservoir. According to the siltation survey carried out in 2015, the capacity of the water conservation decreases to $2.08 \times 10^8 m^3$, which is only 67.4% of its designed storage volume. The siltation survey at Shimen Reservoir for each heavy typhoon event shown in Figure 6. In addition, the loss of water storage may affect water supply and impact existing infrastructure, particularly to outlet works and turbine intakes.

In order to solve the siltation problem, WRA planned to build a desilting tunnel. The project is expected to be completed in 2022.

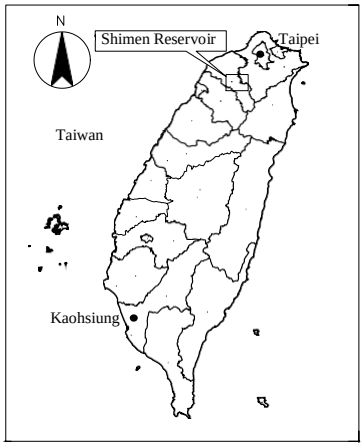

Figure 5. The location of Shimen Reservoir

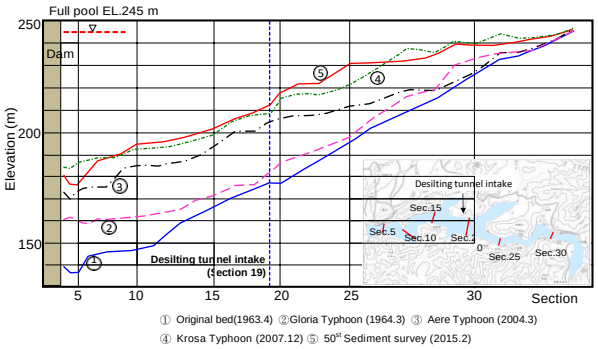

Figure 6. Siltation survey for the typhoon events

3.1 Layout of Desilting Tunnel

The desilting tunnel consists of intake structure, adit, desilting tunnel, sifting facilities, outlet structure, and deposition pool. The general layout is shown in Figure 7. The intake structure is 80 m long and situated at Amuping area, which is 7 km upstream from the dam. The length of the desilting tunnel is 3,702.2 m with a varied slope from 10% to 2.863%. The typical cross section of the desilting tunnel is hood-type with 8 m in width and 7 m in height as Figure 8 shown. Some information and scales about the tunnel are listed in Table 3. An 306 m long adit connected to desilting tunnel at millage of 0k+309 serves as the access route during construction period and also works as the maintenance route after completion.

The desilting tunnel works as a transportation channel in which four steel pipes are installed and the silt dredged by the upstream dredging boats is transported via the pipes. The silt will be screened by sifting facilities at the exit of the tunnel and be separated into coarse sand and fine sand respectively. The coarse sand is valuable and can be used as the mixing materials for concrete. On the other hand, the fine sand will be stored in the deposition pool and discharged to the downstream during typhoon or heavy rainfall period.

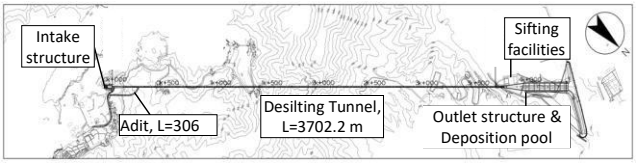

Figure 7. Plan view of the sediment desilting tunnel at Shimen Reservoir

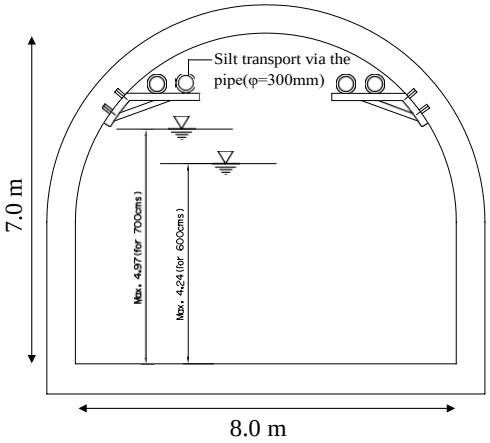

Figure 8. Typical desilting tunnel cross section

In addition, the intake structure is designed by the following critia:

- The design flood-discharging capability for tunnel is 600 m^3/s (El. 242 m) and the maximum discharge is 700 m^3/s.
- Ensure the required freeboard in the tunnel and the safety of operation while desilting operate (The freeboard remains 25% with 600 m^3/s and 15% with 700 m^3/s).
- To avoid the flow chock happening, the shape of intake is designed as streamline shape. The width at the entrance of tunnel is 14.2 m, as shown in Figure 9.

Table 3. Information and scales of desilting tunnel

Sat.	*0k-010 ~ 0k+000*	*0k+000 ~ 0k+070*	*0k+070 ~ 0k+110*	*0k+110 ~ 0k+150*	*0k+150 ~ 0k+200*	*0k+200 ~ 3k+692*
Width [m]	14.2~ 12	12	12~8	8	8	8
Height [m]	11.1~ 8	8	8~7.5	7.5	7.5~7	7
Lining thickness [cm]	80	80	60	60	60	60
Slope [%]	10	10	10	8~ 2.863	2.863	2.863
Flow velocity [m/s]	9.7~ 11.9	11.9~ 16.1	16.1~ 17.0	17.0~ 17.7	17.7~ 17.9	17.9~ 20.2
Section type		Var.			Std.	

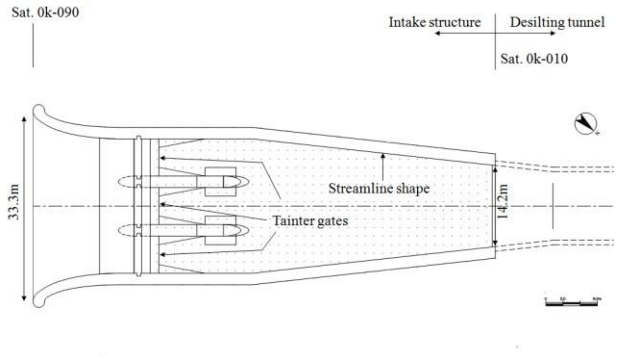

Figure 9. Plan view of intake structure

3.2 Objectives

Two major objectives arise from the desilting tunnel:

- Enhance the desilting capability and decrease sediment of the reservoir.
- Enhance the flood-discharging capability to ensure the safety while extreme hydrology events happened.

WRA has proposed a integrated desiltation strategies to solve the problem of severe siltation. By adopting the methods of mechanical removal, dredging, and hydraulic desilting, the sediment discharge amount is up to 2.07×10^6 m^3/yr recently. Furthermore, the Amuping desilting tunnel, which is a bypass tunnel for the reservoir, will be built and is expected to discharge silt 6.4×10^5 m^3 per year.

The desilting tunnel is expected to provide 600 m^3/s flood-discharging capability and enhance the safety of Shimen Reservoir as well.

3.3 Multifunction of Desilting Tunnel

Recently, the processing and elimination of silt from the reservoir becomes more and more serious problem. Therefore, WRA plan to dredge upstream, where the percentage of coarse sand (diameter $\geqq$ 0.1 mm) is over 50%. The silt transport via the pipe in the tunnel and be screened by sifting facilities at the exit of the tunnel. The coarse sand is screed by the facilities and is separated from the fine sand, then be sold and reused. Besides, unnecessary water storage from the reservoir will be drained by the desilting tunnel, and the fine sand, which is stacked in the deposition pool, will be flushed toward downstream at typhoon period. Thus, the desilting tunnel not only solves the problem of sediment of the reservoir but also the problem of silt elimination.

Furthermore, the desilting tunnel can be used as an access road which provides the trucks pass by during drought period. As the reservoir level below El. 210 m, the mechanical machines can dig directly on the river bed at Amuping area, which elevation is around El. 236 m. It's definitely a more efficient method compared with dredging. The multifunction of the desilting tunnel is shown in Figure 10.

3.4 Reused by Sifting Facilities

According to the efficiency concern, one vibrating screen, three sand washers and three sand separators are designed to install, along with the area about 6,000 m^2 including the storage area. The silt is separated by the facilities and can be divided into 4 parts:

- Gravel or wood, which retained above No.4 (4.76 mm) sieve.
- Coarse sand, which passing the No.4 and retained on the No.18 (1.00mm) sieve.
- Fine sand, which passing the No.18 and retained on the No.200 (0.074mm) sieve.
- Scourable particles, which passing the No.200 sieve and store in the deposition pool.

The process and layout of the sifting facilities shown

as Figure 11. The vibratory screen with No.4 sieve screened out gravel and wood first. The rest is transported to sand washers and sand separators, then be separated into fine sand and coarse sand. A sand washer and a separator connect as a set in series and parallel for three sets. It is assumed that over 50% of the siltation will be selected and then be reused, the amount is about 3.2×10^5 m^3 per year.

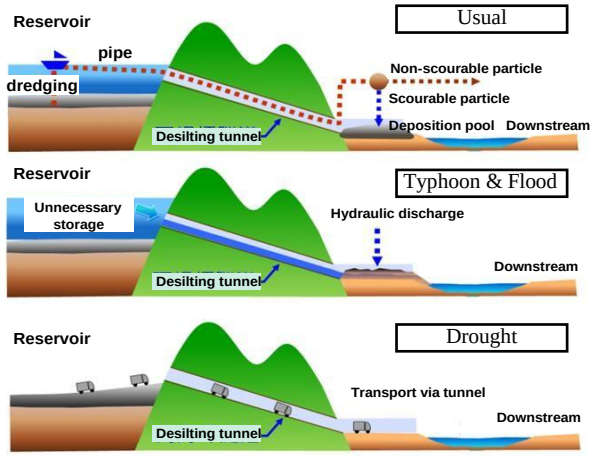

Figure 10. Multifunction of the desilting tunnel

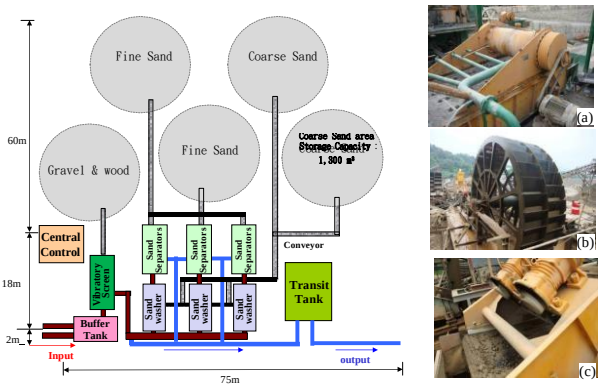

Figure 11. Process and layout of the sifting facilities (a) vibratory screen (b) sand washer (c) sand separators

4 Conclusions

Due to the climate change, extreme hydrology events have occurred frequently, large amount of sediment is flushed into the Shimen Reservoir. The capacity of the water conservation decreases from 3.09 $\times$ 10^8 m^3 to 2.08 $\times$ 10^8 m^3, which is 67.4% of its designed storage volume. Heavy rainfall and landslide had caused reservoir to lose capacity rapidly and cut-off water supply.

In order to sustain the life and ensure the safety of Shimen Reservoir, WRA has done lots of methods such as soil erosion control of the upstream areas, digging and dredging, flushing and sluicing. Considering all of the remediation measures, hydraulic desilting proves to be the most economical and rapid method.

Taking effectiveness and economical efficiency into account, a desilting tunnel is planned to construct and is expected to enhance the desilting and flood-discharging capability. The purpose is to deal with 6.4×10^5 m^3 silt per year and provide 600 m^3/s flood-discharging capability.

References

[1] Northern Region Water Resources Office, WRA, MOEA (2016). Desilting Tunnel Project of Shimen Reservoir (First Stage) The Basic Design Report of Amuping Tunnel.

[2] Taiwan Construction Research Institute (2014). Flexibility Assessment of Sediment Removal at Amuping Tunnel.

[3] Northern Region Water Resources Office, WRA, MOEA (2015). Feasibility Study of Amuping Desilting Tunnel Project for Shimen Reservoir.

[4] Chien-Hsin Lai (2017). Hydraulic desilting of reservoir in Taiwan. In *Proceedings of 2nd IWSBT*.

[5] Kondolf, G.M, Gao, Y., Annandale, G.W., Morris, G.L. Jiang, E., Zhang, J. Cao, Y., Carling, P., Fu, K, Guo, Q., Hotchkiss, R., Peteuil, C., Sumi, T., Wang, H.-W., Wang, Z., Wei, Z., Wu, B., Wu, C., Yang C.T. (2014). Sustainable sediment management in reservoirs and regulated rivers: Experiences from five continents. *Earth's Future*, 2(5), 256–280AuthorSurname C. and AuthorSurname D. A conference paper. In *Proceedings of the conference*, pages 12–34, Sydney, Australia, 2014.

Assessing rainfall thresholds for large-scale landslide

H.L. Kuo[a], G.W. Lin[a], C.Y. Lee[b], H.Y. Yin[b], S.K. Lee[b]

[a]Department of Earth Sciences, National Cheng Kung University, Taiwan
[b]Soil and Water Conservation Bureau, Council of Agriculture, Taiwan
E-mail: kuo1195@gmail.com, gwlin@ncku.edu.tw, ea10401@mail.swcb.gov.tw, sammya@mail.swcb.gov.tw, agrikuen99@mail.swcb.gov.tw

Abstract –

Large-scale landslides caused by extreme rainstorm has become a new challenge of early warning for slope hazard in recent years. However, due to the insufficient observational records in the past, analyzing critical rainfall conditions are fairly obstructed. The information of occurrence time of landslide could be extracted from the seismic signal recorded by adjacent seismic stations. The study collected the seismic records of the Broadband Array in Taiwan for Seismology (BATS) to identify the ground motions triggered by the landslides occurring during 2005-2014 in Taiwan. After eliminating the signals from local and teleseismic earthquakes, 62 landslide-induced seismic signals were interpreted. The seismic signals provided the occurrence time of landslide to assess the rainfall conditions including rainfall intensity (I, mm/hr), duration (D, hr), and cumulative rainfall (R, mm). The comparison between three common rainfall threshold modes (I-D, I-R, and R-D) reveals that duration and cumulative rainfall should be the crucial factors to evolve an early warning mode. Besides, a critical water mode, (I-1.04)•D = 452 mm, involving triple-factors has been established through the analysis of rainfall information from the 62 occurred large-scale landslides.

Keywords –

large-scale landslide; seismic signal; rainfall threshold; early warning

1 Introduction

In recent years, as the frequency of extreme rainfall events has increased globally, the number of large-scale natural disasters has also increased around the world (Tu and Chou, 2013; Saito et al., 2014). These large-scale natural disasters (e.g. landslides, floods, etc.) not only caused huge economic losses but also accompanied by casualties of life. In mountainous area, the occurrence of large-scale landslides will change landscape and erosion process as well. Several previous studies reported that the characteristics of a large-scale landslide may include: (1) extremely rapid mass movement, (2) huge landslide volume, and (3) deep-seated excavation into rock formation (Chigira and Kiho, 1994; Lin et al., 2006). However, the discrimination between large-scale and non-large-scale landslides is still indistinct. Because in practice velocity of mass movement and depth of excavation are both difficult to be measured, landslide area is commonly regarded as an indicator of the scale of landslide. Therefore, in this study, large-scale landslide (LSL) is defined as the landslide having disturbed area larger than 0.1 km2, while the rest is called as small-scale landslide (SSL). It is well known that although there are many factors (e.g. rainstorm, earthquake, melting snow, etc.) that lead to landslide, rainfall is considered to be one of the important factors that trigger landslide. In order to reduce the calamity losses, it is expected to find out the critical rainfall conditions that trigger large-scale landslide, and a rainfall threshold is used as a warning mode to execute disaster prevention and mitigation.

However, in the past researches, it was difficult to estimate the threshold of precipitation convincingly due to the lack of accurate information on the occurrence time of large-scale landslide. In recent studies on geophysics (Kanamori et al., 1984; Surin˜ach et al., 2005; Lin et al., 2010; Ekstro¨m and Stark, 2013), it is believed that the mass movement process of large-scale landslide would generate a series of ground motions. If these ground motions are recorded by seismic stations, the occurrence time information of large-scale landslide can be extracted from seismic records. The problem about lack of time information on estimate critical rainfall can be resolved.

By applying various rainfall factors into statistical analysis, building a statistically threshold is one of commonly strategies to explore the critical rainfall conditions of landslide occurrence, such as using rainfall intensity and duration to define rainfall threshold curves (Caine 1980; Saito et al., 2010; Chen et al., 2015). Those rainfall thresholds provide valuable information for disaster prevention and mitigation. In this study, we used the seismic data recorded by the network of Broadband Array in Taiwan for Seismology

(BATS) and landslide maps interpreted form satellite images to obtain the exact occurrence time and locations of large-scale landslides, then made the rainfall thresholds for large-scale landslides in Taiwan.

2 Study method

2.1 Large-scale landslide interpretation

In order to know the locations and basic characteristics of large-scale landslides, more than 100 satellite images from 2005 to 2014 are collected and used to map rainfall triggered landslides. The Figure 1 shows one of the synthetic image which contains 52 individual SPOT images and is used to interpret landslides trigged by the 2009 typhoon Morakot. After image interpretation, contrasting the interpretation results with 1:5000 topographic map and checking terrain features, then we can exclude the area of interpretation misjudgement. Eventually, large-scale landslides and small-scale landslides are distinguished by an area of 0.1 km^2. In order to avoid reactivated landslides, we compared the interpretation results before and after typhoons or heavy rainfall events, then we could obtain the distribution map of new generation large-scale landslide.

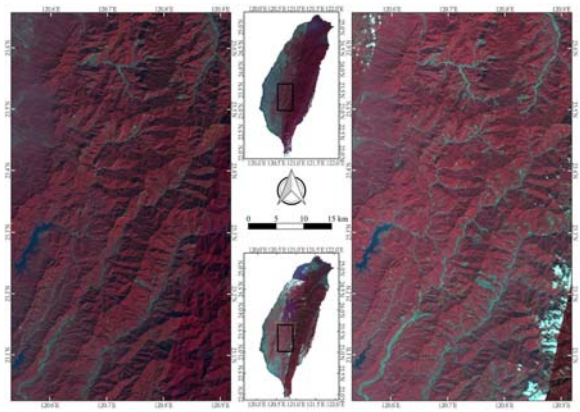

Figure 1. Comparison of satellite images between pre and post Typhoon Morakot. (a) The SPOT image taken in the period of January to June in 2009. (b) The SPOT image taken in the period of September to December in 2009.

2.2 Interpretation of ground motions induced by large-scale landslides

There will be some different motion processes such as sliding, impacting, acceleration and deceleration during the movement of landsliding mass. The complex motion processes acting on ground surface will generate a series of ground motions (Kanamori et al., 1984; Ekström and Stark, 2013). As these signals were recorded by adjacent seismic stations, the landslide-related pattern in spectrogram inherits a triangular time/frequency signature in 1-3 Hz frequency band (Surinach et al. 2005; Chen et al. 2013).

The seismic data during the typhoons and heavy rainfall events having maximum cumulative rainfall of exceeding 500 mm from 2005 to 2014 were collected and the seismic signals of local earthquakes, regional earthquakes and teleseismic were excluded. After removing instrument response, mean, and linear trend, eventually manual identification of landslide-related triangular signature in spectrogram was executed to to find the characteristic signals generated by the landslides (Figure 2).

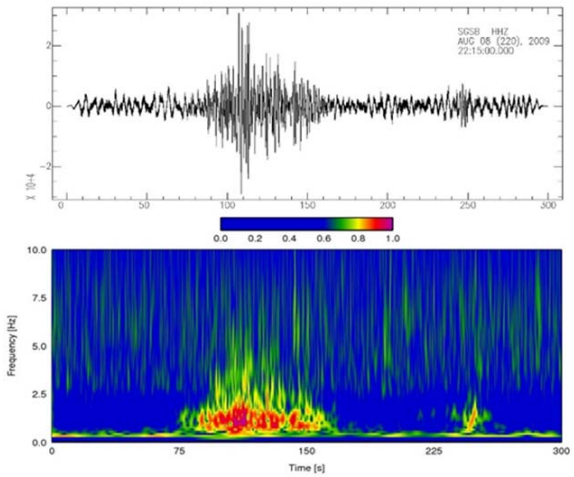

Figure 2. The spectrogram of vertical seismic record at station MASB. The pattern of landslide characteristic signatures is visible in the figure.

In order to realize which landslide generated ground motion, it is necessary to locate the source of signal. However, the arrival time of P-wave and S-wave of landslide-induced ground motion can not be clearly distinguished. As a result, the cross-correlation method was used to calculate the correlation between the envelope functions of the seismic signals received by different seismic stations and the Monte Carlo method was used to locate the landslide-induced signals (Chen et al. 2013).

Finally, the locating result of landslide-induced seismic signal was compared with the exact location of large-scale landslide interpreted from satellite images. If the pairing succeeds, the occurrence time of the landslide could be obtained, and further can be applied to rainfall data analysis.

2.3 Analysis of rainfall threshold for large-scale landslide

In the study, rainfall data are collected from the records of ground rainfall stations. While typhoon event is the major rainfall event analyzed in the study, the scatter of precipitation during typhoon events is closely related to the typhoon track and the position of the windward slope. The density and distribution of rainfall stations in mountainous area will directly affect the results of rainfall threshold analysis. If the landslide location and the selected rainfall station are located in different watershed, it is very likely to get the rainfall information that can not represent the rainfall condition for the landslide. Therefore, in the study, the selection criteria for rainfall station is that the rainfall must be located within the same watershed with landslide and the straight distance should be shorter than three kilometers.

In the process of rainfall analysis, the beginning of a rain event is defined as the time while hourly rainfall is greater than 4 mm, and the rain event ends while continuous 4-hours rainfall intensity is less than 4 mm/hr. The critical rainfall condition for a landslide is calculated form the beginning of rain event to the occurrence time of the landslide. In this way, average rainfall intensity (mm/hr), cumulative rainfall (mm) and rainfall duration (hr) for each large-scale landslide are taken as the factors of rainfall threshold analysis. In addition to the three factors mentioned above, the antecedent seven-days daily rainfall before the beginning of rainstorm is considered as antecedent rainfall. The sum of antecedent rainfall and principal event rainfall are regarded as total effective rainfall (Rt).

Based on different rainfall factors, the critical rainfall analysis for large-scale landslide will result in different relations between rainfall factors. In this study, three common rainfall threshold analysis methods were used. The first method is the I-D method with the commonly formula: $I = aD^{-b}$, while "a" is the intercept of the threshold curve, and b is the slope. (Caine, 1980, Wieczorek, 1987 and Keefer et al., 1987). In the study, the 95% lower I-D rainfall threshold curve is calculated by the method proposed by Brunetti et al. (2010). The second method is the I-Rt method (Jan and Lee, 2004). In the I-Rt method, rainfall intensity and cumulative rainfall were plotted and used to calculate the cumulative probability of the product value of I and Rt by the Weibull distribution method (Jan and Lee, 2004). The cumulative probability of 5% is taken as the I-R rainfall threshold. The third method is the Rt-D method (Aoki, 1980 and Fan et al., 1999). In the Rt-D method, the 5% cumulative probability of the product value of R and D by the Weibull distribution method is taken as the Rt-D rainfall threshold.

2.4 Critical water mode

Whether a given slope produces a landslide is depended on the the balance between the shear strength of the slope material and the downslope component of the gravitational force imposed by the weight of slope material above a potential slip surface. A critical water mode proposed by Keefer et al. (1987) is used in the study to built a rainfall threshold which involves three major rainfall factors. The mode is derived form existing slope stability theory with some simplifying assumptions. The shear strength of material at a point within a slope is expressed as:

$$s = c' + (p\text{-}u_w)tan\phi' \quad (1)$$

While c' is the effective cohesion of the material, p is the total stress perpendicular to the potential sliding surface, u_w is the pore water pressure, and ϕ' is the effective friction angle of the slope material. The main cause of the slope disaster is rainfall infiltration into the slope and accumulation above the impermeable layer, which increases the pore water pressure of the slope material, with the increase of pore water pressure (u_w), the shear strength (s) decreases, which eventually leads to the failure of the slope. A critical value of pore water pressure u_{wc} exists on each slope, assuming an infinite slope composed of a non-cohesive material (c=0), and the sliding surface parallel to the surface, the pore water pressure threshold can be calculated as:

$$u_{wc} = Z \cdot r_t[1 - (tan\,\theta / tan\phi')] \quad (2)$$

Z is the vertical depth of the sliding surface, r_t is the unit weight of the slope material, and θ is the slope angle.

Increasing the pore water pressure u_w to the pore water pressure threshold u_{wc} requires a critical quantity of water Q_C which can be represented by the unit length of the slope and is calculated as

$$Q_C = (u_{wc}/\gamma_w) \cdot n_{ef} \quad (3)$$

Where u_{wc} is the critical value of pore water pressure, γ_w is the unit weight of water, and n_{ef} is the effective porosity, that is the residual porosity of the slope material under free gravity drainage. It is also assumed that all the water will penetrate into the saturated zone above the potential sliding surface after the rainfall start. The drainage rate of saturated zone is represented by the average value I_o, and the unit is mm/hr. Then in a heavy rainfall event, the critical water quantity of causing the slope disaster is defined as:

$$Q_C = (I - I_o) \cdot D \quad (4)$$

3 Results

3.1 Topographic features of large-scale landslide

The result of satellite imagery interpretation showed that a total of 686 landslide events with area greater than 0.1 km^2 occurred in Taiwan mountainous area from 2005 to 2014 (Figure 3a). Most of these large-scale landslides (LSLs) had the area ranging between 0.12 to 0.15 km^2, and their slope angles were concentrated between 30° and 40° (Figure 3b). The number of landslide with slope angle of exceeding 40° had increased obviously after 2010. The increase is most likely due to the fact that during the 2009 typhoon Morakot extremely heavy rainfall, more than 2000 mm in four days, caused huge amount of landslides on lower slopes and made the steeper slope less stable in the following years. LSLs were major concentrated on the slope with elevation ranging from 1000 m to 2000 m (Figure 3c), but the distribution of the highest and lowest elevation of these LSL shows that the average vertical displacement of these LSLs was greater than 500 m.

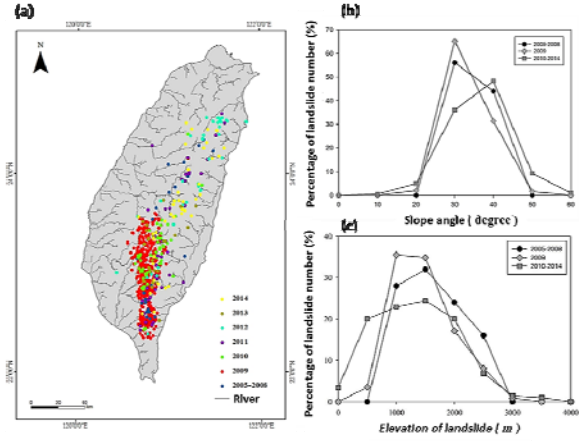

Figure 3. (a) The distribution map of large-scale landslide during 2005 to 2014 in Taiwan. (b) The number distribution of slope angle of the LSLs presented in percentage. (c) The number distribution of elevation of the LSLs presented in percentage.

3.2 The critical rainfall conditions for triggering LSLs

A total of 62 LSLs were obtained with their occurrence time by the interpretation of landslide-induced seismic signal, 41 of which occurred when the total effective rainfall was more than 1000 mm (Figure 4). The statistical results of rainfall intensity at the time of LSL occurrence show that more than half of the LSLs occurred as the rainfall intensity was less than 20 mm/hr. Only seven of LSLs occurred when rainfall duration is less than 24 hours, and the rainfall duration of theses seven events are all longer than 10 hours. The results of single rainfall-factor analysis indicated that the effects of rainfall duration and cumulative rainfall were much more remarkable for LSLs, and the rainfall intensity at the time of landslide occurrence was not the main influence factor for LSLs.

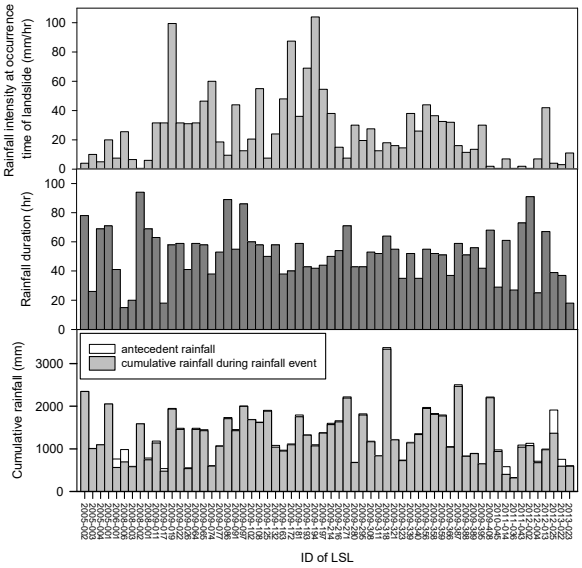

Figure 4. Single-factor rainfall analysis. Most events had the rainfall duration of more than 24 hours, cumulative rainfall of more than 1000 mm, and rainfall intensity of less than 20 mm/hr.

4 Rainfall thresholds for LSLs

4.1 The dual rainfall-factors analysis of I-D, I-Rt, and Rt-D threshold

According to single rainfall-factor analysis, there was no significant correlation between landslide and rainfall intensity at the time of LSL occurrence. In the dual rainfall-factor analysis, the I-D rainfall threshold was assessed by using the mean value of rainfall intensity and rainfall duration. The obtained I-D threshold is $I = 71.9D^{-0.47}$ ($D > 24$ hr) (Figure 5). Besides, we compared the rainfall information obtained from the small-scale landslides (SSLs) occurred in the period from 2005 to 2012, and it seems that the I-D rainfall threshold line for LSL also fits the lower boundary of the rainfall condition of SSLs. In addition, the distribution of the rainfall duration indicates that the SSLs were distributed evenly in the interval of 3 to 70

hours of rainfall duration, while the LSLs were mostly above 20 hours; but the rainfall intensity can not effectively distinguish these two kinds of slope disasters. Even under the same condition of rainfall duration, there are a lot of rainfall intensities of SSLs are higher than LSLs. This result sufficiently demonstrated that using rainfall intensity hardly distinguished between SSLs and LSLs. Therefore, the I-D threshold may cause a situation that disaster scale can not be assessed. It can be found that most of the LSLs with larger area were concentrated in the rainfall duration more than 50 hours, but average rainfall intensity doesn't have a good correlation with landslide area. The average rainfall intensity of the SSL was very high at short duration, but the duration of the SSLs was much lower than LSLs. Therefore, continuous high-intensity rainfall is more likely to cause LSL.

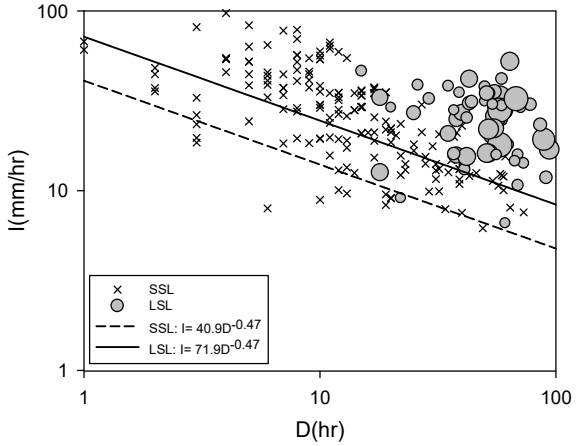

Figure 5. I-D rainfall threshold

Moreover, we compare the I-D rainfall thresholds obtained in the study with other previous studies which were focused on shallow landslide or debris flow (Figure 6). The comparison reveals that the I-D threshold line for LSL is much higher than other threshold lines for shallow landslide or debris flow.

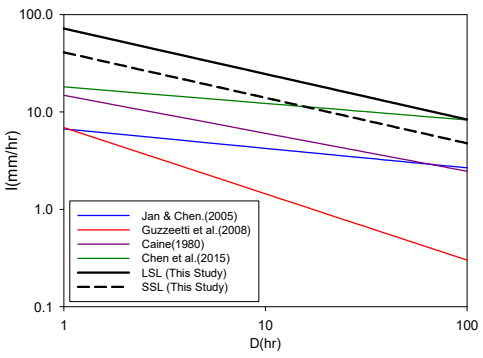

Figure 6. I-D threshold by different studies

The results show that the product of Rt and D for LSL, with a cumulative probability of 5%, is 12773 mm·hr (Figure 7), the rainfall threshold is also much larger than the 5% cumulative probability of SSL (487 mm·hr). This Rt-D threshold value means when the rainfall duration exceeds 24 hours, the critical Rt should be 532 mm. In other words, the critical rainfall duration should be 12.7 hours when the total effective rain exceeds 1000 mm. There is a considerable difference in total effective rainfall between LSLs and SSLs. Most of SSLs had the total effective rainfall below 500 mm, but only few SSLs occurred as total effective rainfall exceeded 1000 mm. As the result of the disparity of the Rt-D threshold curves for LSL and SSL, it can determined the Rt-D analysis can be used to distinguish SSL to LSL effectively.

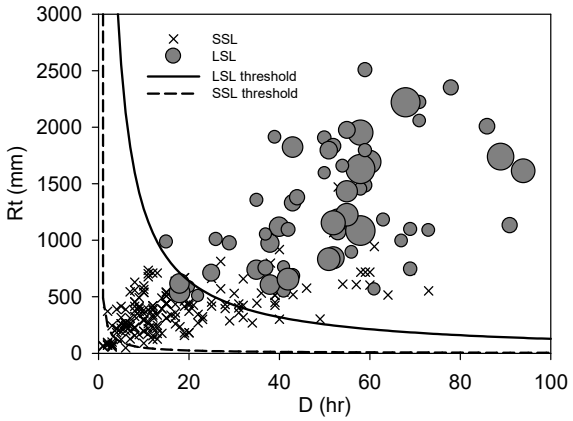

Figure 7. Rt-D rainfall threshold

Based on the analysis of relationship between average rainfall intensity (I) and total effective rainfall (Rt), the product value of both factors for 5% cumulative probability is 5640 mm^2/hr (Figure 8). The I-Rt threshold curve for LSL is not much higher than SSL (1541 mm^2/hr). The I-Rt threshold represents a critical rainfall intensity of 5.6 mm/hr when the total effective rainfall reaches 1000 mm, in contrast, when the rainfall intensity exceeds 10 mm/hr, the total effective rainfall is 564 mm. Combination of the results of three kinds of rainfall threshold analyses reveals that the critical rainfall conditions for SSL is considered to include high average rainfall intensity but relatively low cumulative rainfall, while the rainfall condition for LSL should include long rainfall duration and high effective cumulative rainfall.

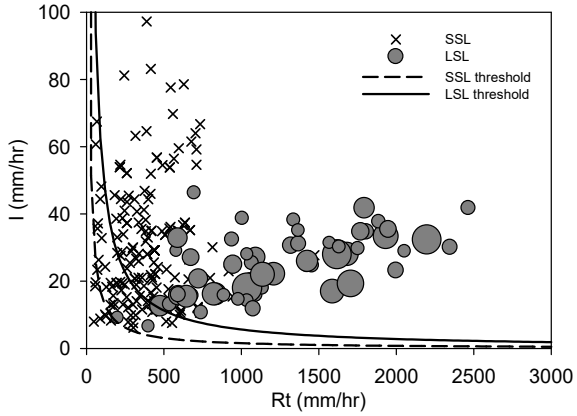

Figure 8. I-Rt rainfall threshold

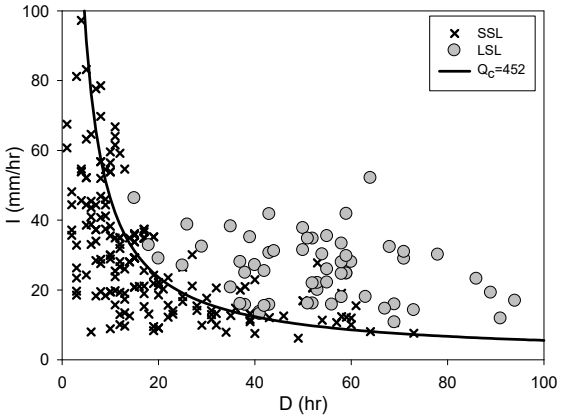

Figure 9. Threshold of the critical water mode

4.2 The critical water mode for LSL early warning

Using the geological material parameters of the study area (Table 1), the critical water quantity Q_C on the sliding surface was calculated to be 452 mm. The Q_C value is taken into $Q_C = (I-I_0)\cdot D$ to obtain the I_0 value of 1.04 mm/hr, which is more suitable for LSL, and the threshold curve is rewritten as $(I - 1.04) \cdot D = 452$. In the application of this threshold curve to average rainfall intensity and rainfall duration, almost all the LSLs can be effectively warned, the application show good results in this mode as a rainfall alert mode that triggers landslides (Figure 9). Besides, the threshold curve can be used to distinguish LSL and SSL clearly. This advantage can reduce the false judgment of early warning operation. The critical water mode combines statistical and deterministic approaches on the assessment of critical rainfall. Therefore, the parameters using to calculate Qc value can be adjusted based on regional geologic and topographic environment within a specific area.

Table 1 Parameters for calculating Qc

Parameter	Value
Z	10 m
γt	2.65 t/m2
θ	32°
ϕ'	37°
nef	0.1

5 Conclusion

In this study, using the seismic signal recorded by broadband seismic network, the exact occurrence time of large-scale landslide (LSL) was successfully obtained, and the rainfall threshold for LSL was assessed statistically based on the time information. Based on the rainfall information of the 62 LSLs occurring during 2005-2014 in Taiwan, the rainfall conditions for triggering LSL include total effective rainfall of more than 1000 mm, rainfall duration of more than 24 hours, rainfall intensity of more than 17.5 mm/hr. After the rainfall threshold analyzed by I-D method, Rt-D method and I-Rt method, the rainfall thresholds based on different dual factors triggering LSL are obtained. Besides, a critical water mode combining statistical and deterministic approaches is developed to figure out a triple-factors threshold for LSL. The rainfall information and geologic/topographic parameters finally were applied to obtained the threshold curve, $(I-1.04)\cdot D = 452$, where average rainfall intensity I in mm/hr and rainfall duration D in hr. The new critical mode can be used to improve the early warning system for LSL and would not lead to confusion between SSL and LSL.

References

[1] Brunetti, M. T., Peruccacci, S., Rossi, M., Luciani, S., Valigi, D., and Guzzetti, F. Rainfall thresholds for the possible occurrence of landslides in Italy. *Natural Hazards and Earth System Sciences* 10:447-458, 2010.

[2] Caine, N. The rainfall intensity: duration control of shallow landslides and debris flows. *Geografiska Annaler. Series A. Physical Geography* 62:23-27, 1980

[3] Chen, C. W., Saito, H., and Oguchi, T. Rainfall intensity–duration conditions for mass movements in Taiwan. *Progress in Earth and Planetary*

Science 2:1-13, 2015.

[4] Chen, Y. C., Chang, K. t., Chiu, Y. J., Lau, S. M., and Lee, H. Y. Quantifying rainfall controls on catchment-scale landslide erosion in Taiwan. *Earth Surface Processes and Landforms* 38:372-382, 2013.

[5] Chien, F. C., amd Kuo, H. C. On the extreme rainfall of Typhoon Morakot (2009). *Journal of Geophysical Research: Atmospheres* 116(D5104): 22, 2011.

[6] Ekström, G., and Stark, C. P. Simple scaling of catastrophic landslide dynamics. *Science* 339: 1416-1419, 2013.

[7] Fan, J. C., Wu, M. F., Peng, G. T. The Critical Rainfall Line of Debris Flow Occurrence at Feng-Chiou. *Sino-Geotechnics* 74:39-46, 1999.

[8] Guzzetti, F., Manunta, M., Ardizzone, F., Pepe, A., Cardinali, M., Zeni, G., and Lanari, R. Analysis of ground deformation detected using the SBAS-DInSAR technique in Umbria, Central Italy. *Pure and Applied Geophysics* 166:1425-1459, 2009.

[9] Ishihara, Y., and Kobatake, S. Runoff model for flood forecasting. *Bulletin of the Disaster Prevention Research Institute* 29(1):27-43, 1979.

[10] Jan, C. D., Lee, M. H. A Debris-Flow Rainfall-Based Warning Model. *Journal of Chinese Soil and Water Conservation* 35:275-285, 2004.

[11] Kanamori, H., Given, J. W., and Lay, T. Analysis of seismic body waves excited by the Mount St. Helens eruption of May 18, 1980. *Journal of Geophysical Research: Solid Earth* 89:1856-1866, 1984.

[12] Keefer, D. K., Wilson, R. C., Mark, R. K., Brabb, E. E., Brown, W. M., Ellen, S. D., and Zatkin, R. S. Real-time landslide warning during heavy rainfall. *Science* 238:921-925, 1987.

[13] Lin, C., Kumagai, H., Ando, M., and Shin, T. Detection of landslides and submarine slumps using broadband seismic networks. *Geophysical Research Letters* 37(L22309):1-5, 2010.

[14] Saito, H., Nakayama, D., and Matsuyama, H. Relationship between the initiation of a shallow landslide and rainfall intensity—duration thresholds in Japan. *Geomorphology* 118:167-175, 2010.

[15] Aoki, S. Critical rainfall triggering debris-flow disaster. *National Research Institute for Earth Science and Disaster Prevention* 38:22-26, 1980. in Japanese

[16] Suriñach, E., Vilajosana, I., Khazaradze, G., Biescas, B., Furdada, G., and Vilaplana, J. Seismic detection and characterization of landslides and other mass movements. *Natural Hazards and Earth System Science* 5:791-798, 2005.

[17] Tsou, C. Y., Feng, Z. Y., and Chigira, M. Catastrophic landslide induced by typhoon Morakot, Shiaolin, Taiwan. *Geomorphology* 127: 166-178, 2011.

[18] Wieczorek, G. F. Effect of rainfall intensity and duration on debris flows in central Santa Cruz Mountains, California. *Reviews in Engineering Geology* 7:93-104, 1987.

[19] Wu, C. H., Chen, S. C., and Chou, H. T. Geomorphologic characteristics of catastrophic landslides during typhoon Morakot in the Kaoping Watershed, Taiwan. *Engineering Geology* 123:13-21, 2011.

Installation Plans of Rainfall Stations for the Maintenance Management of Freeway Slopes

B.S. Lin[a], J.Y. Wei[a], L.P. Shi[b], J.C. Liao[b] and X.H. LIN[b]

[a]Taiwan Area National Freeway Bureau, MOTC, R.O.C.
[b]Taiwan Construction Research Institute, R.O.C.
E-mail: lepnhsu@tcri.org.tw

Abstract –

After the maintenance management system has been built up for freeway slopes, the installations of precipitation stations used for early warning are considered. The QPESUMS data were compared with insitu rainfalls, it is quite different between them. The plans of rainfall stations installed by TANFB and CWB are described. Two stages of early warning are proposed. The landslide accumulated rainfall thresholds established by NCDR is used as early warning value in the first stage. After the complete precipitation stations are set up and the relationships between rainfalls and ground water levels are established, the early waring can be made by real time rainfall monitoring in the second stage.

Keywords –

Rainfall; Slope Maintenance; Early Warning

1 Introduction

Taiwan Area National Freeway Bureau (TANFB) has built up slope maintenance organization and execution system since the huge landslide disaster occurred suddenly at 3.1k of No. 3 National Freeway on April 25, 2010. The slope maintenance manual was revised according to many domestic and foreign references and was made progressive revisions to increase maintenance effect and efficiency according to the practice experience. Except the maintenance operation regulations, the reservation and utilization of database, individual training and maintenance effect management are also included in the manual [1]. The lifecycle-based maintenance and management cloud based system has been established. All the data of slope patrol and inspection, comprehensive ground anchor detection, monitoring, geological investigation, slope stability analysis and slope reinforcement design, etc., were input into this system. The techniques of Geographical Information System are utilized for the system visualization. It makes the management interface more intuitive and friendly to use. Inspection can be easily done by portable tools which connect with internet.

The cloud based system is not only providing the functions of data collection, storing, classification, inquiry, but also supports the functions of situation reciprocation and processing tracing, waiting list notice and tracing, abnormal event notice, focus section monitoring and controlling are also developed. Because rainfall has a close relationship with slope stability and can be quickly noticed its information, TANFB proposed an installation plan of rainfall station. The rainfall information can be used to increase the maintenance efficiency and obtain some early warning strategies.

2 Advantages of Rainfall Monitoring

In order to prevent landslide disaster, the rainfall has been used in Directorate General of Highway (DGH) as the judgement for the road closure in mountain area. It is also used by Soil and Water Conservation Bureau (SWCB) as early warming for debris flows. The governments have a lot of experience using rainfall to prevent natural disasters. There are several advantages using rainfall monitoring described as follows:

2.1 Appropriate Time to Start Special Inspection

When 24 hour accumulated rainfall reaches over 200 mm or 3 hour accumulated rainfall over 100 mm, it should start the slope special inspection according to TANFB manual regulation. The rainfall announced by Central Weather Bureau (CWB) is the basic data to decide whether to begin special inspection. It is very often that the actual rainfall on freeway slope may not follow CWB announcement. Therefore, it needs representative precipitation for every freeway slope by

the rainfall installation to make a better decision.

2.2 Early Warning

The slope stability is largely influenced by the ground water level. The landslide may occur when the driving forces are greater than resistance among ground layers due to water level rising. There are 315 water level observation wells along the national freeway slopes. If we have the relationship between rainfall and ground water level, we can predict slope stability by the evaluation using rainfall data. Then it will be easy to make early warning by rainfall monitoring. On the other hand, the surface erosion or shallow landslide can also be predicted by rainfall monitoring and the records of actual sliding cases.

2.3 Corporation between TANFB and CWB

The freeway slopes are distributed all over in the Taiwan hill area. The installation of rainfall station can help TANFB for slope maintenance management, it can also provide CWB very useful data for weather forecasting. So there were some discussions to share rainfall data between TANFB and CWB,

3 Rainfall Station Installation Plan

The QPESUMS precipitations were compared with insitu rainfall monitoring at freeway and the plans of rainfall stations installed by TANFB and CWB are described here.

3.1 QPESUMS Data

CWB has built up QPESUMS (Quantitative Precipitation Estimation and Segregation Using Multiple Sensor) monitoring and warning system for severe weather condition. It has established precipitation distribution along national freeway for every 1 km. QPESUMS can provide from accumulated 10 minute., 1 hour, 3 hour, 6 hour, 24 hour to 72 hour rainfall data. This customized information for TANFB is shown on website [2].

In order to find out the correlation between QPESUMS and insitu precipitation monitoring at freeway. We utilized rainfall data of Soudelor typhoon that hit Taiwan on Aug. 8, 2015. There are 4 rainfall station data can be compared with QPESUMS, Two of them are shown in Table1 and Table 2. The accumulated rainfalls are quite different between QPESUMS estimated and TANFB measured at national freeway slope. The QPESUMS data is evaluated by 4 Doppler weather radars using the reflectivity. The local precipitations are estimated from planes to points, it cannot have the same trends in accordance with the insitu rainfall. TANFB needs to build up its own rainfall monitoring system.

Table 1 QPESUMS data compared with TANFB rainfall station accumulated in mm on Aug. 8, 2015

No. 1	RA0103XS-231642DR1200200-01				
Duration.	1 hr.	3 hrs.	6hr.	12 hr.	24 hr.
QPESUMS	0.1	1.9	19.1	109.2	168
TANFB	0	0.5	19	65.5	108

Table 2 QPESUMS data compared with TANFB rainfall station accumulated in mm on Aug. 8, 2015

No. 2	RA0106XT-017685B00000000-01				
Duration	1 hr.	3 hrs.	6hr.	12 hr.	24 hr.
QPESUMS	0.1	0.1	7.9	34.9	83.3
TANFB	0	0	18.5	68.5	94

3.2 Rainfall Stations Used for Monitoring

TANFB has installed 20 rainfall stations along national freeway shown in Figure 1. The locations for rainfall station installations are based on inspection data, monitoring data, ground anchor detection results and slope stability analysis results. The tipping bucket rain gauge with resolution more than 0.5 mm is used to measure rainfall.

The precipitation stations set up by CWB were also considered for freeway slope safety monitoring. There are 499 CWB precipitation stations located I km near national freeway. After overlay mapping, judgement by contour line and excluding the stations not on the same side of slopes, there are only 9 precipitation stations can be used for slope monitoring as shown in Figure 1.

3.3 Suggested Installation Plan for CWB

CWB also wants to install precipitation stations at national freeway slopes for weather forecasting. Excluding 29 rainfall stations used for freeway slope monitoring, we surveyed the other excavation slopes which are dip slope with sliding plane exposed, sliding

risk scale above medium or one of landslide causative geological factors above medium. It is suggested that the locations of precipitation stations are shown in Figure 2. There are 61 rainfall stations for slope height greater than 15 m or 50 rainfall stations for slope height greater than 20 m.

Figure 1 Twenty-nine rainfall stations along national freeway

(a) Slope height h >15m

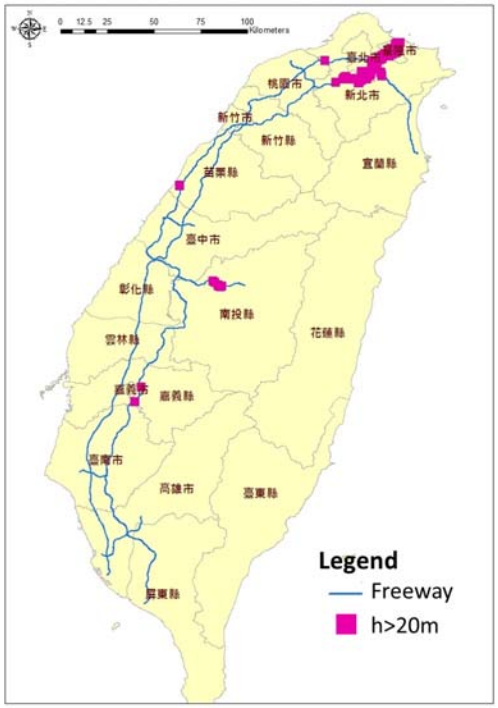

(b) Slope height h >20m

Figure 2 Suggested precipitation stations for CWB (a) Slope height h >15m and (b) Slope height h >20m

4 Strategies of Early Warning

The strategies of early warning of national freeway slopes were considered into two stages. The first stage is before the relationships between rainfalls and ground water levels have been built up; the second stage is after their relationships have been built up.

4.1 The First Stage

National Science and Technology Center for Disaster Reduction (NCDR) has integrated the information of CWB, SWCB, DGH, CGS (Central Geological Survey) etc., to establish the landslide accumulated rainfall thresholds for the local regions. TANFB can use their data for early warning. For example, the 24 hour landslide accumulated rainfall threshold of the Wenshan District of Taipei City provided by NCDR is 500 mm [3] as shown in Figure 3. It can be used as referred early warning value for the maintenance client and company of freeway slope in this area. It should take particular notice for the slope safe condition, if precipitation over 500 mm. On the other hand, if the landslides happen below 500 mm, it needs to adjust the threshold value of early warning.

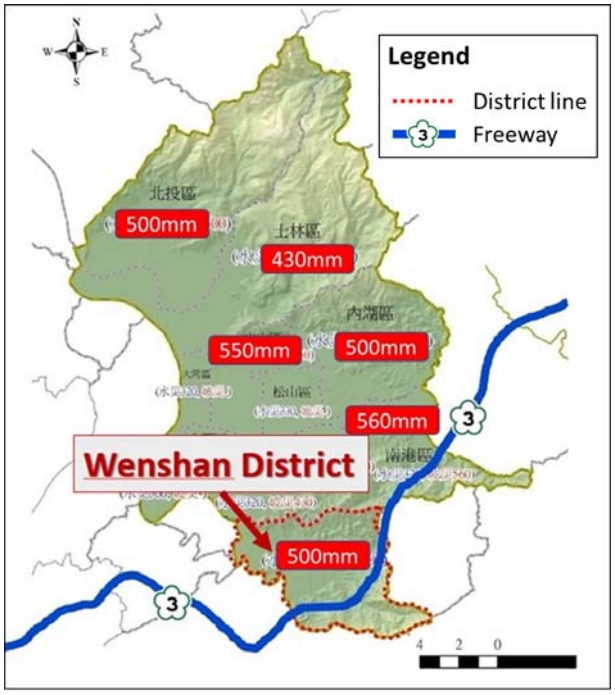

Figure 3 Twenty-four hour landslide accumulated rainfall threshold in Taipei City

4.2 The Second Stage

After all the precipitation stations at the national freeway slopes are set up by CRB, and 29 installed rainfall stations included, and the relationships between rainfalls and ground water levels are established, it comes to the second stage of early warning. The freeway slope stability can be predicted and early waring can be made by real time precipitation monitoring.

5 Conclusions

TANFB has established the freeway slopes of the maintenance management system and its practice manual. The major advantage using rainfall monitoring is for the early warning of landslide disaster. After comparing the QPESUMS data with insitu rainfall monitoring and evaluating the locations of rainfall stations installed by TANFB and CWB, it is concluded as follows:

(1) The accumulated rainfalls are quite different between QPESUMS estimated and TANFB measured at national freeway slope on the day Soudelor typhoon hitting Taiwan. TANFB needs to build up its own rainfall monitoring system for early warning.

(2) After assessing several hundred locations of the precipitation stations set up by CWB, there are 9 of them can be used for slope rainfall monitoring. The corporation between TANFB and CWB for installations of precipitation stations are taken into consideration.

(3) Two stages of early warning are proposed. The landslide accumulated rainfall thresholds established by NCDR is used as early warning value in the first stage. It can be used as referred early warning value for the maintenance client and company of freeway slope before the relationships between rainfalls and ground water levels are established.

(4) After the complete precipitation stations are set up and the relationships between rainfalls and ground water levels are established, the early waring can be made by real time rainfall monitoring in the second stage.

References

[1] Taiwan Area National Freeway Bureau, MOTC，*Maintenance Manual of Freeway*, Chapter 3, 2017.

[2] Central Weather Bureau, MOTC, On-line: http://210.242.179.103/taiwan-html/freeway

[3] National Science and Technology Center for Disaster Reduction, MOST, On-line: http://eocdss.ncdr.nat.gov.tw/ncdrwebv2/.

Evolution and Stability Analysis of a Deep-Seated Landslide in Lantai Area, Taiwan

M.L. Lin[a] and T.W. Chen[a] K.C. Hsia[a]

[a] Department of Civil Engineering, National Taiwan University, Taipei, Taiwan

E-mail: linml@ntu.edu.tw, acura0308@gmail.com, kennys11006@gmail.com

Abstract –

With the fragile geology and more than 2,000 mm annual accumulated rainfall, Taiwan suffered the unstable slope and landslide hazard from time to time. The Lantai study area is on the Yilan Special Route No.1 in the Taipinshan National Forest Recreation Area in Taiwan. The Yilan Special Route No.1 is the only road to the Taipin Mountain Forest Recreation Area. Based on identification using aerial photos and satellite images, the Lantai deep-seated landslide occurred before 1982. Analysis was conducted using remote-sensing images to identify the scars and evolution of the landslide. Luodong Forest District Office and Ministry of Science and Technology installed 2 borehole inclinometers to monitor the landslide. Two additional boreholes were drilled to investigate the stratum with rock cores and ultrasonic mapping at the Lantai deep-seated landslide. The rock core of shear zone was used for the laboratory test and material properties thus determined were used for stability analysis. Field investigation was conducted to verify the landslide evidence. Particle image velocimetry (PIV) analysis was conducted on time series remote sensing images to identify the evolution and sliding direction of deep-seated landslide. Based on the above analysis results, the stability analysis was conducted to locate the possible sliding surface and position of Lantai deep-seated landslide. The possible sliding surface consisted with the main scar of Lantai deep-seated landslide well and the identified possible sliding depth was consistent with LTW01 borehole shear zone. It appeared that the research method established in this research provides identification of the scars, evolution of landslide, possible sliding position and depth of the Lantai deep-seated landslide well.

Keywords –

Deep-seated landslide; Remote sensing; Stability Analysis; PIV Analysis

1 Introduction

Taipingshan National Forest Recreation Area in Taiwan is an important national park and has many precious forests like Taiwan Cypress and Taiwan Beech. The Yilan Special Route No.1 was the only access road to the Taipingshan National Forest Recreation Area. The Yilan Special Route No.1 have been damaged by heavy rainfall events such as typhoon Haitang, typhoon Kalmaegi, typhoon Fung-Wong, typhoon Sinlaku, typhoon Jangmi and typhoon Soudelor.(Huang(2011)[1], Central Geological Survey(2011)[2], Luodong Forest District Office[3]). The Lantai deep-seated landslide is one of the active landslide areas in the Yilan Special Route No.1 with several records of mass movement of the slope. This research used remote sensing images to identify the scar development and evolution of the Lantai deep-seated landslide. Field investigation was conducted to locate the detail sliding evidence in order to determine the possible range of the landslide. The Luodong Forest District Office(2014)[3] and Ministry of Science and Technology(2015)[4] had deployed 4 boreholes for investigating the potential shear zone location of the landslide and to determine the material property of the shear zone for stability analysis. Ultrasonic mapping of one borehole was conducted to identify distribution and attitude of the shear zone. Accordingly, the stability analysis of the deep-seated landslide was conducted to understand the possible condition of the landslide..

2 Study Area

The Lantai area is in the Taipingshan National Forest Recreation Area in north Taiwan as shown in Figure 1. The Taipingshan National Forest Recreation Area is in Datong Administrative District, Yilan County, in the north east Taiwan under the jurisdiction of the Luodong Forest District Office. The red line in Figure 1 marks the study area with the Yilan Special Route No.1 shown in the figure. The river near the study area is the

Tianguer River which is the affluent of Lanyang River. The length of the Tianguer River is about 15 km, and area of the river basin is 34 km^2. The abundant rainfall in Taipingshan National Forest Recreation Area often causes landslides and erosion and damages the Yilan Special Route No.1. The blue dotted line in Figure 1 is the main exposed scar of the Lantai deep-seated landslide. The lower slope is near Tianguer River and the rainfall induces gully erosion developed toward the upper slope. Another area with significant effects of landslide was the Zig-zag road in the left bottom of Figure 1.

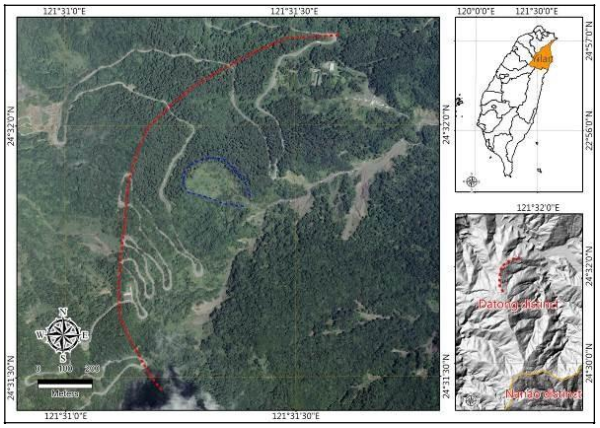

Figure 1. Lantai study area is in the Taipin Mountain Forest Recreation in north Taiwan.

The geology map of the study area is as shown in Figure 2. In Figure 2, the Lushan Formation Jentse Member and Lushan Formation Chingshuihu Member are the two major formations in the area. The Lushan Formation is Miocene Tertiary stratum of grey black weathered slate with some shale. Lushan Formation Jentse Member contains light grey to grey argillite or argillite and thin meta-sandstone interlayer. Lushan Formation Chingshuihu Member contains thick black gray shale and with well-developed cleavages. Due to the well-developed cleavages and being easily eroded of the slate, landslides or erosions often occurred in the study area when encountering heavy rainfall or earthquake.

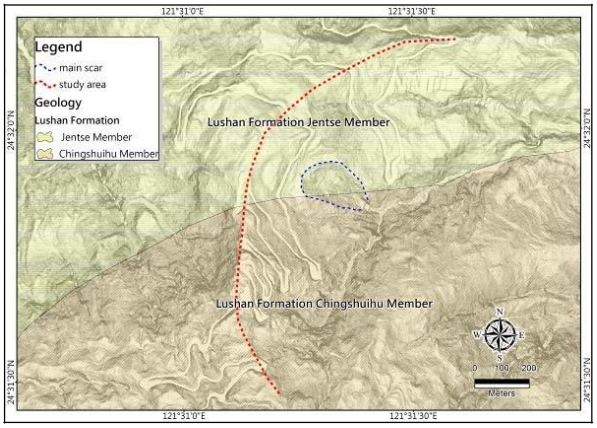

Figure 2. Geology of the Study area.

3 Remote Sensing and Field Investigation

3.1 Investigation Using Remote Sensing Images

As the remote sensing technique improved, the remote sensing images (e.g. SAR satellite ERS1/2, ENVISAT, RADARSAT-1, TerraSAR-X, COSMO-SkyMed) have been proved to be useful for analyzing landslides (Ciampalini et al., 2015) [5]. Remote sensing was use to map the high landslide potential area in the world (Hong et al., 2007) [6]. The aerial photos and SPOT satellite images were used to identify and study the evolution of the Lantai deep-seated landslide. Field investigations were conducted from 2014 to 2017 and the EGNSS technique was used to register the landslide evidence including cracks and subsidence along the Yilan Special Route No.1.

The main scar in Lantai deep-seated landslide could be identified and occurred before year 1982 by the geographic base map. The SPOT 5 satellite images from year 2004 to 2011 of Lantai deep-seated landslide area are shown in Figure 3 with the red dotted line marking main scar. Another linear structure could be identified above the main scar from year 2004 to 2005. The main scar progressed backward and enlarged from year 2005 to 2006. In year 2007, the remediation facilities were installed in the main scar area to prevent erosion. From year 2008 to 2011, the main scar of Lantai deep-seated landslide enlarged a little and some barren land was covered with vegetation.

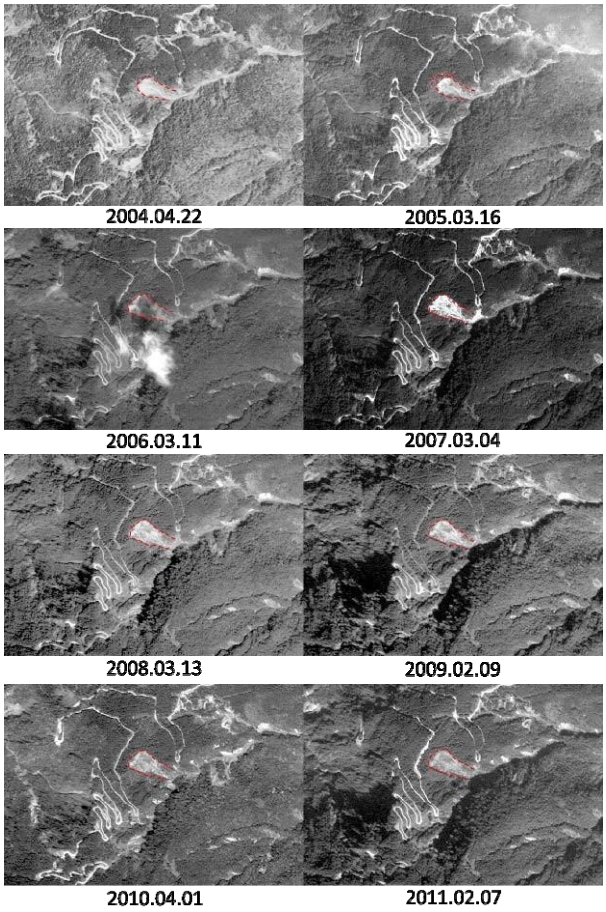

Figure 3. Spot 5 satellite images from year 2004 ~ 2011 of the Lantai deep-seated landslide study area.

3.2 Field Investigation

For understanding the Lantai deep-seated landslide stratum and the shear zone distribution, Luodong Forest District Office (2014) [3] installed two inclinometer boreholes, namely B5 and B7, to monitor the slope displacement. Ministry of Science and Technology (2015) [4] also drilled 2 boreholes, namely LTW01 and LTW02, were shown in Figure 4. In Figure 4 the boreholes were located near the crown of the Lantai deep-seated landslide. Ultrasonic borehole scanning was conducted in LTW01 to map the attitudes of shear zone and discontinuity from inside of the borehole. The rock cores obtained from the boreholes were mapped and the shear zone distribution was identified. Laboratory tests were conducted on specimens of the shear zone to determine the material property.

Figure 4. Locations of the investigation boreholes and inclinometers.

The field investigation was conducted from year 2014 to 2017 to locate the ground evidence of slope displacements and main scar in Lantai area as shown in Figure 5 and Figure 6. The color points in the Figure 5 were cracks recorded on the Yilan Special Route No.1 near the main scar in different years. The subsidence of the crack in some area was about 3 cm and the pavement was repaved every year. The same phenomena could be seen in Figure 6. In Figure 6 it was found that the investigation points distributed along the road and the length of road cracks was about 30 m to 70 m. Observations of the aerial photos and satellite images also confirm the pavement being repaved in different locations. Observing both Figures 5 and 6, the cracks appeared to form linear structures suggesting possible locations of scars in the crown area and the Zig-zag road area and being very active.

Logging of borehole cores was performed and the shear zones and fractures were identified of borehole LTW01 and LTW02 as shown in Figure 7. The shear zones in LTW01 located at about 20 m ~ 26 m, 30 m ~ 44 m and 55 m ~ 65 m below ground surface. The shear zones in LTW02 located at about 23 m ~ 33 m, 42 m ~ 45 m, 57 m ~ 59 m, 64 m ~68 m, 71 m ~77 m and 81 m ~ 94 m below ground surface.

The multi-stage tri-axial compression test and direct shear test were conducted on specimens obtained from the shear zone cores to determine the material properties parameters. The resulting effective stress cohesion and friction angle were 29.9 kPa and 31.1∘, respectively, and the residual friction angle was 23.8° .

The ultrasonic borehole scanning was executed immediately after completion of LTW01 borehole. The travel time and the reflection amplitude signals of the ultrasonic wave were captured, and the frequency of 6 Hz and 1 mm resolution of the borehole data were applied. The shear zone attitude thus determined was N152° / 26° , and the attitude of the bedding plane was

N 128° / 58° .

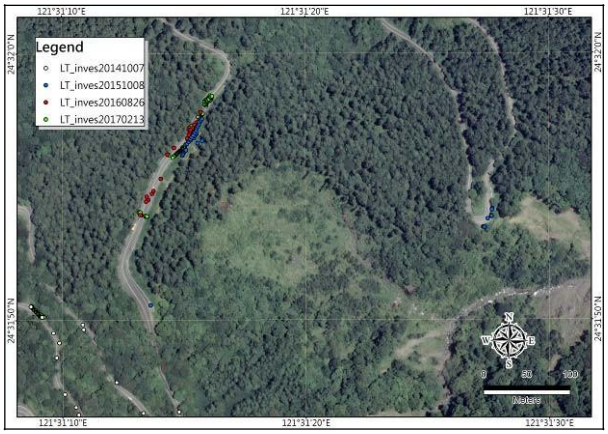

Figure 5. Field investigation points near the crown of the Lantai deep-seated landslide.

Figure 6. Field investigation points in the Zig-zag road area.

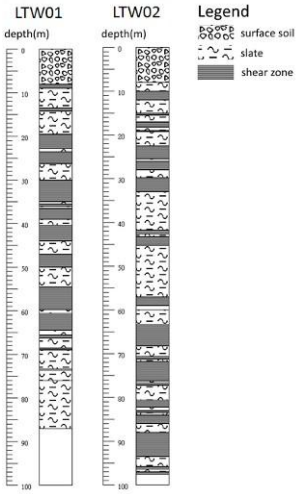

Figure 7. Logging and identification results of LTW01 and LTW02 boreholes.

4 Evolution of Lantai Deep-seated Landslide

The moving direction and the migration of the Lantai deep-seated landslide could be used particle Image Velocimetry (PIV) method to analyze. PIV is a non-touchable based on the 2D image flow field measurement technique, and could non-disturb and accurate measure the 2D flow velocity distribution. The equipment of the PIV is using high speed camera to record the continue images then analyzed two continue images to find displacement of same point change and time difference to calculate the whole velocity field distribution. (Raffel et al.， 2007) [7]

Tseng (2006) [8] used PIV method with the aerial photos successfully analyzed the sliding direction of the Hungtsaiping landslide. Hsieh (2007) [9] used PIV method to classify the sliding direction of Hungtsaiping landslide and found that PIV method help to find the sliding displacement well. Wang and Lin (2011) [10] success used PIV method to trace the displacement of slope model, also could find the initial crack position and moving velocity and direction. The PIV analysis method could use on the remote sensing images well and find the possible sliding direction and range, and these results could provide stability analysis.

The Yilan Special Route No.1 near the main scar area of the Lantai deep-seated landslide was damaged by many typhoons in past, thus the area was the important study area to research. For understanding the landslide migration of the main scar of the Lantai deep-seated landslide, we executed PIV method to analyze. The typhoon Soudelor in Lantai study area brought more than 1,000 mm accumulated rainfall, and the SPOT satellite images before and after typhoon Soudelor could identify some erosion gully in the main scar of the Lantai deep-seated landslide. The Figure 8 and Figure 9 were the results of PIV analysis. The Figure 8 was the PIV analysis results shown in vector map, it could be seen the larger displacement was in the erosion gully and the landslide position. The Figure 9 was the PIV analysis results shown in contour map, which could clearly find the larger displacement change in the erosion gully, landslide area and the riverbank landslide area. Some no landslide area was identified had large displacement, by rechecking the satellite images we found the error identification area was the cloud cover, so when executed the PIV analysis must be carefully executed.

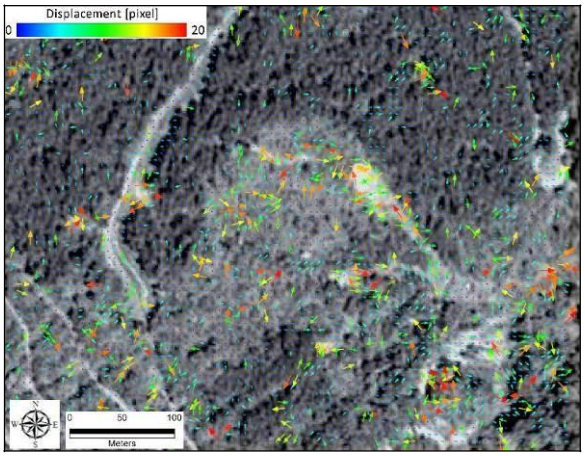

Figure 8. PIV analysis results in vector map at main scar in Lantai deep-seated landslide area (2015.07.14 ~ 2016.06.16).

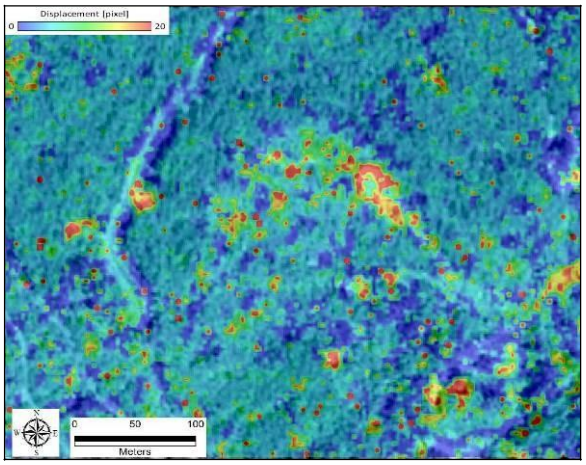

Figure 9. PIV analysis results in contour map at main scar in Lantai deep-seated landslide area (2015.07.14 ~ 2016.06.16).

The Zig-zag road area also use the satellite images before and after typhoon Soudelor to execute the PIV analysis to find the landslide displacement change. The Figure 10 and Figure 11 was the results of PIV analysis in Zig-zag road area. The Figure 10 was the PIV analysis results shown in vector map, it could be seen the larger displacement in the riverbank landslide in the lower right of Figure 10 and some displacement in the Zig-zag road area. The Figure 11 was the displacement result shown as contour map that could clearly see that the larger displacement position in the riverbank landslide and some displacement change spread in the Zig-zag road area.

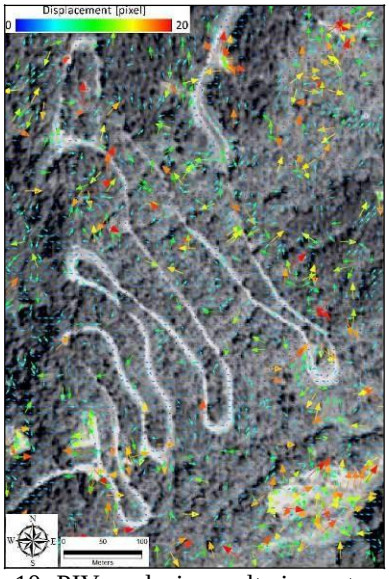

Figure 10. PIV analysis results in vector map at Zig-zag road area in Lantai deep-seated landslide area (2015.07.14 ~ 2016.06.16)

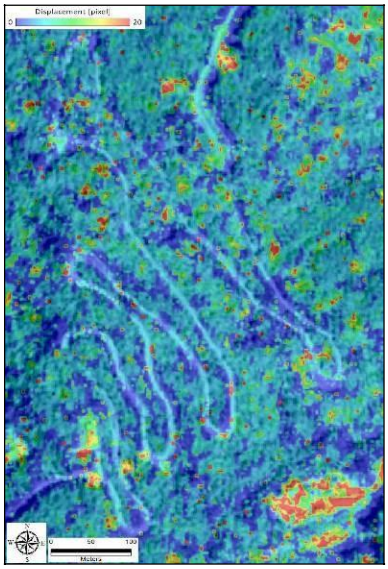

Figure 11. PIV analysis results in contour map at Zig-zag road area in Lantai deep-seated landslide area (2015.07.14 ~ 2016.06.16).

For understanding the long term migration of Lantai deep-seated landslide in main scar, this research use multi group aerial photos with high resolution and satellite images to execute PIV analysis to understand the landslide moving condition. Figure 12 was the PIV analysis result of main scar in Lantai deep-seated landslide which used aerial photo from 2009.06.07 to 2015.06.30. From the Figure 12 could see the better detail results than used the satellite images due to the

higher resolution in aerial photos. Figure 12 also could find the displacement in main scar had larger change than other area and the near the Yilan Special Route No.1 also had larger displacement which was due to the retaining wall be constructed at lower slope of the road after year 2012.

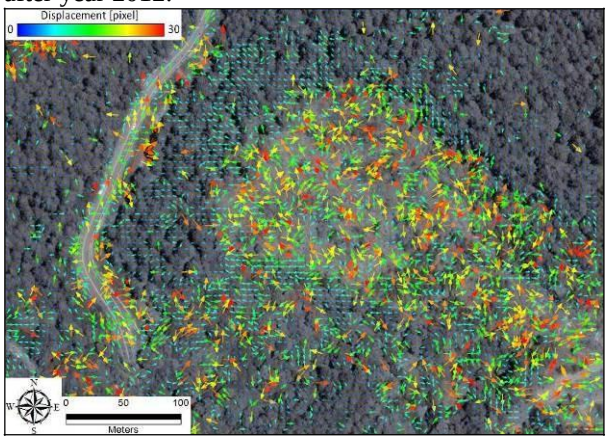

Figure 12. PIV analysis results of main scar in Lantai deep-seated landslide from aerial photos (2009.06.07 to 2015.06.30).

By doing statistic with the multi group analysis results could get the moving direction was E28.9° S, the inclinometer borehole B5 and B7 (Luodong Forest District Office, 2014) [3] also monitor the close results as B5 was E22.6° S, B7 was E20.5° S. The B5 and B7 inclinometer moving direction was a little different from the PIV analysis could be constraint by the retaining wall or the B5 and B7 boreholes located at the different landslide mass. The multi remote sensing group analysis of PIV analysis results and the field investigation results from year 2014 to 2017 were overlay together as shown in Figure 13. Form the Figure 13, the curve lines were the identification scars by PIV analysis and the main scar position almost at the same position, but the upper scars on the Lantai deep-seated landslide were different. The upper scars seemed separated into two group and the inclinometer B5 and B7 located on the different scars that could explain why the moving direction of B5 and B7 were different. The field investigation also mapped in the Figure 13, we could find that the road cracks position were the same with the upper scars well, so the right upper scars were more activity with the left upper scar on the Lantai deep-seated landslide.

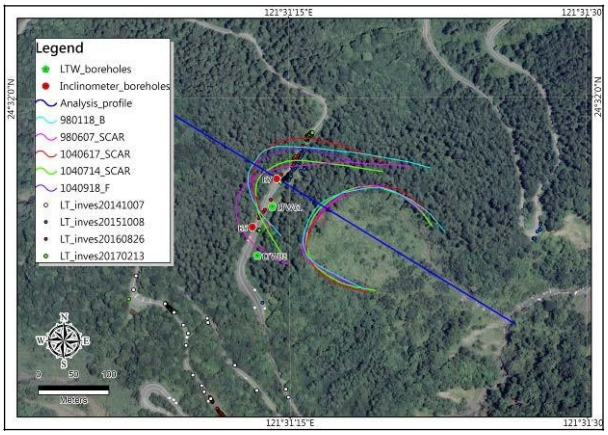

Figure 13. Scars determined from multi PIV analysis results and slope profile for stability analysis.

5 Stability Analysis of Lantai Deep-seated Landslide

For understanding the possible sliding potential and sliding surface of the Lantai deep-seated landslide, a commercially available finite difference program, FLAC, was used to conduct the stability analysis of slope. The slope profile for stability analysis was extracted from 5 m resolution Digital Elevation Model derived from the aerial photos of year 2003~2004 by the Forestry Bureau Aerial Survey Office. The possible sliding direction of Lantai deep-seated landslide was decided from the PIV analysis results. The ground water depth decided by the ultrasonic test of the LTW01 borehole was about 45 m below ground surface. The steady state ground water level was assumed and determined based on Casagrande (1937) [11]. The material property of stability analysis was determined from the laboratory test results and modified from results of back analysis.

Based on previous discussions, the main scar of Lantai deep-seated landslide area was selected for stability analysis. The location of slope profile with the sliding direction of E28.9° S was illustrated as the blue line in Figure 13. The slope profile for the stability analysis is as shown in Figure 14, in which the irregular orange line indicated the slope profile extracted from the DEM, while the blue line marked the ground water level determined using the Casagrande (1937) [11] and modified to fit the ground surface. The material shearing strength parameters used for analysis were with cohesion of 100 kPa and the friction angle of 28° .

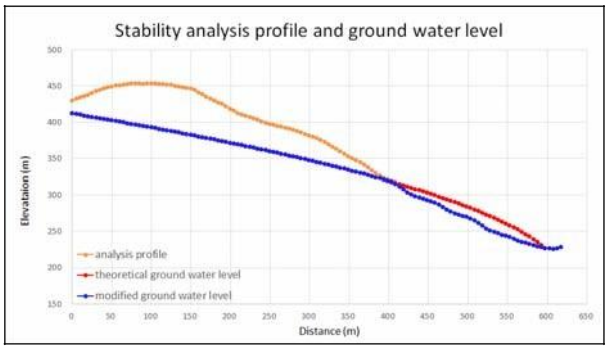

Figure 14. Slope profile and ground water level used for the stability analysis.

The result of stability analysis is as shown in Figure 15. The overall factor of safety was 0.92 and the color band indicated the shear strain distribution which was considered as the possible sliding locations. From the figure two zones with high shear strain concentration developed during the analysis with approximately circular shape. The location of the lower possible sliding zone was consistent with the main scar. The location of the upper possible sliding zone passed through the LTW01 borehole at the sliding depth of about 60 m, which also compared well to the shear zone distribution of the LTW01 borehole logging.

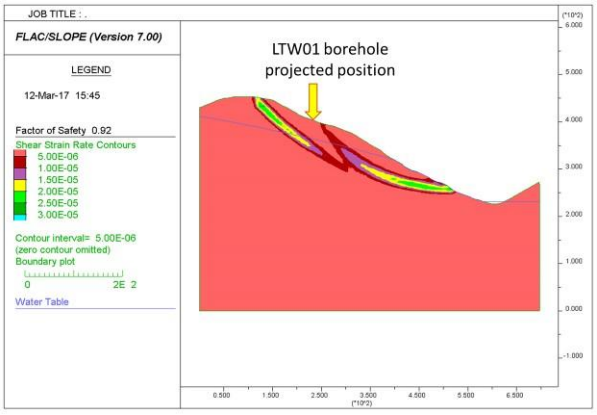

Figure 15. Stability analysis results in main scar of the Lantai deep-seated landslide.

The Figure16 was the PIV analysis and stability analysis results comparison. The red line was the possible sliding surface of the Lantai deep-seated landslide and the green X notation was the multi possible sliding at the ground surface get from the Figure 15. The lower position of the X notation fitted the bottom of the main scar well, and the middle X notation also close to the top of the main scar. But the top of the X notation was higher than the PIV analysis identification position, we speculated the Lantai deep-seated landslide could have other possible multi sliding surface to make the other sliding surface occurred.

Using stability analysis with the appropriate material parameter could find out the possible sliding position and depth in Lantai deep-seated landslide. Hoping this analysis method could apply in other deep-seated landslide case and could provide for slope disaster mitigation and reduce the damage of the deep-seated landslide.

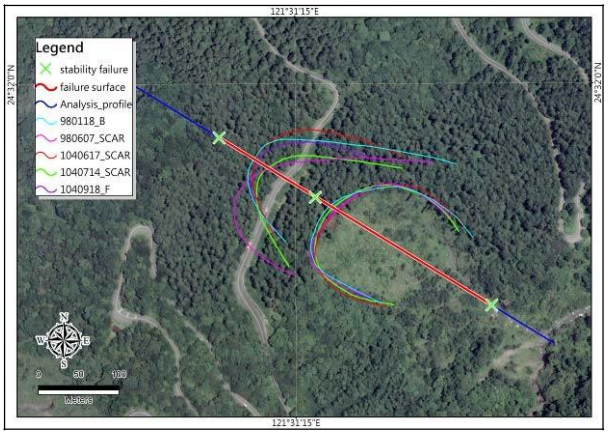

Figure 16. Stability analysis result in comparison with PIV analysis results.

6 Conclusion

This research combined many analysis study methods included remote sensing images identification, field investigation, borehole and ultrasonic investigation, particle image velocimetry method and the stability analysis. Remote sensing images identification could find the migration of the main scar at long term change condition. Field investigation could confirm the landslide evidence like subside and road cracks. Borehole investigation could find the shear zone, and the ultrasonic borehole could find the attitude of the shear zone and bedding of stratum. Shear zone rock core laboratory test could get the material property and supply for the stability analysis. PIV analysis with the time sequence remote sensing images could understand the scars migration of Lantai deep-seated landslide, and found the potential sliding area and direction. The PIV identification result showed that could had two different sliding mass in the Lantai deep-seated landslide. The stability analysis with the appropriate parameter and profile set up could find the possible sliding depth and area of Lantai deep-seated landslide. The depth of the possible sliding surface fitted the LTW01 borehole shear zone well, and the sliding area compared to main scar also favorable. This research method apply to the deep-seated landslide identification, finding possible sliding surface and sliding depth fine. Hope this research could contribute to the sliding condition of

deep-seated landslide and the landslide hazard prevention.

Using the remote sensing images collaborating particle image velocimetry method could find out the migration of the Lantai deep-seated landslide and the possible sliding direction. Combination with above analysis could build up the stability model to find out the possible sliding position of the Lantai deep-seated landslide.

Acknowledgement

This research was supported by the Ministry of Science and Technology (MOST), Taiwan, project number: MOST104 - 2119 - M006 - 008.

References

[1] Huang C.Y. Study on the Landslide Site along Lantai Nursery, Master Thesis of Department of Civil Engineering, National Ilan University, 2011.

[2] Central Geological Survey, MOEA. Investigation and monitor of Lantai landslide, 2010 research announcement representation of Central Geological Survey, MOEA, 2010.

[3] Luodong Forest District Office. 2014 monitor landslide and anchor of Yilan Special Route No.1 report. Luodong Forest District Office, Forestry Bureau, Council of Agriculture, Executive Yuan, 2014.

[4] Lin C.W., Lin M.L., Chen R.F., Chen C.C., Hsu Y.J., Kuo C.Y., Chen H.Y., Wang K.L. and Huang A.B. Establishment of a comprehensive monitoring system and study of monitoring data and sliding mechanisms: An example of Tai-Ping Shan Lan Tai area. Final report of Ministry of Science and Technology, 2015. (project number: MOST104 - 2119 - M006 - 008.)

[5] Ciampalini, A., Raspini, F., Bianchini, S., Frodella, W., Bardi, F., Lagomarsino, D. and Casagli, N. Remote sensing as tool for development of landslide databases: The case of the Messina Province (Italy) geodatabase. *Geomorphology*, 249, 103-118, 2015.

[6] Hong, Y., Adler, R., and Huffman, G. Use of satellite remote sensing data in the mapping of global landslide susceptibility. *Natural Hazards*, 43(2), 245-256, 2007.

[7] Raffel, M.; Willert, C.E.; Wereley, S.T.; Kompenhans, J. Particle image velocimetry - *a practical guide*, 2007.

[8] Tseng C.H. Non-Catastrophic Landslides Induced by the Mw 7.6 Chi-Chi Earthquake in Central Taiwan Revealed by the PIV Analysis. Master Thesis of Department of Geosciences, National Taiwan University, 2006.

[9] Hsieh C.P. Monitoring landslide by Image Multitemporal Analysis Geodesy : application of Huangtsaiping landslide. Master Thesis of Department of Earth Sciences, National Cheng Kung University, 2007.

[10] Wang, K.L. and Lin, M.L. Initiation and displacement of landslide induced by earthquake - a study of shaking table model slope test. *Engineering Geology*, Vol. 122, Issue. 1-2, pp. 106-114, 2011.

[11] Casagrande, A. Seepage through dams. *New England Water Works Association*. Vol. LI., No. 2, pp. 131-172, 1937.

Determination of Drying and Wetting Soil Water Characteristic Curves by Flow Pump Technique

Y.-W. Chen[a], M.-C. Chu[a] and L. Ge[a]

[a]Department of Civil Engineering, National Taiwan University, Taiwan
E-mail: r04521113@ntu.edu.tw, d05521005@ntu.edu.tw, louisge@ntu.edu.tw

Abstract

Soil water characteristics curve (SWCC) is an essential constitutive relationship for solving geotechnical engineering problems involving unsaturated soils, such as slope stability, retaining walls and collapse of surface soil due to rainfall infiltration. Over the past few decades, many standard tests have been developed to evaluate and obtain the SWCC. Among them, the pressure plate method has been widely used due. However, it is difficult in determining whether the specimen reaches a steady state because the only evaluated method is observing its drainage condition. It causes the experimental duration too longer, approximately one to three months to obtain a SWCC.

In this paper, a flow pump was incorporated into a triaxial system for SWCC measurement. The developed also utilizes 3D printing technology, axis translation technique and modified suction drop method to establish an experimental system. Fine quartz sand was to demonstrate the effectiveness of the testing apparatus. Results show that this experimental system is able to obtain the drying and wetting SWCC efficiently, costing less experimental time.

Keywords –

Flow pump; SWCC; Axis translation

1 Introduction

Many geotechnical problems, such as slope stability, retaining walls and collapse of surface soil due to rainfall infiltration, etc., occur in an unsaturated condition. Therefore, understanding of unsaturated soil mechanics is required for preventing geotechnical structures being improperly designed. The soil water characteristic curve (SWCC) represents the constitutive relationship between soil suction and soil water content of unsaturated soil. Various soil materials have a corresponding and unique SWCC.

Numerous laboratory and field methods have been developed to measure and obtain the SWCC in the past years. These common methods include tensiometers, filter paper test, centrifuge test, axis translation techniques, thermal conductivity sensors, humidity-controlled techniques, thermocouple psychrometers and so on. Among them, the pressure plate method, applied axis translation technique has been widely used due to its convenience and reliability. However, the steady state of the specimen is sometimes difficult to identify because the is only determined by observing its drainage condition. It normally causes the experimental duration too long; therefore, several new SWCC measurement and prediction methods were developed gradually.

The concept of axis translation [2] is the most important technique of soil suction measurement in laboratory. Olsen [6] proposed a flow pump technique to improve the measurement of the saturated hydraulic conductivity. Few decades later, Znidarcic et al. [10] applied a similar flow pump technique in developing a new method called “Maintained Suction Measurement”. In addition, Hwang [3] proposed a new method called “Suction Drop Measurement”. Both of them are considered as appropriate and time-saving SWCC measurement methods.

2 Testing Apparatus

The flow pump method, proposed by Olsen [6], controlling the flow rate entering or leaving the specimen, enables the permeability measurements to be more rapidly by recording and observing the pore water pressure difference induced across the specimen. It minimizes numerous experimental errors by avoiding the direct flow rate measurements. In spite of the limit from the testing environment, it is still an appropriate method for soils with either low or high permeability, e.g. [8], [7], [1], [10], [4], [5].

Since applications of flow pump method are very wild, it is also used to improve the SWCC measurement technique. In the past few years, two main measurement method: “Maintained Suction Measurement” [10] and “Suction Drop Measurement” [3] are developed. Both of them combine flow pump method, conventional

triaxial system and axis translation technique to establish an entire measurement approach. Advantages of these measurement method are shorter the experimental duration, capable of obtaining continuous drying and wetting curves, and easier evaluating the condition of the specimen (steady or not) by directly measuring soil suction. The details and the results of comparison between two measurement methods are described after.

2.1 Flow Pump

The flow pump used herein is manufactured by YMC Company, model YSP-201, shown in Figure 1. The flow pump is connected to the bottom of the specimen. Its function is giving a controlled force to push or pull the syringe above it to obtain a constant flow rate into or leaving the soil specimen. Since the maximum bearable force of the flow pump is limited, the pore water pressure in the specimen is also limited during the test. Actually, the limit of pore water pressure is determined by maximum force of the flow pump and the diameter of the syringe. when the diameter of the syringe increases, the limit of pore water pressure reduces. Therefore, the 25-ml Hamilton gas-tight syringe is selected for our experimental tests after evaluation. By used this syringe, the flow pump could be operated precisely from 3E-04 to 21.24 ml/min.

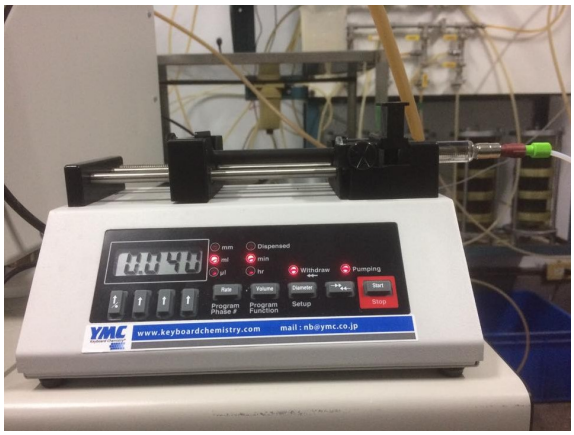

Figure 1. Flow pump

2.2 Pressure Transducer

The pressure transducer used herein is manufactured by Humboldt Mfg Company. Its function is to measure the pore water pressure, where the measured data are continuously recorded by Humboldt software system. Instead of deploying a differential pressure transducer, two pressure transducers are used for measuring pore water (air) pressures at the bottom and top of the specimen in this study. In addition, the resolution of pressure transducer is about 0.5-cm H_2O and the calibrated accuracy of them is 99%.

In the verified test, two pressure transducers measure the difference of pore water pressures between bottom and top of the specimen. However, in the SWCC test, transducers measure the difference between the pore air pressure at the top of the specimen controlled by the back pressure and the pore water pressure at the bottom of the specimen induced by the flow pump.

2.3 High Air Entry Ceramic Plates

The HAE ceramic plate used herein is manufactured by Soilmoisture Equipment Corporation Both of them have 66.68 mm in diameter and 7.11 mm in thickness. When the HAE ceramic plate is saturated, the surface tension in the pores of it separates the air and water pressure. Additionally, the water flow is still able to go through it. Thereby, the axis translation technique (Hilf 1956) could be applied. The effective pore size of the HAE ceramic plate controls the maximum difference between the air pressure and water pressure. The “Bar” of the HAE ceramic plate is commonly determined by this value, such as 1 Bar or 3 Bar HAE ceramic plate.

The HAE ceramic plate is only used in the SWCC test and installed between the specimen and the bottom porous stone. The approach to saturate the HAE is to soak it in the de-aired water, and then use the vacuum pump to provide -76cm Hg (absolute zero pressure) above the de-aired water. It could be found that there is a lot of air existing in the HAE ceramic plate in the beginning of the saturation procedure. After about 12 hours, no air appears from the HAE ceramic plate. In this situation, the HAE ceramic plate is actually considered as being saturated.

2.4 Specimen Mold and Preparation

In order to shorten the experimental duration in the SWCC test, new experimental molds with less height should be produced. Different from general metalworking, new experimental molds for specimen preparation were made by 3D printing. Their materials used are Polylactic Acid (PLA), the most commonly used eco-friendly plastic in the 3D printing. By this new technology, there are many advantages being provided, such as significantly shortening the production time and reducing the cost. In addition, it makes the test for researching the effect of different size of the specimen more convenient. Moreover, the SWCC measurement by the flow pump method could be more easily popularized to other academic institutions over the world.

In this study, the SketchUp Pro software was selected to draw the 3D model of the experimental mold. After that, the exported STL file was opened in the

MakerBot Print software to set up parameters and check the situation of the finished product. Finally, the 3D printing started. Settings of parameters herein are 50% infill, 0.2-layer height, 2 shells, raft and support. Finished products of the experimental mold are shown in Figure 2.

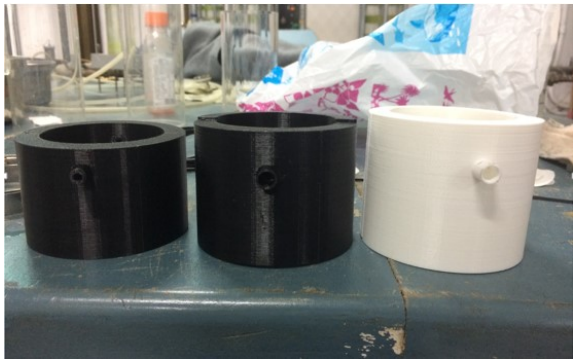

Figure 2. Experimental molds

Fine quartz sand was chosen as the SWCC test material. The specific gravity of fine quartz sand is 2.65. This soil has 15% passing the #100 sieve and be classified as "SP" according to the Unified Soil Classification System (USCS). Since there are many uncertain behaviors in the SWCC measurement and possible error sources in the experimental system, fine quartz sand was selected for relatively stable behavior.

In order to provide an approximately no air condition within the HAE ceramic plate, firstly the tube in the bottom platen was filled with de-aired water. The porous stone and the HAE ceramic plate were placed on the bottom platen, then several 1 mm thickness O-rings sealed around the HAE ceramic plate. The split mold, made by 3D printing was mounted on the bottom platen and the rubber membrane is stretched to fit the mold by applying vacuum. After that, fine quartz sand was poured into the mold through a funnel to desired height. The specimen was divided into 3 layers to be compacted. The porous stone and the top platen were placed on the specimen, and then the rubber membrane rolled over the top platen fastened with O-rings. Vacuum was applied to the top of the specimen to keep the shape of the specimen. To prevent air passing through the space between the HAE ceramic plate and rubber membrane during the SWCC test, other split mold was mounted on the bottom platen for compressing several O-rings sealed around the HAE ceramic plate, shown in Figure 3. The specimen was initially 67.4 mm in diameter, 35.4 mm in height and 50.22 cm3 in pore volume. Finally, the specimen was put in the triaxial chamber and connected to the triaxial system and the flow pump.

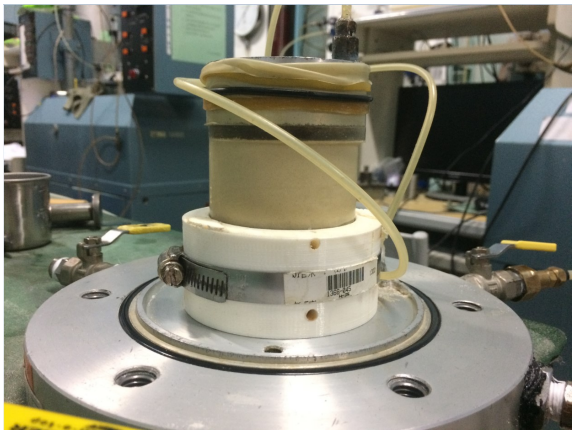

Figure 3. Specimen preparation

3 Testing Procedure

Figure 4 presents the simple schematic drawing of the SWCC test. The procedure of the SWCC test is presented as follows. Firstly, valves (G and H) were closed and then applied the air pressure to the top of the specimen (D). The value of this air pressure was maintained constant at 300 kPa, as the same as the back pressure during the test. Then, the valve (G) was opened and waited for few minutes to make the air pressure and the pore water pressure be balanced. Started the flow pump (A) to remove the water at the top portion of the system, such as the top platen, the top porous stone and the tube. The volume of the removed water was almost 16 cm3. After that, the degree of saturation of the specimen (D) was reached 100% and the SWCC test was started.

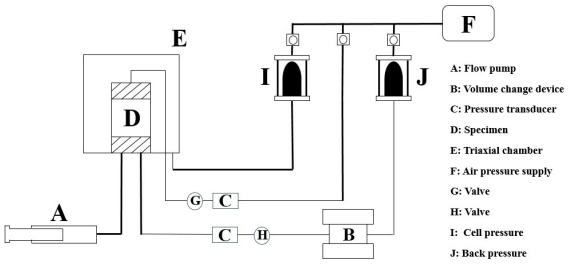

Figure 4. Schematic illustration of the SWCC testing apparatus

The desired outflow rate was applied to the bottom of the specimen (D) by the flow pump (A) and the induced suction at the bottom was measured by two pressure transducers (C). Once the degree of saturation reached the target value, the flow pump (A) was stopped. The induced suction at the bottom of the specimen (D) dropped gradually and reached a steady state after few minutes to several hours. Then, an equilibration point of

the SWCC during drying cycle was obtained and the same procedure was repeated several times to obtain many equilibration points. After obtaining the last equilibration point in drying cycle, the flow pump was changed to the infusion mode. Following the same procedure with the desired inflow rate for several times, many equilibration points in wetting cycle can be obtained.

4 Results and Discussion

Figures 5 and 6 present the suction response of the specimen 2 during the SWCC test. From the suction response of both tests, the steady state of the suction value could be easily and conveniently determined by this measurement method. Thereby, the experimental duration required to obtain an equilibration point could be significantly reduced to about few hours. Besides, the applied flow rate was conservative in tests, which means this measurement test still have many potential to be improved.

although some results in wetting cycle are unacceptable, the wetting SWCC could still be tried to be drawn by using equilibration points (17%~60%) and assuming the saturated degree of saturation is 80%. Therefore, drying and wetting SWCCs are obtained (test 2).

In drying cycle of the test 2, the instability of the suction make the steady state was difficult to be reached. Since this situation is caused by the small cyclic pressure variation, the most possible reason is considered as voltage instability. In wetting cycle of the test 2, at first the suction value is becoming lower with larger degree of saturation and the suction value at the equilibration point is lower than in the drying cycle, shown in Figure 5. These performances are conformed the common behavior of the wetting SWCC and the effect of the hysteresis is also observed. However, the suction value began gradually becoming larger in the later step, shown in Figure 6

From the suction response of both tests, shown in Figure 7, the steady state of the suction value could be easily and conveniently determined by this measurement method. The fitted equations shown in Figure 7 were given in [9]. Thereby, the experimental duration required to obtain an equilibration point could be significantly reduced to about few hours. In addition, the applied flow rate was conservative in tests, which means this measurement test still have many potential to be improved.

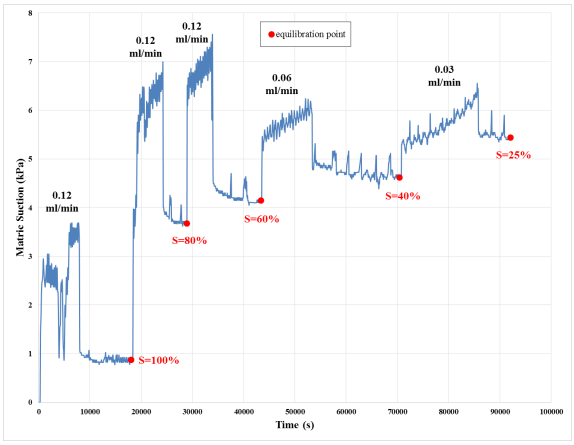

Figure 5. Suction response and equilibrium points (wetting path)

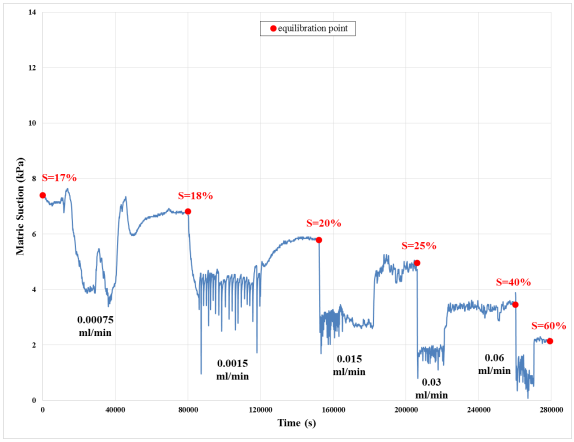

Figure 6. Suction response and equilibrium points (drying path)

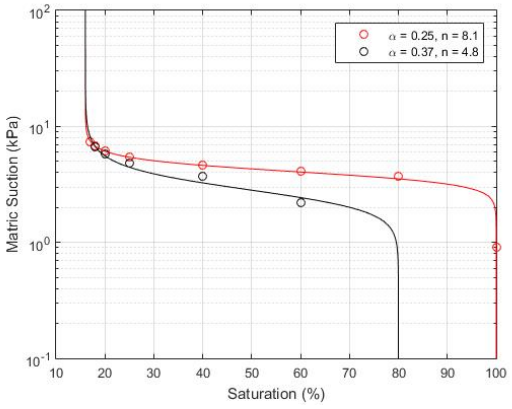

Figure 7. Drying and wetting paths of SWCC

5 Conclusions

The soil-water characteristic curve (SWCC) represents an essential constitutive relationship and plays an important role in unsaturated soil mechanics. To characterize the SWCC, a reliable and convenient experimental measurement method is required. Moreover, shortening the experimental duration of it is also the goal of many researches. In this study, our flow pump is firstly be verified appropriate for the geotechnical laboratory test. Then, a new SWCC measurement system and procedure is established by combing the conventional triaxial system, the flow pump system, the 3D printing technology, the axis translation technique and the modified suction drop measurement method. The drying SWCC of Quartz fine sand is obtained in about 3 days ~ 1 week.

References

[1] Aiban, S. A. and Znidarcic, D. Evaluation of the Flow Pump and Constant Head Techniques for Permeability Measurements. *Géotechnique*, 39(4), 655-666, 1989.

[2] Hilf, J. W. *An investigation of pore-water pressure in compacted cohesive soils*. Ph.D. dissertation, Technical Memo (654), U.S. Department of Interior, Bureau of Reclaation, Design and Construction Devision, Denver, Colorado, 1956.

[3] Hwang, C. *Determination of Material Functions for Unsaturated Flow*. Ph.D. thesis, University of Colorado at Boulder, 2002.

[4] Lee, J. and Znidarcic, D. Flow Pump System for Unsaturated Soils: Measurement of Suction Response and the Soil-Water Retention Curve. *Geotechnical Testing Journal*. 36(5), 2013.

[5] Menezes, L. P. et al.. Determination of the Soil Water Retention Curve Using the Flow Pump. R. Esc. Minas, Ouro Preto, 68(2), 207-213, 2015.

[6] Olsen, H.W. Darcy's Law in Saturated Kaolinite. *Water Resources Research*, 2(6), 287-295, 1966.

[7] Olsen, H.W., Morin, R.H. and Nichols, R.W. Flow Pump Applications in Triaxial Testing. In *Advanced Triaxial Testing of Soil and Rock, ASTM STP 977*, Robert T. Donaghe, Ronald C. Chaney, and Marshall L. Silver, Eds., American Society for Testing and Materials, Philadelphia, 68-81, 1988.

[8] Pane, V., Croce, P., Znidarcic, D., Ko, H.-Y., Olsen, H.W. and Schiffman, R.L. Effects of Consolidation on Permeability Measurements for Soft Clays. *Géotechnique*, 33(1), 67-72, 1983.

[9] Van Genuchten, M.T. A closed-form equation for predicting the hydraulic conductivity of unsaturated soils. *Journal of Soil Science Society of America*, 44, 892-897, 1980.

[10] Znisarcic, D., Illangasekare, T., and Manna, M. Laboratory Testing and Parameter Estimation for Two-Phase Flow Problems. In *Proc. Of the Geotechnical Engineering Congress*, Mclean et al (ed.), Boulder, Colorado, ASCE, New York, 1991.